



CONFERENCE PROCEEDINGS 2024

11th June - 13th June 2024, Nuremberg, Germany

est
The European Society
of Telemetry

airbus.com



PIONEERING SUSTAINABLE AEROSPACE FOR A SAFE AND UNITED WORLD

Through an unwavering commitment to decarbonisation, Airbus is pioneering sustainable aerospace for a safe and united world. Discover more about how our technological developments are shaping a brighter future for generations to come.

AIRBUS

Proceedings

European Test and Telemetry Conference – ETTC 2024

These proceedings cover the manuscripts of the lectures of the ETTC 2024 Conference.

The authors are responsible for form and content of the papers.

AMA Service GmbH accepts no responsibility for the correctness and completeness of the details and the consideration of private rights of third parties.

Herausgeber / Publisher:

AMA Service GmbH
Von-Münchhausen-Str. 49
31515 Wunstorf / Germany
Tel. +49 5033 9639-0
info@ama-service.com
www.ama-service.com / www.sensor-test.com
www.ama-science.org



ISBN 978-3-910600-02-7

© AMA Service GmbH, 2024

Dear Testing Community,

the European Test and Telemetry Conference ETTC has been a pillar of the telemetry and testing community for more than 30 years, bringing together experts from the fields of test, instrumentation, telemetry and data processing from all over the world.

Unique platform for innovation and exchange

The ETTC is characterized by its unique combination of exhibition and conference, which provides both space for the presentation of innovative products and solutions and for intensive exchange between experts. Accompanied by the traditional Bavarian evening, the conference offers a comprehensive program that provides both technical input and networking opportunities.



Common challenges and opportunities

Even sometimes in competitive environments, the testing community is united by the common challenge of actively shaping the future of the industry. Topics such as testing icing conditions or less-intrusive measurements require joint efforts of the testing community to address the needs to the industry for the specific testing tasks.

Sustainability in focus of the transport industry

Sustainability is the overarching theme in the transport industry. New technologies and concepts are being developed. Testing must adapt to these new requirements.

Machine learning revolutionizes the testing industry

Testing can immensely benefit from machine learning, as vast amounts of data from testing programs are available. However, like any training-based method, the results depend on the training data. We must ensure data quality and clarity for machine learning models.

Joint commitment to frequency use

With the utilization of radio frequencies for telemetry applications, the ETTC reports on the status of the current and future plans of the World Radio Conference WRC for the allocation of usable frequency bands.

As the RF spectrum becomes increasingly crowded, the availability of protected frequency bands for telemetry is becoming increasingly critical. Share your expertise, participate in relevant working groups, and lend your voice to ensure that the needs of our community are considered in spectrum allocation decisions.

Standardization as the key to safety and efficiency

Open and applicable standards play a central role in increasing safety and standardization in the testing industry.

They promote the acceptance of new technologies and ensure objective verifiability. The advantages of a standardized approach should be a motivation for all testers to actively apply these standards and to participate to the evolution of the standards.

ETTC: Focus on technology and methods

Our mission is to foster a platform where specialists from the fields of technology and engineering can converge, share innovative ideas, and explore the latest advancements in testing methodologies. At the ETTC, the spotlight shines on the practical applications of innovative technologies. We encourage participants to showcase their experiences and insights, not just to promote their products or services. This exchange of real-world examples serves as a valuable resource for the entire community, identifying areas where solutions are needed and sparking collaboration to address industry challenges.

By bringing together experts from diverse backgrounds and fostering an environment of open dialogue, we collectively push the boundaries of what is possible and shape the future of testing.

In conclusion, I would like to thank everyone who has contributed to the success of the ETTC 2024:

The sponsors: Your financial support allows us to offer the conference at an affordable price and to put together a high-quality agenda.

The exhibitors: You present the latest products and solutions from the industry and enable participants to learn about the latest state of the art.

The members of the program committee: You have carefully reviewed the submitted conference papers and built the foundation for the high-quality conference program.

The session chairs: You ensure the smooth running of the conference and moderate the discussions competently and objectively.

The keynote speakers: You have given new inputs with your inspiring presentations and taken the participants into the exciting world of testing technology.

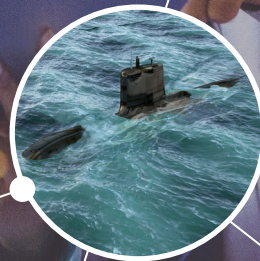
The participants: You are the heart of the ETTC and contribute to the success of the event with your commitment and eagerness to learn.

The ETTC 2024 would not have been possible without the support and commitment of all of you!

ELECTRONICS & DEFENSE

OBSERVE, DECIDE, GUIDE

INTELLIGENCE ONBOARD



SAFRAN ELECTRONICS & DEFENSE, INTELLIGENCE ONBOARD

Day after day, you face critical challenges. The products and services developed by Safran Electronics & Defense, whether civil or military, deliver the technological superiority, effectiveness, reliability and competitiveness you expect. We're with you every step of the way, building in the intelligence that gives you a critical advantage in observation, decision-making and guidance. You can count on Safran Electronics & Defense, your strategic partner on land, at sea, in the air and in space.

safran-electronics-defense.com

🐦 : @SafranElecDef



A1 Sensor Session I

Chair: Jack Vinella, The Boeing Company

- A1.1 The use of LIDAR to measure the flexion and torsion of a wing** 10
I. López Herreros, F. Arevalo Lozano, J. Barrera Rodríguez, A. Egido Fernández, Airbus Defence and Space, Getafe-Madrid (Spain), M. Chimeno, P. García-Fogeda Núñez, Universidad Politécnica de madrid, Madrid (Spain)
- A1.4 H175 Deicing Flight Test Campaign Focus on Flight Test Instrumentation** 18
F. Monteil, Airbus Helicopters SAS, Marignane (France)

A2 ML & AI Session I

Chair: Pedro Rubio Alvarez, Airbus Defence and Space, Getafe (Spain)

- A2.1 Decentralized Reinforcement Learning for Adaptive Transmission Parameter Optimization of a LoRa Transceiver** 22
J. Gissing, Technische Universität Berlin, Berlin (Germany), C. Brockmann, Fraunhofer Institute for Reliability and Microintegration (IZM), Berlin (Germany)
- A2.2 Towards Edge AI in Flight Test Data Acquisition: A Proof of Concept for Anomaly Detection in Aircraft Electrical Networks** 32
R. Pelluault, G. Guerrero, S. Sivakumaran, Safran Data Systems, Les Ulis (France)
- A2.3 Link Resource Scheduling Technology of Networked Telemetry System for LEO Constellations** 40
J. Hao, J. Zhang, Y. Wang, Beijing Institute of Astronautical Systems Engineering, Beijing (China)

A3 Time - Space - Positioning

Chair: Heiko Körtzel, Airbus Defence and Space GmbH, Manching (Germany)

- A3.1 High-Accuracy Time Space Position Information (TSPI) - Field Test Results** 47
B. Kupferschmidt, R. Docimo, Curtiss-Wright, Newtown (USA)
- A3.2 Detection and Monitoring of Jamming and Spoofing of GPS/GNSS Signals in Harbours and Industrial Areas** 54
K. von Hünerbein, Lange-Electronic GmbH, Gernlinden (Germany)

A4 International Consortium for Telemetry Spectrum

Chair: Murat Imay, Deutsche Aircraft GmbH, Wessling (Germany)

- A4.1 Telemetry Spectrum Reallocation Risk Update: An Update on Threats to Telemetry Spectrum** 61
T. Chalfant, GMRE Inc.,

A5 Sensor Session II

Chair: Mario Linde, Airbus

- A5.1 IN FLIGHT OPTICAL FIBER MEASUREMENT ON FLIGHT TEST AIRCRAFT** 68
L. Mennebeuf, B. Mouchet, D. Cumer, K. Veerabadrán, L. Malard, Airbus Operations S.A.S,
Toulouse (France)
- A5.2 Comparing FBG Strain Sensors with Electrical Strain Gauges on a Helicopter
Rotor Blade during Whirl Tower Test** 74
S. Weber, R. Rammer, F. Kurfiss, B. Köhr, Airbus Helicopters Deutschland GmbH,
Donauwörth (Germany), V. Camerini, M. Asselin, Airbus Helicopters S.A.S., Marseille Provence
International Airport (France)

A6 ML & AI Session II

Chair: Nelson Leite, Instituto de Pesquisas e Ensaios em Voo, Sao Jose dos Campos (Brasil)

- A6.1 AITA.AI applications to Testing Activities** 80
F. Coll Herrero, P. Rubio Alvarez, Airbus Defense and Space, Getafe-Madrid (Spain)
- A6.2 Multiplatform sensor fusion. Drawing a common tactical scenario** 87
M. Arévalo Nogales, Airbus Defence and Space, Getafe-Madrid (Spain)

A7 XidML

Chair: Florian Mertl, Airbus Helicopters Deutschland GmbH, Donauwörth (Germany)

- A7.1 The open XidML Standard - What are the Advantages for Users** 96
F. Mertl, Airbus Helicopters Deutschland GmbH, Donauwörth (Germany)

A8 Networks & Architectures

Chair: Murat Imay, Deutsche Aircraft GmbH, Wessling (Germany)

- A8.1 Feature Creep for Efficiency!** 100
M. Weir, Ampex Data Systems Corporation, Hayward (USA)
- A8.2 Power Over Ethernet in FTI, Suitability and Challenges** 106
P. Quinn, Curtiss-Wright, Dublin (Ireland)
- A8.3 TRMC Support for the TM Community** 110
G. Hudgins, Juana Secondine TENA Software Development Activity (SDA), Niceville (USA)
- A8.4 Design and Implementation of a New Generation of Space Ground TT&C
Software Architecture Based on Container Cloud** 118
W. Zhong, W. Feng, BeiJing Research Institute of Telemetry, BeiJing (China)

A9 Imaging & Video

Chair: David Cumer, Airbus Operations & Airbus Group, Toulouse (France)

- A9.1 AI based object recognition for telemetry applications** 125
S. Hardt, M. Faber, Safran Data Systems GmbH, Bergisch Gladbach (Germany)
- A9.2 Introduction of Smart Hi-Speed Airborne Camera with Embedded Real-Time
Tracking Algorithm for Store Separation Flight Tests** 130
R. de Paulo, N. Leite, L. Sousa, Instituto de Pesquisas e Ensaios em Voo (IPEV), São José dos
Campos (Brazil) D. Loubach, Instituto Tecnológico de Aeronáutica (ITA), São José dos Campos (Brasil)

A10 Networks & Data Acquisition

Chair: Patrick Quinn, Curtiss-Wright, Dublin (Ireland)

- A10.1 Improving Rotorcraft Flight Tests Safety and Efficiency with Real Time Wind Mapping 137**
 G. Eket, Airbus Operations SAS, Toulouse (France), S. Schmid, R. Urli, Airbus Helicopters
 Deutschland GmbH, Donauwörth (Germany), L. Rocchi, Airbus Helicopters SAS, Toulouse (France)
- A10.2 Network Management of Flight Test Installation equipment 145**
 J. A. Pablos Palomino, Airbus Defence & Space, Seville (Spain)

B1 Data Acquisition I

Chair: Jürgen Kallup, tukom GmbH, Schondorf (Germany)

- B1.1 Innovative Measurement Technology Solutions for Thermal and Mechanical Testing
 of HV Batteries 155**
 T. Eich, CSM Computer-Systeme-Messtechnik GmbH, Filderstadt (Germany)
- B1.2 FTI Thermal Modelling using Rough Order Model 160**
 D. Doyle, Curtiss-Wright, Dublin (Ireland)
- B1.4 Tornado FTI Refurbishment: Bridging Legacy and Modernity in Aerospace Engineering 166**
 J.-F. Gineste, H. Körtzel, J. Ockerse, Airbus Defence and Space GmbH, Manching (Germany)

B2 Data Acquisition I

Chair: Jürgen Kallup, tukom GmbH, Schondorf (Germany)

- B2.1 Automating Data Conversion 175**
 F. Hacıömeroğlu, R. Uzun, M. Kekeç, A. T. Kaymak, Turkish Aerospace, Ankara (Turkey)
- B2.2 A Review of FFT Algorithms and A Real-Time Algorithm Development for Airborne
 Vibration Testing Applications 181**
 O. B. Ozseven, Turkish Aerospace, Istanbul (Turkey), M. Helvaci, Istanbul Technical University,
 Istanbul (Turkey), S. Tambova, eRC-System GmbH, Ottobrunn (Germany)
- B2.3 Integration of FTI Configuration Management with Flight Test Database for an
 Enhanced Digital Twin Development 195**
 A. T. Kaymak, M. Kekeç, R. Uzun, S. Aydin, Turkish Aerospace, Ankara (Turkey)

B3 Data Management Standards

Chair: Didier Schott, ArianeGroup, Verneuil sur Seine (France)

- B3.1 IQRFF® Communication Standard: Reliability for Lossy, Low Rate Wireless Mesh Networks . . 200**
 V. Šulc, IQRFF Tech s.r.o., Jicin (Czech Republic)
- B3.2 Flight Test Instrumentation System: Tailoring MBSE Methodologies for Prototype Aerial
 Systems Development 204**
 C. Pérez Rus, S. Le Gal, Airbus Defence and Space, Sevilla (Spain)
- B3.3 Encryption of Packet Telemetry: A Risk Analysis 214**
 C. Tavernier, Hensoldt, Plaisir (France), J.-G. Pierozak, Hensoldt Nexeya, Montescot (France)

B4 Sustainable Testing & Materials

Chair: Sergio Penna, Instituto Superior de Engenharia do Porto, Porto (Portugal)

- B4.1 Quality Assurance through Leak Testing of Telemetry Components during Production 220**
J. Lapsien, CETA Testsysteme GmbH, Hilden (Germany)
- B4.2 Achievements and Challenges in Catalytic Combustion Hydrogen Sensors: Commercial Use in Fuel Cell Vehicles and Miniaturization using MEMS Technology 226**
G. Yamamoto, S. Nakao, H. Miyazaki, New Cosmos Electric Co. Ltd., Miki (Japan)

B5 Data Acquisition II

Chair: Ghislain Guerrero, Safran Data Systems SAS, Courtaboeuf Cedex (France)

- B5.1 Measuring the aeroelastic properties of a tiltrotor aircraft in a wind tunnel model 232**
B. van der Meulen, M. Bardet, T. ter Meer, Royal NLR – Netherlands Aerospace Centre, Amsterdam (The Netherlands), E. Brehl, DLR Deutsches Zentrum für Luft- und Raumfahrt FT, Braunschweig (Germany), K. Soal, DLR Deutsches Zentrum für Luft- und Raumfahrt AE
- B5.2 High Innovative Telemetry Solutions for Demanding Applications in the Aerospace Industry . . 242**
S. Manner, E. Manner, J. Manner, MANNER Sensortelemetrie GmbH, Spaichingen (Germany)

B6 HIL & HTB - challenges and solutions

Chair: Jörg Collrep, United Electronic Industries an Ametek Company, Siegsdorf (Germany)

- B6.1 HIL & HTB - challenges and solutions 246**
J. Collrep, B. Judd, E. Goethert, United Electronic Industries., Norwood (USA)
- B6.3 A Hybrid Approach Using Near-Field Scanning in Combination with Field Simulations 248**
D. Schröder, C. Hedayat, Fraunhofer ENAS, Paderborn (Germany), A. Weiß, H. Kuhn, Fraunhofer ENAS, Chemnitz (Germany)

B6 RF Design I

Chair: Guy Williams, Air Force Test Center, Tehachapi (USA)

- B7.3 Research into equivalent Bidirectional Telemetry 254**
F. M. Fernandez Casuso, Airbus Defence and Space, Getafe-Madrid (Spain)
- B7.4 Comparing architectures for bi-directional telemetry ground stations 260**
S. Bonnart, Safran Data Systems, La-Teste-de-Buch (France), P. Klaeyle, Safran Data Systems, Colombelles (France)
- B7.5 First experimental Results and Beamforming Features of Ground Antenna Implementing AESA Technology 266**
C. Mellé, A. Robert, B. Lesur, G. Kipfer, C. Deville, Safran Data Systems, La Teste de Buch (France)
- B7.6 Embedded recording in Flight Test Telemetry Receiver 272**
F. Sandoz, Safran Data Systems, Courtaboeuf Cedex (France), G. Blanc, M. Cariou, P. Klaeyle, Safran Data Systems, Colombelles (France)
- B7.7 A modified OQPSK detection for MIL-STD SOQPSK in the satellite communication 279**
D. Xingwen, S. Jianyong, C. Ming, L. Manhong, Beijing Research Institute of Telemetry, Beijing (China)

Key Words 284

The Use of Lidar to Measure the Flexion and Torsion of a Wing

Israel López Herreros^{1,3}, Felix Arevalo Lozano¹, Jesús Barrera Rodríguez¹, Andrés Egido Fernández¹, Marcos Chimeno², Pablo García-Fogeda Núñez²

¹ Airbus Defence and Space, John Lennon S/N 28906 Getafe-Madrid, Spain

² Department of Aircraft and Space Vehicles, ETSIAE, Universidad Politécnica de Madrid, Madrid, Spain

³israel.lopez@airbus.com

Abstract:

In the field of aerospace, photogrammetry is one of the traditional technologies used to monitor deformations in components such as aircraft wings or other structures, providing valuable data for structural design and evaluation. For these kind of use cases normally two synchronized cameras are needed, they have to be separated by a certain distance to ensure good triangulation.

The current challenge is to assess a new testing technology something less intrusive and less time-demanding in post-processing than photogrammetry methodology. Lidar-based techniques emerge as promising alternatives. Airbus Defence and Space has evaluated the lidar for in-flight relative positioning between two aircrafts, acquiring the knowledge, advantages, and disadvantages of this technology. The objective is to assess this new sensor to measure the flexion and torsion of a wing.

This paper will explain the methodology applied to the point cloud coming from the lidar to characterize the deformation of a wing. Fusion with camera image, clustering algorithms and vibration analysis will be fundamental elements of this process. Simulation and ground tests on a wing mockup will be used to validate the methodology and will allow to choose the best configuration before flight tests.

Key words: lidar, wing deformations, flexion, torsion

1. Introduction

In the field of aerospace, photogrammetry is one the traditional technology used to monitor deformations in components such as aircraft wings or other structures, providing valuable data for structural design and evaluation. For these kind of use cases normally two synchronized cameras are needed, they have to be separated by a certain distance to ensure good triangulation. In some cases irregular dot pattern stickers are used. Applying this methodology in big wings is not an easy task [1].

The current challenge is to assess a new testing technology something less time-consuming in post-processing than photogrammetry methodology. Lidar-based techniques emerge as promising alternatives. Airbus Defence and Space has evaluated the lidar for in-flight relative positioning between two aircrafts [2], acquiring the knowledge, advantages, and disadvantages of this technology. The objective is to assess this new sensor to measure the flexion and torsion of a wing.

2. Lidar

A modern lidar functions by scanning its surroundings with one or more laser beams, which are steered precisely to cover its field of view and that are reflected by the environment back to the scanner. These reflections are transformed into electronic signals by a photodetector, which are then filtered and processed. A 3D point cloud corresponding to the scanned environment as well as the intensities of the reflected beams constitute the output of a lidar system (see Fig. 1). Such a system can be divided into two main components:

- The laser rangefinder: which comprises the laser transmitter, collimated by optics that is shone on the target; photodetector, that generates an electronic signal from the reflected photons that are focused on it by optical elements; and signal processing electronics for estimating the distance between sources and reflecting sources.

- The scanning system: which typically steers the laser beam, following different azimuths and vertical angles. This element defines the system's field of view.

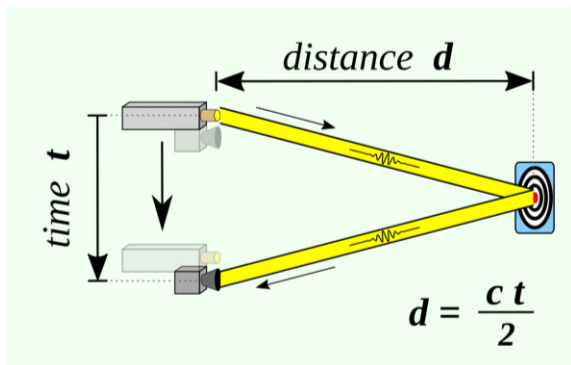


Fig.1. Lidar technological principles

3. Lidar Use Case

The aircraft models used to calculate loads and aeroelastic instabilities need to be validated with ground and flight tests. The most important ground test to obtain the stiffness properties of the aircraft flexible structure is the Ground Vibration Test (GVT). On the other hand, the Flight Vibration Test (FVT) is the most relevant test to characterize the in-flight aircraft flexible response. The FVT is mainly focussed on the transient response of the structure subjected to control surfaces rotations (ailerons, elevators or rudder) and the main objective is to assess that the aircraft, as a system, does have positive damping. The FVT instrumentation is reduced (telemetry-related restrictions) and mainly based on accelerometers located on fuselage and tips of lifting surfaces (wing, HTP, and VTP) and, although the response is well captured in terms of frequency and damping, the deformation shape is hardly characterized with only this instrumentation. Lidar-based techniques could be used to complement the information coming from the FVT, giving additional information as the in-flight steady deformation or the in-flight transient motion due to external perturbations. The lidar-based tools are non-invasive and, with a reduced cost, could be developed to obtain valuable information on the aircraft flexible deformation.

In fact, a prototype beta version of the hardware and software described in this paper will be on-board of an A330-MRTT of Airbus Defence and Space (Airbus-DS) to measure wing elastic deformation, with

emphasis on obtaining the local translations/rotations of the underwing refuelling pods (see Fig. 2).

After these tests, future evolutions of this technology are intended to be applied on subsequent prototypes of Airbus-DS.



Fig. 2. A330-MRTT aircraft refuelling two fighters through the underwing pods

3.1 Mockup Properties, Design, and Manufacturing

A mockup with a high aspect ratio has been manufactured using a 3D printer. The objective was:

1. Create a model to represent the new developments in high aspect ratio wings aimed to reducing emissions while providing high lift/drag ratios.
2. Ensure that the model has a low first bending eigenfrequency for future investigation into the aeroelastic behaviour due to geometrical nonlinearities in the vibration of the mockup.

The mockup has the following geometrical properties:

- Aspect ratio: 18
- Air foil section NACA 4414
- Taper ratio 0.65
- Half span $b/2$ 1m
- Root chord c_r 0.1347m
- Tip chord c_t 0.0875m

A sketch of the wing model can be seen at the fig. 3.

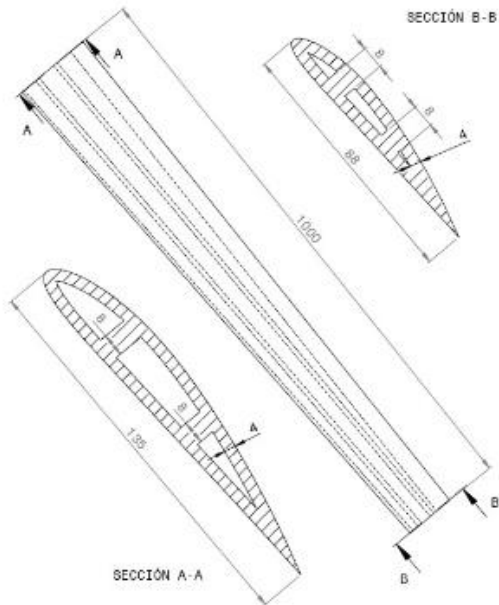


Fig. 3. Wing model

The printing material used was polylactic acid (PLA), a biodegradable thermoplastic polyester produced from renewable sources. It is characterized by a low melting point, a low coefficient of thermal expansion, as well as high flexural strength. The nominal properties of PLA are as follows:

- Elastic modulus E [GPa] 2.5
- Density [kg/m^3] 1250
- Poisson's ratio [-] 0.36

However, the experience acquired from previous bending tests on segmented, 3D-printed, and assembled beams has revealed a change in the mechanical properties of the printing material during the printing process. Therefore, an empirically determined value of $E=1.75\text{GPa}$ (approximately 70% of the filament's nominal Elastic modulus) must be used henceforth for the analysis of the mockup. This adjusted value has been validated through mechanical tests performed on the mockup post-manufacturing.

The first bending frequency of the model is of 4hz, which is considered low enough for conducting studies related to the second objective.

3.2 Structural Model

In order to have an additional comparison against lidar results, a Finite Element Model (FEM) of the mockup structure has been built and computations of static and

dynamic tests have been performed. This model has been defined with the same data (geometry, materials, etc.) which were stated in section 3.1 using quadrilateral 2D elements with shell properties ("CQUAD4" and "PSHELL" in NASTRAN notation). Additionally, a structural damping of $g=2.7\%$ has been considered to take into account the decaying response after release. This coefficient has been estimated with the results from the analysis of the accelerometers during the dynamic tests.

Three kinds of analyses have been carried out with this model:

- Linear static (SOL 101): to obtain the static deformation under the own weight of the mockup plus the additional mass at the wing tip
- Modal analysis (SOL 103): to check the eigenfrequencies and modes of the structure before dynamic analysis.
- Modal transient response (SOL 112): to compute the dynamic response after the release of the wingtip load.

Tab. 1 registers the first eigenfrequencies of the model whereas fig. 4 shows the static deflection of the full model under its own weight and a 200g mass located at its wingtip.

n	Frequency [Hz]	Mode description
1	3.82	1 st bending mode
2	19.29	2 nd bending mode
3	23.28	1 st for-aft mode
4	50.16	3 rd bending mode
5	67.92	1 st torsion mode

Tab. 1. First eigenfrequencies of the model

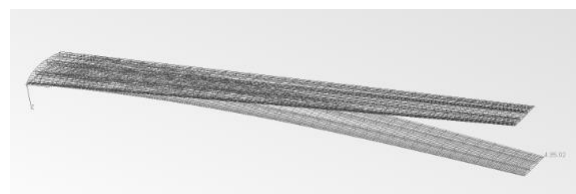


Fig. 4. Full model static deformation

3.3 Tests Requirements

In order to validate the feasibility of the lidar-based techniques to experimentally characterize the deformation of wing-like flexible structures ground tests are requested. The test specimen for the ground test is the wing mockup explained in the previous sections.

Two types of ground tests are requested:

- **Static tests:** Intended to cause a static deformation of the mockup due to the addition of calibrated masses at the wing tip. Two positions along the wing chord are specified for getting both pure bending deformation and bending + torsion deformation.
- **Dynamic tests:** Intended to force a dynamic response of the mockup due to the release of a calibrated mass stored at the wing tip. Four lidar sampling frequencies (10, 16, 24 and 30hz) are requested to characterize the dynamic response of the mockup.

All the steps of the planned test sequence are summarized in the following table:

Test Case	Excitation Method	Excitation Point	Mass	Sampling Frequency
-----------	-------------------	------------------	------	--------------------

0	N/A	N/A	N/A	SP1: 1 Hz
1	Static Load	EP1 (Bending)	50 g	
2	Static Load		100 g	
10	Static Load		150 g	
3	Static Load		200 g	
4	Static Load	EP2 (Bending and Torsion)	50 g	
5	Static Load		100 g	
6	Static Load		200 g	

7	Load Release	EP1 (Bending)	200 g	SF2: 10 Hz
8	Load Release			SF3: 16 Hz
12	Load Release			SF4: 24 Hz
9	Load Release			SF5: 30 Hz

Tab.2. Planned test sequence

4. Lidar Methodology

This section will explain the lidar-based methodology to measure the flexion and torsion of a wing. The output from this methodology will be a time history with several positions of the wing. The following stages will be applied for each frame:

4.1 Point cloud recovery

The first step of the pipeline consists of obtaining the raw point cloud corresponding to the current frame where the wing should be within the lidar's field of view (see Fig. 1).

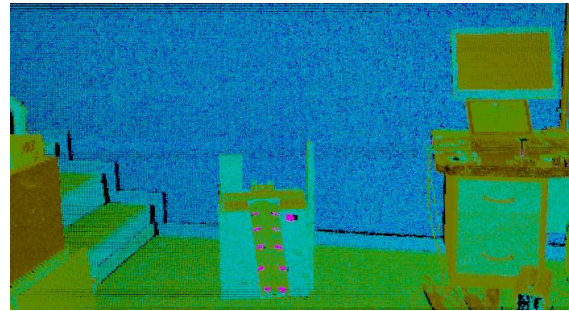


Fig. 5. Point cloud of the wing mockup

4.2 Filter by reflectance

Reflective stickers will be used to filter the point cloud and keep the relevant information. Most of the point cloud disappears, this speeds up the rest of the stages (see Fig. 6).



Fig. 6. Point cloud filtered by reflectance

4.3 Filter by geometry

A geometry filter will be used to remove points outside of the wing (see Fig. 7).

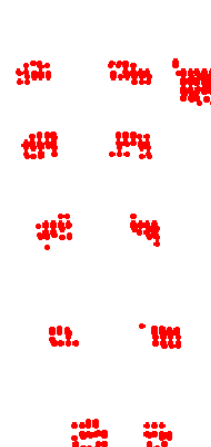


Fig. 7. Point cloud filtered by geometry

4.4 Clustering

A density-based algorithm for discovering clusters in large spatial databases with noise is applied in this stage. Two parameters will have to be adjusted:

- eps: specifies how close points should be to each other to be considered a part of a cluster.
- minimum points: Minimum number of points to form a cluster

These two parameters should be taken into account in the arrangement of the stickers. On one hand, if two stickers are very close it may not be possible to generate two clusters. On the other hand, if the stickers are too far from the lidar it may lead to not having enough points to define properly a cluster.

Each cluster will play the role of a position sensor to characterize the wing deformation (see Fig. 8).

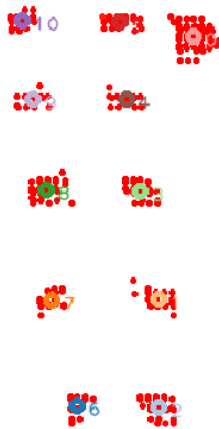


Fig. 8. Clusters of the wing mockup

4.5 Filter by size

When the wing is moving the clusters can significantly vary their geometry producing some noise in the cluster position. To protect this kind of situations a size-based filter is applied. The clusters will need to have a geometry similar to the sticker.

4.6 Centroid calculation

For each cluster, its position will be calculated as the mean of the points that compose it.

4.7 The coherence of the clusters

The density-based algorithm does not have history, that means that the clusters from one frame are not related to the clusters of the following frame. A Neighbourhood-based algorithm is applied to maintain the coherence of the clusters. A maximum cluster displacement is used. This parameter has to be adjusted for the use case.

4.8 Surface reconstruction

To interpretate the resulting point cloud correctly it is very useful to stitch the points to

form a mesh. A surface reconstruction algorithm is applied in this stage (see Fig. 9).

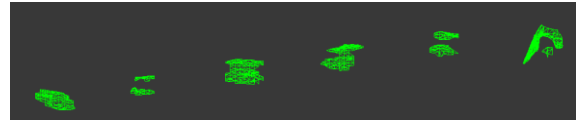


Fig. 9. Mesh generation for each cluster

4.9 Position of the clusters respect to a reference

To characterize the wing deformation is very useful to compare the deformation against other deformations. In this stage each cluster position will be calculated relative to a cluster reference.

The main output from this pipeline is the time series with the position of the clusters. There are some small gaps in the signal that will be reconstructed using interpolations (see Fig. 10).

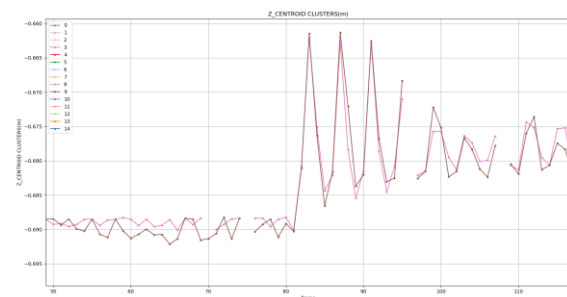


Fig. 10. Time series with the position of the clusters

A vibration analysis based on power spectral density (see Fig. 15) and spectrograms is applied to these signals to obtain the vibration modes lower than half of the lidar sampling rate according to the Nyquist theorem.

5. Test Means

The following means were used to execute the tests.

5.1 Laser distance meter

Used to measure with high accuracy ($\pm 1.5\text{mm}$) the height of the stickers during the static tests (see Fig. 11).



Fig. 11. Laser measurements

5.2 Lidar

Used to measure (range precision $< 2\text{cm } 1\sigma$, 50m) the 3D position of the stickers during the static and dynamic tests. The maximum number of horizontal lines are 640 at 1hz. This number of lines is inversely proportional to the rate, it means that if the rate is 10hz the maximum number of horizontal lines will be 64. Therefore the lidar resolution decreases with the rate.

5.3 Reflective stickers

Reflective stickers will be used to filter the point cloud and keep the relevant information (see Fig. 11).

5.4 Accelerometers

For the dynamic tests, accelerations at the ten locations of the reflective stickers were measured by means of piezoelectric accelerometers. The sensors were installed in the lower surface of the wing to avoid interfering in the cloud point processing (see Fig. 12).



Fig. 12. Accelerometers in the lower surface to measure the dynamic tests response

The accelerations were measured by a set of CCLD Bruel & Kjaer accelerometers acquired through a LDS Dactron Focus II system with a time resolution of $3.9 \cdot 10^{-3}\text{s}$ in the time domain and 0.125hz in the frequency domain.

6. Test Execution and validation

Following sections present the tests results obtained with the different sources. Static torsion tests will not be presented because the effect on the wing is negligible.

6.1 Static results

Static test T0 (0g) will be used as the reference for the rest of the static tests. Several static loads were performed with increasing load at the wing tip: 50gr (T1), 100gr (T2), 150 gr (T3) and 200gr (T4).

T4 analysis will be displayed in this paper for producing the most severe deformation. Similar results were found in T1, T2 and T3. Fig. 13 shows the displacement of the wing in the z-axis respect to the reference during the static tests T4 (200g). There are four series corresponding to the different sources: Nastran model in blue, laser data in orange, lidar data in purple and the integration from the accelerometers in red. The orange zone outlines the laser's confidence band.

The purple zone outlines the lidar's confidence band necessary to make the lidar data compatible with the rest of the sources. In this case use the precision of the methodology using the lidar is 2.5mm.

There are some discrepancies among the different sources but they all have a similar trend.

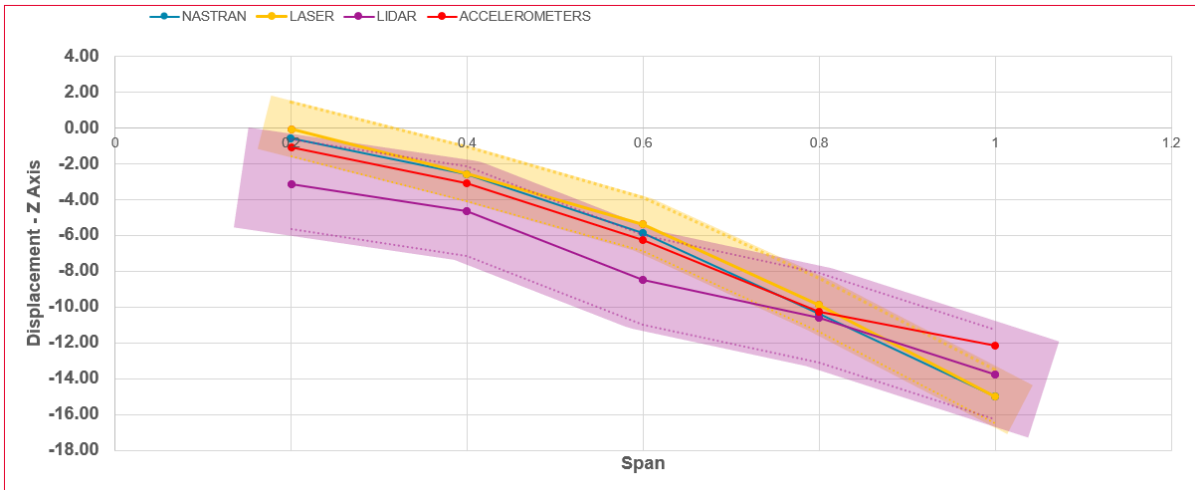


Fig. 13. Wing deformation with static load of 200g

6.2 Dynamic Results

The 200g load release test has been repeated with the following lidar sampling: 10, 16, 24 and 30hz. The ideal lidar configuration for these dynamic tests is the one that has maximum sampling without losing the cluster identification. In this use case the best sampling has been at 16hz.

Fig. 14 shows the oscillations at the wingtip in the z axis during the test T8 (16hz). There are

three sources of data: lidar in blue, Nastran in yellow and the integration from the accelerometers in black. The structural damping coefficient (g) in the Nastran model has been re-estimated using the accelerometer data because it has more precision than the lidar.

Maximum amplitude and damping are coherent in the different sources, however the lidar data has a higher level of noise due to its calculation methodology.

Time History [ID = 11; f = 16Hz]

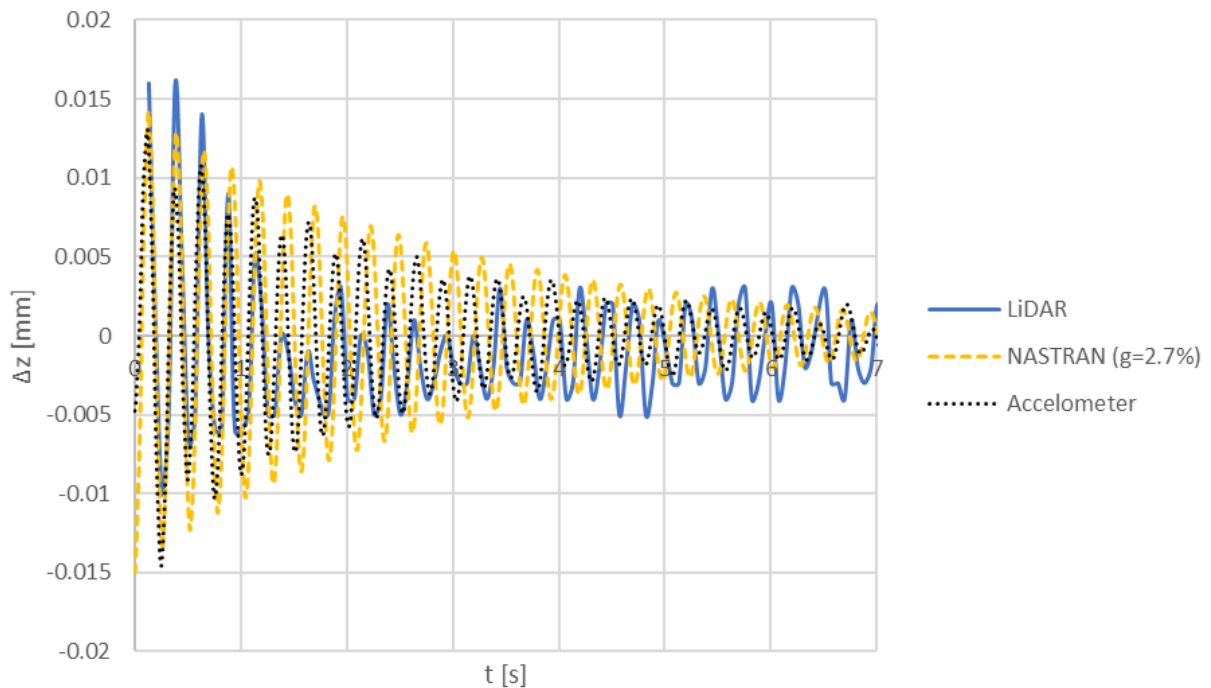


Fig. 14. Dynamic test lidar (16hz)

The power spectral density is applied to the different sources obtaining a similar frequency in the wingtip (see Fig. 15, 16 and 17). The dynamic response is coherent with the first bending mode (See Table 1). The limited lidar sampling rate does not allow identifying other vibration modes.

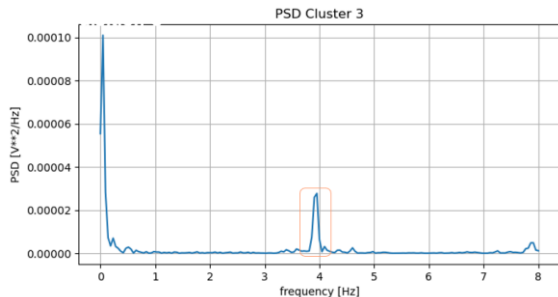


Fig. 15. Lidar PSD wingtip (16hz)

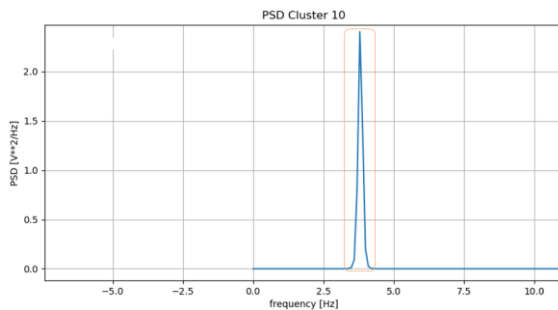


Fig. 16. Nastran PSD wingtip (2000hz)

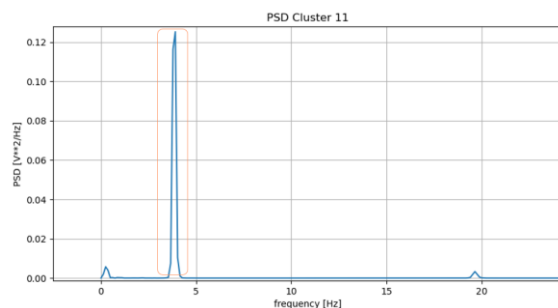


Fig. 17. Accelerometers PSD wingtip (250hz)

7. Conclusions

This lidar-based methodology is applied to measure the flexion and torsion of a wing mockup wing in static tests with a precision of 2.5mm.

For dynamic tests, the lidar sampling rate chosen was 16hz for having maximum sampling without losing the cluster identification. This limits the identification just to the first 4hz vibration mode of the wing mockup, therefore the analysis is restricted to this mode.

This work has been done with a specific lidar coming from the automotive sector. Currently, lidars are seen as a key ingredient to autonomous driving. In the future, lidars with

better performance in terms of precision, range, and sampling are expected to be available.

This work paves the way to the use of the lidar technology to measure the flexion and torsion of the wing of a real aircraft or any other structure. This methodology could be also applied to measure structure deformations in ground tests.

Acknowledgement

I'd like to acknowledge the contribution of Francisca Coll Herrero to support the implementation of the vibration analysis.

References

- [1] F. Boden, T. Kirmese, T. Weikert, T. Wofl, C. Petit, H. W. Jentink: "Application of a new optical measurement technique for non-intrusive wing deformation measurements on a large transport aircraft", SFTE 2010
- [2] Israel López Herreros: "Lidar for in-flight accurate relative positioning", ETTC 2023

Glossary

LIDAR:	Light Detection and Ranging
GVT:	Ground Vibration Test
FVT:	Flight Vibration Test
HTP:	Horizontal Tail Plane
VTP:	Vertical Tail Plane
MRTT:	Multi-Role Tanker Transport
DS:	Defence and Space
PLA:	PolyLactic Acid
PSD:	Power Spectral Density

H175 De-icing Flight Test Campaign – Focus on Flight Test Instrumentation

Floriane Monteil

*Airbus Helicopters SAS, Aéroport International Marseille Provence, 13700 Marignane
Floriane.monteil@airbus.com*

Abstract:

Among flight test campaigns required for certifications, the flights in icing conditions are challenging both for the aircraft system but also from the Flight Test Instrumentation (FTI) perspective. It requires a specific organization, scheduling, resources with expertise and particular means of measurement when it comes to instrument the aircraft for campaigns in icing areas.

Such data must be collected in given icing conditions to be considered as valid data from the certification authorities. It might take time to meet such conditions, thus one possibility to increase these statistics is to run parallel campaigns in several locations. The benefits are there, but come at the cost of some points to be particularly aware of to ensure that both field tests run smoothly.

The instrumentation required to perform those acquisitions has its own complexity and specificities. The choice of the various parts (icing measurement probes, video system, weather station) shows a major importance to withstand the harsh icing environment.

Key words: Flight Test Campaign, Instrumentation, Icing Probes, Video, Weather

De-icing Flight Test Campaigns from FTI perspective

In the frame of the H175 helicopter certification in icing conditions, specific Flight Test Instrumentation installations have been designed and integrated to ensure two campaigns in parallel. The flight tests took place in Canada (London/Ontario) from October, 2023 to April, 2024 and in Norway (Trondheim/Alta) from February, 2024 to April, 2024. Two aircraft were fully instrumented to perform those campaigns in good conditions.

The management of two campaigns simultaneously brings additional challenges, as well as important added-values. The number of measurements increase, thanks to various icing conditions in different locations, which is a major argument to undertake those challenges. As the instrumentation is quite specific, it is important to ensure the availability of the required equipment but also spare parts to face any potential issue with a high reactivity. The resources are shared on two foreign locations in different time zones, increasing the difficulty to communicate between the teams and the third support team located in the main site in France. All the teams must be somehow composed by people experimented with such

types of campaigns, to not miss a chance to perform proper flight tests and adequate measurements.

The parallel campaigns allowed a clear speed up in the certification process, ensuring the availability of all required data by the certification authorities in one go, to justify the sustainability of the aircraft and its de-icing system in such a harsh environment. Good preparation ahead of those campaigns is mandatory in order to obtain the required results from the various flight tests sessions. Ensuring a sufficient number of well-trained resources, as well as equipment availability along with enough spare parts, comes as a prerequisite in addition to a proper schedule organization upfront and during the campaigns.

FTI Overall Architecture

Nowadays, most of the flight test installations are based on a network architecture. This implies as basic components several network switches to ensure the interconnection between data acquisition units, recorders, data displays, control units... When it comes to such de-icing campaigns instrumentation, a huge amount of equipment is added as an extension to the existing typical instrumentation system. An additional network switch is used as gateway

between the existing system and the de-icing specific system, collecting data from the cameras via video encoders, from the de-icing probes via a given computer and feeding dedicated data displays to show the weather data and icing-related measurements.

All in all, it gathers more than 500 analog parameters, as well as 16 video cameras installed inside and outside of the aircraft collected by 4 video encoders, along with 30 ARINC429 lines to store various information coming from the aircraft and several Ethernet busses to exchange data between the equipment.

FTI Specificities for De-icing

De-icing flight test campaigns require some specificities in terms of instrumentation. As a non-exhaustive list but still covering the main components: the icing measurement probes, the video system and the weather station; all considered in the harsh environment of icing conditions.

- **Icing Measurement Probes:** this type of probe is fully specific to this kind of measurement; therefore, they are not often used and the list of suppliers is quite reduced. This implies a strong link with the chosen supplier, in terms of communication, training, implementation but also regarding support during the campaign and potential on-site maintenance. The technology integrated into the means of measurement itself is crucial and might evolve from one campaign to the next one; so obsolescence might appear, which can be seen as an opportunity to improve the efficiency of data collection. Mainly three distinct criteria must be measured:
 - Water concentration, via a “King Probe”, range [0,05; 3,00] g.m⁻³;
 - Small water drops, via a “Cloud Droplet Probe” (CDP), range [2; 50] μm;
 - Big water drops, via “Scattering Spectrometer Probe” (SSP) or “Cloud Imaging Probe” (CIP), range [1; 950] μm;

Those measurements are processed together with the True Air Speed data (TAS) of the aircraft taken from a static pitot probe. All those probes can be considered separately, but as an alternative, new technologies propose one single system called Cloud

Combining Probe (CCP). Working with a dedicated embedded computer, those data can be processed in real-time and provide final parameters useful for the validation and certification process. In addition, it helps defining directly whether the droplets present in the clouds respond to the requirements for such data, or if the particles cannot be used in the frame of certification.

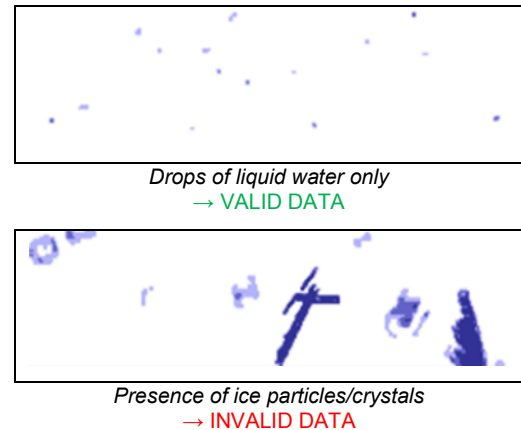


Fig. 1. Icing particles going through the CIP to define the validity of the data for two different kinds of clouds.[1]

The fact that data processing starts in real-time during data collection reduces the time needed for post-processing, improving the overall efficiency regarding the high amount of data to consider other than the icing particles themselves. This however requires the presence of an additional computer linked to the probes. This brings up a new challenge regarding its integration in the FTI system, but it allows timestamping the data coming from the probes via Network Time Protocol (NTP) and aligning them with other acquired data;

- **Video System:** The video system plays a key role in such testing campaigns. Having a literal view on the icing conditions outside helps during interpretation of the measured data, the evaluation of ice quantity all over the campaign by the aircraft and to prepare the crew for the different flight testing phases to perform.
 - *SDI cameras* have been designed specifically to withstand icing conditions by adding a self-heating resistors ring around the lens. One of the main points of interest is to verify the icing accretion and good operation of the de-icing system from the helicopter on the

blades. The pictures taken by the cameras must offer a clear view of the accumulation of the ice without any blurring due to the rotation of the blades. This is ensured thanks to a second key feature of the cameras, allowing to trigger the picture on an external synchronization signal coming from the rotor blades. Other cameras are oriented towards so-called icing indicators, which are installed all over the aircraft at strategic locations with graduations allowing the measurement of ice aggregation. Keeping the same customized model of camera for all shots helps the interchangeability, the mechanical and the electrical integration in the aircraft;



Fig. 2. Camera clearly showing ice accretion on rear rotor blades in 26 seconds thanks to the synchronization of picture capture on the blade frequency.

- *Video encoders* are used to capture the SDI stream from the cameras and compress them with the best possible ratio (H.265 compression algorithm). This is a trade-off between the quality of the resulting compressed videos and the data rate transferred to the rest of the FTI architecture. Each video encoder collects up to 4 video cameras and outputs a single Ethernet stream, sent in parallel to the recorder and data display.

The video system represents a significant data rate transferred over the FTI installation. The calculation of each rate and support by the various equipment receiving the stream must

be planned upfront to setup the system accordingly.

- **Weather station:** weather data provides important information used to identify cloud type and location, as potential sources of valid data. It guides the crew to navigate to the interesting locations and hopefully quickly meet the right icing conditions. Such a system [2] can be connected to the IRIDIUM satellite constellation to provide weather data to experts on ground, in the air or at sea. By processing such data in real-time and combining these with the GPS location of the aircraft, the experts can communicate with the crew to provide them a cartography of the real-time weather conditions. Finding right away adequate icing conditions drastically improves the time required to collect the required parameters with the right quality.

Those specificities about the FTI system increased the integration efforts in more typical FTI architectures, both regarding software and hardware in a general way. However, those technologies and technical choices made it possible to cover all necessary measurement points required by the certification authorities in a limited time range. Appropriate icing conditions being available only in a narrow time window during the year, usually in quite remote locations, it would otherwise have been necessary to wait for one additional year to be able to complete the missing points and complete the flight test campaigns.

- **Harsh environment:** everything has to function properly notwithstanding the harsh environment naturally imposed by the icing conditions. More than ever, the sensors, harnesses and various parts of the instrumentation exposed to the icing conditions must be protected. Damages can appear fast and a high level of repair, maintenance and reactivity become a key success factor. Issues and side effects can appear in unexpected areas. Due to the high responsiveness required during campaigns while facing damaged parts, it is not always possible to wait for repair before flying again and adaptability must be accounted for upfront. As an example, if the static pitot probe from the CCP is damaged during a campaign and becomes inoperative, the data analysis team must be trained to use the static pitot

data acquired from the aircraft and apply the proper formula, to finally calculate the resulting correct icing measurements without this being done automatically by the dedicated computer.

Summary

In addition to the typical harsh environmental conditions met during deicing campaigns which put a heavy stress on the instrumentation, especially as it needs to maintain the highest standards from a metrological perspective, the real challenge behind the H175 deicing campaign was to manage and follow two campaigns happening simultaneously in different locations and timezones.

First, the management of equipment inventories requires an important level of organization and

coordination (ensuring spare parts, facing obsolescence).

Second, the management of the teams requires dedicated attention, regarding the availability of a relevant group of specialists, but also from a communication and planning point of view.

Last but not least, the technical challenges are highly present: from the integration of new probes to the complexity of a customized video system, over the necessary evolution of the network architecture... and all that under time constraints and particularly challenging environmental conditions! But in the end, the resulting benefits in terms of lead time of the certification process proved the challenge to be worth the effort!

References

- [1] Cloud Imaging Probe data measurement analyzed with LaMP laboratory:
<https://lamp.uca.fr/recherche/instruments-modeles/plateforme-de-mesures-aeroporrees#/admin>
- [2] ATMOSPHERE PLANET 9770 FTI Terminal providing weather data:
<https://www.iridium.com/products/atmosphere-planet-9770-fti-terminal/>

Decentralized Reinforcement Learning for Adaptive Transmission Parameter Optimization of a LoRa Transceiver

Julius Gissing¹, Carsten Brockmann²

¹*Technische Universität Berlin, Straße des 17. Juni 135, 10623 Berlin, Germany*

²*Fraunhofer Institute for Reliability and Microintegration (IZM), Gustav-Meyer-Allee 25, 13355 Berlin, Germany*

julius.gissing@izm.fraunhofer.de

Abstract:

In wireless sensor networks (WSN), a large share of the energy demand arises from wireless communication, especially in wide area networks where transmission distances are at the scale of kilometers. Ensuring reliability of communication links while optimizing energy demand requires heterogeneous radio configurations throughout the network demanding for an automated process for identifying suitable transceiver settings in order to mitigate the effort of manual configuration during deployment. Furthermore, wireless links are susceptible to dynamic influences such as environmental conditions and interference from concurrent channel usage, rendering static radio configuration impractical. Therefore, autonomous organization and self-configuration of wireless communication networks, such as transmission parameter optimization, drastically reduce cost and effort for installation and maintenance of large-scale sensor systems. Such dynamic adaptive behavior can be achieved by local execution of decentralized methods that enable decision-making at the network edge, while also inherently offering advantages such as enhanced system robustness and scalability. In this work, we present a method that exemplifies this approach and experimentally evaluate its performance on real hardware. The adaptive algorithm optimizes the transmitter configuration of a *LoRa* transceiver by employing a model-free reinforcement learning approach based on an actor-critic setup using a parameterized stochastic policy and state-value function approximation. Experimental results show that the approach surpasses a standard approach in terms of long-term energy demand. Furthermore, the method's capability of adapting to dynamic wireless channels is demonstrated.

Key words: Reinforcement Learning, Decentralized Systems, Wireless Sensor Networks, LoRa, Energy Efficiency

Introduction

The number of interconnected devices in the Internet of Things (IoT), among which, wireless sensor nodes constitute a large share, is growing steadily during the last years. In light of 25 Billion devices forecasted by the year 2030 [1], the effort for installation, maintenance and administration is tremendous. To address this challenge, devices should be highly resource-efficient, ensuring a long lifespan and extended maintenance cycles. Furthermore, autonomous configuration and organization of distributed devices improve the ease of use, save efforts during deployment and improve system robustness. Achieving these advancements requires individual devices to make decisions autonomously at runtime and in coordination with other network participants. These decisions encompass various tasks of network organization, such as establishing connectivity,

selecting appropriate transceiver configurations and realizing efficient routing. This approach relies on the concept of decentralized systems, in which, unlike in centralized architectures, the edge nodes of the network contribute the essential functionality of the entire network.

This work will present an approach of reinforcement learning to support local decision making of distributed devices in decentralized systems. The paper is structured as follows. First, related work with focus on machine learning in wireless sensor networks and in specific in *LoRa* and *LoRaWAN* networks will be discussed. Next, the essential fundamentals of smart sensor systems, decentralized systems, reinforcement learning, and the networking standard *LoRa/LoRaWAN* will be outlined. Thereafter, the developed algorithm for transmission parameter optimization will be introduced and the results of experiments are

presented. Finally, the findings are summarized in a conclusion.

Related Work

Cui et al. emphasize the importance of learning and intelligent algorithms from the field of machine learning for the Internet of Things in their article [2]. The applications they discuss include device identification within networks, data security measures, network traffic prediction, and various examples from edge computing. The significance of edge computing is particularly highlighted for reducing server load, minimizing energy consumption, and supporting low-latency applications.

In [3], the authors describe a learning method for wake-up control of sensor nodes in a sensor network for compressed data acquisition. The goal is to evenly distribute energy consumption and thereby extend the network's lifespan. The approach is based on reinforcement learning, intended to be executed locally on the sensor node. The achieved results demonstrate an improvement in network lifespan compared to similar approaches. The simulation used, consisting of 512 uniformly distributed sensor nodes, assumes that all nodes know the shortest transmission path to the base station and can be woken up at any time by a radio message.

In their article [4], Zhang et al. describe the optimization of *LoRa* radio parameters aimed at achieving a fair allocation of network resources and minimizing overall network energy consumption. Their approach is based on integer linear programming, which is approximated using a combination of an evolutionary algorithm and the Gurobi solver. Compared to conventional resource allocation strategies, their simulations show a reduction in energy consumption by more than 20% while also decreasing packet collisions. The approach relies on a high-performance server and a centralized system architecture.

Farhad and Pyun [5] provide an overview of current machine learning techniques for enhanced resource management in *LoRa* and *LoRaWAN* networks. The methods described rely on learning algorithms executed by the network server within a centralized network architecture. These algorithms can therefore access information from all nodes in the network or from an offline dataset. Evaluation of the techniques is based on simulations.

González et al. [6] employ various machine learning algorithms to predict path loss and shadowing effects in a *LoRa* connection based on environmental factors. They propose a method for calculating efficient radio parameters by executing a pre-trained model on the network

node. The algorithm's evaluation is conducted through simulation.

Azizi et al. introduce an algorithm for parameter optimization of a *LoRa* radio module, based on reinforcement learning and algorithms from the field of multi-armed bandits [7]. The primary goal is to optimize the packet delivery rate of message transmissions, demonstrated in a simulation involving 100 nodes. The authors limit the radio configuration to a maximum of 18 parameter combinations and demonstrate that their approach significantly improves the delivery rate compared to the standard used in *LoRaWAN*.

There are several promising approaches to resource allocation and configuration optimization in *LoRa* networks, with some occasionally adopting the approach of distributed, decentralized execution. To our knowledge, there are no existing works that implement these concepts on real hardware and evaluate them in experiments outside of simulations.

Smart Sensor Systems

With developments towards the internet of things, the notion of smart sensors included more advanced signal processing and data fusion techniques on the device, especially intelligent algorithms and concepts of artificial intelligence that improve the usability of the system in terms of integration and extraction of information [8]. In recent years the number of operational systems is quickly growing and each system may consist of a large number of end nodes, making it impossible to configure and manage each device manually. Additionally, node failure, replacement or network extensions are common practice in WSNs. Especially large-scale networks are prone to failure of single nodes due to battery depletion or electronic failures over time. Therefore, self-organizing, self-configuration and self-healing capabilities are key factors for a successful WSN deployment [9, 10]. These requirements demand the behavior of individual nodes to be more autonomous and self-adaptive, pushing sensor nodes more towards actual intelligent behavior in order to form a system that is capable of adapting to many circumstances and possibly generalizing over different application domains. Promoting intelligent behavior of individual nodes inside a WSN may enable the system to fulfill described expectations of modern sensor systems.

Decentralized Systems and Decision Making

Many techniques that are used in recent time rely on centralized cloud servers, connected to base stations that organize the network and roll

out configurations to network entities. Though the centralized approach has the advantage of using powerful servers as the network backbone and opening up the opportunity of using computationally heavy algorithms on the sensor data, it also comes with a range of issues. Each central base station has a limited number of devices that it is able to manage due to the limited bandwidth and duty-cycle. Configuration of nodes that are far away may require communication over relay nodes which further increases communication overhead. Generally, centralized control of end-devices by a base station impedes scalability of the network and decreases operational robustness. In order to address these challenges, decentralized data processing and network management has become a research focus. Decentralized network management aims to organize network nodes and resources led by end-devices, with minimal need for manual intervention. Without centralized control, individual nodes aim at optimizing global objectives by the means of localized decision making. Each node must observe its environment by using sensors and communicate with its neighbors. Based on that information and processing capabilities of end nodes the local decision making process is employed with the goal of optimal behavior independent of the place of installation and circumstances present. Sensor nodes are enabled to adapt according to the network's needs in changing conditions. Meeting this objective requires increased functionality of individual end nodes, specifically, higher complexity of firmware components that controls task sequencing and decision making. This goes along with higher demand on the computational power and resources [11].

Reinforcement Learning

Reinforcement learning (RL) is a subclass of machine learning that aims at finding a (nearly) optimal behavioral policy of an agent acting in an unknown environment. The agent optimizes its policy by the means of trial and error, supported by a reward signal that evaluates the taken actions. The goal of a learned policy is to maximize the long-term cumulative reward. The formalization of reinforcement learning is based on a Markov decision process (MDP) which is a tuple $(\mathcal{S}, \mathcal{A}, P, R)$ where the state space \mathcal{S} is the set of all states in the environment and the action space \mathcal{A} is the set of actions the agent can take. $P(s'|s, a)$ is the state transition probability and $R(s, s', a)$ is the reward the agent collects for transitioning from state $s \in \mathcal{S}$ to $s' \in \mathcal{S}$ given that action $a \in \mathcal{A}$ was performed. For most environments, especially in the real world, the transition probability function is unknown, which

means the agent has to explore the environment in order to find a policy that yields maximum cumulative reward. On the other hand, if an agent always explores its environment it can never exploit the behavior that is believed to generate most reward. Balancing the trade-off between exploring the environment and exploiting what has been learned to effectively gain reward is one of the fundamental problems in RL and has been studied intensively. At each time step t the agent has to choose an action a_t , given the current state $s_t \in \mathcal{S}$, which may be exploratory or greedy. It does that by evaluating the current behavioral policy π_t that maps the current state $s_t \in \mathcal{S}$ to an action $a_t \in \mathcal{A}$. In general, the policy can be deterministic or stochastic and is given by a probability distribution.

$$\pi(a|s) = \mathbb{P}(a_t = a | s_t = s)$$

After taking an action the agent observes the successor state s_{t+1} and the gained reward r_t . During exploration of the environment the agent has to acquire knowledge about the potential of long-term reward of each state, in order to adapt its policy. A common concept of evaluating a state is to estimate the value function. The state-value function $V_\pi(s)$ is defined as the expectation of the discounted long-term reward under policy π when starting in state s .

$$V_\pi(s) = \mathbb{E}_{a \sim \pi, s \sim P(s'|s, a)} \left[\sum_{k=0}^{\infty} \gamma^k r_{t+k} \mid s_t = s \right]$$

Note, that the expectation also takes into account the transition probability of the environment. However, this will be the case for every expectation used from here on, so the subscript will be omitted to simplify the notation ($\mathbb{E}_{a \sim \pi, s \sim P(s'|s, a)}[\cdot]$ from here on denoted as $\mathbb{E}_\pi[\cdot]$). The discount rate γ is a parameter $0 \leq \gamma \leq 1$ that determines the importance of future reward in contrast to immediate reward, besides, it is particularly important for an infinite planning horizon, because it ensures the sum to be finite. The sum of the discounted future rewards is also referred to as the return G . Similarly to the state-value function, the action-value function $Q_\pi(s, a)$ can be defined as the expected return when starting in state s , taking action a and following the policy π thereafter.

$$Q_\pi(s, a) = \mathbb{E}_\pi \left[\sum_{k=0}^{\infty} \gamma^k r_{t+k} \mid s_t = s, a_t = a \right]$$

A distinctive characteristic of RL is the ability of agents to learn from observations and locally available information. As opposed to supervised

learning, there is no need for data that is labeled by an expert. An RL agent collects information and incorporates it into the future decision process, which makes it an inherently adaptive class of algorithms that is able to cope with uncertain environments. A key idea that allows to immediately learn from examples that are generated from interactions with the environment is called temporal difference (TD). TD learning takes experienced samples and uses them to incrementally approximate the state or state-value function. In order to update estimates of the value function of a certain state, they rely on their current value estimate of the next state (bootstrapping).[12]

$$V(s_t) \leftarrow V(s_t) + \eta(r_t + \gamma V(s_{t+1}) - V(s_t))$$

Where η is the learning rate (or step size) and $V(s)$ is the current estimate of the value if in state s . For a sufficiently small step size and following a certain policy during interaction, the approximation is guaranteed to converge to the actual value under that policy. When TD prediction is applied to estimate action-values instead of state-values, it can be used for optimizing an agent's policy. During operation, the action with the highest action-value ($\operatorname{argmax}_a Q(s, a)$) is executed. This means no more exploration of the state space and requires sufficient prior experience in the environment by the agent. Furthermore, this kind of policy leads to deterministic decisions which may lead to optimal behavior in deterministic environments. In stochastic and dynamic environments it has been shown that stochastic policies may yield to better results [13].

Instead of defining behavioral policies directly through action-values, an additional stochastic function can be defined to map states on action probabilities. Policy gradient methods define a parameterized policy and optimize the parameters with respect to the expected return the policy is generating. For a parameterized policy $\pi_\theta(a|s)$ it can be shown that an optimization step for the function weights θ in direction of the gradient of the expected return,

$$\theta_{t+1} \leftarrow \theta_t + \eta \nabla_\theta V(s_t),$$

can be computed using the return and the gradient of the policy, without explicit knowledge of the transition probabilities of the environment.

$$\nabla_\theta V(s) = \mathbb{E}_\pi [\nabla_\theta \log \pi_\theta(a|s) G]$$

When the expectation is replaced by sampled data, this is called the REINFORCE estimator [14]. A characteristic of the REINFORCE estimator is its need for the full return of a state. This can become an issue for tasks that do not

follow an episodic structure, since it means long trajectories need to be sampled in order to compute the policy gradient and optimize the parameters. Fortunately, instead of using the actual return, it can be replaced by an approximate of the state-value or action-value function, as it is learned in the TD-learning setup. Algorithms that use a value function estimate to update the policy are called actor-critic methods, since they learn a policy (actor) by optimizing it in direction of the value function that evaluates its actions (critic) [15]. A typical choice for the critic is the advantage function $A_\pi(s, a)$, which can be described as the advantage of taking action a over taking another action $a^* \neq a$, when in state s . It is defined as the difference between the action-value function $Q_\pi(s, a)$ and the state-value function $V_\pi(s)$.

$$A_\pi(s, a) = Q_\pi(s, a) - V_\pi(s)$$

Instead of learning a state- and action-value estimate in parallel, the advantage can be estimated by the action-value and the gained reward only.

$$\begin{aligned} Q_\pi(s_t, a_t) &= \mathbb{E}_\pi \left[\sum_{k=0}^{\infty} \gamma^k r_{t+k} \mid s_t, a_t \right] \\ &= r_t + \gamma \mathbb{E}_\pi \left[\sum_{k=0}^{\infty} \gamma^k r_{t+1+k} \mid s_{t+1} \right] = r_t + \gamma V_\pi(s_{t+1}) \\ A_\pi(s_t, a_t) &= r_t + \gamma V_\pi(s_{t+1}) - V_\pi(s_t) \end{aligned}$$

Therefore, the critic can be estimated by learning an approximate state-value function $\hat{V}_\pi(s) \approx V_\pi(s)$, for example with on-policy TD-learning. The policy optimization rule for an actor-critic algorithm is given by

$$\theta_{t+1} \leftarrow \theta_t + \eta \nabla_\theta \log \pi(a_t | s_t) \hat{A}_\pi(s_t, a_t).$$

Since it may take many exploration and learning steps until the state-value estimator converges to reflect the true state-value under the current policy, the state-value and policy parameters are optimized concurrently. The true value function is changing under the constantly optimized policy, as a consequence, the state-value approximation may be inaccurate. Other reasons for wrong value estimates may be delayed reward or non-Markovian property of problems [12, 16]. A standard procedure to counter these problems are eligibility traces. Eligibility traces are a discounted accumulation of the gradients that are used in the optimization step. In case of eligibility traces for the actor optimization, this means, the gradient $\nabla_\theta \log \pi_\theta(a_t | s_t)$ at times step t is not only

influencing action a_t at time step t but also at the following time steps $t + 1, t + 2, \dots$, etc.

Aforementioned RL techniques necessitate the use of function approximation to model state value and policy function. The implementation can range from simple approaches, such as tabular methods, to complex, nonlinear representations, such as artificial neural networks. Since tabular representations require substantial memory in multi-dimensional state spaces and artificial neural networks demand significant computational power for optimization algorithms, both methods are not well-suited for resource-constrained microcontrollers. An efficient approach to function approximation is provided by linear methods in combination with nonlinear projections of the state variables [17]. One effective projection method is tile coding, which divides the state space into partitions (tiles) of arbitrary size. The partition containing the input vector is activated (1), while others remain inactive (0). Multiple overlapping tilings enable function approximation to generalize across nearby input values, as different partitions can be activated in different tilings. [18]

LoRa & LoRaWAN

LoRa (Long Range) is a proprietary modulation technology for wireless communication, developed by *Semtech* that is based on the technique of chirp spread spectrum. In this process, a communication signal is spread in the frequency domain, resulting in a signal with increased bandwidth but the same total power. Due to the enlarged bandwidth, the signal becomes less susceptible to disturbances such as multipath fading, interference, or the Doppler Effect [19]. Demodulating the signal back to the base frequency allows the receiver to benefit from processing gain, enabling the detection of signals below the noise floor with high accuracy [20]. Thus, robust communication over long distances can be achieved with minimal energy use. *LoRa* offers flexible parameterization of the radio module which enables balancing the trade-off between link quality and energy demand. Transmit power (TP), spreading factor (SF), bandwidth (BW), and coding rate (CR) can be configured to meet the requirements of specific applications. The flexible selection of parameter combinations creates a complex search problem for the optimal configuration of the radio module [21].

The recommended networking layer to establish a working communication network with *LoRa* is the open-source protocol *LoRaWAN*. In *LoRaWAN*, network participants are organized in a star topology which allows for communication exclusively between end nodes and gateways. Since there is no widespread

networking protocol based on a meshed or multi-hop topology, the *LoRaWAN* standard will be the benchmark for further evaluation during this work. The standard describes a procedure for parameter optimization of the radio module, called adaptive data rate (ADR) [22]. The concept is based on the range versus data rate tradeoff and consists of increasing data rate as much as possible while maintaining a stable communication link. Higher data rate goes along with shorter transmission time, leading to less energy consumption and shorter communication range. Along with decreased energy usage, channel efficiency benefits from short time on air, resulting in larger channel capacity and mitigating risk of message collision. ADR is a link-based approach, meaning that the transmission parameters for communication between end-node and gateway are determined by the network server in a centralized fashion. If an end-device uses ADR or not is decided by the application and the process is initiated by the device. The network server collects some messages of the node in question and issues a downlink including the ADR command through the gateway with the best communication link to the node. The optimal data rate is computed by the server, taking link budget and a margin for error into account. After a predefined number of messages the node requests an ADR acknowledge from a gateway to ensure a stable connection. If the connection was lost, it gradually decreases its data rate in a standardized back-off scheme until the communication link is reestablished. The link-based ADR approach has several shortcomings that have been reported especially with increasing network size [22, 23]. ADR commands and ADR acknowledgement creates a traffic overhead in the network that leads to increased channel occupation. This lowers the packet delivery ratio due to message collisions. Lost ADR acknowledgment also leads to undesired data rate increase even if low data rates are applicable. Moreover, gateways servicing many end-devices easily exceed duty-cycle limitations on unlicensed frequency bands due to the requirement to send acknowledgment and ADR frames to all connected devices. These issues with centrally managed ADR schemes lead to interest in network-aware concepts that follow a distributed approach, meaning that end-devices determine optimal transmission parameters locally [23]. Furthermore, ADR is only applicable to static end-nodes because a constant propagation environment is assumed during link probing. If the wireless channel is dynamic, by the time an ADR command is issued through the gateway, the estimated link budget is not valid anymore [22].

Online Reinforcement Learning for Transmission Parameter Optimization in LoRa

At the time of deployment, the quality of the channels between participants of a WSN is unknown and may be heterogeneous across the network. Optimal parameter settings of a radio transceiver minimize energy consumption while ensuring communication reliability. The choice of transmission parameters can be optimized in a decentralized fashion by employing reinforcement learning (RL) on the end nodes. The exact method and procedure for this is described in the following.

First, the problem needs to be described in form of a Markov decision process (MDP) in order to make use of an RL approach. The state of the process should provide precise contextual information of the learning agent's situation. It is composed of the radio configuration of the transceiver and the measured signal quality using that configuration. The signal quality is described by the received signal strength indication (RSSI) value and the signal-to-noise ratio (SNR), it is sent as a feedback by the receiving entity. In order to move around in the state space, the agent is endowed with a set of actions that change the radio configuration in a differential way. The reward is constructed to reflect importance of successful transmissions and minimization of energy consumption jointly. In particular, a state s_t at a discrete time step t is defined as the tuple

$$s_t = (SF_t, TP_t, RSSI_t, SNR_t),$$

with $RSSI_t$ and SNR_t denoting the observed signal values when using spreading factor $SF_t \in \{SF5, SF6, \dots, SF12\}$ and transmission power $TP_t \in \{0 \text{ dBm}, 1 \text{ dBm}, \dots, 14 \text{ dBm}\}$ for a transmission. The agent then evaluates its policy $\pi_t(a_t|s_t)$ and chooses a differential action a_t from the discrete set of actions

$$\mathcal{A} = \{\text{inc}(SF), \text{inc}(TP), \text{stay}, \text{dec}(SF), \text{dec}(TP)\},$$

where $\text{inc}(\cdot)$ and $\text{dec}(\cdot)$ denote increasing and decreasing of a radio parameter respectively, and stay means to remain in the current transceiver configuration. After execution of the chosen action a_t the agent observes the successor state s_{t+1} and the gained reward r_t that is given by the following function.

$$r_t = \begin{cases} E(SF_t, TP_t)^{-1}, & \text{if transmission successful} \\ -p, & \text{if transmission not successful} \end{cases}$$

$E(SF, TP)$ provides the energy required for a transmission with spreading factor SF and transmission power TP . Therefore, the reward is

positive for all successful transmissions, inversely proportional to the required energy and constant negative for unsuccessful communication attempts.

The first part of the algorithm is to estimate the state-value for any arbitrary state. In order to enable generalization over nearby states and avoid the need to explore every existing state in the state space, a linear function approximation scheme with a nonlinear feature projection using tile coding is employed.

$$V_\pi(s) \approx \hat{V}_\pi(s; \mathbf{w}) = \psi(s)^T \mathbf{w}$$

Where $\psi(s)$ denotes the projection of the tile coding and \mathbf{w} denotes the function weights of the linear approximator. Optimizing the function weights can be realized using gradient descent on the squared error \mathcal{L}_{SE} between the actual state-value and the approximation.

$$\mathcal{L}_{SE}(s, \mathbf{w}) = \left(V_\pi(s) - \hat{V}_\pi(s; \mathbf{w}) \right)^2$$

$$\nabla_{\mathbf{w}} \mathcal{L}_{SE}(s, \mathbf{w}) \propto (V_\pi(s) - \hat{V}_\pi(s; \mathbf{w})) \nabla_{\mathbf{w}} \hat{V}_\pi(s; \mathbf{w})$$

Since the true state-value $V_\pi(s)$ is unknown, it is replaced using bootstrapping, as typical for the TD learning procedure. A complete optimization step with learning rate η_w uses the TD error δ as follows.

$$\delta = r_t + \gamma \hat{V}_\pi(s_{t+1}; \mathbf{w}_t) - \hat{V}_\pi(s_t; \mathbf{w}_t)$$

$$\mathbf{w}_{t+1} = \mathbf{w}_t + \eta_w \delta \nabla_{\mathbf{w}} \hat{V}_\pi(s_t; \mathbf{w}_t) = \mathbf{w}_t + \eta_w \delta \psi(s_t)$$

This method learns approximating the long term discounted reward of a given state, when following a certain policy π , but it does not provide inference about taking a certain action. Therefore, a parameterized stochastic policy is defined, that is then successively trained using the learned value estimate. The policy π_θ , parameterized by θ , is defined as a normalized exponential function (softmax) over action preferences $H(s, a; \theta)$. The action preference is estimated using a linear function approximation and employing a feature mapping in form of tile coding.

$$\pi_\theta(a|s) = \frac{e^{H(s, a; \theta)}}{\sum_{b \in \mathcal{A}} e^{H(s, b; \theta)}}$$

$$\text{with } H(s, a; \theta) = \phi(s, a)^T \theta$$

$\phi(s, a)$ signifies the feature encoding for a state-action pair in form of tile coding and θ represents the function weights that need to be optimized. For policy optimization, the derivative of the log-probabilities given by the policy is needed.

$$\nabla_{\theta} \log \pi_{\theta}(a|s) = \phi(s, a) - \sum_{b \in \mathcal{A}} \pi_{\theta}(b|s) \phi(s, b)$$

The policy gradient is used for the optimization of the parameters θ with learning rate η_{θ} .

$$\theta_{t+1} = \theta_t + \eta_{\theta} A_{\pi}(s, a) \nabla_{\theta} \log \pi_{\theta}(a|s)$$

The advantage $A_{\pi}(s, a)$ is estimated by the state-value TD-error as previously described. Alternatively to using only the policy gradient of the current step, eligibility traces accumulate the gradients over consecutive learning steps, improving learning stability and sensitivity for delayed reward.

With the two given components, an actor-critic learning algorithm can be implemented. Since a good state-value estimate is needed to provide meaningful guidance for the actor, usually the critic learns at a higher rate than the actor, which will be achieved by tuning the learning rates, such that $\eta_w > \eta_{\theta}$. An outline for the resulting learning procedure is given in Alg. 1.

Alg. 1: Actor-Critic algorithm for radio parameter optimization

```

 $\eta_w, \eta_{\theta} \in (0, 1)$       ▷ Initialize learning rates
 $\gamma \in (0, 1), \lambda \in (0, \gamma)$   ▷ Initialize discount factors
 $\mathbf{w}, \theta = \mathbf{0}$           ▷ Initialize function parameters
 $D = \mathbf{0}$                 ▷ Initialize eligibility traces
 $s_1 \in \mathcal{S}$             ▷ Initialize starting state
for  $t = 1, \dots, T$  do
   $a_t \sim \pi_{\theta}(a|s_t)$       ▷ Sample action from Policy
   $s_{t+1} \sim P(s|s_t, a_t)$   ▷ Observe successor state
   $r_t = R(s_t, s_{t+1}, a_t)$   ▷ Receive reward
   $\delta = r_t + \gamma \hat{V}_{\pi}(s_{t+1}; \mathbf{w}) - \hat{V}_{\pi}(s_t; \mathbf{w})$   ▷ Compute TD-error
   $\mathbf{w} \leftarrow \mathbf{w} + \eta_w \delta \psi(s)$   ▷ Optimization state-value
   $D \leftarrow \lambda D + \nabla_{\theta} \log \pi_{\theta}(a_t|s_t)$   ▷ Update eligibility traces
   $\theta \leftarrow \theta + \eta_{\theta} \delta D$   ▷ Optimization policy
end

```

Implementation and Preliminaries

The method described has been developed to enable learning on low-power end-devices with constrained computing capabilities, such as sensor nodes. In order to evaluate the algorithms, they were implemented on real hardware and experimentally tested under real world conditions. The hardware platform chosen for experimentation is based on the *STM32WL5x* system-on-chip (SoC), that embeds a low-power Cortex-M4 microcontroller and a sub-GHz radio based on *Semtech's* SX126x.

During the experiments two radio modules are used, one takes the role of an end-node that sends messages to the second module acting as the receiving node or base station. Unlike dedicated gateway radio chips, the used wireless module cannot listen on different channels simultaneously. Thus, the radio configuration for an upcoming message transmission is communicated with the previous transmission. Feedback for a transmission is sent over the same channel as the message. If a transmission fails, the last successfully used channel is used. In case this fails due to dynamic influences, a backup channel that is defined as highest spreading factor (SF12) with highest transmission power (14 dBm) is used.

The computation of the reward for the RL algorithm is based on the required energy for a transmission. This is calculated using a simple energy model consisting of a product of the real transmission power P_{TX} and the time on air T_{OA} of the transmitter. The real transmission power was measured with a digital multi meter and stored on the microcontroller as a lookup table for every configurable transmission power. The time on air can be computed using a formula based on the used radio configuration [24].

The function approximation scheme to estimate the state-value $\hat{V}(s; \mathbf{w})$ and the action preference $H(s, a; \theta)$ both use tile coding to encode the state features. The number of tilings, their offset and size of partitions need to be defined. These hyperparameters set the trade-off between generalization over similar states and accuracy of feature representation. The used values are given in tab. 1.

Tab. 1: Parameters for encoding of state variables using tile coding with 5 tilings

State Variable	# Tiles	Offset per Tile
SF	3	1
TP	4	2
RSSI	4	5
SNR	4	4

In case of the RSSI and SNR value, one tile is reserved for the event of a failed transmission. If this happens, the offset is ignored, thus, the same tile is activated in all tilings. In case of the action preference $H(s, a; \theta)$ the state-action pair has to be encoded. Since there are $|\mathcal{A}| = 5$ discrete actions, each action uses a separate state encoding.

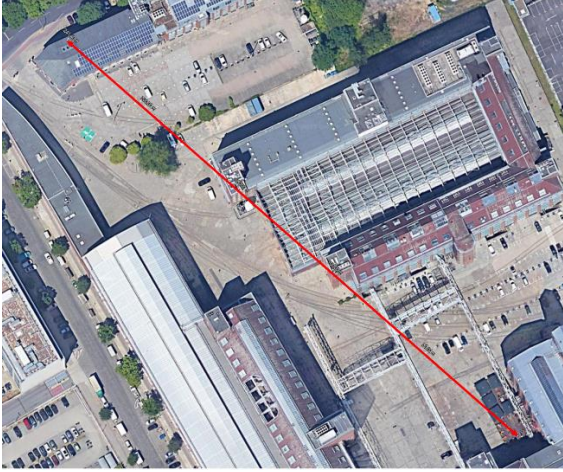


Fig. 1. Satellite view of the urban setting for communication. Distance between transmitter and receiver is 241 m. (©2023 CNES/Airbus, GeoBasis-DE/BKG, GeoContent, Maxar Technologies, Kartendaten ©2023)

The goal of the algorithm is to identify near optimal parameter selection to save energy while ensuring communication reliability. To reflect the importance of the long term energy savings the discount factor is set to $\gamma = 0.99$, this mean the agent tries to maximize its long term future reward. The discount factor for eligibility traces is set to $\lambda = 0.9 \gamma$. The learning rates are set to $\eta_w = 0.6$ and $\eta_\theta = 0.4$ for the critic and policy respectively.

To accurately assess the energy demand, it is important to account for both the transmission energy E_{TX} and the energy overhead E_{Opt} caused by additional computations on the end node. The time for sampling actions based on the policy function is insignificant, optimizing the value weights takes 4 ms per step and updating the policy parameters takes 21 ms, this results in a total time for optimization of 25 ms per step. At 48 MHz clock speed and supply voltage of 3.3 V the controller consumes 3.5 mA.

Experimental Comparison with ADR in LoRaWAN

The ADR scheme is the standard procedure for data rate and parameter optimization in LoRaWAN. There exists no specification how ADR has to be implemented but *Semtech* gives a recommendation for a baseline algorithm [25] that is used during this experiment. Although, LoRaWAN It will be compared experimentally to the developed method described in this work, mainly in terms of long term energy demand. The setting of the experiment is in an urban environment, an overview is shown in Fig. 1. The distance between the receiver and transmitter are 241 m. The walls of the building, cars and other objects in between the two radio

transceivers cause some varying channel degradation.

In the experimental setting, the transmitter sends 5,000 packets of 20 bytes each using the radio parameters proposed by the optimization algorithm. The parameters are recorded and evaluated after the experiments. Fig. 2 shows the accumulated energy consumption after each transmission for the experiment. It includes the energy for transmission itself and the consumption induced by the processing overhead. Five runs of optimization were analyzed, the plot shows the range between the least and most energy efficient run, as well as the mean over the runs. It can be seen that the ADR mechanism in LoRaWAN quickly determines a radio configuration after a short probing phase and keeps it throughout the whole duration, which results in a linear energy consumption over time. In different runs, ADR used slightly different data rates, which results in a difference in energy consumption over time. In case of the implemented actor-critic RL algorithm, the transmitter behaves randomly and seems less goal oriented in the beginning. It needs many samples (transmissions) until a stable configuration for the transmitter is reached and kept. However, due to the long lifetime of wireless sensor systems, even small energy savings scale over time and may accumulate to long term savings.

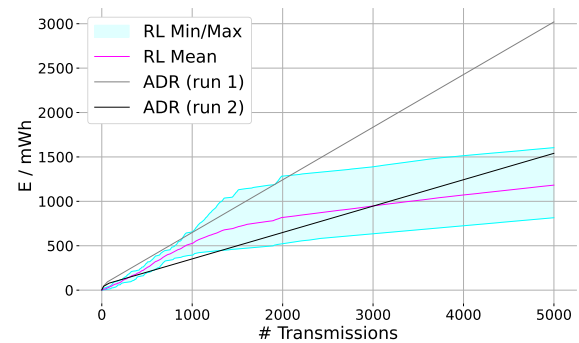


Fig. 2. Cumulative energy consumption of the two methods for comparison in urban setting. ADR converges to a reliable setting quickly but the utilized configuration differs in the two runs. The RL based method need more trial and error but eventually converge to a more efficient configuration.

Comparing the energy consumption with the more efficient ADR run, the RL based approach breaks even at around 3000 message transmissions on average. If an application with one transmission every 15 minutes is assumed, this would mean the energy demand breaks even at around 31 days, which is usually only a fraction of the desired lifetime of a wireless sensor.

Adaption to a Dynamic Wireless Channel

ADR in *LoRaWAN* is not supposed to be used in dynamic channels, e.g. when the transmitting unit is changing its position over time. The RL algorithm supports decision-making by locally incorporating contextual information to determine the appropriate transmitter configuration for the next operation. This means, channel degradation or improvement can be monitored in real-time and addressed by adjusting the radio configuration adaptively. This creates opportunities for mobile sensor nodes and enables the exploration of new network topologies. The end nodes are not dependent on the network server for parameter provisioning, thus, improving their capability of communicating effectively with each other, which is essential in multi-hop or meshed networks.

To demonstrate this behavior the node is set to two different locations where it learns to adapt to the respective condition, the first channel is set to be worse than the second (greater distance to the receiver). The agent is left to converge on the first position for 2000 steps, then, the position is changed to the second location. It can be observed, that the process of finding efficient parameters is quicker than in the first case, showcasing some degree of generalization. After 2000 initial transmissions on each channel, the position is switched back and forth two more times, with 1000 transmissions on each channel. The time for adaption to the new channel is accelerated each time, the agent observes a changed channel condition. This observation can be depicted by comparing the average energy consumption during the process, which is shown in fig. 3. Note, that the energy consumption in the second channel is so much smaller, that it appears to be zero in parts of the plot.

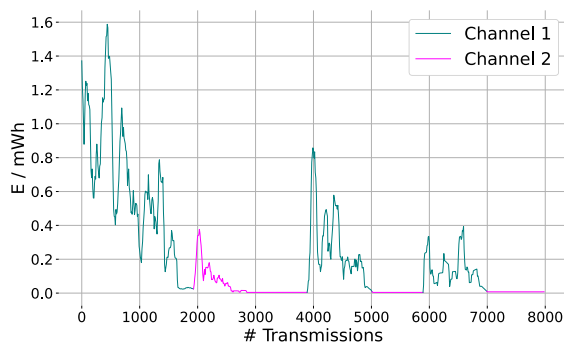


Fig. 3. Energy consumption of the RL method in an alternating channel. Process of finding efficient parameters for the changed channel is faster in every iteration. Energy consumption averaged over 10 steps for smoother visualization.

Conclusion

This work presents an approach to enable low-power sensor nodes to utilize algorithms from

the field of reinforcement learning. This opens opportunities across a wide range of application domains, exemplified here by applying it to radio parameter optimization. Other conceivable use-cases include tasks such as network routing, or timing and balancing of data acquisition, processing, and communication. Moreover, the algorithm's versatility allows for adaptable optimization across diverse objectives, such as maximizing data throughput, enhancing energy efficiency, and ensuring robustness against failures. Decentralized organization in general and adaptive mechanisms such as self-healing and self-configuring capabilities are desired properties of wireless sensor systems in the future. These needs highlight the appeal of intelligent behavior of sensor nodes in the context of wireless sensor networks, which marks a paradigm shift as learning algorithms are commonly associated with substantial computational power typically found in cloud servers.

The implementation of RL algorithms has been described with a special focus on resource constrained hardware as it is common for low-power sensor devices. The outlined algorithm was customized with the goal of developing a decentralized and adaptive learning algorithm that aims at optimizing energy demand of WSNs.

The developed method was implemented and its performance was experimentally evaluated in comparison to a state-of-the-art concept for parameter optimization in the networking standard *LoRaWAN*. Despite the approach of decision making on the device, the presented algorithms showed to be able to compete in a realistic experimental setting. The ability of saving a significant amount of energy long-term helps maximizing the lifespan of sensor nodes in a network. However, ADR doesn't need the amount of downlink communication in direction of the end-node, which serves its purpose in large star networks where a single gateway services thousands of nodes. Locally optimizing radio configurations in real-time opens up opportunities for exploring different network topologies for *LoRa* networks and may help improving overall network efficiency. The method showed promising results in the experimental setup. Nevertheless, it will be a part of future research to further evaluate its performance based on diverse and long-term deployments.

References

- [1] A. Jay, Number of Internet of Things (IoT) Connected Devices Worldwide 2022/2023: Break-downs, Growth & Predictions, *FinancesOnline*, (Access: 20.05.2024) <https://financesonline.com/number-of-internet-of-things-connected-devices>
- [2] L. Cui, S. Yang, F. Chen, Z. Ming, N. Lu, J. Qin, A Survey on Application of Machine Learning for Internet of Things, *International Journal of Machine Learning and Cybernetics* 9 (2018); doi:10.1007/s13042-018-0834-5
- [3] X. Wang, H. Chen, S. Li, A Reinforcement Learning-Based Sleep Scheduling Algorithm for Compressive Data Gathering in Wireless Sensor Networks, *EURASIP Journal on Wireless Communications and Networking* (2023); doi:10.1186/s13638-023-02237-4
- [4] H. Zhang, Y. Song, M. Yang, Q. Jia, Modeling and Optimization of LoRa Networks under Multiple Constraints, *Sensors* 23 (18) (2023); doi: 10.3390/s23187783
- [5] A. Farhad, J.-Y. Pyun, LoRaWAN Meets ML: A Survey on Enhancing Performance with Machine Learning, *Sensors* 23 (15) (2023); doi: 10.3390/s23156851
- [6] M. González-Palacio, D. Tobón-Vallejo, L. M. Sepúlveda-Cano, S. Rúa, Machine-Learning-Based Combined Path Loss and Shadowing Model in LoRaWAN for Energy Efficiency Enhancement, *IEEE Internet of Things Journal* 10 (12) (2023); doi: 10.1109/JIOT.2023.3239827
- [7] F. Azizi, B. Tyemuri, R. Aslani, M. Rasti, J. Tolvaneny, P. H. J. Nardelli, MIX-MAB: Reinforcement Learning-based Resource Allocation Algorithm for LoRaWAN, *2022 IEEE 95th Vehicular Technology Conference* (2022); doi: 10.1109/VTC2022-Spring54318.2022.9860807
- [8] Sensors (Open Access journal): Intelligent Sensors (Zugriff: 15.05.2024) https://www.mdpi.com/journal/sensors/sections/Intelligent_Sensors
- [9] F. Fraternali, Towards Large-Scale Autonomous Wireless Sensor Networks, *arxiv:1906.12001* (2019)
- [10] C. Yan, Q. Ji-hong, Application Analysis of Complex Adaptive Systems for WSN, *2010 International Conference on Computer Application and System Modeling (ICCASM 2010)* 7, S. 328-331 (2010); doi: 10.1109/ICCASM.2010.5620113
- [11] Z. Zhou, X. Chen, E. Li, L. Zeng, K. Luo, J. Zhang, Edge Intelligence: Paving the Last Mile of Artificial Intelligence with Edge Computing, *Proceedings of the IEEE 2019*, 107 (8), 1738–1762 (2019); doi: 10.1109/JPROC.2019.2918951
- [12] R. S. Sutton, A. G. Barto, Reinforcement Learning: An Introduction, *The MIT Press*, Cambridge, Massachusetts, second edition (2018)
- [13] S. P. Singh, T. Jaakkola, M. I. Jordan, Learning Without State-Estimation in Partially Observable Markovian Decision Processes, *Machine Learning Proceedings 1994*, 284–292 (1994); doi: 10.1016/B978-1-55860-335-6.50042-8
- [14] R. J. Williams, Simple statistical gradient-following algorithms for connectionist reinforcement learning, *Machine Learning*, 8(3-4), 229–256 (1992); doi: 10.1023/A:1022672621406
- [15] V. R. Konda, J. N. Tsitsiklis, On Actor-Critic Algorithms, *SIAM Journal on Control and Optimization*, 42(4), 1143–1166 (2003); doi: 10.1137/S0363012901385691
- [16] S. P. Singh, R. S. Sutton, Reinforcement Learning with Replacing Eligibility Traces, *Machine Learning*, 22(1/2/3), 123–158 (1996); doi: 10.1007/BF00114726
- [17] M. G. Lagoudakis, Value Function Approximation, *Encyclopedia of Machine Learning and Data Mining*, 1311–1323, Springer US, Boston (2017); doi: 10.1007/978-1-4899-7687-1_876
- [18] A. A. Sherstov, P. Stone, Function Approximation via Tile Coding: Automating Parameter Choice, *Abstraction, Reformulation and Approximation*, volume 3607 of Lecture Notes in Computer Science, 194–205, Springer, Berlin, Heidelberg (2005); doi: 10.1007/11527862_14
- [19] A. Bensusky, Communication Protocols and Modulation, *Short-range Wireless Communication*; 85–127, Elsevier (2019); doi: 10.1016/B978-0-12-815405-2.00004-X
- [20] Semtech Corporation: AN1200.22 LoRa Modulation Basics. *Semtech Corporation* (2015)
- [21] M. Bor, U. Roedig, LoRa Transmission Parameter Selection, *2017 13th International Conference on Distributed Computing in Sensor Systems (DCOSS)*, 27–34, Ottawa, ON (2017); doi: 10.1109/DCOSS.2017.10
- [22] Semtech Corporation: Understanding the LoRa Adaptive Data Rate, *Semtech Corporation* (2019)
- [23] R. Serati, B. Teymuri, N. A. Anagnostopoulos, M. Rasti, ADR-Lite: A Low-Complexity Adaptive Data Rate Scheme for the LoRa Network, *arXiv: 2210.14583* (2022); doi: 10.48550/arXiv.2210.14583
- [24] Semtech Corporation: AN1200.13 SX1272/3/6/7/8: LoRa Modem Designer's Guide, *Semtech Corporation* (2013)
- [25] Semtech Corporation: LoRaWAN – simple rate adaptation recommended algorithm, *Semtech Corporation* (2016)

Towards Edge AI in Flight Test Data Acquisition: A Proof of Concept for Anomaly Detection in Aircraft Electrical Networks

Rémy Pelluault¹, Ghislain Guerrero¹, Sangaran Sivakumaran¹
¹ Safran Data Systems, 5 Avenue des Andes, 91940 Les Ulis, France

remy.pelluault@safrangroup.com
ghislain.guerrero@safrangroup.com
sangaran.sivakumaran@safrangroup.com

Abstract:

In recent years, the proliferation of artificial intelligence (AI) technologies and their associated use cases has been observed across various industrial and consumer domains. Within the field of instrumentation, the longstanding trend of acquiring and digitizing physical measurements captured by sensors has been further bolstered by the rise of edge computing, enabling early data-to-information transformation. Consequently, the emergence of edge AI becomes a natural extension of this evolution.

However, the deployment of edge AI in the realm of embedded instrumentation introduces new possibilities while also challenging fundamental aspects of the field, including metrology, determinism, miniaturization, and power saving. In light of these considerations, Safran Data Systems has developed a Proof of Concept aimed at integrating an edge AI capability into a flight test data acquisition unit. The primary objective is to leverage this technology for anomaly detection in time series data pertaining to aircraft electrical networks monitoring.

This paper presents the technological approach employed, highlighting its unique features and advantages. Furthermore, the outcomes and results obtained through experimentation are shared, shedding light on the effectiveness and potential of the implemented edge AI solution. Additionally, the paper explores future use cases and potential enhancements, paving the way for continued research and development in this area.

Key words: Machine learning, anomaly detection, time series analysis, on board processing

Introduction

More Electrical Aircraft (MAE) represents a significant advance in the aeronautical sector, aimed at reducing CO₂ emissions and promoting decarbonization. This innovation is transforming aircraft design by replacing combustion engines and traditional mechanical systems with electrical technologies.

The transition to MAE poses several major challenges for aircraft manufacturers, and by extension, for Safran Data Systems. A disruptive innovation in the aeronautical industry requires special care during certification to ensure compliance with

organizations such as the EASA or FAA, which translates into a massive multiplication of measurement points and data, to ensure the aircraft's nominal operation. However, current on-board-to-ground data transmission technologies are often limited in data rate, exceeding just a few tens of Mbits, which may prove insufficient to efficiently manage the increasing volumes of data generated as required by aircraft manufacturers.

And this trend doesn't just apply to future electric aircraft. Generally speaking, in flight testing, the doctrine is to record as much as possible, to oversize the acquisition, even if it means exploiting only a tiny fraction of what we

collect. The price of an unsuccessful test flight is extremely dissuasive, which leads to two statements: "Prevention is always better than cure". In addition, when a problem occurs: "track down the root cause of the disturbing event". This leads to an oversizing of the aircraft measurement plan: more sensors, more storage capacity, increased throughput, etc... If normality is expected, anomaly is unacceptable.

So how can we manage these constantly growing quantities of data? From a technical point of view, we can always improve throughput, storage, computing power, telemetry... However, in terms of human resources? How can we effectively leverage this huge amount of data, which will often just be recorded without ever being processed due to a lack of human resources? Data is more and more the heart of our industries and we still need to be able to extract information from data in an efficient and relevant way.

One innovative solution is the use of Artificial Intelligence (AI). Such algorithms could be used cleverly to process part, or even all, of the data, which would otherwise probably just be recorded without ever being considered. The use of AI in this context comes up against a number of constraints. Traditionally, the flight test domain requires deterministic approaches to ensure the reliability and predictability driven by certification and safety. The somewhat 'black-box' aspect of AI, where decision-making processes are not entirely transparent, poses a problem in an environment where every component must be fully certified and justifiable. Nevertheless, there remains significant potential for AI to assist test operators. In our example, we would like to propose an algorithm for real-time anomaly detection, helping engineers to identify potential problems more quickly and accurately. Of course, the role of such an AI must remain that of an assistant, not a decision-maker. AI, and anomaly detection, is not entirely new in the world of instrumentation [1], but there is currently very little embedded and real-time application, which could remain relevant for specific use-cases

Anomaly detection

The project implies the creation of an algorithm integrated into an airborne platform. This algorithm will be specifically designed to supervise an aircraft's electrical networks in order to detect any anomalies.

Today, it is of course possible to monitor these electrical networks using "conventional" methods such as Total Harmonic Distortion (FFT), but these on-board techniques have

certain limitations, particularly when it comes to detecting complex anomalies.

Indeed, the application of these methods requires manual definition of normality thresholds. For example, an operator might judge an electrical AC signal to be nominal if it is between 110 and 120 V with a THD lower than 5%, no carrier current present, etc...

However, this approach only detects predefined events, potentially allowing signals to slip through which might subjectively be judged as abnormal, but which do not correspond to the established criteria. This restriction represents a significant drawback, as it limits the system's ability to identify only a finite set of anomalies, thus increasing the risk of non-detection of new anomalies or variants of previously uncharacterized anomalies. The idea would be that, using AI, we could train it on signal considered valid and warn us if the monitored signal diverges from this normality.

AI creation

The project has the significant advantage of generating easily large-scale artificial datasets.

It is possible to generate sinusoidal signals considered to be valid (for example, at 400 Hz and 115V) as well as signals with various anomalies such as overvoltages, spikes, noise, carrier current or modulations. Subsequently, we will be able to validate the model with real data, extracted from an arbitrary generator, in order to test its robustness and accuracy under a variety of conditions.

Initially, our architecture was based on an artificial intelligence system with supervised learning. In this approach, the model was fed with both anomaly-free data and data containing one or more categorized anomalies.

The objective of the algorithm was to classify the inputs as "nominal" or "abnormal". However, this approach was quickly discarded. The main drawback of this method lies in its intrinsic limitation: it could only detect a finite number of predefined anomaly categories. As a result, the model could only identify anomaly types for which it had been explicitly trained for, making it inefficient to detect new anomalies or previously uncharacterized variations. In the end, our algorithm was not much of an evolution compared with more "classic" methods, since here again, the algorithm was not able to adapt itself to new situations.

The real revolution is unsupervised learning: a program that learns by observing "normal" or typical data. Later, when used, this program can alert us if something unusual happens,

something that does not look like what it initially learned. To develop such a system, we will explore different methods and architectures.

Let us start with the basics: the neuron. The simplest type of neuron is called a **perceptron**. It is often the first model used for simple tasks in machine learning. It works as follows: it takes an input, multiplies it by a weight, adds a bias (a fixed adjustment), then applies what is known as an activation function to obtain a final result. Despite its simplicity, the perceptron is widely used in machine learning

However, the perceptron is very limited especially for time series analysis. In a time series, each value shall be considered in its context, because information is not just a series of independent, isolated numbers. A value at a given moment ($x(t)$) has a given meaning because it is part of a sequence of values. The standard perceptron, which process isolated inputs as single values, is therefore not at all suited to time series and lead us to consider an improved version of the perceptron: the **RNN** (Recurrent Neural Network). This type of network is designed to take into account the time or order of the data.

To achieve this, in addition to the usual input, weights, bias and activation function, the RNN uses a kind of feedback loop. This means that information is not just processed and forgotten; instead, it circulates back through the network. For example, information from two previous time steps $x(t-2)$ influences information from previous time step $x(t-1)$, which in turn affects current information $x(t)$.

It is similar to an IIR (Infinite Impulse Response) digital filtering system, where the current output $y(t)$ depends not only on the current input $x(t)$ but also on all previous inputs. In this way, RNNs are able to "remember" past data, which is crucial for processing time series. However, RNNs have a limitation: although they are affected by recent inputs, their ability to remember older information is limited. This means they tend to have a "short-term memory", which can be a problem when learning or recalling details of older data in a long sequence.

To overcome the short-term memory limitations of RNNs, **LSTM** (Long Short-Term Memory) networks were developed. These networks are an advanced variant of RNNs, designed specifically to avoid the problem of memory loss of old information.

LSTMs operate with a more complex structure, enabling them to retain information for long periods. They incorporate so-called "gates" -

mechanisms that decide which information to keep and which to discard.

Thanks to these gates, an LSTM can efficiently recall important events in a sequence, even if they occurred a long time ago. This makes it particularly useful for tasks such as time series prediction. We choose this neural network architecture for our project.

A quick note about transformers: there are very promising for anomaly detection and time series analysis thanks to their attention mechanism. However, they require a large number of parameters to perform correctly, and are still relatively recent, which may be incompatible with embedded architecture. Their operation is completely different from perceptrons, RNNs and LSTMs. However, these architectures are very interesting when computing power is not a limiting factor, such as for ground stations and post-flight processing.

In addition to LSTMs, we will be using an auto-encoder system.

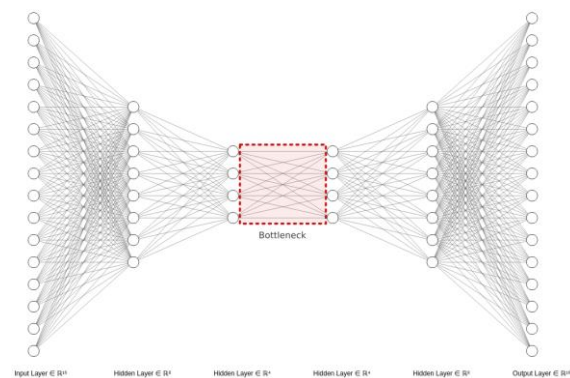
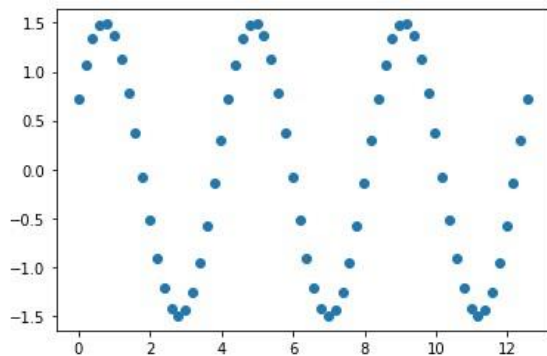


Fig1: An example of autoencoder architecture

The aim of an auto-encoder is to reproduce as output what it receives as input. Assume we feed it a sine wave curve, with the intention that the output replicates this same sine wave. This may seem uninteresting at first glance, but the interest of the auto-encoder lies in its double-funnel structure. In the center, the feature space (called latent space) is smaller than at the ends. This means that, to successfully reproduce the input sine, our model must find a simplified way of representing it, with very few parameters.

We can draw an analogy with human reasoning: it is a bit like a person having to draw a sine wave.

If we give an individual the following vector:



And ask him to remember it, he could learn all 64 values that make it up. But more likely he will recognize a sine wave, and so, using a simple formula like $A \sin(x\omega + \phi)$, he will memorize just 3 values: amplitude, frequency and phase shift. Therefore, instead of storing 64 separate values for our sine wave, we would only need 3 parameters, which is a encoded (or compressed) version of the original signal.

The same applies to our algorithm. The model is trained ingesting signals that the user considers nominal. Once the training is completed, the parameters are set, and the auto-encoder can reproduce the learned signal. An auto-encoder trained on a sine wave is fed by such signal, it will output a sine wave with similar characteristics (amplitude, phase shift and frequency). But if it is fed by a different signal, such as a square wave, the output will be very different from the input, as it is not possible to represent a square waveform adjusting A , ω and ϕ of the function $A \sin(x\omega + \phi)$. An output radically different from the input indicates an anomaly.

The denser and larger a neural network is, with many layers and connections, the more it can learn to recognize complex functions. The monitoring of simple sine waves does not really need very large neural networks. However, this type of system is also capable of processing signals far more complex than simple sine waves, such as detecting events in signals coming from vibro-acoustic, dynamic strain or pressure measurements.

Learning these tasks is surprisingly simple: the system listen to a signal considered nominal to learn and recognize it. Once it has done this, it will be able to detect anomalies on its own. In short, by listening to and memorizing what is normal, the neural network learns to identify

what is not, signaling any deviation as an anomaly. This makes these systems extremely efficient for monitoring and detecting problems without continuous human supervision.

Testing the PC model

We use a simple method to decide whether a signal is normal or abnormal: we compare the model prediction with the actual input. If our model and the signal are perfect, the result of this comparison (i.e. the difference between prediction and input) should be a zero vector. If the values of the output vector deviate from zero, this indicates that the incoming signal could be abnormal.

To decide whether a signal is normal or abnormal, we have several options:

- 1. Sum of absolute values:** We add up the absolute values of the points on the output vector. If the total exceeds a certain threshold, which we call ϵ . If the total exceeds a certain threshold (ϵ), then the signal is considered abnormal.
- 2. Least squares method:** This method gives greater weight to values that deviate significantly from zero. If the sum of the squares of the deviations exceeds the threshold ϵ , the signal is considered abnormal.
- 3. Examining each value:** We examine each point of the output vector individually. If any of these values exceeds the ϵ threshold, we classify the signal as abnormal.

In our case, we prefer to use the third method as it gave better results for our application. But the important thing to remember is that whatever method we choose, it is crucial to define a value for ϵ . This ϵ value is essential as it helps maximizing the accuracy of our model by allowing us to effectively distinguish between normal and abnormal signals. We will soon delve deeper into how to choose this value optimally.

Our first computer tests are very encouraging. We use synthetic data to train our model, then test it on real data taken by a data acquisition unit fed by an arbitrary function generator. The results show that our model is effective.

We evaluate the quality of a model by creating a data set consisting of real signals recorded by a data acquisition unit. This dataset is divided in two: one half contains nominal data and the other, "abnormal" data. Anomalies can be caused by a variety of factors, such as the addition of even and odd harmonics, frequency

or amplitude shifts, or the presence of carrier currents.

When we compare different models to determine the most effective, it is essential to harmonize our approach to the ϵ threshold. If ϵ is too small, even slight noise could cause a signal to be classified as "abnormal", resulting in many false positives (the model reports an anomaly when there is none) and most likely no false negatives. Conversely, a ϵ too large could cause our model to consider all signals as healthy, increasing false negatives and eliminating false positives.

So, how do we choose the right ϵ for each of the models we want to test? We decided to set ϵ at a level where there are no false positives. This approach standardizes the basis of comparison for all the models we will evaluate in the future, enabling a fair and consistent evaluation between them.

It is important to note that according to the concept of operation (CONOPS), we would probably prefer to have zero false negatives, even if this implies accepting some false positives. False positives can be re-evaluated by a human operator to confirm whether they really represent an anomaly, while a false negative could remain permanently undetected. The choice of the ϵ threshold we use to compare our models is based on ease of comparison between them. However, nothing prevents us from adjusting ϵ later on to modify the sensitivity of our model according to the specific needs of final user.

Our first auto-encoder model was of the following size and architecture:

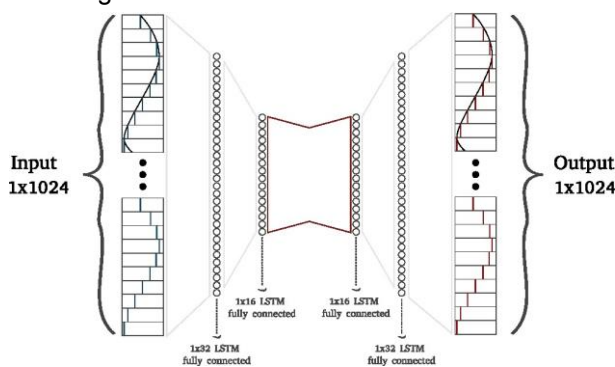


Fig2: First autoencoder+LSTM model

Relatively frugal with its 15,000 parameters, our model had the following already promising performances

		Predicted values	
		0	1
True values	0	497	0
	1	17	486

Fig3: Confusion matrix of first model

The next step is to port this architecture to the host target.

Embedding software

We are now going to integrate our current model into the XMA systems, one of the most advanced modular DAU. We will leverage the OBP, or On-Board Processing module. OBP is designed to run C-language programs. It is specifically used to process data, whether periodically sampled or aperiodically produced, in an XMA system. This module also offers local serial ports and discrete I/Os, as well as a Gigabit Ethernet interface.

The OBP is particularly customizable, making it ideal for quick prototyping needs. It is equipped with a Zynq-7020, a System On chip (SOC) that combines a FPGA and a processing unit running an optimized Linux to be more responsive (Preempt-rt). Users can develop their own applications [2] thanks to an SDK that provides the necessary tools and guidance.

To begin with, we are going to try and implement our algorithm in the software part of the SOC. The OBP, being an optimized embedded system, does not directly support complex frameworks like Keras. Therefore, we need to compile the code in C or C++ to run our algorithm on the target. To convert models created in Keras to C code, we used a tool called Keras2C.

We have successfully integrated our model into our OBP module and can now read data from a sensor acquired by a generic analogue module, like the ANA module. This system captures signals at a frequency of 32 768 Hz. The model works well, and can correctly identify anomalies in the signal when artifacts are artificially added with a generator. The performance obtained in terms of accuracy is comparable to the PC version algorithm. However, this first non-optimized implementation does not allow real time signal processing.

Our model processes a 1024-point window as input. To keep pace in real time, this means processing 32,768 points per second, or 32 windows per second, giving an ideal processing time (known as "inference time") of 31 milliseconds. At this stage, without optimization, our model requires 5 seconds to infer a single window

To improve this, we are considering two main optimizations:

1. Quantization: the original model weights are stored in 32-bit format (FP32). We could convert them to smaller formats, such as FP16 or especially INT8. Calculating with integers rather than floating-point numbers could dramatically reduce computation time and potentially double inference speed. It would also reduce the memory footprint; although this is not the main concern (the non-optimized model size is just about 256 KB).

2. Pruning: This technique consists of removing non-significant neural connections to lighten the model. Fewer connections means fewer calculations and therefore faster inference, which is crucial for real-time applications and resource-constrained devices. This approach can maintain high accuracy while improving speed, with the potential to double inference speed, albeit at the cost of some effort and perhaps a slight drop in quality.

Even with the optimizations envisaged, achieving an inference time of 31 milliseconds remains a considerable challenge. We will probably have to explore more radical options to get there.

A long-term solution could be to consider a different type of hardware. Traditional processors (CPUs) are not particularly efficient for matrix computation, which are at the heart of machine learning algorithms. The GPU (Graphics Processing Unit), known for its ability to handle such computations efficiently, offers a better balance between performance enhancement and development simplicity. However, neither OBP nor any other XMA

module currently incorporates a GPU as of today. The GPUs have a large footprint, consume and dissipate a lot, making them difficult to embed in compact DAU modules like the XMA. However, other flight test instrumentation systems, such as the MDR (Modular Data Recorder), have GPU-capable platforms. Another option would be to use an FPGA (Field-Programmable Gate Array), designed for parallel computing and promising excellent performance in terms of inference time and energy efficiency. However, development and deployment on FPGAs are more complex. It is an attractive solution, but for this proof-of-concept, we decided to explore the full potential of the CPU implementation. We will consider this solution for future developments.

Coming back to our inference time problem, another option would be to modify the auto-encoder model itself, reducing the number of parameters. By progressively reducing the size of our auto-encoder, we have achieved promising results and similar accuracy, with an even more resource-efficient model.

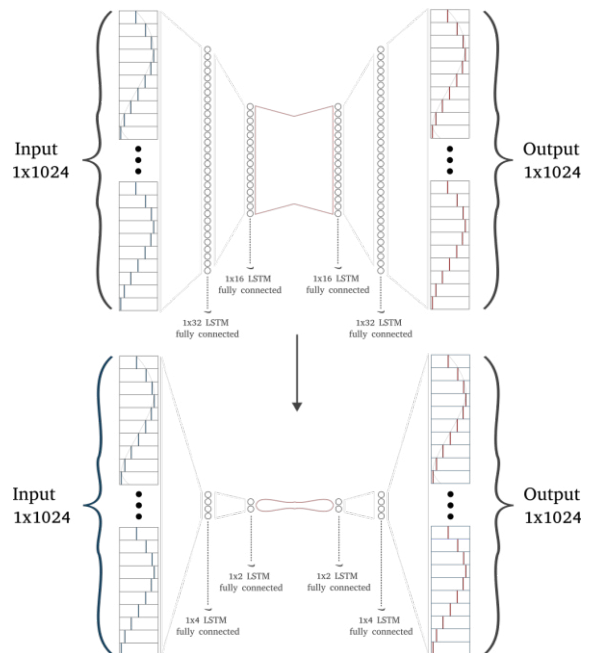


Fig4: shrinking down the precedent model

Just as deep, but 10 times narrower, this model has only 300 parameters, 50 times less than before, with limited impact on accuracy.

Parameters	Accuracy	TPR
15 000	98,8	97,7
300	96,9	93,9

The inference time for this new model on our target system is 80 times faster, or about 60

milliseconds. We are not yet fast enough for real time processing, but we are getting close. In fact, with a little more effort, it would be quite feasible to analyze a signal in real time using our on-board CPU. The performance we have achieved is considered well enough for a demonstrator. For the future, it does not seem wise to continue fine-tuning our current model for this CPU configuration. It would be more appropriate to develop a solution based on specific hardware acceleration.

What's next?

We are now concentrating on hardware acceleration, in particular using an FPGA. The next logical step would be to develop a dedicated hardware acceleration to perform the necessary computation directly on the FPGA. The expected performance of the FPGA is very promising, and should greatly surpass the performance currently achieved with the CPU.

Here is a comparison between the current performance of our implementation and the performance we hope to achieve in the near future with an FPGA, maintaining the same accuracy:

Type	Inference (ms)	Architecture	Parameters
CPU	60	16x4x4x16	0.3 k
FPGA	1	4x2x2x4	15 k

Using the FPGA of the same platform as before, but with a little further development, we anticipate offering the same real-time accuracy, process several signals in parallel, and use larger models.

Model size is a crucial aspect for the future. We have already shown that a simple network can deliver comparable performance. So why consider a larger network? In our current case, which involves monitoring AC electrical networks, the small size of our model is not a problem. However, for the future, it would be interesting to detect anomalies or event of interest in much more complex time series, such as those arising from vibro-acoustic phenomena. For these cases, a larger model, capable of modelling complex phenomena almost perfectly, would be required. While a 300-parameter model may be enough for predictable periodic signals such as sine waves, initial results shows that a larger model will be able to monitor much more sophisticated signals.

Another option would be to use a GPU, which offers many advantages. GPUs, especially those from NVIDIA with CUDA, make it much easier to deploy neural networks, offering

excellent performance. It is almost certain that if we deploy our model on a GPU-equipped platform, we will achieve real-time performance without difficulty. While it is entirely possible to integrate neural networks on FPGAs, GPUs, with their ability to perform matrix calculations and store large amounts of information in their VRAM, are often preferred to FPGAs

The MDR (Modular Data Recorder), designed by Safran Data Systems, is a modular flight test recorder with internal media for storing data from the aircraft.

The MDR is larger and more powerful than the XMA, and can be used for computationally intensive applications, such as video encoding, which may require the use of GPUs. Like the XMA-OBP, the MDR provides a user processing module and embeds a more complex platform, including a CUDA-compatible NVIDIA GPU. It would therefore be entirely feasible to integrate our temporal analysis algorithms. This has already been done for object detection algorithms in the past [3]. In addition to its function as a multimedia recorder and telemetry gateway, the MDR is also designed to capture all the data streams generated by the flight test installation of a test vehicle, making it a strategic choice for the implementation of anomaly detection algorithm, allowing the user to incorporate edge-computing activities into his measurement plan.

On the other hand, we could also consider positioning our algorithms even closer to the source of the measurements than our current XMA.

Given that models as frugal as 300 parameters offer satisfactory performance, we might consider deploying these nano-models, such as the one for anomaly detection in power grids, in an IoT-like context. In particular, this could be achieved using μ MA [4], a miniaturized and distributed data acquisition unit, enabling physical deployment as close as possible to the measurements.

Throughout this document, we have discussed a machine learning algorithm for power network analysis. However, the main objective is to demonstrate the ability of our equipment to integrate machine learning algorithms. One of the target would be to offer a software package (SDK, framework) enabling the instrumentation engineers to integrate their own algorithms as easily as possible. Currently, it is possible to integrate algorithms on the CPU of an OBP, as we have done. However, for custom ML algorithms, the hardware acceleration offered by the GPU (in the MDR) or FPGA (in the XMA) would be preferred.

Conclusion

In the near future, we anticipate a considerable increase in the amount of data to be transferred, stored and analyzed during flight testing campaigns. To maximize the support that Safran Data Systems can offer to aircraft manufacturers, it will become necessary to go beyond the simple acquisition, recording and uploading of signals. Each link in the chain should become an active agent, leveraging AI to facilitate and accelerate test set-up and data processing.

We have already explored anomaly detection, but time series analysis offers far more possibilities.

With the right algorithms, we could, for example, consider the automatic detection of sensors when configuring data acquisition units, or the automatic labeling of data to identify different phases of flight. We can easily imagine greatly simplifying "preflight-check", where each agent (XMA/MDR/ μ MA) checks the behavior of each signals before a flight to ensure that everything runs smoothly.

Generally speaking, multiplying small algorithms would save operators a considerable amount of time. By increasing efficiency, we are convinced that we could save many flight or engineering hours, whether by offering our own algorithms or by allowing users to implement their own models. This can be done via a centralized computing approach, or by deploying at the edge of the system more frugal nano-models.

Glossary

AI: Artificial Intelligence

CPU: Central Processing Unit

DAU: Data Acquisition Unit

EASA: European Union Aviation Safety Agency

FAA: Federal Aviation Administration

FFT: Fast Fourier Transform

FPGA: Field Programmable Gate Array

FTI: Flight Test Instrumentation

GPU: Graphical Processing Unit

IoT: Internet of Things

LSTM: Long Short-Term Memory

MDR: Modular Data Recorder

MAE: More Electrical Aircraft

ML: Machine Learning

MOE : More electrical aircraft

OBP: On-Board Processing

PoC: Proof of Concept

RNN: Recurrent Neural Network

SDK: Software Development Kit

SDS: Safran Data Systems

SOC: System On a Chip

Sps: samples per second

THD: Total Harmonic Distortion

XMA: eXtra Modular Acquisition unit

References

- [1] F. Morel, C. Barreyre, A. Charcosset, O. Coustie, J-E. Denis, L. Hammoud, N. Hans, B. Rouzier, Anomaly detection: a first AI based application for OASIS, *ETTC 2023, Toulouse, 2023*.
- [2] V. Belaud, G. Guerrero, R. Pelluault, Q. Lecoq, On-Board Processing: A Decade of Experience Opening to new Applications, *ETTC 2023, Toulouse, 2023*.
- [3] Hardt, S. & Faber, M. (2023). Vlab – Enhanced Video and Data Pre- Processing. International Telemetry Conference Proceedings, 58.
- [4] G. Guerrero, V. Chomel, F. Monteil, O.Pinto. A new modular electronics approach applied to instrumentation units, *ETTC 2020 (Virtual)*.

Link Resource Scheduling Technology of Networked Telemetry System for LEO Constellations

Jingwei Hao¹, Jingang Zhang¹, Yan Wang¹

¹ Beijing Institute of Astronautical Systems Engineering, Fengtai Strict, Beijing, China
hjwbit@163.com

Abstract:

In recent years, many mega Low Earth Orbit (LEO) satellite constellation plans to provide global Internet services have emerged internationally. The Tracking, Telemetry and Command (TT&C) system is the life line to ensure the normal operation of LEO satellites, and the telemetry system is the key in monitoring the operation status of LEO satellites. The networked telemetry system which is based on High Earth Orbit (HEO) and Medium Earth Orbit (MEO) satellites has no coverage blind area, is applicable to various types of LEO constellations and can serve LEO satellites with abnormal attitudes. Concerning the stable-burst hybrid transmission requirements of LEO satellite telemetry data, we studies the distributed scheduling algorithm of ISL resources in the networked telemetry system. Based on the multi-agent deep reinforcement learning architecture, each MEO satellite dynamically allocates MEO beam and time slot resources according to the latest state of the system, and prioritizes the transmission of high-valuedata to increase the value of the total transmitted data of the system. Meanwhile, we designs a deep Q-network architecture to reduce network traning and storage overhead. The simulation results show that the value of the total telemetry data transmitted by the system is not less than 85% ofthe upper bound.

Key words: LEO constellations, Networked telemetry system, Satellite telemetry data, Resources, Deep Q-network.

1 Introduction

In recent years, numerous large-scale Low Earth Orbit (LEO) constellation projects providing global internet services have emerged internationally. These include the Starlink constellation, consisting of 41,926 LEO satellites[1]; the OneWeb constellation, composed of 648 LEO satellites[2]; and the Kuiper constellation, comprising 3,236 LEO satellites[3]. As of February 2023, SpaceX has successfully launched over 3,580 satellites. The OneWeb constellation, with its 648 LEO satellites, aims to provide high-speed broadband internet services to rural and remote areas. In April 2019, Amazon announced the deployment of its large broadband satellite internet constellation, Kuiper, to offer broadband internet connectivity to remote areas. This project plans to deploy 3,236 satellites within a decade, distributed across 98 orbital planes at altitudes of 590 km, 610 km, and 630 km.

In addition to these mega-LEO constellations, there are also various smaller LEO constellations currently in existence. These constellations serve purposes such as Earth observation, meteorology, disaster mitigation,

and communication. As of June 2023, the global number of LEO satellites has surpassed 7,500, encompassing a wide range of functionalities. With the advancement of mega-LEO constellation projects and various functional LEO constellation plans, the number and variety of LEO satellites worldwide are expected to further increase in the future.

2 LEO Satellite Telemetry Systems

LEO satellite telemetry systems are primarily categorized into three types: traditional ground-based telemetry, space-based telemetry via LEO inter-satellite networks, and space-based telemetry via medium to high Earth orbit inter-satellite networks.

(a) As shown in Fig. 1, the traditional ground-based telemetry system mainly includes a mission center, a network of ground control stations, and the LEO constellation itself. When an LEO satellite is outside the line of sight of a ground control station, the telemetry data generated by the satellite can only be temporarily stored in local buffers. Once the satellite comes within the line of sight of a ground control station, it transmits both the real-time generated telemetry data and the buffered telemetry data to the ground control station via

the satellite-to-ground link. Finally, the telemetry data is transmitted to the mission center through the ground network for further processing[4].

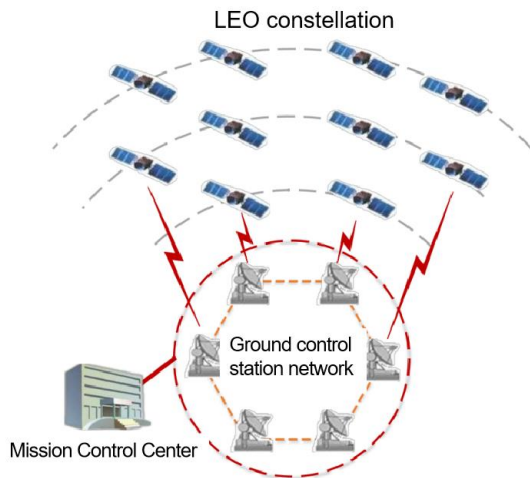


Fig. 1. Ground-Based Telemetry System

(b) As illustrated in Fig.2, space-based telemetry systems utilizing LEO inter-satellite networks establish inter-satellite links among the LEO satellites. When an LEO satellite is not visible to a ground control station, the telemetry data can be relayed hop-by-hop through the LEO inter-satellite network to a satellite that is within the line of sight of the ground control station. The data is then transmitted to the ground control station via the satellite-to-ground link[5].

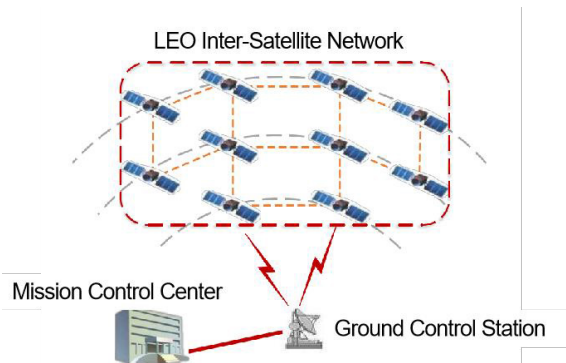


Fig. 2. Space-Based Telemetry System Utilizing LEO Inter-Satellite Networks

(c) As depicted in Fig.3, networked telemetry systems consist of LEO constellations and medium to high Earth orbit (MEO/HEO) constellations, with inter-satellite links existing between adjacent MEO/HEO satellites and LEO satellites. Regardless of whether the LEO satellites are visible to ground control stations, they can transmit telemetry data to the control stations and the mission center through the MEO/HEO inter-satellite network and the MEO/HEO satellite-to-ground links.

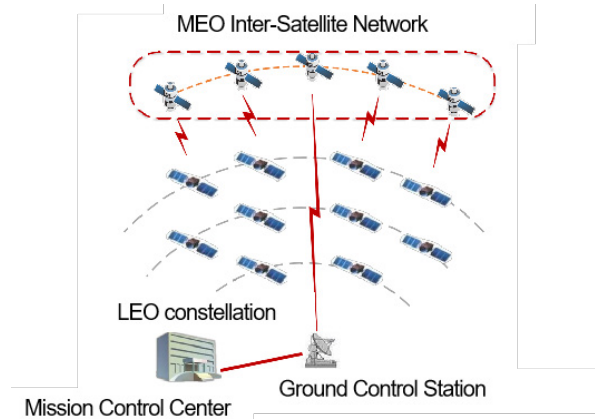


Fig. 3. Space-Based Telemetry System Utilizing MEO/HEO Inter-Satellite Networks (Networked Telemetry)

For ground-based telemetry systems, the return of telemetry data relies on direct line-of-sight satellite-to-ground links. Most countries find it challenging to establish control stations globally, resulting in significant telemetry coverage blind spots. Consequently, satellites outside domestic borders struggle to transmit telemetry data to the mission center in a timely manner. However, for networked telemetry systems, when LEO satellites are not visible to ground control stations, telemetry data can be transmitted continuously and without blind spots through the MEO/LEO inter-satellite network[6].

In contrast, for telemetry systems based on LEO inter-satellite networks, although multi-hop transmission through the LEO inter-satellite network can achieve continuous and blind-spot-free telemetry data transmission, this is only applicable to LEO constellations with inter-satellite links. For LEO constellations without inter-satellite links, this method is ineffective. Comparatively, networked telemetry systems do not rely on LEO inter-satellite links and are thus applicable to various types of LEO constellations. Additionally, the inter-satellite links in LEO communication constellations typically use laser or broadband microwave links. If a satellite experiences attitude anomalies, the beam of the inter-satellite link cannot be aligned, resulting in a transmission interruption. In this scenario, telemetry systems based on LEO inter-satellite networks cannot transmit telemetry data. On the other hand, networked telemetry systems use narrowband microwave links between MEO/LEO and LEO satellites, with LEO satellites using omnidirectional antennas. Therefore, even if an LEO satellite experiences attitude anomalies, it still can transmit telemetry data.

Tab.1 compares the characteristics of the three telemetry mechanisms mentioned above. From the analysis, it is evident that networked

telemetry systems eliminate coverage blind spots, are applicable to various types of LEO constellations, and can service satellites with attitude anomalies. Therefore, they are more suitable for transmitting telemetry data for LEO constellations.

Tab. 1: Comparison of Characteristics of Different Telemetry Mechanisms

Characteristic	Traditional Ground-Based Telemetry System	Telemetry System Based on LEO Inter-Satellite Networks	Networked Telemetry System
Telemetry Data Transmission Relies On	Yes	Yes	Yes
Coverage Blind Spots	Yes	No	No
Applicability	No	No	Yes
Service for Satellites with Attitude Anomalies	No	No	Yes

3 Main Research and Contributions

In LEO constellations, satellite transmission power is typically limited. Additionally, to ensure telemetry data transmission even during attitude anomalies, LEO satellites are usually equipped with omnidirectional control antennas, inevitably resulting in lower transmission gains compared to directional antennas. Moreover, the distance between LEO and MEO satellites is considerable, leading to significant signal propagation attenuation in inter-satellite links between LEO and MEO satellites, thus limiting the transmission rate[7].

In a networked telemetry system, LEO satellites transmit telemetry data using omnidirectional antennas, while MEO satellites employ directional beamforming to receive telemetry data. Due to the narrow beamwidth, each MEO satellite beam can only serve one LEO satellite in a single time slot.

The term "link resources" refers to the transmission resources of different MEO satellite beams in different time slots. The orthogonal transmission resources of a single MEO satellite beam in a single time slot are defined as a single channel. Networked telemetry systems use orthogonal allocation of link resources to ensure stable and reliable telemetry data transmission.

As illustrated in Fig.4, in the MEO-LEO networked telemetry system, LEO satellites first generate telemetry data, including health status data, fault diagnosis data, program execution

data, etc. This data is then transmitted via MEO-MEO links to the MEO satellites directly connected to the ground station. Finally, the MEO satellites connected to the ground station unload the telemetry data via the MEO-ground link, which is further stored and processed at the mission center. Considering that the data generation state of LEO satellites is a mixed constant-random state, this paper proposes a distributed dynamic resource scheduling architecture. In this architecture, each MEO satellite dynamically allocates MEO-LEO inter-satellite link beam and time slot resources based on the latest system state, prioritizing the transmission of high-value data to improve the overall transmission data value of the system.

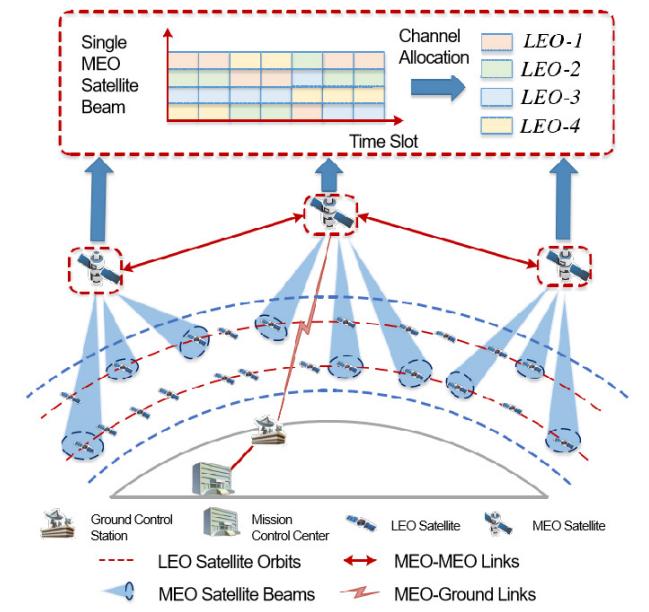


Fig.4. Distributed Link Resource Scheduling in Networked Telemetry System

4 Method

4.1 System Model

Considering that the data generation state of LEO satellites is a mixed constant-random state, MEO satellites utilize deep reinforcement learning to dynamically determine the channel allocation scheme. The training experience required for reinforcement learning is initially recorded locally by MEO satellites and then offloaded and stored at the mission center. Subsequently, the mission center utilizes this experience to train the Deep Q-Network (DQN) used to formulate the channel allocation scheme. Finally, the trained DQN is uploaded and deployed to the MEO satellites.

Upon completing the initial training and deployment of the DQN, the overall process of telemetry data transmission in the system is as shown in Figure 5: At the beginning of each time slot, the LEO satellite first informs the

current state to the MEO satellite. Each MEO satellite possesses a wide beam to specifically collect status information from LEO satellites within its coverage area. Frequency division multiplexing is used within the wide beam to collect status information from different LEO satellites. The propagation delay between MEO and LEO is approximately 0.03s, while each time slot length is 0.25s, allowing MEO satellites to promptly obtain status information from LEO satellites. Then, based on the trained DQN, the MEO satellite determines the channel allocation scheme and broadcasts it to different LEO satellites in the current time slot. Finally, the LEO satellites transmit telemetry data to the designated MEO satellite on the allocated channels.

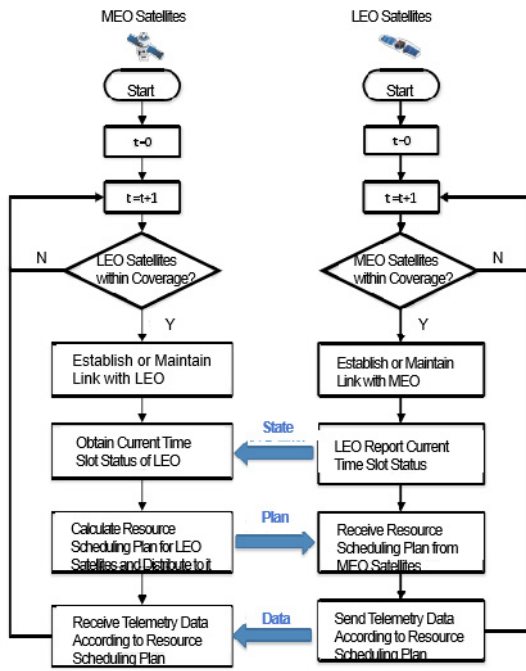


Fig. 5. Distributed Resource Scheduling and Data Transmission Process

This section outlines the system model and operational mechanism, detailing the utilization of deep reinforcement learning for dynamic channel allocation and the subsequent telemetry data transmission process between LEO and MEO satellites as depicted in Figure 5.

4.2 Problem Optimization

In the system, there are a total of I LEO satellites, each equipped with one omnidirectional antenna with a transmission power of P . There are also J MEO satellites in the system, with each satellite equipped with K movable directional beams with a bandwidth of B . The system allocates channels for T time slots, with each time slot having a length of T_S . In each time slot, a directional beam from an

MEO satellite can only serve one LEO satellite. Here, we define the set of LEO satellites as $\mathcal{I} = \{1, 2, \dots, I\}$, the set of MEO satellites as $\mathcal{J} = \{1, 2, \dots, J\}$, and the set of time slots as $\mathcal{T} = \{1, 2, \dots, T\}$. The link transmission matrix is defined as $A_{I \times J \times T}$, with its matrix elements denoted as $a_{i,j}(t) = 1$. If the i -th LEO satellite transmits data to the j -th MEO satellite in time slot t , then $a_{i,j}(t) = 1$, otherwise $a_{i,j}(t) = 0$.

In order to maximize the total transmission data value of the networked telemetry system, this paper optimizes the link transmission matrix $A(t)$ and the cache transmission matrix $B(t)$. Accordingly, the objective function can be constructed as:

$$\max_{\{A(t), B(t)\}} \lim_{T \rightarrow \infty} \frac{1}{T} \sum_{t=1}^T V(t) \quad (1)$$

In addition, the constraints of the networked telemetry system are as follows:

1) Each LEO satellite can be served by at most one MEO satellite in each time slot. Therefore, for $\forall i \in \mathcal{I}, t \in \mathcal{T}$, we have $\sum_{j=1}^J a_{i,j}(t) \leq 1$.

2) Since each MEO satellite has K beams, at most K LEO satellites can be served by the same MEO satellite in each time slot. Therefore, for $\forall j \in \mathcal{J}, t \in \mathcal{T}$, we have $\sum_{i=1}^I a_{i,j}(t) \leq K$.

3) Each LEO satellite can transmit only one type of data in each time slot. Therefore, for $\forall i \in \mathcal{I}, t \in \mathcal{T}$, we have $\sum_{l=1}^L b_{i,l}(t) \leq 1$.

Based on the analysis of the objective function and constraints mentioned above, this paper formulates the optimization problem as follows:

$$\max_{\{A(t), B(t)\}} \lim_{T \rightarrow \infty} \frac{1}{T} \sum_{t=1}^T \sum_{i=1}^I \sum_{j=1}^J \sum_{l=1}^L v_l \cdot W_{i,l}^D(t)$$

$$\begin{aligned} \text{s.t.} \quad & \sum_{j=1}^J a_{i,j}(t) \leq 1 \quad \forall i \in \mathcal{I}, t \in \mathcal{T} \\ & \sum_{i=1}^I a_{i,j}(t) \leq K \quad \forall j \in \mathcal{J}, t \in \mathcal{T} \\ & \sum_{l=1}^L b_{i,l}(t) \leq 1 \quad \forall i \in \mathcal{I}, t \in \mathcal{T} \\ & a_{i,j}(t), b_{i,l}(t) \in \{0, 1\} \quad \forall i \in \mathcal{I}, j \in \mathcal{J}, l \in \mathcal{L}, t \in \mathcal{T}. \end{aligned} \quad (2)$$

In order to maximize the total transmission data value of the system, it is essential to fully utilize the K beams of each MEO satellite. Clearly, through inference, the original problem is transformed into a problem solely related to $A(t)$:

$$\begin{aligned} \max_{\{A(t)\}} \lim_{T \rightarrow \infty} \frac{1}{T} \sum_{t=1}^T \sum_{i=1}^I \max_{l \in \mathcal{L}} \left(v_l \min \left(D_{i,l}(t), \sum_{j=1}^J C_{i,j}(t) \right) \right) \\ \text{s.t.} \quad & \sum_{j=1}^J a_{i,j}(t) \leq 1 \quad \forall i \in \mathcal{I}, t \in \mathcal{T} \\ & \sum_{i=1}^I a_{i,j}(t) = K \quad \forall j \in \mathcal{J}, t \in \mathcal{T} \\ & a_{i,j}(t) \in \{0, 1\} \quad \forall i \in \mathcal{I}, j \in \mathcal{J}, t \in \mathcal{T}. \end{aligned} \quad (3)$$

Therefore, the original decision space size is reduced from $2^{I \times J \times T} \times 2^{I \times L \times T}$ to $2^{I \times J \times T}$.

4.3 Markov Decision Process

The above formula represents an optimization problem with stochastic variables, which is difficult to solve using traditional static optimization algorithms [8]. Therefore, this paper considers using reinforcement learning to dynamically allocate channels. It is worth noting that the inter-satellite and satellite-to-ground link propagation distances between LEO satellites, MEO satellites, and ground stations

are far, resulting in significant propagation delays. If a centralized channel allocation architecture is adopted, the mission center will find it challenging to promptly obtain the latest status of LEO satellites and perform channel allocation. Therefore, this paper proposes letting each MEO satellite dynamically allocate channels to the LEO satellites within its coverage area. Specifically, as shown in Fig.6, each MEO satellite can be viewed as an agent, and its channel allocation can be modeled as a Markov decision process.

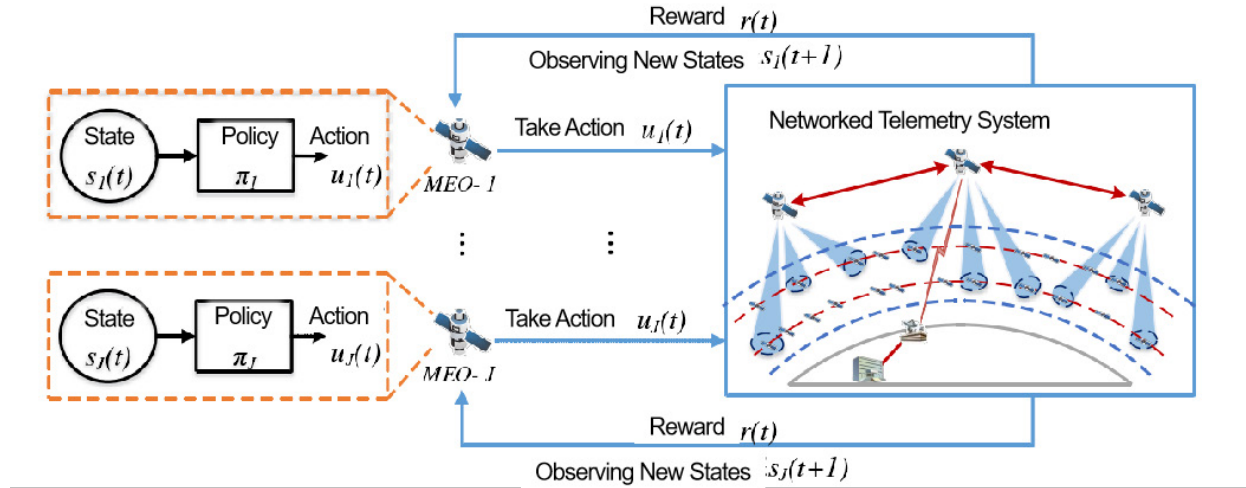


Fig.6. Markov Decision Process Model for Distributed Scheduling Problem

4.4 Deep Reinforcement Learning Method

For the j -th MEO satellite, after taking action u in state s , it receives reward $r(s,u)$ and transitions to state s' . For the traditional Q-learning algorithm, the Q-value is updated according to the following formula:

$$Q_j(s, u) = (1 - \alpha)Q_j(s, u) + \alpha(r_j(s, u) + \gamma \max_{u'} Q_j(s', u')). \quad (4)$$

Where $\alpha \in (0,1]$ is the learning rate. The traditional Q-learning algorithm stores all action values in a Q-value table. However, when the state and action spaces are large, it is challenging to store a massive amount of action values in the Q-value table. Therefore, we adopt the method of Deep Q-learning, which uses a Deep Q-Network (DQN) with low-dimensional parameters to approximate the high-dimensional action values in the Q-value table, thus significantly reducing storage costs. The j -th MEO satellite utilizes $Q_j(s, u; \theta_j)$ computed by a DQN with parameters θ_j to approximate the actual $Q_j(s, u)$. The optimal

policy generally involves selecting the action u with the highest value given state s [9], i.e.:

$$\pi_j^*(s, u) = \begin{cases} 1 & u = \operatorname{argmax}_{u'} Q_j(s, u') \\ 0 & \text{else} \end{cases}. \quad (5)$$

The specific training process of DQN is shown in Fig.7 After completing the network training of the j -th MEO satellite, the Q-function $Q_j(s, u; \theta_{j,train})$ used to evaluate action values can be obtained. The channel allocation for the j -th MEO satellite will follow the optimal policy defined by Equation (5) to maximize long-term rewards.

Although DQN possesses strong fitting capabilities and can compute the values of different actions under different states, training the network can still be challenging when the action space is too large. Therefore, considering decomposing action values into combinations of sub-action values through Q-function decomposition is proposed to directly determine the connections of the network output layer, aiming to reduce network training and storage costs.

The DQN employs a fully connected structure, as depicted in Fig.8

```

# Input: learning rate a for network training, number of training episodes N, exploration p
# Output: DQN parameters  $\theta_{(j,target)}$  for each satellite  $j \in \mathcal{J}$ 

# Initialize the experience memory  $D_j$  for each satellite  $j \in \mathcal{J}$ 
for  $j = 1$  to  $\mathcal{J}$  do
    Initialize experience memory  $D_j$  as an empty set
endfor

# Randomly initialize parameters for training and target networks for each satellite  $j \in \mathcal{J}$ 
for  $j = 1$  to  $\mathcal{J}$  do
    Randomly initialize parameters for training and target networks:  $\theta_{(j,train)} = \theta_{(j,target)}$ 
endfor

# Training loop for N episodes
for episode  $n = 1$  to N do
    # Initialize states  $s_{1(1)}, \dots, s_{\mathcal{J}(1)}$  for all satellites at time slot 1
    Initialize states  $s_{1(1)}, \dots, s_{\mathcal{J}(1)}$  for all satellites

    # Loop through each time slot
    for time slot  $t = 1$  to T do
        # Choose actions for each satellite  $j$  with  $\epsilon$ -greedy policy
        for  $j = 1$  to  $\mathcal{J}$  do
            # Choose action  $u_{j(t)}$  with exploration probability  $\epsilon$  or according to the optimal policy
            if random  $< \epsilon$  then
                Choose a random action  $u_{j(t)}$ 
            else
                Choose action  $u_{j(t)} = \text{argmax}_u Q_j(s_{j(t)}, u; \theta_{(j,train)})$ 
            endif
        endfor

        # Get rewards and next states for all satellites
        Get rewards  $r_{1(t)}, \dots, r_{\mathcal{J}(t)}$  and next states  $s_{1(t+1)}, \dots, s_{\mathcal{J}(t+1)}$ 

        # Store experiences in memory  $D_j$  for each satellite  $j$ 
        for  $j = 1$  to  $\mathcal{J}$  do
            Store  $(s_{j(t)}, u_{j(t)}, r_{j(t)}, s_{j(t+1)})$  into experience memory  $D_j$ 
        endfor

        # Sample a mini-batch of experiences from  $D_j$  and update parameters  $\theta_{(j,train)}$ 
        for  $j = 1$  to  $\mathcal{J}$  do
            Sample a mini-batch of experiences from  $D_j$ 
            Update parameters  $\theta_{(j,train)}$ 
        endfor

        # Update target network parameters for each satellite  $j$  by copying parameters from the training network
        for  $j = 1$  to  $\mathcal{J}$  do
            Update target network parameters:  $\theta_{(j,target)} = \theta_{(j,train)}$ 
        endfor
    endfor
endfor
    
```

Fig. 7. Deep Q-Network (DQN) training

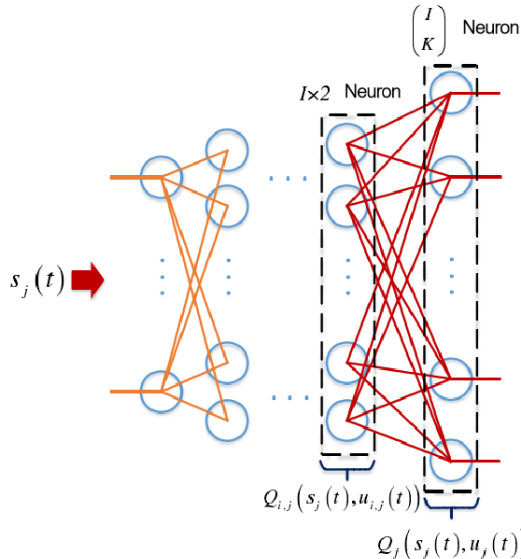


Fig. 8. the architecture of the DQN network.

5 Simulation Results

Firstly, we constructed a MEO-LEO satellite constellation for simulation, as shown in Fig. 9. The MEO constellation consists of 11 satellites evenly distributed on a circular orbit 8000 kilometers above the Earth's equator, with orbit

parameters referenced from O3bmPower. The LEO constellation comprises 1584 satellites deployed in the first phase of Starlink, with orbit parameters referenced from [10]. The topological structures of the MEO and LEO constellations are illustrated in the Fig.9.

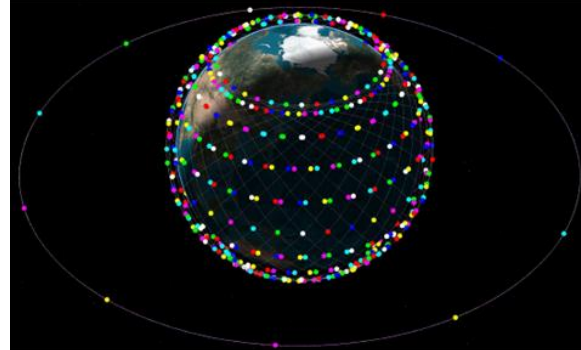


Fig. 9. Topological Structures of the MEO and LEO Satellite Constellations

As shown in Fig.10, after 3000 training episodes, the total transmitted data value of the system converges and tends to stabilize. Fig.11 displays the data value transmitted in different time slots after 1000, 2000, 3000, 4000, and 5000 training episodes. The transmitted data value in different time slots significantly increases as the number of training episodes increases from 1000 to 3000. Subsequently, as the number of training episodes increases from 3000 to 5000, the transmitted data value in different time slots remains relatively stable.

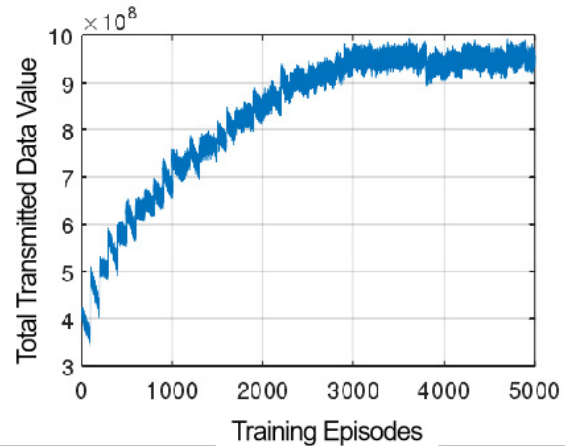


Fig. 10. Convergence of the Distributed Scheduling Algorithm

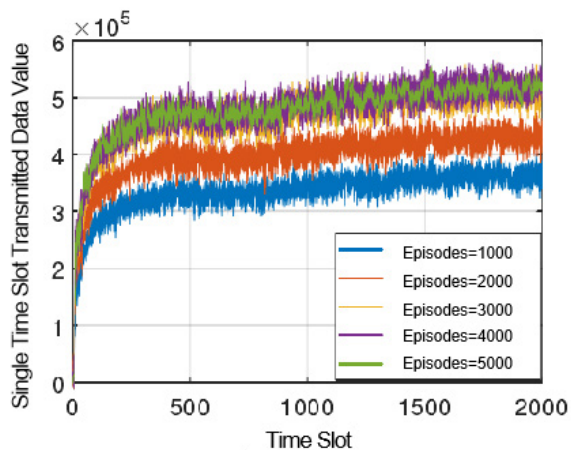


Fig. 11. The Data Value Transmitted in Different Time Slots after Training with Varying Numbers of Episodes.

6 Conclusion

This paper constructs a Markov Decision Process (MDP) based on multi-agent reinforcement learning framework for dynamic channel allocation. Considering the vast state and action space of the Markov Decision Process, a Deep Q Network (DQN) is employed to compute action values. The original action function is decomposed into a combination of Q functions for multiple sub-actions, and the output layer connections of the Deep Q Network (DON) are further designed to significantly reduce the training and storage overhead of the DQN. Finally, numerical simulations are conducted to verify the performance of the proposed channel allocation algorithm under different system parameters. Simulation results demonstrate that the proposed channel allocation algorithm achieves higher total transmitted data value compared to other benchmark algorithms, surpassing 85% of the performance upper bound.

References

- [1] Wang I, Li L, Qin Z, et al. Capacity analysis of LEO mega-constellation networks[J].IEEE Access, 2022, 10:18420-18433.
- [2] Chen Q, Chen X, Yang L, et al. A distributed congestion avoidance routing algorithm in mega-constellation network with multi-gateway[l].Acta Astronautica, 2019, 162:376-387
- [3] Lai Z, Li H, Li J. Starperf: Characterizing network performance for emerging mega-constellations[C]//2020 IEEE 28th International Conference on Network Protocols (ICNP). IEEE, 2020: 1-11.
- [4] Garg V K, Sharma C D. Engineering and performance evaluation of TTC ground station[J]. IETE Technical Review, 1989, 6(5): 380-386.
- [5] Pan X, Zhan Y, Zeng G, et al. TT&C capacity analysis of mega-constellations: How many satellites can we support?[C]//ICC 2022-IEEE International Conference on Communications. IEEE, 2022: 2393-2398.
- [6] Zhan Y, Zeng G, Pan X. Networked TT&C for mega satellite constellations: A security perspective[J]. China Communications, 2022, 19(9): 58-76.
- [7] Jia L, Zhang Y, Yu J, et al. Design of mega-constellations for global uniform coverage with inter-satellite links[J]. Aerospace, 2022, 9(5): 234.
- [8] Sutton R S, Barto A G. Reinforcement learning: An introduction[M]. MIT press, 2018.
- [9] Arulkumaran K, Deisenroth M P, Brundage M, et al. Deep reinforcement learning: A brief survey[J]. IEEE Signal Processing Magazine, 2017, 34(6): 26-38.
- [10] Albulet M. SpaceX v-band non-geostationary satellite system[J]. Federal Commun. Commission, Washington, DC, USA, Tech. Rep. SAT-LOA-20161115-00118, 2017.

High Accuracy Time Space Position (TSPI) Field Test Results

Ben Kupferschmidt¹, Rocco Docimo¹

¹ *Curtiss-Wright, 15 Terry Dr., Newtown, PA 18940, USA*

bkupferschmidt@curtisswright.com, rdocimo@curtisswright.com

Abstract:

Flight test applications require accurate data to verify and validate the test article's performance. This data is most useful when it is properly correlated with other contemporaneous test data. This includes ensuring that all collected data can be cross-referenced with the aircraft's position and orientation in space. This enhances one's knowledge of what is happening during different maneuvers, allowing engineers to better determine the limits of an airborne platform.

Time Space Position Information (TSPI) systems deliver this positional data. TSPI systems are able to provide very accurate data by combining highly accurate and precise internal sensor components with careful installation and calibration. This paper discusses Curtiss-Wright's new MiTSPI nTTU-2600 Miniature TSPI device and presents some real-world test data that demonstrates its performance.

Key words: TSPI, GPS, INS, IMU, GNSS

Introduction

Time Space Position Information (TSPI) systems provide extremely accurate position, orientation, velocity, and acceleration data about test articles. This data can be combined with other conventional flight test data from analog sensors and digital buses to greatly improve the overall situational awareness for the flight test engineers who are tasked with monitoring and analyzing the results of a flight test. This information is also very useful in determining the overall capabilities and limitation of a test article, since the TSPI data allows the measurements taken by the conventional flight test data acquisition system to be correlated with specific maneuvers.

In this paper, we will introduce the technologies that are used to generate TSPI data. We will then introduce Curtiss-Wright's new miniature TSPI product, the MiTSPI nTTU-2600. Finally, we will present the results of a series of real-world tests that Curtiss-Wright has performed to measure the accuracy and precision of the TSPI data generated by the nTTU-2600.

How Do TSPI Devices Work?

The best way to determine the position of a test article today is through the use of an Inertial Navigation System (INS) that is comprised of two components. These components are a Global Navigation Satellite System (GNSS) and an Inertial Measurement Unit (IMU). The original and most widely used GNSS system is the US

government's Global Positioning System (GPS). Some other commonly used GNSS systems include the Galileo system operated by the European Union, the GLONASS system operated by Russia, and the BeiDou system operated by China.

Commercial GNSS receivers have a positional accuracy that varies between meters to sub-meter due to several factors including the number of simultaneous satellite systems that are being tracked and if the receiver has single or multiple (differential) receivers. In addition, the GNSS data is typically updated at lower rates (5 to 20 Hz), which can be too slow to catch some course change information. For example, a missile traveling at Mach 2 traverses about 780 m/s, equating to a significant possible gap in position information when relying solely on GNSS with updates at 5 Hz.

There are many potential sources of error with GNSS systems, including:

- The location of the GNSS antenna, and multi-path effects on the test article.
- The type of GNSS receiver used, e.g., multi-constellation and/or differential GPS (DGPS).
- Atmospheric uncertainty due to charged particles can introduce errors up to a few dozen meters.

- Clock errors – even a few nanoseconds could mean a one-meter error.
- Ephemeris error, i.e., the difference between theoretical and actual satellite position.

An unlucky combination of these errors could result in location data that is too inaccurate to be useful for some test scenarios.

Additionally, GNSS receivers do not provide orientation information, such as the roll, pitch, and yaw of a platform, although some models compute a trajectory/velocity, albeit at low data update rates. The orientation information, along with the trajectory information, form the six degrees of freedom (6DOF) data that is critical to help correlate aircraft sensor data with maneuvers to assess an aircraft's performance and operation limits accurately. In contrast, INS units typically provide the 6DOF information to help achieve a better correlation of measured platform flight test dynamics with the stresses experienced by the platform during these maneuvers.

An INS generally consists of a GNSS and an Inertial Measurement Unit (IMU) which uses accelerometers, gyros, and inclinometers to detect changes, at high sample/update rates, in the forces impacting the test platform and thereby accelerations relative to an inertial frame of reference. Modern IMUs have high updates rates up to 800Hz and can be used to derive velocities and spatial positions in 6DOF without any additional external inputs.

Since the IMU units essentially calculate position and orientation information by calculating differences from a starting reference point, errors accumulate and propagate over time, and in-flight recalibrations may be necessary for continued accurate readings.

TSPI units rely on fusing data from the GNSS and the IMU to provide higher accuracy and higher update rates by using the lower update and relatively more accurate GPS receivers to provide the "truth" data on the platform position and the higher update rate IMU data to estimate the platform position and 6DOF data through data fusion/filtering techniques such as Kalman filters.

Flight Test Requirements For TSPI

Since modern aerospace platforms are typically space-constrained, it is important for the TSPI unit to be optimized to reduce its size, weight, and power (SWaP). It is also important that the TSPI unit integrates well with the rest of the flight test data acquisition system and how data is telemetered to the ground and/or stored for post-

flight access. Both real-time and post-test data are required, so the TSPI unit must be able to provide both. In real-time, the TSPI and trajectory information needs to be formatted for efficient transmission while still being easily decoded by the onboard/ground station software for flight test point clearance and safety reasons. The limited RF downlink bandwidth and real-time processing of data in the ground station, during the flight test, place a premium on ensuring that the critical data is quickly transmitted to the ground for decisions on safety and/or to repeat a test point.

In contrast, post-test data analysis can provide higher fidelity by using the full INS dataset, including all acceleration and rate sensor measurements, captured by the TSPI unit at higher update rates. Due to the need for transmitting a quick summary of the data along with the need to record all of the data for post-flight analysis, it is important for the TSPI unit to have the ability to locally record all of the GNSS and IMU/INS data.

Introducing The MiTSPI nTTU-2600

Curtiss-Wright has developed a compact and accurate TSPI solution called the MiTSPI nTTU-2600. The nTTU-2600 is a network tactical TSPI unit with an integrated recorder. The unit provides user-selectable TSPI information for real-time telemetering via Ethernet and/or IRIG-106 Chapter 4 PCM (Clock and Data) and for simultaneous data recording as IRIG-106 Chapter 10 for post-flight retrieval and analysis.

The nTTU-2600 contains sub-systems / functional blocks for both acquisition and recording, as shown in Figure 1 and Figure 2.



Figure 1. MiTSPI nTTU-2600

- **MINS-600-1:** The Miniature INS (MINS) module interfaces with an external GPS antenna to receive the GPS signals and to process them for the “truth” data. In addition, the MINS includes a miniature IMU that computes the 6DOF data. The MINS combines both the GPS and IMU data to estimate, using Kalman filters and with appropriate translations of the leverage arms data, the test platform’s TSPI and 6DOF data relative to its preferred datum which is often the platform’s Center of Gravity (CoG).
- **MREC-601-1:** The miniature recorder module is used for recording the TSPI data provided from the MINS-600-1. An industrial-temperature rated CompactFlash Express (CFexpress) memory card, available in 512GB capacity, is accessible through a sealed, hinged door on the front of the MREC.
- **MPPC-600-3:** The processor module for the data acquisition system performs the necessary overhead functions and processes the TSPI data for real-time telemetry and for recording locally.
- **MACQ-600-1:** The overhead acquisition module for the data acquisition system provides the functionality to create IRIG-106 Chapter 4 PCM (Clock / Data) for real-time telemetry output as an RF telemetry stream. In addition, the MACQ outputs real-time multicast TSPI output on its Ethernet port.
- **MPFM-461/MPSM-2005-3:** Power filtering and power supply module for the TSPI unit, accepting a MIL-STD-704F 28VDC prime power.

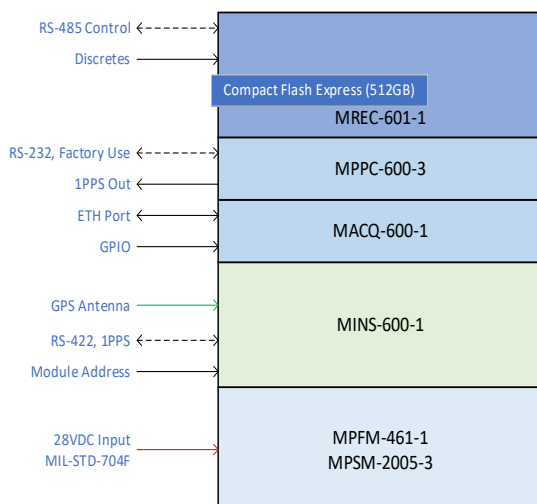


Figure 2. nTTU-2600 Block Diagram

The nTTU-2600 can transmit real-time serial and Ethernet TSPI data at up to 20 Mbps. However, in almost all cases, the nominal rate is less than 2 Mbps based on the TSPI sensor data rates.

The real-time serial and Ethernet multicast outputs can be configured to send user-selected navigation (fused) parameters, position/position error in Earth-Centered-Earth-Fixed (ECEF) or North-East-Down (NED) formats, 6DOF data in ECEF or NED formats, accelerations, and angular rates in body-frame references, and GNSS statistics. Additional IMU data, such as delta velocity and delta angles for coning and sculling, Quaternions, Rotation Matrix, and health status, can be locally recorded for post-test analysis.

A well-calibrated and well-installed nTTU-2600 unit provides the following performance during GNSS lock conditions:

Table 1: nTTU-2600 Specifications

Parameter	Accuracy / Specification
Heading (magnetometer only)	2.0° rms
Heading (above 5.0 m/s, with GPS lock)	< 0.1° rms
Pitch (static)	< 0.08° rms
Pitch (dynamic)	< 0.03° rms
Roll (static)	< 0.08° rms
Roll (dynamic)	< 0.03° rms
Horizontal Position	< 1.0 m, rms (0.01 m with RTK)
Vertical Position	< 1.5 m, rms (0.01 m with RTK)
Velocity accuracy	< 0.02 m/s
TSPI update rate	Up to 400 Hz

Configuring The nTTU-2600

The nTTU-2600 is configured using Curtiss-Wright’s TTCWare setup software. Several items need to be properly configured to get high quality data from the TSPI unit.

First, the location of the GNSS antenna relative to the nTTU-2600 mounting reference must be entered. After that, the lever arm and boresight measurements need to be entered to establish the distance and angles of the nTTU-2600 mounting, to the desired datum and reference planes of the test article. This has the effect of offsetting the GPS data which is received at the antenna and the local IMU measurements and shifting the position and orientation to match the test article’s datum and desired reference planes.

Next, the content of the actual data packets needs to be defined. The nTTU-2600 allows the engineer who is configuring it, to define up to three packets. Each packet can be recorded locally, multicast on the Ethernet, or both. The idea is that one packet which is intended for

telemetry purposes would have a low update rate and only contain essential information. The next packet could have different information at a higher update rate but be intended for recording. Finally, the third packet might have all information enabled for recording at a low update rate. In this manner, the engineer can satisfy multiple use cases with the same TSPI unit.

For each packet, the available parameters are categorized into five main groups: Time, IMU, GNSS, Attitude, and INS. The engineer can select the parameters that are required for their test.

Packets are multicast on the Ethernet using Curtiss-Wright’s DARv3 format. The local recording onboard the nTTU-2600 uses the IRIG-106 Chapter 10/11 recording standard. For the multicast data, the Curtiss-Wright nGWY-2000 network to PCM gateway can be used to receive the Ethernet packets from the nTTU-2600 and other network sources. The nGWY-2000 selects the parameters of interest and inserts them into the IRIG-106 Chapter 4 PCM stream for transmission to the ground via the telemetry link.

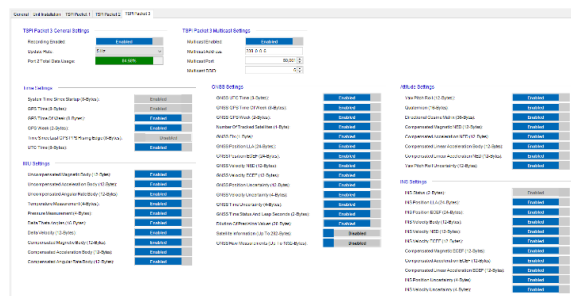


Figure 3. nTTU-2600 Packet Setup

Real-World Testing

As part of the nTTU-2600 development and verification, Curtiss-Wright conducted road tests, using a cargo van as the test platform, to demonstrate the accuracy and precision of the data generated by the nTTU-2600. This could not be demonstrated with laboratory testing alone because the IMU sensors require actual motion in order to be fully exercised. A precisely defined route (shown in Figure) comprised of multiple turns and straight-line stretches was used to test the capabilities of the nTTU-2600. Each drive lasted about fifteen (15) minutes and generated approximately 400,000 data points at a 400 Hz update rate.

The nTTU-2600 requires the platform to be travelling at more than five (5) meters per second for the GNSS receiver to generate accurate heading estimates. Similarly, the IMU requires multiple changes in direction to exercise the rate sensors before accurate data can be measured. Each test drive commenced from a stationary

“rest” position in the Curtiss-Wright parking lot. Roughly the first 30 seconds of each drive was done at low speeds within the parking lot. Due to these factors, the data collected during the first 35 seconds of each test was excluded from the analysis. Also, all data below five (5) meters per second was excluded as the test platform does not travel an adequate distance for accurate GNSS heading estimates.



Figure 4. Test Drive Route For TSPI Data Analytics

For the test, two nTTU-2600 units, mounted in different orientations approximately one (1) meter apart (as shown in Figure 5), were used to validate the leverage arms and boresight calculations, unit performance, and to compare measurements. One nTTU-2600 unit was mounted with a roll of 45 degrees and a yaw of 135 degrees, while the other was mounted with a roll of 30 degrees and a yaw of -30 degrees. The orientations were such that the two units experienced forces in different directions and magnitudes, as the test platform (cargo van) was driven around the prescribed test route. The two nTTU-2600 units were provided identical GPS RF signals from a GNSS antenna, using a GNSS splitter. In an ideal scenario, both nTTU-2600 units should provide nearly identical values for all TSPI parameters, after accounting for the leverage arms, boresight, and orientations corrections. The nTTU-2600 units were also provided with a synchronized IEEE-1588 time using an Ethernet switch. The same switch was used to route data from the nTTU-2600 devices to a laptop computer.

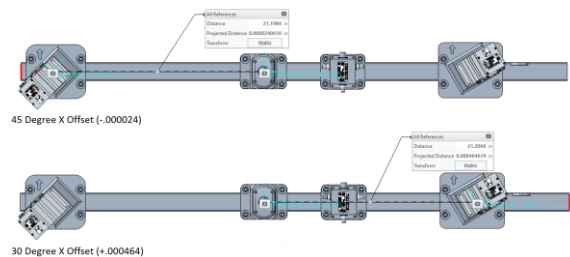


Figure 5. nTTU-2600 Test Fixture Design

Establishing Test Criteria And Limits

Multiple road test runs were conducted, and various TSPI parameter data were collected for

analysis. The parameters included physical locations (latitude, longitude, and altitude) and orientation (heading/yaw). The physical locations measured and estimated by the two nTTU-2600 units were compared to Google maps, and with one another. In order to verify the precision and accuracy of the data, much of the data analysis was done by comparing the results from the two nTTU-2600 units.

The nTTU-2600 design accuracy is provided in Table 1. Each parameter's accuracy is specified as a root-mean-square (rms) value, given the stochastic (random) nature of the errors from the GNSS and IMU sensors. Additionally, the processed results of the two nTTU-2600 units would have a larger rms values, by a factor $\sqrt{2}$, given that they are linear combinations of stochastic variables[1]. A good example of this is the relative location errors calculated by subtracting identical parameters like latitude or longitude.

In this paper, we present the (i) Distance and (ii) Heading/Yaw results of two separate drives, Drive 1 and Drive 2 as described below.

- Drive 1: GPS Antenna offset to each nTTU-2600 unit was set to zero (0) meters, requiring each nTTU-2600 to provide identical location estimates and similar heading values after the boresight, leverage arms, and orientation corrections are applied. This assumes that the relative physical mounting of the two units is within the heading parameter's accuracy.
- Drive 2: GPS Antenna offset to each nTTU-2600 unit was half of the 1.076878 meter distance between the units. This requires each nTTU-2600 to provide location estimates that are at a distance of 1.076878 meters and similar heading values after the boresight, leverage arms, and orientation corrections are applied. Again, we assume that the relative physical mounting of the two units is within the heading parameter's accuracy.

Horizontal Position / Distance Results

The horizontal position/distance between the two nTTU-2600 units were calculated using the Haversine formula[2] for both Drive 1 and Drive 2.

As Drive 1 used a zero (0) offset for the GPS Antenna location, the relative distance between the two nTTU-2600 estimates is expected to have a mean value of zero (0) meters and be within the unit's rms (standard deviation) value of 1 meter increased by a factor of $\sqrt{2}$, thus imposing a limit of 1.414 meters for the calculated values rms (standard deviation).

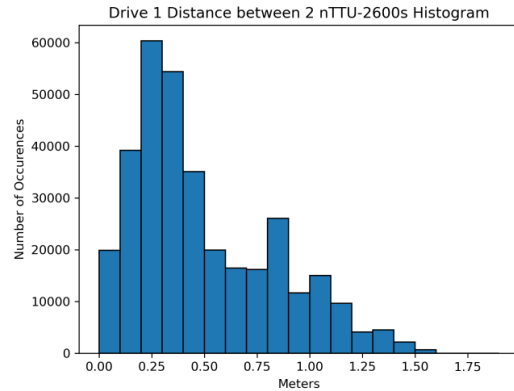


Figure 6. Drive 1 Distance Histogram

Likewise, as Drive 2 used a GPS Antenna offset of 1.076878 meters, the relative distance between the two nTTU-2600 estimates is expected to have a mean value around 1.076867 meters and be within the unit's rms (standard deviation) value of 1 meter increased by a factor of $\sqrt{2}$, thus imposing a limit of 1.414 meters for the calculated values rms (standard deviation) about the 1.076878 meters mean value.

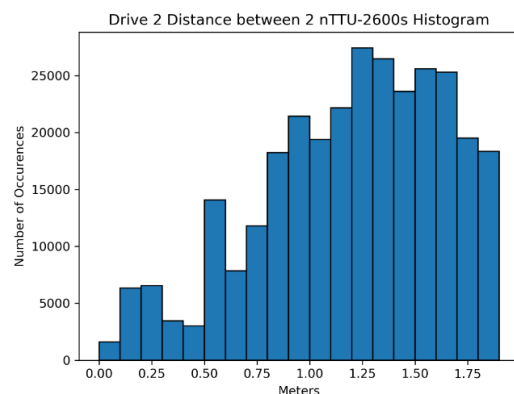


Figure 7. Drive 2 Distance Histogram

For Drives 1 and 2, the calculated distance between the two nTTU-2600 units is shown as histograms in Figure 6 and Figure 7 respectively.

Figure 6, for Drive 1, shows a peak around 0.25 meters instead of the expected zero (0) meter mean value, but almost all of the 400,000 data points are within the 1.414 meters limit for the calculated rms (standard deviation) for the location. In fact, a significant number of the data points are within 1 meter, implying that the native nTTU-2600 location accuracy is much better than the stated 1 meter rms accuracy.

Figure 7, for Drive 2, shows a peak around 1.25 meters instead of the expected 1.076878 meter mean value, but almost all of the 400,000 data points are within the 1.414 meters limit for the calculated rms (standard deviation) about that mean value. In fact, a significant number of the

values are between 0.75 meters and 1.75 meters, implying that the native nTTU-2600 location accuracy is much better than the stated 1 meter rms accuracy.

The distance between the two units, as a function of time, are provided in Figure 8 and Figure 9 for Drive 1 and Drive 2 respectively.

Figure 8, for Drive 1, shows the expected zero (0) mean value as a green line and expected rms (standard deviation) of 1.414 meters as a red line. The calculated relative distance between the two nTTU-2600 units is almost always within the expected rms value of 1.414 meter. The dotted blue line shows the calculated standard deviation value of 0.335 meters for all the Drive 1 relative distance measurements, as compared to the 1.414 meter limit, a difference of 0.675 meters better performance than the limit.

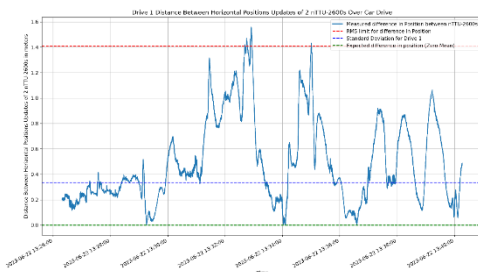


Figure 8. Distance Between The Two TSPI Units – Plotted For Drive 1

Figure 9, for Drive 2, shows the expected 1.076878 meter mean value as a green line and expected rms (standard deviation) limit of 2.491 meters (1.414 meters rms + 1.076868 meter mean) as a red line. The calculated relative distance between the two nTTU-2600 units is almost always within the expected rms value of 2.491 meter. The dotted blue line shows the calculated standard deviation value of 1.752 meters for all the Drive 2 relative distance measurements, as compared to the 2.491 meter limit, a difference of 0.738 meters better performance than the limit.

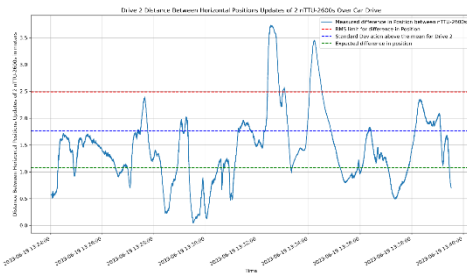


Figure 9. Distance Between The Two TSPI Units – Plotted For Drive 2

Heading / Yaw Results

The heading/yaw results from the two nTTU-2600 units, are compared for Drive 1 and Drive 2. In contrast to the location calculations, the yaw results for both units and for both drives are expected to be identical as the nTTU-2600 boresight, leverage arms, and orientation corrections would remove the mounting dependencies. Our carefully designed experiment used 3-D printed mounting blocks to achieve the roll of 45 degrees and a yaw of 135 degrees for one unit, while the other was mounted with a roll of 30 degrees and a yaw of -30 degrees. However, both units were mounted to the cargo van’s roof rail using U-bolts and there might be slight mismatches in relative orientation leading to a bias in the measured/calculated yaw results, as described below.

The heading/yaw results from each nTTU-2600 were converted to a range between -180 degrees and +180 degrees relative to true north, and then subtracted from one another. Ideally, the subtracted values should provide a zero (0) mean and be within the specified nTTU-2600 rms values increased by a factor of $\sqrt{2}$ for the linear processing of two stochastic variables.

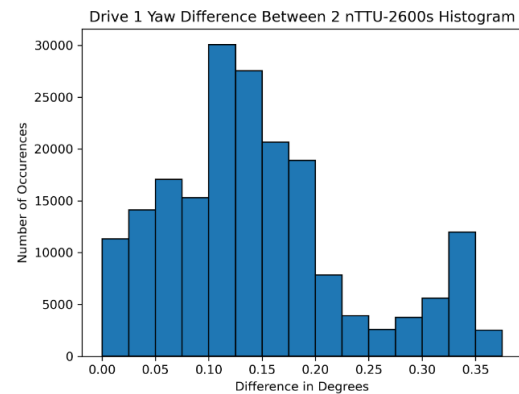


Figure 10. Yaw Difference For Drive 1

Figure 10 shows the histogram of calculated heading/yaw differences between the two nTTU-2600 units for Drive 1. The peak value is about 0.11 degrees and shows a possible bias in the relative mounting between the two units. However, the maximum difference in yaw estimates between the two units is less than 0.35 degrees thereby highlighting the highly accurate estimates from the nTTU-2600 units.

Figure 11 shows the histogram of calculated heading/yaw differences between the two nTTU-2600 units for Drive 2. The peak value is about 0.19 degrees and shows a possible bias in the relative mounting between the two units. Also note that for Drive 2, the nTTU-2600 is also using the relative distance of 1.076878 meters in its

calculations as it arrives at a yaw solution, thus possibly accounting for the difference between the Drive 1 and Drive 2 end results. However, the difference in yaw estimates between the two units is still less than 0.35 degrees thereby highlighting the highly accurate estimates from the nTTU-2600 units.

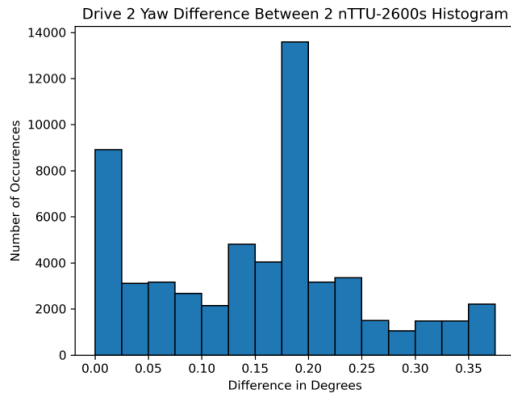


Figure 11. Yaw Difference Drive 2

Conclusion

This paper presents details of a miniature TSPI unit, model nTTU-2600 from Curtiss-Wright that provides high accuracy TSPI data within 1 meter rms horizontal and 1.5 meter rms altitude and less than 0.1 degrees rms for pitch, roll, and yaw. The nTTU-2600 includes a GNSS receiver that also supports Satellite-Based-Augmentation-System (SBAS) and a miniature IMU, for navigation solutions calculated by a Kalman filter at updates rates up to 400 Hz. The field tests carried out by Curtiss-Wright demonstrate and validate the specifications of the nTTU-2600. Additional results from current field tests and from airborne tests, if available, will be provided at our presentation during the International Telemetry Conference 2023.

References

- [1] Propagation of uncertainty, https://en.wikipedia.org/wiki/Propagation_of_uncertainty#Linear_combinations
- [2] Haversine formula, https://en.wikipedia.org/wiki/Haversine_formula
- [3] Ben Kupferschmidt, Brandon Rosso: "Miniature High-Accuracy Time Space Position Information (TSPI) Data Acquisition", ETTC Proceedings, 2023.

Detection and Monitoring of Jamming and Spoofing of GPS/GNSS Signals in Harbours and Industrial Areas

Karen von Hünerbein¹

¹ Lange-Electronic GmbH, Rudolf-Diesel-Str. 29A, 82216 Gernlinden, Germany
kvh@lange-electronic.com

Abstract:

GPS/GNSS plays a key role for navigation in autonomous vehicles.

For industrial areas and harbour terminals there is a need to use autonomous or remotely controlled vehicles, for more efficient and safe operation and transport among containers and assets.

Such industrial and harbour areas can be complex and confusing for untrained personell and external lorry drivers, who are usually unfamiliar with the structure and floor plan of container stacks, walls of boxed materials and building compounds. These container stacks and other structures reduce overall visibility for a human operator, making visual navigation more difficult. When drivers are confused they take a long time and use more fuel before arriving at the intended location for loading and unloading of bulk goods. Autonomous vehicles can be pre-programmed with a safe and efficient trajectory.

In order to navigate properly in any terrain, autonomous vehicles require a redundant navigation system, usually consisting of GNSS (Global Navigation Satellite Systems) and INS (Inertial Navigation System) and additional sensors. One disadvantage is that the GPS / GNSS environment can be and will be degraded in a complex area with a lot of metal structures and possibly jamming signals. Thus it is important to check and monitor the quality of the signal environment for smooth continuous operation of all vehicles on the ground. In this paper, we present a novel Interference Detection and Monitoring System, GIDAS, by OHB-Digital, capable of detecting and monitoring GPS/GNSS signal jamming and spoofing, 24/7 and capable of analysing and classifying the interferer types. In addition GIDAS will store snapshots of the interference signals and alert the operator of the harbour / industrial area. GIDAS allows localization of the interference source and detailed analysis in post-processing..

Key words: GPS/GNSS interference monitoring, increased efficiency, autonomous vehicles

Introduction

Harbour areas are equipped with many large metallic structures, among which vehicles, such as lorries need to find their way and arrive at predefined locations, e.g. loading areas and docks. Metallic structures include cranes and containers, some of them form a complex and variable topography and obstruct visual line of sight, making it hard for drivers to find their destination.

In order to increase efficiency of transport inside such areas, it is easier and safer to use remotely piloted or autonomous robots and vehicles for moving and transportation among the complex metallic structures and topography of an industrial area and harbour.

Most vehicles with and without drivers use GPS/GNSS satellite navigation signals for localization and navigation. These signals are very weak (at -120dBm to -130 dBm) and can

be obscured and reflected from metal surfaces, which are present abundantly in harbours and industrial areas. Reflections, especially when there are a lot of them, can cause issues for a GPS/GNSS receiver, because it needs to identify the correct navigation signal for calculation of an accurate and precise position. If the receiver uses a reflected navigation signal (multipath), which is attenuated and has a different path length compared to the line of sight signal, this may result in a less accurate position fix. In a multipath rich signal environment it can also become difficult for a receiver to acquire and process any useful signal at all.

In addition these weak satellite navigation signals can be easily interfered with by other RF signals as unintentional interference, or by intentional jamming signals. Such interference and jamming events have been observed frequently in the last 10 years. [5], [6]

In a study by Fraunhofer CML and Fraunhofer IML it has been shown that in a harbour environment efficiency and sustainability can be improved by using automated and remotely controlled vehicles. [1,2].

In this paper we would like to present how efficiency can be increased by use of automated vehicles in harbours and by monitoring the signal environment to detect and analyze jamming and spoofing signals detrimental to GPS/GNSS signal reception.

Automated Vehicles in Harbour Areas

Harbours and container terminals are full of high metallic structures and machines such as cranes and stacks of containers, which reflect and obscure GPS/GNSS satellite system signals and obstruct vision and driving routes for human drivers. Reduced visibility and complex arrangement make it harder for any lorry driver to spot and drive to the appropriate loading/unloading and other destinations inside a harbour area and inside many industrial areas.

In 2022, Fraunhofer Institute Center of Maritime Logistics (Fraunhofer CML) and Fraunhofer Institute for Material Flow and Logistics (Fraunhofer IML) have conducted a simulation study, in order to assess the potential for efficiency gains in container terminals when operating automated vehicles and lorries instead of lorries with human drivers. [1,2]

The project is called SALT: Simulation automatisierter LKW in Häfen und Terminals, meaning **S**imulation of **A**utomated **L**orries in harbours and **T**erminals. This study was conducted in a reference container terminal and the surrounding access roads and streets. [1,2]

In the simulation, input data were real data of traffic flow and data of control signals for the traffic lights by the Hamburg Port Authority. In addition, all relevant operational processes for lorry handling inside the harbour were included in the simulation and analysis, including OCR2-Gate, interchange, different container storage areas, and customs offices. Traffic routes and lorry trajectories were implemented in the statistical model, plus additional vehicles and all sorts of other traffic inside the terminal. Data and logic of the simulation model were validated by expert interviews. Fraunhofer CML researchers set up and ran different simulation scenarios with various conditions, e.g. different levels of automation, and various amounts of automated vehicles in relation to non-automated vehicles, because mixed traffic is occurring especially on the access roads.

Fraunhofer researchers calculated and evaluated parameters such as throughput times, traveling times and length of traffic jams, in order to analyze efficiency gains.

Results showed that no efficiency gains could be achieved on the surrounding access roads, due to crossings, merging of lanes, traffic lights and lane changes in mixed traffic. Good gains of average throughput time could be achieved on the area of the container terminal with automated vehicles of SAE levels (Safety Levels) 4 and 5: 15% improvement of throughput time in mixed traffic and even 29% of throughput time with fully automated traffic. This is due to faster shunting maneuvers and removal of manual processes.[1,2]

Positioning of Autonomous Vehicles

Autonomous and automated vehicles are generally equipped with a variety of multiple sensors and positioning technologies in order to ensure a high degree of safety and security while driving on roads, industrial areas or inside container terminals.[3,4,16,17]

At higher levels "of autonomy, we see more and more sensors built into vehicles. Radar, LIDAR, vision and ultrasonic sensors are all in the mix, offering relative positioning capability. In other words, they can tell us how far away other objects are from the vehicle, and, by sensing the distance from landmarks, they can also be used to position it relative to the reference frame defined by these landmarks. For some use cases, however, a truly absolute positioning sensor is needed, and this is where GNSS or, more typically, GNSS fused with inertial sensors comes into the picture " [4]

Using a combination of sensors provides redundancy for safety, robustness for use cases and an optimized cost balance.[11,16]

GPS/GNSS Reception

A reasonable or good GPS/GNSS reception with 8-12 satellites in view is a key element of the positioning in autonomous vehicles. While GPS/GNSS signal reception is generally good at sea or in rural areas, it can be degraded or severely restricted in mountainous areas, urban canyons or harbour areas, where there are a lot of high structures such as cranes and stacks of containers. The main issue in these areas is obscuration, since the high structures block GPS/GNSS signals from satellites, much like steel and rock structures blocking the direct sunlight.

In addition, certain materials reflect the GPS/GNSS electromagnetic waves and lead to

signal distortions or inaccuracy of the PNT solution (PNT: position, navigation and timing) in the receiver. GPS/GNSS signals can also be affected and drowned out by electromagnetic interference and spoofing.

“In recent years, there have been increasing concerns about intentional and unintentional interference with GPS signals [9]. GPS signals are weak at around -130 dBm, so weak that they disappear in the normal thermal background noise, and can be easily disrupted.” [9]

“A jammer produces stronger RF signals in the same RF band, and simply overwhelms the GPS receiver by sheer noise. When a receiver is disrupted by a jammer, it is clear to the receiver and to the user that there is a signal problem. Spoofing on the other hand is a hidden attack misleading the receiver with erroneous information, to make it believe it has different position, velocity or time than it actually has. In this case it is not clear to the receiver and the user, that there is a signal problem. Spoofing has not been observed so far in the civil world, but it has been demonstrated to work in demonstration field test” [9,11]. In the last two years, spoofing has been observed in civil life, with passenger jets being affected. [21]

Interference of GPS and GNSS Signals

One way of dealing with degraded signal environments is by monitoring the GPS / GNSS signals at the location of interest. Such monitoring measurements have already been performed in several studies around Europe.

One of them was the STRIKE3 Project: STRIKE3 was a “European initiative to support the increasing use of GNSS within safety, security, governmental and regulated applications. The aim of STRIKE3 was to develop international standards in the area of GNSS threat reporting and GNSS receiver testing.[12] Using thousands of threats collected from their network over a three-year period, STRIKE3 has developed a baseline set of threats that can be used to assess performance of different GNSS receivers under a range of typical real-world interference/jamming threats” such as: wide swept frequency with fast repeat rate, narrow band signal at L1 carrier frequency, triangular and triangular wave swept frequency and tick swept frequency.” [12].

A recent paper in Inside GNSS reports about interferences observed in the Baltic Sea: “Automatic Dependent Surveillance (ADS)-B messages broadcast by aircraft are an important source of information regarding the

timing and effects of GNSS RFI, and this information is now readily available online (e.g., at GPSJam, managed by John Wiseman [15], which uses data from ADS-B Exchange” [14]. The GPSJam Website is showing plenty of GPS interference around the Baltic Sea from December 2023 to February 2024, which is believed to be emitted and caused by Russian military.

In a study from 2016 conducted together with the institute of flight guidance (IFF) of the technical university of Braunschweig, we observed 238 interference events on a nearby motorway A2 within two weeks, and 34 of them with a high signal strength and severity. [6].

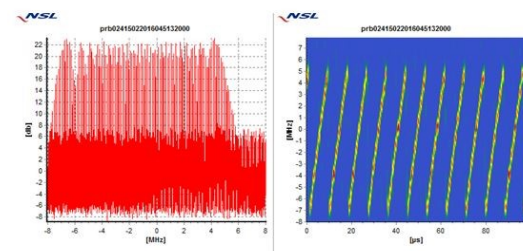


Figure 6: Chirped saw tooth (up) interference event (Feb. 15 2016, 04:51:32 UTC)

Fig. 1. Chirp Saw Tooth Up Interference in 2016

Interference Detection and Monitoring

To address these challenges, there have been several systems developed to detect, classify and store interference events.

One of them was the DETECTOR system by Nottingham Scientific laboratory NSL described in our paper from 2016 [6].

Another one has been developed by Fraunhofer IIS in Germany in 2017 [20]. Fraunhofer IIS developed a configurable and customizable GNSS interference detection station. With up to three GNSS bands with a bandwidth of up to 80 MHz and a resolution of up to 8 bit can be continuously analyzed.” [20]

The interference monitoring system, which we would like to present in this paper is the GIDAS System: GNSS Interference Detection and Analysis System by OHB Digital in Austria [7]. This system is based on a set of algorithms and has been implemented in three different versions:

- as a stationary system, which can be useful for permanent monitoring in industrial areas and harbours, or other critical infrastructure
- as a portable system in a suitcase for field testing in various locations
- as an embedded system, where the software detector algorithms are

integrated into GPS/GNSS receivers or other electronic systems.

The algorithms use a set of different detector parameters, which are combined and weighted to allow a secure and clear detection of both spoofing and jamming. [7]

The detector parameters are:

1. Power Spectral Density Detector
2. Received Power Detector
3. Carrier to Noise Ratio
4. Correlation Peak Detector
5. Clock Detector
6. Position solution
7. Number of tracked satellites

“The **power spectral density** (PSD) of the signal describes the power present in the signal as a function of frequency, per unit frequency.” [18]. In GIDAS, it is possible to define different thresholds to optimize the interference detection to the jamming types relevant to the use, e.g. narrowband thresholds, wide-band thresholds or the ICAO mask (for civil aviation), see figures 3 and 4 for an example. [7]

The **received power detector** measures the absolute received signal power within the monitored frequency band. In case of interference, the received power is usually significantly stronger and thus overwhelms the GPS/GNSS receiver frontend.

Carrier to noise ratio (C/No), is the signal to noise ratio. In case of interference, a strong drop of the carrier to noise ratio is observed, while in case of spoofing there usually is an increase in C/No, because the fake signals add to the signal strength of the original GPS/GNSS signals. Also the spoofer can try to take over the receiver tracking loops by transmitting the fake signals with a slightly increased signal strength.

The combination of these three parameters PSD, C/No and overall received power are used to detect interference in GIDAS. The combination of different parameters is considered advantageous for a low false alarm rate [7]. When the interference is strong there will also be a failure of the receiver to fix a position solution. This results in a denial of GPS/GNSS service. Sometimes the receiver carries on providing position outputs to the user, however, in the presence of medium strength interference, these position fixes can become inaccurate and unreliable.

“The **clock-based spoofing detector** operates on the assumption of non-perfect synchronization of the spoofed signals with respect to their authentic counterparts. A GNSS receiver continually estimates its own clock bias relative to the system time within the PVT solution. After receiver initialization, large jumps in the estimated clock bias are typically not expected due to the clock steering algorithm. In case of spoofing takeover, however, such a jump is expected (it is the combined effect of non-perfect time synchronization of the spoofer and nonperfect spoofer as well as victim receiver position estimation)” [7]

Correlation Peak Detector: In case of spoofing there are two correlation peaks for each satellite signal: the true signals are still present and in addition there is a fake spoofing signal for each satellite. Thus a determination of the amount of correlation peaks for each satellite is a good indication of the presence of a Spoofer.

In summary a weighted combination of clock detector, correlation peak detector and carrier to noise ratio is used to detect spoofing.

The number of tracked satellites shows whether the GPS/GNSS receiver has enough satellites in view to be able to calculate a PNT solution: position, navigation and timing. A GPS receiver needs at least four satellites to do so. If the number of tracked satellites is low, there can be various reasons. Lack of sufficient amount of satellites can be caused by interference, or it can also be caused by high structures obscuring satellite view.

Lack of sufficient number of satellites is thus a reason for alert and countermeasures, even if no spoofing or jamming is detected. [7]

Overall Functionality of the GIDAS System

The GIDAS system uses the above mentioned detector algorithms and provides a real-time 24/7 monitoring of jamming and spoofing signals for all GNSS systems on L1, and for GPS on L1,L2,L5, Galileo E1 and E5, GLONASS L1 and L2 with a maximum bandwidth of 81 MHz. The events are classified and saved for later analysis. They are also listed in the GUI and stored in a database with time of occurrence and duration. The direction of arrival of the interference systems can be determined, with an antenna with two or more antenna elements. The GIDAS system is hardware agnostic, thus different antennas can be attached. Users are alerted via E-Mail or via a custom alert interface. Information can be viewed remotely via a webbased graphical user interface. The graphical user interface displays

a map and detailed information about the interference events, all detector parameters are displayed. “Since GIDAS automatically captures and stores raw baseband signal snapshots for every interference event, it is even possible to gather more detailed insights on the jamming signals by post processing analyses.” [5]

Longterm results of a fully operational stationary GIDAS system with several monitoring stations at 3 locations around an airport are described in a whitepaper from 2023: “Since May 2022 we operate a permanent GIDAS installation at a European airport, together with the local air navigation service provider. The goal of the commonly operated GNSS quality assurance system is to gather data-based evidence for future decision-making and strategy definition on how to handle GNSS interference, inflicting air traffic surrounding the airport premises. The first eight months of operation show, that especially along motorways and construction sites, the quantity of interference signals in the restricted GNSS bands is even higher than expected. Between the 17th of May 2022 and the 18th of January 2023 (246 days of operation), the system detected 630 interference events with a severity classified as an alarm (which means that there was an actual degradation of the GNSS

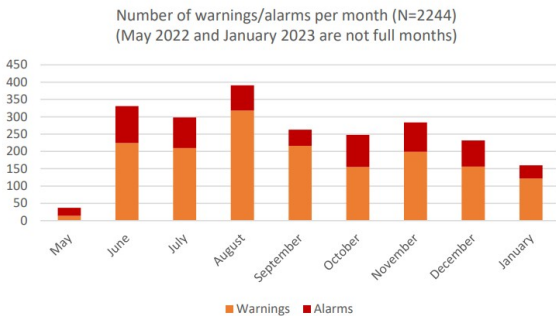


Fig. 2. Number of warnings alarms per month

measurement quality). During this period an additional number of 1614 interference events with a severity classified as a warning has been captured.” [5]

In their results they found that interference events occur on a daily basis, especially along motor ways and that a significant amount of such events correlate with daily rush hours and working hours.

“The highest number of interference alarms and warnings has been recorded at” at two monitoring sensors, “both close to either a motorway or a busy country road. In total, a number of 98 interference events have been critical enough to be recorded at least at two sites in parallel.” [5]

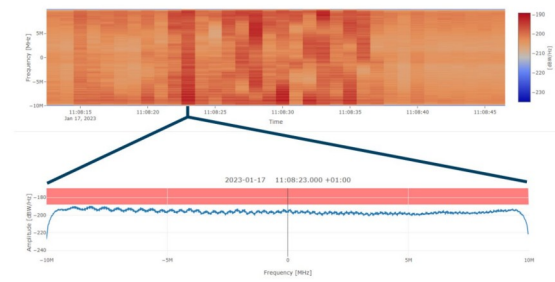


Fig. 3. A typical recorded interference event on the L1 frequency. [5]

Results from Interference Monitoring in a Harbour

In 2021 the GIDAS system was installed in the port of Tallin, and operated for 2 years. Within 11 days in November 2021 the GIDAS system recorded 1231 interference events in the L1/E1 band, 51 of them were strong enough to cause an alarm, this means interference with a high probability of negatively impacting GPS/GNSS receivers. Some events lasted several minutes, the longest one approximately 13 hours. The GIDAS installation in Tallin recorded a total of distinct 5 interference events, classified as GNSS jamming events. The most significant event started at 2021-11-21 14:39 UTC+1 and lasted for an approximate duration of 13 hours. [19]

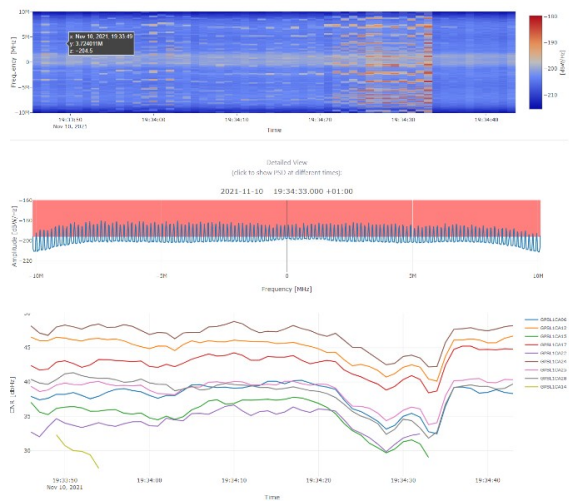


Fig. 4. Jamming event at port of Tallin 10th, Nov, 2021 [19]

The jamming event in figure 4 lasted for 3 min with an alarm duration of 45 sec. The red area in the PSD of figure 4 (plot in the middle) shows the power above the alert threshold. The satellite signals’ C/No clearly drops to much lower levels in the bottom part of figure 4, with tracking loss of 2 satellites. The top plot shows a waterfall diagram with power levels: x-axis

Time, y-axis frequency (MHz), powerlevel: color code (dBW/Hz).

Effects of Monitoring

Even though monitoring does not eliminate unintentional interference, jamming or spoofing, it increases situational awareness and provides alerts. Alerted operators can pass this information on to their automated vehicles and allow them to switch over to other sensors, such as inertial sensors and to disregard the GPS/GNSS information for a certain period of time. In addition operators can decide to stop the automated vehicles and freeze their position, while the GPS/GNSS outage lasts, which can help to prevent accidents, due to false PNT solutions and thus save loss of material and damage. Other countermeasures can be a hand over to remote control steering of the automated vehicle. Since GIDAS also allows to localize interference sources, it is possible to search for them and to remove the interference transmitters. This contributes to overall smoothness of operation and thus better sustainability.

Conclusions:

Reduction of throughput time of lorries in harbour container terminals by operation of automated vehicles will lead to an improvement in efficiency thus contributing to sustainability.

In recent years more and more interference events have been observed in Europe and other areas of the world. We have presented the GNSS monitoring system GIDAS, capable of analyzing and classifying interference events, and issuing alerts in case of such events. The GIDAS system was installed at an airport and at the harbour of Tallin and in both locations a high amount of jamming and interference has been observed. Monitoring the GNSS signal environment ensures enhanced awareness of GPS/GNSS availability or blackouts and thus allows to optimize the operation of autonomous and automated vehicles, which in turn leads to a more efficient and sustainable operation.

Acknowledgements

I am grateful for the support and data from Sina Willrodt, Fraunhofer CML, and the support and unpublished data from Sascha Bartl, from OHB-Digital and would like to thank them for their support and cooperation.

References

- [1] S. Willroth, I. Völkel; Einsatz automatisierter LKW in Häfen und Terminals; Schiff und Hafen, March 2022, S.54-55.
- [2] S. Willrodt, P. Zimmermann. Simulationsbasierte Analyse Automatisierter Verkehrsflüsse In Häfen und Terminals. 2022. Fraunhofer-Allianz Verkehr Newsletter.
- [3] O Julien, R Bryant, C Hide, I Sheret. Tight Position Bounding for Automotive Integrity. Inside GNSS May/June 2021: 34-41.
- [4] S. Igarashi et al. Autonomous Driving Control of a Robotic Mower on Slopes Using a Low-Cost Two-Frequency GNSS Compass and an IMU, January 2022. Journal of the ASABE 65(6):1179-1189, DOI: 10.13031/ja.15032
- [5] M. Kadletz. Jamming and Spoofing of Safety Critical Infrastructure. January 2023. Whitepaper by OHB-Digital
- [6] M. Stanisak, K. Hünerbein K, U. Bestmann, W. Lange, (2016) "Measured GNSS Jamming Events at German Motorways", Proc. of POSNAV ITS, DGON Conference, Berlin, Germany, 5th-6th July, 2016.
- [7] S. Bartl, M. Kadletz et al. (2022) Mitigating the Threat of Jamming and Spoofing to Aeronautics. Inside GNSS Sep/Oct 2022, vol. 17, no. 5: 46-55.
- [8] P. Gutierrez, (2014) A GNSS Wake Up Call for Europe; Apr 2014, European Navigation Conference in Rotterdam, Netherlands
- [9] K. Hünerbein, W. Lange, A New Solution of Generation of Spoofing Signals for GNSS Receivers. DGON Conference CERGAL 8th-9th July 2014, in Dresden. International Symposium on the Certification of GNSS Systems and Services.
- [10] M. Jones, "The Civilian Battlefield", Inside GNSS, March/April 2011, vol. 6, no. 2, pp. 40-49
- [11] M. Baus. Safe GNSS/Inertial Positioning for Highly Automated Driving. Presentation. 2018 Munich satellite Navigation Summit in Munich, 2018
- [12] M Creadie, M. Pattinson, M Dumville, Standardisation Of GNSS Threat Reporting And Receiver Testing Through International Knowledge Exchange, Experimentation And Exploitationstrike3, Final Report. 2019.
- [13] M. Petovello, How can we ensure GNSS receivers are robust to real-world interference threats? Inside GNSS Jul/Aug 2018, Vol 13 No 4: 33-37.
- [14] Z. Liu, S Lo et al. Solutions: What do we know about recent observations of GNSS Interference and Spoofing in Eastern Europe?... Inside GNSS March April 2024 Vol19, No2: 28-35
- [15] J. Wiseman; GPSJam: Daily Maps of GPS Interference, <https://gpsjam.org>
- [16] SA Negru, P Geragersian, I Petrunin, W Guo. (2024). Resilient Multi-Sensor UAV Navigation with a Hybrid Federated Fusion Architecture. Sensors, 24(3).<https://doi.org/10.3390/s24030981>

- [17] Ruwisch F., Schön S. (2022): GNSS Feature Map: Representation of Signal Propagation-related Features in Urban Trenches, Proceedings of the 2022 International Technical Meeting of The Institute of Navigation, Long Beach, California, January 2022, pp. 701-711. DOI: 10.33012/2022.18171
- [18] https://en.wikipedia.org/wiki/Spectral_density#Power_spectral_density
- [19] Sascha Bartl, OHB Digital (2024) personal communication.
- [20] A Rügamer et al (2017) Versatile and Configurable GNSS Interference Detection and Characterization Station; Proceedings of the ION Pacific PNT 2017 Conference, ION PNT 2017, Honolulu, Hawaii, May 1-4, 2017
- [21] S Schweitzer (2024) Jamming of a Parked Passenger Jet: Sensitivity of the aircraft to Jamming with Varying Power. European Navigation Conference in Nordwijk, NL, May 22-24, 2024

Telemetry Spectrum Reallocation Risk Update: An Update on Threats to Telemetry Spectrum

Tim Chalfant¹, Sergio Penna²

¹ *GMRE, Inc., supporting the U.S. Department of Defense Test Resource Management Center,
Arlington, VA, USA,*

² *Instituto Superior de Engenharia do Porto, Porto, Portugal
timothy.chalfant.1.ctr@us.af.mil*

Abstract:

A review of spectrum issues that can challenge the future use of radio frequency telemetry. The International Consortium for Telemetry Spectrum (ICTS) will present the status of World Radiocommunications Conference items that address telemetry that were considered at the 2023 World Radiocommunication Conference and may be planned for future World Radiocommunications Conferences. International telemetry vendors, suppliers, and users need to be aware of, and potentially engage with their national administrations on these items.

The ICTS (www.telemetryspectrum.org) was formed in 1999 and is chartered under the sponsorship of the International Foundation for Telemetry (IFT). The IFT (www.telemetry.org) is a non-profit organization dedicated to serving the professional and technical interests of the telemetry community. This paper provides an update to potential spectrum allocation issues for each telemetry band perceived by the ICTS as of interest to the international telemetry community.

Key words: Telemetry spectrum, Frequency spectrum encroachment, Airborne Mobile Telemetry.

Introduction: Higher Demand

Several factors within and outside of the telemetry community have revolutionized demand for electromagnetic spectrum, including spectrum allocated for flight test telemetry. These factors include:

- Commercial radio frequency (RF) spectrum utilization is increasing rapidly, particularly for mobile broadband, and this trend is expected to continue.
- Real-time data and video telemetry is critical to the economic viability of the commercial aeronautical industry.
- Frequency bands used for telemetry have been reallocated for other uses.
- Telemetry data rates are increasing, thereby increasing the RF bandwidth needed for each mission.

Telemetry users are caught between a proverbial rock (telemetry demand is increasing) and a hard place (less spectrum is available for telemetry).

As an example, CTIA (the cellular industry trade association) has filed a chart with the U.S.

Federal Communications Commission (FCC) presenting a list of target bands for future cellular use (4G/5G) (Figure 1). Several of these bands are currently allocated for telemetry. While carriers still prefer exclusive licenses, the spectrum is congested, and clearing a band of incumbents to auction those frequencies may no longer be practical. If telemetry bands become targeted for repurposing, telemetry operations could become further cramped and congested whether via band clearing or spectrum sharing.

Globally the bands in Figure 1 – which are critical to Aeronautical Mobile Telemetry (AMT) and associated operations (telemetry command and control and time-space-position information, or TSPi) – are covered by three bands: L-Band, S-Band, and C-Band. These bands reside in an RF spectrum “sweet spot.” This region between 300 MHz and 3 500 MHz is well-suited for mobile communications due to its RF propagation characteristics (penetration of atmospherics, buildings, terrain). This region is ideal for AMT, where the transmission of data over long distances using low-power transmitters on maneuvering test articles, is typical. It is also attractive for cellular operators for many of the same reasons.

Low-Band					
406.1-608 MHz	960-1164 MHz	1300-1350 MHz	1427-1518 MHz	1780-1850 MHz	
Mid-Band					
3100-3550 MHz	4400-5000 MHz	5925-7125 MHz	7125-8400 MHz	10-10.5 GHz	
High-Band					
25.25-27.5 GHz	28.35-31.3 GHz	31.8-36 GHz	42.5-47.2 GHz	50.4-52.6 GHz	Over 95 GHz

Figure 1. Desired 4G/5G Bands (CTIA)

WRC-23 Results

The International Telecommunication Union (ITU), chartered by the United Nations, manages the ITU’s Radio Regulations at periodic World Radiocommunications Conferences (WRCs).

The ITU manages this regulation within three regions (Fig 2). The recent World Radiocommunications Conference was just completed in December in Dubai (WRC-23). Several of the AMT-related radio regulations (RR) were amended or modified at this Conference. Many changes were administrative only, some were substantive or critical. A synopsis of WRC-23 AMT-related radio regulation discussions and updates follows.

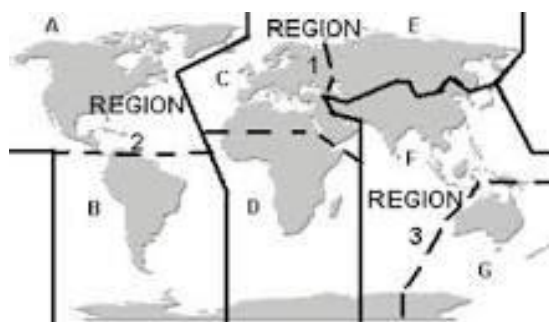


Figure 2 ITU Regions

L-Band

IMT. The appetite for spectrum to support International Mobile Telecommunications (IMT) efforts (IMT-2000, IMT-Advanced and IMT-2020, cell phones, wireless, broadband) is driven by the vision of global mobile access – providing telecommunication services on a worldwide

scale regardless of location, network, or terminal used. Much of the ITU focus is on frequency bands below 3 GHz.

There has been a tremendous growth in mobile communications driving an increasing demand for spectrum – already encroaching in some regions on several heavily used AMT bands (1 435-1 535 MHz, 1 710-1 885 MHz, 2 300-2 400 MHz, 4 400-4 800 MHz, 5 091-5 250 MHz...). As a result, one administration added themselves to the use of 1 452-1 492 MHz for IMT, a critical AMT band in the United States and other areas. The following regulation was discussed at WRC-23:

- RR 5.346 In Algeria, Angola, Saudi Arabia, Bahrain, Benin, Botswana, Burkina Fao, Burundi, Cameroon, Central African Republic, Congo (Rep. of the), Côte d'Ivoire, Djibouti, Egypt, United Arab Emirates, Eswatini, Gabon, Gambia, Ghana, Guinea, Iraq, Jordan, Kenya, Kuwait, Lesotho, Lebanon, Liberia, Madagascar, Malawi, Mali, Morocco, Mauritius, Mauritania, Mozambique, Namibia, Niger, Nigeria, Oman, Uganda, Palestine**, Qatar, Dem. Rep. of the Congo, Rwanda, Senegal, Seychelles, Somalia, Sudan, South Sudan, South Africa, Tanzania, Chad, Togo, Tunisia, Zambia, and Zimbabwe, the frequency band 1 452-1 492 MHz is identified for use by administrations listed above wishing to implement International Mobile Telecommunications (IMT) in accordance with Resolution 223. (Rev.WRC-19/23).

This regulation was revised at WRC-23 to modify the affected countries (Somalia was added). Asterisks were added to Palestine to note the

use by Palestine of the allocation to the mobile service.

S-Band

Upper S-Band. The WRC approved revision of RR 5.394 to increase the affected telemetry band from 2 360-2 390 MHz to 2 360-2 395 MHz.

- RR 5.394 In the United States, the use of the frequency band 2 360-2 395 MHz by the aeronautical mobile service for telemetry has priority over other uses by the mobile services. In Canada, the use of the frequency band 2 360-2 400 MHz by the aeronautical mobile service for telemetry has priority over other uses by the mobile services. (WRC-23)

S-S Links. WRC-23, noting that there is growing interest for utilizing space-to-space satellite links for a variety of applications, adopted the following agenda item 1.11 for WRC-27:

... to consider the technical and operational issues, and regulatory provisions, for space-to-space links among non-geostationary and geostationary satellites in the frequency bands 1 518-1 544 MHz, 1 545-1 559 MHz, 1 610-1 645.5 MHz, 1 646.5-1 660 MHz, 1 670-1 675 MHz and 2 483.5-2 500 MHz allocated to the mobile-satellite service, in accordance with Resolution 249. (Rev.WRC-23)

The accompanying Resolution 249 provides:

- RESOLUTION 249 (Rev.WRC-23) Study of technical and operational issues and regulatory provisions for space-to-space transmissions in the frequency bands 1 518-1 544 MHz, 1 545-1 559 MHz, 1 610-1 645.5 MHz, 1 646.5-1 660 MHz, 1 670-1 675 MHz and 2 483.5-2 500 MHz.

This resolution notes that in Region 2 the frequency band 1 435-1 525 MHz is used by the aeronautical mobile service for telemetry in the United States. It seeks studies of the technical and operational characteristics of different types of non-geosynchronous-orbit (non-GSO) space stations that operate space-to-space links with non-GSO systems or GSO networks for space-to-Earth direction in the frequency bands 1 518-1 525 MHz, among others.

This new agenda item for a WRC-27 decision could affect AMT operators in the United States and other administrations. This would also include the space-to-Earth direction in the frequency band 1 518-1 544 MHz.

Supplemental Space Coverage. The Conference also discussed possible allocations to enable supplemental coverage from space (SCS) via

direct connection with IMT terminals. WRC-23 noted the growth in demand for mobile-satellite systems (MSS) is making it difficult to sustain MSS services on a long-term basis in the existing bands. Believing that new allocations to the MSS would be consistent with the International Telecommunication Union's objective of promoting access to telecommunication services, particularly in remote and rural areas, it adopted the following WRC-27 agenda item 1.13:

...to consider studies on possible new allocations to the mobile-satellite service for direct connectivity between space stations and International Mobile Telecommunications (IMT) user equipment to complement terrestrial IMT network coverage, in accordance with Resolution COM6/9. (WRC-23)

The agenda item and accompanying Resolution COM6/9 (WRC-23) provide that the studies will deal with the frequency range between 694/698 MHz and 2.7 GHz, which includes several AMT bands.

C-Band

Protection from IMT. WRC-23 Agenda Item 1.1 The upper portion of the 4 GHz band, namely 4 800-4 990 MHz, is identified for IMT in numerous countries (including China, South Africa, Russia, Nigeria, Gambia, Uruguay, and Iran). WRC-23 agenda item 1.1 called for studies to consider measures to protect stations of the aeronautical and maritime mobile services located in international airspace and waters from IMT operations in the 4 800-4 940 MHz band. France, the United States, Canada and other administrations sought to protect Aeronautical Mobile Service systems (AMS; note AMT is included in AMS) and Maritime Mobile Service (MMS) systems. Russia, supported by China, Iran, and others, sought changes that would weaken existing protection for AMS/MMS in international airspace and waters.

5.441B In Angola, Argentina, Armenia, Azerbaijan, Benin, Botswana, Brazil, Burkina Faso, Burundi, Cabo Verde, Cambodia, Cameroon, Chile, China, Colombia, Congo (Rep. of the), Côte d'Ivoire, Djibouti, Eswatini, Russian Federation, Gabon, Ghana, Guinea, Iran (Islamic Republic of), Iraq, Kazakhstan, Lao P.D.R., Lesotho, Liberia, Madagascar, Malawi, Mali, Mongolia, Namibia, Niger, Uganda, Uzbekistan, the Dem. People's Rep. of the Congo, Kyrgyzstan, the Dem. People's Rep. of Korea, South Sudan, South Africa, Chad, Togo, Viet Nam, Zambia and Zimbabwe, the frequency band 4 800-4 990 MHz, or portions thereof, is identified for use by administrations wishing to implement International Mobile

Telecommunications (IMT). This identification does not preclude the use of this frequency band by any application of the services to which it is allocated and does not establish priority in the Radio Regulations. The use of IMT stations is subject to agreement obtained under No. 9.21 with concerned administrations, and IMT stations shall not claim protection from stations of other applications of the mobile service. In addition, before an administration brings into use an IMT station in the mobile service, it shall ensure that the power flux-density (pfd) produced by this station does not exceed -155 dB (W/m² · 1 MHz) produced up to 19 km above sea level at 20 km from the coast, defined as the low-water mark, as officially recognized by the coastal State. Resolution 223 (Rev.WRC-23) applies. (WRC-23)

WRC-23 made no change (i.e., no relaxation) to the power flux density protection level for aeronautical mobile systems (which includes AMT as noted above) in the relevant ITU Radio Regulations. At the Conference, Mexico stated its intention to deploy IMT in 4 800-4 990 MHz, which could lead to potential AMT interference. Telemetry operators in this region should pay close attention to bi-lateral negotiations for protection of these operations. The Conference did not remove the part of Resolution 223 exempting administrations (including Russia and China) from that protection.

Wireless Access Systems. WRC-23 also addressed the need for additional wireless access systems (WAS), including radio local area networks (RLANS) and the need to protect existing primary services in these bands (5 150-5 350 MHz and 5 470-5 725 MHz). There is concern that this expansion could interfere with AMT operations in 5 150- 5 250 MHz in Region 1 (and other administrations).

- RESOLUTION 229 (REV.WRC-23) Use of the frequency bands 5 150-5 250 MHz, 5 250-5 350 MHz and 5 470-5 725 MHz by the mobile service for the implementation of wireless access systems including radio local area networks

This resolution was revised at WRC-23 to enable additional WAS and RLANS in this band. This resolution notes that this band is also allocated to AMT (see RR 5.446C) and notes the need to protect the existing primary services in the bands. It also specifies emission limits for WAS and RLANS implementations. As 5 150- 5 250 MHz is widely used in Region 1 including Europe and several other administrations for AMT, this is a watch item for telemetry users in this band.

IMT Implementation. WRC-23 approved WRC-27 Agenda item 1.7 to consider the use of the frequency bands 4 400-4 800 MHz, for IMT.

...to consider studies on sharing and compatibility and develop technical conditions for the use of International Mobile Telecommunications (IMT) in the frequency bands 4 400-4 800 MHz, 7 125-8 400 MHz (or parts thereof), and 14.8-15.35 GHz taking into account existing primary services operating in these, and adjacent, frequency bands, in accordance with Resolution COM 6/26 (WRC-23)

It also adopted a resolution on IMT that could affect the 4 400- 4 940 MHz band used for AMT. The resolution discusses the necessary studies for the use of International Mobile Telecommunications (IMT) in several bands, including 4 400-4 800 MHz (Region 1 and 3 only), to implement IMT. The resolution references relevant protective information relating to previous sharing studies including ITU-R M.2116 (but not M.1459).

- RESOLUTION COM 6/26 (WRC-23) Sharing and compatibility studies and development of technical conditions for the use of International Mobile Telecommunications (IMT) in the frequency bands 4 400-4 800 MHz, 7 125-8 400 MHz (or parts thereof), and 14.8-15.35 GHz for the terrestrial component of IMT

Use of 4 400-4 800 MHz for telemetry in Region 1 and 3 (and other administration) can be at risk. The Region 2 allocation for AMT in this band appears unaffected.

RNSS Spectrum. WRC-23 adopted a preliminary agenda item for WRC-31 as follows:

...to consider possible allocations to the radionavigation-satellite service (space-to-Earth) in the frequency bands [5 030-5 150 MHz and 5 150-5 250 MHz] or parts thereof, in accordance with Resolution COM6/19 (WRC-23)

The accompanying resolution, presented by the European Conference of Post and Telecoms (CEPT) per a proposal initiated by the European Space Agency (ESA), was adopted for studies of the proposed new allocation:

- RESOLUTION COM 6/19 (WRC-23) Studies on possible new allocations to the radionavigation-satellite service (space-to-Earth) in the frequency bands [5 030-5 150 MHz and 5 150-5 250 MHz] or parts thereof

Parts of these bands are currently used by AMT (5 091-5 150 MHz globally and 5150-5250 in Region 1 (and others). This resolution, in support of the ESA's R&D activities on the European Global Navigation Satellite System (EGNSS) and Positioning, Navigation and Timing in Low Earth Orbit (LEO-PNT), asks for new frequency bands and allocations suitable for very wide band PNT signals. Clearly, these new services could be exploited by all other RNSS users, including aeronautical transportation systems. It is felt that these potential new signals cannot be supported in the existing allocations.

ITU-R Studies on sharing and compatibility between RNSS and the incumbent services may be considered at WRC-27 with the result depending on confirmation of the preliminary agenda item for WRC-31.

Domestic Issues

While ITU regulations are determined at the WRC, each administration (country) has national regulations in place apart from the ITU regulations. This section addresses a few spectrum regulatory issues of particular note for each band used for AMT in specific administrations as reported to the ICTS.

L-Band

Cellular Interference (U.S.). While the band is currently not perceived as threatened, it is on several target lists due to its proximity to other low-band spectrum. While 1 300-1 350 MHz is being considered for repurposing, the National Telecommunications and Information Administration (NTIA) noted that this would also apply to equipment certification requests for all stages in 1 240-1 390 MHz; in other words, repurposing will impact usage in the entire band, not just 1 300-1 350 MHz.

There is a concern that TSPI data links (Advanced Range Data System (ARDS), Common Range Integrated Instrumentation System (CRIIS), 1 350-1 390 MHz) may be affected by adjacent channel interference from cellular operation below 1 350 MHz. This is a watch item for test and training ranges that rely on GPS-based TSPI instrumentation as the susceptibility of the TSPI data link operations to Long Term Evolution (LTE) interference is unknown as this time. Efforts to access this susceptibility, and necessary protection criteria, are needed to analyze this threat.

IMT (Region 2). The International Telecommunication Union (ITU) Radio Regulations give AMT priority over IMT in 1 435-1 535 MHz in Region 2 (North and South America). RR 5.343. It remains high on the list of encroachment concerns for ICTS as it resides in the low band "sweet spot" for RF propagation characteristics for international mobile communications. ITU Recommendations M. 1459 is particularly relevant for AMT protection criteria.

Ligado (U.S.). The upper part of the L-band is home to several global positioning systems (GPS). Along with AMT operations below 1 525 MHz, one of these signals is potentially threatened. L1 (encrypted precision code, coarse acquisition code), at 1 575.42 MHz, could receive interference from a terrestrial data link proposed by Ligado Networks (Reston, VA) in the United States. Despite major pushback from the Department of Defense (DoD) and other federal agencies over GPS interference concerns, the FCC initially granted the Ligado application for a terrestrial Internet of Things (IoT) network. Several agencies and commercial interests filed Petitions for Reconsideration due to concerns about interference to GPS. If this IoT network is implemented, it could have significant impact on GPS-dependent systems (like TSPI). The U.S. Congress has enacted legislation intended to protect DoD spectrum uses against the possibility of Ligado interference.

Ligado has filed a lawsuit alleging "theft" of its L-band spectrum by the U.S. Government, but the Department of Justice has moved to dismiss the Ligado lawsuit. Several groups and companies have indicated their support for the Government's motion.

AWS-3 Auction (U.S.). In 2014, the FCC in the United States started the process of auctioning 65 MHz of spectrum to meet the goals of the National Broadband Plan. This was the last of three auctions required for funding FirstNet, the public safety broadband network, and other services. Previous auction results had raised nearly \$1.6 billion of the \$7 billion needed. The AWS-3 (Advanced Wireless Services) auction generated \$44.9 billion in revenue. As a result, several government users were compensated to vacate the band. AMT operations, previously in the band 1 755-1 780 MHz, were compressed into the remaining spectrum between 1 780 and 1 850 MHz. The ICTS is concerned that commercial interests may not be satisfied with the 65 MHz.

Lower S-Band

Commercial Space Launch (U.S.). In the United States, the FCC is considering potential

allocation of several additional bands for commercial space launch – including 2 360-2 395 MHz. Last year the FCC adopted rules for a new allocation in the 2 025-2 110 MHz band for space operations on a secondary basis, expanded the spectrum available for commercial space operations on a secondary basis in the 2 200-2 290 MHz band from four channels to the entire band, and adopted licensing and technical rules for space launch operations. The Office of Engineering and Technology is to issue a public notice opening a new docket for comments on expanded federal earth station use of non-federal satellite bands. The Aeronautical and Flight Test Radio Coordinating Council, Inc. (AFTRCC) has proposed that it to coordinate non-Federal space launch requests with the DoD area frequency coordinators.

C-Band

Allocation Restrictions (Germany). In a recent decision the German administration decided that new allocations in the future will only be granted in the range 5 091-5 150 MHz, not in the range 5 150-5 250 MHz. No new or temporary allocation on a new test site will get granted in the 5 150-5 250MHz. Current allocations in the range 5 150-5 250 MHz will remain.

Non-Federal AMT Use (U.S.). In the United States, AFTRCC has submitted a proposal to the FCC for a non-federal AMT allocation in the band 4 400-4 940 MHz with DoD support. AFTRCC would coordinate use of any such allocation, if approved, with DoD area frequency coordinators. This is not considered a “threat” since AFTRCC member companies work hand-in-glove with DoD personnel in the development of new and modified aircraft and missiles for the Department.

RADAR-Alt Interference (U.S.). In the band below 4 400-4 940 MHz, there has been major controversy regarding 5G compatibility in the band 3 700-3 980 MHz, with radar altimeters (R-Alt) operating in the band 4 200-4 400 MHz. A Federal Aviation Administration (FAA) Special Airworthiness Information Bulletin calls on R-Alt vendors and others to provide data on specific R-Alts, and to assess the need for further mitigation. Meanwhile, AT&T and Verizon have agreed to delay deployment of certain 5G operations in 3 700-3 980 MHz.

Future Spectrum Legislation (U.S.). Several proposed bills currently being considered by the U.S. Congress, would require NTIA to study the 4 400-4 490 MHz band for possible future reallocation and auction. This band remains of great interest to cellular and broadband users.

Global AMT Band (All Regions). While 5 091-5 150 MHz is the globally harmonized band

allocated for aeronautical telemetry world-wide, its utilization is a domestic issue. Global telemetry users are encouraged to make use of this AMT band. AMT use may need to co-exist with airport ground communications depending on the administration.

Upper C-Band (5 925-6 700 MHz) Unlicensed Wi-Fi (U.S.). In the United States, the FCC concluded 5 925-7 125 MHz could be utilized for unlicensed Wi-Fi and very low-power devices for high data rate applications, such as wearables, augmented-reality, and virtual-reality. The band is also used for point-to-point microwave links; terrestrial microwave operators (mainly public safety and utilities) have unsuccessfully opposed the FCC’s Wi-Fi plans. While the FCC has tabled any AMT assignments/allocations in the band, DoD has studied new spectrum aggregation technologies.

New National Spectrum Strategy (U.S.). The draft Implementation Plan for the National Spectrum Strategy was released in November along with a Presidential Memorandum; a draft Implementation Plan has been developed by NTIA. While data is not telemetered to the ground using the five bands targeted, several “Outcomes” address topics with significant potential to affect telemetry users as the NSS seeks additional spectrum for the study pipeline. Several outcomes talk of the need to develop/field new spectrum management tools, metrics, and utility specifications. U.S. telemetry users will need to be prepared to articulate spectrum utilization and sharing potential.

Articulation of spectrum utilization in telemetry and Flight Test can be difficult. Flight Test use of telemetry is one link in the test and evaluation chain of events that are required to complete a test program. Telemetry is a “late-in-the-cost-chain” asset where a failure (mission cancellation) could cause significant down-chain impact (cost/schedule) in a test program (targets, test environments, test assets, ranges). Capturing and articulating these costs can be very difficult.

Conclusions

Significant encroachment challenges to telemetry spectrum exist both domestically (in the United States) and internationally (ITU/WRC). The encroachment of incompatible services in- band and adjacent to bands used for AMT, can degrade telemetry data and result in test failure, loss of test articles, and even pose hazards to life. Adequate RF spectrum for telemetry operations is critical for flight test and other scientific applications.

The information in this paper is presented so that telemetry practitioners are aware of

developments that could affect the business of telemetry.

Acknowledgment

The International Consortium for Telemetry Spectrum, chartered by the International Foundation for Telemetry, is dedicated to serving the professional and technical interests of those in the telemetry community.

This work was supported by the CISTER Research Unit (UIDP/UIDB/04234/ 2020), financed by National Funds through FCT/MCTES (Portuguese Foundation for Science and Technology), and by project Aero.Next Portugal (ref. C645727867-00000066), funded by the EU/Next Generation, within call n° 02/C05-i01/2022 of the Recovery and Resilience Plan (RRP).

References

- [1] CTIA, <https://www.ctia.org/the-wireless-industry/wireless-industry>
- [2] "The Great Radio Spectrum Famine," Mitchell Lazarus, *Institute of Electrical and Electronics Engineers Spectrum Magazine* (30 Sept. 2010). <http://spectrum.ieee.org/telecom/wireless/the-great-radio-spectrum-famine>
- [3] International Consortium for Telemetry Spectrum (ICTS), www.telemetryspectrum.org
- [4] International Foundation for Telemetry (IFT), www.telemetry.org/who-we-are/
- [5] Aeronautical and Flight Test Radio Coordinating Council, Inc. (AFTRCC), <https://aftrcc.org/>
- [6] International Telecommunications Union, Radiocommunications Sector, <https://www.itu.int/en/ITU-R/Pages/default.aspx>
- [7] World Radiocommunication Conference 2023 (WRC-23) Provisional Final Acts, ITU Publications, International Telecommunication Union, Radiocommunication Sector

IN FLIGHT OPTICAL FIBER MEASUREMENT ON FLIGHT TEST AIRCRAFT

Laetitia MENNEBEUF, Benjamin MOUCHET, David CUMER,
Karounen VEERABADRAN, Laurent MALARD

Affiliation : Airbus Operations S.A.S, 316 route de Bayonne, 31060 Toulouse Cedex 09, FRANCE

Abstract

For many years, the Airbus Test Center has explored new ways of measuring with the optical fiber, mainly Fiber Bragg Grating sensors for temperature, stress, bending... This low intrusive instrumentation procures the advantage to be almost transparent, making aerodynamic effects negligible. Moreover, the insensitivity to the electrical environment due to its high level of galvanic insulation, enables measurement in a high Voltage environment which was nearly impossible with classical sensors.

This presentation will describe the main difficulties, benefits and results obtained in the frame of several Flight Tests campaigns.

Key words: Optical fiber sensors; Fiber Bragg Grating

Introduction

For more than a decade, Airbus Commercial Aircraft Test Center has been interested in optical fiber. Known to the general public for its qualities in the communication industry, the optical fiber presents many advantages such as: small size, low weight, insensitivity to EMI (Electromagnetic Interference), ability to be used in ATEX (ATmosphere EXplosive) environment, ... but it also has sensing properties. The sensitivity to temperature and strain had particularly caught our attention. Several implementations were done in order to decouple these two phenomena. Metrological tests were realized in Lab with successful results and allowed us to continue to evaluate in flight tests conditions.

The objective of this paper is to provide an overview of several flight tests realized on Airbus aircraft with an OFDR (Optical Time Domain Reflectometry) based on distributed Fiber Bragg Grating (FBG) with different implementations. In the first part, the integration of optical fiber sensors in aerodynamic environment will be described. In the second part, we will focus on the integration in an electrical environment.

Part 1 : Installation in an aerodynamic environment

1. Detection of laminarity along the A340-300 MSN001 wing

In September 2017, Airbus launched the Breakthrough Laminar Aircraft Demonstrator in Europe (BLADE) project to evaluate the reduction of the friction drag over the wing.



Fig. 1: A340-300 MSN1 laminar wing demonstrator

The aircraft was the A340-300 MSN 1, fitted with two 8m-long laminar profile wings. A specific instrumentation had been developed to assess the performance of the laminar flow wings.

This BLADE project offered the opportunity to install and expose the optical fiber sensors to assess their ability to detect the transition line between the laminar flow and the turbulent flow all over the wing. The transition line is characterized by a temperature variation between 2°Celsius and 10°Celsius along a laminar wing profile. This temperature variation is usually measured either by Pt100 or InfraRed (IR) cameras. The optical fiber was a good candidate for such measurements as well. Despite the low intrusiveness of the optical fiber and its capillary, their total thickness was too high (~1mm) to directly measure the temperature without disturbing the laminar flow. The optical fiber sensors were integrated using a sandwich of very thin and smooth stickers as described here after.

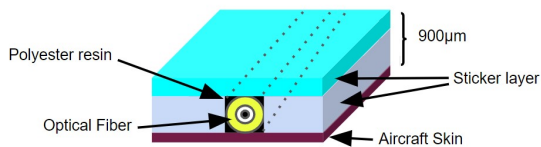


Fig. 2 : Schematic diagram of the optical fiber integrated within layers of stickers



Fig. 3: Picture of the installation before upper sticker application



Fig. 4 : Installation finalized

Two optical fibers measured the temperature distribution along four wing chords during

several flight tests and their results were compared to IR cameras (figure 5).

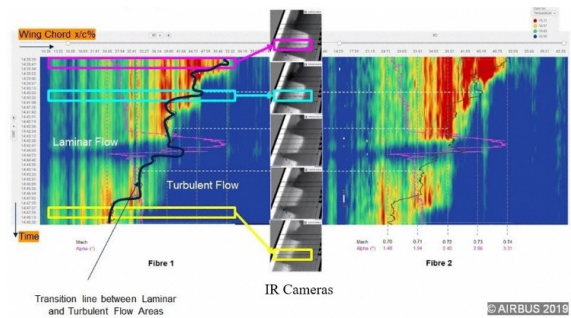


Fig. 5 : Visualization of the transition between laminar and turbulent flow area on 2 optical fibers

For each optical fiber, it was possible to detect the transition between the laminar and turbulent flow areas and there was a good coherence between them. Besides, the results showed an excellent correlation between optical fibers sensors and the IR cameras, spatially and over the time, as shown on figure 5. As the sensors are spaced 6.35mm apart, a very accurate resolution is achieved. This system can be valuable solution for areas where no direct view is possible for an IR camera.

2. Air inlet skin temperature measurement

Another application of the Optical Fiber temperature measurements in flight has been done on the engine inlet of an A350 aircraft.



Fig. 6 : A350-900 MSN1 aircraft

The request of the Design Office was to find a solution to measure the skin temperature of the air inlet without disturbing the air flow and without drilling any holes or cavities. The usual measurements are done with thermocouples

bonded on the surface and covered with resin. Nevertheless, this installation is spatially limited (a few points only), complex (several wires to be routed) and considered aerodynamically too intrusive (a few millimeters thick and an uneven surface finish) as shown on the following pictures.

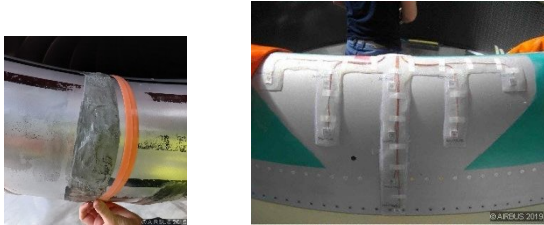


Fig. 7 : Pictures of thermocouples installation

To ease the routing of the optical fiber and to ensure the bonding, a dedicated fairing has been designed to encapsulate and maintain the optical fiber sensors.[1]

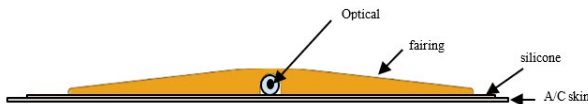


Fig. 8 : Schematic of the airbus patented fairing [1]

The integration of this concept was done on the A350-900 MSN1 at the end of 2019 and flew for a year. Four sections were instrumented with optical fiber sensors.

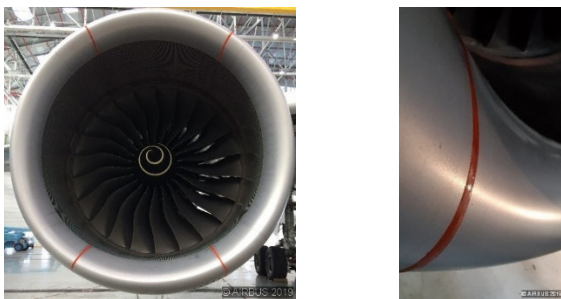


Fig. 9 : Pictures of the optical fibers' integration on an aircraft engine inlet

As shown on figures 8 and 9, the intrusiveness of this solution is negligible with a smooth and homogeneous profile. Besides the very small thickness of the installation, FBG optical sensors provide a huge number of measurements. Analysis has permitted the visualization of the effect of the Inlet de-icing activation. All along the four sections, the

temperature distribution profile has been characterized as described in the figure 10.

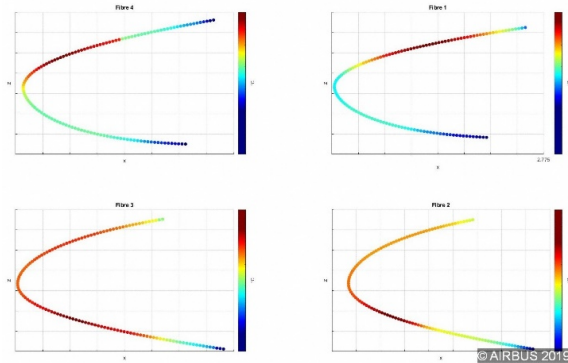


Fig. 10 : Temperature distribution measured by the four optical fiber sensors installed on A350-900 MSN1

The lesson learnt of this integration has shown several advantages:

- The sensors installation is flush and the aerodynamic impact is negligible,
- The lead time installation is reduced regarding the number of measurements,
- The post-treatment of the measurements is reduced with the absence of correction thanks to the low intrusiveness of the installation compared to the thermocouples and their resin cover.
- The optical fibers offer a fine spatial analysis compared to a few thermocouples.

3. Wing bending on A350-1000 MSN059 aircraft

In 2008, the National Aeronautics and Space Administration (NASA) presented its results to measure strain and wing bending on their Ikhana test vehicle [2, 3, 4, 5]. After several studies, the Airbus Flight Test Center has launched a study to evaluate the applicability of this method on a wider wing. The installation was done in 2021 on the A350-1000 MSN059. Eight optical fibers sensors were installed along the wing on the front spar area: four fibers were glued on the lower and the upper wing surfaces, dedicated to strain measurements and four other fibers were inserted inside a capillary to measure the temperature distribution. As the strain measurements are sensitive to temperature variations, a temperature compensation is necessary to improve the accuracy of the strain

data. The optical fiber sensors were installed just after the engine pylon up to the winglet area, as described on figure 11 over a length of 23 meters.



Fig. 11: Schematic diagram of the optical fiber sensors installation on the A350 wing

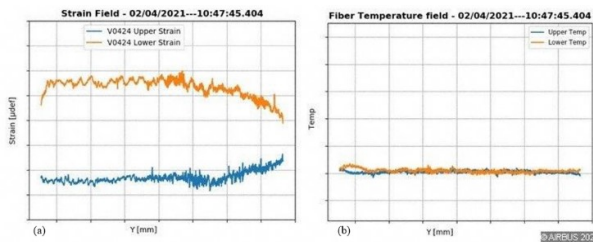


Fig. 12 : a) Strain field along the wing, b) Temperature distribution along the wing

In cruise conditions, the optical fiber sensors showed that the typical temperature distribution along the wing is quite homogeneous over the span but also between the upper and lower surfaces, the variations being a few degrees only. Using this result, confirming the numerical simulation, the model has been simplified from the temperature compensation. Applying the theory of Kho, Eq.1, from the strain measurements [5], the bending of the wing in cruise condition can be deduced:

$$\frac{d^2y}{dx^2} = \frac{\varepsilon(x)}{c(x)} \quad (1)$$

in which y is the vertical displacement, x is the span-wise coordinate, c is the uniform beam half depth and $\varepsilon(x)$ is the bending strain at the beam bottom (or top) surface.

The measurements done in flight with the optical fibers had been compared to a set of inclinometers, the current reference measurements. These inclinometers are installed into the wing, on the spars and are used to measure the wing twist and bending for this aircraft.

After post-processing, inclinometers and optical fiber measurements are consistent with a maximum deviation of 10 mm at the wing tip,

when comparing the wing vertical displacements. This result offers the possibility to simplify the installation as the fiber is glued on the surface whereas the inclinometers should be wired inside the wing.

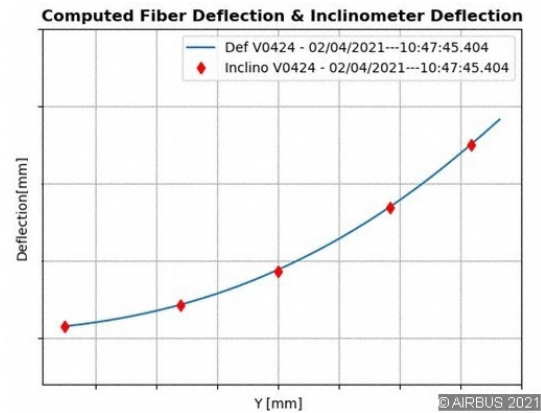


Fig. 13: Comparison between the inclinometers and the optical fiber measurements along the wing span

The next step is the investigation of the wing twist measurements as the fiber can provide a fine spatial resolution enabling to notice every twist variation over the span.

PART 2 : INSTALLATION IN ELECTRICAL ENVIRONMENT

1. Instrumentation of Beluga XL battery



Fig. 14: Beluga XL

In the frame of the Beluga XL development, we had a request to monitor the temperature inside a battery installed in the avionic bay. For safety reasons, the conventional electrical measurement with PT100 or thermocouple, has been refused, due to the risk of short circuit. Thanks to the high level of galvanic insulation of the fiber, Test Center Instrumentation teams have proposed to insert 8 optical FBG sensors

between the different cells without affecting the integrity of the battery. Here after, you can see the integration of the optical fiber sensors and the 3D visualization of the thermal mapping.

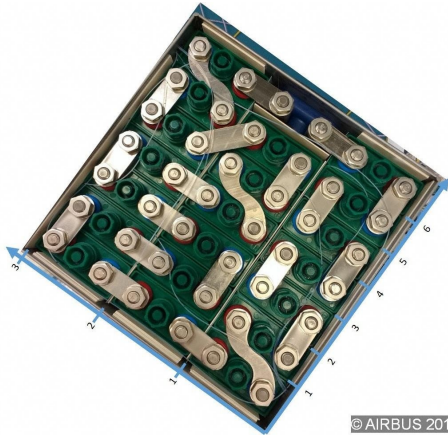


Fig. 15 : picture of the batterie with the optical fiber

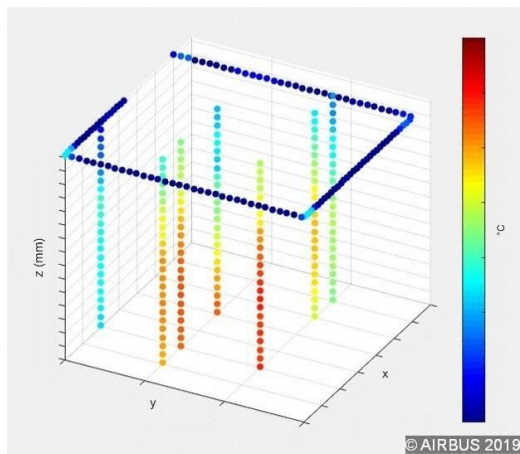


Fig. 16 : visualization of the thermal mapping

2. Temperature monitoring for High Voltage wiring

The future generation of Airbus aircraft will be more and more electric, involving new electrical power generators and converters, using higher voltage levels. In this frame, Airbus works on the characterization of new electrical cables and connectors. The thermal dissipation of these new wires and connectors pins, is an important parameter that we want to analyze at different levels of current injection. For this purpose, conventional electrical Pt100 or thermocouple are not recommended in Lab and forbidden in flight.

That's why, we have decided to implement optical fiber technology, all along the wires and above electrical components, in order to have

the temperature mapping and monitoring in the core of this harsh environment. Another advantage of the optical fiber is the immunity to the EMI (Electro-Magnetic Interference) constraints, which is a favorable asset to get accurate values in this kind of environment.

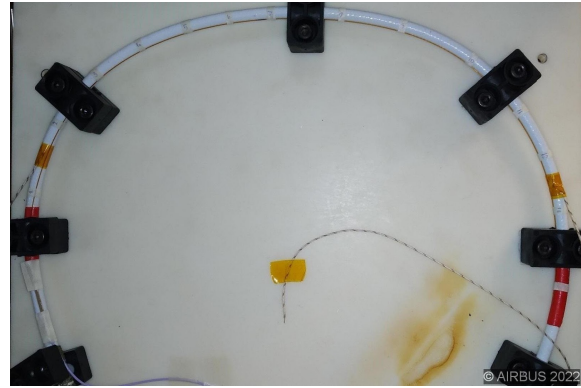


Fig. 17: temperature monitoring with optical fiber sensors of electrical cable

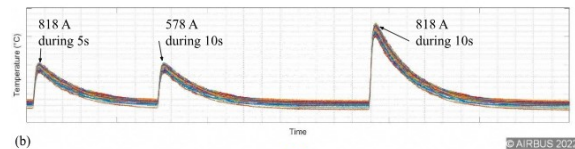


Fig. 18 :graph showing the temperature monitoring after several current impulsions

On the curves above, we can observe the temperature measurements mapping along the cable.

CONCLUSIONS

15 years ago, the Airbus Flight Test Center considered the optical fiber as a promising temperature and stress sensor. After many years of Lab testing and a long period of COTS devices evaluation, metrology verification and installation rules definition, we have been able to expose this technology in Flight, these last 5 years. The results have confirmed the promising hopes.

Thanks to the EMI immunity, galvanic insulation, low intrusiveness, ..., the optical fiber sensors are well adapted to the future aircraft ambitions of Airbus. All these characteristics are in line with the challenges and needs of the new aircraft development roadmap. The number of measurements able to be collected along an optical fiber provides a measurement mapping very useful for the design office in order to improve their design models.

To continue further, our expectations are now:

- to have small and ruggedized systems able to be embedded and installed in any aircraft areas;
- to collect measurements in real time;
- to be connected with our FTI over IENA Ethernet protocol (Specific application layer developed by AIRBUS);
- to explore other kinds of physical measurements requiring a higher data rate: pressure, acoustics, ...
- to continue the technical survey on different optical means (punctual, semi-distributed, fully distributed).

References

- [1] "Structure having a wall equipped with an optical sensor measuring device surrounded by a flexible envelope closely attached to the wall, and method for installing the device" Airbus U.S. Patent No US2021181038 (A1) Jun. 17, 2021
- [2] Dr. Lance Richards, Allen R.Parker, Dr. William L.Ko, Anthony Piazza, "Real-time In-Flight Strain and Deflection Monitoring with Fiber Optic Sensors" Space Sensors and Measurements Techniques Workshop Nashville, TN August 5, 2008
- [3] Francisco Pena Armstrong Flight Research Center, Edwards, California "Fiber-Optic Strain-Based Deflection and Twist Sensing for a High-Aspect-Ratio Swept Wing"
- [4] Francisco Peña, Dr. Lance Richards, Allen. R. Parker, Jr., Anthony Piazza, Patrick Chan, and Phil Hamory "Fiber Optic Sensing System (FOSS) Technology - A New Sensor Paradigm for Comprehensive Structural Monitoring and Model Validation throughout the Vehicle Life-Cycle"
- [5] Deformed Shape Predictions of the Doubly-Tapered Ikhana Wing, NASA/TP-2009-214652, January 2009. 9. Ko, William L., and William Lance Richards, "Method for Real-time Structure Shape-Sensing," U.S. Patent No. 7,520,176 B1, issued April 21, 2009
- [6] <https://lunainc.com/solution/thermal-mapping-batteries>

Comparing FBG Sensors with Electrical Strain Gauges on a Helicopter Rotor Blade during Whirl Tower Test

Simone Weber¹, Raphael Rammer¹, Valerio Camerini², Maxime Asselin², Florian Kurfiss¹, and Benedikt Köhr¹

¹Airbus Helicopters Deutschland GmbH, Industriestr. 4, 86607 Donauwörth, Germany,

²Airbus Helicopters S.A.S., Marseille Provence International Airport, France
simone.weber@airbus.com

Abstract:

Fibre Bragg grating strain sensors and conventional electrical strain gauges were deployed on an Airbus Helicopters H145 rotor during a dedicated whirl tower test to examine the accuracy of the optical fibre sensors. Data was streamed wirelessly from the rotor hub-mounted sensor interrogator to a ground station. Changes in strain and vibration signatures in response to a sequence of controlled hydraulic actuator inputs were successfully identified and the parameters of interest of both sensing solutions compared against each other. The outcome of this work demonstrates the potential of using optical fibre sensors for flight testing and providing in-service operational data on helicopter blade dynamics.

Key words: Fibre Bragg grating sensors, optical fibre sensors, electrical strain gauges, helicopter rotor blade, helicopter blade dynamics.

Introduction

Electrical strain gauges (SG) have been used for the measurement of aircraft structural loads for more than 70 years [1,2]. Some reports highlight the deployment of SG in the late 1970s to measure in-flight rotor blade loading in hover and forward flight conditions of a Boeing CH-47A [3,4]. Work conducted in the 1980s adopted a combination of SG and pressure sensors to predict the aerodynamic loading and rotor blade structural deformation for the hover case and for a variety of forward speeds on a Puma helicopter [5]. However, methods using SG have numerous disadvantages. These range from operational limitations, such as high sensitivity to precipitation to long installation times due to tedious wiring of each sensor. Moreover, the large amount of wiring interferes with the aerodynamic and dynamic behaviour of the blade and it is not uncommon that SGs fail during the testing. Robust and reliable measurement of rotating blade deformation is challenging and the search for new non-intrusive measurement techniques have been the subject of numerous studies. While imaging approaches have been trialled in wind tunnels and on whirl rigs [6], their in-flight use is hampered by the large observation angle and depth of field required to measure along the entire length of the blade, along with issues related to background light and to the fouling of

the blade surface. Optical fibre-based approaches with optical fibre Bragg gratings (FBGs) have the potential to meet both the measurement requirements and the demands of the measurement environment, with recent reports of their deployment on rotorcraft components in laboratory conditions [7-9], and under flight, or flight-equivalent, conditions [10–15]. In [10], surface-mounted FBG sensors were utilised to monitor the strains on a rotor blade during take-off, a low altitude hover, and landing, using six sensors connected to a battery powered interrogator, with the data logged locally for later processing. The data was post-processed to provide information on the flap, lead-lag and torsion deformation. Recently, as part of the BladeSense programme [11], two optical fibre-based sensing techniques were deployed on the rotor blades of an Airbus Helicopters H135: optical fibre FBG and fibre segment interferometry-based direct fibre optic shape sensing, live-streaming data during a series of ground runs with controlled pilot inputs. Aspects of the work and the findings have been presented previously [12-14], where it was shown that both sensing approaches were capable of detecting the 1/rev rotation frequency, and its harmonics, and of detecting some of the operational modes excited by specific pilot inputs. To increase the acceptance of optical fibre sensors in the aerospace

industry, they need to be benchmarked against SGs. In a previous study a good agreement with a maximum error of 1.8% was achieved during real flight that compared measured dynamic strains of SGs and FBGs on a rotor blade [15].

The work done in this paper focuses on determining the accuracy and reliability of FBG strain sensors compared to conventional SGs during a dedicated whirl tower test on an Airbus Helicopters H145 rotor applying a sequence of controlled hydraulic actuator inputs for rotor load determination and identification of modal properties. Outcome of the test campaign is presented with a clear recommendation for the potential use of optical fibre sensors for flight testing.

Sensors and instrumentation

Three FBG sensor arrays were applied to the flexbeam of the bearingless main rotor of an Airbus Helicopters H145, each containing 4 wavelength-division multiplexed FBGs in Ormocer coated 125 μ m single mode optical fibres, with the sensors distributed along a 0.4m length of the fibre. The FBG sensor arrays were bonded to the upper and lower surfaces of the flexbeam (see Fig. 1) using adhesive AE10, while Gagekote #8 was applied on top of the FBG as a first protective layer. The entire length of each fibre optic cable was covered with Silicone 3140 RTV to protect the fibres from detaching. Standard electrical SG instrumentation was deployed as a reference during the test campaign. It was ensured that the FBGs were located as close as possible to the SGs despite limited available space due to the required wiring of each single SG on the flexbeam structure. The SGs form a full bridge configuration, meaning they are arranged symmetrically around the neutral axes, similar to the set-up presented in Fig. 1(b). The different sensor locations are depicted in Fig. 1(a) showing the positions of the SGs and the fibre sensors that were deployed on the lower surface of flexbeam, with FBGs G1a to G4a on the leading edge and G1b to G4b on the trailing edge. A different fibre array set-up in Fig. 1(b) shows two FBGs on the upper surface and two FBGs on the lower surface. Fig. 1(c) depicts an image of the final instrumented flexbeam highlighting the limited installation space of FBGs G1c to G4c. It should be noted that the FBG sensor positions presented in this paper are the ones that remained functional after the final blade assembly, in which the flexbeam and the pitch control cuff were merged together. As part of repair measures FBGs G1c to G4c were glued to the upper and lower surfaces once the rotor blade was fully assembled.

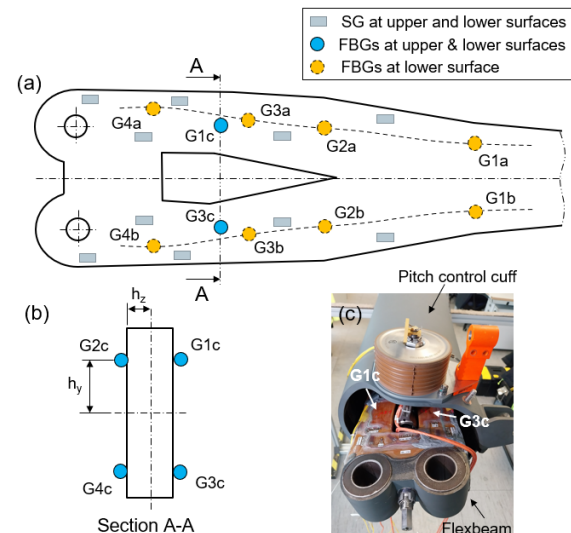


Fig. 1 (a) Diagram depicting positions of the SGs and the fibre sensors deployed on the lower surface of the flexbeam, with FBGs G1a to G4a on the leading edge and G1b to G4b on the trailing edge, (b) only showing fibre sensors mounted on the upper and lower surfaces of the flexbeam with FBGs G1c to G4c, (c) image of the sensor positions G1c and G3c.

The whirl tower test arrangement is presented in Fig. 2. The FBG sensor arrays were interrogated using a 4-channel FBG sensor interrogator mounted on top of the rotor mast, running at a data rate of 2.5 kHz during the whirl tower test campaign. A sampling rate of 0.5 kHz was used for the Airbus internal measurement and control system that allows the determination of bending moments with respect to the SG measurements, calibrated to flap (out-of-plane) and lead-lag (inplane) moments.

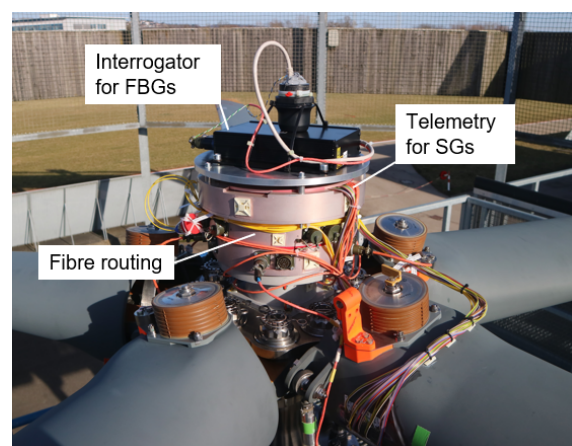


Fig. 2: Whirl tower test: Deployment of FBG strain sensors and electrical SGs with their dedicated data transfer and acquisition devices on an H145 rotor system

In this case, the data transfer from the rotating to the fixed frame was achieved via an inductive Manner telemetry system connected to the

ground station, while the FBG strain sensor data was streamed wirelessly. It was not possible to synchronise the data of the FBGs with the SGs by means of a precision time protocol during the test. Instead, the synchronisation had to be done manually before the data analysis.

Experimental conditions

A whirl tower test was carried out to identify the rotor loads and the modal properties of the main rotor blade, such as natural frequencies and related damping in flap and lead-lag directions. Sufficient excitation of the rotor blade is achieved by providing input with three hydraulic actuators reproducing the collective and cyclic control inputs to the blade via the pitch links (see Fig. 3). The actuators are mounted vertically in the fixed frame of the whirl tower test rig and are located on the same radius around the rotor shaft with an equal spacing of 120° , providing input to the non-rotating part of the swash plate. A cyclic periodic excitation from the actuators to the main rotor is achieved with a sine signal that consists of the same amplitude for all three actuators and a 120° phase shift between the actuators resulting in a 240° phase shift between the first and third actuator. For a steady collective setting all three actuators are moved and fixed in a given position.

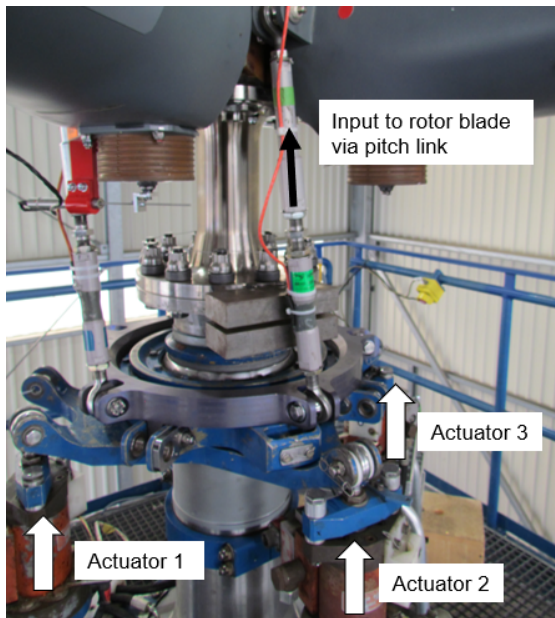


Fig. 3: Actuator arrangement

The required rotor blade loads for flap and lead-lag moment comparison are generated with steady cyclic control inputs, while the excitation of the natural frequencies of the blade is typically achieved with a sine sweep. In case of exciting the flap frequencies of interest as well as the 2nd lead-lag frequency the sine

signal is swept within a certain frequency range with one dedicated setting of collective controls and zero cyclic controls. For assessing the 1st lead-lag frequency and associated damping parameters, the same actuator setup was used, but driven at larger amplitudes at a fixed cyclic periodic excitation frequency. This exact value of the input signal was estimated through a short frequency sweep in the range of the estimated lead-lag frequencies. Once a stable condition with large lead-lag moments is obtained, the excitation is stopped instantaneously allowing the identification of frequency and damping of the 1st blade lead-lag mode from measured lead-lag moment decay curves. The same approach is repeated for several steady collective control angles as well as for steady zero and one steady non-zero cyclic control angle.

Results

During the test campaign data totalling around nine hours was collected. While all of the FBG sensors survived the test campaign, one of the SG measurements failed during the whirl tower test. The malfunctioned SG was one of the flap moment measurement positions, which was mounted in a radius range, where large strains occur. This behaviour can often be observed during whirl tower testing or in early flight test phases since the experienced strains at some locations along the flexbeam of a bearingless main rotor are within a range that exceeds fatigue strength of common SGs.

The FBG strain measurements ϵ on opposing sides of the structure were converted to moment to allow a comparison with the SG sensing system that directly outputs bending moments. The flap and lead-lag bending moments, M_{flap} and M_{lag} , are dependent on time t and the radial spanwise location r and are determined as follows:

$$M_{flap}(r, t) = \frac{\epsilon_2(r, t) - \epsilon_1(r, t)}{2 h_z(r)} EI_{flap}(r) \quad (1)$$

$$M_{lag}(r, t) = \frac{\epsilon_4(r, t) - \epsilon_2(r, t)}{2 h_y(r)} EI_{lag}(r) \quad (2)$$

for which h_z and h_y are defined as the distance between the neutral axis in vertical and horizontal directions (chordwise), respectively (Fig. 1(b)). EI_{flap} and EI_{lag} are the structural bending stiffness in flap and lead-lag directions. By using strain measurements ϵ on opposing sides, the effect due to temperature, centrifugal loading, and either flap or lead-lag movement is compensated, assuming that the sensors, e.g.

G1c to G4c are on the same spanwise location and arranged symmetrically around the neutral axes.

Since it was difficult to position the FBGs G1c to G4c on the flexbeam surface (refer to Fig. 1(c)) an analysis was performed in which the FBG sensor locations were varied in radial and chordwise locations. The outcome provides some understanding of the effect of positioning errors of ± 10 mm on the resulting flap and lead-lag bending moments. As shown in Eq. (1) and Eq. (2) a variation of sensor position in radial direction will alter the values of EI_{flap} , EI_{lag} , and h_z which were modified in accordance with the changing flexbeam geometry, while a deviation in chordwise position influences the value of h_y . Fig. 4 and Fig. 5 present the obtained error on flap and lead-lag moments for different spanwise locations due to the effect of radial and chordwise position deviations, respectively.

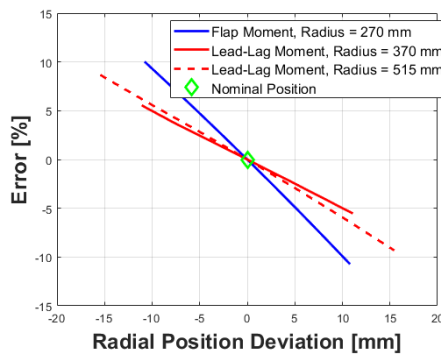


Fig. 4: Resulting error between FBG and SG due to radial position deviation

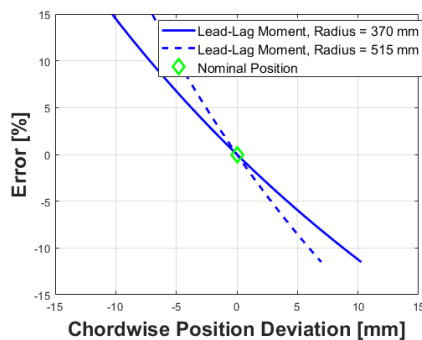
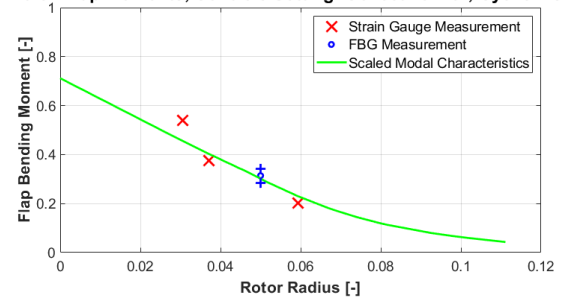


Fig. 5: Resulting error between FBG and SG due to chordwise position deviation

As can be seen in the two graphs, a position error leads to a noticeable difference in the flap and lead-lag moment comparison between both sensing solutions. It should be noted that this is true for both, FBG and SG positioning accuracy. The error due to angular consistency to the blade neutral axis is not considered here, but can lead to further discrepancy within the bending moment comparison.

For the comparison of the flap and lead-lag bending moments a harmonic analysis of the moments, derived from SG and FBG measurements, was performed with an inhouse software. Data without dynamic cyclic excitation was extracted for different collective control angles. The static cyclic control angle was set to approximately 3.4° to introduce a 1/rev loading on the blades. Fig. 6 and Fig. 7 depicts the resulting flap and lead-lag bending moment amplitudes, respectively, determined with the SG and FBG measurements for different collective control angles and sensing positions. The moments determined with FBGs are shown with a ± 10 mm sensor variation in radial position and chordwise position, respectively. Additionally, a modal moment distribution for the 1st flap and 1st lead-lag modes was computed and scaled by the mean value of measured 1/rev moments and introduced in the graphs as a reference. Since the scatter from FBGs and SGs around the reference lines exhibit similar behaviour, it is concluded that both sensing solutions deliver similar accuracy for obtained flap and lead-lag bending moments. Possible reasons for such discrepancies are due to the dependency of the SG and FBG sensor positions relative to the neutral axes and subsequently its underlying structural information, needed for the strain to moment conversion. Slight variations of the sensor position will impact the consequential bending moment.

1/rev Flap Moments, Controls Setting: Collective = 0° ; Cyclic = 3.4°



1/rev Flap Moments, Controls Setting: Collective = 8° ; Cyclic = 3.4°

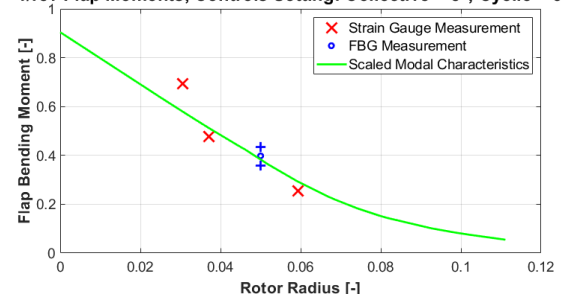


Fig. 6: Flap bending moment comparison, normalised to its maximum moment. The moments determined with FBGs are shown with a ± 10 mm sensor deviation in radial position.

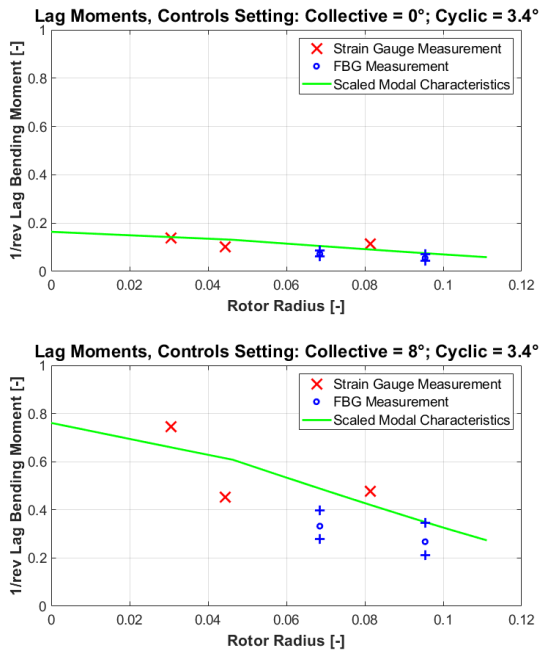


Fig. 7: Lead-lag bending moment comparison, normalised to its maximum moment. The moments determined with FBGs are shown with a ± 10 mm sensor deviation in chordwise position.

As for both, FBGs and SGs, no dedicated device apart from measuring tape was applied to position the sensors, a deviation in position and angle from nominal values is very likely. Additionally, as some of the fibres were broken during the flex-control-unit assembly and had to be replaced on the already assembled unit, it was difficult to place the FBG sensors symmetrically around the neutral axes due to stringent space restrictions, see also Fig. 1(c).

For characterising the modal properties the excitation signal from the hydraulic actuators have to be transformed to the rotating frame to create transfer functions of the SG and FBG measurements. Therefore, the measured strokes of the three actuators were transformed to multi-blade-coordinates. By means of the rotor turn marker and rotor speed measurements, the excitation in the fixed frame was transformed to individual-blade-coordinates in the rotating frame. Afterwards, transfer functions were established and evaluated by means of an inhouse software and the natural frequency and damping were identified. Tab. 1 lists the error between natural frequency Δf and between the related damping ratio $\Delta \zeta$ obtained with FBG and SG sensors. While the natural frequencies obtained from FBGs and SGs are in very good agreement, with a percentage error of less than 0.6%, the damping ratio exhibited a percentage error of about 80% which were both of the 2nd flap mode. The identification of the damping coefficient is particularly challenging due to its dependency

on measurement noise, sensor placement and identification method [16]. While SGs were distributed in radial direction all over the flexbeam and blade, FBG sensors were only available at inboard radial positions at the flexbeam. A better distribution of FBG sensors would significantly improve the identification of the modal properties of the blade.

Tab. 1: Natural frequency Δf and damping ratio $\Delta \zeta$ error of FBG relative to the SG measurements.

Mode	Δf (%)	$\Delta \zeta$ (%)
1 st lead-lag	-0.2	1.8
1 st flap	Not identified with SG or FBG	
2 nd flap	0.6	-79.9
3 rd flap	0.0	-11.5
1 st torsion	Not identified with FBG	
2 nd lead-lag	0.0	-11.1
4 th flap	0.2	0.0

Summary

Fibre optic cables with integrated FBG strain sensors were installed on the surface of the flexbeam with the aim to examine the accuracy of the optical fibre sensors compared to conventionally deployed electrical SG. Data was streamed wirelessly from the rotor hub-mounted sensor interrogator to a ground station.

The determined flap and lead-lag bending moments, as well as modal properties were comparable between FBG and SG sensors with a percentage error of less than 0.6% for the natural frequencies and a percentage error of about 80% for the related damping that was subject to the specific FBG sensor position which was not ideal for identifying this particular mode. Since both sensing systems exhibit a dependency on their position relative to the neutral axes of the flexbeam, a full characterisation of the flap and lead-lag modal properties require careful consideration of sensor location in the chordwise and radial directions. It was also demonstrated that a slight deviation of FBG sensor position in radial and chordwise directions can lead to significant errors in the determination of flap and lead-lag moments.

During the test campaign data totalling around nine hours was collected. While all of the FBG sensors survived the test campaign, one of the SG measurements failed during a whirl tower run with higher flexbeam loading. This behaviour from SGs on flexbeams of bearingless main rotors is already known from past experience, since SGs are loaded at or

above their fatigue limit during whirl tower and subsequent flight testing. It is expected that the optical FBGs exhibit a much longer lifetime compared to SG. While the test preparation was carried out according to industry standards it was shown that the FBG sensors have to be handled in a slightly different manner than components equipped with SGs. After the merging of flexbeam and control cuff and application of varnish several fibres were broken and had to be replaced. Due to the limited accessible space once the blade was fully assembled, slight positioning errors were likely.

While key challenges remain in the area of interrogator miniaturisation, robust data transfer from the rotating to the fixed frame and accurate time synchronisation between all acquisition systems, the outcome of this work demonstrates the potential of using optical fibre sensors for flight testing and providing in-service operational data on helicopter blade dynamics.

References

- [1] T.H. Skopinski, W.S.J. Aiken, W.B. Huston, "Calibration of strain-gage installations in aircraft structures for the measurement of flight loads," NACA Report 1178, 1954.
- [2] E. Kottkamp, H. Wilhelm, D. Kohl, "Strain gauge measurements on aircraft," AGARDograph Vol. 7, (160), 1976.
- [3] R. Golub, W. McLachlan, "In-flight measurement of rotor blade airloads, bending moments, and motions, together with rotor shaft loads and fuselage vibration, on a tandem rotor helicopter," Volume I. Instrumentation and in-flight recording system. Technical Report 67-9A, U.S. Army Aviation Materiel Laboratories, Virginia, USA, 1967.
- [4] W.J. Grant, R.R. Pruyn, "In-flight measurement of rotor blade airloads, bending moments, and motions, together with rotor shaft loads and fuselage vibration, on a tandem rotor helicopter," Volume II. Calibrations and instrumented component testing. Technical Report 67-9B, U.S. Army Aviation Materiel Laboratories, Virginia, USA, 1967.
- [5] J. Riley, G.D. Padeld, J. Smith, "Estimation of rotor blade incidence and blade deformation from the measurement of pressures and strains in flight," 14th European Rotorcraft Forum, Milano, Italy, 1988.
- [6] F. Boden, B. Stasicki, K. Ludwikowski, "Optical Rotor-Blade Deformation Measurements using a Rotating Camera," The European Test and Telemetry Conference, 147–154 (2018), doi:10.5162/ettc2018/7.4
- [7] S. Weber, T. Kissinger, E. Chehura, S. Staines, et al., "Application of fibre optic sensing systems to measure rotor blade structural dynamics," *Mechanical Systems and Signal Processing*, 158, 107758 (2021).
- [8] M. Hajek, S. Manner and S. Susse, "Blade root integrated optical fiber Bragg grating sensors a highly redundant data source for future HUMS," *American Helicopter Society 71st Annual Forum Proceedings*, Virginia Beach, Virginia, USA, May 2015.
- [9] F. Berghammer, B. Sosa, V. Heuschneider, I. Yavrucuk, "Testing of a Fiber-Optical Sensor System for Rotor Blade HUMS," *Vertical Flight Society's 79th Annual Forum & Technology Display*, West Palm Beach, Florida, USA, May 2023.
- [10] J. Serafini J, G. Bernardini, L. Mattioni, V. Vezzari, C. Ficuciello, "Non-invasive dynamic measurement of helicopter blades," *J. Phys.: Conf. Ser.* 882, 012014 (2017).
- [11] S. Weber, D. Southgate, K. Mullaney, S.W. James, et al., "BLADESENSE – A novel approach for measuring dynamic helicopter rotor blade deformation," 44th European Rotorcraft Forum, Delft, The Netherlands, September 2018.
- [12] S. W. James, T. Kissinger, S. Weber, K. Mullaney, et al., "Fibre-optic measurement of strain and shape on a helicopter rotor blade during a ground run: 1. Measurement of strain," *Smart Materials & Structures*, Vol. 31, (7), 075014 (2022), DOI 10.1088/1361-665X/ac736c.
- [13] S. W. James, T. Kissinger, S. Weber, K. Mullaney, et al., "Fibre-optic measurement of strain and shape on a helicopter rotor blade during a ground run: 2. Measurement of shape," *Smart Materials & Structures*, Vol. 31, (7), 075015 (2022), DOI 10.1088/1361-665X/ac736c.
- [14] S. W. James, T. Kissinger, S. Weber, K. Mullaney, et al., "Dynamic Measurement of Strain and Shape on a Rotating Helicopter Rotor Blade: The Measurement Challenge," 28th International Conference on Optical Fiber Sensors, Hamamatsu, Japan, November 2023.
- [15] H. Zhang, Z. Wang, F. Teng, P. Xia, "Dynamic Strain Measurement of Rotor Blades in Helicopter Flight Using Fiber Bragg Grating Sensor," *Sensors*, 23, 6692 (2023).
- [16] X. Wang, K. Liu, H. Liu, Y. He, "Damping Identification with Acceleration Measurements Based on Sensitivity Enhancement Method", *Shock and Vibration*, Vol. 28, Article ID 6476783, <https://doi.org/10.1155/2018/6476783>.

AITA.AI applications to Testing Activities ETTC 2024

Francisca Coll Herrero¹, Pedro Rubio Alvarez¹
¹ Airbus Defense and Space, Av John Lennon s/n Getafe, Spain
Francisca.coll@airbus.com, Pedro.R.Rubio@airbus.com

Abstract:

Most test analyses are repetitive and therefore can be automated, instrumentation of prototypes is increasingly heavy and all parameters require validation. Most test analysis tasks are manual, time-consuming and prone to human error. Documentation grows exponentially, making it very difficult to find it when needed. Test tasks can be optimized, etc.

AITA is an Airbus R&T project with the aim of developing a framework based on AI to automate and facilitate most of these tasks.

Currently, the areas that are part of the AITA project are:

- Automatic FTI validation using a machine learning technique based on decision tree item [1].
- Automatic manoeuvre detection/validation using wavelets.
- NORDOC (Not Only Relational DOCument.Tool): Tool based on Natural Language Processing to find Test documentation.
- TABAI [2]: Chatbot to help Test Activities.

For each of these areas, proof of concepts has been developed with very promising results. The idea is to progress towards ultimately developing the AI-based framework.

This article describes the progress achieved in the AITA project in particular in the automatic detection of maneuvers, storage of maneuvers and analysis results in a non-relational database, Elasticsearch and finally the **AITAVIEW** tool will be presented, which is the interface used to find the manoeuvre information.

Key words: AI: Artificial Intelligence, decision tree, wavelets, CWT: Continuous Wavelet Transform, Elasticsearch, R2: correlation coefficient, pattern recognition.

Introduction

Airbus Defense and Space has grown significantly in recent time, particularly in the area of Flight Testing. With multiple prototypes to test and abundance of parameters to validate and analyze.

To address this challenge, ADS Test organization is developing a framework based on AI to streamline the process and make it more efficient.

The name of the project is AITA (Artificial Intelligence for Test Application).

The AITA project is an in-house software composed of a set of functions developed in Python and in C++ for reading data and heavy calculations.



Figure 1, AITA Logo

*This information is of origin Airbus Defense and Space/Spain and does not contain any export controlled information
 Airbus Amber releasable to ETTC
 ETTC 2024– European Test & Telemetry Conference*

This document will provide an overview of the project's advancements and enhancements in the area of automatic detection of manoeuvres, in the storage of this information in a no-SQL database, specifically Elasticsearch, and the manoeuvre visualization and search tool known as AITAVIEW will be presented.

Automatic Manoeuvre Detection

The Automatic Manoeuvre Detection is based on Pattern identification. The analysis methodology used consists of building adaptive wavelets in the sense of least squares to a specific pattern. Once the wavelet is available, the CWT (Continuous Wavelet Transform) is used to find the pattern in the time history.

This methodology is an improvement of the one included in the BMAD [3] (Big-data Manoeuvre Automatic Detection) project. Besides improving the pattern generation, including new parameters that help determine the manoeuvres validation, the data access and pattern search library has been optimized by migrating python library to C++ and parallelizing the process.

What is a wavelet?

Wavelet analysis is used in digital signal and image compression.

A wavelet is a mathematical function $\psi \in L^2(\mathbb{R})$ with zero average (i.e. $\int_{\mathbb{R}} \psi = 0$), normalized (i.e. $\|\psi\| = 1$), and centred in $t = 0$.

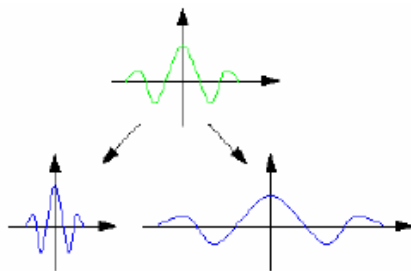


Figure 2.Harr Wavelet

Let $\psi_{u,s}$ be a family of translations u and dilations s of a wavelet ψ named wavelet mother.

$$\psi_{u,s}(t) = \frac{1}{\sqrt{s}} \psi\left(\frac{t-u}{s}\right), \quad u \in \mathbb{R}, s > 0. \quad (1)$$

*This information is of origin Airbus Defense and Space/Spain and does not contain any export controlled information
Airbus Amber releasable to ETTC
ETTC 2024– European Test & Telemetry Conference*

Given f , the Continuous Wavelet Transform (CWT) at time u and scale s is defined as:

$$Wf(u, s) = \int_{-\infty}^{+\infty} f(t)\psi_{u,s}^*(t)dt \quad (2)$$

The CWT is used to find the dilations and translations of the wavelet in the time series f .

Automatic Manoeuvre Detection Process

The steps to be followed are as follows:



Figure 3.steps

- Select a pattern to detect

The first step is to construct wavelets adaptable, as well as possible, in the least squares sense, to the specific pattern. The procedure is described in the chapter 7 of the item [3].

A Python application has been developed to generate the pattern library, which consists of XML files for each maneuver (GenWavelet.py). Initially, a time slice of a parameter that represents the maneuver is selected, as illustrated by the example of a Rapid Rolling maneuver during an actual Eurofighter flight. The lateral pilot stick serves as the parameter for defining the pattern.

The figure below depicts the interface of the application used to generate the patterns, specifically showcasing the Rapid Rolling pattern in this instance.

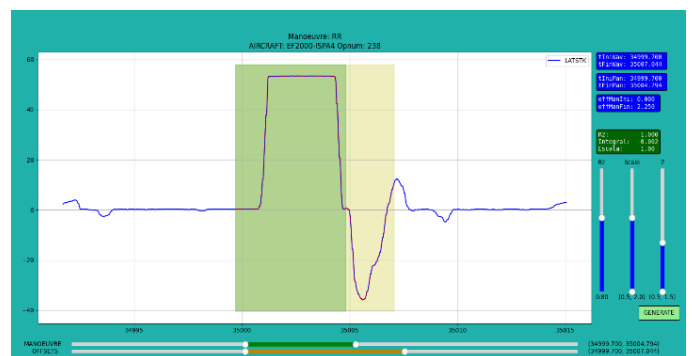


Figure 4.Rapid Rolling pattern

The time slice included in the dark green rectangle corresponds to the pattern that characterizes a Rapid Rolling, but this pattern doesn't meet the wavelet properties.

Hence, an additional light green rectangle is manually delineated by utilizing the lower slices until the pattern conforms to a wavelet shape.

$$\int_R \Psi = 0 \tag{3}$$

$$\|\Psi\|_{L2} = 1 \tag{4}$$

• Manoeuvre selection criteria

As previously stated, the Continuous Wavelet Transform (CWT) is employed to identify dilations and translations of a wavelet pattern within a time history, where horizontal and vertical dilations correspond to the scale and Z criteria, respectively.

In order to enhance the maneuver detection process, a new criterion has been introduced, which measures the R2 correlation between the actual data and the manoeuvre pattern.

Hence, within the application interface, the criteria for maneuver detection are outlined as follows:

- Scale: minimum and maximum horizontal axis scale applied to the wavelet pattern.
- Z: minimum and maximum vertical factor applied to the wavelet pattern.
- Minimum R2: between real data and the manoeuvre pattern in the dark green rectangle.

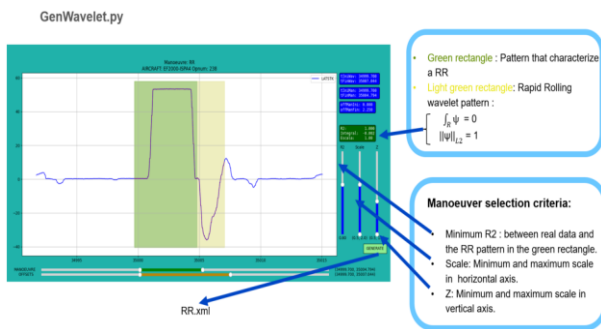


Figure 5. Manoeuvre Selection Criteria

• Add additional constrains and calculus

In the following figure, all the information contained in the XML file can be seen. This Information includes:

- Creation date.
- Name of the Pattern.
- Information of the flight, parameter used, time slice.

*This information is of origin Airbus Defense and Space/Spain and does not contain any export controlled information
Airbus Amber releasable to ETTC
ETTC 2024– European Test & Telemetry Conference*

- Wavelet characteristics: Integral value, wavelet pattern criteria, if is symmetric, R2 etcetera.
- Constraints can be imposed on parameters other than the one utilized to define the pattern. In the case of RR, the parameter phi (roll) is implicated and must complete a full turn within the manoeuvre.
- Calculations associated with the manoeuvre, such as the average MACH, Altitude and Airspeed, minimum and maximum of pitch and AOA angles within the manoeuvre.
- Numerical wavelet values.

The figure shows an XML file named 'RR.xml'. The XML content includes metadata (SOURCE, opnum, paramName, rate, tFti), preprocessing code, constraints (maxSTICK, MACH, HEIGHT, minPITCH), calculations (maxPITCH, minAOA, maxAOA), and data points. Blue arrows on the right side of the XML code point to specific sections: 'Pattern information' points to the metadata, 'constraints' points to the <CONSTRAINTS> block, 'calculations' points to the <CALCULATIONS> block, and 'wavelet' points to the <DATA> block.

Figure 6 . RR.xml

Find pattern in flight

The continuous wavelet transform (CWT) is used to find the wavelet pattern in a flight. Findpatterninflight.py is a Python application that searches wavelet patterns in a flight.

The application is run by applying the following command.

```
python findPatternInFlight.py -ac EF2000-ISPAA -opnum 240 -man RR -plot
```

It can also be executed automatically, storing the results in an elasticsearch database.

```
python findPatternInFlight.py -ac EF2000-ISPAA -opnum 240 -man RR -db
```

In this case, the Rapid Rolling manoeuvre is searched in a real flight of the EF2000. The following figure shows the temporal data with the identified manoeuvres at the top and the spectrogram is represented at the bottom. Item [4].

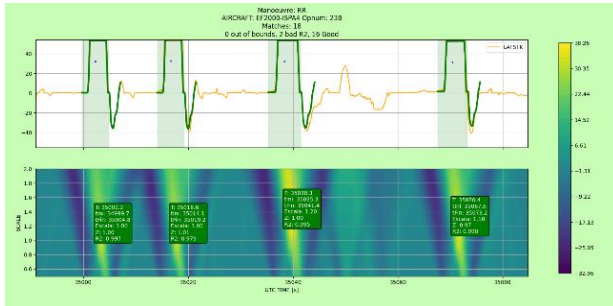


Figure 7. Find RR in flight

The relative maxima of the scalogram (yellow colour) indicate the temporal location of the wavelet, while the corresponding y-axis represents the horizontal scale applied to the wavelet pattern.

The green lines represent the detected wavelets, while the time slice encompassed by the green rectangles corresponds to the Rapid Rolling manoeuvre.

Validate patterns

The first step is to identify the wavelet pattern within the time series using CWT and then validate the detected manoeuvres. To do this, a section of the wavelet pattern that corresponds to the manoeuvre has been defined (manoeuvre pattern) and a minimum R2 value between the real data and the manoeuvre pattern.

Sometimes, this is not enough to detect all the real manoeuvres especially in cases where the wavelet pattern is much larger than the part corresponding to the manoeuvre.

The search for maneuvers has been enhanced as follows: once the center of the wavelet pattern is detected, the pattern moves along the x-axis, applying horizontal and vertical factors until identifying the maneuver pattern that best aligns with the real data.

Furthermore, by defining constraints with other parameters such as phi in the case of RR, the maneuvers are now perfectly identified.

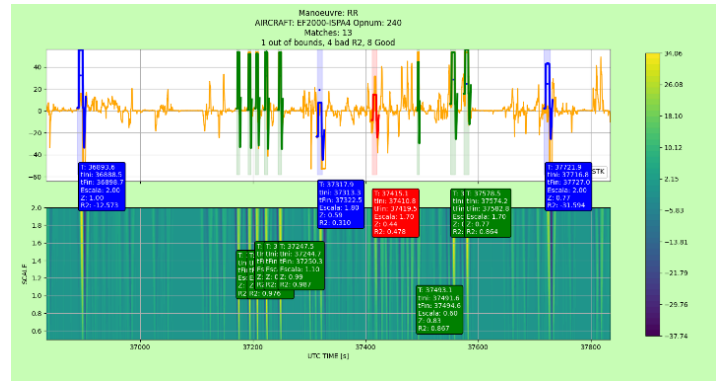


Figure 8. validate patterns

The green colour of the rectangle indicates whether the manoeuvre is well detected, in red if the R2 is lower than the required in the pattern definition, or in blue if it does not meet any of the constraints.

A 3D visualization of the manoeuvre has also included in the application by clicking on one of the rectangles.

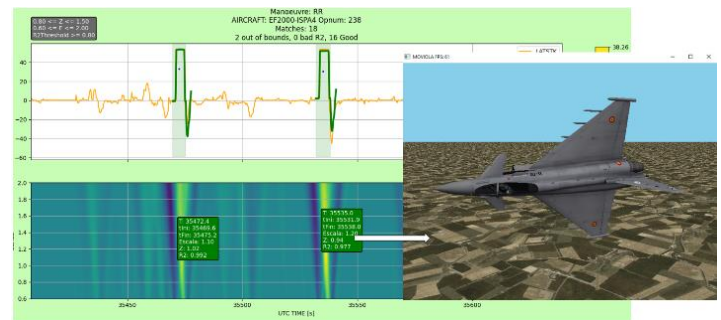


Figure 9. 3D manoeuvre visualization

Patterns Library

Currently the manoeuvres that are identified for each aircraft are:

Eurofighter: Rapid Rolling, Wind Up Term and Lateral-Directorial and Longitudinal manoeuvres generated by FBI (Function Bias Input).

C295: SHSS (steady Heading Side Slip), using DR (Rudder deflection) as pattern.

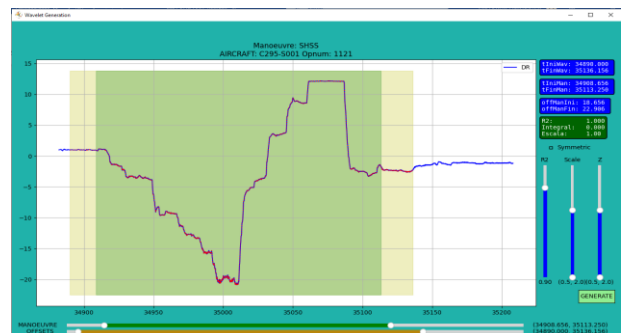


Figure 10. C295 – SHSS

This information is of origin Airbus Defense and Space/Spain and does not contain any export controlled information Airbus Amber releasable to ETTC ETTC 2024– European Test & Telemetry Conference

C295: BTB (Bank to Bank), using PHI (bank angle) as pattern.

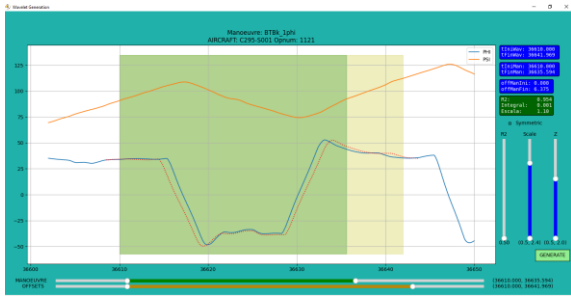


Figure 11. C295 – BTB

C295: TO (take off), using THETA (pitch angle) as pattern.

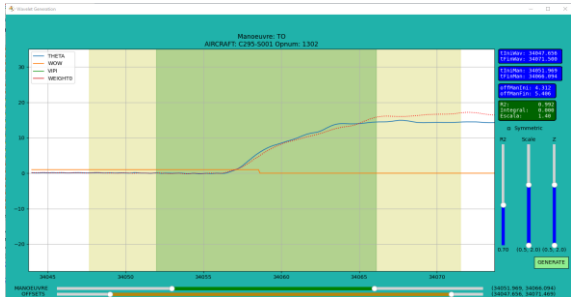


Figure 12. C295 TO

C295: DUCHROLL using DR as pattern.

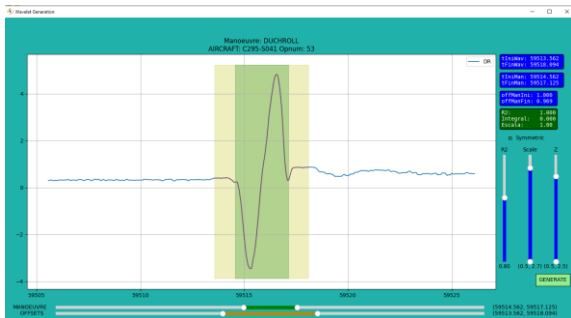


Figure 13. C295 DUCH ROLL

C295: STALL using AOA (angle of attack) as pattern.

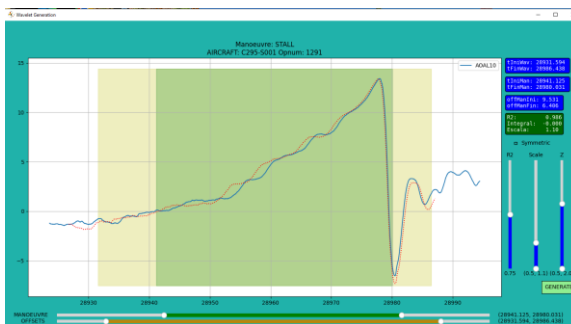


Figure 14. C295 STALL

This information is of origin Airbus Defense and Space/Spain and does not contain any export controlled information
Airbus Amber releasable to ETTC
ETTC 2024– European Test & Telemetry Conference

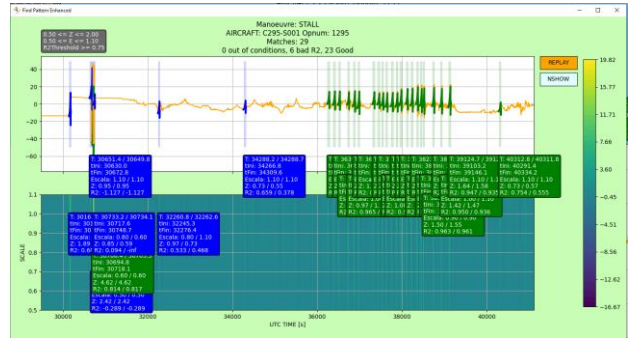


Figure 15. Find STALL in a flight

The following figure shows the 3D simulation of the manoeuvre.

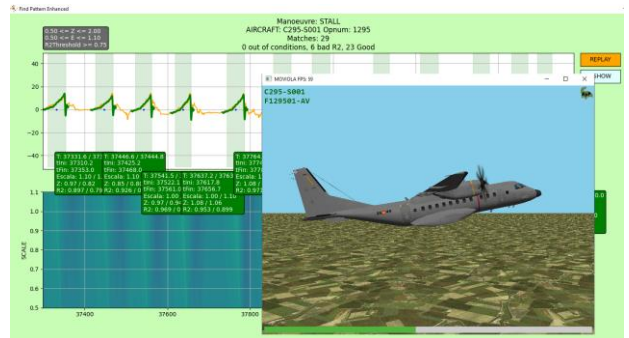


Figure 16. 3D manoeuvre visualization

By clicking on the NSHOW icon, a plotting tool will appear displaying the time histories of the key flight parameters of the manoeuvre, including all the time stamps corresponding to the manoeuvre.

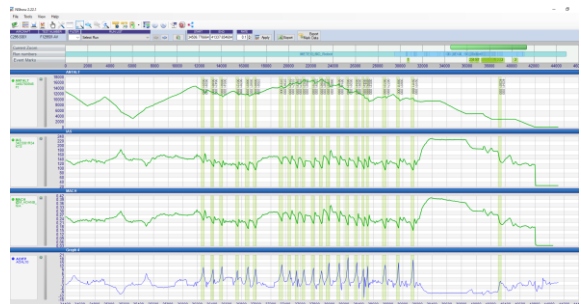


Figure 17. NSHOW

Store manoeuvres in an Elasticsearch

Initially, maneuver information was stored in relational database tables, but the data within these tables lacked relational structure. For instance, in-flight refuelling manoeuvres need storing data such as the fuel transferred, contact duration, or the aircraft receiver however these values do not make sense in other maneuvers such as aerial delivery tests.

What is elasticsearch?

- Elasticsearch is a distributed and document-oriented database
- Elasticsearch is an open, free and distributed search and analytics engine.
- Elasticsearch is commonly used for log analytics, full-text search, security intelligence, business analytics, and operational intelligence use cases.

The elasticsearch database had already been used in the NORDOC application, which is part of the AITA project based on Natural Language Processing, obtaining surprising results.

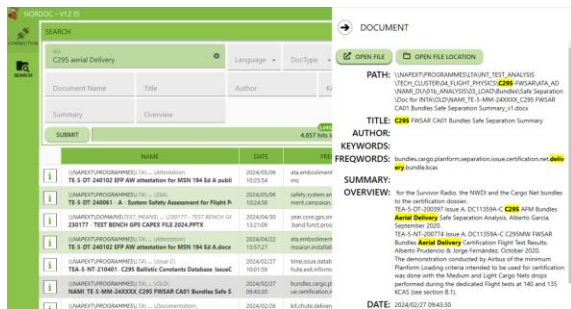


Figure 18. NORDOC

Elasticsearch databases have been created for each aircraft where all automatically detected maneuvers are stored with the fields that characterize each maneuver.

Kibana is the standard open-source data exploitation and visualization tool designed for Elasticsearch, but with the objective of facilitating access to maneuver databases and being able to connect them to Test applications and databases, it was decided to develop a specify tool: AITAVIEW.



AITAVIEW is an in-house Tool designed to access, visualize and filter maneuver databases.

Initially, you select the database you want to access. Currently, there are two options available, corresponding to Eurofighter and C295.

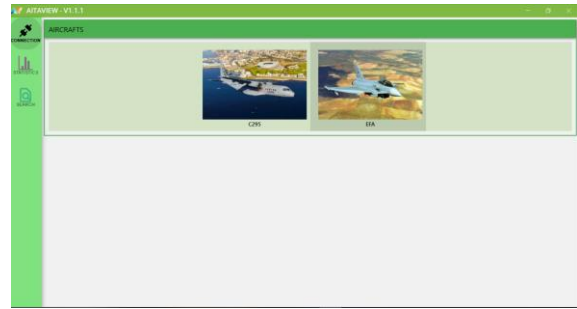


Figure 19. AITAVIEW. Database Selection

Once the database is selected, in this case C295, information regarding the number of aircraft and maneuvers contained within the database is displayed.

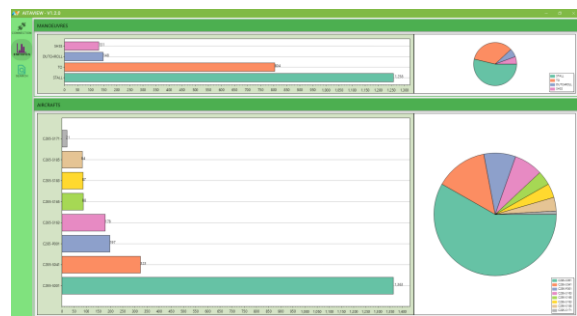


Figure 20. AITAVIEW Statistics

By clicking on the SEARCH button, searches can be performed by selecting aircraft and maneuvers.

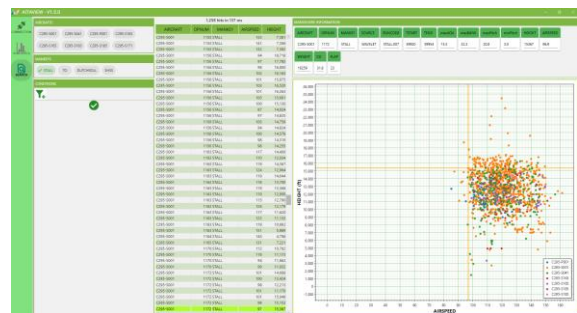


Figure 21. AITAVIEW SEARCH

In the center of the interface, the list of selected maneuvers appears, with a graph displayed on the right showing the airspeed versus altitude where these maneuvers were performed.

You can hover the mouse over the graphic, orange lines, and see the corresponding maneuver highlighted in green in the list, along with its characteristic parameters at the top of the interface.

Additionally, other filtering conditions can be defined using all available fields in the database.

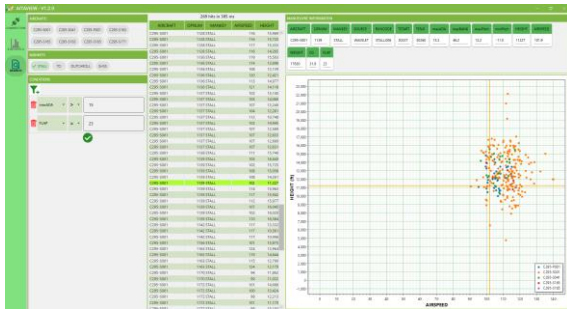


Figure 22. AITAVIEW Filter conditions

A 3D replay of a manoeuvre can be seen by selecting it with the right mouse button.

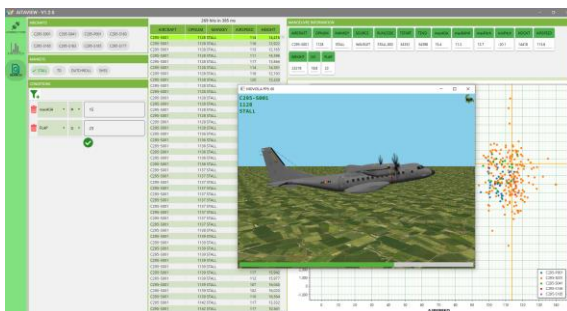


Figure 23. AITAVIEW 3D replay

You can also see the time history of the significant parameters of the manoeuvre using NSHOW plot Tool.



Figure 24. AITAVIEW NSHOW

Conclusions

The technique of automatic manoeuvre detection based on pattern recognition using Continuous Wavelet Transform has been optimized in accuracy and speed.

The method has been checked for some manoeuvres in Eurofighter (RR,FBI,WUT) and C295 (BTB,SHSS,TO,STALL,DR) with promising results.

An Elasticsearch database containing all the manoeuvres detected has been created.

A tool named AITAVIEW has been developed to view and filter the manoeuvre database.

The next steps are to store in Elasticsearch all the manoeuvres of all the aircraft, whether

*This information is of origin Airbus Defense and Space/Spain and does not contain any export controlled information
Airbus Amber releasable to ETTC*

ETTC 2024– European Test & Telemetry Conference

identified with patterns or other techniques, and to expand the functionalities of AITAVIEW.

References

- [1] Francisca Coll Herrero, Pedro Rubio Alvarez “*AITA. Automatic Validation of Parameters*”. ETTC-2023 ,13 Jun
- [2] Francisca Coll Herrero, Pedro Rubio Alvarez “*TABAI. Test Assistant base on artificial intelligence*”. ETTC-2022 ,10-12 May
- [3] Francisca Coll Herrero “*BMAD. Automatic detection of flight manoeuvres using wavelets*”. ETTC-2020. 23-24 June
- [4] V.J. Bolos,R. Benitez .”*The wavelet scalogram in the study of times series*”. XXIII Congreso de Ecuaciones Diferenciales y Aplicaciones .9-13 sep 2013

Multiplatform sensor fusion Drawing a common tactical scenario

Miguel Arévalo Nogales¹

¹ Airbus Defence and Space, John Lennon Av, Getafe Madrid, Spain
miguel.arevalo@airbus.com

Abstract:

Recent years have proven the importance of sharing sensor data in complex scenarios. The platforms in play are wildly heterogeneous, from small, unmanned vehicles to aircrafts, land units or vessels. This paper explains the concept of Common Operational Picture, a tactical scenario where multiple participants share sensory data to draw a single vision, improving data quality and reliability through data fusion. The main topic to be covered will be the data fusion and integration techniques used to enhance quality and reliability and the machine learning methods used for decision making with the data being stored.

The root of the problem lies in the origin of data, as it is provided, processed, and stored by different participants and later on shared with others. This pipeline brings some challenges such as different timing systems, sensor hysteresis, and connectivity problems which burden data quality. Artificial intelligence and machine learning offer several solutions in this regard: bandwidth can be reduce using dimensionality reduction techniques, data anomalies, outliers, can be detected and analyzed using support vector machines and a greater situational awareness can be achieved.

Key words: Sensor, machine learning, data fusion, common operational picture, connected environment.

Introduction

Recent years have marked a huge improvement in sensors and networking, making information ubiquitous and cheap. This fact, combined with the improvement in calculus capabilities and the advent of single board computers means large amounts of information can be read, processed, and shared, easily and conveniently, between many devices.

Some specific area of interest is a situation where vehicles, manned or unmanned, possibly helped by other actors (ground stations, satellites), participate in a joint operational environment, e.g. a rescue or surveillance mission. Sharing a common view of the scenario, fostering collaboration, and enhancing their situational awareness is a very welcomed feature provided by communication advances. This scenario is what is commonly known as the common operational picture.

The objective of this paper is to study how machine learning techniques can be applied to sensor fusion and the enhancements this methodology provides to a common operational picture that all these actors are trying to depict together.

The paper will analyze the problems, algorithms and opportunities that must be faced when trying to work a common scenario where sensors are not managed by a single entity but transmitted over networks and shared between many participants.

Working on a Common Operational Picture

When we are talking about sensor fusion we should have a clear objective, sensor data is being merged and processed to provide a Common Operational Picture to all the participants in a joint operation.

The objective is to share data and create additional sensors that provide a better view of the scenario being operated.

Normal scenarios, such as monitoring disputed areas, mean several participants collaborate and bring data together. Navy ships can act in the field with sonar, radar and thermal cameras, satellites can provide images and reconnaissance aircrafts can provide radar (ISAR/SAR), sonobuoys (and acoustic processing), additional imagery (FLIR, etc.), as well as IFF interrogators and/or AIS-SART. These sensors are normally managed through the tactical system of the participants where they are displayed to an operator. Datalinks can

*This information is of origin Airbus Defense and Space/Spain and does not contain any export controlled information
Airbus Amber releasable to ETTC
ETTC 2024– European Test & Telemetry Conference*

provide some sort of interconnection between participants so data is shared, but if not properly classified we can find the information to be overwhelming and misleading. The need for some classification and data fusion algorithms is clear[1].

STANAG 4676 and nomenclature

Since the objective of the project is to collaborate in a common operational picture it is necessary to define a standard language for the participants to talk. NATO defines a series of standardization agreements or STANAGs, these agreements cover many topics, but we will focus on STANAG 4676[2] which is the Intelligence Surveillance Reconnaissance Tracking Standard. This agreement specifies a data model which can be used among all participants.

Before getting into the model itself it is important to know the basic nomenclature:

- NITS: Operation being performed.
- Tracker: A tracker is an active actor participating in the operation. It generates information using its sensors.
- Product: Products are a collection of sensors, they can be, but are not limited to, actors in the scenario, for example, a system that provides several sensors, is a product, but an actor can have many products.
- Sensor: Each and everyone of the measurement units in a product, a product may have many of them (e.g. a multicamera pod).
- Track: Information of an object provided by a sensor, it normally focuses on position, speed, and acceleration but it is not limited to them.

STANAG4676 data model is quite complex, supporting not only ID, position, and speed of different objects, but also the source of this measurements, and more complex features such as coordinates transformations, the basic model diagram can be seen in Fig 2.

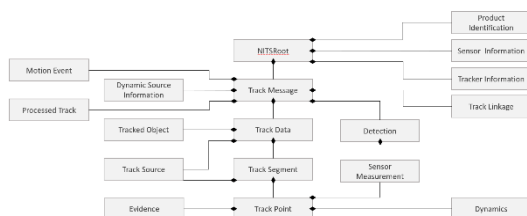


Fig.1.STANAG4676 model. First level.

The model can be understood as a tree, NITS is a common entity, shared by all participants, that

hosts all the information: sensor definition, trackers, messages, etc. This entity can be used to add new data or to forward current information to other participants.

All participating actors (trackers) register themselves, providing tracker, product, and sensor information.

Messages are the basic entity containing transmitted data, a single NITS can contain many messages, or a single one if historical information is not transmitted. Messages are linked to several other entities, motion events, track data or their source.

Track Data is the primary entity containing a track, it is defined by a set of tracked objects, tied to a track source (tracker, product and / or sensors) and linked to a segment which is made of a set of track points.

Track Points are the key to understanding the model, a track point is tied to a detection, comes from a sensor measurement or a sensor composition, and is linked to a set of evidence. Tracked object position is stored in a dedicated entity itself linked to a track point: Dynamics. This entity can store position, speed, and acceleration, in addition to the coordinate system used by the data.

Composed sensors are supported by means of transformations, so they can be traced back to originating sensors. The transformation itself can be also described.

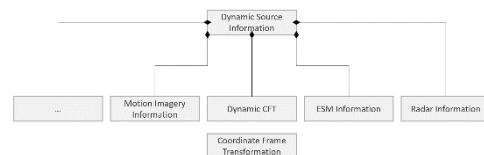


Fig.2.STANAG4676 Source - Sensor relationship.

The reason for choosing STANAG 4676 as the data model lies in the features it supports: data transformation, track stitching, confidence definition, track merging, etc. It fits nicely with the concept of sensor fusion.

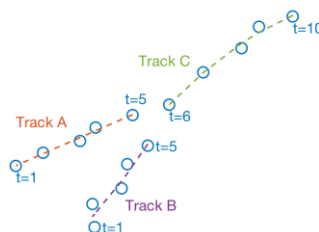


Fig.3.STANAG4676 Track merge example.

*This information is of origin Airbus Defense and Space/Spain and does not contain any export controlled information
Airbus Amber releasable to ETTC
ETTC 2024– European Test & Telemetry Conference*

Algorithm description

Algorithms used for the project are not exclusive to sensor fusion, but generic machine learning ones.

For the sake of better understanding how the algorithms are being used for sensor fusion a brief section describing the methods being used has been included.

Principal component analysis

Principal component analysis (PCA)[3] is a technique used to describe a data set in terms of new, uncorrelated variables (eigenvectors). These variables are ordered by the amount of variance, from the original dataset, that they are describing (eigenvalues). The original idea was to reduce the dimensionality of the data.

The whole process can be reversed losing some of the original information, this way we are reducing the bandwidth being used but we keep most relevant data.

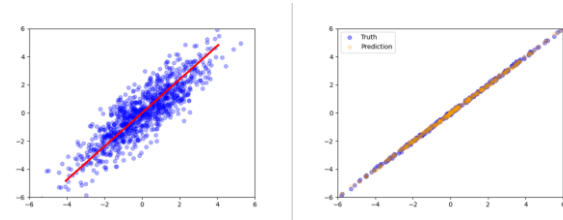


Fig.5. Original dataset, PCA and reconstruction.

PCA can be reconstructed using equation (1).

$$PCA_R = PC_{score} * Eigenvector + Mean \quad (1)$$

There is another relevant use case as hinted by Fig. 5 which is reducing the amount of noise in a dataset.

Autoencoders

Autoencoders [4][5] are an unsupervised type of neural network used to learn codings (features) of unlabelled data. This can be used to compress data and later on decompress (reconstruct) data to its original form.

They are composed of three parts:

- Encoder. It is a layer, or set of layers in case of multi-layered autoencoders, used to compress (encode) the input data into a reduced set of features.
- Latent space. It is a position on the space describing, using a different set of variables, the original position coming from the input space. Since normally latent space is chosen to have a reduced dimension to input space the dimensionality is reduced.
- Decoder. Layer, or set of layers, used to decompress (decode) the latent space

representation of some data into another representation into the original data space. Since the dimension of the latent space is normally smaller than the original data space reconstruction is lossy.

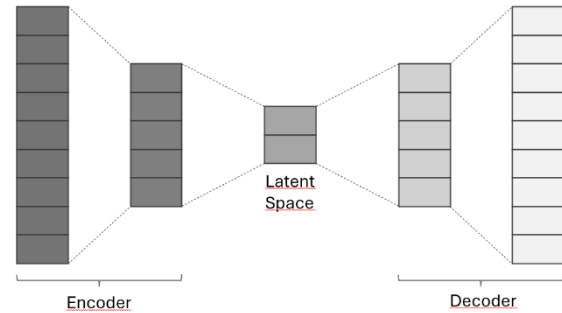


Fig.6. Autoencoders.

Support Vector Machines (SVM)

This supervised learning method is a max-margin model used for classification or regression. The original idea was to find a vector which divided a set of points in two different groups, hence classifying new points based on the original points that were used for training and obtaining the vector.

SVM have evolved into new techniques such as kernel support vector machines (KSVM), which transform the original two-dimensional space into a higher dimensionality one using a kernel trick.

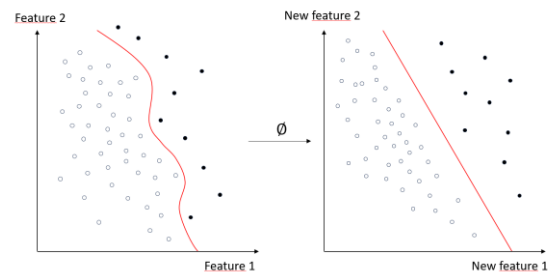


Fig.7. Kernel function.

SVMs robustness to outliers can be used to separate them and curate datasets [6][7].

K-Nearest Neighbor (k-NN)

Not to be confused with k-Means, k-NN [8][9] is a supervised learning algorithm used for classification or regression.

When used for data classification a point is assigned a class based on the classes of its neighbors, the most frequent class is assigned to the point, k is the number of neighbors to be considered.

If used for regression the output is the property (measurement) value of the object, for example

if the sensors measuring the property failed. The value is the average of the nearest k neighbors.

A normal modification of the algorithm is the addition of weights to the neighbors. This way averages consider a factor that modifies the relevance of the neighbor (the weight) into the result. This weight can depend on many things, distance to the original data, neighbor index (closer ones weigh more than farther ones, but distance is not considered), etc.

Introduction to sensor fusion

Sensor (or data) fusion is the process of merging several measurements to get a better understanding of the status of a system.

Previous definition is intentionally broad to cover very different use cases, let's try to clarify it by making it more precise.

A system can be many things, a human being, a set of moving objects or a computer cluster connected to a network. The status is dependent on the system, for a set of moving objects it makes sense to be interested in their relative position whereas for a computer cluster it may be a single measurement providing its health / resource usage.

Finally, sensors can be any kind of information coming from the system, bandwidth, resource usage or latency if speaking from a computer environment, blood pressure and heart rate in case of a medical monitoring system, or position, speed and direction in the case of a moving object. These measurements are normally registered over a time frame, providing some sort of guidance or evolution.

Sensor fusion can be divided based on the stage or level where the fusion is performed.

- Low-level Fusion (a. in Fig. 2): Raw sensory data is fused together to get a more accurate measurement. It is the most common type of sensor fusion; we are normally merging homogeneous sensors which may differ in type but provide the same kind of measurement (e.g. taking several samples of a fingerprint scan and merging them together to get a single value or using several images coming from different source to identify an object).
- Mid-level Fusion or Feature Level Fusion (b. in Fig. 2): Multiple heterogeneous measurements are fused together into a single entity, for example biometrics sources such as fingerprints, iris scanner and face / image recognition are brought together to identify a person. This is done by detecting correlated measurements and merging them into a single dimension.

- High-level fusion or decision level fusion (c. in Fig. 2): As its name implies, decision level fusion is aimed at making decisions: selecting a single hypothesis from a group of hypotheses based on the information provided by a set of sensors, which may be identical or not. For example, in a car, several sensors, some of them already fused (external temperature, speed, route, weight) can be merged to decide if the driver has to be notified to change route or stop in a gas station / electric vehicle charging station because he is not going to make it to destination.

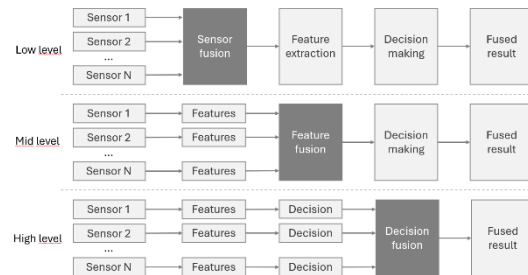


Fig. 8. Sensor fusion classification by levels.

Sensor fusion is also divided in two main categories depending on where it occurs:

- Centralized: Participants simply forward the information to a central processing entity which merges the information, if clients are not relevant actors they might not be notified back with the results.
- Decentralized: All actors can perform some level of data fusion and have some degree of autonomy in decision-making. This is normally the case on edge / fog computing environments.

Data fusion: bandwidth usage reduction

Although the focus of the paper, and the techniques being used, is mid and high-level data fusion, there is a specific use case that has to do with low level fusion: bandwidth enhancement in fog / edge computing.

There is a perennial problem in connected environments, which is sharing data between participants. Bandwidth is normally limited, so the amount of data that can be shared is scarce, this hits precision and decision making.

A straightforward application of machine learning techniques is dimensionality reduction using PCA analysis / autoencoders: by reducing the dimensions of data we can minimize used bandwidth at the cost of precision.

Autoencoders can detect relevant features from a dataset and compress it into a latent space, this space's dimensionality is lower than the

*This information is of origin Airbus Defense and Space/Spain and does not contain any export controlled information
Airbus Amber releasable to ETTC*

ETTC 2024– European Test & Telemetry Conference

initial space, improving bandwidth usage. Once the information is received it can be decompressed and reconstructed into a similar space to the original one, the resulting space is not equal since we are losing some fidelity, but the tradeoff is the amount of data being sent is significantly reduced.

Another method of bandwidth reduction being studied is the creation of an adaptive rate using sensor data [10]. The basic idea is to adapt the transmission rate to the data being read so we can make better use of the available bandwidth.

To properly adapt the rate, we should be first doing a PCA analysis of the sensors, this determines which ones are more relevant to the use case.

The idea is to classify sensors into groups using PCA. These groups are defined as most relevant sensors to the scenario being studied, for example in a COP where we are receiving positional data from hundreds of tracks, we may discard most information from all tracks in an area to focus / improve data transmission of tracks in a relevant area, in this way information from secondary tracks is consuming less bandwidth. Doing this classification at sensor level means that we can focus on specific measurements (e.g. position) relegating others (e.g. speed) to a secondary role / transmission.

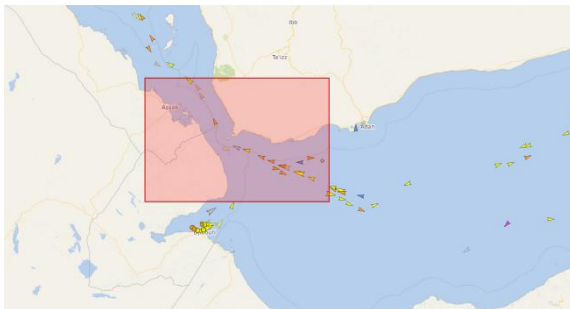


Fig.9.Example: priority area for track transmission.

Once sensors are classified, the value difference from the sensor to previous measurement is compared to a threshold, so even non relevant values are sent when the variance is large enough (or a certain time has passed).

This method is similar to a QoS in networks but done based on what sensor information is more relevant to our use case.

There are several caveats with these techniques:

- We are using compression techniques that are reducing the fidelity of the data being sent (lossy compression), this means we may be missing some relevant information.

- We are saving on bandwidth at the cost of computing power, which is not always a good tradeoff.

Feature fusion: confidence definition

There is a straightforward application to mid-level fusion for STANAG 4676: obtaining the uncertainty of a measurement. Sensors do not know the real position or speed of an object being tracked, in fact STANAG 4676 model has a placeholder to define the confidence of a measurement, but how can it be obtained? A method has been developed to provide an expected value for this field.

The algorithm relies on comparing previous measurements from the same set of sensors and comparing them with a set of well-known data, incorporating contour conditions such as tracker heading, distance to tracked object, etc.

For the use case under analysis, we are basing our training in AIS data, there are several reasons to do this.

- If data comes from some well-known participants the quality of the data is very high, as the participant is already making corrections to it by means of low-level data fusion.
- AIS data directly comes tagged with its originator, so we have no uncertainty on the originator of the trace and the is no obscuring.
- AIS data is transmitted through the network and there are historical databases that can be checked and used. This eases the training of the models.

To create new, data-quality, sensors the first step was to make a simple comparison between AIS data and sensor data from historical records. This comparison provides, given the sensor type and contour conditions an estimation of the expected error (certainty) for any given sensor and measurement.

At this stage the influence of the variables in the error is not known, this is what the model is going to analyze and provide to us.

Once we have the dataset a multi-variable regression algorithm is trained (k-NN was used but others are under evaluation). This model is trained for a single error / certainty, if we want to distinguish between different types of measurement errors (e.g. speed, position) we should train different models.

These steps (model training) are done before the operation (real object tracking) is performed.

During the operation the sensor suite from the tracker is generating sensor data. The measurements can be validated if the object being tracked is also providing AIS data or not, if, as is usually the case in disputed environments or with hostile tracks.

In any case, the next step in the algorithm is to enhance the sensor dataset with contour conditions. These conditions are expected to be the same ones used during the training: tracker position and heading, time and day, meteorological, etc.

If the object being tracked is also providing AIS data, we can use all this information to further train the model, moreover, this data will be given higher priority since it is providing closer to reality contour conditions (meteorological, etc.). Certainty is calculated directly and not through the model.

If, on the other hand, the tracked object does not provide AIS data we can use the model to calculate the certainty of the measurements. To calculate this value, we simple use the model to predict an expected certainty.

This method has validated some logical assumptions for example, it has been found that images taken against the sun (so sun position is relevant) provide worse detection quality than the ones being taken in normal conditions. The same can be said about lightning conditions, when the attitude of the camera is not adequate, or the object being tracked is too far away.

The additional sensor information (certainty) can be then fed to image recognition algorithms to enhance them or take into consideration when processing the image.

Abnormal track detection

Decision level data fusion may be the core reason to have a COP where several participants (trackers) collaborate and bring information together. Merging all this information produces better informed decisions and a level situational awareness not attainable when working alone.

One of the most important areas of analysis in a COP is detecting abnormal behaviors. This behavior may be due to technical problems (e.g. The Dali colliding with the Francis Scott Key Bridge) or deliberate as in unsafe driver's behavior [11].

STANAG 4676 supports several sensors to classify the track, there is already plenty of work doing with abnormal behavior identification using cameras [12], but project's development has focused on typical sensor information such as position, heading or speed.

The basic idea of the algorithms being implemented is to provide operators a measurement on the level of suspiciousness of certain tracked object.

The first approach to identify if a tracked object had an abnormal behavior was to use data classification algorithms.

A one-class SVM [13] was trained with AIS data available online. This type of SVM uses a kernel function to map the input data into a higher dimension space, this way point distance is larger, and the algorithm can distinguish between different points.

Since naval routes are well defined it is easy to identify if a ship is deviating from a typical route.

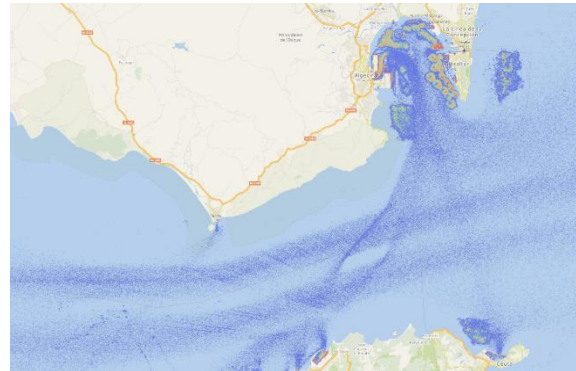


Fig.10. Historical AIS data in the Gibraltar strait area.

This approach is not without its problems:

- Only X/Y position is considered, no speed, acceleration or heading is taken into account for the decision criteria.
- Points are seen as independent variables, they are not linked in a time series, strange routes within the valid area are considered normal by the algorithm.

These problems highlight that working with trajectories (tracks) has some additional challenges. First, tracks are not a disjointed set of points, they have a direction, this variable needs to be considered since it has an impact on what the normal behavior is for a given trajectory. Secondly, and linked to previous problem, trajectories are made of a set of ordered points, this poses a problem for typical ML algorithms that are focused on non-ordered sets.

The first problem can be solved by having two different instances of the algorithm trained with different datasets, one for each direction or lane.

The second problem on the other hand means that basic classification algorithms may not be able to detect abnormalities in trajectories, and additional data conditioning techniques are needed to properly analyze data.

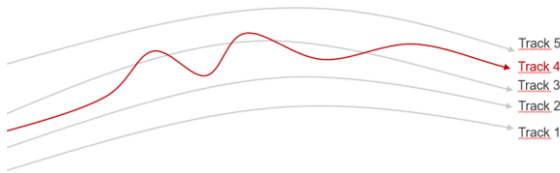


Fig.11. Abnormal track within trajectory boundaries.

A typical approach to solve the timing problem is to divide the track into different tiles or windows. Partitioning the data into fixed size windows means that every point in the trajectory P_i (2) is encoded into a fixed size attribute vector V_P (3), along with other relevant variables for the point.

$$P_i = \{X, Y, V^x, V^y \dots [\overline{XY}] \} \quad (2)$$

$$V_P = \{P_0 \dots P_N\} \quad (3)$$

All windows must have the same number of points, for these trajectories must be resampled, and each point has to be composed of the same set of variables, creating matrixes (4) for each window.

$$\begin{bmatrix} X_0 & Y_0 & V_0^x & V_0^y & \dots & [\overline{XY}_0] \\ \vdots & \vdots & \vdots & \vdots & \ddots & \vdots \\ X_N & Y_N & V_N^x & V_N^y & \dots & [\overline{XY}_N] \end{bmatrix} \quad (4)$$

These matrixes are defining the behavior of a track in any given tile but even more so, they can be compared to extract common values and patterns among tiles.

This windowing is based on Li et al. [14] work, which focused on hierarchical feature classification using a rule-based classifier, this was the core of their moving objects anomaly detection algorithm (ROAM). Other examples include Lee et al. [15] who also used trajectory partitioning for their outlier detection algorithm.

Once data is partitioned, we can analyze each window separately using traditional machine learning algorithms.

The workflow is quite basic: a classification algorithm is trained using the basic information for a window (V_P), we have as many instances of the algorithm as windows, which is interesting as it highlights abnormalities per zones.

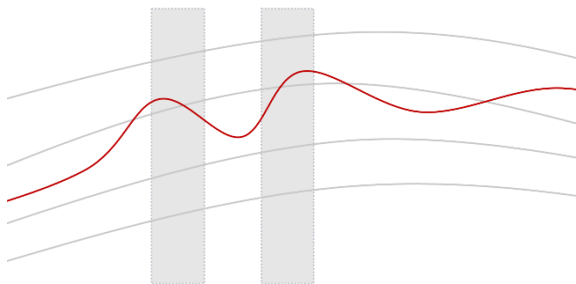


Fig.12. Windowed data where we can find anomalies.

The track data is then measured by the tracker, using the windowing criteria a window is selected and the associated instance is fed with the data. The algorithm outputs if the data is within boundaries or is an outlier.

Once the theory has been presented, we can discuss the algorithms are being used and how they are being trained.

First thing to do is define a partitioning criterion for the data, in our specific use case, and since we are focused on trajectories, we are using geospatial positioning for windowing. The area under analysis is divided into a tile matrix, the size of each tile must have into account the responsiveness of the objects being tracked.

Now complete trajectories are created, ensuring the track being analyzed has the right dimension (all tiles must have the same number of sample), for this we resample the track using linear interpolation. We can think of this procedure as a resampling in the space domain instead of time. It is in this step that additional parameters are added to the dataset, e.g. distance to other objects.

Now a set of tiles are selected based on the position / trajectory of the tracked object, this defines the set of trained models that will be used for analyzing the behavior.

Once divided and assigned to tiles a similar approach to the first algorithm can be used: a one-class SVM. A matrix of tile objects, each one tied to a OneClassSVM object is kept in memory. This SVMs have been trained using AIS data and reproduce what a normal behavior should be, considering not only position but speed, direction, distance to nearest track, etc.

In real time a measurement is made and buffered, if the data is enough to reconstruct a trajectory in the given tile, then the proper instance is invoked with the track's data for that tile, this way the algorithm can predict if the measurement is an outlier (behavior is not normal) or not.

Several things must be considered when training the algorithm:

- Tile size has a huge impact on the precision of the decisions provided by the ML algorithm.
- Kernel function and gamma must be tuned to match the type of variables being measured.

To put both problems into context, slow cruising ships or transports, very slow moving and with highly limited routes allow for larger tiles and smaller gamma, highly maneuverable objects,

on the other hand require smaller tiles and are much harder to fine tune.

Both these algorithms offer several advantages on their own, but the real value is obtained when combining both.

Simple naval route comparison is fast and does not need windowing, it provides a fast glimpse on how probable is to find a track in certain area and what the typical values for his speed and position would be. If combined with a windowing method additional, time related information is obtained: track direction, speed, acceleration and if the trajectory is normal or not. This information takes longer to be processed and is not readily available because of the windowing.

Conclusions

To summarize the work done, we have seen how sensor data can be collected and transmitted between different participants in a scenario, depicting a common operational picture that improves situational awareness for all participants.

The studied scenario has been one dealing with surveillance and reconnaissance with different actors, naval, aerial, etc. but can be extended to other situations such as cars driving in a highway, provided they have V2V connectivity, and collaborate to depict a common picture.

Once the scenario, the roles and communications have been defined we have studied what machine learning methodologies can be applied to sensor data, going beyond low-level and focusing more on mid-level and high-level data fusion.

Mid and high-level data fusion can benefit from machine learning in several ways. Mid-level data fusion can create new sensors, such as data quality sensors, based on original sensor types, position, or speed. We can go further and create a transmission rate sensor using trained information.

High level data fusion revolves around decision making, and in this aspect machine learning is also useful. Models can be trained to determine the normality of a behavior, detecting inconsistencies in the measurements, inconsistencies that do not necessarily have to do with invalid data but with abnormal behaviors that reveal that one of the monitored participants is having a problem. New sensors can be built measuring the level of certainty on the abnormality of the behavior.

Two types of machine learning algorithms have proven to be suited to this kind of sensor creation:

- Classification algorithms.
- Anomaly detection algorithms: Support Vector Machines & Principal Component Analysis.

Nevertheless, the usage of machine learning is not without its problems. There are two problems that are inherent to machine learning:

- Training. Most of the algorithms used for machine learning require the training of the system, this means many of the applications are only meaningful if applied to a dataset within the training margins, which is not always possible, for example anomaly detection for cargo boat trajectories is normally tied to the area where the model was trained, moving to another area changes the model and means some retraining is necessary.
- Overfitting. This is the result of trying to get exceptionally meaningful results, we may end up in fitting our model so much that is only relevant for the training dataset.

Finally, there is a specific problem for our use case, it has to do with how data is used. One of the use cases for the project was using data fusion in disputed areas. The problem is if the rivals know the algorithm being used and its results, in which case they can adapt their techniques and behavior to go unnoticed, effectively cheating the system.

References

- [1] R. Nowak, R. Biedrzycki and J. Misiurewicz, Machine learning methods in data fusion systems, 2012 13th International Radar Symposium, Warsaw, Poland, 2012, pp. 400-405, doi: <http://dx.doi.org/10.1109/IRS.2012.6233354>
- [2] G. Van Nederveen, NATO intelligence surveillance reconnaissance tracking standard NATO STANAG 4676, IET Seminar on Target Tracking and Data Fusion: Algorithms and Applications, 2008, doi: <https://doi.org/10.1049/ic:20080063>
- [3] Shlens, Jonathon. A tutorial on principal component analysis, doi: <https://doi.org/10.48550/arXiv.1404.1100>
- [4] David Charte, Francisco Charte, Salvador García, María J. del Jesus, Francisco Herrera, A practical tutorial on autoencoders for nonlinear feature fusion: Taxonomy, models, software and guidelines, Information Fusion, Volume 44, 2018, <https://doi.org/10.1016/j.inffus.2017.12.007>.
- [5] Chen S, Guo W. Auto-Encoders in Deep Learning—A Review with New Perspectives. Mathematics. 2023; 11(8):1777, doi: <https://doi.org/10.3390/math11081777>
- [6] Marta Baldomero-Naranjo, Luisa I. Martínez-Merino, Antonio M. Rodríguez-Chía, A robust

- SVM-based approach with feature selection and outliers detection for classification problems, Expert Systems with Applications, Volume 178, 2021, 115017, ISSN 0957-4174, doi: <https://doi.org/10.1016/j.eswa.2021.115017>.
- [7] Tsyurmasto, Peter & Zabaranin, Michael & Uryasev, Stan. (2014). Value-at-risk support vector machine: Stability to outliers. Journal of Combinatorial Optimization. 28, doi: 10.1007/s10878-013-9678-9.
- [8] K. Taunk, S. De, S. Verma and A. Swetapadma, A Brief Review of Nearest Neighbor Algorithm for Learning and Classification, 2019 International Conference on Intelligent Computing and Control Systems (ICCS), Madurai, India, 2019, pp. 1255-1260, doi: 10.1109/ICCS45141.2019.9065747.
- [9] Guo, Gongde & Wang, Hui & Bell, David & Bi, Yaxin & Greer, Kieran. (2003). KNN Model-Based Approach in Classification. Lect Notes Comput Sci. 2888. 986-996, doi: 10.1007/978-3-540-39964-3_62.
- [10] C. Z. Liu and M. Kavakli, Data-aware QoE-QoS management, 2016 IEEE 11th Conference on Industrial Electronics and Applications (ICIEA), Hefei, China, 2016, pp. 1818-1823, doi: 10.1109/ICIEA.2016.7603882.
- [11] Lattanzi E, Castellucci G, Freschi V. Improving Machine Learning Identification of Unsafe Driver Behavior by Means of Sensor Fusion. Applied Sciences. 2020; 10(18):6417. doi: <https://doi.org/10.3390/app10186417>
- [12] R. Srinath, J. Vrindavanam, V. P. Vasudev, S. Supreeth, H. Raj and A. Kesarwani, A Machine Learning Approach for Localization of Suspicious Objects using Multiple Cameras, 2020 IEEE International Conference for Innovation in Technology (INOCON), Bangluru, India, 2020, doi: 10.1109/INOCON50539.2020.9298364.
- [13] Y. Wang, J. Wong and A. Miner, "Anomaly intrusion detection using one class SVM," Proceedings from the Fifth Annual IEEE SMC Information Assurance Workshop, 2004., West Point, NY, USA, 2004, pp. 358-364, doi: 10.1109/IAW.2004.1437839.
- [14] Li, Xiaolei & Han, Jiawei & Kim, Sangkyum & Gonzalez, Hector. (2007). ROAM: Rule- and Motif-Based Anomaly Detection in Massive Moving Object Data Sets, doi: 10.1137/1.9781611972771.25.
- [15] Lee, Jae-Gil & Han, Jiawei & Li, Xiaolei. (2008). Trajectory Outlier Detection: A Partition-and-Detect Framework. 140-149. doi: 10.1109/ICDE.2008.4497422.

The open XidML Standard - What are the Advantages for Users

Florian Mertl

Airbus Helicopters Deutschland GmbH, Industriestrasse 4, 86609 Donauwörth
 Florian.mertl@airbus.com

Abstract:

XidML is the “eXtensible Instrumentation Definition Markup Language”. It is an XML-based, open and vendor-neutral standard to describe any type of FTI (Flight Test Instrumentation) configuration. XidML aims to store and exchange all information about how data are acquired, processed and packaged for transmission.

XdefML is part of the XidML standard. As for XidML, the XdefML schema is open, vendor-neutral. It is designed to describe all properties, specifications and parameter of an equipment. It is often called “electronic datasheet” and so it does e. g. not describe the actual value of a specific setting, but the limits of it.

XdefML can be adopted solely, it does not rely on XidML. User can take benefit of just implementing XdefML in their toolchain to having a standardized interface to describe FTI equipment.

The available schemata for XidML and XdefML allows the creation, parsing, verification and validation of XidML and XdefML files.

Key words: Open Source, vendor-neutral, electronic datasheet, markup language, data management standard

What is XidML?

XidML was born in 2004. At that time, it was mainly driven by single user/supplier in the field of flight test instrumentation. The idea was to find a way to describe, how FTI systems store and exchange information. The solution was found by developing a derivate of the XML eXtensible Markup Language. XML is both human- and machine readable. The structure of an XML file is based on tags (like e. g. HTML). One key element of XML is that XML files can be validated by applying a schema. A schema is a separate file which defines the legal structure of an XML file. Tools can validate XML to ensure the data integrity and that the file is well-formed (valid tags, order, data types etc.). In 2004, the XML schema was adapted to the needs for flight test instrumentation and this extension was named as XidML, where “id” stands for “Instrumentation Definition”. To ensure availability, flexibility, a wide acceptance and to foster collaboration, all information should be made free and open available. The initial focus was mainly the description of data acquisition systems, although the adoption to telemetry or recorder systems was already considered by the XML-based utilization.

Over the years, XidML evolved from version 2 to the current version 3

According to [1], XidML files consists of up to 8 main elements:

- **Auxiliary Files:** This element lists all the auxiliary files associated with the XidML document
- **Documentation:** This element can be used to document a XidML file. It can include information such as short and long descriptions, the creation date, who the author of the XidML file is, references to technical specifications, and other miscellaneous information.
- **Parameters:** This element contains a list of all globally defined parameters and their properties sourced or generated by the acquisition system(s) described in the XidML document.
- **Packages:** This element contains a list of all the packages used by acquisition system(s) described by the XidML file.

- **Algorithms:** This element contains all the algorithms used by the acquisition system(s) described in a XidML file.
- **Instrumentation:** This element lists all the instrumentation used by an acquisition system along with associated setup information.
- **Links:** This element contains a list of all the Links used by acquisition system(s) described by the XidML file.
- **Addenda:** This element contains a list of "Addenda" that can be used to place any information that is not catered for in XidML.

XdefML was introduced in parallel to XidML

As the name already implies, XML allows to extend the

Where does XidML & XdefML affect FTI

XidML and XdefML can have an impact in different areas in the daily FTI life, like:

- **FTI Configuration management:** When looking for new FTI devices, systems or sensors (instruments), there are multiple requirements which must be fulfilled by the candidate. Beside the technical specifications and properties, it is also important, how to integrate this new instrument in the existing toolchain. Every user needs to find a way to link tests to instruments to sensors to calibration information to movements and so on and on. This toolchain can reach from a simple spreadsheet approach to highly complex and customized databased framework solutions. Bringing new hardware in the loop should be easy and efficient. Due to the standardized format of XidML files, the configuration of an instrument can be easily imported in the toolchain. With the built-in version control information in the XML files, it's easy to keep track of modification and configuration evolutions. Implementing XML parser along with the XidML and XdefML schemata (XSD), allows the validation of an imported file to ensure a valid and consistent configuration of the instrument.
- **FTI Asset management:** Instruments like sensors requires regular calibration. Other devices should undergo maintenance. Information like

calibration or maintenance interval can be implemented in the XdefML file. This could simplify any notification or alerting by the toolchain to remind the user about upcoming maintenance actions. Instruments in the FTI world are not meant to stay on the same place for its entire life time. They are shipped for maintenance/repair or they are being used during test campaigns somewhere around the globe. To comply with the national/international laws about export control and customs, but also to company-specific classification rules, dedicated information can be placed in the XdefML description to enable e. g. automated tagging of the instruments for e. g. shipping notes.

XdefML – the electronic datasheet

XdefML is a way to describe instruments, in particular it's specifications, available settings and their limits. As for XidML, there's a schema available to validate XdefML files to ensure a valid file. The XdefML schema provides up to three main elements [2]:

- **Instrument Identification:** Contains all information required to identify the instrument. Required elements are ManufacturerName and PartReference. (optional e. g.: SerialNumber, ModelReference)
- **Instrument Specification:** Contains information on the physical and logical characteristics of the instrument as well as some additional information. Required elements are MechanicalClass and FunctionalClass. (optional e. g.: Standalone, SlotsOccupied)
- **Instrument Configuration:** Contains all configuration options for the instrument. Typical elements are Parameters, Settings, Channels.

It's important to note that a XdefML file does not contain the actual configuration of an instrument. It provides information about the instrument settings, especially which setting are available and what are the constraints for these settings. It also holds information about which parameter are provided by the instrument and how they are defined. The interfaces of an instrument are described by Channels (CAN, Serial, AR429, Ethernet...). Their definition is also part of the XdefML files.

Combine XidML & XdefML

XidML and XdefML can be adopted solely, but combining both leads to that unique benefit of “decoupling” instrument configuration from instrument specification. Compared to other description standards, this combination adds another validation layer to ensure that an instrument is configured in accordance to its limits.

- **XML:** an XML parser with syntax highlighting provides feedback, if the file is “well formed”. That means for e. g. that every opening tag has also a closing tag. It does not check if the minimum required elements are present.
- **XdefML:** A valid XdefML file ensures that the instrument description in this file is valid against the XdefML schema. Any violation (missing/unknown element, value out of bound) will be reported by the tool.
- **XidML:** As for the XdefML, a valid XidML file means that the instrument configuration is valid. All elements required are present. But in this stage, a wrong setting (e. g. Channel Gain out of bounds) is not detected.
- **XidML & XdefML combined:** Having the possibility to read XidML files and validates them with the schema, but also with the associated XdefML files for the instrument, ensures that the instrument is correct configured and all setting values are within the instrument perimeter.

Collaboration

Standards like XidML are driven by collaboration. There are several ways to increase the collaboration level:

- **Open Standard:** An open standard is more visible to the SW developer community. This wider recognition scope allows a broader adoption of the standard across different FTI ecosystems.
- **Visibility and Transparency:** All XidML & XdefML information are available in the Internet for free use. Along with the documentation and schemata, there are also sample files available for free download. This fosters trust and wider acceptance within the community.
- **Change Requests:** If a user requires a modification of the schema, a change request process was established to

submit that request via the webpage [3].

- **Vendor-neutral:** The open approach prevents vendor lock-in. This allows vendors and users to develop tools to handle XidML & XdefML. It helps to foster a more innovative community.
- **Community driven:** XidML & XdefML is a community driven project, which aims not be a product or a service provided a single vendor. In fact it targets the contribution of all stakeholder in the FTI community. These standards should benefit from the huge level of experience in the FTI toolchain development community. A large community accelerates the development of tools.
- **Standardization Body:** The XidML Working Group acts as the standardization body. Its member are from ever Anybody interested in the standard can participate. Regular working group meetings ensures a certain ritual, allows newcomer to join and provides the possibility to exchange the various topics around XidML & XdefML. Submitted change requests will be discussed and decisions will be taken accordingly. This working group lends credibility to the standard and it's open access is intended to eliminate any entry barrier.

Tools

When working with XidML & XdefML files, user can choose different solutions to create, modify and validate the files:

- **Notepad++ :** With the XML plugin it is possible to assign the XidML or XdefML schema and to validate those files accordingly. Users can edit, view and validate files. Notepad++ is free to use
- **XdefML Assistant:** The application is available on the XidML.org webpage for download and free usage. XdefML files can be created, modified and validated. It supports different views.
- **Altova XMLSpy:** XMLSpy is a professional XML editor with enhanced edit functionality. It provides multiple views and automatic validation. User can even create and modify the schema. It's a license-based application with different variants.

Summary

XidML and XdefML can help FTI users in various domains due to its open approach, its

vendor-neutrality and the resources it provides to adopt the standards. Everyone is welcome to get familiar with the schemata and the

documentation and to contribute to the evolution and wider acceptance of these standard.

References

- [1] XidML.org XidML Schema definition:
<https://www.xidml.org/library/XidML-3.0.0.html/html/XidML-3.0.0.html> (accessed 20.05.2024)
- [2] XidML.org XdefML Schema documentation:
<https://www.xidml.org/library/XdefML-3.0.0.html/html/XdefML-3.0.0.html> (accessed 20.05.2024)
- [3] XidML.org Change Request :
<https://xidml.org/change-requests/> (accessed 20.05.2024)

Feature Creep for Efficiency

Malcolm Weir¹

¹ Ampex Data Systems Corporation, Hayward, California USA,
mweir@ampex.com

Abstract:

For most project managers, additions to the scope of a project are problematic: not only must the project complete its original goals, but also new ones. And while cost is naturally important, perhaps the biggest challenge is adapting the design of a system to incorporate new functionality, which may lead to inefficiency in development and implementation. This paper describes the sequence of scope changes to a data collection system, and how collaboration between the customer, the end user and the suppliers increased the functionality of the solution as the capabilities expanded. The result is a system which started as a simple data collection device and has evolved into a traffic management system handling data format conversion, security oversight, instrumentation command and control, traffic routing, and, still, data collection. This paper provides insight into the process by which the new functionality was implemented, illustrating how economies of power, mass and volume can be achieved by the use of specialist software running on versatile hardware. That process is in contrast to the more traditional "one box, one function" approach with hardware modules, which is undoubtedly elegant but also less efficient than a software-centric design."

Key words: Data acquisition & networks, Networks & Architecture, Data Management, Applications, Data Management Standards, Security of data, links and networks.

Introduction

Over the past 20 years or so, the composition of telemetry and instrumentation systems has changed. For most of those years, there has been presentations, discussions, papers and exhibits on how the "new" technology can be used to deliver various advantages over the "old" approaches.

This is another such paper.

But unlike those earlier write-ups, this one is oriented from the problem-solving perspective: how can a device serve the required purposes.

It must be noted that this paper is "loosely based" on a real project, but it does not focus on the specifics of that program, for two main reasons: first, no two projects are identical, so whatever challenges and solutions one program team identifies, the chances are very likely that another effort would have, at best, similar-but-different tasks, and the second reason is that the a deep-dive into a single program is likely to be both irrelevant to even well-versed readers, and may also contain proprietary or even confidential information.

Accordingly, this paper describes a "lightly fictionalized" program, based on a real effort but with excessive detail omitted for the sake of readability.

Similarly, the specific detailed capabilities of the test equipment used in the program isn't described unless that capability is relevant to the narrative. For example, efforts required to work around specific limitations of test equipment (ours or that of other vendors) are not particularly interesting to anyone who isn't using that specific set of equipment, so are omitted regardless of the amount of effort involved in the work-around – unless, of course, the limitation was a product of a standard or architectural model that would apply to a whole class of devices.

Background

At first glance, the requirements of the program for a Mission Data Recorder were not particularly onerous: a few hundred megabits of data and a few terabytes of storage. The I/O interfaces were straightforward Ethernet, the recording format should be IRIG-106, *Inter-Range Instrumentation Group (IRIG) 106 Chapter 10 Digital Recording Standard*, with the only marginally unusual feature being a requirement

that the recorder be able to act as a Grand Master time source in accordance with IEEE/1588, *Institute of Electrical and Electronics Engineers Standard for a Precision Clock Synchronization Protocol for Networked Measurement and Control Systems*, version 2.

Certainly, there were also atypical file retrieval specifications: in accordance with IETF RFC 959, *File Transfer Protocol*, using Transport Layer Security (TLS) in accordance with IETF RFC 4217, *Securing FTP with TLS*. However, perhaps the atypicality of this is remarkable mostly by the fact that *all* FTP connections aren't routinely secured with TLS!

There were also requirements for video manipulation (changing frame rates and compression ratios), but these were fairly localized to a particular retrieval channel.

The environmental requirements were fairly conventional, with the exception of those for radiation exposure; since the vehicle was designed for extreme altitudes, the objective was for the solution to be "rad hard"; or to be exact, tolerant of higher-than-normal radiation levels; see Figure 1.

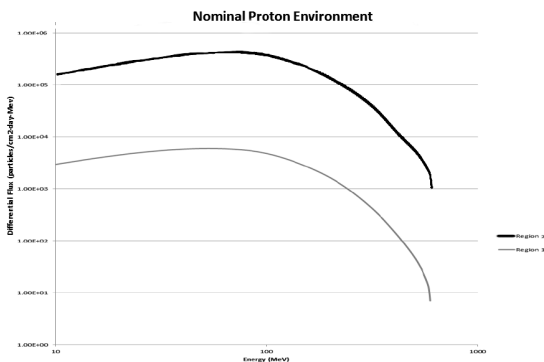


Figure 1 Radiation Levels

The relevance of the radiation tolerance may seem slight when viewed in the context of the topic of this paper, but as will be seen it is a critical factor in identifying solutions.

Trimming Chapter 10

As noted earlier, the requirements started by specifying an IRIG 106 Chapter 10 recorder.

However, Chapter 10 contains multiple disparate sections, some of which are organized into Chapters of their own: Chapter 6 for Command and Control, Chapter 9 for Metadata Description and Configuration, and Chapter 11 for Packet Formats.

And in addition to those sections in separate Chapters, there are significant functional requirements remaining in Chapter 10, which are relatively independent in isolation but combine to

define a particularly specific and interoperable recorder. See Figure 2 for the visual guide to the standard from the 2019 version of the standard, which is a little out of date but not inherently incorrect (the Data Format & Packetization Definition that is referenced as being in section 10.6 is actually now in Chapter 11, but section 10.6 now effectively states "see Chapter 11").

In addition to requirements for an on-board recorder, Chapter 10 reaches beyond the device to mandate practices for naming files once downloaded, and even when modified. Obviously, this sort of detail is overreach for the standard's stated purpose, but relatively harmless and easily ignored without breaking much, if anything. (Things like the naming of files properly belong in a "best practices" handbook, not a formal standard).

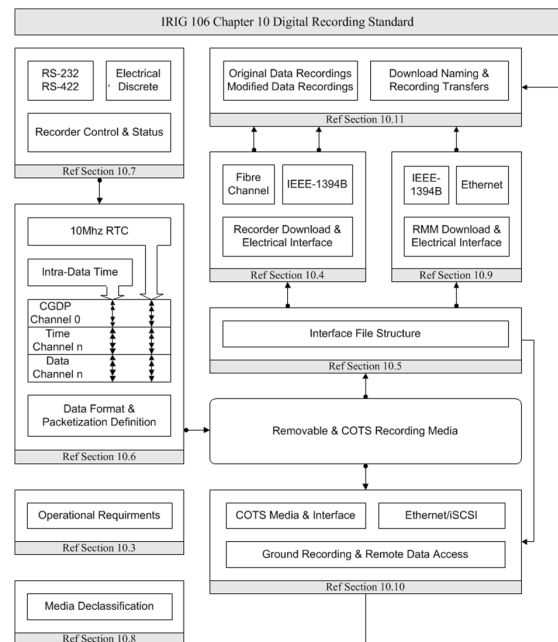


Figure 2 Diagram of Chapter 10 Standard (2019)

The Disk and Filesystem Problem

One of the challenges of using Chapter 10 for more than just instrumentation data collection (in this case, and for example, general file storage using FTP) is that Chapter 10 embraces a simplistic model of storage devices and requires a primitive filesystem to be used.

The first challenge is that the standard requires that the sector at Logical Block Address (LBA) 1 on the device be used for the "root" of the filesystem (i.e. the first directory block), and that LBA 0 is "reserved", which is interpreted as being set to all zeroes. These two requirements prevent the use of any commonly used volume/partitioning scheme (as LBA 0 technically must be zeroes), and prevent the use of one physical storage device to hold two or

more Chapter 10 filesystems (as the root of the filesystem has to be in LBA 1).

Of course, sophisticated storage controllers can easily get around those issues by combining and then dividing one or more physical devices into multiple targets, each of which appears to be an independent device. But this sort of work-around creates additional complexity as Chapter 10 mandates particular device addresses for the download interface and does not embrace the concept that there may be multiple devices on a single interface.

Given, then, that Chapter 10 only comfortably supports one filesystem, it is unfortunate that the filesystem it mandates is unsuited to general purpose applications.

This filesystem is adapted from a NATO standard, STANAG 4575. However, the intent of that STANAG was (and is) to define a “virtual” filesystem that manufacturers of Intelligence, Surveillance, and Reconnaissance (ISR) recorders could use as a common interface between their internal systems and a NATO download station. It was always envisaged (by the STANAG) that a processor could be in the data path during the download operation, so the filesystem was designed to be an easy “virtualization” of the underlying structures; the STANAG is explicitly designed to be usable without read/write access to the media.

But Chapter 10 adopted the STANAG filesystem in an architecture where there was no expectation of a processor in the download data path, instead expecting a bridge between the download interface and the storage interface (which was most often an industry-standard one like IDE or SATA and so to commodity storage devices like SSDs, although at least one recorder implemented the media interface directly to raw flash chips).

The biggest problem with the filesystem is that it requires all files to occupy (apparently) contiguous storage; that is, if the first sector of a 1,000-sector file is at LBA 1234, then the last sector will be at LBA $(1234+1000-1) = 2233$. This makes it challenging to support writing/appending to more than one file at a time. Of course, there are ways to mitigate this problem to a greater or lesser degree, such as by performing operations like the old Windows “Defragment” utility to move isolated chunks of one logical file into a single location, but these all impose costs in time, performance and capacity (or all three).

However, the Chapter 10 download interface, and the related filesystem / partitioning constraints, was designed for a use case where

a single ground installation (e.g. a test range) would be retrieving test data from a variety of different recorders. But for this specific application, the logistics dictate that the media would only ever be directly accessed in one or two designated facilities, and perhaps not even then since the data can be extracted from the recorder *in situ* using the FTP interface, which might be quicker than waiting until the recorder can be accessed, the media extracted and transported to the facility where it would be accessed.

Therefore, it was agreed that the parts of Chapter 10 relating to the download interface were unnecessary and could be excluded from the requirements with which the recorder must comply that are derived from Chapter 10.

Solution Approach

The first design decision to be made is regarding the product baseline. Obviously, a solution that reuses an existing product is likely to be lower cost and lower risk than one which starts with a “clean sheet”, with the tradeoff that a modified product may be less efficient by one or more metrics (size, weight, power, etc.).

The two viable “reuse” options would be to start with a classic “Chapter 10” recorder and add the file server features (support for secured FTP, etc.), or to start with a file server product and add Chapter 10 capabilities. As previously discussed, the filesystem issues inherent with a “pure” Chapter 10 system were moot, so the analysis of the two options boiled down to assessing how much of the workload was classic Chapter 10 data acquisition, and how much was related to post-acquisition processing.

With a view particularly to the video manipulation requirements, a decision was made that a file server platform adapted to handle Chapter 10 would be most appropriate.

A side benefit of using a server platform is that the hardware and software environments are more scalable: if more CPU power is needed, that’s usually an easy upgrade.

Chapter 10 Data Type Fidelity

In the development of the Chapter 10 standard, a lot of attention was paid to the idea that the recorder should not manipulate the acquired signals, and therefore recordings made on different products from different vendors could be compared.

This led to a slightly unexpected resistance within the standard-making body to certain “obvious” data types, initially centered around Time, Space, Position Information (TSPI) data: since that data was usually acquired through a

RS-232 serial port in accordance with the NMEA 0183 standard supported by many GPS receivers, it should be stored in the recording as RS-232 serial data, even though the data was TSPI data and it would be much more convenient if analysis/exploitation software could process it as expected.

The counterpoint to those resisting the sort of manipulation needed to pull TSPI data out of a data stream received over a serial port is simply that treating a serial port as a data type is similarly inappropriate: it should properly (using that logic) be captured as a stream of “1” / “0” pulses, or even a sequence of analog voltage levels. While obviously a preposterous approach, it illustrates the inflexibility of the “no manipulation” position.

This position extended especially to Ethernet: the interface type was Ethernet, therefore the recorder should (only) record data as a series of low-level Ethernet frames. While that might be useful for test instrumentation engineers building a test system (“Is the network working?”), in general that’s less useful than, for instance, pulling out a video streamed over Ethernet and storing it as a video, eliminating as irrelevant the fact that it was transported by Ethernet for at least part of the journey from camera to recorder.

Obviously, for this program, and indeed for all traditional programs, the decision as to how a particular data stream should be recorded belongs solely with the program, and standards should not interfere with the preferences and decisions of the people designing the solution.

This feature represents the first extension of the nominal set of requirements: instead of a pure “Chapter 10 Recorder”, the program needs a recorder that will repackage received data into the appropriate data types, regardless of how that data was delivered.

This feature extension also drives the need either for a more powerful processor and suitable software, or for a dedicated subsystem, likely based on an FPGA and customized firmware. While the latter is likely more efficient by many metrics, the former is more flexible and easier to implement in stages.

Hardening

Having identified that a fileserver system was the best choice on which to base the solution, the next step was to explore how to meet the radiation requirements.

This involved extensive discussion with the customer’s subject matter experts. Given that the recording system wasn’t critical for flight, it was determined that some core “data integrity”

steps (such as Error Correcting Codes on the memory interfaces) and thickened chassis walls would likely address data corruption, while a watchdog circuit would be sufficient to protect against the system locking up or crashing.

Component selection for the system as a whole would include radiation considerations; for example, the CPU was selected to use a 22nm FinFET process, which has shown excellent radiation performance, and MOSFETs were derated to 75% of their operating voltages to reduce the probability of a “single event gate rupture”. In addition, lead-based solder was used in place of lead-free processes, and so on.

Obviously, the watchdog circuit would have to be manufactured out of radiation hardened components, as would the power supply, but beyond those two subsystems, everything else could be fairly standard. The watchdog was implemented in a FPGA using a Triple Module Redundancy, to provide an overall system monitor providing a series of counters, checks and responses to provide a fault detection, isolation and recovery (FDIR) methodology.

The only additional design decision was to switch the bulk data storage from being NVMe based on PCI Express back to SATA, since it was considered more likely that an radiation event upset on an NVMe interface could impact more of the system (as PCI Express is the main system bus), while a SATA controller can be reset without restarting the whole machine.

One curious aspect of this specific project is that the mission length is significantly longer than is typical for regular terrestrial flight tests. With a single mission estimated to last about 11 weeks, and the design life of the system required to be for 15 missions, this equates to approximately three years in the high-radiation environment. So while the dosage rates are quite low, the overall dose is not insignificant.

Chapter 10 Data Types, Redux

The implications of the radiation hardening extended beyond the recorder enclosure: since the data acquisition that arrived at the recorder did so over Ethernet, at some point in the overall instrumentation architecture there had to be Data Acquisition Units (DAUs).

The challenge for the recorder is that, because the DAUs *also* had to be radiation tolerant, the number of vendors / product options was extremely limited; in fact, only one vendor offered a range or “rad tolerant” DAUs. Unfortunately, these DAUs are manufactured by a European company, and so their adherence to the Chapter 10 standard was effectively nil; while they collected data and sent it out over Ethernet,

they used the IENA protocol, not the Chapter 10/11 format.

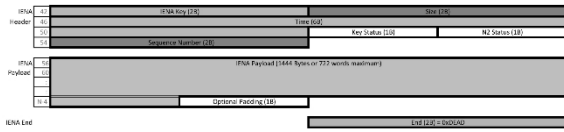


Figure 3 IENA Packet Format

This creates a new problem: since at least one of the customers for the data is a US Government agency, Chapter 11 data packets are a *de facto* requirement. So some degree of data conversion would be required. And the conversion would have to be much more sophisticated than was the case with video.

CHANNEL ID		PACKET SYNC PATTERN		Packet Header
PACKET LENGTH				
DATA LENGTH				
DATA TYPE	PACKET FLAGS	SEQUENCE NUMBER	DATA TYPE VERSION	
RELATIVE TIME COUNTER				(Optional) Packet Secondary Header
HEADER CHECKSUM		RELATIVE TIME COUNTER		
TIME (LEAST SIGNIFICANT LONG WORD [LSLW])				
TIME (MOST SIGNIFICANT LONG WORD [MSLW])				
SECONDARY HEADER CHECKSUM		RESERVED		
CHANNEL-SPECIFIC DATA				Packet Body
INTRA-PACKET TIME STAMP 1				
INTRA-PACKET DATA HEADER 1				
DATA 1 WORD 2		DATA 1 WORD 1		Packet Trailer
DATA 1 WORD N		:		
[FILLER]				
DATA CHECKSUM				

Figure 4 Chapter 11 Packet Structure

To expound on that point: video carried over Ethernet is (usually) “just” a series of MPEG Transport Stream (TS) packets placed in UDP/IP datagrams, while video in Chapter 10 is the same TS packets dropped into a Chapter 11 packet type, with some added header and trailer information. But other data types generally carry assumptions that may or may not align with a different standard.

The most prominent example is with time. A Chapter 11 packet has a “Relative Time Counter” in the header (48 bits), an optional time field in the Packet Secondary Header (64 bits), and an Intra-Packet Time Stamp in the payload (for some data types only, either 48 or 64 bits long). The IENA packet only has a single time field at 48 bits in length. Mapping the two packet formats requires understanding how the time is measured in each architecture.

And this is where the significance of the radiation requirements comes in: because the DAUs were COTS products, modifying them to output Chapter 11 packets would require significant software/firmware modifications, and possibly even hardware revisions. Therefore, the conversion had to happen at the recorder, not the DAUs.

Fortunately, there was a very limited number of data types, and despite the DDU vendor being unwilling to cooperate directly, we could

establish a mapping between the IENA fields and values and Chapter 11 ones. This mapping is not universal and might not work too well for other applications, but it is sufficient for this specific project.

Parameter Extraction

Once the core data acquisition system, including the format conversion, was completed, the next added task was to implement a scheme to usefully reduce the data rate, so as to accommodate a very limited telemetry downlink channel. As may be expected, the greatest challenge was to define a very flexible control interface, so that the user could specify the parameters to extract and the rate at which to send the extracted samples; also considered, but ultimately rejected as unnecessary for this application, was whether provide averaging or min/max functions to the down-sampled parameters.

The control language was implemented by vendor extensions to IRIG 106 Chapter 9, the Telemetry Attributes Transfer Standard (TMATS). While pretty much universally disliked, the overwhelming advantage of TMATS is that it is widely understood, and tools to manage and manipulate TMATS records are relatively abundant.

The telemetry packets were assembled into a standard Chapter 10 UDP Data Transfer stream and dispatched to the address of the downlink transmitter. In this specific application, the downlink channel is an established radio network, but architecturally it could just as well be an IRIG 106 Chapter 7 Packet Telemetry Downlink implementation.

Vehicle Infrastructure Management

Once the radiation-hardened recorder system was designed, the program started to consider using it for additional tasks.

The first of which is the management of the networks and gateways within the vehicle. In addition to the on-board operational networks (such as the data acquisition networks), there are networks designed to be used by payloads carried by the vehicle. Naturally, the vehicle operators want to be able to isolate and connect those payload (cargo) networks to limit connectivity to various gateway points at various times during the mission, so the recorder (by now renamed the Multi-Function Data Recorder) was selected as the control node through which all other network functions were managed.

This obviously had relatively little to do with “recording”, but it reflects the fact that the device hosting the recording software was central to the overall vehicle network, and thus represents a

good site for non-mission-critical *ad hoc* command and control.

As it turns out, on this specific program the implementation of the software to support these additional capabilities was via code written by Ampex. However, on other programs, the recorder was configured to support “containers” such as Docker and LXC.

In many ways, containers are similar to virtual machines, but instead of having a whole operating system and a virtual machine hypervisor, a container uses the same operating system kernel as the supporting system, much reducing the overhead involved: a container running on a particular operating system calls exactly the same library and kernel software as a traditional application would; the only significant difference is that containers use more storage space as they duplicate all the files and libraries needed so as to ensure integrity of the container (all the pieces are present).

It should be noted that supporting a full hypervisor/virtual machine architecture is also perfectly possible and allows additional capabilities such as the use of different operating environments (classically, Windows and Linux, with the former used for analysis and the latter collection and manipulation) and more rigorous cybersecurity boundaries.

This facility allows third parties to develop lightweight, self-contained software packages that will not interfere with each other or with the main recording application.

Cargo Management

Following on from the concept of controlling the network access points that various payloads may use, it’s an obvious extension to provide health and status interfaces to the various payloads.

This includes both the generic capabilities provided by the vehicle, such as control of cameras and floodlighting, but also passing commands to the various payloads (in both the pressurized and unpressurized compartments) and returning the responses to the origin. In that way, the vehicle can carry “third party” payloads and provide access to them through the MDR interface.

Summary

Traditionally, an instrumentation recorder is perceived as an “endpoint” device: data flows to it, but the only data flows from it are downloading or streaming.

But as the requirements for data acquisition shift inexorably towards networks and DAUs, so does

the role of the “recorder”: no longer is it just an endpoint, but now it becomes a central hub.

Naturally, it’s still possible to record network data using a traditional purpose-built recorder, but the very limitations of network recording -- primarily the non-deterministic delivery of packets -- means that general-purpose systems with a software-defined recorder are not only viable, but more flexible.

And as the flexibility of the network hub recorder gets recognized, additional functionality inevitably migrates to the recorder. And the use of “packaging” technologies such as containers show one approach that will allow even greater versatility from these formerly “one trick” devices!

Acknowledgements

The author acknowledges the contributions and hard work of Paul Carrion, Peter Chan, Kevin Hudson, and Hal Steger without whom this solution would have remained a hypothetical though experiment, instead of an operational space-going Multi-Function Recorder.

Power Over Ethernet in FTI, Suitability & Challenges

Pat Quinn, Product Line Manager, Data Acquisition
Curtiss-Wright, Dublin, Ireland
pquinn@curtisswright.com

Power Over Ethernet in FTI, Suitability & Challenges:

This paper discusses why Power Over Ethernet (POE) is ideally suited to Flight Test Instrumentation (FTI) and details some of the challenges of designing in POE into FTI hardware and discusses some of the considerations that must be taken when architecting a Flight Test Instrumentation system with POE components.

Key words: Data Acquisition, Power Over Ethernet (PoE), Distributed Networks, Reduced Wiring, SWaP Optimized

What is Power Over Ethernet (PoE)?

Power Over Ethernet (PoE) ^[1] is a method of distributing power and data to networked devices over the same twisted pair Ethernet cabling. PoE has been standardized by IEEE since 2003.

Power Over Ethernet (PoE) Terminology

In order to understand Power Over Ethernet (PoE) there are some common terms used to describe PoE devices that must be explained.

1) Powered Devices (PD) ^[2]

Powered Devices (PD) are defined as any networked device that is powered by PoE.

2) Power Sourcing Equipment (PSE) ^[3]

Power Sourcing Equipment (PSE) are devices that send power and data over the Ethernet cabling to the Power Devices (PD)

3) PoE Switches

Network Switches that support Power over Ethernet (PoE) directly from the switch itself.

4) Power Injectors

Power Sources that add power to the Ethernet cabling from non PoE capable switches to the Powered Devices (PD)

Types of Power Over Ethernet (PoE)

There are 4 main types of PoE, with the IEEE standards defining a link negotiation protocol on power up in order to determine the level of power required to be delivered from the PSE to the PD. The differences between them relate to the max power that can be delivered, and the voltage levels at the PSE.

Passive PoE ^[4]

No link negotiation protocol on power up

PoE - IEEE 802.3af-2003 ^[5]

POE Link negotiation protocol, 44-57V at PSE, Max of 15.4W at PD – Type 1 Devices

PoE+ - IEEE 802.3at-2009 ^[6]

POE Link negotiation protocol, 50-57V at PSE, Max of 25.5W at PD – Type 2 Devices

PoE++ / 4PPoE - IEEE 802.3bt-2018 ^[7]

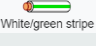
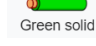


POE Link negotiation protocol, 50-57V at PSE, Max of 51W at PD – Type 3 Devices. Max of 71.3W at PD – Type 4 Devices





Power Over Ethernet (PoE) Wiring Options

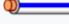



The PoE standards define two wiring schemes for both PSE and PD devices.

For 10/100BT Ethernet speeds, Mode A, 4 wire wiring, puts the DC voltages over the same physical wires as the data, with DC+ on the RX pair and DC- on the TX pair.

Tab. 1: 10/100 BT Mode A Wiring ^[8]

Wire	10/100 MODE A (4 wire)
 White/green stripe	Rx+ / DC +
 Green solid	Rx- / DC +
 White/orange stripe	Tx+ / DC -
 Blue solid	Unused

 White/blue stripe	Unused
 Orange solid	Tx- / DC-
 White/brown stripe	Unused
 Brown solid	Unused

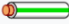






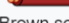
 White/blue stripe	TxRx C-
 Orange solid	TxRx B- DC-
 White/brown stripe	TxRx D+
 Brown solid	TxRx D-

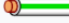



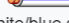


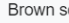
For 10/100BT Ethernet speeds, Mode B, 8 wire wiring, puts the DC voltages on the other 4 wires in the standard Ethernet cables.

For 1000BT speeds, Mode B puts the DC voltages on the C and D bidirectional pairs.

Tab. 2: 10/100 BT Mode B Wiring [8]

Tab. 3: 1000 BT Mode B Wiring [8]

Wire	10/100 MODE B (8 wire)
 White/green stripe	Rx+
 Green solid	Rx-
 White/orange stripe	Tx+
 Blue solid	DC+
 White/blue stripe	DC+
 Orange solid	Tx-
 White/brown stripe	DC-
 Brown solid	DC-





Wire	1000BT MODE B (8 wire)
 White/green stripe	TxRx A+
 Green solid	TxRx A-
 White/orange stripe	TxRx B+
 Blue solid	TxRx C+ / DC+
 White/blue stripe	TxRx C- / DC+
 Orange solid	TxRx B-
 White/brown stripe	TxRx D+ / DC-
 Brown solid	TxRx D- / DC-

For 1000BT speeds, Mode A puts the DC voltages on the A and B bidirectional pairs.

Why is Power Over Ethernet (PoE) a great fit for FTI?

Tab. 4: 1000 BT Mode A Wiring [8]

The arguments for PoE in FTI are simple, reduced wiring weight and ease of installation. In traditional FTI systems data and power are delivered over separate cables to each device in the FTI system architecture. By leveraging PoE the number of cables required to get both Power and Data to and from the devices is potentially halved.

Wire	1000BT MODE A (8 wire)
 White/green stripe	TxRx A+ / DC+
 Green solid	TxRx A- / DC+
 White/orange stripe	TxRx B+ / DC-
 Blue solid	TxRx C+

Every Flight test engineer is aware of the paperwork and approvals needed for FTI installation drawings and document management, reducing the wiring leads to less overhead required for their installations.

Today, typical FTI installations are distributed throughout the airframe, requiring power and data cables to be routed all over the airframe,

through bulkheads and around critical systems. Reducing the number of cables here makes perfect sense.

However, given the nature of the FTI hardware and the power required by them, not all of them are suitable for PoE implementation. Take for example a Data Acquisition unit running multiple strain channels, this could easily exceed the power levels available from the PoE standards.

As stated before, FTI architectures are, these days, distributed throughout the airframe, getting the Data Acquisition closer to the sensors is in-fact a much greater weight saver than just combining the power and ethernet cables to the DAU. Reducing the length of the cable harness from the sensor back to the data acquisition unit by making the unit miniaturized and SWaP optimized and PoE capable balances all the above. The challenges and considerations of such a system architecture are discussed in the next sections.

The challenges of designing miniature, SWaP optimized PoE FTI hardware.

The target for the design of PoE capable FTI hardware can be summarized as:

- 1) Keep it small.

For mounting in restricted spaces, closer to the sensors, the smaller you can make the design the better.

- 2) Use standard connectors if possible.

Flight test hardware uses many different connector types already, typically either flying leads or crimp able field rewireable connectors.

- 3) Simple to manufacture.

It should not be so complex to build that the costs of manufacture make it unfeasible.

- 4) Flexible design

There are a multitude of analog sensors used in flight test, and many different avionic busses that are captured in flight test campaigns. In the hardest to reach places on the airframe these are typically analog measurements for Strain / voltage / temperature / vibration. As many of these should be supported as possible.

- 5) Daisy chainable

Running PoE cables to each device would be one approach, but better to make the devices possible to daisy chain so a single cable can deliver the power and data to multiple devices in the same location on the airframe.

- 6) Compatible with existing products on the same network

Bearing in mind that these devices are most likely to be part of a larger FTI system they must be supported by the same configuration tools and generate the same data formats as the rest of the system.

7) Getting Power and Data to the devices

While there are many PoE switches and power injectors available, very few of them are suitable for FTI applications. Networked FTI systems use PTP IEEE 1588 to synchronize and there are very few PoE switches available that support PoE. Therefore, a method of delivering the power and data to the system as part of a flight qualified FTI system is a concern.

To expand on one of these topics in more detail, Daisy chaining, let us consider what this entails.

From a PoE point of view a daisy chainable PoE device must act as both a Powered device (PD) and as Power Source Equipment (PSE). It must be able to take power in from the source and deliver power down to all the devices in the chain. It must also be able to aggregate the data from all downstream devices back to the main network. A consideration here would be what happens if the chain breaks, due to wiring damage or other causes of failure. Potentially, all the data down stream from the fault would be lost.

If the device chain supported loop back wiring, where the devices could be powered from both the input and output ports and could be designed to automatically switch the traffic flow direction in the case of a single device failure, loss of data could be minimized.

Considerations for Architecting PoE as part of an FTI system

Power Over Ethernet (PoE) brings a very different set of challenges and considerations that should be taken into account when architecting your FTI system.

Cable Power Losses

PoE uses high voltages out of the PSE's to account for loss over the cable itself. There must be enough voltage left at the end of the cable to power the device.

CAT5E has a cable resistance of 0.188Ω/meter^[9]. From a 48V PSE source to a chain of 8 PoE devices, each drawing 4W over a 100 Meter total chain length would result in a voltage drop of about 25% by the end of the chain.

For CAT6, with a cable resistance of 0.14 Ω/meter^[10] the same setup would have about a 19% drop.

Chain Throughput

The aggregated data from the chain of PoE devices is also something to consider. How you construct and schedule your traffic is important to be aware of, so as not to over run the capacity of your link. For example, an 8 channel device sampling at 50Ksps could produce up to 60Mbps if each channel was sampled in its own high rate / short packet. The same sample rates can be achieved using slower larger / packets reducing the device throughput to about 6Mbps.

Power

The number of devices drives the power requirement of the full chain. Each device must be able to provide enough power to power the rest of the devices downstream from it, and the PoE Power budget for the PSE must be able to provide enough power for the full chain.

Summary

This paper has shown how Power over Ethernet (PoE) is ideally suited to Flight Test applications, considering the advantages of reduced wiring weight, especially for distributed networked FTI systems when designed into SWaP optimized, daisy chainable miniature devices.

References

- [1] IEEE 802.3af-2003, June 2003
- [2] IEEE 802.3af-2003, June 2003
- [3] IEEE 802.3af-2003, June 2003
- [4] Tycon Power Green Power Accessories (archive.org), June 2010
- [5] IEEE 802.3af-2003, June 2003
- [6] 802.3at Amendment 3: Data Terminal Equipment (DTE) Power via the Media Dependent Interface (MDI) Enhancements, September 11, 2009
- [7] IEEE 802.3bt 145.1.3 System parameters, 2018
- [8] IEEE 802.3af/at/bt standards, 2003, 2009, 2018
- [9] "SuperCat OUTDOOR CAT 5e U/UTP" (PDF). Archived from the original (PDF) on 2012-03-16.
- [10] "Cat6A Interactive Reference Guide" (PDF). Archived (PDF) from the original on 2019-10-31.

TRMC Support for the TM Community

Gene Hudgins, Juana Secondine
 TENA Software Development Activity (SDA), Niceville, FL, USA
bobby.g.hudgins.ctr@mail.mil, juana.d.secondine.ctr@mail.mil

Abstract:

The nature of telemetry often requires operators to be on location with receive system(s) or remote consoles, resulting in costly TDY and possibly a shortage of operators to support all scheduled events. To mitigate these issues, the Test Resource Management Center (TRMC) has developed a remote-control capability (along with centralized data collection) to eliminate existing personnel requirements at both locations, **greatly reducing operational costs** and providing **real-time insight** to system status. The TRMC's Joint Mission Environment Test Capability (JMETC) is a distributed LVC capability using a hybrid network solution for all classifications and cyber, and the Test and Training Enabling Architecture (TENA) is the middleware selected for use in JMETC Secret Network (JSN) events. TENA provides for real-time system interoperability, as well as interfacing existing range assets, C4ISR systems, and simulations - fostering reuse of range assets and future software systems. These capabilities allow the most efficient use of current and future TM range resources via range resource integration, critical to validate system performance in a highly cost-effective manner. This presentation will inform the audience as to the current impact of TRMC capabilities on the T&E community; as well as their expected future benefits to the range community and warfighters.

Key words: TENA, JMETC, BDA, multi-site, multi-domain

TRMC Solutions for the Telemetry Community

As in the past, present telemetry (TM) support requires operators to be on location with the TM receive system or at a remote TM console (with a remote TM antenna control unit). This often results in temporary duty (TDY) for operators and potentially an insufficient number of operators to support all scheduled operations. The capability to remotely operate the telemetry system (i.e., perform status monitoring, data distribution, and/or command and control from a centrally-located, manned site) greatly reduces operational costs of TDY to remote TM sites. A remote-control capability could altogether eliminate the existing requirement for personnel at both the local TM system antenna site as well as the TM control facility, alleviating previous manpower issues (Figure 1).

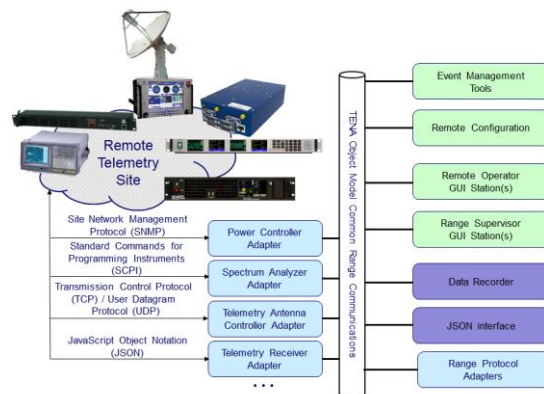


Fig. 1. Architecture to a Remote TM Site.

The original design of the DoD test and training range infrastructure was not intended to be interoperable, and rapidly became inadequate in this new era of warfare. The cost-effective integration of range data and telemetry resources is critical to ensuring the war-worthiness of today's advanced weapon systems and platforms which populate the air, land, sea, and cyber areas of operations. To ensure the advantages of range interoperability are available across the DoD, the OSD Test Resource Management Center (TRMC) Central Test and Evaluation Program (CTEIP) developed and is constantly refining the Test and Training Enabling Architecture (TENA).

TENA is a common architecture providing real-time software system interoperability and the capability to interface existing range assets, systems, and simulations at distributed facilities. Government-owned and free for anyone to use, TENA allows the most efficient use of current and future range resources via range resource integration. This integration invariably fosters interoperability and reuse within the test and training communities – critical in validating system performance in a highly cost-effective manner.

TENA provides a middleware software component and can be used on any internet protocol (IP)-based range or distributed network, such as the Joint Mission Environment Test Capability (JMETC) networks and the Joint Staff (JS) J7 Deputy Director Joint Training (DDJT) Joint Training Enterprise Network (JTEN).

Upgrading an existing range system to TENA can be achieved in a drastically shorter time frame than traditional software integration efforts. Additional benefits include the cost-effective replacement of unique range protocols, enhanced exchange of mission data, and organic TENA-compliant capabilities at sites which can be leveraged for future events, enhancing both reuse and interoperability.

The JMETC Secret Network (JSN), which leverages the Secret Defense Research and Engineering Network (SDREN) for connectivity, is the test and evaluation (T&E) enterprise network solution for secret testing. SDREN is a network established to support research, development, testing and evaluation, and science and technology activities in the DoD. The persistent JSN infrastructure includes sites at Defense industrial facilities and peering with sites on other DoD networks at like classification such as the Secret Internet Protocol Router Network (SIPRNet).

JMETC also offers a network capability to its customers with a requirement for higher-than-secret classifications of distributed testing, cyber testing, or unique requirements that don't fit the JMETC JSN model. The JMETC Multiple Independent Levels of Security (MILS) Network (JMN) is the enterprise network solution for higher test event classifications, as well as those which are cyber-specific.

The primary product of T&E is the data and knowledge gained through the collection of information about a system or item under test. The amount of information needed to acquire this knowledge is growing exponentially due to more complex systems needing to operate in System of Systems (SoS), Family of Systems

(FoS), Joint, and Coalition environments. With many DoD tools and methods remaining largely the same for decades, the T&E infrastructure necessary to collect and analyze this information has not evolved alongside this increased complexity, becoming increasingly deficient and ineffective. By contrast, corporations have dramatically changed their methodologies – modernizing their analytics capabilities to keep up with the massive influx of data.

To properly test and evaluate today's advanced military systems, the T&E community must leverage new algorithms using the equivalent processing power of many computers in parallel to effectively analyze large amounts of data. This process is called "big data analytics (BDA)" and the Test Resource Management Center is taking the initiative to develop better tools and techniques to empower DoD analysts to make better and faster decisions using more of the collected data than was previously usable.

Current Telemetry Applications

OmegaNExT TENA Adapter (X-5000 Decommutator TENA Adapter): The TENA OmegaNExT Adapter (Figure 2) is a TENA-enabled application that receives telemetry data from an OmegaNExT X-5000 decommutator and converts that data into TENA State3D Data and TENA DataTable Data. Once the OmegaNExT data is converted into TENA Data, the State3D Object and the DataTable object can interact with other TENA-enabled applications within the same Execution.

The TENA Adapter is able to receive live or recorded data from a running OmegaNExT Client.

Text boxes within the adapter Graphical User Interface (GUI) enable the user to enter the names of parameters within the OmegaNExT Stream. The user can find the parameters in the OmegaNExT Client that correspond to a specific measurement (example: finding the parameters that respond to ECEF-X, ECEF-Y, and ECEF-Z or parameters that respond to latitude, longitude, and height above the ellipsoid). Settings involving the type of Position (Geocentric or Geodetic), Angle Unit (Radians or Degrees), or Orientation Types (Euler or Yaw/Pitch/Roll) can also be selected depending on the stream.

Custom parameters that may not fit in the State3D Parameter categories can be added to a data table at the bottom of the GUI. The parameter type (int, float, etc.) and the parameter unit (meters, radians, degrees, pressure) can be selected as well.

The update frequency can be set to whenever a certain parameter updates or when any parameter updates.

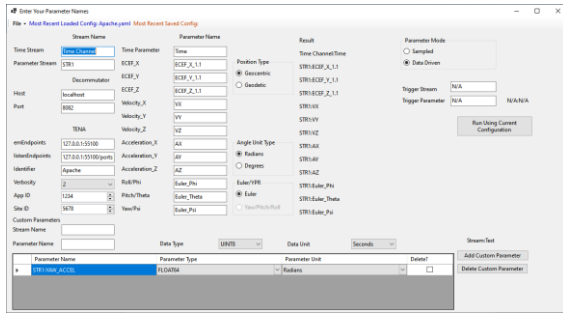


Fig 2. OmegaNEXt Adapter GUI Display.

Automatic Dependent Surveillance-Broadcast (ADS-B) Adapter: Starting January 1, 2020, aircraft must be equipped with an air traffic control “Automatic Dependent Surveillance-Broadcast (ADS-B) Out” to fly in most controlled airspace. ADS-B is a surveillance technology in which an aircraft determines its position via satellite navigation, and periodically broadcasts position (and other information), enabling it to be tracked. The TRMC is creating a library of software products called Range System Adapters which present a common distributed communication mechanism for the remote configuration, monitoring, and control of range systems. As such, the TENA Software Development Activity (SDA) has developed an ADS-B Adapter – a software application designed to expose a common communication interface to an existing range system by wrapping the system’s custom external interface.

The ADS-B Adapter is a computer process separate from the software running an existing system. By “wrapping” the existing ADS-B system, there is no modification of the existing system, allowing use on legacy systems that cannot be updated or have limited communication capabilities. The ADS-B Adapter translates identification and position information sent by aircraft and interfaces an application called a dump1090 server (Transmission Control Protocol (TCP)/IP connection), which translates signals received by the Software Defined Radio (SDR) to a data stream that makes it available via a TCP service.

The TRMC-developed ADS-B Adapter provides a low-cost solution to acquire live/local aircraft information: an SDR radio and antenna costs >\$100 and the dump1090 server software is freely available, open-source software and works with a variety of SDRs and antennas. The ADS-B Adapter is free, government-off-the-shelf (GOTS) software and when used in

conjunction with the TENA Data Collection System (TDCS), captures/replays repeatable and realistic local air traffic scenarios in simulated environments (Figure 3).

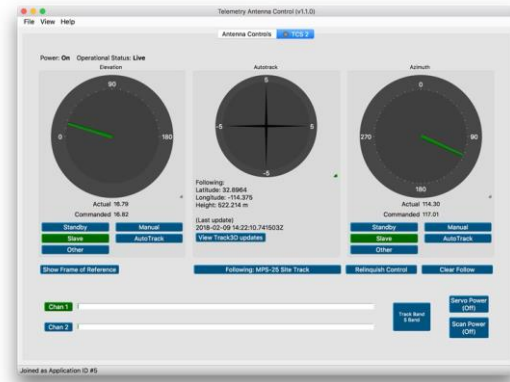


Fig 3. TENA ADS-B Adapter Telemetry Antenna Control Display.

TENA Plugin for SIMDIS: SIMDIS is a Naval Research Laboratory (NRL) set of software tools that provide two and three-dimensional interactive graphical and video display of live and post-processed simulation, test, and operational data. SIMDIS has evolved from an NRL display tool for the output of missile models, to a premier GOTS product for advanced situational awareness and visual analysis (Figure 4). The TENA plugin for SIMDIS allows a set of TENA Stateful Distributed Objects (SDOs) and messages to be used in SIMDIS (e.g. SIMDIS can be used in conjunction with the TENA ADS-B Adapter to provide a display of local aircraft identification and position).

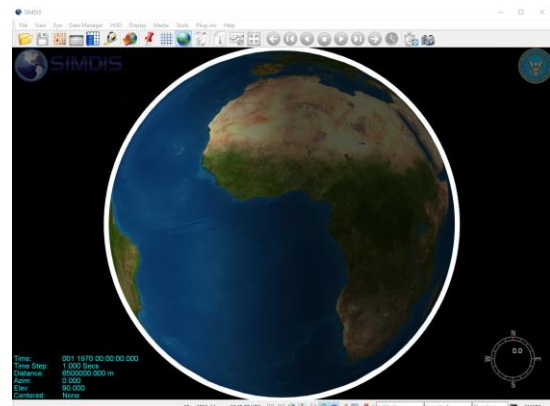


Fig 4. SIMDIS GUI Display.

TENA Interface for Yuma Proving Ground (YPG) TCS Antenna: YPG, located in Yuma, Arizona has chosen to add a TENA interface to their TCS Antenna Control Unit (ACU) model M1 used on their TM pedestals. The Antenna Control System SDOs created by the ACU adapters are visible on SIMDIS and the Instrument System Assignment Tool (ISAT),

where SIMDIS shows the system with a beam indicating where it is pointed and ISAT allows users to select a Track SDO to send cueing data to the ACU. The operator then uses the data to point the system. Operational testing is currently underway on the remote monitoring and control capabilities of the telemetry antenna system using TENA.

Cloud Hybrid Edge-to-Enterprise Evaluation & Test Analysis Suite (CHEETAS) Tool: The TRMC has developed and successfully demonstrated a rapid Knowledge Management/Big Data Analysis capability to support hypersonic flight test. During a recent high-priority hypersonic test mission at Edwards Air Force Base, CA, post-test data processing (download, conversion, and validation – all necessary steps that must occur prior to data analysis) took approximately ten hours using existing capabilities. Working with the 419th Flight Test Squadron the following week, the TRMC team processed the same raw mission data with the CHEETAS tool in less than 15 minutes. Using CHEETAS cut the time required to get the test data into the hands of analysts by over 95%.

The CHEETAS framework provides a common tool suite for building evaluation infrastructure for disparate acquisition portfolios. Developed and supported by TRMC, CHEETAS is provided to the test community for free and is currently in use at multiple locations throughout the test community. CHEETAS is vendor- and hardware-agnostic, and can run on anything from a laptop to a full GPU-enabled, hyper-converged cluster, to a commercial cloud environment. CHEETAS is providing game-changing knowledge management and big data analysis capability both pre-flight and post-mission to support the testing of hypersonic boost-glideweapons and other systems requiring large-scale test data collection.

Data Processing Timeline: Traditional Software vs. CHEETAS		
Description	Traditional Software <i>(what was used for ARRW mission)</i>	TRMC CHEETAS GOTS Software <i>(evaluated week after ARRW mission)</i>
Data Size	57 GB DTD X 3 DTDs	57 GB DTD X 3 DTDs
Dataset Used	BIMDAS Data Collection Memory Modules	BIMDAS Data Collection Memory Modules
Ingestion Equipment Capacity	Single RMM Reader <i>(serial process)</i>	8 RMM Read Simultaneously <i>(parallel process utilizing multi-cartridge reader)</i>
Data Ingestion Time 1 Module	55 minutes	3 minutes 7 seconds
Data Conversion Time 1 Module	9 hours 39 seconds	11 minutes 4 seconds <i>(included data validation)</i>
Data Available for Analyst Use	Approx. 10+ hours post-test	Approx. 15 minutes post-test
Computer System	Data Ingestion Workstation	Spare 4-year-old High Performance Desktop

CHEETAS Enables Timely Delivery of Validated Data to Analysts for Future Tests

Fig 5. CHEETAS Data Processing Time.

Past TM Uses of TENA

Eglin Gulf Test Range (EGTR) Gulf Range Enhancement (GRE) Program: As in the past, present telemetry Theater Missile Defense (TMD) missile systems are designated to provide regional defenses against present and future conventional, chemical, biological, or nuclear ballistic, cruise, or air-to-surface guided missiles that can endanger deployed U.S. forces as well as U.S. friends and allies throughout the world. Eglin Air Force Base (AFB) in Florida is enhancing the capability of the EGTR to conduct TMD programs via the GRE program. This development includes the selection and construction of land-launch facilities; the modification of land, sea, and air safety zones; and the subsequent conduct of TMD missile system test and training flights within the enhanced EGTR. When complete, this expansion will allow launched target missiles to be halted by interceptor missiles with the intercepts occurring in the airspace over the Gulf of Mexico.

The EGTR expansion will provide greater flexibility in test scenarios than is possible using other ranges, and permits more realistic testing of TMD interceptor systems. This next-generation architecture is expected to be completely remote controlled when classification allows.

To make this happen, GRE engineers met with representatives of the TENA Software Development Activity (SDA) concerning the many TENA capabilities which would benefit this new architecture. TENA, chosen for the command and control (C2) portion of the GRE plan, will support remote operations of numerous Joint Gulf Range Complex test assets. TM equipment currently identified to be accessed via TENA adapters and controlled by TENA interfaces include the following: ACUs, digital switches, Time to Live (TTL) splitters, data link test set / Bit Error Rate Test (BERT), monitoring systems, spectrum analyzers, Global Positioning System (GPS) receivers, oscilloscopes, TM receivers, telemetry recorders, power strips, dehydrators, IP cameras, and uninterruptible power supplies (UPS). The long-term plan is for all GRE devices to be retrofitted with TENA adapters and interfaces.

Naval Air Station (NAS) Patuxent River, MD (Pax River) Atlantic Test Range (ATR): The Pax River ATR is another excellent example of how beneficial TENA can be for TM control. Before work began to develop and field an enterprise approach to remotely monitor and operate all components of remote ATR ground telemetry systems, Pax River was faced with

four major, and incredibly common, TM range issues: operator proximity, lights-out operations, a generalized interface, and Information Assurance (IA) requirements.

The existing approach at Pax required TM operators to be on location with the TM ACU during missions. Any near-term remote operations concepts required a one-to-one correlation between the remote ACU and remote TM Antenna, and no sub systems were supported. They also had no ability to fully power-on, configure, operate, or obtain the status of their remote Auto-Tracking Telemetry System (ATAS) and Mobile Telemetry Acquisition System (MTAS) systems, therefore requiring personnel on-site to perform power-on and to configure all systems with no distributed status available from TM system components.

Vendor-specific interfaces and data models were used, which meant operators had to gain proficiency on each system component. This generalized interface prohibited uniform operator consoles, and limited the ability to easily access and share relevant metrics and engineering data. Furthering the problem was that Pax River had a limited ability to meet evolving IA requirements and Security Technical Implementation Guides (STIG) on system components.

Working alongside members of the TENA SDA, NAS Pax River developed an enterprise approach to remotely manage and operate all components of remote ground telemetry systems. This method provides a common architecture (TENA) which interfaces system components, regardless of system manufacturer. Upon completion, this effort now provides for single operator control of several remote TM systems, therefore reducing travel and manning requirements at remote sites. It also allows TM status information, setup, and control to be distributed to appropriate destinations for system verification and operations.

Additional Applications: Other TM applications of TENA are ongoing at White Sands Missile Range (WSMR) in New Mexico and Vandenberg AFB in California. WSMR reached out to the TENA SDA seeking a TENA-capable range interface unit (RIU) for existing radars; a TENA-capable Telemetry Tracker pointing data interface (as a modification to the existing RIU); and a persistent, distributed TENA capability through WSMR's Inter Range Control Center (IRCC). TENA is currently being used to connect FPS-16 radars, telemetry systems, and optics systems. Future plans at WSMR include the use of TENA for Real-Time

Data Processing (RTDPS). Redstone Test Center also used TENA to pull real-time Time, Space, Position Information (TSPi) data via a "Data Adapter Tool" which fused other real-time TSPi sources. The Data Adapter Tool allows operators at RTC to now transport data via TENA using the Standard platform object model.

Understanding TENA

Understanding composability is the ability to rapidly assemble, initialize, test, and execute a system from members of a pool of reusable, interoperable elements, the TENA architecture is a technical blueprint for achieving an interoperable, composable set of geographically distributed range resources (both live and simulated) that can be rapidly combined to meet new testing and training missions in a realistic manner. TENA is made up of several components, including a domain-specific object model that supports information transfer throughout the event lifecycle, common real-time and non-real-time software infrastructures for manipulating objects, as well as standards, protocols, rules, supporting software, and other key components.

The TENA Middleware (currently at Release 6.1.0beta2 and available for free download at the TRMC web site: <https://www.trmc.osd.mil>) combines distributed anonymous publish-subscribe and model-driven, distributed, and object-oriented programming paradigms into a single distributed middleware system. This unique combination of high-level programming abstractions yields a powerful middleware system that enables TENA middleware users to rapidly develop complex yet reliable distributed applications.

The TENA object model consists of those object/data definitions derived from range instrumentation or other sources, which are used in a given execution to meet the immediate needs and requirements of a specific user for a specific range event. The object model is shared by all TENA resource applications in an execution. It may contain elements of the standard TENA object model although it is not required to do so. Each execution is semantically bound together by its object model.

Therefore, defining an object model for a particular execution is the most important task to be performed to integrate the separate range resource applications into a single event. In order to support the formal definition of TENA object models, a standard metamodel has been developed to specify the modeling constructs

that are supported by TENA. This model is formally specified by the Extensible Markup Language (XML) Metadata Interchange standard and can be represented by Universal Markup Language (UML). Standards for representing metamodels are being developed under the Object Management Group Model Driven Architecture activities. The TENA Object Model Compiler is based on the formal representation of this metamodel, and TENA user-submitted object models are verified against the metamodel. However, it is important to recognize the difference between the TENA metamodel and a particular TENA object model. The object captures the formal definition of the particular object / data elements that are shared between TENA applications participating in a particular execution, while the object model is constrained by the features supported by the metamodel.

Another significant benefit for TENA users is auto-code generation. The TENA Middleware is designed to enable the rapid development of distributed applications which exchange data using the publish-subscribe paradigm. While many publish-subscribe systems exist, few possess the high-level programming abstractions presented by the TENA Middleware. The TENA Middleware provides these high-level abstractions by using auto-code generation to create complex applications, and these higher-level programming abstractions (combined with a framework designed to reduce programming errors) enable users to quickly and correctly express the concepts of their applications. Re-usable standardized object interfaces and implementations further simplify the application development process.

Through the use of auto code generation, other utilities, and a growing number of common tools, TENA provides an enhanced capability to accomplish the routine tasks performed on the test and training ranges in support of exercises. The steps in many of the tasks are automated, and thanks to the enhanced software interoperability provided by TENA, the information flow is streamlined between tools and the common infrastructure components.

TENA utilities facilitate the creation of TENA-compliant software and the installing, integrating, and testing of the software at each designated range. This complex task falls to the Range Developer who, in this phase, performs the detailed activities described in the requirement definitions and event planning, as well as the event construction, setup, and rehearsal activities of the range's Concept of Operations. While some manual exercise and

event setup is required at ranges, TENA tools, as they are developed and become accepted across the range community, make exercise pre-event management easier.

Support for TENA Users

The TENA SDA has developed a website that provides a wide range of support for the TENA user, including an easy process to download the Middleware, free of charge. The website also offers a helpdesk and user forums that will address any problems with the Middleware download and implementation. The TENA SDA is very aware of the need to inform range managers and train TENA users, and the TENA SDA presents regular training classes that are designed to meet attendees' needs; from an overview or technical introduction of TENA, all the way to a hands-on, computer lab class on the TENA Middleware.

TENA's continuing evolution in its support of the test and training range community is managed by an organization of users and developers. TENA is maintained according to a consensus of its users, which assemble as the JMETC Configuration Review Board (JCRB). These meetings are generally held at technical exchanges JMETC holds each year called the JMETC Technical Exchange (JTEX). At these meetings, users are updated on TENA usage, problems, and advancements. Although the agenda involves briefings, it is open to wide-ranging discussions. This ensures the users' concerns and inputs are understood, recorded, and action items are made if necessary. Of equal importance, TENA developers and management have had a long and mutually beneficial relationship with the Range Commanders Council.

Conclusion

Although it was a technological and software evolution that was the impetus for TENA's growth in its enabling of range interoperability and resource reuse, the Middleware found its needed validation on DoD test and training ranges. On these ranges, the U.S. Military evaluates the warfighting equipment, personnel, and concepts that are deployed in support of ongoing missions around the globe. Unfortunately, test and training events only provide the opportunity for evaluation. It is the data collection and analysis that determines the war-worthiness of the equipment or concept; this data can quickly and definitively illuminate any necessary improvements needed to ensure effective and safe weapon system operation and training. TRMC TENA, JMETC, and Big

Data Knowledge Management are time-tested, proven, integral parts of that equation.

JMETC reduces the time and cost to plan and prepare for distributed events by providing a persistent, readily-available network, and the TENA common integration software is easily-integrated into telemetry environments and applications. Even the remote-control capability alone alleviates previous manpower issues and greatly reduces operating costs for the telemetry community.

The TRMC is constantly building on a DoD T&E data management and analysis capability that leverages commercial big data analytic and cloud computing technologies to improve evaluation quality, reduce decision-making time, and reduce T&E cost. This vision encompasses a big data architecture framework – its supporting resources, methodologies, and guidance – to properly address the current and future data needs of weapon systems testing.

Transforming the current T&E data infrastructure to one employing a Big Data approach will support both current warfighter T&E needs and the developmental and operational testing of future weapon platforms. The T&E community will be able to realize improvements in cost avoidance and cost reductions, in faster and more accurate T&E responses, and in overall T&E capabilities. Using TENA, JMETC, and BDA, Test Directors can put their focus back where it needs to be – on the warfighter and the task at hand.

For more information, contact Ryan Norman, Chief Data Officer and Lead, Joint Mission Environments, E-mail: jmetc-feedback@trmc.osd.mil or tena-feedback@trmc.osd.mil. For the Unclassified, Controlled Unclassified Information (CUI), U.S. Government / Contractor website, go to <https://www.trmc.osd.mil>; for Distribution A, non-U.S. Government / Contractors, please visit <https://www.tena-sda.org>.

Acknowledgement

The authors acknowledge the contribution of their colleagues to this work.

Glossary

ACU: Antenna Control Unit
ADS-B: Automatic Dependent Surveillance – Broadcast
AFB: Air Force Base
ATAS: Auto-tracking Telemetry System
ATR: Atlantic Test Range

BDA: Big Data Analytics
BERT: Bit Error Rate Test
C2: Command and Control
CHEETAS: Cloud Hybrid Edge-to-Enterprise Evaluation and Test Analysis Suite
CTEIP: Central Test and Evaluation Investment Program
CUI: Controlled Unclassified Information
DDJT: Deputy Director Joint Environment
EGTR: Eglin Gulf Test Range
FoS: Family of Systems
GOTS: Government Off-the-Shelf
GPS: Global Positioning System
GRE: Gulf Range Extension
GUI: Graphical User Interface
IP: Internet Protocol
IRCC: Inter Range Control Center
ISAT: Instrument System Assignment Tool
JCRB: JMETC Control Review Board
JMETC: Joint Mission Environment Test Capability
JMN: JMETC MILS Network
JS: Joint Staff
JSN: JMETC Secret Network
JTEN: Joint Training Enterprise Network
JTEX: JMETC Technical Exchange
MILS: Multiple Independent Levels of Security
MTAS: Mobile Telemetry Acquisition System
NAS: Naval Air Station
NRL: Naval Research Laboratory
RIU: Range Interface Unit
SDA: Software Development Activity
SDO: Stateful Distributed Objects
SDR: Software Defined Radio
SDREN: Secret Defense Research and Engineering Network
SIPRNet: Secret IP Router Network
SoS: System of Systems
STIG: Security Technical Implementation Guide
TCP: Transmission Control Protocol
TDCS: TENA Data Control System
TDY: Temporary Duty
T&E: Test and Evaluation
TENA: Test and Training Enabling Architecture
TM: Telemetry
TMD: Theater Missile Defense

TRMC: Test Resource Management Center
TTL: Time to Live
UML: Universal Markup Language
UPS: Uninterruptible Power Supply

WSMR: White Sands Missile Range
XML: Extensible Markup Language
YPG: Yuma Proving Ground

Design and Implementation of a New Generation of Space Ground TT&C Software Architecture Based on Container Cloud

Zhong WeiHong¹, Feng Wei¹

¹ Beijing Research Institute of Telemetry, BeiJing China
zhongwhong@qq.com

Abstract:

With the continuous development of space technology, in view of the increasing types and number of in-orbit spacecraft led to the increasing demand for ground measurement and control equipment. To address this issue, this paper puts forward a new generation of space ground TT&C software architecture based on container cloud. Based on the virtualization container cloud technology, we divide the space ground TT&C software, and dynamically reorganize the resources required for different system types of tasks. In practice, the architecture effectively improves the flexibility, reusability, availability and resource utilization of complex space ground TT&C software.

Key words: TT&C Software, Resource Reorganization, Virtualization, Container Cloud, Kubernetes.

Introduction

Today is the era of space, the space launch missions are becoming increasingly dense in the world. Multi-band, new systems and new model task are emerging, and the number of spacecraft in orbit has been significantly increased. The TT&C mode has changed from a few traditional systems to multiple types of systems, the number of tracking targets has increased from single target to multiple targets, and the whole system is also developing towards the trend of digitalization. For the multi-task TT&C system, the space ground TT&C software needs to quickly adapt to the requirements of task resource reorganization.

In the traditional modular space TT&C software architecture, the coupling degree between modules is high, and an exception in a small module may cause the entire system to crash, which greatly reduces the stability and fault tolerance of the system. Due to the high correlation between the functions of the system, the development of one functional module also depends on another functional module, which reduces the efficiency of software development and increases the development cycle. Meanwhile, the traditional TT&C software is directly run on a real physical machine with one machine running one software. In order to improve the fault tolerance of the system, a software often runs both primary and backup simultaneously. In this case, a TT&C software

needs to occupy two machines at the same time, resulting in low resource utilization. Different software runs on different environment with different configuration, and the maintenance of configuration is quite difficult. Moreover, there are many dependency issues and low deployment flexibility.

To solve these problems, this paper introduces the container cloud technology, which runs the TT&C software in the containers and manage them uniformly through the container cloud technology. At the same time, a new software architecture is designed, which is based on the multi-task planning to divide the space ground TT&C software. Each software runs independently in a different container, and a machine can run multiple container software, which improves the utilization rate of internal resources of the system. In the event of software abnormalities or machine outage, there is no need to manually restart the software or replace the machine. The system can quickly restart the software automatically or rerun the outage service on another available machine, improving the availability of the system without reducing the resource utilization. The container cloud platform could manage the software configuration centrally. Different software has their own configuration in its own independent container operating environment, which is not affected by the deployment environment, and greatly enhances the flexibility.

Docker

In this paper, the space ground TT&C software is divided and the resources are reorganized, which requires the virtualization technology to isolate the computer resources. Mainstream virtualization technologies include two kinds: virtual machine (VM) and container technology. As we use virtual machine software such as VirtualBox need to simulate the whole machine, including virtualized hardware and its independent operating system, which is relatively heavyweight.

Docker is an open-source container engine and a way to implement container virtualization. As shown in Figure 1, unlike virtual machines, Docker containers and hosts share the same operating systems. It is more lightweight with extremely low performance. The container contains applications and all dependency packages by sharing kernels with other containers, and runs in user space with separate processes in the host operating system.

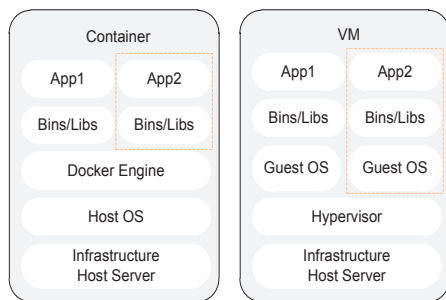


Fig. 1. Difference between container and VM.

Through Docker container technology, we can easily package the code, configuration, and dependencies of applications, turning them into easy-to-use building blocks, enabling applications to more efficiently utilize system resources, deploy faster and more efficiently, and achieving environmental consistency and high application reliability.

Kubernetes

Kubernetes is the most popular container management platform. It can realize a series of basic functions such as application deployment, scheduling and monitoring, and also supports service discovery, automatic restart, automatic scaling and many other functions.

Kubernetes is Google open source container cluster management platform, which provides a complete set of easy-to-use RESTful API (Representational State Transfer Application Programming Interface) for external service interfaces. The core idea of the Kubernetes management platform is to provide a highly available set of cluster self-healing mechanisms

for container applications running on it, leaving the applications running on it in the expected state of users.

The architecture of Kubernetes is shown in Figure 2, which can be divided into two parts: control plane and working node. The control plane mainly includes components such as API Server, Controller Manager, Scheduler, and etcd key value database, which realizes the control functions of making global decisions on clusters (such as scheduling), detecting and responding to cluster events; while the working node is the physical machine actually running by the application service, each node runs multiple Pod, each Pod can run multiple containers, and multiple Pod of the same type jointly form one application service. Working nodes mainly include the kubelet and kube-proxy components, which can maintain the Pod running on the node and provide a running environment for each node.

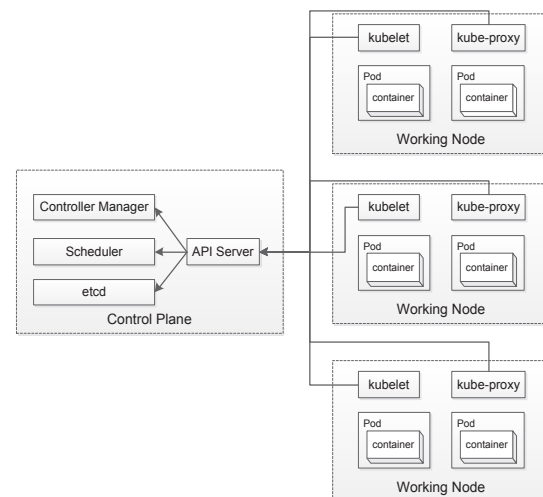


Fig. 2. Kubernetes architecture diagram.

Architecture Design

The architecture of general application software is usually categorized into two types: traditional physical machine deployment architecture and virtual machine deployment architecture. Traditional physical machine deployment architectures generally deploy applications on physical machines, but the failure to define resource boundaries for applications in a physical machine may lead to resource preemption between applications. One solution is to deploy different applications on different physical machines, running only one application per physical machine, but this makes the resource utilization too low per computer. The virtual machine deployment architecture allows multiple virtual machines running on a single physical machine, allowing applications to run between virtual machines and perform resource isolation and process isolation, enabling better

use of resources on the physical machine. Container technology is similar to virtual machines, which also provides a certain degree of isolation, with its own file system, CPU, memory, process space, etc. Whereas a virtual machine is like virtualizing a complete computer running all its components (including its own operating system) on virtualized hardware, while a container is lighter and only shares the operating system between applications.

Compared to the first two general architecture deployment way, due to the lightweight characteristics of container, it creates more simple and quick, start fast, build simple, can support the application of rapid construction, deployment and update. So this paper based on container cloud technology, divide the space ground TT&C software into different application services, and dynamically restructure the resources.

The overall architecture of the new generation of space ground TT&C software based on container cloud is shown in Figure 1, which includes three layers: basic support, operations management and application service. The bottom level is the basic support layer, including the CPU, GPU, memory, network, storage and other resources required by the system, as well as the container cloud platform and various service images, which is the basis of the system operation. The second layer is the operations management, which mainly manages the operation and maintenance of the system, including image management, resource management, task management, resource scheduling, storage management and log management. The upper layer is the application service layer, in which the space TT&C software is divided into storage and forwarding software, data interaction software, system monitoring software, signal acquisition software, signal processing software and data processing software.

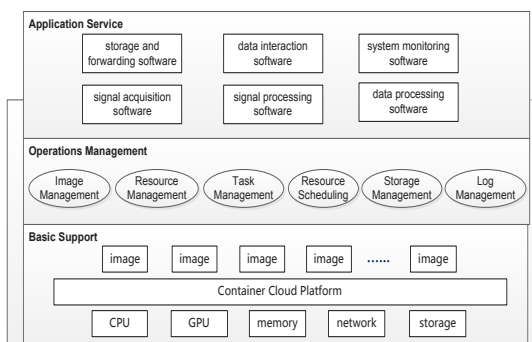


Fig. 3. System Architecture.

The entire system takes the task as the core, resolving the task when it comes. And the

system resources are allocated and scheduled to meet the needs of the task operation. Select the relevant application service image to start the task software, the log and data will be collected and stored uniformly during the task, and the relevant software is withdrawn at the end of the task with the resources released.

Container Cloud Platform

The container cloud platform is the basis of the entire system. It consists of four components: Keepalived, Haproxy, Docker and Kubernetes. Keepalived is a LVS service high availability scheme based on the VRRP protocol, it can check the status of the server, if a server problems, Keepalived will remove it from the system, always keep the system has a server available to provide service. Haproxy is a high-performance load balancing software, which is responsible for balancing the access to Kubernetes to each control plane. Keepalived and Haproxy are to ensure the high availability of the system, only running on the control plane, while Docker and Kubernetes are the basis of container operation and management, running on each node.

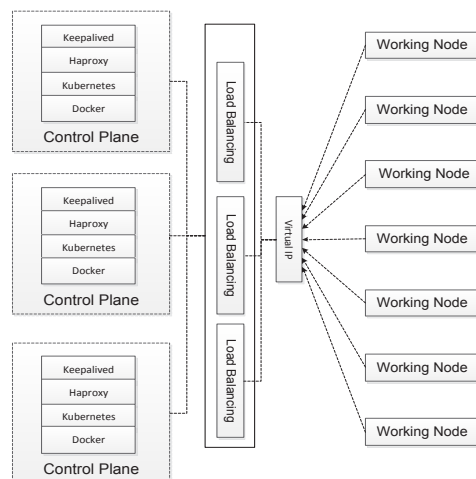


Fig. 4. Container Cloud Platform Topology.

The container cloud platform topology is shown in Figure 4. Keepalived component runs on each control plane, which virtually creates a unified IP, and the working node accesses the control plane through the virtual IP. On each control plane, there is also a Haproxy load balancer, which is responsible for diverting the requests of the working nodes and assigning them to the API servers of different control planes for processing.

Image Management

In the container cloud platform, each application software runs in the container in the form of services. The container encapsulates the computing resources and packages the CPU,

GPU, memory, network, storage and other resources for the service use. The container where the service is located uses Linux's container technology to realize process isolation. The service seems to run in a separate operating system, with its own independent namespace such as file system, network, etc. Like the directory of ordinary applications, the container has its own "directory"---image. Image is the basis of the container operation, which includes the file system and program data needed for the container to run. As shown in Figure 5, different service containers can be packaged into different service images and stored in the image repository for unified management. When the task comes, it can dynamically download the task-related service image files from the image repository, and then start the container and run the related application services.

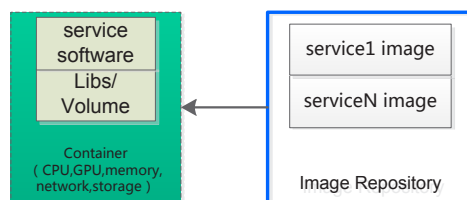


Fig. 5. Container and Image Repository.

The image repository is implemented using harbor technology. In order to ensure the high availability of the image repository, this paper has deployed harbor image repository on multiple servers. The image repository on different servers is configured with automatic synchronization. The image in any repository changes, and other repository can be automatically synchronized. The image management module visits the harbor image repository through the unique IP virtual out of the Keepalived. Even if the server of one or more of the repository in the cluster is down, as long as there is a image repository, it can ensure the normal operation of the image management function and ensure the high availability of the system.

The image management module consists of five sub-functions according to requirements: building image function, uploading image function, querying image function, downloading image function and deleting image function. Different from the virtual machine image, one of the unique characteristics of container image is image layer. Different image layers are joined together through union mount technology, and different images can share the same image layer. Thus, the same underlying part of different image in one machine only need to download and storage once, it can greatly

reduce the image data transmission and storage, for the image stored in the shared image repository created convenient conditions.

Image is the basis of container operation, different tasks use different application service software, so you need to build different images according to the different application services and the environment on which they rely. When the task requirements change, you only need to delete and rebuild the corresponding image in the image repository to adapt to the changing requirements. After building the image, the image can only be used locally. In order to allow the rest of the container cloud platform machines to use the built image, the image needs to be uploaded to the harbor image repository. Other servers can query what images are in the image repository, and they can download the required images to the local in advance. When the task comes, there is no additional time and network bandwidth to download the images from the image repository.

Resource Management

The resource management function is to manage the resources that need to be scheduled in the system, including resource monitoring and the increase, deletion, isolation of resources. The resources here include two meanings: business resources and basic resources. Business resources refer to the antenna, channel, signal processing and other resources that implement business functions, which are combined into various TT&C task systems by dispatching the business resources. Basic resources refer to CPU, GPU, memory, network, storage and other operation support resources, which are the lowest level management and scheduling unit to realize business resources.

We can choose to monitor the use of resources in the system from three different perspectives. First, treating the system as a whole to view the number of used resources and the total number of resources in the system, and graphically shows the proportion of the current system used resources to easily analyze and monitor the overall resource use of the whole system. Secondly, the resource usage can be viewed according to the different resource types in the system. For example, it can list all the computers in the system and its real-time resource usage separately to analyze whether a computer in the system is overloaded with operation. Finally, the resources can be monitored from the perspective of the application service container, lists all the service containers managed in the system, display the real-time resource occupation and

the proportion of allocated resources, analyze whether the service is resource-limited.

When the system needs to expand and shrink, it needs to increase and delete resources. When the resources in the system are insufficient to meet the daily task requirements, the insufficient resources can be manually added for the use of the tasks. When some resources in the system are damaged, the fault resources will be automatically isolated to prevent the task execution failure caused by selecting the wrong fault resources during resource scheduling. If the resource cannot be repaired, the failed resource can be removed manually.

For space TT&C software, there are requirements of continuous operation and online upgrade. The applications developed based on traditional platforms must apply for downtime in advance when upgrading, and conduct the outage update verification in the gap of the tasks, which increases the

complexity of the plan and the inadequacy of verification for the busy space mission. The software in this system is running in the container in the form of service. The containers are isolated from each other. As long as the resources in the system are sufficient, some resources in the system can be isolated for non-stop test and verification of the software without affecting the task operation.

Task Management

In this paper, the TT&C system software is task-oriented, and the relevant TT&C software that needs to be used in the task is divided and resource reorganized. The input of the task can be resolved by remote plans or created locally. The service containers running in the system are created and deleted dynamically according to the start and end of the task.

As shown in Figure 6, the task management module includes the configuration management, plan resolution, manual management and real-time monitoring.

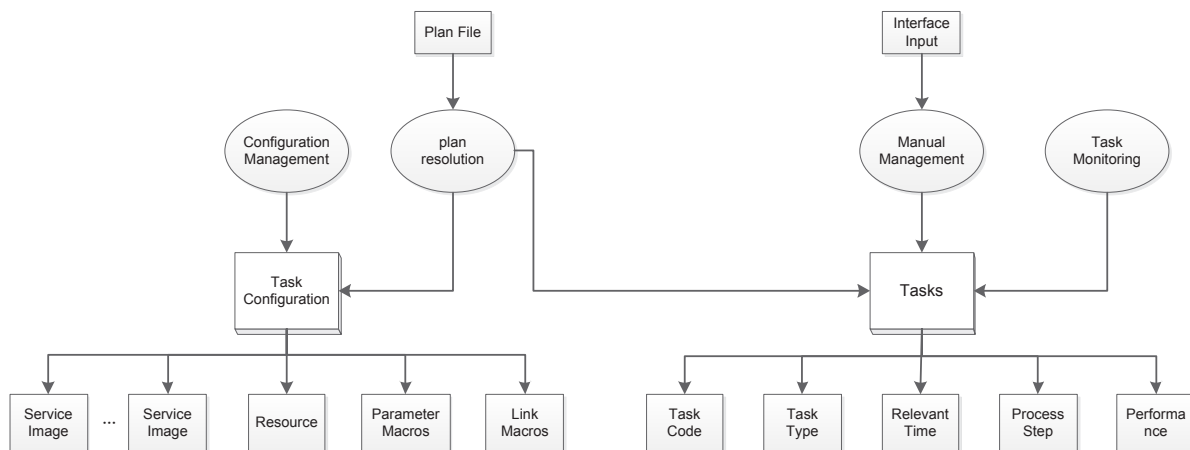


Fig.6. Task Management Functions.

The configuration management is mainly managing the relevant configuration of the tasks. The configuration of a task includes which service images it relies on, which resources it needs to occupy, parameter macros, link macros, etc. For example, for the TT&C task of a USB system, it is necessary to configure USB signal processing software image, USB data processing software image, USB system monitoring software image, etc. Then, the types and quantities of antenna resources, channel resources, computing resources and other resources used by it are also need to be configured in advance for resource scheduling. Each system has its own unique parameter list and related link configuration. Different tasks need to be configured separately. During the task execution process, the system monitor software reads the parameter macro and the link macro,

and sets the macro to each stand-alone device in the system.

The plan resolution receives a remote task plan file, parses it according to the protocol format, and transforms it into an input recognized by the system. In the process of resolving the plan file, first judge whether the file format is correct, if error then reject and generate the format error rejection response. For task creation plans, the plan files are decomposed into independent tasks to read the task-related configuration from the configuration management. Then judge the legitimacy of tasks and the rationality of resource use, if failure then also produce the task-level plan failure response. After the plan is resolved, tasks are created and displayed through the real-time monitoring. For task cancellation planning, cancel the locally created

tasks that did not start according to the task code.

The manual management is that the user manually CRUD tasks through interface. When creating a task, enter the task code, type, preparation time, start time, end time, resource scheduling policy, and then assign the resource scheduling module for resource conflict judgment. If the resource conflict, then the user is prompted to create the task failure. After creating the task, if parameters such as task execution time change, you can manually edit the task parameters on the interface.

The task monitoring is responsible for monitoring the running status of tasks, including real-time tasks and historical tasks. Real-time task monitoring can view whether the task has started, where the process has started, whether it is performed smoothly, and other task overview information. To view the task details, you can open the system monitoring software interface to view. Historical task monitoring can view the performance of historical tasks, including the actual start time, actual end time, execution success and other information.

Resource Scheduling

When creating a task, system need to schedule the resources according to the resource allocation information of the task. Resource scheduling is one of the core functions of the system, and it needs to consider the following points: 1) *Resource utilization: this is the core indicator of resource scheduling. In resource allocation and scheduling, tasks need to comprehensively evaluate the use of all resources in the system, adopt appropriate scheduling strategies, and try the best to run the most tasks under the condition of limited resources;* 2) *Flexibility: Different tasks require different resources, and different times will run different tasks, so we need to support a variety of scheduling policies for flexible resource scheduling;* 3) *Real-time: In a large-scale system with complex environment, the number of tasks and resources is huge, it can be dispatched efficiently without affecting the normal operation of tasks.*

The flow of resource scheduling is shown in Figure 7. After creating the task, the resource scheduling module first obtains the resources required by the task, and classifies them according to the resource types such as CPU, GPU, memory, and so on. The second step is to obtain all the current resources and resource occupation in the system from the resource management module. The third step is to pre-select all the required equipment according to the resource demand and resource surplus.

Finally, using the corresponding scheduling strategy according to the actual situation calculate the priority weight and select the best resources. The scheduling strategy can be manually specified by the user or automatically select the optimal policy.

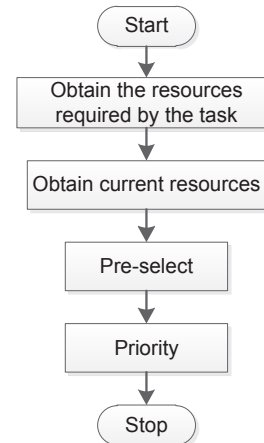


Fig. 7. Resource Scheduling Flowchart.

After deleting task, release the resources for other tasks.

Log Management

The system log mainly records the running status of the program and user's operation behavior, which plays a very important role for the post-hoc analysis of the system. Log records are categorized into three different levels, error, warning and normal. Error log refers to the log that affects the normal operation of the system and must be avoided; the warning log is a log with potential risks and should be avoided as far as possible; the normal log is some user-perceived events generated during the normal operation of the system.

By checking the process content of the program in the log, the software developers can quickly find out where the bugs appear, the defects of the system operation and quickly repair the loopholes. Meanwhile, with the development of big data technology, the log, as an important data source in the program, can improve the level of the system intelligence and monitor the system operation to improve the performance and detect faults through data mining technology.

In this paper, the program is distributed in the various containers of the cluster in the form of application services, so the log information generated by the system is also scattered in the isolated containers, which brings some difficulties to the collection of logs, and the collection of logs from different services becomes a particularly important function. At

the same time, once the container is destroyed, the data in it is gone, and the host where the container is located will dynamically schedule according to the resource load of the system, so it brings challenges to the storage and unified query of logs.

To sum up, the log management in the system mainly includes three functions: log sending, log storage and log query. The log sending function can provide an interface for each application service in the system. Through this interface, the application services running in different containers of different nodes in the cluster can send the logs rather than directly stored in the container. Log management uses redis's message queue mechanism to receive log forwarding and store them uniformly in a database that can be accessed when needed to query all logs produced in the platform. Log query supports a variety of combinations, such as can separately query a certain time period, a certain task, a certain log level log and display, to improve the efficiency of log analysis.

The full flow chart of log management is shown in Figure 8, during the log-sending process, the application service first connects the redis node in the cluster. When log information is generated during the run, application send the log by calling the message sending interface of redis; The log storage function calls the message receiving interface to receive log information sent from different application services, then connect on the local MySQL database, store the received logs in the database in an order; the log query function, according to the query conditions selected by the user, perform the corresponding sql statement to query the logs in the database. Finally, the log is displayed on the interface for user analysis.

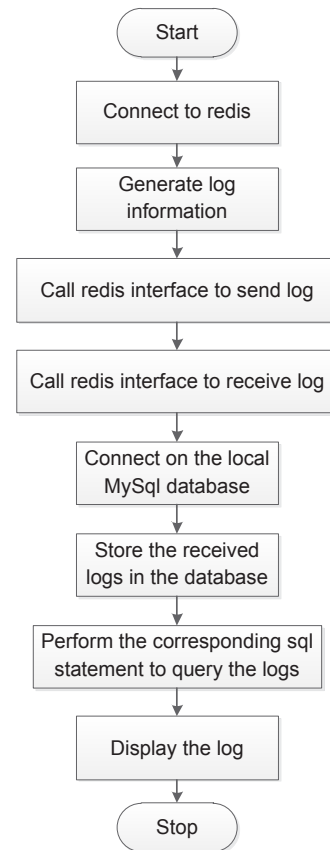


Fig. 8. Log Management Flowchart.

Future Prospects

This paper studies the container cloud technology, divides the space ground TT&C software into different application services and runs in different containers, so as to design a new generation of space ground TT&C software architecture. Using this architecture as a framework, the application services and basic resources required by different tasks are dynamically reorganized. The system has high flexibility, good maintainability, and has the advantages of high availability and high resource utilization. In the future, we can study how to divide application services into smaller microservices to reduce the coupling of software in the system, and a single service with smaller granularity requires less resources, which can effectively reduce scattered resources in the system and improve resource utilization. All the software in this system is running locally. In the future, we can study how to reduce the delay of remote communication, so that different types of software can be deployed in different places according to the needs to realize unmanned stations and ultra-remote TT&C. At the same time, other space application software similar to the TT&C software architecture can be studied to expand the business scope and improve the compatibility of the system.

AI based object recognition for telemetry applications

Simon Hardt, Marc Faber

Safran Data Systems GmbH, Friedrich-Ebert-Str. 75, Bergisch Gladbach - Germany

Simon.Hardt@SafranGroup.com, Marc.Faber@SafranGroup.com

Abstract

In today's Flight Test Instrumentation (FTI), the bandwidth of data to be analyzed is constantly increasing. This is mainly due to the need for more video channels in parallel and higher resolution video signals. This raises the problem of how to transfer all the relevant image information to the ground station during the flight.

A common solution to this problem is to use a reduced bitrate or reduced framerate of the video channels for the telemetry downlink to a ground receiving station. This reduction in signal quality can cause problems during data analysis.

This paper presents an approach that uses **Artificial Intelligence** (AI) based **object recognition** to detect the relevant image content of a video signal. Based on this AI detection, different actions can be performed, e.g. the detected content can be extracted and only this information is streamed in high quality to the ground station.

An embedded video toolbox is provided for the instrumentation engineer to configure the AI system. The instrumentation engineer has the ability to define custom compositions and extraction of video streams.

The defined outputs create video streams that contain only the relevant information of the image content in an extremely **bandwidth saving** manner.

Key words: AI, Telemetry, Bandwidth, On Board Processing

Introduction

In the course of the FTI evolution, a change from pure data recording devices to real data processing devices is taking place. The use of state-of-the-art hardware components opens up completely new possibilities, especially in the area of data analysis, data merging and data pre-processing. The wide range of AI functions implemented in modern CPUs/GPUs enables automated data usage and interpretation, providing instrumentation engineers entirely new tools.

For all on-board data processing approaches, it is elementary that the original task of data acquisition + recording must not be negatively influenced or even disrupted by the processing units. All-data acquisition and recording, especially in the event of anomalies, must continue to be carried out with priority no. 1. A strict separation of the necessary data paths and processing units is therefore inevitable and must be provided for in the appropriate design architecture.

Applications based on video capture are a good approach to implementing the diverse possibilities of on-board processing, be it to save telemetry bandwidth, speed up post processing or to meet security requirements.

In addition, FTI device control and A/C structure analysis can also be reconsidered when using AI. This paper shows various possibilities on these topics. The technical possibilities in the area of today's image and audio interpretation and compilation are immense especially when conservative data optimizations are merged with AI capabilities.

Efficient usage of TM video bandwidth

The telemetry data transmitted from the air to the ground must be carefully selected due to bandwidth limitations. In today's applications, video data is recorded in high quality on board, while parallel generated video streams are transmitted to the ground at a lower bit rate. The processors used in data recorders allow even

more possibilities to utilize the available telemetry bandwidth more efficiently. Video signals from different sources can be combined and unnecessary image content can be overlaid with necessary information (advanced picture in picture). This allows the instrumentation engineer to easily compile the best and most effective video stream for his application.

Another possibility to use the TM bandwidth effectively is the time-shifted transmission of video signals. In this way, various data can be transmitted in real time and other video data recorded in parallel can be retransmitted in a subsequent time slot.

Furthermore, the introduction of an AI in the on-board recorder allows also objects to be identified and only these objects to be embedded in the telemetry data stream. In this way, non-essential image content is removed automatically, thus saving transmission bandwidth.

As another approach to data reduction, it is also possible to recognize text + voice content via AI and then transmit it in native text form in a bandwidth-efficient manner.

Picture in Picture

The first step in improving the telemetry bandwidth for the application in video data transmission is to use only the areas of video that are really needed. In most applications, the user is transmitting video areas that are not needed by the operator on the ground. Therefore, these areas in the video data streams can be optimized to reduce the overall bandwidth. The first step here is to be able to combine different input video data streams into one output video data stream. To do this, we implemented a picture-in-picture mode on our on-board processing platform. As shown in Figure 1, it is possible to just combine 4 different input video streams into one output video stream. This saves bandwidth, because all input video data streams are rescaled to a lower resolution. However, this is not a good solution in all cases. Therefore, a better approach for a picture-in-picture mode is to be able to select different ROIs (Region of Interest) in all our input video streams and be able to map these ROIs to one output video data stream what we call Advanced Picture in Picture Mode (see Figure 2). By reducing four 1920x1080 video streams to just one 1920x1080 video stream, the module can save up to 75% of the bandwidth used to stream all four video streams.

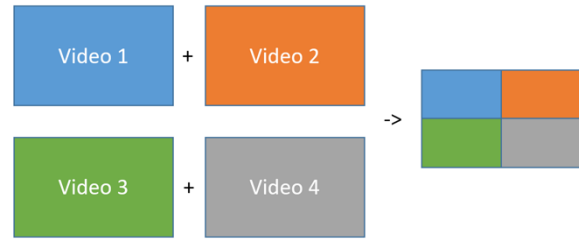


Fig. 1. Picture in Picture Mode

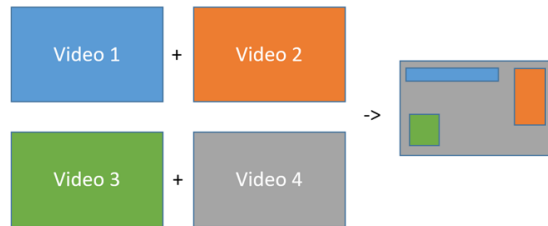


Fig. 2. Advanced Picture in Picture Mode

Video manipulations for security reasons

In some applications the telemetry downlink should not include all areas of the video. For example, for security reasons, there may be some areas in a video data stream that contain sensitive information. One approach is to gray out certain areas as shown in Figure 3. As with the ROI, the user can select these areas in the input video data streams and these areas will not be visible in the output video data stream and will have a gray out area of a user selected color.

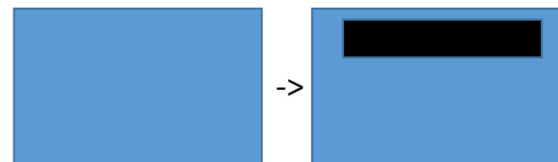


Fig. 3. Grayout Area for Security Reasons

Artificial Intelligence (AI) - Overview

After these initial “basic” approaches, additional Artificial Intelligence (AI) algorithms can be used to further improve the bandwidth utilization and speed up post-processing time.

The following chapter gives an overview of different AI algorithms and their possible use cases. In particular, the work of post-processing the data can thus already be implemented during the test flight. To save TM bandwidth, these AI algorithms can also be used to transmit only the results of these algorithms via telemetry instead of transmitting all the raw data during a test flight.

Basically, all AI algorithms work on the same principle. Each of them has a neural network in the background that actually does the work. Depending on the size of the neural network and

the training, the results are better. Each of these neural networks consists of an input layer, “N” hidden layers, and an output layer (see Figure 4). During the training of the neural network, the weights and values in the hidden layer were trained to produce the right result in the output layer. Training the neural network is the real work for an AI algorithm. To train it, means that it needs a large training data set and the results for each of the training data to automate the training process. The actual production of the result is often called “inference”, meaning that the trained model is used to predict outcomes from new observations. Because in an actual use case of the neural network, the network is not trained with the actual outcome of a real example, it has only been trained with a training data set. For the on-board processing application, we use an NVidia module, which has the advantage that NVidia has been in the AI field for a long time and is used in a lot of areas [2]. It also has the advantage that it comes with a lot of libraries to set up, train and use the neural network, e.g. the Tensor RT framework gives great advantages when it comes to an efficient and easy way to train and do the setup for a new use case. In the following chapter we will describe some use cases that are possible with the used NVidia module and that are feasible for some first real-world examples and tests.

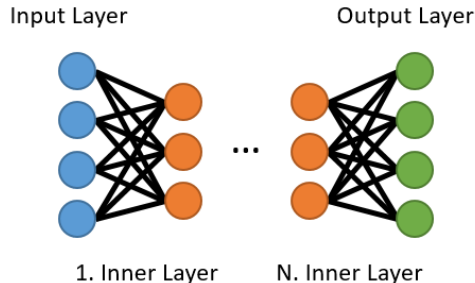


Fig. 4. Structure of Neuronal Network

AI – Object recognition & Extraction of relevant content

If it is necessary to track an object during a flight, an object recognition algorithm is a good solution. In this case, a neural network can be trained on the object to be detected. These trained objects can then be tracked (see Figure 5) during the flight with the same network. During test flights, only a portion of the video stream containing the object can be downlinked to the ground station. This saves a lot of bandwidth because the whole video stream does not have to be transported and the operator on the ground does not have to track the object himself. Instead, they receive a truncated video stream that contains only the object they are tracking. In many video streams, these tracked objects are

in a small part of the video. For example, if only a quarter of a video stream needs to be transmitted, only a quarter of the required telemetry bandwidth is needed.

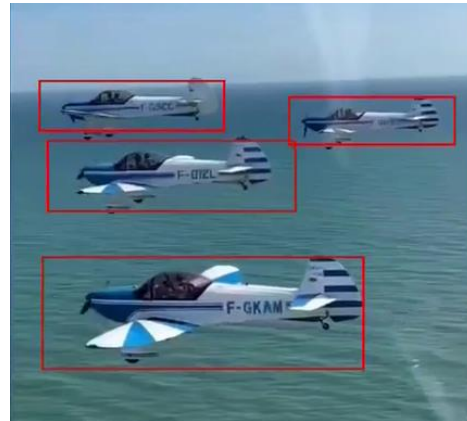


Fig. 5. Tracking of Airplanes

AI – Intelligent cockpit digitalization

In modern aircraft, almost any information that is displayed on a cockpit display is also available on some kind of data bus. But in situations where this information is not available, or for some reason it is not allowed to record the data bus, intelligent display recognition can be used. In this case, the information from the display is extracted into a digital form, e.g. the value from a gauge can be extracted or the changed color of a light can be detected [1]. This detected digital information can be sent to the ground, stored on the recording or an overlay of this digitized information can be created on a video stream. This helps the operator on the ground to get the requested information w/o any additional effort.

This cockpit digitization is focused on a specific set of gauges - the 6-pack (see Figure 6). This includes six gauges that are present in almost every aircraft and provide the pilot with critical information about the aircraft. To process multiple gauges simultaneously, it is necessary to process them in parallel and use the same neural network. In this use case, YOLOv8 from Ultralytics provides a good starting point for a neural network specialized for object detection.

In order to automatically retrieve the value of a gauge, it is necessary to find key features that facilitate detection. Each gauge has its own AI that is trained to recognize the key features of that gauge. Once the position of the needle or virtual plane is known, this information is converted to an angle and compared to the reference measurement. The result is a value for each sensor which can be transmitted or recorded in any necessary Chapter 10 Format.



Fig. 6. Cockpit Digitalization (markings in green).
Heading: Left/Descent, Turn: Right, Airspeed: 50
Knots, Heading: 6 Degree, Altitude: 1544 Knots,
Vertical speed: -1 fpm

AI – Control via voice

In today's world, many things can be controlled by voice. For example, when you walk into a room, you can tell your smart speaker what music to play or how you want the lights in your room to be. The same can be done during a test flight. When the voice is recorded, the same information can be used to control actions on the recorder. During a test flight campaign, the recording process can be started or stopped as needed. Or, if the pilot says some keywords, this can be transmitted as a specific event to the ground station via the telemetry downlink. This lets the operator know that a special scenario is occurring without having to process all the available data directly. Some more advanced actions can also be used to trigger some events or some other internal action. Like changing the recorder's save set or triggering any post-processing algorithm directly while the flight is still in progress.

AI – On the fly data analysis with event trigger

Another approach on the onboard processing module is to trigger events on online data analysis. A typical use case for this is load monitoring, but it could also be used for any other data. In many test flight campaigns, load monitoring in the post-processing phase is a part that can take a lot of time. The idea here is to do this post-processing online during the flight phase and to monitor this load. If a peak is too large or too long, an event can be triggered. This means that the operator on the ground gets this information directly, without any post-processing. In this case, he can react directly to the occurrence of this event. This saves a lot of time in the post-processing phase, and in some cases the post-processing phase can be skipped for this type of event. The algorithm used in this case can vary from a simple Peak Valley

algorithm to a more advanced online structure analysis. [4]

Furthermore, an AI can also help to identify other anomalies in the recorded data during the test flight and mark the corresponding locations in the recordings with events. Intelligent event detection, insertion and logging is thus possible. During the download, these data fragments can be downloaded with priority and in a short time to quickly gain initial insights.

AI – Gesture Detection

Another approach is to use gesture recognition. Currently, most planes or aircraft use some kind of button handling to detect some action of the pilot. For example, to start a recording or trigger an event. But if the cockpit has a camera installed, gesture recognition can be used instead [3]. Then the pilot can make gestures with his hands, and the recorder can react based on the gesture. This means that an event can be triggered, a recording can be started/stopped, or any other operation is possible. This approach also has the advantage of requiring less wiring and less testing of wiring, since some of the contact remote inputs can be saved or used for additional functions.

AI – A/C structure analysis during flight

Video applications with high speed cameras also allow vibration and oscillation analysis which can be performed directly from the on-board equipment. This is a non-contact method of performing a vibration test on the aircraft (A/C) structure. The advantage here is that no traditional sensors need to be attached to the structure to be tested. Even areas that are difficult to access can be analyzed efficiently with this methodology.

A high-speed camera is used to capture a video of a previously marked structural area. Using an algorithm in the vibration analysis software, the vibration motion is visualized and then the results are analyzed. The AI approach helps to intelligently detect changes in the color gradient caused by external picture changes such as light and shadow. These induced changes in the video must be compensated for, so that the actual measurement results are not negatively affected.

AI – Speech to text conversion

Almost everyone has used some kind of voice-to-text conversion in their daily life. You can talk to your smartphone, and the smartphone translates your voice directly into a text that is sent to someone. The next step now is to do the same thing in an airplane. The pilot's voice is usually recorded during test flights. This means that this information can also be used in the on-

board processing module. Here it is possible to convert the pilot's voice into native text messages and send this text to the ground station with very low bandwidth requirements. In some situations, the pilot's voice is recorded in a noisy environment, so in this case text conversion could help the operator to better understand the pilot.

AI – Conclusion

New processing capacities in on-board data recorders allow new possibilities for effective data reduction and data interpretation, and this already during the test flight and without disturbing the all data recording running in parallel.

The available computing power can be used to make the best use of the available telemetry bandwidth and to reduce the necessary post-processing time through the use of AI.

Further applications are manifold and range from active object and gesture recognition to security applications and possible A/C structure analysis using high-speed video evaluation.

The way is paved to apply these approaches in the FTI area and thus provide the responsible instrumentation engineers with new powerful tools and possibilities.

References

- [1] B. Howells, J. Charles and R. Cipolla, "Real-time analogue gauge transcription on mobile phone" in Mobile AI workshop in conjunction with CVPR, 2021
- [2] Stephen Cass, "Nvidia makes it easy to embed AI: The Jetson nano packs a lot of machine-learning power into DIY projects" in IEEE Spectrum (Volume: 57, Issue: 7, July 2020)
- [3] Heng Yang, Marco Pavone, "Object Pose Estimation with Statistical Guarantees: Conformal Keypoint Detection and Geometric Uncertainty Propagation" in IEEE/CVF Conference on Computer Vision and Pattern Recognition (CVPR) 2023
- [4] Ghislain Guerrero, Valentin Belaud, Remy Pelluault, Quentin "How to reconcile COTS components and tailored future-proof Data Acquisition System in Flight TestInstrumentation?" in International Telemetry Conference 2023

Introduction of Smart Hi-Speed Airborne Camera with Embedded Real-Time Tracking Algorithm for Store Separation Flight Tests

Rodrigo C. de Paulo^{1,2}, Nelson P. O. Leite¹, Lucas B. R. Sousa¹, Denis S. Loubach²

¹ Instituto de Pesquisas e Ensaios em Voo (IPEV), Pça Mal. Eduardo Gomes nº 50, Vila das Acácias, São José dos Campos, SP, 12.228-901 - Brazil,

² Instituto Tecnológico de Aeronáutica (ITA), Pça Mal. Eduardo Gomes nº 50, Vila das Acácias, São José dos Campos, SP, 12.228-900 - Brazil

rodrigorc@fab.mil.br, nelsonnpol@fab.mil.br, lucaslbrs@fab.mil.br, dloubach@ita.br

Abstract:

For efficiency and flight safety improvement in Store Separation Flight Testing (SSFT) IPEV's R&D efforts over the past 10 years were focused on the development and validation of an Airborne Real-Time Optical Tracking System (SisTrO), to provide the ejected store Time-Space Position Information (TSPI) in real-time and expressed in 6 Degrees-of-Freedom (6DoF) parameters (i.e., 3-D Linear and Angular Displacement). The current SisTrO architecture employs Hi-Speed airborne cameras connected to a tracking processor through the CoaXPress (CXP-12) interface. The recent introduction of airborne hi-speed cameras where the users can integrate their own application into the camera FPGA, opens new frontiers where the tracking algorithm is embedded into the camera processing unit, making possible the development of "Hi-Speed airborne smart cameras" to be used in flight testing, such as SSFT campaigns to provide a real-time efficient solution in a smaller form factor. Furthermore, using Perspective-n-Point techniques opens new frontiers for developing an advanced algorithm to compute the 3D 6DoF trajectory parameters with sufficient accuracy from a single camera and therefore to improve SisTrO reliability and in a smaller form factor. Given this context, the present paper evaluates the implementation of different tracking algorithms in CPU/GPU used in SisTrO I/II with the new small-factor FPGA hardware architecture. The evaluation parameters are real-time performance (i.e., execution time), object tracking effectiveness, and operational environment (flight tests). Results show that while the SisTrO CPU/GPU architecture has better computation performance, the FPGA can execute the tracking algorithms fulfilling the real-time constraints with reduced form factor and weight.

Keywords: Store Separation Flight Test, Photogrammetry, Object Tracking, Hardware Architecture.

Introduction

Store Separation Flight Tests (SSFT) are fundamental to guarantee a safe separation condition of the load over its entire operational envelope. Since there is a real chance of collision of the store with the aircraft due to unexpected or unknown aerodynamic coupling, and wing servo-aeroelasticity flexion in a given Store Separation Flight Test it should be verified if the store has some tendency to collide with the aircraft.

To perform this task the Instituto de Pesquisas e Ensaios em Voo (IPEV – "Flight Tests and Research Institute") (IPEV) has used high-speed camera image frames to evaluate and compute the trajectory of the store after launching.

In general, photogrammetry techniques [01] are often used to reconstruct the store trajectory in time-consuming post-mission operations, which may take hours or even days. To reduce flight hours and flight test campaigns, costs, reworking, and re-flights and to allow 2 or more launches in the same flight, IPEV has been developing and validating an Airborne Real-Time Optical Tracking System (SisTrO) to provide the ejected store Time-Space Position Information (TSPI) in real-time and expressed in 6 Degrees-of-Freedom (6DoF) parameters.

After two successful campaigns, with two different approaches, one as an improvement of the other, IPEV can now perform real-time object tracking with two different system architectures embedded in a photogrammetric POD. However,

with the evolution of hardware architecture and systems as well as sensors, nowadays it is possible to find COTS high-speed cameras that allow users to access the camera processing unit, in general, by giving access to its reconfigurable hardware (e.g., FPGA), which permits the users to integrate their own application on-site to run into the camera.

This work uses such advances in hardware architectures and sensors to develop a novel real-time object tracking system in small-factor (centimeters units) by employing the expertise and knowledge gathered in the previous campaigns by using a novel high-speed reconfigurable camera, which not only allows real-time processing but also reduces the equipment count and volume required to perform this task. In summary, this work presents the design of an object tracking system in FPGA and compares it with the previous developments that used a different hardware architecture.

SisTrO I

IPEV has developed and validated two versions of the Optical Tracking Systems (SisTrO) described as follows.

The initially pursued architecture was derived from an application presented in ETTC 2013 that used an iPhone 4S (Figure 01) to track and compute aircraft trajectory in the Air Data System calibration Flight test campaign by using the Tower-Fly-By method [2]. In such application, the deep integration between the video camera and processor resulted in satisfactory real-time performance where the time to compute the aircraft altitude and speed of a 720p image frame was $599\text{ms} \pm 19\text{ms}$ @ 1σ , exceeding the camera connected to a processor traditional architecture by using an Ethernet connection.



Fig. 01 - Screen of iPhone4S Snapshot.

The first development was the SisTrO I, which was successfully tested in a flight test campaign in 2019 and performed object tracking in real time. The initial objective was to use an airborne

hi-speed (i.e., up to 400 fps) hi-resolution (i.e., 1080p) camera with provisions for integrating a user application into the camera processing unit. However, at that time, finding a supplier with such a camera was not possible, mostly due to Intellectual Property (IP) issues. Therefore, the solution was to use a processing unit connected to a camera. However, the asynchronous Gigabit Ethernet connection introduces significant delays in hi-rate (i.e., 19.91Gb/s) data transfers of image frames, resulting in unsatisfactory performance for real-time applications.

The introduction of the CoaXPress (CXP-6) protocol [3] that supports up to 25 GB/s sustained (i.e., 100% duty cycle) data transfers solved the issue of transferring real-time live image frames from the high-speed camera to an image processor. After a long search, it was possible to build such processor with a CXP-6 interface fully compliant with MIL-STD-810G for airborne applications.

Thus, it was possible to define SisTrO I architecture, which was composed of (Figure 02):

1. Two high-speed cameras, each one connected to an image processor, which detects and tracks the store Reference Marks (RM); and
2. A Trajectory Processor, that computes the 3D trajectory from the detected 2D coordinates of the tracked RM; and
3. An IRIG-B GNSS time base and PtP v.2. grandmaster.

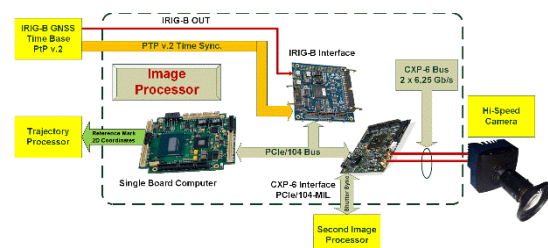


Fig. 02 – SisTrO I Architecture

SisTrO I uses the CAMSHIFT technique to perform the 2D tracking of RM. It is initialized with the positions of the RM in the first frame and searches in sequential frames the corners in a local window.

Although SisTrO I RM 2D measured tracking performance (i.e., 75,13%) provides enough satisfactory information for computing the 3D trajectory of the ejected store in all flight test points, it was observed that once the tracking

algorithm can't detect a given RM, such RM is permanently lost for all remaining image frames.

SisTrO II

SisTrO II development was aimed to improve SisTrO I tracking and real-time performance and also to encompass 3D solution redundancy. In this case, the image processor executes the 2D RM detection & tracking and the 6DoF store trajectory estimation by using a RANSAC Perspective-N-Point algorithm.

To improve 2D tracking the enhanced algorithm uses an ArUco Markers [4] for image segmentation (i.e., for area selection where each RM is most possible located) and neural network techniques. Such solution made it possible to reacquire a given RM tracking that was not identified in previous image frames due to image blur or low/excessive light and as a consequence improve algorithm 2D performance.

After image segmentation, the algorithm performs sub-pixel corner detection for RM tracking. A Convolutional neural network (CNN) was designed and trained to perform the marker identification obtaining successful results as detailed in [5], however, the flight test campaign was executed with the classical computer vision algorithm OpenCV cornersubpixel.

Corner Detectors

There are several ways to identify an object. In classical computer vision, it is common to use some features like edges, corners, and contours. More specifically, corners have proved to be a good feature to track as demonstrated in the Harris corner detector [6], the Shi-Tomasi corner detector [7], and the Förstner Operator [8]. This paper uses the Harris corner detector to find the RM location that was placed on the store surface, since the criterion to find a corner uses less operations than, for example, the Shi-Tomasi, which has to compute square roots [9].

As described in [9], the simplest possible matching criterion for two image patches is the weighted summed square difference, as described in (1):

$$E_{WSSD}(u) = \sum_{i=1}^n w(x_i) [I_1(x_i + u) - I_0(x_i)]^2 \quad (1)$$

Where:

- I_1 and I_0 are two images;
- $u = (u, v)$ is the displacement vector;
- $w(x)$ is a spatially varying weighting function; and
- $\sum_{i=1}^n$ is over all pixels in the segment.

Considering small variations in the same image and using a Taylor series expansion of the image function, we have:

$$I_0(x_i + \Delta u) \approx I_0(x_i) + \nabla I_0(x_i) \cdot \Delta u \quad (2)$$

Now it is possible to approximate the weighted summed square difference as:

$$E_{AC}(\Delta u) \approx \sum_{i=1}^n w(x_i) [I_0(x_i) + \nabla I_0(x_i) \cdot \Delta u - I_0(x_i)]^2 \quad (3)$$

$$= \sum_{i=1}^n w(x_i) [\nabla I_0(x_i) \cdot \Delta u]^2 \quad (4)$$

$$= \Delta u^T A \Delta u \quad (5)$$

Where:

- $\nabla I_0(x_i)$ is the image gradient at x_i then:

$$\nabla I_0(x_i) = \left(\frac{\partial I_0}{\partial x}, \frac{\partial I_0}{\partial y} \right) (x_i) \quad (6)$$

And the matrix A:

$$A = w \begin{bmatrix} I_x^2 & I_x I_y \\ I_x I_y & I_y^2 \end{bmatrix} \quad (7)$$

Where the weighted summations were replaced by discrete convolutions with the weighting kernel w .

So, the Harris criterion [6] to differentiate interesting key points and localize corners is described in eq (8) with α between [0.04,0.06] and $R \gg 0$.

$$R = \det(A) - \alpha \text{trace}(A)^2 \quad (8)$$

Hardware Architecture

Different kinds of hardware architecture operate in different ways. The work [10] made an overview of the cyber-physical system's architecture concerning machine learning and described the main difference between them.

Up until now, the IPEV has been using the Central Processing Unit (CPU) architecture, as shown in the previous section, which follows the von Neumann or Harvard architecture and uses superscalar pipeline and multi-threading as forms of parallelism [10].

On the other hand, a Field-Programmable gate array (FPGA) consists of an array of programming logic blocks with programming routes between the blocks, which allows a configuration after manufacturing by a designer. The work [10] states that an advantage of an FPGA is the flexibility of refine and replace implementations in the target, and has presented performance over commercial off-the-shelf architectures.

The architectures that mix more than one hardware architecture are known as heterogeneous architecture. An example of this architecture is the System-on-chip that encapsulates a CPU with reconfigurable hardware as an FPGA.

High-Speed Camera

This work uses the high-speed camera EoSens® Creation 2.0CXP2 developed by Mikrotron SVS-Vistek with the capacity of recording 2,247 fps in a 1920 X 1080 pixel resolution (1080p) as a platform of tests. It is a monochrome camera with the CoaXPress high-speed interface which allows real-time sustained transfer rates of up to 12,5 Gb/s.

Such a smart camera provides users access to its internal FPGA (i.e., Kintex UltraScale KU053-2, 2G DDR4).

Besides that, the camera is enclosed in a compact and solid full metal housing robust enough to allow its use in an airborne environment with dimensions of 80 x 80 x 84.6 mm and a C-mount mechanical interface for lens installation.

Reference Marker Tracking Process

The RM tracking (Figure 3) process is composed of 3 steps as follows:

1. Pre-flight operations (i.e., Test setup);
2. Image segmentation to dynamically estimate where each RM is possibly located; and
3. Corner detection.

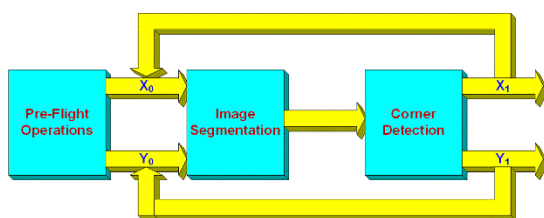


Fig. 03 – 2D Marker Tracking Process

For test setup, it should be executed the following steps:

1. Initially it should be installed several RM's and the ArUco on the store surface and it should be measured their 3D coordinates expressed in the aircraft coordinate reference system with a Total Station;
2. Then it should be computed the camera's intrinsic and extrinsic parameters by using a Stereo Camera Calibration Algorithm [11]. For this step, it should be noticed that the

photogrammetric POD translucent window glass also distorts the image. Therefore, to provide better and more accurate results [12], this calibration should be executed with the cameras installed into the POD. Such calibration process:

- a. Computes the camera intrinsic parameters;
 - b. Then using as reference, the pinhole camera model, it estimates the optical distortion radial and tangential error minimization compensation parameters; and
 - c. It combines the results of all cameras to optimize the solution and to compute the translation and rotation matrices between the master camera and all slaves (i.e., one or more).
3. Finally, it should be determined the translation and rotation matrices between the master camera and the aircraft reference systems.

Once the calibration is performed the position of the RM will be used for tracker initialization, for this reason, it is not possible to move the cameras or the store anymore.

Once the tracking system is initiated the next step is to segment the image framed to define a fixed searching window for corner detection centered in the previously known or initial RM 2D position.

The tracker will search in the subsequent frame for the new position of the RM. Since a high-speed camera is used the new position of the RM will be close to the previous one, which simplifies the tracking process.

The Harris Corner detection algorithm will be used to locate the RM 2D position in the next frame (Figure 4).

The corner detection section initially computes the gradient in x and y of the segmented image and then builds the A matrix as depicted in eq. (7).

To execute as many operations as possible in parallel, the steps in the same stage will be computed in parallel in the FPGA.

This technique can optimize and reduce the execution time in this reconfigurable architecture as compared to a traditional CPU.

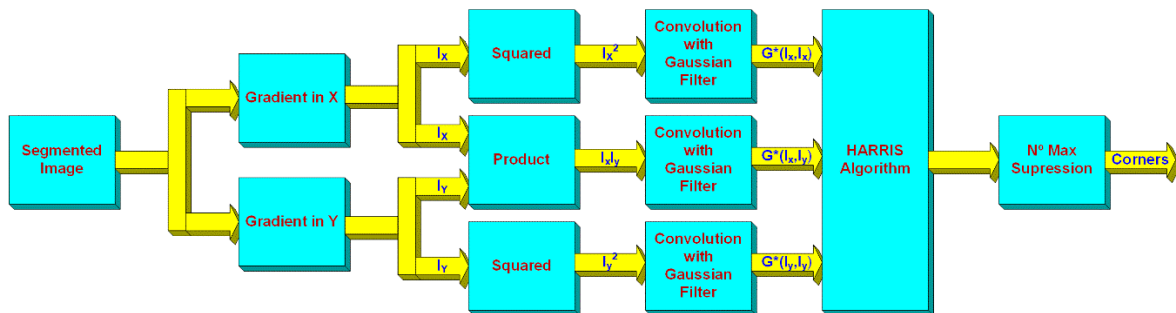


Fig.4. Harris Corner Detection as in [14]

After the computation of the Harris quantity, a non-maximum suppression operation is required to avoid that corner concentration in areas with high contrast.

The new RM position will be used to define the searching window position (i.e., Image segmentation area) updating the tracking.

It is worth mentioning that some works use a prediction step, like a Kalman filter, however, for this application, and since a high-speed camera is used, this step is avoided to reduce the computational load.

Discussion

As mentioned above the two previous flight test campaigns (i.e., SisTrO I and SisTrO II) were satisfactorily executed in conformance with the requirements presented in the Advisory Group for Aerospace Research & Development document AGARD-AG-300-Vol.5 [13].

The errors in the x, y and z axis, measured in the SisTrO I flight test campaign were respectively $-0.16 \text{ mm} \pm 0.97 \text{ mm}@1\sigma$; $-0.11 \text{ mm} \pm 1.42 \text{ mm}@1\sigma$; and $-0.26 \text{ mm} \pm 1.21 \text{ mm}@1\sigma$.

Besides the fact that SISTRO II fulfilled the AGARD-AG-300-Vol.5, requirements it also improves SisTrO I, in some aspects such as faster execution time, and 3D trajectory solution from a single camera for introducing redundancy.

However, a point that has to be observed is that SisTrO I uses an i7 Quad Core @2,4GHz, 8GB DRAM @1600 MHz processor to perform the real-time processing while this present paper designs a solution for an embedded FPGA Kintex UltraScale KU053-2, 2G DDR4 with limited capability as compared to the first one.

Therefore, the CPU architecture used in the SisTrO I achieves better performance than the FPGA architecture.

For this reason, all forms of parallelism and operations optimization should be applied.

Furthermore, the workload to execute the object tracking algorithm and the amount of data that high-speed video produces are the main issues for this work.

Therefore, using FPGA parallelism and Harris corner detector simplifies the tracking processing.

For example, the work in [14] developed a Harris Corner detection algorithm in FPGA aiming for processing high-speed data. The results of the work are presented in Table 1.

Tab. 1: Resource comparison in [14].

Implementation	[14]	[15]	[16]
LUTs	8035	9849	6267
FF	8404	4335	-
BRAM(18K)	17	5	11
BRAM(36K)	0	64	0
DSP	0	0	0
Frame/s	626	144	295

However, the difference between this paper and the referenced one [14] is that in our work the background is considered to be fixed and it was possible to engineer the store with the RM's that simplifies the knowledge of tracking pattern, while theirs tracks natural targets.

In addition, the exact position of the RM's can be accurately measured, and this particular feature speeds the processing algorithm and benefits the real-time tracking performance.

The FPGA Kintex UltraScale KU053-2 contains more hardware resources than was necessary to perform the referenced work [14] (Table 2).

In addition, the camera and its embedded FPGA unit are designed to satisfactorily operate in an airborne environment, such as the camera POD.

Tab. 2: Hardware resource of FPGA Kintex UltraScale KU053-2.

Elements	KU053-2	70% availability
LUTs	20328	14229
FF	406256	284379
BRAM(18K)	1080	756
BRAM(36K)	540	378
DSP	1700	1190

Conclusion

This work presented a marker tracking design to execute real-time target tracking in an FPGA inside a small-factor high-speed camera, and it was compared with the two previous flight test campaigns (SisTrO I/SisTrO II) that used a regular embedded computer with a CPU.

The results in the CPU architectures in SisTrO I and SisTrO II showed small errors and the fulfillment of the AGARD-AG-300-Vol.5. Since they have more computational capacity they achieve better performance compared with the reconfigurable architecture that has limited computational capacity and memory.

However, it was seen that an FPGA, with some parallelism and a reduced operations algorithm (e.g. Harris corner detector), can process the object tracking in high-speed video accomplishing the flight test form factor and environmental requirements.

Suggested future works are to execute real flight tests to obtain and compare the results of the RM tracking design, find other algorithms to perform the corner detection or the object tracking, verify the performance of a prediction step like a Kalman filter, use a deep learning algorithm and an FPGA accelerator to perform the inference and perform the 3D trajectory estimation from a single high-speed camera.

Acknowledgment

This work is supported by the funding agency FINEP under the FAEV project (Ref.: 01.22.0545.00).

References

- [1] Forsman, Ed & Getson, Scott & Schug, David & Urtz, Greg. (2008). IMPROVED ANALYSIS TECHNIQUES FOR MORE EFFICIENT WEAPON SEPARATION TESTING. DOI:10.13140/RG.2.1.4539.0240
- [2] Forni, A. L. C., "Manual de Aerodinâmica, Documento nº 20-R-AH", Chapter 3, Divisão de Ensaios em Voo, 1995.
- [3] JIAA; JIAA CXP-001-2015 CoaXPress Standard, The Standardization Committee CoaXPress Working Group, Japan Industrial Imaging Association (JIAA), 2015, Available at: http://jiaa.org/wp-content/themes/jiaa/pdf/standard_dl/coaxpress/CXP-001-2015.pdf, accessed on August, 20th, 2018.
- [4] Romero-Ramirez, Francisco J.; Muñoz-Salinas, Rafael; Medina-Carnicer, Rafael. "ArUco: a minimal library for Augmented Reality applications based on OpenCV".
- [5] Melo, Gabriel Adriano, Marcos Máximo, and Paulo André Castro. "High Speed Marker Tracking for Flight Tests." IEEE Latin America Transactions 20.10 (2022): 2237-2243. DOI: 10.1109/TLA.2022.9885171
- [6] Harris, Christopher G. and M. J. Stephens. "A Combined Corner and Edge Detector." Alvey Vision Conference (1988). DOI:10.5244/C.2.23
- [7] Shi, Jianbo. "Good features to track." 1994 Proceedings of IEEE conference on computer vision and pattern recognition. IEEE, 1994. DOI: 10.1109/CVPR.1994.323794
- [8] Förstner, Wolfgang, and Eberhard Gülch. "A fast operator for detection and precise location of distinct points, corners and centres of circular features." Proc. ISPRS intercommission conference on fast processing of photogrammetric data. Vol. 6. 1987.
- [9] Szeliski, Richard. Computer vision: algorithms and applications. Springer Nature, 2022. DOI:10.1007/978-3-030-34372-9
- [10] Loubach, Denis S. "An Overview of Cyber-Physical Systems' Hardware Architecture Concerning Machine Learning." 2021 IEEE/AIAA 40th Digital Avionics Systems Conference (DASC). IEEE, 2021. DOI: 10.1109/DASC52595.2021.9594429
- [11] ZHANG, Z.; "Flexible Camera Calibration by Viewing a Plane from Unknown Orientation". In Proceedings of the 7th IEEE Conference of Computer Vision, pp 666-673 vol. 1, DOI: 10.1109/ICCV.1999.791289

- [12] de Vasconcelos, Luiz Eduardo Guarino, et al. "Store separation: Photogrammetric solution for the static ejection test." *International Journal of Aerospace Engineering* 2019 (2019). DOI: 10.1155/2019/6708450
- [13] Arnold, R. J., and C. S. Epstein. "Agard flight test techniques series. volume 5. store separation flight testing." *Agard Flight Test Techniques* (1986).
- [14] H. Zhou et al., "A High-Speed Parallel FPGA Implementation of Harris Corner Detection," 2020 IEEE International Conference on Integrated Circuits, Technologies and Applications (ICTA), Nanjing, China, 2020, pp. 71-72, doi: 10.1109/ICTA50426.2020.9332111.
- [15] Chao, Tak Lon and Kin Hong Wong. "An efficient FPGA implementation of the Harris corner feature detector." 2015 14th IAPR International Conference on Machine Vision Applications (MVA) (2015): 89-93. DOI: 10.1109/MVA.2015.7153140
- [16] A. Ben Amara, E. Pissaloux, R. Grisel and M. Atri, "Zynq FPGA Based Memory Efficient and Real-Time Harris Corner Detection Algorithm Implementation," 2018 15th International Multi-Conference on Systems, Signals & Devices (SSD), Yasmine Hammamet, Tunisia, 2018, pp. 852-857, doi: 10.1109/SSD.2018.8570491.

Improving Rotorcraft Flight Tests Safety and Efficiency with Real-Time Wind Mapping

EKET Gabriel¹, SCHMID Sebastian², ROCCHI Lilian³, URLI Renaud²

¹ Airbus Operations SAS, France,

² Airbus Helicopters Deutschland GmbH, Germany,

³ Airbus Helicopters SAS, France,

gabriel.eket@airbus.com, sebastian.schimd3@airbus.com, lilian.rocchi@airbus.com, renaud.urli@airbus.com

Abstract

Helicopter testing plays a critical role in ensuring their operational readiness, safety, and performance optimization. At Airbus Helicopters Flight Test Center in Donauwörth, procedures are conducted to validate helicopter performance and systems, involving maneuvers such as power reduction, recovery, and low altitude landing procedures. Traditionally, weather data for these tests was obtained from ground and tower measurements. However, this approach falls short in providing precise wind data within the helicopter's vicinity.

This paper presents efforts aimed at enhancing safety, efficiency, and performance evaluation by providing real time wind data at various altitudes proximate to helicopters during testing operations. To achieve this, the study explores different approaches, with particular focus on a commercially available ground wind LIDAR system.

The system demonstrated promising results in providing wind speed data comparable to traditional cup anemometers, although limitations in wind measurement were noted.

The findings underscore the potential of wind LIDAR to enhance the understanding of test conditions, mitigate risks associated with maneuvers, and facilitate post-test analysis for rotorcraft testing. Nevertheless, optimization of the LIDAR is necessary to improve reliability and further integration tests are needed to validate the system's compatibility for real time use with current Flight Test Instrumentation.

Key words: Rotorcraft, Testing, Instrumentation, Wind, LIDAR.

I. Introduction

Helicopter testing stands as a cornerstone in ensuring the operational readiness, safety, and optimal performance of rotorcraft. At the Airbus Helicopters Flight Test Center in Donauwörth, procedures are in place to validate various aspects of helicopter performance and systems. These procedures include maneuvers, such as power reduction, recovery, and low-altitude landing procedures, typically conducted between 10 to 60 meters above ground level. However, relying solely on ground and tower weather measurements fails to provide accurate wind data within the vicinity of the helicopter.

This challenge was addressed by proposing a solution to enhance safety, efficiency, and performance evaluation through real-time wind data mapping. Furthermore, the solution enables wind data measurement at altitudes of interest while being operable in controlled

airspace, as testing operations often extend beyond Airbus facilities

To achieve this objective, various solutions have been explored, with a focus on leveraging a commercially available ground wind LIDAR system.

The paper will outline the methodology employed to meet these objectives, discuss encountered challenges, and present achieved results. Additionally, it will explore the potential benefits and implications of this solution while offering insights into future directions for further refinement and implementation.

II. Solutions Overview

To identify potential solutions, a review of existing weather measurement technologies was conducted. This research covered both emerging solutions and established methods available on the market. The aim was to identify concepts that could feasibly address the challenge of precise weather data collection at low altitudes.

Building upon this preliminary research, multiple concepts were generated. Each concept was evaluated against a set of criteria, including accuracy, cost-effectiveness, safety, regulatory compliance, and compatibility with controlled airspace.

The following subsections presents the three main concepts that emerged from the preliminary research, highlighting their potential benefits and drawbacks.

A. Tethered aerostat

This concept employs a helium-filled balloon anchored to the ground to elevate sensor units to the desired altitudes for weather data collection. Stability is ensured by aramid cables, minimizing movement for accurate measurements. Sensor units, linked to the balloon and ground via tensioned aramid cables, consist of off-the-shelf weather sensors and wireless modules transmitting data to a base station. The base station communicates data to both the test helicopter and ground teams.

Upfront cost of such a solution is expected to be in the 8,000€ and 18,000€ price range with a maintenance cost mostly coming from the calibration and verification of sensors.

Advantages:

- Extended operational durations, lasting up to two days without frequent maintenance.
- Ability to withstand high wind speeds, thanks to the aerostat design and aramid cables.
- Compact transmitter units within the sensor modules enhance autonomy and reduce weight.

Disadvantages:

- Potential impact of wind-induced movements on measurement accuracy.
- Requirement for a clear radius around the attachment point, potentially limiting deployment (e.g., for a 60-meter flight, a 60-meter clear radius around the center attachment point is necessary).

- Regulatory challenges for flying in controlled airspace and public traffic areas.

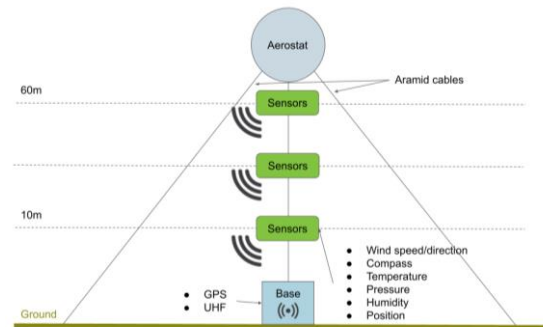


Fig. 1. Tethered aerostat concept illustration.

B. Drones

The drone-based solution shares similarities with the aerostat concept but employs drones to lift and position sensor units at specific altitudes. The drones can be either wired or wireless, each presenting its own set of advantages and challenges. To ensure accurate measurements, sensors are fixed away from the perturbations generated by the drone's blades.

Upfront cost of this solution ranges between 10,000€ and 20,000€. Ongoing maintenance costs mainly revolve around sensor calibration, verification, and drone upkeep.

Advantages:

- Easy deployment, reduced setup time.
- Portable design for effortless mobility.

Disadvantages:

- Similar challenges to aerostats.
- Maintenance concerns due to drones not being designed for extended flight durations.
- Requirement for active operator control.
- Significant increase in costs, operator needs, and space requirements for simultaneous data collection at multiple altitudes.

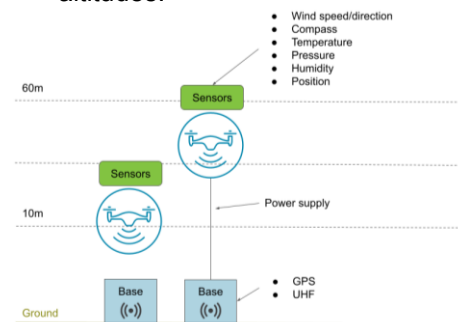


Fig. 2. Drone concepts illustration.

C. Wind LIDAR and SODAR

LIDAR (Light Detection and Ranging) and SODAR (Sonic Detection and Ranging) concepts are based on remote sensing devices that measure wind speed and direction using different techniques.

LIDAR shoots laser beams into the sky. These beams hit particles and aerosols in the air that reflect them back at the instrument. Wind speed and direction are then derived from the reflected light [1]-[4].

SODAR uses a similar principle. It transmits via speakers a short acoustic pulse into the air, then listens for return signals. By analyzing sound waves that are scattered back by temperature variations in the air the device then determines wind speed and direction [5]-[6].

Price of such a solution is expected to be in the 30,000-100,000€ price range with a maintenance cost mostly coming from periodic verification.

Advantages:

- Ground-based measurements without the need for airborne units.
- Capability to provide wind measurements at various altitudes for wind mapping.
- Measurements do not disturb airflow.

Disadvantages:

- Limited to wind speed and direction measurements.
- Potential challenges in calibrating the devices as they need to be calibrated against a multiple anemometer fixed on a mast and such installations are not widely available.
- Fog, rain and snow are reducing measurement availability and accuracy.
- Effectiveness declines with low aerosol quantity.
- SODAR emits audible sound and accuracy is reduced by environmental noise.
- LIDAR's laser can be a hazard.

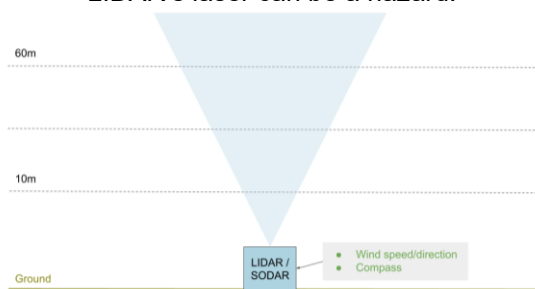


Fig. 3. LIDAR concept illustration.

III. Solution Selection

After consideration of the various concepts the LIDAR solution emerged as the preferred option.

It was chosen over other flying concepts because it presents fewer constraints in terms of regulatory compliance, logistical intricacies, and the need for additional development efforts.

Furthermore, the decision was made to opt for LIDAR over SODAR because noise generated by helicopters can interfere with SODAR measurements, leading to reduced accuracy. LIDAR's reliance on laser beams eliminates this concern.

Additionally, the noise emitted by SODAR during its operation could pose challenges not only in terms of personnel comfort and safety but also regarding its compatibility with installation in environmentally sensitive areas during campaigns, such as protected wildlife zones.

IV. Wind LIDAR Market Overview

The wind LIDAR market offers a diverse range of solutions tailored to various industries, with over 30 commercially available products identified in our research. These solutions span a spectrum of functionalities and price points, with vertical scan versions typically averaging around 70,000€.

In the evaluation process, the selection was narrowed down to three vertical scan wind LIDAR devices, of which one was tested. Other products were mainly excluded due to their inability to measure at the required minimum altitude of 10 meters and within the required temperature range. This limitation is largely attributed to the predominant focus of these devices on serving the needs of the renewable energy sector, offshore platforms, and airports.

V. Wind LIDAR Risks

To ensure safety of the use of the LIDAR system, a risk assessment was conducted.

Three main risks were identified and a risk assessment matrix was employed to evaluate the overall risk level of each identified risk by combining likelihood and severity.

Based on this assessment, it was determined that with the implementation mitigation strategies, the risks could be effectively managed.

For instance, the possibility of measurement errors posing significant risks during testing was identified. To address this, procedures such as periodic verification, pre-operation checks, and

automated cross-verification with ground and tower measurements could be implemented.

Moreover, although the risk of the LIDAR laser damaging devices like aircraft rangefinders is very low, precautions are necessary. Hence, implementing a laser shutdown when not in use and taking steps to prevent aircraft from entering the laser's path could be implemented.

Additionally, laser beams can be harmful to the eyes if observed directly with magnifying devices. Even though this situation is improbable, mitigation steps like placing eye hazard warning signs on the device and its surroundings, along with implementing physical barriers such as fencing to prevent unauthorized access to the laser observation area are best practice.

VI. External Studies on Selected LIDAR

To gauge the performance of the considered wind LIDAR, an evaluation was conducted, first considering external studies.

In one study [7], the LIDAR was deployed alongside a mast for a seven-week period. Data collection occurred at various heights, including 20m, 45m, 70m, and 91m. The analysis generated scatter plots that demonstrated the correlation between the LIDAR measurements and the mast data. The results showed deviations remaining within 2% of class 1 anemometry instruments across all measured heights.

In another study [8], conducted by a renewable energy consultancy group in a calibrated wind tunnel, the LIDAR showed an average deviation of 0.4% compared to a Pitot tube across speeds ranging from 5m/s to 75 m/s.

VII. Internal Study

In addition to external assessments, a study based on field data provided by the LIDAR's manufacturer and data gathered during a test of the LIDAR system at Airbus Helicopters Donauwörth was conducted to confirm its performance.

The data provided by the manufacturer compares LIDAR measurements against measurements from a guyed lattice anemometer mast. The test provides wind measurements at a 1Hz measuring rate. Measurements are done on different heights, leading to a measurement at a given height approximately every 20 seconds. Complete data was only provided for the 91m measuring height. However, this setup has limitations as the references had an accuracy of 0.2%, while the targeted accuracy for the LIDAR was 0.5%. Consequently, the Test Accuracy Ratio (TAR)

[10] for this study was 2.5, signifying that the reference standard's accuracy was 2.5 times greater than the targeted accuracy of the LIDAR.

Data gathered during tests on Airbus site were compared to measurements provided by an ultrasonic anemometer installed on Airbus Donauwörth heliport tower. However, conditions for comparison were not ideal due to installation constraints. It was tried to find the best compromise in positioning of the unit, but turbulence caused by the surrounding buildings and air traffic had an influence on the LIDAR system. There were also slight height and alignment offsets between the reference and the LIDAR. Different filtering methods were developed to compensate for noise induced by testing conditions.

Measurements were done at a fixed height of 10m and a sampling rate of 1Hz. Compared to the manufacturer test, this leads to more data points per time at the given height.

This sampling rate was chosen to answer real-time data requirements for flight testing. The wind industry in comparison mainly uses 10-minute averages.

Tests performed by the LIDAR manufacturer and Airbus both measured data in a timespan of approximately two months.

VIII. Internal Study Methodology

Stochastic evaluation methods (e.g., linear regression plots) were used to compare the LIDAR with the references. Measurements also were visualized over longer time periods, to further validate in which scenarios deviations occur. The manufacturer provides data analysis for the test performed against the guyed lattice anemometer mast. These are used for comparison to analysis conducted by Airbus Helicopters, to validate the precision of the measurement unit.

Data from tests on Airbus site required additional filtering and averaging methods to compensate for errors caused by the unfavorable testing conditions. Data otherwise would be too noisy and could not match the test data of the manufacturer, performed under scientific conditions.

Filters like the wind directional and wind velocity filter remove data based on an average of the data provided by LIDAR and Tower.

For some evaluations only data without air traffic was used (weekends, nights).

The LIDAR used during the manufacturer and Airbus site tests can show a 180° offset in

directional measurements. This is a known issue, which will be removed in future LIDAR hardware versions. A filter using the tower reference data is used to remove the faulty data. Data are considered as faulty if the direction difference between tower and LIDAR is greater than 90° .

Turbulence is filtered out using turbulence intensity calculations. Average and standard deviation of wind speed in a 10-minute interval are used to get a percentage value indicating the intensity of turbulence [11]. The method is often used in the wind power industry. Data with intensity values bigger than a given intensity threshold is removed.

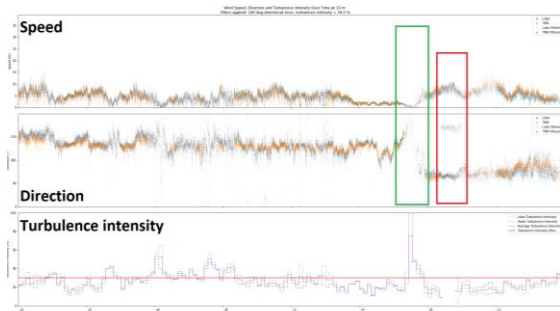


Fig. 4. Time plot of wind speed and direction as well as turbulence intensity. Example: one day on Airbus site.

Figure 4 shows an example of a visualization over time of the raw data. Data that was removed by the 180° filter (red) and the turbulence filter (green) can be seen. Removed data is visualized in gray tones. The bottom plot shows the turbulence intensity and its threshold.

A 30 second running average is used to smoothen the 1Hz measurements. This method is often used when working with real-time wind measurement applications. A vectorial based average method is used, separating the wind vector in x and y parts to be averaged. The averages then are transformed back in speed and direction components (polar coordinates). This considers the circular nature of the data.

Filters were not always used. The result section will state which ones were used.

IX. Results Manufacturer Data

The manufacturer tests have less noise caused by the environment. The analysis at Airbus Helicopters therefore mostly applied no additional filters except the 180° shift correction. The manufacturer applied filters to remove data collected in the shadow of the guyed lattice mast. The mast provides multiple reference measurements at different heights. Filters were applied by the manufacturer, removing data

where the reference measurements had too big discrepancies. [11]

A. Wind speed

The manufacturer test data showed good correlation of wind speed measurements. The visualizations over time suggested a good correlation. To check this, a linear regression was performed.

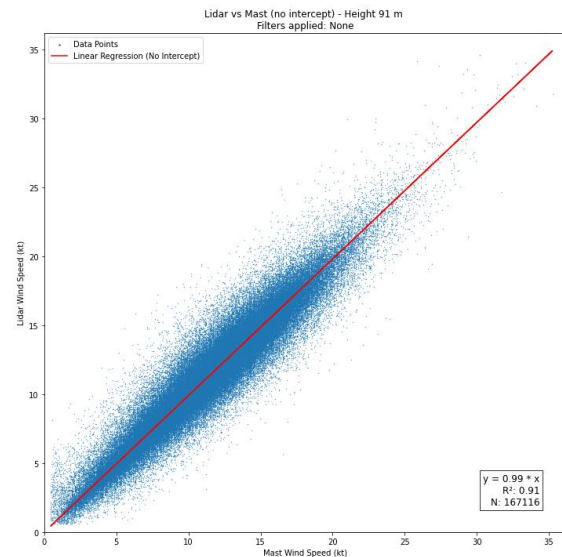


Fig. 5. Linear regression of wind speed at 91 m (manufacturer data).

Figure 5 shows the result of a linear regression forced through the origin without applying any filters. The result confirms the good correlation between Mast measurements and Lidar measurements with a slope of 0.99 and a r squared value of 0.91. A linear regression was also performed by the manufacturer, leading to the same results. The manufacturer gets a slope of 0.99 and a r squared value of 0.909 [8]. Given the data from the manufacturer test, both analyses confirmed the good correlation between the measurement methods.

B. Wind direction

For the direction, a linear regression was performed, with the same settings the manufacturer used. Meaning the direction data was shifted to consider the circular nature of it, allowing for linear regression. Data with velocity less than 4 m/s was filtered, as direction is poorly defined for low-speed data. The 180° shifts are also filtered.

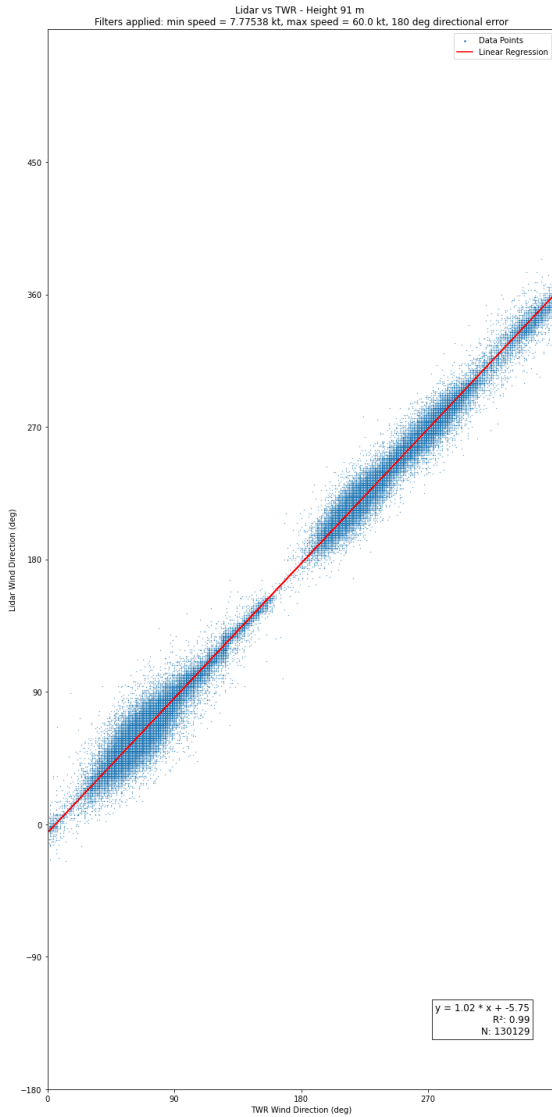


Fig. 6. Linear regression of wind direction at 91 m with filter (manufacturer data).

Figure 6 shows the results. Similar to the manufacturer plots, the line was not forced through the origin. The resulting line is almost exactly the same as with the analysis of the manufacturer. The result indicates very good correlation with a r squared value of 0.99. This is also similar to the manufacturer with a r squared value of 0.995 [8]. The line shows a slight offset from the origin by -5.75.

X. Results Donauwörth Data

A. Raw wind speed data

Section VII showed the issues with the tests in Donauwörth and explained differences to the manufacturer test. Section VIII showed different approaches in filtering to compensate for the imperfections. The necessity of the filters will be illustrated in this section. Tests in Donauwörth were all measured at a height of 10 m. For performance comparison the 20 m

measurement of the manufacturers test will be used. [8]

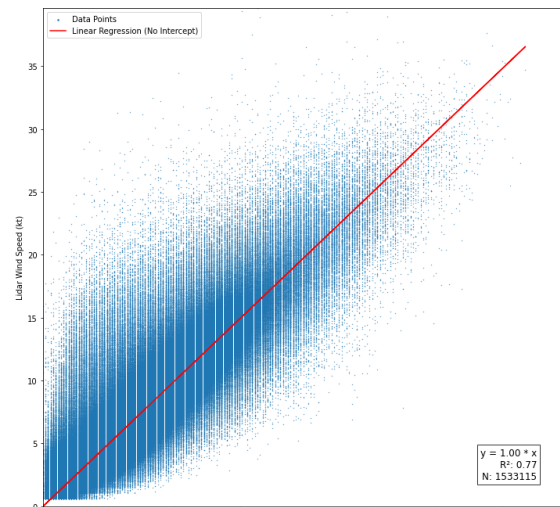


Fig. 7. Linear regression of wind speed at 10 m on Airbus site.

Figure 7 shows the linear regression result for wind speed in Donauwörth without applying any filters. The raw data leads to a slope of 0.99 and an r squared value of 0.77. The lowest measurement available of the manufacturer tests is at 20 m. The resultant slope of that measurement is 0.999 and the r squared value 0.881 [8]. The low correlation of the Donauwörth test indicates the need for filtering, allowing for less noisy data analysis.

B. Wind speed

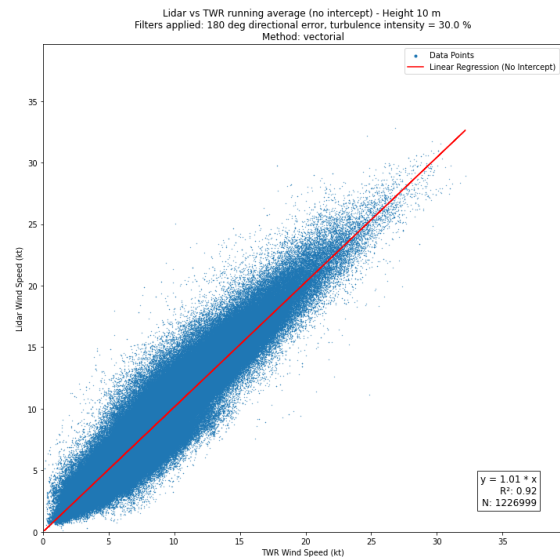


Fig. 8. Linear regression of filtered wind speed at 10 m on Airbus site.

The turbulence intensity filter in combination with the 180° shift filter and the 30 second running average allowed for better data analysis. The turbulence intensity filter was set to filter intensities bigger than 30%.

Figure 8 shows the linear regression after applying these filters. This results in a slope of 1.01 and a r squared value of 0.92. The plot allows for comparison with figure 6 that applied no filtering. The filters applied are meant to improve the data quality and remove any noise. At the same time, they should not be a method to embellish the results. For this reason, only these few filters were applied, which are commonly used in the wind industry.

C. Wind direction

A linear regression analysis for wind direction at a height of 20 meters was not performed by the manufacturer, rendering direct comparison impossible. To address this, modifications were made to the regression approach to align more closely with the method used for evaluating wind speed.

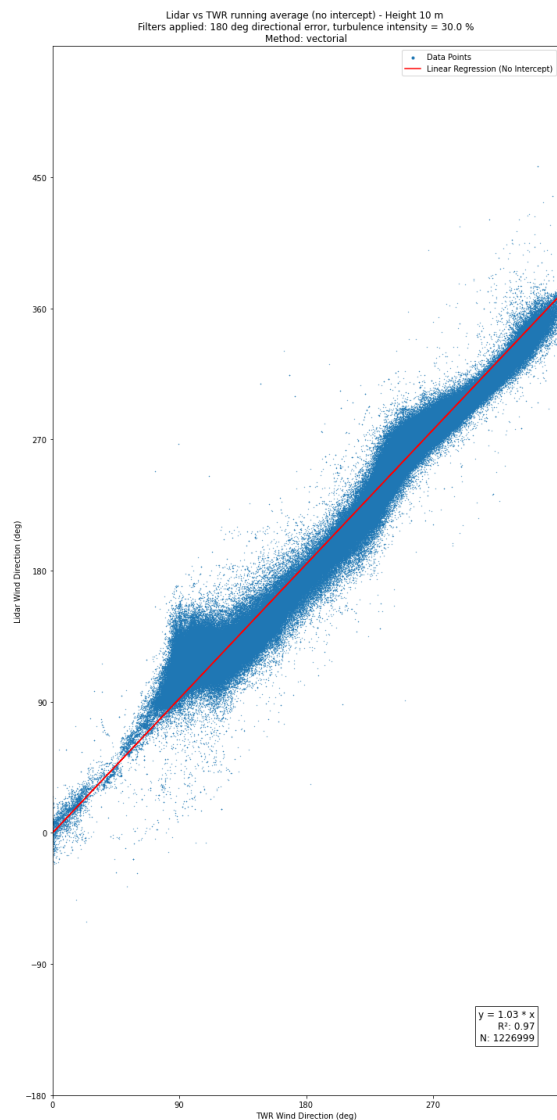


Fig. 9. Linear regression of filtered wind direction at 10 m on Airbus site.

Without any filters, the wind direction plots exhibited similar noise levels to those observed

in the speed plots. To mitigate this noise, a 30-second running average, a turbulence intensity filter with a 30% threshold, and a 180° directional filter were applied. The linear regression was forced through the origin.

Figure 9 depicts the resulting plot with a slope of 1.03 and an r squared value of 0.97. These correlation values are good and similar to the results obtained for the manufacturer's data at other heights.

XI. Conclusion and Perspectives

Despite suboptimal testing conditions and the use of filters to compensate for this limitation during trials on Airbus site, results show the capability of the LIDAR to provide wind speed and direction with an accuracy comparable with traditional anemometers.

These findings corroborate manufacturer tests which were conducted under more controlled conditions and showed a strong correlation with anemometers without filters.

However, the current hardware exhibits an issue with direction determination, where the direction can temporarily shift by 180°. This makes the current hardware unsuitable for real-time applications.

The manufacturer has acknowledged this issue and plans to address it in future hardware iterations. Consequently, faulty data was removed during analysis. Future tests with the updated hardware are necessary and should be conducted under more controlled conditions. Additionally, new testing scenarios will be performed as in our study only one scenario with measurements at a height of 10m was considered.

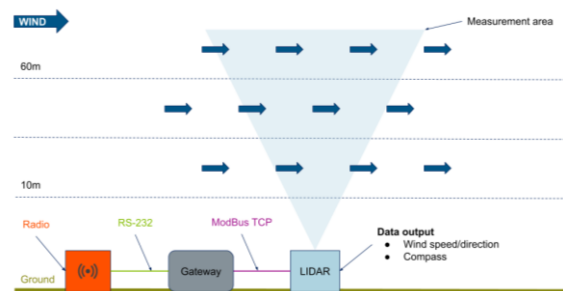


Fig. 10. Diagram of envisioned architecture for Wind LIDAR data stream during Flight Test.

Lastly, the flight test use case requires further integration of the hardware in the instrumentation architecture, e.g., for real-time display of the measured values in the cockpit of the aircraft in using an adequate RF link as depicted Figure 10.

As an extension of this first use case, a multiplication of the ground unit on the test site

can provide a matrix view of the wind conditions around the test aircraft. A relevant network architecture on the ground shall support the data transfer for control and measurement.

References

- [1] Liu, Zhengliang, et al. "A Review of Progress and Applications of Pulsed Doppler Wind LiDARs." *Remote Sensing*, vol. 11, no. 21, 2019, p. 2522, <https://doi.org/10.3390/rs11212522>.
- [2] E. Simley, L. Pao, K. Neil, B. Jonkman, Bonnie, R. Frehlich. LIDAR Wind Speed Measurements of Evolving Wind Fields, 50th AIAA Aerospace Sciences Meeting, July 2012; doi: 10.2514/6.2012-656.
- [3] Shangguan, Mingjia, et al. "Doppler Wind Lidar from UV to NIR: A Review with Case Study Examples." *Frontiers in Remote Sensing*, vol. 2, 2022, <https://doi.org/10.3389/frsen.2021.787111>.
- [4] N.D. Kelley, B.J. Jonkman, and G.N. Scott. "Comparing Pulsed Doppler LIDAR with SODAR and Direct Measurements for Wind Assessment." *Nrel.gov*, July 2007, <https://www.nrel.gov/docs/fy07osti/41792.pdf>.
- [5] Muradyan, P., and R. Coulter. "Sonic Detection and Ranging (SODAR) Wind Profiler Instrument Handbook." *Arm.gov*, https://www.arm.gov/publications/tech_reports/handbooks/sodar_handbook.pdf.
- [6] Nappo, Carmen J. "Sodar" *International Geophysics*, Elsevier, 2012, pp. 231–278.
- [7] Power, Natural. Natural Power's ZephIR Wind Lidar Demonstrates World-first Matched Performance in High-performance Wind Tunnel. Aug. 2011.
- [8] ZXlidars. Comparisons Between ZX 300 Lidar and A Reference Mast Using 1Hz Data. 19 April 2024.
- [9] ZXlidars. UK Remote Sensing Test Site: 91 m Mast Specification. 21 December 2017.
- [10] Mimbs, Scott M. "Measurement Decision Risk - the Importance of Definitions'." *Nasa.gov*, <https://ntrs.nasa.gov/api/citations/20130012508/downloads/20130012508.pdf>.
- [11] Morales, A., Wächter, M. and Peinke, J. (2012), Characterization of wind turbulence by higher-order statistics. *Wind Energ.*, 15: 391-406. <https://doi.org/10.1002/we.478>

Network Management of Flight Test Installation equipment

Joaquín Antonio Pablos Palomino¹

¹ Airbus Defence &Space, San Pablo Sur FTC, Seville, Spain,
joaquin.pablos@airbus.com

Abstract :

Monitoring the status of flight test instrumentation components and networks has been a key element to ensure flight test operations. Originally the monitoring was implemented using the remote acquisition units data format (IENA, Inet-x, ..) but new flight test devices adopted SNMP (Simple Network Management Protocol) to provide network management of ethernet equipment. As a natural evolution acquisition units have improved SNMP capabilities to be managed as standard ethernet devices. Adoption of SNMP provides new functionalities such as control, authentication functions and standardization of objects to be monitored but it requires update of flight test software tools and support of hybrid architectures.

This paper describes the evolution of monitoring capabilities of flight test instrumentation equipment and different options for management of SNMP devices in flight test. Future needs for monitoring and control of FTI equipment and SNMP contribution are also analyzed.

Key words: Flight Test Network Management, SNMP, FTI monitoring.

Introduction

System management of flight test instrumentation in IP networks has been based on monitoring data encapsulated in FTI protocols (IENA, INET-X, CH10) [16] provided by data acquisition systems. With the adoption of Ethernet new equipment such as Ethernet Network recorders, Ethernet switches, or printers appeared in FTI Ethernet data networks that needed to be managed. Commonly this equipment didn't support FTI protocols to report status and the management was initially limited, being difficult to integrate in flight test monitoring displays.

Fortunately, this new flight test instrumentation equipment supported Simple Network Management Protocol. This protocol was introduced in 1988 for supporting the management of Internet Protocol (IP) networks being widely accepted by vendors as a standard.

The support of this standard for monitoring flight test networks has become essential to anticipate to problems and provide new functionalities as configuration setting not covered by standard reporting of acquisition systems.

New scenarios of flight test networks, operating in system-of-systems environments, will make even more critical to provide monitoring of network equipment in different locations.

This paper introduces first how FTI components and networks are currently monitored, why SNMP is relevant, an introduction to SNMP framework, its evolution, and the adoption by TmNS for network management.

Secondly it provides an overview of the current support of SNMP by FTI components and the solutions to integrate SNMP onboard in Airbus DS so far.

Thirdly it describes functions provided by standard network management tools and the software solution developed by Airbus DS to cover flight test activities.

Finally, new FTI scenarios are presented to show how FTI networks will be more complex so the need of tools supporting SNMP to monitor and control the equipment and network will be even more important.

Monitoring of FTI networks

In addition of light indicators and digital outputs for signalling status, most of the remote acquisition units provide internal parameters using FTI protocols as IENA (see Fig. 1) to be easily integrable in standard monitoring displays. Some acquisition systems provide even a dedicated alarm card dedicated to this function.

The number of parameters is dependent of the manufacturer but usually parameters like the following are acquired:

- Out of range input voltage, internal temperature and voltages.
- Communications and synchronization errors.
- Built-in test results.
- Firmware version.
- Detection of connectors.
- Synchronization status.
- Loss of messages.
- General statistics.

The data parameters are configured in the same way of aircraft signals tapped, usually with a low sampling rate of 1 sample per second for most of the them.

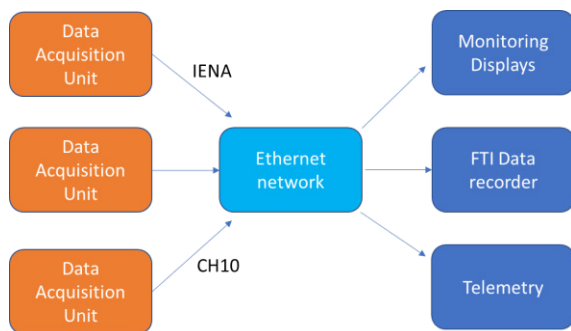


Fig. 1. DAU Internal parameters transmission in IENA / CH10 format to data processing destination.

In addition to status monitoring using FTI protocol, flight test data acquisition systems and data recorders have implemented serial and Ethernet protocols to be configured and controlled. These capabilities are vendor dependent although some of them use standards such as SNMP or IRIG 106 Chapter 6 [1].

The monitoring of other FTI devices is done connecting some of their digital / analogue outputs or serial buses to the FTI acquisition systems that provide standard data using a FTI acquisition protocol (see Fig. 2).

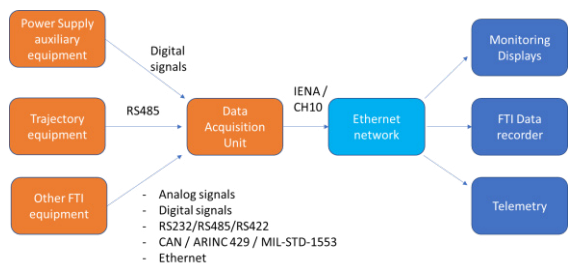


Fig. 2. FTI Status parameters acquisition using DAU.

The FTI monitoring data is processed and shown in monitoring displays dedicated to FTI status. These displays are key to:

- Validate flight test installation.
- Check that FTI is operative, and status in preflights and postflights review.
- Warn flight test engineer about any problem during flight test.

Usually, a general status display is defined for flight test engineer (see Fig. 3), and additional specific displays are defined for operation teams to analyse and detect problems during preflights and verification of installation.

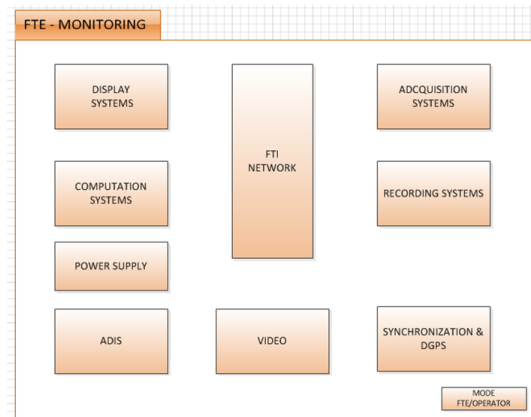


Fig. 3. Global FTI monitoring display for FTE.

If a problem has been detected only during flight, data can be analysed after flight with same tools used by analysis team to check FTI status parameters.

Although this solution has covered successfully the monitoring of data acquisition units, the use of new flight test components with ethernet connectivity but without IENA/Chapter 10 output makes necessary to implement new ways of monitoring. Fortunately, most of them provide plenty of status data using SNMP capabilities, but what are the advantages of SNMP?

Introduction to SNMP

The Simple Network Management Protocol (SNMP) is a full internet standard and was originally focused to manage nodes in the Internet community. The original standard [2] included a description of SNMP architecture and the protocol definition.

The architecture is based in a collection of components (See Fig. 4):

- Network management station, that controls and monitors all the network elements.
- Network elements that include a management agent that performs the

functions required by the network management station.

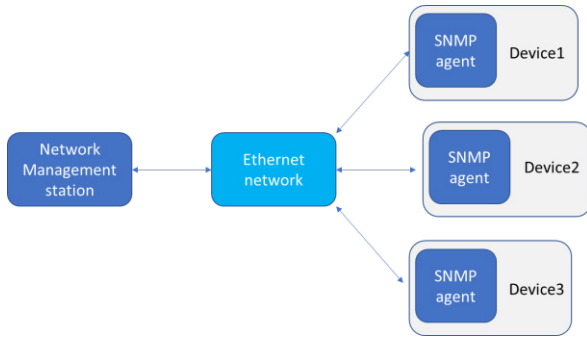


Fig. 4. Components in an SNMP system.

For representation of the management information, it was defined a sub-set of ASN.1 [3] language and created an Internet-standard Structure of Management Information (SMIv1) [4]. It included descriptions of an object information model for network management along with a set of generic types used to describe management information. For identifying objects this standard uses the concept of "OBJECT IDENTIFIER", a sequence of integers which traverse a global tree.

The root node of this tree has at least three children depending of the organization who administers it: ccitt(0), iso(1) and joint-iso-ccitt(2). The internet community has allocated the following one:

```
internet OBJECT IDENTIFIER ::= { iso org(3) dod(6) 1 }
```

Inside this tree the Internet Activities Board (IAB) has defined the following nodes (see Fig. 5):

- directory OBJECT IDENTIFIER ::= { internet 1 }
- mgmt OBJECT IDENTIFIER ::= { internet 2 }
- experimental OBJECT IDENTIFIER ::= { internet 3 }
- private OBJECT IDENTIFIER ::= { internet 4 }

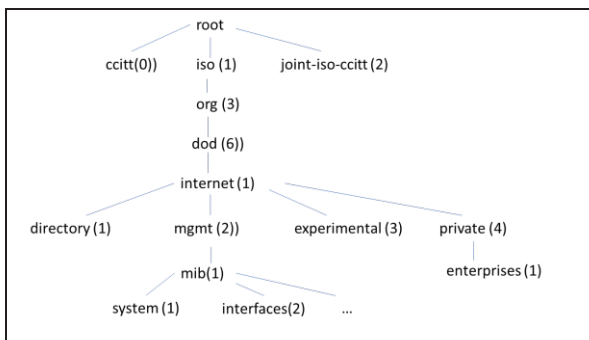


Fig. 5. OID tree.

The most important nodes are the mgmt and private ones:

- Mgmt: identify objects which are described in IAB-approved documents.

The Internet Assigned Numbers Authority assigns object identifiers when a new RFC containing standard Manage Information Base is published.

- Private: is used to identify objects defined unilaterally. Initially, this subtree has at least one child:

```
enterprises OBJECT IDENTIFIER ::= { private 1 }
```

This allows to enterprises to receive a subtree where they can define new objects.

In RFC 1155[4] the following objects syntax is defined:

- Primitive types: integer, octet string, object identifier, and null.
- Aggregate types: "sequence" type allows to generate lists and tables.
- Defined types: some application-wide types are defined as NetworkAddress, IpAddress, Counter, Gauge.

The definition of an object should include: object descriptor (textual name), syntax, definition (description), access (read-only, read-write, write-only, not accessible), status (mandatory, optional, obsolete).

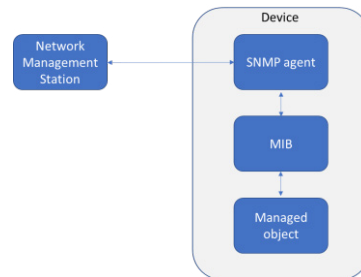


Fig. 6. Components in an SNMP device.

This allows to define MIB databases that will be accessible through SNMP (see Fig. 6), as an example the ifOperStatus of an interface is defined in MIB-II [5]:

```
ifOperStatus OBJECT-TYPE
SYNTAX INTEGER {
    up(1), -- ready to pass packets
    down(2),
    testing(3) -- in some test mode
}
ACCESS read-only
STATUS mandatory
DESCRIPTION
    "The current operational state of the interface.
    The testing(3) state indicates that no operational
    packets can be passed."
::= { ifEntry 8 }
```

SNMPv1 messages include a version identifier, an SNMP community name and a protocol data unit. The protocol entities receive messages at UDP port 161, except for those that report traps that do at port 162. The PDU originally defined were:

- GetRequest-PDU: the receiver will send a GetResponse-PDU with the name and value of the variable requested.
- GetNextRequest-PDU: the receiver will send a GetResponse-PDU with the name and value of the immediate successor of the object requested.
- GetResponse-PDU: it is generated by a protocol entity when receiving a GetRequest-PDU, GetNextRequest-PDU, or SetRequest-PDU.
- SetRequest-PDU: after receiving this message an entity will set the variables with the values sent in the message. A GetResponse-PDU of identical form and error-status field of noError will be generated.
- Trap-PDU: is generated by an SNMP entity and sent to a specific IP address (Network Manager). Includes information of the generic trap type (coldStart, warmStart, linkDown, linkUp, authenticationFailure, egpNeighborLoss, enterpriseSpecific), time stamp and variable list.

The authentication scheme to define administrative relationships is based in SNMP community. Each SNMP community is named by a string of octets, that is called the community's name for said community. This community string is sent in readable text when a query is made, being a security issue.

For any network element, a subset of objects in the MIB that pertain to that element is called a SNMP MIB view. An element of the set { READ-ONLY, READ-WRITE } is called an SNMP access mode. A pairing of a SNMP access mode with a SNMP MIB view is called an SNMP community profile. A SNMP community profile represents specified access privileges to variables in a specified MIB view. A pairing of a SNMP community with a SNMP community profile is called a SNMP access policy.

Finally in addition to object descriptions and protocol definition, a standard Management Information Base (MIB-II) [5] was defined. It contained the definition of essential elements related with the following groups: System, Interfaces, Address Translation, IP, ICMP, TCP, UDP, EGP, Transmission and SNMP. The

implementation of them is mandatory for all systems and provide essential information for network management.

Internet equipment vendors adopted this standard and the deployment was fast [2]. In parallel new revisions of SNMP were published to increase security and capabilities.

SNMPv2c and SNMPv3 improvements

A second version of SNMP was defined in RFC 1901, named Community-based SNMPv2 (SNMPv2c) [6]. It defined new protocol operations described in RFC 1905 [7]:

- GetRequest, GetNextRequest, Response, SetRequest with similar function to SNMPv1.
- GetBulkRequest: request the transfer of large amount of data, improving efficiency and performance for transferring large tables.
- SNMPv2-Trap: it includes the objects sysUpTime.0 and snmpTrapOID.0 and following additional optional variable-bindings.
- InformRequest: it allows data transfer between two SNMPv2c entities acting as managers. A response-PDU is sent by the receiver so it is a confirmed event notification.

Furthermore, an updated SMIv2 (RFC 2578) was defined with expanded data types (Counter64, bit strings) and how to update MIB modules.

Although a User-based Security Model for SNMPv2 (RFC1910) was developed it was never used, so SNMPv1 and SNMPv2c standards suffered the same security problems.

SNMPv3 added security capabilities providing data integrity, source authenticity and confidentiality. This solved the main weakness of SNMPv1 and SNMPv2c.

An overview of SNMPv3 standard is described in RFC 3410 and is currently STD 62 of IETF containing RFC3411-3415 documents. This new standard supports:

- A new SNMP message format.
- Security for messages.
- Access Control.
- Remote configuration of SNMP parameters.

SNMP and telemetry standard IRIG 106

The telemetry standard IRIG 106 Chapter 21 defines an introduction to The Telemetry Network Standard (TmNS).

IRIG 106 Chapter 21 [9] mention SNMP as one of the core technologies used for system configuration and management. The system management provides a fault, accounting, performance and security configuration information on the network. Other protocols such as FTP, HTTP and ICMP are used for functions of file transfer, discovery and configuration.

The managed devices execute applications called agents that use the TmNS-defined MIB to provide their internal status and to accept controls and configuration.

The other kind of component is the TmNS Manager that manages TmNS-compliant components.

The use of SNMPv3 is recommended for secure communications within a TmNS system to provide authentication and privacy.

In IRIG 106 Chapter 22 [10] it is defined the protocol standards to be supported by TmNS manageable applications (TMA) as well as the RFCs implementation required for supporting SNMPv2c and SNMPv3.

Tab. 1: TmNS RFC requirements

SNMP	SNMPv3	SNMPv2c
RFC 3411	RFC 3410	RFC 1901
RFC 3413	RFC 3412	RFC 2578
RFC 2579	RFC 3414	RFC 3416
	RFC 3415	
	RFC 3417	
	RFC 3826	

Apart of the specific TMNS-MIB, many TMAs will also implement other public standard Internet Engineering Task Force (IETF) Request for Comments (RFC) MIBs. the TMNS-MIB only contains those concepts that are unique to TmNS components reusing MIB standards when possible.

In IRIG 106 Chapter 25 [11] it is defined the TMNS-MIB OID registered with IANA:

Telemetry Network Standard (tmns):
iso.org.dod.internet.private.enterprise.31409
(1.3.6.1.4.1.31409)

Documentation for the TMNS-MIB is part of the management resource matrix [11]. All management resources that are TmNS-specific

fall under the top-level hierarchy element “tmns” (see Fig. 7).

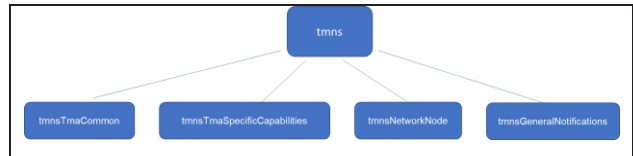


Fig. 7. TmNS tree

The tmnsTmaCommon resource is a container of management resources that shall be available on all TMAs unless otherwise noted. It contains six resource containers (see Fig. 8) referred to identification, fault, configuration, control, status and security.

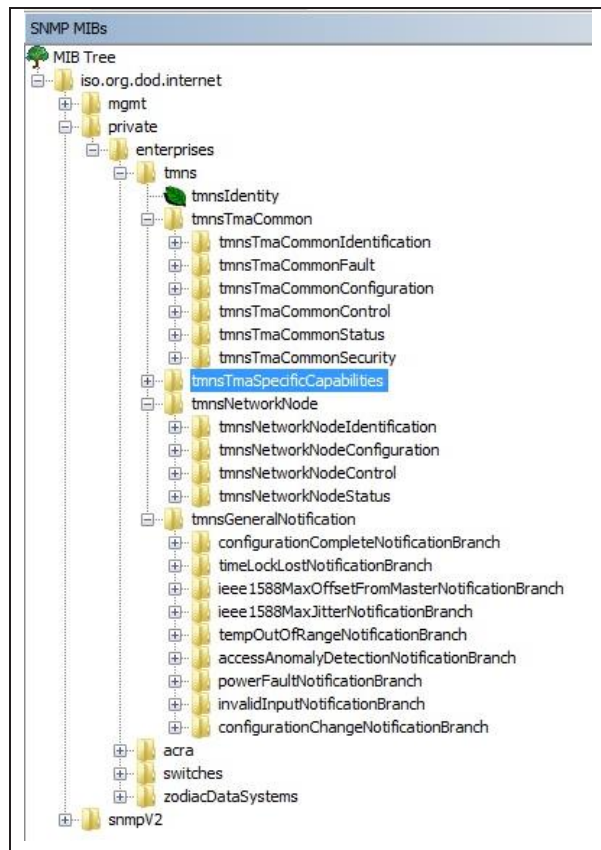


Fig. 8. TmNS MIB tree

The tmnsTmaSpecificCapabilities resource is a container of management resources for application-specific capabilities. Some examples are: tmnsNetworkFabricDevice, tmnsACU, tmnsDAU, tmnsRecorder, tmnsMasterClock, tmnsSSTTx or tmnsSSTRx.

The tmnsNetworkNode resource is a container of management resources that provide status and control capabilities that are specific to the host machine.

All TMAs shall be capable of generating event-based notifications. Management resources regarding general notifications are contained within the tmnsGeneralNotifications container

*This information is of origin Airbus Defense and Space/Spain and does not contain any export controlled information
Airbus Amber releasable to ETTC
ETTC 2024– European Test & Telemetry Conference*

resource. This container resource contains the nine resource containers that are shown in Fig. 8.

Although this standardization work was done in IRIG 106 [17] it has not been implemented in real devices as it is described in next chapter. But it should be the starting point to be used in future standardization initiatives.

SNMP readiness of FTI equipment

Although IRIG 106 MIBs have not been implemented, there are more than 100 standard MIB modules to support network and system management published in "Internet Official Protocol Standards" list and even a greater number of MIBs defined by enterprises.

FTI equipment support both types of MIBs:

- Standard MIBs: for interfaces [5], routing, .. defined by IETF
- Enterprise MIBs: most of FTI system provides specific MIBs to define the parameters that can be monitored or controlled using SNMP.

Most of current FTI systems support only SNMPv2c standard but some of them are starting to support SNMPv3.

Manufacturers of data acquisition systems for FTI support SNMP[19] and have developed their own MIB definitions. The desired solution for final users would be to have a standardized MIB, as IRIG 106, for definition of similar equipment. If needed any manufacturer could extend this definition in the enterprise tree with additional objects. This is a common practice in other sectors that use intensively SNMP.

More even, existing standard MIBs for certain FTI functions are not adopted yet by FTI manufacturers [15]. This is the case of "Precision Time Protocol Version 2 (PTPv2) Management Information Base" defined in RFC 8173 [8]. The information is available but in specific manufacturer OIDs.

This situation makes complex the task to manage the same function with different manufacturers and should be fixed in the future. Using standard MIBs makes simpler for standard network management applications to discover and detect systems and process standard alarms.

The following table shows the monitoring capabilities of FTI components in a standard instrumented aircraft. It describes if they are capable of being monitored and controlled using SNMP, IENA or any other method, the SNMP version they support and if they support standard and enterprises MIBs:

Tab. 2: FTI device monitoring capabilities

FTI device	SNMP mon/cont	IENA	Other mon	SNMP version	MIB std/ent
RDAU1	Low/No	High	No	SNMPv2c	Yes/Yes
RDAU2	Low/No	High	No	SNMPv2c	Yes/Yes
RDAU3	High/Low	High	Yes	SNMPv2c	Yes/Yes
Recorder	High/High	No	Yes	SNMPv2c	Yes/Yes
Switch	High/High	No	Yes	SNMPv2c	Yes/Yes
Video	High/low	No	Yes	SNMPv2c/v3	Yes/No
Cameras	No/No	No	Yes	No	No
Telemetry	High/High	No	Yes	SNMPv2c	Yes/Yes
Computer	High/Low	No	No	SNMPv2c	Yes/No
Control	High/High	No	Yes	SNMPv2c	Yes/Yes

As it is shown most of the DAU support IENA and SNMP but the recorder only supports SNMP. Majority of the devices only support SNMPv2c and support of SNMPv3 is weak so far (only 2 systems are capable).

Reviewing this table, it can be seen that IENA should be complemented with SNMP monitoring to have a full picture of the flight test installation.

Adopting SNMP monitoring we will benefit from the following capabilities to monitor:

- Recorder: remaining time, disk space, recording bit rate, BIT, system health information, synchronization status
- Ethernet switches: status and statistics of interfaces, synchronization status, health information
- Video IP encoder: resolution and status of video input, system health information.
- Rugged PC: system health information, disk space, CPU usage,
- Telemetry equipment: output power, frequency selection, system health information.

It can also be controlled many functions: start/stop recording, enable/disable video streaming, modifying telemetry parameters (frequency, power), ...

Integration of SNMP in Airbus DS

As we have seen in many cases SNMP is the only way to monitor systems. In the past the solution has been to implement ad-hoc solutions to cover the urgent monitoring need as no standard solution was easily integrable in FTI monitoring displays.

The usual case is to use a small IENA proxy-server that can generate IENA streams with data acquired using snmp requests to a certain

*This information is of origin Airbus Defense and Space/Spain and does not contain any export controlled information
Airbus Amber releasable to ETTC
ETTC 2024– European Test & Telemetry Conference*

equipment. In this way data is recorded and available as usual FTI data for monitoring but the solutions are program or even aircraft dependent.

This solution may require a software package to be installed in an existing rugged PC (see Fig. 9) or a new equipment designed to perform this function as the Enhanced Cockpit Control Unit (ECCU) developed for a new fighter prototype [14].

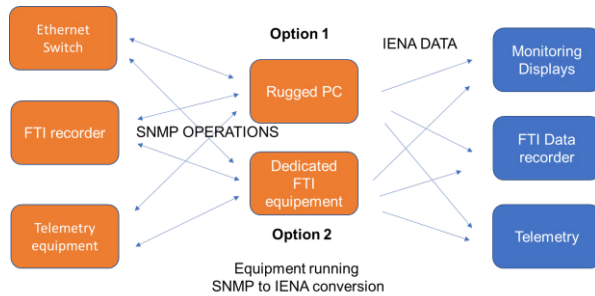


Fig. 9. SNMP to IENA scenarios

Other use case is when FTI data has to be provided to an external system. In this case an SNMP agent is used to receive IENA data from FTI and provide to the external SNMP manager the information through an agreed MIB (see Fig. 10).

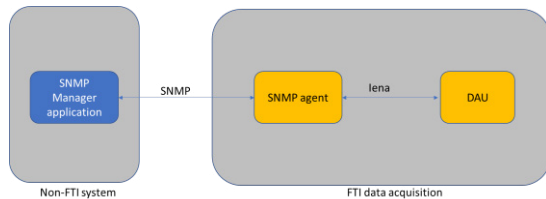


Fig. 10. IENA to SNMP scenario

The objective is to provide a standard solution for FTI and this requires to analyze the tools commonly used for SNMP monitoring in network operators or internet service providers.

SNMP standard monitoring tools

From the beginning of internet, the need of network management was a requirement to ensure a good service level. Most of the network management tools used SNMP as main protocol to acquire data from the systems to be monitored. Some of these historical tools were HP Network Node Manager or IBM Tivoli that have evolved to cover new needs as cloud services or IoT [12].

These powerful tools are used in Network Operating Centres to manage and monitor services, networks and systems. They are capable of discovering the network topology and give visibility of traffic and load of the network using SNMP and managing events providing an alarms console.

The main features of these tools are [13]:

- Discovery of networks: using ICMP and SNMP, the networks that are connected to any device accessible by the network management station are visible.
- Provide preconfigured Device Profiles for known sysObjectID configuring automatically settings.
- Creation of groups of nodes automatically with predefined groups (routers, switches, virtual machines, ...)
- Monitor network health, polling critical devices more frequently than non critical devices to reduce the amount of traffic generated. Configuration of alarms with thresholds and rearm values.
- Definition of user groups for access to visualisation of alarms.
- Advanced features to reduce alarms generation: e.g., if a switch is down, all the interfaces connected to it will also be down, generating excessive alarms for an event.

The cost of these tools is high and would require an additional console to monitor events, new administration and configuration efforts and hardware for supporting the network management software. In addition, some DAU has low implementation of SNMP support. So, it seems not practical to integrate it for onboard FTI monitoring.

Developing a solution capable of providing features included in these standard monitoring tools will provide improvements to take the most out of SNMP.

New FTI alarms console in Airbus DS

As part of network management improvement, a new GUI for monitoring FTI alarms has been designed. It is capable of presenting an alarms history view that will reduce the overload for the operator.

The definition of the alarms requires the following data:

- Define to which system type, system group and message group the alarm will be assigned to.
- Description of the alarm thresholds, parameters calculation related with the alarm (up to three), the severity, the message to be shown to operator and a suggested action if needed.

For simplifying the view, alarms can be filtered depending on:

- A specific system as alarm source
- Severity of alarms (critical, major, minor, warning, normal, unknown).
- System group: DAU, Video, Network, Power, Data servers and Recorders.
- Message group: Network, System performance (CPU, hard disk free space,...), synchronization, environmental (temperature), hardware (BIT, ..)

The console will also allow easily to disable monitoring of a system until a problem is solved to avoid excessive alarms from it.

In case that no data is received for a defined alarm, a message will be shown to warn the operator that is not being processed.

For reducing overload only current status of an alarm is shown in console (see Fig.11) but all alarms are stored and can be consulted. This will allow to detect possible failures in a post-flight check.

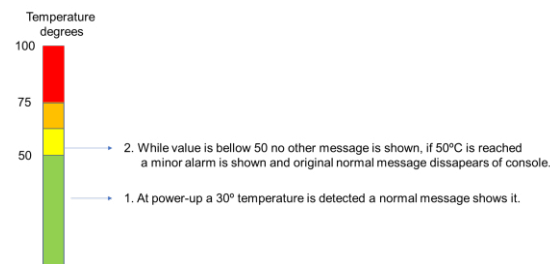


Fig. 11. Alarm message generation.

This software application for alarms visualization (see Fig. 12) receives information from a data server and is independent if this data comes from an IENA or SNMP source.

Host	Date	Level	Message	System Type	System Group	Message Group
9312XA01	09:58:59.352	Normal	9322XA01 Alarms ANA Slot 11	RR291	Data	Hardware
9312XA01	09:58:59.352	Major	9322XA01 Specific alarms ANA	RR291	Data	Hardware
9312XA01	09:58:59.352	Normal	9322XA01 Alarms ANA Slot 11	RR291	Data	Hardware
9312XA01	09:58:59.352	Critical	9322XA01 Alarms ANA Slot 11	RR291	Data	Hardware
9312XA01	09:58:59.352	Normal	9322XA01 Specific alarms ANA	RR291	Data	Hardware
9312XA01	09:58:59.352	Major	9322XA01 Specific alarms ANA	RR291	Data	Hardware
9312XA01	09:58:59.352	Normal	9322XA01 Specific alarms ANA	RR291	Data	Hardware
9312XA01	09:58:59.352	Major	9322XA01 Specific alarms ANA	RR291	Data	Hardware
9312XA01	09:58:59.352	Major	9322XA01 Specific alarms ANA	RR291	Data	Hardware
9312XA01	09:58:59.351	Critical	9322XA01 Alarms ANA Slot 6-1	RR291	Data	Hardware
9312XA01	09:58:59.351	Critical	9322XA01 Alarms ANA Slot 5-1	RR291	Data	Hardware
9322XA	09:57:49.750	Critical	3322XA DGPS trajectory RS raw	XR032	Data	Hardware
9322XA	09:57:49.750	Critical	3322XA DGPS trajectory ZTD raw	XR032	Data	Hardware
9322XA	09:57:49.750	Critical	3322XA DGPS trajectory RT raw	XR032	Data	Hardware
9322XA	09:57:49.750	Normal	3322XA DGPS trajectory roll raw	XR032	Data	Hardware
9322XA	09:57:49.750	Normal	3322XA System DGPS trajectory	XR032	Data	Hardware
3202XA	09:57:49.750	Critical	3202XA Adu fault	WZ009	Data	Hardware

Fig. 12. FTI monitoring History display

This console is fully operative currently and will integrate SNMP data using an SNMP-IENA application (see Fig. 13) that will do the conversion between SNMP OID's and IENA parameter, poll at defined intervals for SNMP parameters and generate IENA data.

This approach will have the following advantages:

- Monitoring software is independent of data source (SNMP and IENA data can generate alarms).
- Data is recorded in standard FTI format and can be consulted with standard analysis tools.
- SNMP data can be sent over telemetry link in the standard way (IENA).

The architecture will support in addition the reception of SNMP traps in the "IENA-SNMP application" and conversion of this data to IENA format.

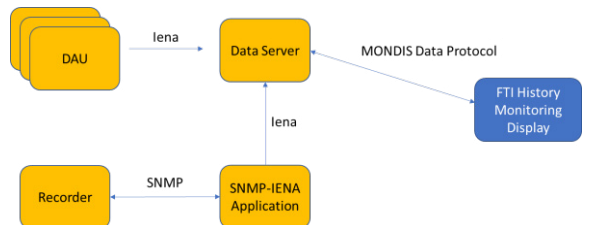


Fig. 13. Architecture for SNMP polling.

For supporting SNMP configuration, a configuration protocol will be used to set SNMP parameters using the SNMP-IENA application. This configuration protocol (see Fig.14) is already used for configuration of FTI devices

using HTTP or sockets applications for video system equipment.

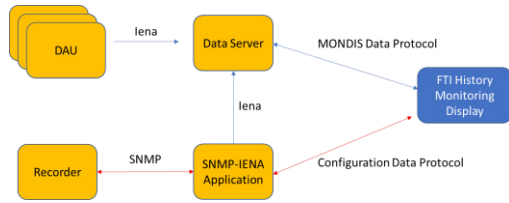


Fig. 14. FTI configuration using SNMP.

The configuration of SNMP-IENA application will be automatically generated from the programming generation tool once the SNMP parameters configuration has been defined.

New monitoring capabilities for new scenarios

Monitoring current FTI architectures can be a difficult task as they include many Ethernet switches, remote acquisition units, recorders and specific equipment for flight test. The new capabilities provided by supporting SNMP will improve the detection of problems of existing flight test installation but will enable also to manage more complex networks.

The development of bidirectional telemetry and mesh networks will allow communication between test articles having FTI installed and ground stations (see Fig.15). This will allow even to monitor and control FTI devices in other test articles if tools are operative.

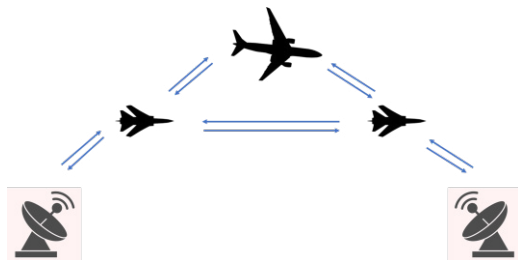


Fig. 15. FTI telemetry mesh network.

SNMP support will be important in these future scenarios [19] utilizing version 3 of the protocol, adding authentication and encryption to the SNMP message exchange. The use of standard TmNS MIBs should be encouraged to simplify monitoring configuration.

The figure 16 shows a FTI architecture in which the flight test engineer of a military transport aircraft could be monitoring FTI data received from drones checking that all parameters are right before launching a flight test, or modifying configuration of drone equipment to prepare the test. This will be possible with bidirectional

telemetry if monitoring & control capabilities are ready.

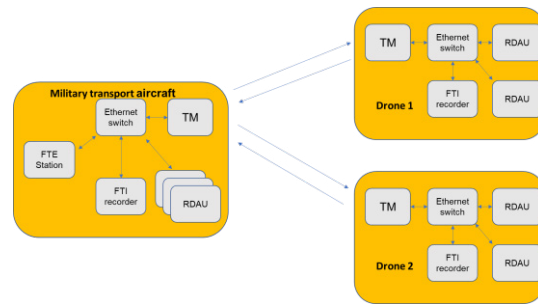


Fig. 16. FTI architecture for MTA and drones.

Conclusions

Network management of FTI requires the adoption of SNMP to be able to monitor most of the components of a flight test network. This is encouraged by the Telemetry Network Standard (TmNS) that adopt SNMP as standard for monitoring, configuration and control and has defined standard MIBs for telemetry components.

The adoption of SNMP requires the use of new software applications to receive the data and to visualize the information received without overloading the operators. The software architecture has also to provide capability to control the systems using SNMP. Airbus DS is developing the flight test software solutions that will allow the management of SNMP devices easily in a multi-program environment.

Finally, the improvement of network management with SNMP support and new software tools is a previous step to cover future needs of flight test activities as System of Systems (SoS) where bidirectional telemetry with mesh networks is expected to be used.

References

- [1] Telemetry Standards, RCC Standard 106-23 Chapter 6 - Recorder & Reproducer Command and Control, July2023 - <https://www.trmc.osd.mil/wiki/display/public/RCC/106+Telemetry+Standards?preview=/168165620/168165605/chapter6.pdf>
- [2] RFC 1157 - A Simple Network Management Protocol (SNMP) - <https://www.ietf.org/rfc/rfc1157.txt>
- [3] Information processing systems - Open Systems Interconnection, "Specification of Abstract Syntax Notation One (ASN.1)", International Organization for Standardization, International Standard 8824, December 1987.

*This information is of origin Airbus Defense and Space/Spain and does not contain any export controlled information
Airbus Amber releasable to ETTC
ETTC 2024– European Test & Telemetry Conference*

- [4] RFC 1155 - Structure and Identification of Management Information for TCP/IP-based Internets - <https://www.ietf.org/rfc/rfc1155.txt>
- [5] RFC 1213 - Management Information Base for Network Management of TCP/IP-based internets: MIB-II - <https://www.ietf.org/rfc/rfc1213.txt>
- [6] RFC 1901 - Introduction to Community-based SNMPv2 - <https://datatracker.ietf.org/doc/html/rfc1901>
- [7] RFC 1905 - Protocol Operations for Version 2 of the Simple Network Management Protocol (SNMPv2) - <https://datatracker.ietf.org/doc/html/rfc1905>
- [8] RFC 8173 - Precision Time Protocol Version 2 (PTPv2) Management Information Base: <https://datatracker.ietf.org/doc/html/rfc8173>
- [9] Telemetry Standards, IRIG Standard 106-23 Chapter 21 - Telemetry Network Standard Introduction : <https://www.trmc.osd.mil/wiki/display/public/RCC/106+Telemetry+Standards?preview=/168165620/168165599/Chapter21.pdf>
- [10] Telemetry Standards, IRIG Standard 106-23 Chapter 22, July2023 - Network-Based Protocol Suite <https://www.trmc.osd.mil/wiki/display/public/RCC/106+Telemetry+Standards?preview=/168165620/168165603/Chapter22.pdf>
- [11] Telemetry Standards, IRIG Standard 106-23 Chapter 25, July2023 - Management Resources <https://www.trmc.osd.mil/wiki/display/public/RCC/106+Telemetry+Standards?preview=/168165620/168165596/Chapter25.pdf>
- [12] What happened to Tivoli? – Ingo Averdrunk 2016 - <https://web.archive.org/web/20180224143553/https://www.ibm.com/blogs/cloud-computing/2016/08/what-happened-to-tivoli/>
- [13] HP Network Node Manager i Software 10.0 - Online Help: Help for Administrators – https://support.microfocus.com/kb/kmdoc.php?id=KM00838328&fileName=hp_man_nnmi_Help_Administrators_10.00_pdf.pdf
- [14] G. Martínez Morán, “Intelligent Networked Flight Test Instrumentation for a new Fighter Prototype”, ETTC 2018; doi:10.5162/ettc2018/11.1
- [15] O. Holmeide, M. Schmitzr ,“PTP version 3 in FTI”, ETTC 2016; doi: 10.5162/ettc2016/1.1
- [16] P. Quinn , “Addressing the Babel’s Tower of FTI Standards in a Network Environment”, ETTC 2020; doi: 10.5162/ettc2020/2.5
- [17] Grace, Thomas B., Bertrand, Allison R., Newton, Todd A. , “Applying the iNET System Management Standard”, International Telemetry Conference Proceedings 2019
- [18] N.Cranley , D.Corry, “Networked Flight Test Instrumentation Data Recording Solutions”, International Telemetry Conference Proceedings 2009
- [19] Pingfan Guo, Ming Liu, Hong Li, Hongxiang Zhu ,” Telemetry System Based on MESH Network and Its Application” , International Telemetry Conference Proceedings 2018

*This information is of origin Airbus Defense and Space/Spain and does not contain any export controlled information
Airbus Amber releasable to ETTC
ETTC 2024– European Test & Telemetry Conference*

Innovative Measurement Technology Solutions for Thermal and Mechanical Testing of HV Batteries

Dipl.-Ing. (FH) Timo Eich¹

¹ CSM Computer-Systeme-Messtechnik GmbH, Raiffeisenstr. 36, 70794 Filderstadt, Germany

Abstract

HV batteries have to endure multiple mechanical and thermal stresses when in service, which have to be extensively examined already in the development phase to prevent battery failures or even vehicle fires caused by thermal runaways. Thermal and mechanical simulations depend on real field data for creating reliable models and verifying such in later development phases against reality. For this reason field testing of HV batteries utilizing measurement technology is key. Unfortunately, testing under high-voltage conditions poses a lot of challenges on the measurement equipment, particularly when acquiring data from sensors like strain gauges, accelerometers and temperatures. In this presentation Timo Eich shows, how CSM GmbH mastered those challenges and solves the needs of car and battery manufacturers for mechanical and thermal testing worldwide with innovative measurement technology solutions.

Key words: High-voltage safety, battery testing, strain gauge measurement, acceleration measurement, temperature measurement

Mechanical stresses on HV batteries

In modern electric and hybrid vehicles, high-voltage traction batteries not only serve as energy storage units, but also perform structural and load-bearing functions in the vehicle, particularly in the passenger car sector, due to their proportion of the vehicle mass and their size and shape (skateboard architecture). This means that - at the latest when HV batteries are integrated into their respective target vehicles - they are confronted exposed to the conditions of the respective vehicle environment. On-road or even off-road environments in particular induce multiple stress influences during driving due to vibrations, impacts and shocks as well as deformations caused by the forces that occur when cornering or, for example, when driving over curbs (torsional forces). These forces, vibrations and deformations not only occur at the outside and surface of the battery housing, but also propagate into the inside of HV batteries with great effect. This results in some high forces on load-bearing elements such as struts, but also mechanical loads on busbars, for example, which connect individual battery modules relatively rigidly and can be subjected to high loads due to their relative movements to each other.

At the same time, the operation of lithium-ion batteries causes swelling, an expansion of the

individual battery cells due to electrochemical and thermal effects, which occurs particularly in prismatic cells. While the major reason for irreversible cell-swelling is the degrading of battery cells, reversible swelling mainly stems from thermal expansion of electrolytes.

Thermal stresses on HV batteries

The performance of HV battery systems heavily depends on the ambient temperature as well as on self-heating effects caused by high currents and electronic and thermal resistances. Effective battery management and the associated sophisticated temperature management are crucial here, especially when it comes to battery safety. This is one of the reasons why thermal testing of HV batteries is of such importance to battery and vehicle manufacturers. While end customers demand performance and a long range in all seasons, manufacturers must also ensure the safety of the battery and thus of the vehicle and its occupants. Above all, worst-case scenarios such as thermal runaways must be avoided.

Testing with measurement equipment is vital

All the effects and phenomena listed above require comprehensive investigations and tests of HV batteries, both in the development phase of batteries and in the near-series testing of

complete vehicles. Thermal and mechanical simulations can already provide valuable insights here - if the corresponding models are reliable and based on real data from road tests. Ultimately, however, even the best simulations cannot fully cover the countless small and large influences of the real world.

This means that testing of HV batteries and complete vehicles with analog measurement technology is crucial in several phases of vehicle development. On the one hand, to create a data basis for modeling and simulation and, on the other hand, to check the simulation results against reality and to improve and refine the models. Road tests are of crucial importance here, as even test benches only reflect the reality of the road to a certain, fixed degree.

Challenges when testing HV batteries with analog measurement equipment

In order to gain comprehensive insights into the physical and thermal processes in HV batteries, they must be equipped with sensors to record vibrations, strains, forces, pressures, deformations and, above all, temperatures. However, there are numerous challenges to overcome when performing measurements in HV batteries. Firstly, the space available for comprehensive instrumentation of HV batteries is very limited, as the batteries are usually very densely packed. Secondly, comprehensive instrumentation of the battery may also have adverse side effects on the actual operation and behavior of the battery, not least due to the numerous breakthroughs required for cables for sensor supply and signal lines. And finally, the measurement technology and sensors are directly confronted with the system voltage, which in HV batteries usually amounts to several hundred volts.

Challenges when measuring in high-voltage environment

The high battery system voltages pose two challenges for the measurement technology: the acquisition of the smallest sensor signals at HV potential and the safety of the measurement equipment and its operators.

Sensors such as accelerometers, force and pressure sensors, but in particular strain gauges and temperature sensors, provide extremely small measurement signals in the millivolt and microvolt range. These fine signals must be measured, digitized and transmitted by the respective measurement amplifier in a high-voltage environment with several hundred volts of potential without interference or superposition. This requires extremely good common mode rejection (CMRR), which is

effective over the entire required frequency range of the physical measured value acquisition.

Current HV safety regulations for HV battery testing

High voltages also pose a particular challenge for the safety of measurement equipment and its operators. Therefore, comprehensive safety measures must be taken under all circumstances to prevent damage to material and personnel. Measurement devices for high-voltage applications must be certified in accordance with DIN EN 61010 and thus have to provide a comprehensive HV safety concept. On the one hand, this concerns the circuit design, which must be implemented with double or extended insulation. On the other hand, sensor cables, connectors, cable sockets and the device housing must also comply with the strict regulations set out in DIN EN 61010.

Insulation and galvanic decoupling demands

Fiber optic cables are only a very limited alternative for two reasons. Firstly, fiber optic cables do not allow the transmission of energy for the sensor supply, which is essential for the operation of bridge-based sensors such as strain gauges, acceleration sensors and resistance thermometers as well as active sensors with conditioned output. On the other hand, fiber optic cables pose a risk of breakage due to the tough mechanical requirements of the road test.

Wireless transmission of the signals is also difficult due to the shielding nature of the HV battery housing. It is therefore necessary to route the supply and signal lines for the corresponding sensors into and out of the battery, also meaning that galvanic decoupling must take place in the measurement device.

CSM's high voltage safety concept

CSM GmbH has developed a comprehensive measurement device concept for use in high-voltage environments, which is based on DIN EN 61010. After 10 years of continuous extension, CSM's HV-safe product line covers almost all physical measured variables to be acquired at high-voltage potential. The core of the HV-safe measurement devices is the analog part of the measurement amplifier circuit, which is designed separately for each measurement channel and is electrically isolated from the digital part of the measurement device by reinforced insulation. This ensures that high voltage reaches the measurement device but not its power supply circuit or the bus system for measurement data transmission, let alone the device housing.

High-voltage connectors specially developed for CSM and a special potting of the plugs and sockets enable an insulation strength of 1,000 volts in the smallest of spaces. In this way, the device housing can be designed very compactly and the required air gap and creepage distances are still maintained – a significant factor in field tests.

CSM's HV safety concept also includes robust and high-voltage-safe special cables that carry sensor signals into the measurement device in an insulated manner and consist of several layers of insulation. It is important that individual signal cables are available for each measured value, which meet the requirements of the respective measured value. For example, signal cables for thermocouples are designed as a sum cable for four sensors in the respective thermocouple material combination, whereby the thermocouple pairs are individually insulated and the sum cable as a whole then has additional insulation.

The following section outlines four applications in the field of mechanical and thermal battery testing that CSM customers have performed with measurement devices from the HV-safe product line.

Battery drop test with acceleration measurement

According to the Korean Motor Vehicle Safety Standard (KMVSS), traction batteries for vehicles must undergo a standardized test in order to be certified for the Korean market. The test involves dropping the HV battery from a height of 4.90 meters onto a hard surface such as concrete. Acceleration signals on the outside of the housing and inside the HV battery are to be measured. The aim is to acquire and document the shock amplitudes of the acceleration transducers and to gain insights into the propagation of the shock wave through the battery. Both objectives require a very high temporal resolution and, in addition, extremely good temporal synchronization of all measurement signals.

In this case CSM's customer utilized a combination of HV-safe and non-HV-safe measurement modules, which were connected via EtherCAT® and clock-mastered by a CSM XCP-Gateway. CSM's HV IEPE3 FL100 measurement device was used for the acceleration signals within the battery, which allows the acquisition of one triaxial or three uniaxial IEPE sensors with a sampling rate of up to 100 KHz per measurement channel. The HV IEPE3 FL100 supplies the IEPE sensor(s) electrically isolated with an impressed current of 3.5 mA. The acceleration measurements on the

surface of the battery, which are not required to be high-voltage safe, were carried out with a CSM AD4 IE1000, which allows the acquisition of four IEPE measurement channels with up to 1 MHz per channel.

By using the EtherCat® bus system and the CSM XCP-Gateway, the measurement signals could be synchronized with an accuracy of 1 microsecond and thus valuable conclusions could be drawn from the measurement data regarding the propagation of the shock waves through the battery.

Vibration measurement on busbars

In corresponding HV battery variants, the individual battery modules move relative to each other under driving conditions. This in turn affects the busbars connecting them, which are exposed to considerable vibrations and forces. In the worst case, the busbars can break and lead to malfunctions or even battery failure. CSM customers therefore wanted to measure how great the accelerations are directly on the busbars within the HV battery. In this case, piezoresistive acceleration sensors are used, which require different signal processing than IEPE sensors. CSM's customer used the HV AD4 IF1000 measurement module, which enables the acquisition of active sensors under HV environmental conditions. The acceleration sensors are supplied with an electrically isolated power supply from this measurement module and the sensor signals are measured back separately and isolated with sampling rates of up to 1 MHz per channel. In this way the safe use of standard sensors in HV environments gets possible.

Strain gauge measurements in HV batteries

Measurements with strain gauges under HV conditions are a particular challenge. Their measurement signals are vanishingly small compared to the battery system voltages, usually only a few microvolts. CSM's customer wanted to apply strain gauge sensors to the surface of the battery in order to measure strain, compression and torsion while driving. On the other hand, strain gauges were also to be attached to the struts between the battery modules in order to investigate the swelling effects. A major challenge here is the different materials for which the measurement device must be able to provide the appropriate measurement ranges, as well as the possibility of subsequently adjusting the measurement ranges and sensor supply voltage after the strain gages have been applied.

CSM was able to solve these requirements with the HV STG4 pro BS20 measurement module. It allows the connection of four strain gauge full

or half bridges with a sense line on both sides. Quarter bridges can also be realized with special external supplementary resistors. The special feature of the measurement module is the bridge supply voltage unit, which can be set individually for each channel between 1 and 10 volts and thus optimally adapted to the material to be measured. In addition, the bridge supply voltage is measured by the measurement module in parallel with the bridge voltage (=measurement signal) itself, so that the measurement signals are not negatively influenced by potential fluctuations in the bridge supply voltage and are therefore extremely accurate and unsusceptible to interference.

Temperature measurement in HV batteries

While battery management systems generally only have a manageable number of temperature sensors, dense temperature monitoring is necessary in the development phase of batteries in order to reliably detect even the smallest anomalies. This requires measurements at cell, module and system level, which can often lead to a total of over 500 temperature measurement points in a battery.

Currently, measurements are often carried out using thermocouples, but these have two major disadvantages. Firstly, the best thermocouples (class 1) with a measurement accuracy of at best 1.5 Kelvin or 0.4 % of the measured value are not accurate enough for many applications such as the verification of temperature models. On the other hand, measurements with many thermocouples also require many feedthroughs through the battery housing, even with cable glands that are suitable for several cables.

Resistance thermometers are more accurate than thermocouples, but only if they are operated in a 4-wire circuit. This means that twice as much cabling is required for the same number of thermocouples. This is not only unfavorable with regard to the necessary openings in the battery housing, but also with regard to the cable routing of the sensor lines within the battery. In addition, they are difficult to position exactly and reproducibly in the same places on several battery cells. Furthermore, the identification of the individual measurement points and their assignment in the measurement data acquisition is prone to errors with large numbers of channels in analog measurement setups. In addition, the sensor signals on analog lines within the battery are exposed to massive fields and interference. Finally, the acquisition of such a large number of sensors also requires many measurement channels and thus measurement modules outside the battery, which consume limited space, especially in road tests.

To meet these challenges, CSM has therefore developed a digital multi-channel temperature measurement system for testing HV components, especially HV batteries. The HV DTemp measurement system consists of digital temperature IC sensors as well as small, compact controller units and a single central unit. The system can measure up to 512 temperatures with an accuracy between 0.1 to 0.25 Kelvin (total system accuracy). Only a single digital cable is routed from the central unit into the battery housing to supply and organize the controllers and sensors and to transmit the measurement data to the central unit.

Thanks to the digital architecture, the sensors can be precisely identified and assigned. The individual sensors each occupy an area of just 1 x 1.5 mm and measure the temperature on the underside with pinpoint accuracy between -40°C and +125°C. Thanks to their low height of 0.5 mm and their robust design, they can also be pressed between battery cells, for example. They are soldered onto ultra-thin, flexible foils, which provide the connections for the cabling and are covered with Kapton foil, thus offering contact reliability of 1,000 volts. Thanks to the direct digitization of the measured values in the sensor, the measurement signals are extremely immune to interference, as no analogue signal lines are used within the system.

The sensors can be designed as individual sensors or combined as sensor assemblies and thus individually adapted to the application. For measurements on cells in particular, custom-designed foils with up to 20 precisely positioned sensors are available, which can then be inserted between battery cells and thus reproducibly measure the temperatures of different cells at exactly the same positions.

The controller units allow the connection of up to 16 sensor modules with 4 sensors each and can therefore manage a total of 64 measurement channels. With their small dimensions of 80 x 10 x 56 mm, they can also be placed in tight battery housings. Their ports are available with different insulation strengths of up to 1,000 V. A total of up to eight controllers can be connected in series, enabling a total of 512 temperature channels. The measurement data from the 512 measurement channels is then fed from the battery to the central unit using just a single sensor cable.

The central unit takes over the supply and management of up to 512 measurement channels on one or two ports (e.g. with different potentials for two test specimens) and then

makes them available for forwarding on a CAN bus connection.

The HV DTemp system thus represents a highly innovative, minimally invasive and precise measurement method for multi-channel temperature measurements for HV batteries. It is already being used extensively by CSM's customers in the automotive industry as well as in electrified aviation.

Conclusion

CSM's HV device family allows almost complete coverage of mechanical and thermal measurements under high-voltage conditions with proven and common standard sensors such as strain gauges and accelerometers as well as with digital temperature ICs. This also enables comprehensive physical tests to be carried out in a safe environment in general electromobility.

FTI Thermal Modelling using Rough Order Model

David Doyle,
Curtiss-Wright, Aerospace Instrumentation Group,
Unit 5 Richview Office Park, Clonskeagh, Dublin 14, D14 X981, Ireland
ddoyle@curtisswright.com

Abstract

There is an industry drive in Flight Test Instrumentation to make the acquisition units smaller and more powerful; smaller with less weight to fit in tighter, more disturbed locations; and more powerful to facilitate fast, powerful, high-speed chips and to provide excitation to sensors.

This drive to minimization and high-power means that thought needs to be given to thermodynamics and the management of heat dissipation. This in turn means that tools and Techniques to predict thermal performance are becoming more and more important.

This paper is a study of a thermal modelling technique using a rough order model and open source pSpice to run the thermal system as an analogous electronic circuit. With this tool we can predict the thermal performance the installation with a view to having a successful flight test campaign.”

Key words: Thermal Modelling, Rough Order Model (ROM)

Introduction

Modelling temperature in a complex electronic system like flight test instrumentation is a very complex and difficult task. There are hundreds of passive and active components on each board each with their own heat dissipation requirements and thermal properties. They all make a very complex thermodynamic system. To be practical, there needs to be an approximation that simplifies the process of modelling the thermodynamic behavior. This is especially true for a modular system where units can be assembled in any combination. The approximation used in this study is a rough order thermal model. This operates with fundamental thermodynamic principles operating on conceptual approximations of the physical units under study.

Rough Order Model

At the center of the rough order model is a node of specific dimensions. This node is assigned thermodynamic properties and is considered to have a heat flow through it as per Fig 1.

In particular, the rate of heat flow is directly proportional to the temperature differential on either side of the node, the cross-sectional area of the heat flow and a constant call the thermal conductivity which is a property of the material.

The rate of heat flow is inversely proportional to the distance across the node in the direction of the heat flow.

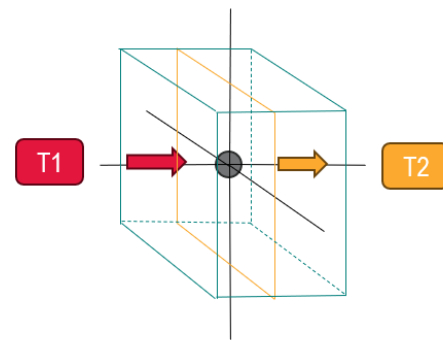


Fig. 1. Representation of a rough order node

$$Q = k A \frac{(T_1 - T_2)}{X_{12}}$$

Q rate of heat flow (W)
 Temperature T1 and T2 (K)
X₁₂ Distance between 1 & 2 (m)
A cross section area (m²)
k Thermal conductivity of medium (W/Km)

Fig. 2. The fundamental thermodynamic equation that governs the ROM node.

The heat flow equation has the same form as like ohms law in Fig 3. This means that we can use freely available electronic circuit simulators to handle the numerical analysis, provided suitable numbers are provided to the model.

$$I = \frac{V1 - V2}{R}$$

I Current flow in (A)
 V1 – V2 Voltage Differential (V)
 R Electrical Resistance (Ω)

Fig 3. Ohms Law

The nodes are generally smaller than the material being modelled and can be combined into a mesh as per figure 3. This allows for a predicted temperature along medium. In the case where there is a break in the medium and a boundary to another, this boundary can be modelled as an extra thermal resistance.

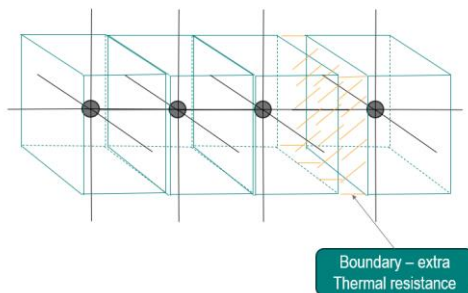


Fig. 4. Mesh of ROM nodes with a boundary condition.

For the purposes of using an electrical circuit simulator to simulate thermal behavior the thermal/electrical equivalents in Fig 5 were used.

Thermal Capacitance (J/K) \approx Electrical Capacitance (F)
 Thermal Resistance (K/W) \approx Electrical Resistance (Ω)
 Power Dissipation (W) \approx Constant Current Source (A)
 Temperature (T) \approx Voltage (V)
 Ambient Temperature (K) \approx Electrical Ground (0V)

Fig. 5. Thermal/Electrical equivalent used in this study

Considering the above, a circuit can be used to predict the thermal system's dynamic and steady state, that is given the thermal properties of the materials involved, the correct boundary conditions and the correct wattages of the heat sources.

Fig 6 shows the 3D image of a data acquisition unit side by side with its equivalent electrical circuit that represents its thermal behaviour. The ROM model is an approximation and that

each PCB is modelled as a single node and a single block. It does not model each of the components placed on the PCB.

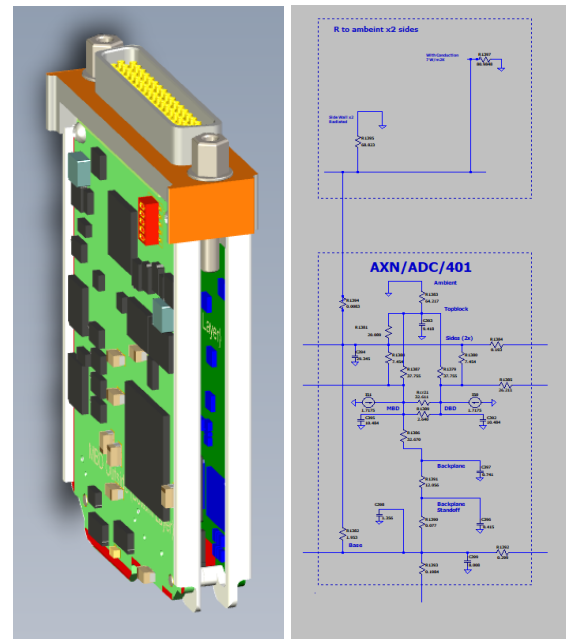


Fig. 6. Representative of physical data acquisition and its equivalent thermal circuit.

The circuit in Fig 6 represents a dual board user module in the data acquisition system. With a library of circuits representing all the available user modules any combination of user modules can easily be assembled into a thermal system representing the physical system.

Finally, to do a thermal simulation the following elements are needed:

1. The system configuration of the planned instrumentation
2. A power calculator tool to establish the power dissipation requirements per board.
3. A library of equivalent thermal circuits that represent user modules and chassis.
4. A thermal model of the physical bracket that the equipment is mounted on if it needs to be modelled (if it can be heated by the equipment)

Procedure

The system in Fig 7 was modelled with the ROM Thermal Model and assembled in reality to compare the thermal model with the experimentation. The system was set up on an AXN/CHS/16U/AB2 which permitted the deployment of heat sinks AXN/HSK/16U/V. The experiment ran the with and without the heat sinks fitted. The unit was not mounted to any plate or bracket during test.

Slot #	Module Selection
Chassis	AXN/CHS/16U/AB1
0	AXN/BCU/402/C
1	AXN/ADC/401
2	AXN/ADC/401
3	AXN/ADC/401
4	AXN/ADC/401
5	AXN/ADC/401
6	AXN/ADC/401
7	AXN/ADC/405/10V
8	AXN/ADC/405/10V
9	AXN/ADC/404/B
10	AXN/ADC/404/B
11	AXN/ADC/404/B
12	AXN/ADC/404/B
13	AXN/MBM/401
14	AXN/MBM/401
15	SPARE
16	SPARE

Fig. 7. User module loadout of the AXN/CHS16U/AB2 test article for the experiment

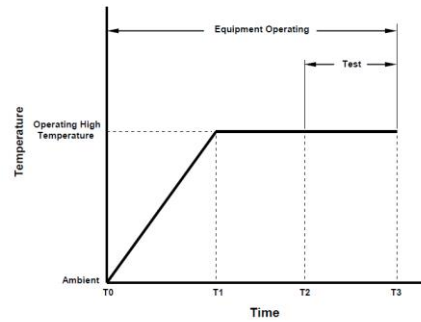
The 6x AXN/ADC/401 are each 8x channel bridge cards and all 48x channels had a 15mA excitation load arranged for the test.

The 4x AXN/ADC/404/B are each 12x channel bridge cards and all 48x of those channels had a 15mA load arranged for the test.

The 2x AXN/ADC/405/10V are each 24x channel differential ended voltage cards. These had a precision voltage applied to all 48 channels.

The 2x AXN/MBM/401 are each 4x Dual redundant MIL-STD-1553 bus monitor cards. One of them had all 4x channels connected to a MIL-STD-1553 simulator.

The test method chosen was the DO160-G Category D2 hot test (70C)



- Note: 1) Temperature change rate from T0 to T1 is not specified.
- 2) T1 to T2 is time for equipment temperature to stabilize.
- 3) T2 to T3 is 2.0 hours, minimum.

Figure 4-4 Operating High Temperature Test

Fig. 8. Temperature profile for DO160-G Category D2 high operating thermal test

The block diagram for the test system is as per Fig 9. and photos of the test article are in Fig 10

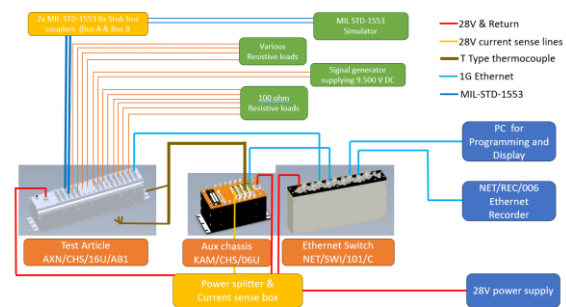


Fig. 9. Temperature profile for DO160-G Category D2 high operating thermal test



Fig. 10. AXN/CHS/16U/AB2 test article in thermal chamber with thermcouple.

In parallel with the experiment, the ROM for each scenario was developed in LTSpice which is an open source circuit simulator package. (Fig 11 and Fig 12)

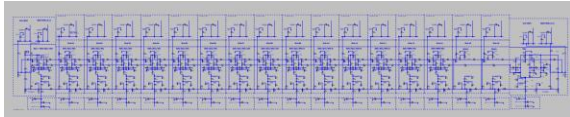


Fig. 11. Equivalent thermal circuit of AXN/CHS/16U/AB2 test article without heat AXN/HSK/16U/V heatsinks

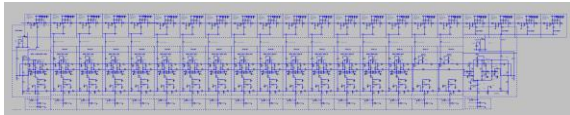


Fig. 12. Equivalent thermal circuit of AXN/CHS/16U/AB2 test article without heat AXN/HSK/16U/V heatsinks

These simulations were run to compare the simulation results with the indicated values in the experiment.

To run the model certain assumptions were made related to heat transfer boundary conditions and power distribution as follows in Fig 13

Air convection with an equivalent Conductance of $26 \text{ W/m}^2\text{K}$

Emissivity ϵ of 0.9 for Axon Chassis for radiation purposes (black body)

Emissivity ϵ 0.16 for exposed based plate

Thermal Interface material between AXN/HSK/16U and chassis with 7.0 W/mK

The potential path to conduct heat away from the DAU through the sensor wiring will not be modelled (and will not cool down the DAU in the simulation)

The potential path to conduct heat through the grill in the oven will not be modelled

Power consumed by user modules as described in the datasheets equally split between mother board and daughter board in dual board user modules

Power consumed externally by sensor excitations do not heat up the test article

Fig. 13. Assumptions used in ROM model

Results

There are two significant measured results, the measured power consumption and the measured temperature at different points on the test article. Two separate experiments were run, one with the AXN/CHS/16U/AB2 test article with AXN/HSK/16U/V heatsinks fitted and the other without the heatsinks fitted.

The power consumption was measured at two points, at the external power supply and inside the test article. The current was measured on the 28V line so power consumption could be calculated. This was compared with the predicted power consumption from the user module datasheet specifications and from the prediction of the Axon power supply unit's losses based on predicted efficiency at the predicted load. The second point where current was measured was on the Axon 15V backplane supply. The results of both are shown in Fig.14

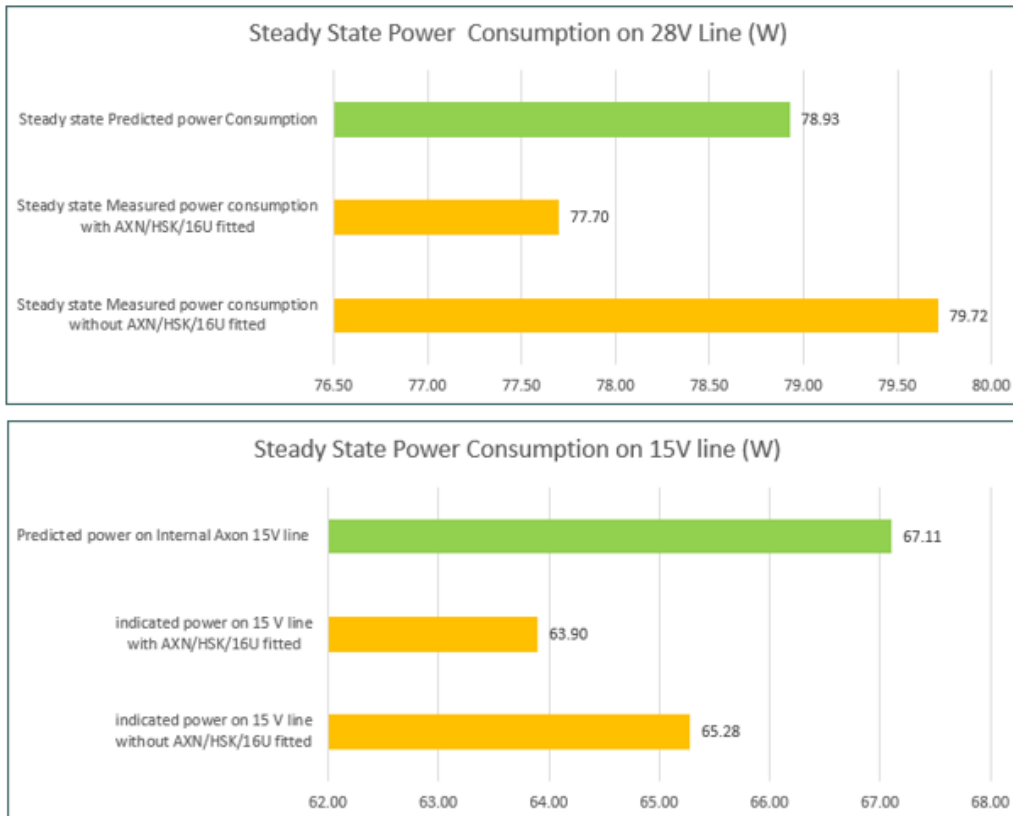
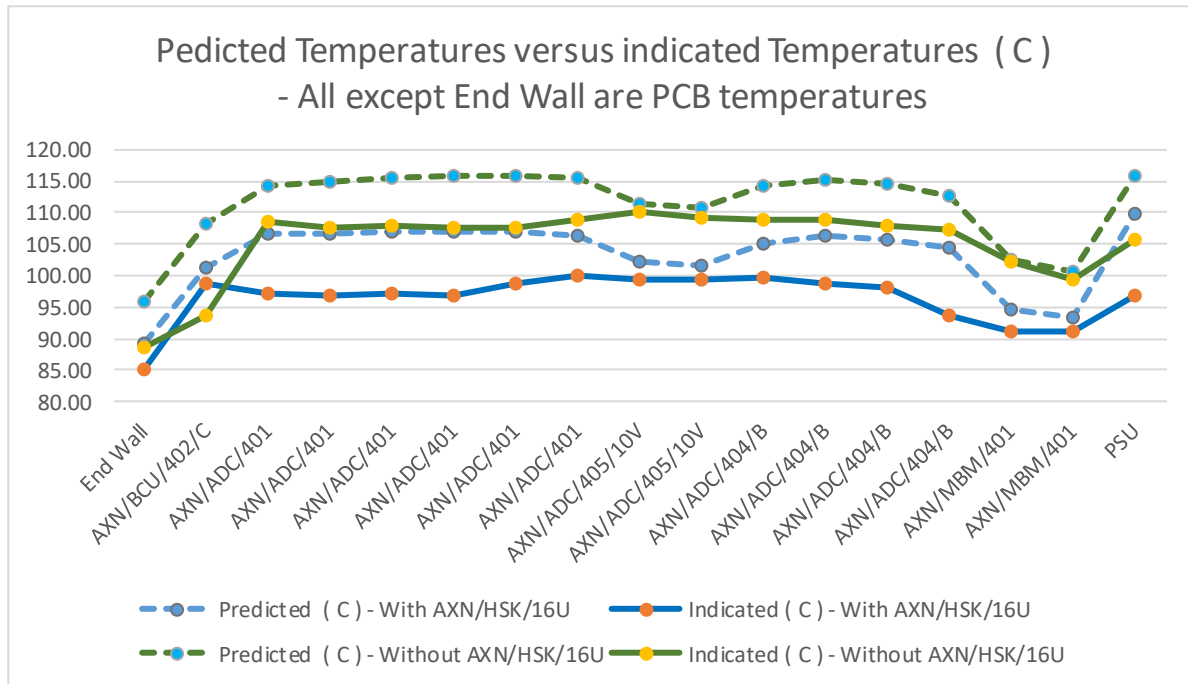


Fig. 14. Predicted and measured power consumption

In each case the measured power consumption with the heatsinks fitted was less than the measured power consumption with the heatsink. The measured power consumption on the 28V line with a heatsink fitted was 2.45% less than predicted, without the heatsink the power consumption was 1% more than predicted. In both cases the expected power consumption figure on the Axon backplane was less than predicted. With the heatsink fitted it was 4.78% less than predicted and without the heatsinks fitted

The indicated temperature points were read directly from the board of the user modules with the inbuilt Axon resistance temperature device. In addition to that the end wall of the AXN/CHS/16U/AB2 had an R-Type thermocouple mounted on it to measure the case temperature. The results from both tests are as shown in figure 15



In both cases, the measured temperatures were below the predicted temperatures.

Fig.15.Predicted Temperatures vs indicated temperatures.

Conclusions

The rough order thermal model was proven to be conservative. This is due to the inbuilt headroom of the model and the assumptions made. This makes it a good tool in terms of risk reduction for flight test instrumentation programs.

The technique has proven to be useful for modular flight test instrumentation systems. The downside of this technique is when the thermal study requires a complex bracket because this can be time consuming to generate.

In practice, the model has been used to assist with the design of the mounting brackets on flight test instrumentation deployment, it has been used to guide thermal risk reduction steps on flight test instrumentation deployments and it has been used to guide product development decisions. In this way the technique has proven its worth.

Further research for this topic is to compare the predicted temperatures with the indicated temperature for the actual flight tests of the flight test instrumentation studies that were made with the model.

The main Acknowledgements

The main body of work that this study is built on the work by Professor Jeff Punch, School of Engineering University of Limerick, Ireland. Jeff specialises in thermal sciences and did extensive work modelling for the Curtiss Wright space team in Dublin Ireland.

References

- [1] RTCA, Incorporated, DO-160G, Environmental Conditions and Test Procedures for Airborne Equipment; doi December 8, 2010.
- [2] Curtiss-Wright, DST/AJ/011, AXN/CHS/16U/AB2; doi 20 Nov. 2023
- [3] Curtiss-Wright, DST/AH/004, AXN/BCU/402/C; doi 21 Apr. 2023
- [4] Curtiss-Wright, DST/AB/019, AXN/ADC/401; doi 19 Jul. 2023
- [5] Curtiss-Wright, DST/AB/019, AXN/ADC/404/B; doi 23 Jan. 2023
- [6] Curtiss-Wright, DST/AB/019, AXN/ADC/405/10V; doi 23 Jan. 2023
- [7] Curtiss-Wright, DST/AF/002, AXN/MBM/401; doi 16 Apr. 2024

Tornado FTI Refurbishment: Bridging Legacy and Modernity in Aerospace Engineering

Jean-François Gineste¹, Heiko Körtzel², John Ockerse³

Airbus Defence and Space GmbH

Rechlinerstraße, 85077 Manching, Germany

¹Flight Test Ground Station

²Flight Test Instrumentation

³EMC department

jean-francois.gineste@airbus.com

heiko.koertzel@airbus.com

john.ockerse@airbus.com

Abstract

The Tornado FTI Refurbishment Project aims to extend the aircraft's service life from its first flight in 1974 until 2030. This holistic modernization involves significant upgrades to the Flight Test Instrumentation (FTI) and Ground Stations (FTGS). Onboard communications are being transitioned from PCM (Pulse Code Modulation) to Ethernet, from S-Band to C-Band and data transmission is evolving from analog (/Ch4) to digital telemetry (SOQPSK/Ch7). Addressing electromagnetic compatibility (EMC) issues was crucial, with a specialized shielding concept ensuring the integration of new hardware with legacy systems. Infrastructure modernization, including upgrading a 30-year-old measurement system, was essential. Performed during the COVID-19 pandemic, the project demonstrated exceptional adaptability and innovation. This presentation explores strategies for managing obsolescence, enhancing EMI resistance, and integrating advanced technologies, offering valuable lessons for future aerospace modernization endeavors.

Key words: Tornado, FTI Refurbishment, EMC, Shielding Concept, Digital Telemetry, Ethernet

1. Introduction

The Tornado aircraft, first flown in 1974, has long been a critical asset for the German Air Force due to its versatile capabilities. Facing the need to delay the replacement of its Tornado fleet, the German Air Force decided to extend the aircraft's operational lifespan to 2030, increasing its flying hours from 6000 to 8000. This extension postpones the immediate need for new aircraft amidst debates between the Eurofighter Typhoon (EFA) and F-18. Consequently, the FTI refurbishment became essential to support this extended service life.

This FTI refurbishment project was driven by the necessity to maintain Germany's capability to carry out NATO's nuclear strike missions. However, it faced significant technical challenges: the 70's Tornado was developed with analog telemetry, non-encrypted FTI, no onboard Ethernet, a weak EMI protection... Additionally, the last major update to the Manching FTGS was over 20 years ago. The project involved a holistic modernization of these outdated systems while ensuring

continuous operational readiness, requiring parallel maintenance of both legacy and refurbished environments.

The global context of COVID-19 and the war in Ukraine further complicated the project, provoking supplier difficulties and necessitating new ways of working. The simultaneous refurbishment of 3 Tornado versions adds another layer of complexity. Modernizing this obsolete infrastructure required meticulous planning and resource management to ensure that both infrastructures remain operational during the transition.

Managing these aspects has required robust project management strategies, effective collaboration across multiple departments (FTI, FTGS, EMC, Design Office, electric cables design), and innovative solutions to logistical challenges.

2. Overview of FTI Architecture and Time Synchronization

2.1 General FTI Architecture

The FTI architecture is designed to handle the complex requirements of modern flight testing, integrating advanced data acquisition, processing, and transmission technologies. The architecture aims to improve data reliability, synchronization, and transmission efficiency.

3.1.1 Key components

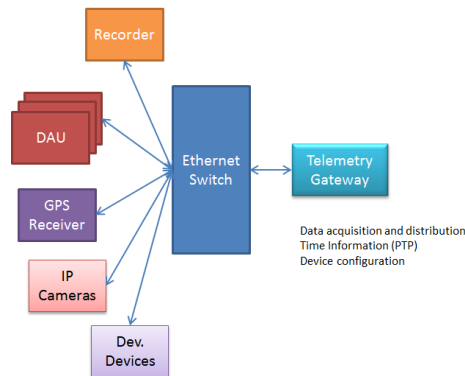


Fig. 1. Ethernet-based FTI architecture.

- **Data Acquisition Units (DAUs)** collect data from various sensors and systems throughout the A/C. These units are critical for capturing accurate and high-resolution data. Each DAU is equipped with multiple input channels that can interface with different types of sensors (temperature, pressure, acceleration, strain gauges...) and converts analog signals from sensors into digital data that can be processed and transmitted over the network.
- **GPS Receiver:** Provides precise time and positional data. The GPS receiver is critical for synchronizing the system clock with global time standards and providing positional data for flight analysis.
- **HD Cameras:** Capture visual data which can be integrated into the FTI system. Used to monitor various parts of the aircraft and provide video data that can be synchronized with other sensor data.
- **Dev. Devices:** Custom HW devices for specific data acquisition tasks. These devices can include specialized sensors, signal conditioners, and custom data processing units.
- **Recorder:** Captures and stores data from various sources for later analysis. Recorders are equipped with high-capacity storage devices and interfaces to receive data from multiple DAUs and other sources.
- **Network Switches** are central elements in the architecture that route data between different components using Ethernet-based communication. They handle data traffic management and ensure that data packets reach their intended destinations. These switches support advanced features such as VLANs, Quality of Service (QoS), and multicast traffic management to optimize network performance and ensure the reliable delivery of critical data streams.
- **Telemetry Systems** are responsible for transmitting the collected data to ground stations for analysis. These systems must handle high data rates and ensure reliable communication over long distances. Telemetry systems typically include RF transmitters, antennas, and receivers. The transmitted data is often encoded and compressed to optimize bandwidth usage and ensure data integrity during transmission.
- **Synchronization Systems** maintain precise timing across all components to ensure data integrity and accurate correlation. These systems are essential for coordinating data collection and ensuring that all recorded data is properly time-stamped. Synchronization is achieved using protocols such as PTPv2 (Precision Time Protocol) and IRIG-B. These systems also compensate for network delays and jitter to maintain high-precision synchronization across all devices.
- **Ethernet Switch:** Central hub for data routing and distribution. The switch connects all networked devices and manages data traffic to ensure efficient and reliable communication.
- **Telemetry Gateway:** Transmits data to ground stations and provides time synchronization and device configuration information. The telemetry gateway encodes and transmits data over RF links to ground-based telemetry stations.

3.1.2 Ethernet-Based Communication

The transition from traditional PCM to Ethernet-based on-board communication provides several advantages:

- **Higher Data Rates:** Ethernet supports much higher data transmission rates compared to PCM, enabling the transmission of large volumes of data efficiently. Ethernet networks in FTI systems can support gigabit and even 10-gigabit speeds,

allowing for the simultaneous transmission of multiple high-bandwidth data streams.

- **Flexibility:** Ethernet allows for multipoint communication, enabling one-to-many and many-to-many data exchanges. This flexibility is crucial for modern FTI systems that need to handle diverse data sources and destinations. Ethernet switches can dynamically manage connections between devices, facilitating flexible and scalable network architectures.
- **Standardization:** Utilizing standard IP-based protocols simplifies the integration of new equipment and technologies, making it easier to upgrade and expand the system. Standard protocols such as TCP/IP, UDP, and PTP ensure interoperability between different vendors' equipment and future-proof the system against evolving technologies.

3.1.3 Data flow and routing

Network switches manage data flow within the FTI system. Data packets are routed based on IP addresses and port numbers, ensuring that they reach the correct destinations. Switches can also prioritize traffic, ensuring that critical data is transmitted with minimal delay. The data flow is designed to minimize latency and maximize throughput, which is essential for real-time data acquisition and telemetry.

2.2 Time-Synchronization in FTI systems

Accurate time synchronization is critical in FTI systems to ensure data integrity and proper correlation of events. The FTI system uses Precision Time Protocol version 2 (PTPv2) for this purpose.

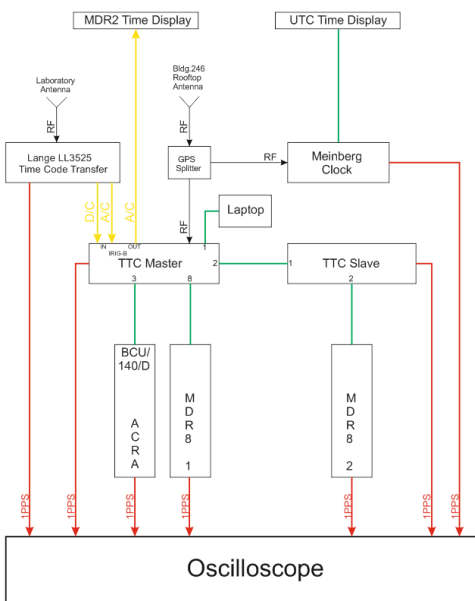


Fig. 2. Test architecture

3.2.1 Time-Synchronization methods

Primary Time Source: GNSS: The primary time source for the FTI system is the Global Navigation Satellite System (GNSS). The TTC master switch acts as the PTP grandmaster clock, continuously synchronized with GNSS. This provides highly accurate timing information to all network components.

PTPv2 Protocol: PTPv2 distributes timing information across the network. The protocol operates based on International Atomic Time (TAI) and compensates for network delays to ensure precise time synchronization. PTPv2 messages include synchronization, delay request, delay response, and follow-up messages to accurately measure and adjust for network delays.

3.2.2 Backup Time Sources

1) **IRIG-B (DC and AC Codes):** IRIG-B signals serve as secondary time sources when GNSS is unavailable. IRIG-B signals provide a reliable means of maintaining synchronization and are widely used in aerospace applications. IRIG-B transmits time information as a serial digital signal, which can be either DC-coded or AC-modulated.

2) **Internal RTC (Real-Time Clock):** The internal RTC of the TTC master switch is used as a last resort when external time sources are unavailable. The internal clock maintains time with a known drift rate, ensuring continuity of operation until external sources are restored. The RTC is periodically calibrated to minimize drift and maintain accuracy over extended periods.

3.2.3 Time Distribution in the Network

1) **Grandmaster Clock:** The TTC master switch, synchronized to GNSS, serves as the grandmaster clock. It provides the reference time for all other devices in the network. The grandmaster clock sends periodic synchronization messages to maintain consistent timing across the network.

2) **Slave Clocks:** Other network components, such as the TTC slave switch, ACRA DAUs, and Heim data recorders, synchronize to the grandmaster clock using PTPv2. This ensures that all components share the same time base. Slave clocks adjust their local time based on the received PTPv2 messages to stay synchronized with the grandmaster.

3.2.4 IRIG-B synchronization

IRIG-B signals are used to synchronize components in environments where GNSS signals are weak or unavailable. The system

can switch between DC and AC codes based on availability.

3.2.5 Priority Order for Time Sources

- a. IRIG-B (DC Code): Preferred source for manual synchronization before flight or test. This code provides high precision and is less susceptible to noise.
- b. GNSS: Primary source for in-flight synchronization, providing the most accurate and stable time reference.
- c. IRIG-B (AC Code): Used if GNSS is unavailable. This code is typically used in noisy environments where DC coding might be impractical.
- d. RTC: Used if no external time sources are available. The RTC provides a fallback timing mechanism with known drift characteristics.

3.2.6 Testing and Validation of Time Synchronization

Various tests were conducted to validate the time synchronization capabilities of the FTI system. The following key results were obtained:

- 1) Timing Difference between Lange Time Code Transfer Unit and Meinberg Laboratory Time Reference:
 - Supplied by different antennas: ~110ns
 - Supplied by the same antenna: ~20ns
- 2) Time Synchronization of TTC Master Switch with GNSS:
 - Offset: ~96ns
 - Jitter: ~37ns
- 3) Time Synchronization with IRIG-B:
 - DC Code: Offset ~240ns, Jitter ~24ns
 - AC Code: Offset ~1.6us, Jitter ~2.1us
- 4) Synchronization of Slave Components:
 - TTC Slave Switch: Offset ~140ns, Jitter ~50ns
 - BCU/140/D: Offset ~62ns, Jitter ~99ns
 - MDR8 Units: Offset ~155ns, Jitter ~34ns

These results demonstrate the system's capability to maintain precise time synchronization across various components and conditions. The tests confirm that the FTI system can achieve nanosecond-level synchronization accuracy, which is essential for high-precision data collection and analysis.

3.2.7 Drift and Resynchronization

The drift rate of the RTC in the TTC master switch was evaluated under two scenarios:

- Power-on drift (without external time sources): 30µs/hour
- Power-off drift (after reconnection and synchronization with GNSS): 1.5ms/h

These measurements indicate that while powered, the internal RTC maintains a low drift but a higher drift rate is observed when powered off.

3.2.8 System Restart & Resynchronization

Several power resets were performed to evaluate the resynchronization behavior:

- Master Switch: 45s to resynchronize.
- BCU/140: 70s.
- Slave Switch: 100s
- MDR8 units: 120s
- Whole system: 140s

The timings indicate the time required for each component to achieve full synchronization post-reset.

3.2.9 Configuration adjustments

The MDR8 unit offers an "OFM-Shift" setting for clock offset adjustments:

- Default setting: 0 ns.
- Adjustments tested: Shifts to 170 ns and -100 ns to optimize synchronization

3.2.10 Recommendations

To ensure the highest level of precision and stability in time synchronization across the FTI system, the following recommendations are made:

- Stabilization Period: Allow at least 3 minutes post power-on before beginning operations to ensure all components are fully synchronized.
- Synchronization Code: Utilize IRIG-B DC code for manual time synchronization to achieve the best stability.
- OFM-Shift: Employ the MDR8 OFM-Shift setting for fine-tuning synchronization, adjusting as necessary based on detailed test results.
- Operational Time Base: Maintain UTC as the operational time base within the FTI system to avoid frequent reconfigurations and ensure consistency

By integrating robust synchronization methods and structured IP/UDP address allocation, the FTI system provides a scalable and high-performance solution for modern flight test requirements, ensuring accurate and timely data for analysis.

3.3 IP Address and Port Allocation for FTI Systems

3.3.1 General principles

Structured IP Address Allocation: The IP address allocation strategy is designed to ensure efficient routing and prevent conflicts within the network. By utilizing a designated IP address range, each subsystem and device can be uniquely identified, which is crucial for seamless communication and integration.

Segmentation by Subsystem and Device Type: To manage network performance and isolate traffic, each subsystem within the FTI architecture is assigned a unique range of addresses. Specific IP address ranges are allocated based on the type of device and its serial number, ensuring clear identification and preventing conflicts between different types of equipment.

Database Integration: When devices are received, they are logged into a component database where IP addresses are assigned according to the established schema. These IP addresses are then configured into the devices to ensure seamless integration into the network.

3.3.2 Destination IP Address Allocation

UDP-Based Communication: The FTI system utilizes UDP extensively due to its low latency and minimal overhead, which are essential for real-time data transmission. Multicast IP addressing is employed to efficiently distribute data to multiple destinations, ensuring that all necessary devices receive the required data streams simultaneously.

Multicast Addressing: A designated range is reserved for multicast traffic, segmented to avoid conflicts and ensure organized data flow. Addresses within this range are allocated by project and data stream, allowing for clear and manageable data distribution.

IGMP Management: The Internet Group Management Protocol (IGMP) is implemented to manage multicast group memberships. Devices use IGMP to join and leave multicast groups as needed, ensuring they receive the relevant data streams and optimizing network traffic.

3.3.3 Routing and Data Management

Switch-Based Routing: Network switches route data based on destination addresses, managing traffic efficiently to ensure prompt transmission. Prioritizing critical data is essential to minimize latency and maintain the high performance required for real-time data acquisition and telemetry.

Multicast Management: Devices use IGMP to signal switches to forward specific multicast streams. This approach minimizes unnecessary traffic, ensuring efficient communication and reliable data delivery across the network.

3.3.4 Destination Port Allocation

Structured Port Allocation: Ports are allocated systematically to ensure clear identification and prevent conflicts. This allocation is based on the function of the service or application and data format, promoting organized and predictable communication patterns.

Protocol Identification: Each subsystem and protocol are assigned specific port ranges to differentiate data streams effectively. Different subsystems and devices use specific port ranges to avoid conflicts and streamline network traffic management, facilitating easier troubleshooting and monitoring.

4 EMI & new shielding concept

4.1 Background and Initial Findings

Our investigation aimed to understand the root causes of EMC/EMI issues in the Tornado aircraft's FTI system. During the initial EMC System Interaction Testing, significant interference was detected on the UHF "Guard Channel" (=emergency channel). The sample measurement shown in Figure 3 illustrates these significant EMI peaks. These issues were particularly concerning as they could compromise the safety of the aircraft.

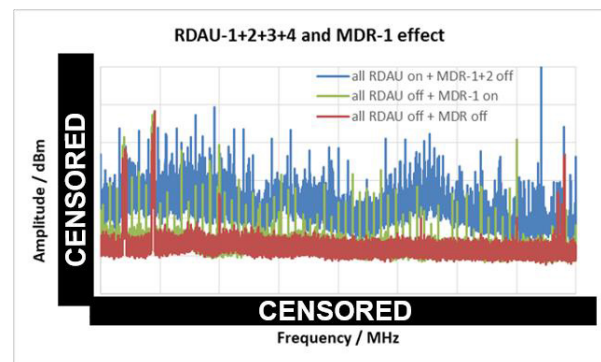


Fig. 3. EMI measures with the legacy shield

High levels of broadband EMI (peaks & higher floor level) were found in the ventral avionics bay containing the RDAU units, covering VHF and UHF bands, and a repetitive "raster" signal near the MDR (Modular Data Recorder) unit in the left-hand bay.

4.2 Problem identification

4.2.1 Shield terminations and grounding

Our assessment of the FTI installation revealed several core issues. Cable shield terminations were often bonded only at one end, and shields

were grounded through connector pins, leading to poor EMI containment.

4.2.2 Use of pigtailed

Some cable shields were connected to ground using long pigtailed (over 30 cm), significantly increasing susceptibility to EMI. EMC engineers commonly identify poor cable shielding and terminations as primary issues associated with system-level emissions. Often, these poor terminations occur when a cable's shield is twisted into a single wire, known as a "pigtail," and connected to ground. While pigtailed were a practical, inexpensive, and easy-to-use solution suitable for the infrastructures of the 1970s, they are now completely inadequate in a modern architecture with much stronger EMI.

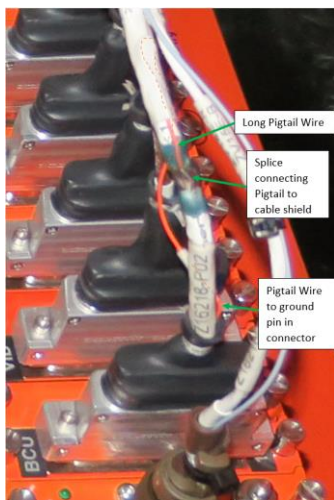


Fig. 4. Example of a bad pigtail: 17cm long, connected via a pin in the connector to the chassis inside the housing

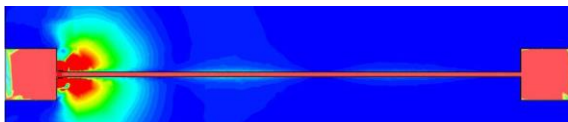


Fig. 5. Illustrative EMI measures of an installation with a pigtail on the left (<http://rfemcdevelopment.eu/>)

4.2.3 Connector Bonding Issues

Connector inspections revealed that paint on the shells prevented proper bonding to the mounting plates and many shields were not correctly bonded to their shells. Figure6 shows on its upper part a shield not bonded to the connector shell with the pigtail fed through a pin while its lower part illustrates a correctly bonded shield.

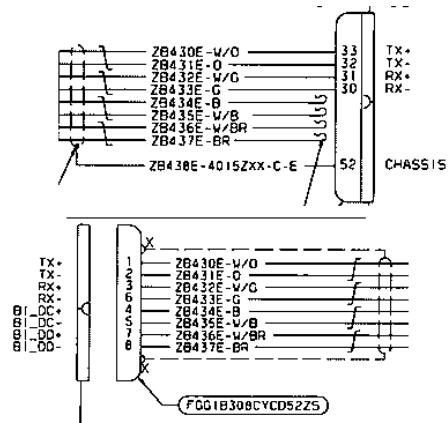


Fig. 6. Old (up) vs new shield (below): from not bonded to connector shell to correctly bonded to connector shell

Further examination indicated that improper shield terminations and liberal use of pigtailed were significant contributors to the high EMI levels observed. Moreover, the presence of paint on the connector shells further impeded effective grounding leading to increased electromagnetic interference.

4.3 Problem resolution

4.3.1 Revised electrical drawings

To address these issues, we revised the electrical drawings (see Figure6) to ensure proper shield terminations.

4.3.2 Corrective Measures

We corrected the bonding at connector backshells, removed the pigtailed (preferring a more expensive but more efficient 360° coverage at the connectors), and ensured all shields were grounded directly to the connector shells or chassis. Additionally, we adjusted the FTI datalink transmission rate to shift the raster signal off the guard channel frequency. The implementation steps included updating the electrical drawings, reinstalling the corrected cables, installing High-Pass filters in the TXs (telemetry transmitters), and verifying the effectiveness of these adjustments as illustrated in Figure5. These corrective measures were developed in consultation with the EMC department to ensure comprehensive resolution of the underlying issues.

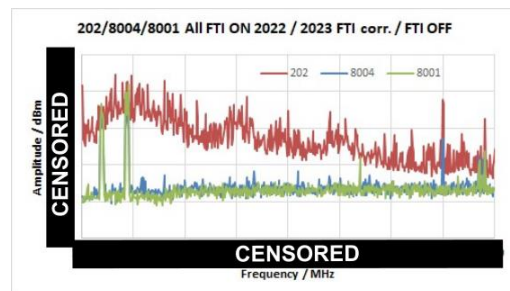


Fig. 7. Old shield (red) vs new shield (blue)

4.4 Verification and assessment

4.4.1 Post-Implementation Measurements

Following the implementation of the corrective measures, we conducted post-implementation measurements to verify their effectiveness. The comparison of EMI levels shows a significant reduction after the corrections, confirming the success of our solutions. The red line (202) represents the EMI levels before corrections, the green line (8001) shows the ambient environment, and the blue line (8004) indicates the levels after implementing the corrective measures.

4.4.2 Antenna Pickup Measurements

Additionally, antenna pickup measurements confirmed the absence of interference (no peak, no floor augmentation) on the guard channel frequency. These results demonstrate the effectiveness of the implemented solutions in mitigating EMI issues and improving overall system performance.

4.5 Specific action for GS-062 and GS-117

4.5.1 Compliance with PAN 6850

Based on EMC recommendations, we ensured all FTI cabling installations complied with PAN 6850. We replaced existing Ethernet cables with higher category cables where necessary and removed the pigtails.

4.5.2 Cable Replacement and Bonding

Proper bonding of all connectors to the chassis or shell was also ensured. The execution plan involved sequencing the refurbishment and testing of GS-062, GS-177 and GS-217, prioritizing immediate testing and verification for GS-062, focusing on electrical drawings creation for GS-217, and final implementation for GS-177.

4.6 Summary of the new shielding concept

4.6.1 Overall shielding approach

Our new shield concept involves utilizing an overall shield for cable bundles, connected with 360° coverage at the connectors, providing superior shielding compared to previous methods. This approach enhances EMI performance, improves signal integrity, and ensures compliance with PAN 6850 standards.

4.6.2 Implementation & cooperation

Moving forward, we will continue to work with manufacturers to improve the EMC characteristics of the MDR telemetry card and monitor and verify EMI levels post-refurbishment to ensure long-term compliance. This comprehensive shielding approach is designed to prevent any electromagnetic interference from affecting the sensitive

instrumentation systems, ensuring reliable data transmission and system performance.

4.6.3 Impact of the new Shield Concept

The implementation of this new shield concept is a significant step towards maintaining the integrity and reliability of our flight test data. Ongoing collaboration with manufacturers will be critical in refining these shielding techniques and adapting them to future technological advancements.

5 FTI & telemetry upgrades

5.1 Context

The refurbishment of the Tornado aircraft's telemetry systems marked a significant technological transition from analog S-Band/FM/Ch4 telemetry to a more advanced digital C-Band/SQPSK/Ch7 system, incorporating a new Modular Data Recorder (MDR). This shift aimed to enhance the capabilities and efficiency of data acquisition and analysis but introduced complex synchronization challenges.

5.2 First implementation: synchronization issues

The initial setup in the upgraded telemetry system, referred to as the 'red solution', involved randomizing data at the transmitter outputs (TX). This configuration did not include randomization between the MDR and the TXs, which necessitated a clock signal due to the absence of randomization in this segment.

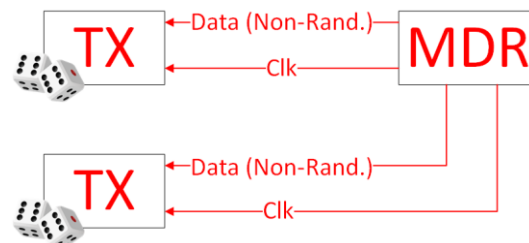


Fig. 8. First implementation: NRZL between MDR and TX. Randomization at TXs level

This initial setup in the upgraded telemetry system, involved randomizing data at the transmitter outputs (TX) level.

Nevertheless, with this setup, synchronization issues were noticed on the received signal at the FTGS.

- FTGS point of view: The FTGS team observed no issues within their receiver (RX), decryptor, or Ground Modular Data Recorder (GMDR) chain, suggesting that the challenge might originate from the FTI configuration itself.

- FTI point of view: The FTI team noted that this setup worked without issue both when used with the Dimona test aircraft and within the FTI labor, the problem may then come from the data processing at the FTGS.

It has been finally discovered that the synchronization problem was occurring on the FTI side, more specifically from the decentralized randomization taking place at the level of the 2 TXs which led to timing discrepancies between outputs. Even small (some ms), they were enough to provoke the signals desynchronization.

Since the Dimona has only a single TX, this problem was not detected when testing this setup with this test A/C in an earlier phase. Similarly, in the FTI labor with 2 TXs, power levels were much different from real cases, and not provoking this symptom.

5.3 New implementation

Recognizing the need to address the transmitter synchronization issue, a new setup was developed, with a centralized randomization at the MDR level, ensuring synchronized outputs and eliminating the discrepancies observed with the first setup.

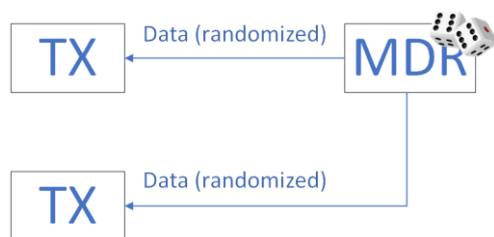


Fig. 9. New implementation: R-NRZL between MDR and TX. Randomization at MDR level

5.4 Temporary mitigation

While identifying the issue developing a fixes setup, a temporary configuration was implemented to maintain system functionality without interruptions: we temporarily used a C-Band/Analogue FM/Ch4 configuration, combining the new standard C-Band frequency with the legacy analog modulation. This setup provided a middle ground by utilizing the new frequency band while maintaining the more synchronization-tolerant FM modulation until the new FTI setup was fully operational.

6 Lessons learnt

- Project Management Complexity: Managing simultaneous refurbishments of multiple Tornado models required meticulous planning and execution. Balancing the integration of new measurement systems, regular maintenance, and synchronization

of updates without disrupting the project timeline underscored the importance of effective project management.

- Strategic Financial and Technical Resource Allocation: Effective financial management was critical for integrating advanced systems and new telemetry infrastructure. Addressing obsolescence in test installations and measurement systems required significant investments in new HW and SW, highlighting the need for strategic resource allocation. A poorly managed refurbishment could cost more than the purchase of a new fleet on the long term.
- Stakeholder relationships: External factors such as COVID-19 and geopolitical tensions complicated supplier management and logistic. This underscored the value of maintaining robust relationships with stakeholders like WTD61 and various suppliers to ensure consistent supply and integration of components.
- Specificities in working with old systems: Working with ancient systems brings specific challenges, including poor documentation and outdated concepts from an era of a.o. low EMI levels and non-encrypted flight transmissions. Some original suppliers no longer exist or have been acquired, complicating spare parts sourcing and upgrades. Adapting to new regulations required detailed engineering assessments and documentation updates, especially for EMC PAN 6850 compliance. Overcoming certification hurdles for older components highlighted the need for reevaluating standards. Be prepared to retest and recertify ancient systems and develop hybrid solutions that integrate legacy technologies with modern standards to ensure compatibility and functionality. These challenges highlighted the importance of a good documentation and extensive personnel trainings.
- Managing Parallel Infrastructures: The FTI refurbishment required the parallel maintenance of two dedicated infrastructures for the Tornado (Legacy & Refurbished): two complete SW chains (FTI to FTGS) and two SW ecosystems on the FTGS side (Pre-Flight/In-Flight/Post-Flight). This added complexity to an already intricate environment, as other programs like the EFA are managed simultaneously. Developing a refurbished version did not eliminate the need to support the legacy version, which continues to operate concurrently.

- Testing under real conditions is irreplaceable: The difference between controlled test scenarios and real operational environments highlighted the need for more robust and realistic testing protocols. Unexpected system behaviors in actual conditions emphasized the importance of thorough real-world testing.
- Value of Cross-Departmental Collaboration: Successful refurbishment relied heavily on collaboration across multiple departments, including FTI, FTGS, EMC, DO, and electrical drawing. This cooperation was vital for solving complex issues and integrating various system components effectively.

7 References

- [1] Heiko Körtzel, Marvin Götze, Karsten Keil.
"Implementing a New Telemetry Architecture into a Fighter Type Aircraft", ettc2021

8 Acknowledgements

I would like to warmly thank my colleagues John Ockerse, Heiko Körtzel, Christian Diederichs, Melissa Schatz and Sven Luboeinski, without whom this white paper would not have been possible.

9 Glossary

ADS	Airbus Defence and Space
a.o.	Amongst Others
BCU	Bus Control Unit
clk	Clock
Dimona	Dimona H-36 D-KARG A/C
DO	Design Office
EFA	Eurofighter
EMC	Electromagnetic Compatibility
EMI	Electromagnetic Interference
FM	Frequency Modulation
FTGS	Flight Test Ground Station
FTI	Flight Test Instrumentation
(G)MDR	(Ground Based) Modular Data Recorder
GNSS	Global Navigation Satellite System
GS	German Strike
GT	German Tactical
IGMP	Internet Group Management Protocol
IP	Internet Protocol
IRIG	Inter-Range Instrumentation Group

NRZL	Non-Return-to-Zero-Level
PAN	Panavia
PCM	Pulse Code Modulation
PTP	Precision Time Protocol
QoS	Quality of Service
RNRZL	Rand. Non-Return to Zero Level
RTC	Real-Time Clock
SOQPSK	Shaped Offset Quadrature Phase-Shift Keying
TOR	Tornado
TTC	Trigger, Timing, and Control
UDP	User Datagram Protocol
UHF	Ultra-High Frequency
VHF	Very High Frequency
WTD	Wehrtechnische Dienststelle

Automating Data Conversion

Fatih Hacıömeroğlu, Raşit Uzun, Mehmet Kekeç, Ali Tahsin Kaymak
Turkish Aerospace, Ankara

fhatiomeroglu@tai.com.tr, rasit.uzun@tai.com.tr, mehmet.kekec@tai.com.tr, alitahsin.kaymak@tai.com.tr

Abstract

Data Acquisition Units provide raw data which needs to undergo a data conversion process, named as either “Engineering-Unit Conversion” for sensor parameters or “Avionic Data Decoding” for avionic parameters. Albeit trivial, this step is crucial, since a simple typo suffices to jeopardize all of the instrumentation efforts. Considering the enormity of the instrumentation, the increased frequency of flights accompanied with changes in sensor and avionic configurations, need for helper tools emerged, to prevent us from relying solely on the attention of the Instrumentation Engineers. In this paper, which is in the same spectrum as the works submitted in the two previous conferences, we present some of the developed utility tools. First one is a tool to generate conversion formulas of all sensor parameters (from Parameter List file and instrumentation definition file (xidml file)) as well as to perform some sanity checks of the Parameter List aiming to minimize human errors. Besides, another tool to compare formulas is presented. This second tool is valuable because it enables to compare formula sets residing in different locations (i.e. hangar computer, lab computer and telemetry room), and to ensure the equivalency of the formulas.

Key words Data Management Applications

Introduction

Starting with the T625 Gökbey Project, the volume of data request increased considerably. It became conventional to use a structured spreadsheet named “Numbered Parameter List” (NPL) for management of the data requests.

Instrumentation architecture of the data acquisition system is Ethernet-based [1, 2].

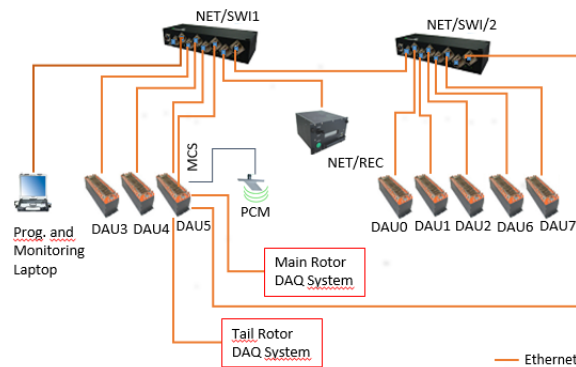


Fig. 1 Instrumentation Architecture in T625

In dealing with numerous parameters, the formula creation becomes an important and critical task, better not performed manually. Relying solely on the attention of the Instrumentation Engineer would not be wise since a simple typo can have severe outcomes. In case of any human error, such as taking wrong calibration coefficient, or wrong sensitivity for a sensor, or using wrong voltage

levels than the ones, which the measurement channel’s gain setting imposes, the output turns out to be erroneous. It is unfortunate that such errors cause not only flight test interruptions, but also doubts in data requesters mind about the instrumentation system, which made them think that any abnormal data is a result of such an error. Although in practice, an abnormal data is normally the result of an anomaly or malfunction in the system of interest. Hence, data analysis process suffers because people starts to shortcut their reasoning and question the instrumentation system rather than the measured system. To prevent such unfortunate interpretations, we cannot emphasize enough the importance of a tool for automating sensor related formula generation.

On the other hand, another difficulty lies in the fact that there are formula sets in different locations. The computers in Lab, in hangar and in telemetry room have their own formula sets. We worked on a tool to ease checking their equivalency (both textually and computationally).

Manual Formula Creation

EU formula converts the raw data obtained from a DAU (Data Acquisition Unit) channel to an Engineering Unit data, amenable to data analysis. As an example, consider a formula for a strain gage, named STR153c.

Here, STR is an acronym for strain measurement, “1” means it is from the location coded as 1 (cabin area), “53” is a number uniquely identifying the sensor (we can infer that there are at least 52 gages defined in cabin area other than this one), finally “c” means that it is a rosette leg (other legs are named as STR153a and STR153b).

$$\text{STR153c} = \text{D2_J6_ADC_135_B_ch3}/65535*(0/009765625-0/0048828125)/2.5*4/(1*2.14)*1e6$$

Fig. 2 An example formula

This formula is entered in our Data Conversion and Monitoring tool (IADS [4]) as a field entry of a table. In the tool, the table to hold Conversion formulas is named as “*ParameterDefaults*” table, and the field, which contains the text of the formula is named as “*DataSourceArgument*” field. Descriptions of the terms, based on their order in the formula are as follows:

- **D2_J6_ADC_135_B_ch3** is the raw parameter that DAU is programmed to output. (has to be fetched from NPL and xidml)
- **65535** comes from 16 bit sampling done by DAU
- **0.009765625** and **0.0048828125** come from the channel gain settings (from maximum and minimum voltages) (they have to be fetched from xidml file, based on the channel information in NPL)
- **2.5** is the voltage excitation of the bridge (has to be fetched from xidml file)
- **4** is a constant term in strain formula
- **1** is the Bridge Factor. It is 1 for “STR” parameters (quarter bridges having one active leg)
- **2.14** is the Gage factor (has to be fetched from NPL)
- **1e6** is a coefficient to obtain EU parameter in terms of microstrain

This structure is used for all of the strain (STR) measurements.

There are various reasons why formula generation can become erroroneous: First, there are different types of formulas for each sensor type. Other than STR, there are 24 different analog data types, such as ACC for Accelerometers, POT for Potentiometer sensors, PRE for Pressure Sensors, etc. Generally the structure is similar and can be reduced to the form given in Equation 1:

$$\text{EU Parameter} = \frac{\text{Measured Voltage}}{\text{Sensitivity}} + \text{Offset}$$

Eq. 1 Generic EU conversion formula for a sensor

where “*Sensitivity*” is in terms of mV/EU and “*Offset*” is EU value when sensor output is 0

mV. However not all of the sensor types can be written in this manner. For example the analog parameters obtained from the 3rd Party Rotating Data Acquisition systems has system specific formulas. Moreover, within a single data source type, we may have more than one formula structure. For instance the structure of the formula for an RTD sensor depends on whether its excitation is done by instrumentation system or excitation is handled by the system in Platform.

Second, the sheer number of parameters is challenging to handle. One can very likely enter a wrong information in one of the formulas if he/she is supposed to enter hundreds of formulas.

Third, there are cases where the structure can have slight changes. For instance, the triaxial vibration sensor parameters may require orientation correction. Similarly; if a triaxial sensor is installed for *VIB101x*, *VIB101y*, *VIB101z* measurement and x/y/z conventions of the Platform are not as the orientation of the sensor as it is installed, then we will need to convert the orientation. For example, we may have a case where we are measuring z axis of the platform from the x channel of the sensor. Oftentimes such conversions are error-prone.

Finally, the IADS’s *ParameterDefaults* table also contains many other fields than the “*DataSourceArgument*” field. For instance; the *Group* and *SubGroup* fields are useful in sensor grouping. Moreover *SubGroups* can be used for easy grouping of parameters for data export groups. More than rarely, when entering such fields, there are inconsistencies that cause confusion. It would be much better to have a standardization, which enforces conventions on the *ParameterDefaults* table.

As a result, for all of the above potential error sources, it is of utmost importance to generate formulas automatically in the process, where severe consequences might occur as discussed in the Introduction section.

Master Formula Generator

We have used Python to implement the tool. Main libraries which are used extensively are:

- **pandas** : for NPL reading, for merging NPL and xidml, for dumping results
- **minidom** : for xidml reading
- **re** : for NPL checks, for xidml and NPL sheet binding in merging process

The tool performs the tasks depicted in the following diagram:

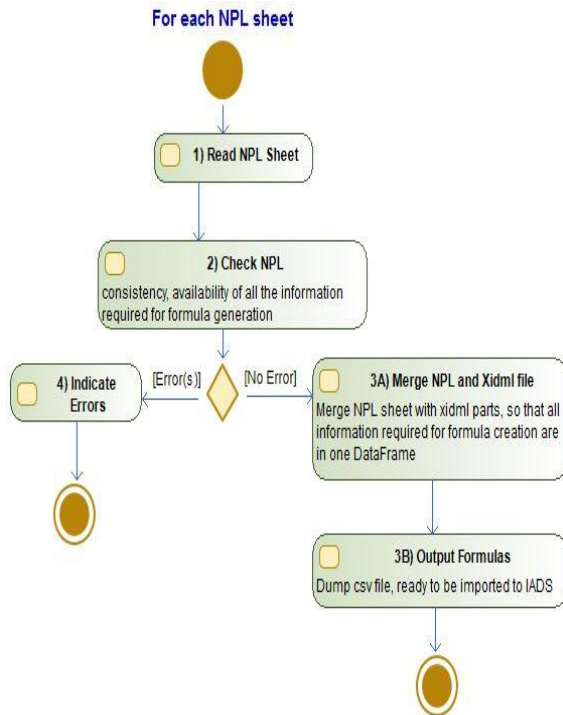


Fig. 3 Activity Diagram of the operations for a single sheet in NPL

STEP 1) Read NPL Sheet

All sheets are read separately, it is logical for the tool to loop each sheet because structure of the formulas depends mainly on the sensor types (hence sheets in NPL’s).

STEP 2) Check NPL

We implemented an architecture to easily define checks on NPL so that we are in a better position to generate formulas. Checks are regular expressions (regex’s) imposed on the content of specific columns of NPL. For instance, the below code snippet shows the checks imposed on the “POT” sheet of NPL (Potentiometer measurements).

```
# POT sheet checks #####
CHECKS['ONE_COLUMN']['POT'] = {(1, 'Unit'): 'ONLY_mm',
                               (2, 'ParameterName'): 'POT_PARAMNAME',
                               (3, 'ParameterNo'): 'POT_PARAMNO',
                               (4, 'RealTimeFrequencyHz'): 'IS_WHOLE_NUMBER',
                               (5, 'Sensitivity'): 'IS_NUMBER_WITH_OR_WITHOUT_mVpm',
                               (6, 'ZeroOffset'): 'IS_NUMBER_WITH_OR_WITHOUT_mm'}
CHECKS['TWO_COLUMN_SUBSTRING']['POT'] = {(1, 'ParameterNo', 'Zone')
                                          : ('GET_ZONE_FROM_PARAMETERNO', 'GET_ZONE_FROM_ZONE')}
```

Fig. 4 Example of NPL checks defined for POT sheet

Each element imposes a rule to check. For instance:

- The “Unit” column must obey the regular expression saved as “ONLY_mm” (which is `^\\s*(?-i:mm)\\s*$`). If it is empty or something else, the check will fail.
- “ZeroOffset” column must obey regex named as “IS_NUMBER_WITH_OR_WITHOUT_mm” (which is `^\\s*(-?\\d+|-?\\d*\\.\\d+)\\s*$|\\s*(-?\\d+|-?\\d*\\.\\d+)\\s*mm\\s*$`). If zero offset is empty or is filled something else, the check will fail.

The above examples are so-called “one-column” checks. Also “two-column” checks can be defined. For POT sheet, one such “two-column” check is defined as below.

- The “ParameterNo” column must obey a regex named “GET_ZONE_FROM_PARAMETERNO” (which is `^\\s*\\w{3}(\\d)(?\\:\\d{2})\\d{1}[a-zA-Z][[a-zA-Z]{2}][xyzXYZabcABC]*\\s*$`)
- The “Zone” column must obey a regex named as “GET_ZONE_FROM_ZONE” (which is `^([0-9])(\\.0)*`). Both must give the same output. For instance if parameter is POT304 (3 being the location (zone) number), the zone column must be 3.

A sheet may have as many checks as desired. For instance, the checks defined for RTD sheet are more than the ones defined for POT sheet. In RTD case, there are “two-column” checks such as checking if “Excitation Current” field is entered in case RTD is an externally excited one (i.e. excited by the system, not by DAU). Note that checks for informations that should not be entered are also defined, for instance if an RTD excitation is done by DAU, its column named “Alpha” should be empty (as the DAU provide the linearized output and we do not need alpha coefficient of the RTD inside the formula for an RTD excited by DAU).

```
# RTD sheet checks #####
CHECKS['ONE_COLUMN']['RTD'] = {(1, 'Unit'): 'ONLY_C',
                               (2, 'ParameterName'): 'RTD_PARAMNAME',
                               (3, 'ParameterNo'): 'RTD_PARAMNO',
                               (4, 'RealTimeFrequencyHz'): 'IS_WHOLE_NUMBER',
                               (5, 'ExcitationSource'): 'IS_PROPER_RT_EXCITATION_SOURCE'}
CHECKS['TWO_COLUMN_SUBSTRING']['RTD'] = {(1, 'ParameterNo', 'Zone')
                                          : ('GET_ZONE_FROM_PARAMETERNO', 'GET_ZONE_FROM_ZONE')}
CHECKS['TWO_COLUMN']['RTD'] = {(1, 'ExcitationSource', 'ExternalExcitation')
                               : ('IS_KANS00_EXCITATION', 'IS_EMPTY'),
                               (2, 'ExcitationSource', 'ExternalExcitation')
                               : ('IS_EXTERNAL_EXCITATION', 'IS_NUMBER_WITH_OR_WITHOUT_mA'),
                               (3, 'ExcitationSource', 'Alpha')
                               : ('IS_KANS00_EXCITATION', 'IS_EMPTY'),
                               (4, 'ExcitationSource', 'Alpha')
                               : ('IS_EXTERNAL_EXCITATION', 'IS_NUMBER_WITH_OR_WITHOUT_ohmPC'),
                               (5, 'ExcitationSource', 'Rref')
                               : ('IS_KANS00_EXCITATION', 'IS_EMPTY'),
                               (6, 'ExcitationSource', 'Rref')
                               : ('IS_EXTERNAL_EXCITATION', 'IS_NUMBER_WITH_OR_WITHOUT_ohm')}
```

Fig. 5 Checks defined for RTD sheet of NPL

As a by-product of this work, more involved checks of some columns of NPL (other than the ones for formula generation) are implemented. For instance we check if serial numbers of sensors are added, whether they are unique,

whether the parameter names follows our convention etc. Note that having lacked time at the beginning of the Project, we contented to use a spreadsheet named NPL for handling parameter requests. Implementing such auxiliary checks is a useful band-aid to make this spreadsheet based Parameter List handling method more robust.

NPL is read as a pandas DataFrame and the checks are actually created using a class named “*DataFrameChecker*”, which first transforms all the DataFrame into strings. The defined rules can be added into a *DataFrameChecker* and the results can be obtained. Using such a method leads to flexibility in adding/removing/applying checks.

STEP 3A) Merge NPL and Xidml File

Below diagram shows the tasks inside the Merge task.

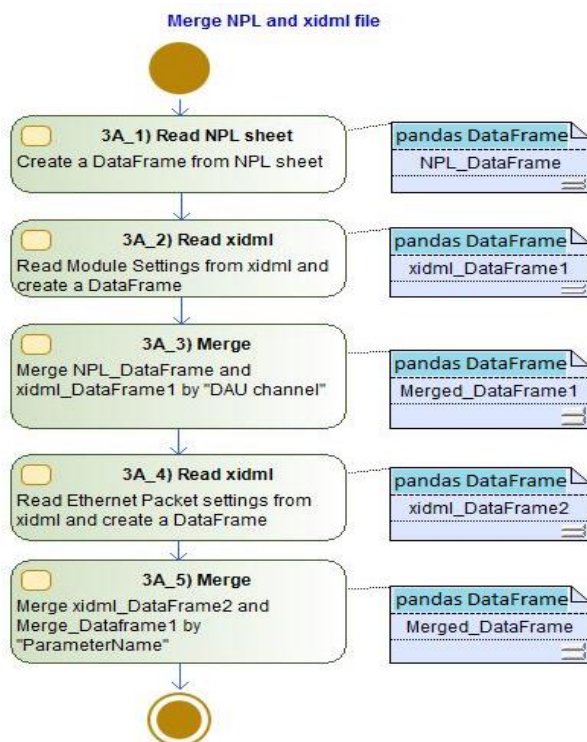


Fig 6 Steps of Collecting Information to use in automatic creation of the IADS's ParameterDefaults table

To create a formula, we need to gather information. For example to generate formula given in Figure 2, we need to collect the parameter name, gage factor, the channel number on which the gage is connected to, the channel settings (maximum and minimum voltages of ADC), excitation setting, etc. IADS's parameter default contains not only the formula string but also other fields that we want to fill automatically. For instance we will set the *SubGroup* as “FTI_STR_1024Hz” for STR153b,

because this parameter is sampled at 1024Hz, which can be inferred from the xidml file. This will be used for grouping for data exporting purposes, so that all parameters having same *SubGroups* will be exported together.

Figure 7 to Figure 10 are screenshots illustrating what the DataFrames in Figure 6 look like (for demonstration purposes, DataFrames for only two accelerometers in ACC sheet of NPL are considered).

Once NPL and xidml are read into DataFrame's, we make use of the pandas' built-in merge capability according to any common content in DataFrames, similar to table joining operations in database tables. We have to read xidml twice, first for channel settings and second for ethernet packet rate settings (from which we calculate parameter recording rates to fill the *SubGroup* field). We also merge twice, first by channel and then by parameter name.

STEP 3B) Create and Output Formulas

Having assembled all the required parameters in a single DataFrame, creating formulas for a specific sheet is a straight-forward task of string concatenations. Figure 13 shows the output for this demo case. As can be seen, two formulas are created for a single channel. For instance for ACC101x channel, we have one formula for EU conversion (ACC101_g) and one formula for the millivolt representation (ACC101_mV) (It is useful to generate such middle parameters, particularly for troubleshooting).

Note that all information are combined either from NPL or xidml file. For instance *SubGroup* columns are different for ACC101 and ACC201 since they are sampled at different rates as deduced from xidml file. Moreover, ACC101 channels are not oriented but the ACC201 ones are. (Note that small blank gaps left in the formula of ACC201 provides a visual hint to indicate that orientation was performed).

STEP 4) Indicate Errors

If there is an error or an inconsistency, the tool indicates the specific parameters where information is not properly entered in NPL. Full reliance to the defined rules is expected. Since the rules can be created per each measurement type, in a flexible fashion by using regex's, this process results in a clarified parameter list from which reliable EU conversion formulas are obtained.

The output provides references to where are the errors as well as what they are. An example for errors and inconsistencies in Parameter List are provided in Figure 11.

-	Parameter No	Zone	Requester	Parameter Name	Unit	Recording Frequency (Hz)	Real Time Frequency (Hz)	Sensor Name	Serial Number	Sensitivity	Orientation
D4_J6_Ch0	ACC101x	1	ATAQ330	ACC101x_CG_g	g	256	256	DC Accelerometer (Dytran 7503D4 25g)	11001	159,2	
D4_J6_Ch1	ACC101y	1	ATAQ330	ACC101y_CG_g	g	256	256	DC Accelerometer (Dytran 7503D4 25g)	11001	159,75	
D4_J6_Ch2	ACC101z	1	ATAQ330	ACC101z_CG_g	g	256	256	DC Accelerometer (Dytran 7503D4 25g)	11001	159,5	
D1_J9_Ch16	ACC201x	2	ATAQ320	ACC201x_AHRS2_g	g	4096	256	DC Accelerometer (Dytran 7503D3)	10876	401,3	CableLEFT StudDOWN
D1_J9_Ch17	ACC201y	2	ATAQ320	ACC201y_AHRS2_g	g	4096	256	DC Accelerometer (Dytran 7503D3)	10876	404,4	CableLEFT StudDOWN
D1_J9_Ch18	ACC201z	2	ATAQ320	ACC201z_AHRS2_g	g	4096	256	DC Accelerometer (Dytran 7503D3)	10876	402,1	CableLEFT StudDOWN

Fig.7 ACC sheet of NPL for this example case

DAU_Slot_Ch	ParameterName	Filter Cutoff	Unit	RangeMax	RangeMin
4_6_0	D4_J6_ADC_112_10V_ch0	0.5	VoIt	10	-10
4_6_1	D4_J6_ADC_112_10V_ch1	0.5	VoIt	10	-10
4_6_2	D4_J6_ADC_112_10V_ch2	0.5	VoIt	10	-10
4_6_3	D4_J6_ADC_112_10V_ch3	0.5	VoIt	10	-10
4_6_4	D4_J6_ADC_112_10V_ch4	0.5	VoIt	10	-10
4_6_5	D4_J6_ADC_112_10V_ch5	0.5	VoIt	10	-10

Fig. 8 DataFrame created from xidml (only ACC101 related part is shown)

Index	ParameterNo	MeasurementName	Unit_NPL	RecordingFrequency/Hz	Sensitivity	Orientation	parameterName_XIDML_PARAM	RangeMax	RangeMin	Stream_ID	inet_Name	Parameter_Name	Occurrences	SampleRate	
0	D4_J6_Ch0	ACC101x	Body Accelerat...	g	256	159.2	NOT ORIENTABLE	D4_J6_ADC_112_10V_ch0	10	-10	60	D4_Voltage_256Hz	D4_J6_ADC_112_10V_ch0	4	256
1	D4_J6_Ch1	ACC101y	Body Accelerat...	g	256	159.75	NOT ORIENTABLE	D4_J6_ADC_112_10V_ch1	10	-10	60	D4_Voltage_256Hz	D4_J6_ADC_112_10V_ch1	4	256
2	D4_J6_Ch2	ACC101z	Body Accelerat...	g	256	159.5	NOT ORIENTABLE	D4_J6_ADC_112_10V_ch2	10	-10	60	D4_Voltage_256Hz	D4_J6_ADC_112_10V_ch2	4	256
3	D1_J9_Ch16	ACC201x	AHRS X	g	4096	401.3	CableLEFT StudDOWN	D1_J9_ADC_112_10V_ch16	10	-10	49	D1_Voltage_4096Hz	D1_J9_ADC_112_10V_ch16	16	4096
4	D1_J9_Ch17	ACC201y	AHRS Y	g	4096	404.4	CableLEFT StudDOWN	D1_J9_ADC_112_10V_ch17	10	-10	49	D1_Voltage_4096Hz	D1_J9_ADC_112_10V_ch17	16	4096
5	D1_J9_Ch18	ACC201z	AHRS Z	g	4096	402.1	CableLEFT StudDOWN	D1_J9_ADC_112_10V_ch18	10	-10	49	D1_Voltage_4096Hz	D1_J9_ADC_112_10V_ch18	16	4096

Fig.9 Merged DataFrame

ParameterDefaults	Parameter	ParamType	ParamGroup	ParamSubGroup	ShortName	LongName	Units	Color	Width	DataSourceType	DataSourceArgument	UpdateRate
FTI_ACC	ACC101x_CG_g	float	FTI_ACC	FTI_ACC_256Hz	ACC101x_g	Body Acceleration from CG X axis	g			Derived	(D4_J6_ADC_112_10V_ch0/65536*20-10)*1000 / 159.2	256
FTI_ACC	ACC101y_CG_g	float	FTI_ACC	FTI_ACC_256Hz	ACC101y_g	Body Acceleration from CG Y axis	g			Derived	(D4_J6_ADC_112_10V_ch1/65536*20-10)*1000 / 159.75	256
FTI_ACC	ACC101z_CG_g	float	FTI_ACC	FTI_ACC_256Hz	ACC101z_g	Body Acceleration from CG Z axis	g			Derived	(D4_J6_ADC_112_10V_ch2/65536*20-10)*1000 / 159.5	256
FTI_ACC	ACC201x_AHRS2_g	float	FTI_ACC	FTI_ACC_4096Hz	ACC201x_g	AHRS X	g			Derived	(D1_J9_ADC_112_10V_ch17/65536*20-10)*1000 / 404.4	4096
FTI_ACC	ACC201y_AHRS2_g	float	FTI_ACC	FTI_ACC_4096Hz	ACC201y_g	AHRS Y	g			Derived	(D1_J9_ADC_112_10V_ch16/65536*20-10)*1000 / 401.3	4096
FTI_ACC	ACC201z_AHRS2_g	float	FTI_ACC	FTI_ACC_4096Hz	ACC201z_g	AHRS Z	g			Derived	(D1_J9_ADC_112_10V_ch18/65536*20-10)*1000 / 402.1*(-1.0)	4096
FTI_ACC	ACC101x_CG_mV	float	FTI_ACC	FTI_ACC_256Hz	ACC101x_mV	Body Acceleration from CG X axis	mV			Derived	(D4_J6_ADC_112_10V_ch0/65536*20-10)*1000	256
FTI_ACC	ACC101y_CG_mV	float	FTI_ACC	FTI_ACC_256Hz	ACC101y_mV	Body Acceleration from CG Y axis	mV			Derived	(D4_J6_ADC_112_10V_ch1/65536*20-10)*1000	256
FTI_ACC	ACC101z_CG_mV	float	FTI_ACC	FTI_ACC_256Hz	ACC101z_mV	Body Acceleration from CG Z axis	mV			Derived	(D4_J6_ADC_112_10V_ch2/65536*20-10)*1000	256
FTI_ACC	ACC201x_AHRS2_mV	float	FTI_ACC	FTI_ACC_4096Hz	ACC201x_mV	AHRS X	mV			Derived	(D1_J9_ADC_112_10V_ch17/65536*20-10)*1000	4096
FTI_ACC	ACC201y_AHRS2_mV	float	FTI_ACC	FTI_ACC_4096Hz	ACC201y_mV	AHRS Y	mV			Derived	(D1_J9_ADC_112_10V_ch16/65536*20-10)*1000	4096
FTI_ACC	ACC201z_AHRS2_mV	float	FTI_ACC	FTI_ACC_4096Hz	ACC201z_mV	AHRS Z	mV			Derived	(D1_J9_ADC_112_10V_ch18/65536*20-10)*1000	4096

Fig. 10 IADS ParameterDefaults Table containing ACC101 and ACC201 formulas

VIB sheet needs correction:
 Column(s) : Sensitivity
 Check Description : IS_NUMBER_WITH_OR_WITHOUT_mVpg_or_pCpg
 Failing Rows : ['D4_J14_Ch3', 'D4_J14_Ch4', 'D4_J14_Ch5', 'D3_J15_Ch9', 'D3_J15_Ch10', 'D3_J15_Ch11', 'D4_J14_Ch8', 'D4_J14_Ch9', 'D4_J14_Ch10']

Column(s) : ParameterNo
 Check Description : VIB_PARAMETERNO
 Failing Rows : ['D7_J15_Ch11']

Column(s) : ('ParameterNo', 'Zone')
 Check Description : ('GET_ZONE_FROM_PARAMETERNO', 'GET_ZONE_FROM_ZONE')
 Failing Rows : ['D7_J15_Ch11']

Fig. 11 Example for indication of errors in VIB sheet

Formula Comparing

Normally, we have IADS sessions in 3 computers. First one is in the Laptop in Hangar, second one is in the Data Monitoring Room where engine tests on ground are performed, and a final one in the Telemetry Room. We are to ensure that all the formulas in these 3 places are same. The created Formula Generation tool is named as “Master” Formula Creation tool, (“Master” word is used in the sense that these formulas are the “original” or the “reference” ones.) A simple text based compare is by itself very helpful but we also did a computation wise comparison using synthetic value injection in places of raw data and middle parameters. In other words, we intend to compare formulas not only textually but also by their results. Basically “b+a+2” and “2+a+b” are considered as equivalent, although not “same” when compared textually.

Inspired from [5], lexical analysers, parsers and interpreters are implemented to evaluate formulas. We scan the formula character by character and match with defined tokens to form a tree, composed of nodes. The nodes can be either a “Leaf Node” (such as a constant of a variable) or a “Tree Node” (which are either operators (like addition and subtraction) or “Function Nodes” (as defined in IADS (such as pow(), byteswap16(), etc.)). Then, upon assigning values for variables (if present), a “Parser” evaluates the tree. Recursive nature of the process handles calculation of nested formulas as well as conditional formulas which are common in the present EU conversion formulas. An example formula and its Tree are given below, where leaf nodes and tree nodes are outlined orange and black respectively. Note that function nodes are also shaded. If it existed, names not known as functions would have been taken as variable names (like raw

data names), to which user could assign/inject values and calculate output of the formula.

$$(3 * \text{pow}(10, 2 * \text{byteswap16}(256)) + 1e2) * \sin(-30 * \pi / 180)$$

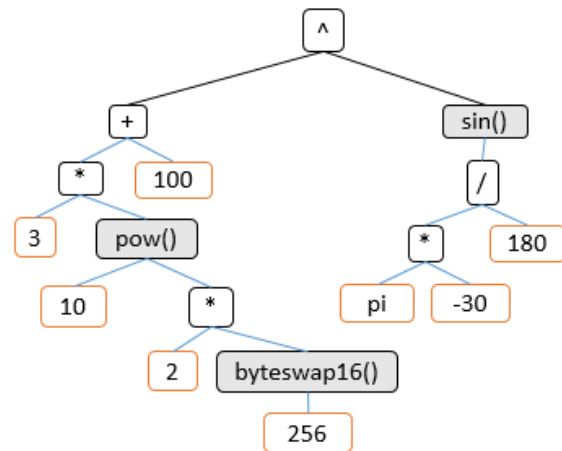


Fig. 12 Example formula and its Tree (outputs 0.05)

Conclusion

An error in an EU conversion formula could have devastating effects on the credibility of the instrumentation system and consequently shift the focus of data analyzers from measured system to the instrumentation system which is traditionally the easy target, the usual suspect, the first place where fingers are pointed in delicate flight test campaign processes. Therefore, it is wise to generate analog parameter formulas in an automatic fashion. We developed a software tool which is built to fetch required information from parameter list (NPL) and from the instrumentation configuration file (xidml file). The tool also performs some consistency checks during the process to enforce instrumentation engineers to prepare NPL and xidml in a structured fashion. The benefit of the tool can better be appreciated by realizing that even the provided minimal ACC examples contain tricky parts (such as orientation correction, subgroup differentiation, etc.). On the other hand a formula comparison tool by means of raw data injection is also developed to ensure that raw data is not subjected to different conversion in the data monitoring locations.

References

- [1] Automated PCM Placement, Fatih Haciomeroglu et al. ETTC 2023
- [2] Evolution of Data Exporting, Fatih Haciomeroglu et al. ETTC 2022
- [3] www.xidml.org
- [4] www.curtisswrightds.com
- [5] Chapter 19 of Programming Python 4th Ed. O'Reilly, Mark Lutz

A Review of FFT Algorithms and A Real-Time Algorithm Development for Airborne Vibration Testing Applications

Osman Birkan Ozseven^{1, 2}, Safak Tambova³, Mustafa Helvacı²

¹ *Department of Avionics and Electrical Systems, Turkish Aerospace, Istanbul 34467, Turkey; osmanbirkan.ozseven@tai.com.tr; +903128111800*

² *Department of Communication Systems, Istanbul Technical University, Istanbul 34467, Turkey; ozseven20@itu.edu.tr (O.B.O.); helvacim@itu.edu.tr (M.H.); +902123657800*

³ *Department of Flight Test Systems, eRC-System GmbH, Ottobrunn 85521, Germany; tambova@erc-system.com; +4915110652823*

Abstract

In Flight Test Instrumentation applications, many types of data are collected, including temperature, pressure, force, digital bus monitoring, etc. However, one type of data has always been popular and has become even more so with the increased use of composite structures: vibration. Vibration is a key measurement for different types of tests such as engine and propulsion system, flutter analysis, structural resonances, etc. In full-size air vehicle prototype testing, thousands or even ten thousand parameters are needed to be transformed over telemetry to the ground station. This operation itself already requires a significant amount of bandwidth in the communication channel and by considering the high-frequency behavior of vibration parameters, this situation becomes even worse. To overcome this problem, some techniques can be performed to increase the efficiency of communication by reducing the payload on the communication stream. The Fourier Transform decomposes a continuous-time signal into its foundational sinusoidal frequencies, bridging between the time and frequency domains. It reveals a signal's spectrum, denoting each frequency's strength and phase. This transformation is pivotal for understanding and isolating specific frequency components in continuous signals. The Discrete Fourier Transform (DFT) adapts the Fourier analysis to discrete-time signals, mapping a finite set of samples to a discrete frequency spectrum. It delineates the amplitudes and phases of sinusoids at distinct frequencies within digital signals. Central to digital signal processing, the DFT's efficiency is notably harnessed via the Fast Fourier Transform (FFT) algorithms. While conventional FFT algorithms are commonly favored, this paper distinguishes itself by adopting an alternative well-established method to achieve a more precise analysis in the real-time vibration analysis. In this paper, a review has been conducted to evaluate and compare well-known FFT algorithms. As a result of this review, the most efficient method has been used to solve a real-life aviation problem. The details of the problem have been given in the case-study chapter.

Key words: Chirp-Z Transform, Fast Fourier Transform, Flight Test Instrumentation, Real-Time Data Acquisition, Signal Processing, Vibration Testing.

Introduction

In the aerospace industry, data collection from air vehicles is crucial during the development or modernization stages while performing testing activities. The data which is obtained via air vehicle parts provides information about the efficiency of the systems. Although integrated systems have some standards, it is critical to see the system integrability with others [1]. To validate, verify, and certify the air vehicle in accordance with relevant standards, it is critical to implement a flight test instrumentation system design. This design should include a data acquisition unit, network switch, and

recorder, all smoothly integrated with the existing aircraft systems throughout the various stages of air vehicle development [2]. Since, there can be a requirement for the installation of additional equipment such as a sensor, transducer, and thermocouple to be able to collect temperature, vibration, strain, current, voltage, pressure, etc. data from the avionics or mechanical parts [3] [4]. In this paper, vibration data is analyzed in detail.

Vibration data collected from sensors contains information about the mechanical behavior of air vehicle components such as avionics, propulsion systems, control surfaces,

gearboxes, and airframe structures. In terms of safety and reliability, excessive vibration may be a reason for mechanical problems or component wear. By monitoring vibrations, aircraft operators can detect issues early, reducing the risk of in-flight failures, accidents, or the health of various components due to mechanical failures [5] [6]. Irregular vibrations can indicate problems such as imbalance, misalignment, fatigue, or damage to these components [7]. Additionally, in the matter of compliance, regulatory authorities generally require aircraft operators to monitor and report on various parameters, including vibration levels. Conformity with these regulations is crucial to ensure the airworthiness and safety of aircraft [8]. In connection with research and development, aircraft manufacturers and researchers may use the obtained vibration data to improve the performance of the aircraft design and material. This data aids in the development of more efficient and reliable aircraft [9].

Fourier Transform (FT) is a fundamental technique that breaks down continuous-time signals into their component sinusoidal frequencies. It connects the time domain (where signals vary over time) to the frequency domain (where signals are represented by their frequencies). In the time domain, signals are complex waveforms formed by overlapping waves, each with its frequency, phase, and amplitude [10]. FT transforms this into a frequency spectrum, showing the strengths and phases of each frequency in the original signal. This is useful for identifying dominant frequencies. For discrete signals in digital applications, DFT is used, which maps a sequence of numbers (discrete signal) to another sequence representing its discrete frequency components. This spectrum reveals amplitudes and phases of discrete frequencies that approximate the original signal when combined [11].

DFT algorithms enable the analysis of signals in the frequency domain. These algorithms are crucial tools for decomposing discrete-time signals into their underlying frequency components. The Cooley-Tukey Radix-2 FFT, a widely used DFT algorithm, excels at efficiently computing the DFT for data lengths that are powers of 2 [12]. Mixed-radix FFT extends this approach to handle data lengths that are not powers of 2 by employing mixed-radix stages. The Prime Factor FFT specializes in efficiently computing the DFT of data with prime factorization lengths. Furthermore, Bluestein's FFT, also known as the Chirp Z-Transform (CZT), is vital when working with signals of

arbitrary lengths, as it transforms them into a format suitable for FFT computation [13]. In the theory section, these algorithms are compared, and the most appropriate method is chosen for addressing the problem under consideration.

In this paper, a practical aviation challenge related to the propulsion system test is addressed. Specifically, during the propulsion system test, the transmission of vibration data to the ground station leads to significant constraints due to communication channel limitations. In response to this challenge, transmitting the vibration signal in its frequency domain format has been preferred, rather than the time domain signal, to facilitate real-time testing [14]. It's worth noting that a subsequent time domain analysis is also conducted during the post-data processing phase for comprehensive evaluation and insights. This approach allows to efficiently address the complexity of real-time data transmission and subsequent analysis in the context of aviation testing. In contrast to the widespread preference for conventional FFT algorithms in [15] and [16], this paper stands out by opting for the CZT Method, a well-established alternative, to attain a more precise analysis. Since, in spectral analysis, the frequency resolution of the FFT is intrinsically tied to the length of the signal window. This means that the resolution is determined by dividing the sampling rate by the number of points in the FFT. While zero-padding is a technique often employed to interpolate between FFT bins, it doesn't increase the genuine frequency resolution. On the other hand, the CZT introduces a significant flexibility. It allows for computation of the DFT samples within a specific region of the z-plane, enabling users to define a starting frequency, an ending frequency, and the desired number of points or frequency resolution between them. This capability of the CZT is particularly beneficial when the focus is on a specific frequency range rather than the entire spectrum. Band-Selectable Fast Fourier Transform (Zoom FFT) also provides targeted frequency analysis [17]. However, while Zoom FFT focuses on a specific frequency range through down-sampling after mixing to baseband, the CZT calculates spectral values across any chosen frequency interval directly. CZT also succeeds in handling non-uniformly sampled data, making it suitable for scenarios where data points are irregularly spaced in time [18].

This paper is organized as follows, a brief introduction to the topic covered by the paper is given in Chapter I. A theoretical comparison is made between different FFT algorithms and the

terms spectral leakage, windowing techniques, zero-padding and oversampling are given in Chapter II. Case study including the subsection of the propulsion system vibration analysis, the methods and techniques used in the CZT algorithm are given in Chapter III. Result analysis is performed in chapter IV. Concluding remarks are stated in Chapter V as performing CZT analysis in real-time.

Theory

In vibration analysis, the vibration data obtained from sensors placed on system components, continuously or at regular intervals are analyzed to predict whether there is a fault or not. Vibration signals taken from different points contain complex waveforms due to various forces and factors. Therefore, determining faults by examining time-waveform graphs is very challenging. The signals obtained in the time domain from vibration sensors are transformed into the frequency domain methods using the Fourier transform [19]. The frequencies within the spectrum provide valuable insights into not only the type but also the source of the fault, aiding in fault diagnosis. Concurrently, the amplitudes associated with these frequencies serve as a clear representation of the damage's severity, allowing for an accurate assessment of its extent. Specific faults occur at certain frequencies, and if the fault is not rectified, the amplitude at that frequency continues to increase. Faults exhibit various symptoms such as increased vibration, temperature, noise, and excessive current until the system malfunctions [7] [20]. Condition monitoring-based maintenance is performed by measuring and evaluating these symptoms. In this way, the risk of economic loss, operation problems and re-work caused by component failure may be reduced.

The Fourier Transform is a mathematical technique used to analyze signals or functions in terms of their frequency components. It decomposes a signal from the time domain into the frequency domain, revealing the individual sinusoidal components that make up the signal [21].

The Continuous Fourier Transform (CFT) is defined by using (1) [22].

$$X(f) = \int_{-\infty}^{\infty} x(t)e^{-j2\pi ft} dt \quad (1)$$

$X(f)$ is the complex-valued representation of the signal $x(t)$ in the frequency domain.

$x(t)$ is the signal in the time domain.

f is the frequency (in Hertz).

j is the imaginary unit.

The Inverse Continuous Fourier Transform (ICFT) is defined by using (2) [21].

$$x(t) = \int_{-\infty}^{\infty} X(f)e^{j2\pi ft} df \quad (2)$$

The DFT holds a significant position in the examination, creation, and realization of algorithms and systems in discrete-time signal processing applications, including but not limited to linear filtering, correlation analysis, and spectrum analysis. Its remarkable significance can be primarily attributed to the presence of highly efficient algorithms for its computation. DFT is equivalent to the samples of the FT at equally spaced frequencies. As a result, computing an N -point DFT involves calculating N samples of the FT of N equally spaced frequencies ($2\pi k/N$ for $k = 0$ to $N-1$) on the unit circle in the z -plane. The main purpose is to use efficient algorithms for computing the N -point DFT, and these algorithms are commonly known as FFT algorithms [22].

When performing the computation of the DFT as outlined in (3), there is an essential involvement of N complex multiplications and $N-1$ complex additions for each $X(k)$ value. Consequently, in the process of calculating N DFT values, the necessity arises for N^2 complex multiplications and $N(N-1)$ complex additions. It's also worth noting that within each complex multiplication, there is an implicit utilization of four real multiplications and two real additions, whereas every complex addition is achieved with two real additions [23]. As a result, for large values of N (the length of the array), computing DFT directly requires a considerable amount of processing. As N increases, the number of operations grows rapidly, and the computation becomes unacceptably time-consuming.

The DFT is defined by using (3). [22].

$$X[k] = \sum_{n=0}^{N-1} x[n]e^{j2\pi kn/N} \quad (3)$$

Where:

$X[k]$ is the complex-valued representation of the signal $x[n]$ in the frequency domain.

$x[n]$ is the discrete signal in the time domain.

k is the discrete frequency index (0 to $N - 1$).

N is the number of data points in the time domain signal.

The Inverse Discrete Fourier Transform (IDFT) is defined by using (4) [22].

$$x[n] = \frac{1}{N} \sum_{k=0}^{N-1} X[k] e^{j2\pi kn/N} \quad (4)$$

The number of applications of the DFT in digital signal processing and other domains increased significantly because of the method created by Cooley and Tukey in 1965 to reduce the computation effort related to the DFT. The previously mentioned method additionally established the foundation for the development of diverse algorithms, commonly referred to as the FFT [24]. They significantly decrease the quantity of operations required for the computation of the DFT, hence enhancing the feasibility of the procedure. The FFT is a very fast and cost-effective algorithm utilized for the computation of the DFT. It offers useful simplification and computational convenience [25].

Spectral leakage is observed when the FFT is applied to a signal that does not contain an exact integer number of cycles within the window utilized for the transformation. This causes the signal's energy, which is concentrated at a single frequency, to be distributed across multiple frequency divisions in the FFT output [26]. The issue of FFT spectral leakage arises when the discrete frequency bins of the FFT do not fully line up with the frequency components of a signal. In other words, spectral leakage is especially pronounced when the signal frequency is not an integer multiple of the frequency bin spacing (bin width), the signal duration is not an integer multiple of the sampling period and the signal is not properly windowed before applying the FFT. To address spectral leakage, it is common practice to employ windowing techniques. These involve multiplying the original signal by a window function that reduces the signal's amplitude towards the edges [27]. This effectively reduces the influence of signal values at the edges of the window, which contributes to spectral leakage. Common window functions include Hamming, Hanning (or Hann), Blackman, and more. These windows taper the signal towards the edges, reducing abrupt changes that contribute to spectral leakage [19]. No leakage, leakage, and windowed sine wave comparison is shown in Fig. 1.

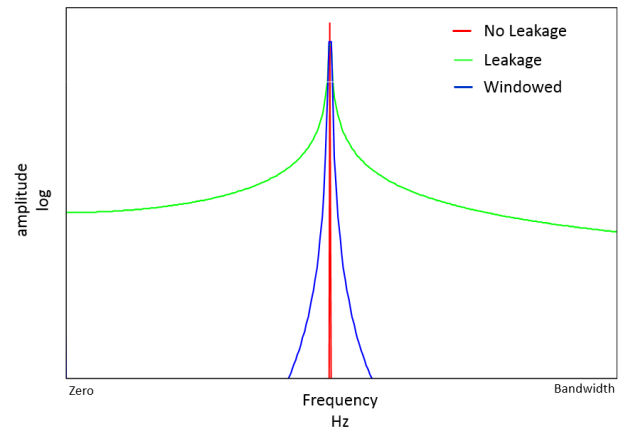


Fig. 1. Sine wave: no leakage, leakage and windowed [28].

The Hamming window, whose formula is given in (5) has a main lobe that's wider than the main lobes of the Hanning and Blackman windows. It offers a good balance between main lobe width and side lobe suppression [29]. Also, it provides better side lobe suppression compared to rectangular (no window) but not as good as Hanning and Blackman.

$$w(n) = 0.54 - 0.46 * \cos\left(\frac{(2 * \pi * n)}{N+1}\right) \quad (5)$$

Where:

$w(n)$ is the value of the Hamming window at the sample.

N is the total number of samples in the window.

n takes on integer values starting from 0 and goes up to $N-1$.

The Hanning window, which is mathematically defined in (6), is frequently known as the "raised cosine" window. The term "raised" or "shifted upwards" to initialize at 0 and conclude at 1 is derived from the geometric configuration of the function. The primary lobe of the window is thinner compared to the Hamming window, leading to greater frequency resolution. The amplitudes of the side lobes have a reduced magnitude in comparison to the Hamming function [27].

$$w(n) = 0.5 - 0.5 * \cos\left(\frac{(2 * \pi * n)}{N+1}\right) \quad (6)$$

Where:

$w(n)$ is the value of the Hanning window at the sample.

N is the total number of samples in the window.

n takes on integer values starting from 0 and goes up to $N-1$.

The Blackman window, as defined in (7), has the narrowest primary lobe when compared to the other three windows. This feature offers optimal side lobe suppression, which means facilitating the reduction of spectral leakage [29]. Due to its strong side lobe suppression, the Blackman window can provide good results for precise frequency analysis.

$$w(n) = 0.42 - 0.5 * \cos\left(\frac{(2 * \pi * n)}{N - 1}\right) + 0.08 * \cos\left(\frac{(4 * \pi * n)}{N - 1}\right) \quad (7)$$

Where:

$w(n)$ is the value of the Blackman window at the sample.

N is the total number of samples in the window.

n takes on integer values starting from 0 and goes up to $N-1$.

All three windowing techniques (Hamming, Hanning, and Blackman) are designed to reduce spectral leakage when performing FFT analysis. The selection of the window to use is contingent on the demands and prerequisites. If frequency resolution and minimizing side lobes are concerned, Hanning or Blackman might be preferred. If a balance between frequency resolution and side lobe suppression is being looked for, Hamming could be a good choice [30]. Experimentation and understanding the signal characteristics help determine the best window for the application. There are some windowing techniques given in Table 1.

When working with vibration signals that contain high-frequency components, it is important to consider the specific characteristics of the signal and the requirements of the application. There are some other methods rather than the windowing method efficiently used while selecting a suitable FFT method such as zero padding, oversampling, etc.

In real-time FFT analysis, zero padding is commonly used to improve the accuracy and clarity of frequency analysis. It refers to the process of adding extra zeros to the end of a time-domain signal before performing the FFT [31]. The frequency resolution of FFT is determined by both the length of the input signal and the sampling rate (or the time duration of the signal). Longer signals provide finer frequency resolution, allowing you to distinguish between closely spaced frequencies more accurately. By adding zeros and increasing the signal length, the frequency resolution of the FFT is enhanced. Zero padding can also be seen as a form of interpolation between the existing signal

samples. This can result in smoother spectral peaks in the frequency-domain representation, making it easier to visualize and analyse the frequency content of the signal [32]. Zero padding is often used in scenarios where frequency components with higher precision are aimed to be analysed, such as identifying closely spaced harmonics in a signal, or visualization of the frequency spectrum with more detail.

Tab. 1: Comparison of windowing techniques [23], [24], [25]

Signal Content	Window
Sine wave or combination of a mix of sinusoidal waves	Hann
Sine wave (with a focus on amplitude precision)	Flat Top
Narrowband stochastic signal (pertaining to vibration data)	Hann
Wideband stochastic signal (resembling white noise)	Uniform
Closely situated sinusoidal waves	Uniform, Hamming
Stimulus signals (akin to a hammer strike)	Force
Outcome signals	Exponential
Signals with undisclosed content	Hann
Two sinusoidal signals with proximate frequencies but distinct amplitudes	Kaiser - Bessel
Two sinusoidal signals with proximate frequencies and nearly identical amplitudes	Uniform
Precise measurement of amplitude in single-tone signals	Flat Top

Oversampling encompasses the act of obtaining and handling an increased number of samples from the vibration signal by utilizing a sampling rate that surpasses the Nyquist rate, equivalent to twice the maximum frequency component found within the signal. In mathematical terms, if the highest frequency component in the signal is f_{max} , then the Nyquist rate $f_{Nyquist}$ is given in (8) [33]. With more samples, better frequency resolution can be achieved. This means that closely spaced frequencies are distinguished more accurately, which can be beneficial in applications like

frequency analysis or spectral leakage reduction. Also, oversampling can help in reducing the impact of noise and quantization errors [34]. By capturing more samples, the noise gets spread over a wider range of samples, leading to a better signal-to-noise ratio (SNR) in the resulting FFT. The other advantage of oversampling is to reduce the effects of aliasing, which occurs when high-frequency components in the signal fold back into the frequency range of interest due to inadequate sampling. A higher sampling rate pushes the Nyquist frequency further away from the frequency range of interest, minimizing aliasing [35].

$$f_{Nyquist} = 2 \times f_{max} \quad (8)$$

There are several other methods and algorithms rather than FFT and DFT used for analysing and processing signals, especially in the field of signal processing and spectral analysis. Although the FFT and DFT are extensively utilized for the transformation of signals from the time domain to the frequency domain, it's important to note the existence of alternative methods like the Wavelet Transform (WT), Short-Time Fourier Transform (STFT), and Hilbert-Huang Transform (HHT). These alternative techniques are designed to address signal processing challenges and provide specific analytical requirements [36]. The WT is a mathematical method and signal processing tool employed to analyse signals and data in both the time and frequency domains. The utilization of this technique proves to be highly advantageous in the capture and analysis of high-frequency, non-stationary, and transient components within signals. The set of fundamental functions, commonly referred to as wavelets, are typically characterized by short durations and are defined at various scales [37]. Additionally, the STFT is a widely used technique in the field of signal processing that is utilized to analyse the changes in the frequency properties of a signal over time. The analysis of non-stationary signals, which exhibit time-varying frequency components, is significant [38]. Moreover, the HHT is a widely employed signal processing methodology utilized for the examination of non-linear and non-stationary data. The purpose of its development is to address the constraints inherent in conventional techniques such as the FFT and the STFT when dealing with intricate signals that change over time. The aim of this technique is to extract the inherent modes, uncover patterns, and analyse the instantaneous frequencies within signals [39]. FFT and DFT offer several advantages compared to other approaches and algorithms stated earlier. These advantages

include improved efficiency and speed, enhanced frequency accuracy, wide applicability, compliance with linearity principles, and simplified implementation [40].

In the circumstance of high-frequency applications, it may be reasonable to explore higher-level algorithms that provide better performance or specific functionalities. An approach that can be utilized for high-resolution frequency analysis of signals with non-uniformly spaced frequency components is the Chirp Z-Transform (CZT) which is an extension of the DFT [41]. a contour adheres to the pattern as specified in (9).

$$z_k = AW^{-k} \quad (9)$$

Where:

k serves as the frequency index, spanning from 0 to $M - 1$.

M is an arbitrary integer (not always equal to N , the point number of the desired complex spectrum).

A and W represent arbitrary complex numbers as defined in (10) [43].

$$A = A_0 e^{j\theta_0}, W = W_0 e^{j\varphi_0} \quad (10)$$

Where:

A is the contour starting point.

θ_0 is the starting angle.

W determines the rate at which the contour spirals inward or outward from a circle with a radius denoted as A_0 .

φ_0 signifies the angular separation among the various frequencies.

When $A_0 = W_0 = 1$, $\theta_0 = 0$, $\varphi_0 = \frac{2\pi}{N}$ and $M = N$, the contour encompasses the full unit circle, and the CZT is essentially identical to the DFT.

Firstly, it is excellent at detecting transient events in the data due to its ability to provide high-resolution time-frequency information. FFT and DFT may be less effective in isolating and characterizing these events. Secondly, the CZT provides significant utility in the analysis of non-stationary signals or signals exhibiting time-varying frequency components and is better suited to capture these variations accurately [44]. In contrast, the FFT and DFT assume constant frequency content over the entire signal duration. Thirdly, if the signal contains chirping or rapidly changing frequencies, the CZT can track these changes in a way that FFT and DFT cannot. The CZT's chirp modulation

aligns with such frequency variations. Fourthly, the CZT can handle signals with arbitrary data lengths without requiring zero padding, making it versatile for various datasets [45]. FFT and DFT are most efficient when applied to data lengths that are powers of 2 [46].

The algorithm is used to compute the Z-transform of a sequence on a finely selected region of the Z-plane. When applied to vibration data analysis, especially in data acquisition (DAQ) systems the CZT can be beneficial in several ways such as focused frequency analysis, data compression, higher resolution, reduced noise, optimized data transmission and better feature extraction that can reduce the payload on a communication channel. In terms of focused frequency analysis, unlike the standard FFT that computes the spectrum uniformly across a wide frequency range, the CZT allows the user to focus on a specific frequency band of interest. This is especially useful when analysing vibration data where specific frequency bands are of interest [47]. Focusing on specific bands means fewer data points are needed, leading to less data to transmit. Regarding data compression, since only considering a particular frequency range, fewer data points are obtained than sending the entire frequency spectrum. By transmitting only the relevant frequency components, the amount of data can be reduced sent over a communication channel. Concerning higher resolution, using the CZT can yield higher resolution results within the specific frequency band of interest compared to a standard FFT applied to the same data. The CZT has the potential to identify anomalies or features that could go unnoticed when using alternative methods. In connection with reduced noise, in the case of focusing on a specific frequency band, irrelevant frequency components (which might be just noise or other undesired vibrations) can be excluded. This can result in a cleaner signal representation, requiring less data for effective transmission or storage. In the matter of optimized data transmission, in wireless DAQ systems, where bandwidth might be a constraint, sending only crucial or relevant information becomes a necessity. By utilizing CZT, it is essentially sending only the most pertinent information, thus optimizing the use of available bandwidth [41]. About better feature extraction, the CZT can help in extracting more meaningful features from vibration data by focusing on the relevant frequency components, which could be of a much smaller size than the original data, thus reducing the payload. Comparison of FFT, DFT and CZT is given in Table 2.

Tab. 2: Comparison of FFT, DFT and CZT [22], [23], [24]

Feature	FFT	DFT	CZT
Computational Efficiency	Highly efficient ($O(N \log N)$)	Standard ($O(N^2)$)	Depends on the algorithm used
Time-Domain Input	Finite-length sequence	Finite-length sequence	Finite-length sequence
Frequency-Domain Output	Discrete frequencies	Discrete frequencies	Discrete frequencies
Frequency Resolution	Fixed based on signal length	Fixed based on signal length	Adjustable
Time-Frequency Analysis	Limited (non-time-localized)	Limited (non-time-localized)	Effective (time-localized)
Application Range	General spectral analysis	General spectral analysis	Time-varying signals
Real vs. Complex Output	Complex	Complex	Complex
Suitable for Linear Chirps	No	No	Yes
Computational Complexity	Lower for large N	Higher for large N	Depends on the algorithm used

Case Study

As detailed in Chapter I, vibration testing has remarkable importance in the aerospace industry, surrounding the assessment of aircraft components, systems, and even entire airframes to ensure their dependable and safe operation across diverse flight conditions. In this case study, the primary objective is to subject the prototype propulsion system to strict vibration analysis. After a detailed evaluation of available analysis methods, the decision has been made to employ the CZT technique to handle the challenges that appeared in the case study.

The exact frequency range of interest for vibration tests using the CZT depends on the specific goals of the test and the components being analyzed. The primary frequencies of interest here are associated with the engine's rotational speed and harmonics. This can vary from low frequencies like large turbofan engines to higher frequencies such as smaller engines or propellers. The CZT algorithm's ability to outline the specified frequency range with remarkable resolution enables effective "zooming in" on this specific range to identify

the engine harmonics relevant to the investigation [48].

Planned engine tests are set to run at 2000 RPM, meaning the engine completes 2000 rotations per minute, corresponding to a fundamental harmonic with a frequency determined by using (12) of $2000/60 = 33.33$ Hz. This knowledge serves as a vital reference point for identifying the specific frequencies of interest during the frequency analysis. The choice of a frequency range spanning from 1 Hz to 512 Hz is planned, aimed at providing clear insight into the motor's harmonic behavior. Even when considering the 10th harmonic, the corresponding frequency value is calculated as 330 Hz using (11). Therefore, preferring a wide frequency range makes logical sense, as it ensures the capture of all potential frequency components, even if higher harmonics are not the primary focus.

$$f_{\text{harmonic}} = n \times f_{\text{fundamental}} \quad (11)$$

Where:

f_{harmonic} is the harmonic frequency.

n is the harmonic number.

$f_{\text{fundamental}}$ is the fundamental frequency.

If the given parameters are substituted into (11),

$$f_{\text{harmonic}} = 10 \times 33.33$$

$$f_{\text{harmonic}} = 330.33$$

f_{harmonic} is rounded to 330 Hz.

The provided algorithm (see Appendix A for the pseudocode) contains the methodology and computational steps for simulating real-time vibration data processing. Using the CZT, the provided algorithm emphasizes the specific frequency components, offering a detailed perspective on the signals in the frequency domain [49].

The given algorithm in the paper consists of vibration data extraction, defining key parameters, desired spectral resolution, pre-processing, CZT configuration, real-time processing simulation, visualization, playback, and performance assessment stages. In the data extraction stage, the algorithm loads vibration data from a TDMS (Technical Data Management Streaming) file. The acceleration values and corresponding time stamps are extracted from the data [50]. In the defining key parameters stage, key parameters are set, including the sampling frequency $f_s = 2048$ Hz denotes how frequently data is sampled, the $windowSize = 512$ samples defines the data

segment length for spectral analysis, the $overlap = 256$ samples ensures smooth transitions between consecutive data segments and the $segmentSize = 512$ samples, which denotes the data chunk processed in one iteration.

In the iteration establishment stage, to process the vibration data in segments, the number of iterations (chunks) is determined by using (12).

$$Iterations = \frac{\text{length of full data}}{\text{segments size}} - 1 \quad (12)$$

Equation 12 ensures that each data chunk consists of non-overlapping segments, optimizing the computational efficiency.

In the spectral resolution and pre-processing stage, the vibration data is segmented into overlapping windows using the calculated parameters. Windowing helps reduce spectral leakage and improve frequency resolution. The process of oversampling with a 512-point Hann window and a sampling rate of 2048 Hz strengthens the resolution of frequency analysis [51]. The increased resolution facilitates an in-depth investigation of the frequency spectrum. It provides opportunities for advancements when necessary and enhances the precision with which high-frequency harmonics are detected, which allows for a greater understanding of the engine's behavior and performance.

The Hann window is utilized for the CZT analysis in this paper thanks to its numerous benefits. The selection of the Hann window is inspired by its ability to prevent spectral leakage, hence increasing the accuracy of frequency analysis [52]. It provides a consistent frequency response, facilitating the accurate identification of spectral peaks. Furthermore, this technique achieves a harmonious equilibrium between the width of the primary lobe and the suppression of side lobes, so increasing the resolution of frequencies while limiting the occurrence of unwanted sidelobe artefacts. Additionally, the Hann window is favored for its simplicity and ease of implementation, requiring minimal computational resources [53].

In a CZT, the desired resolution is computed by using (13) [54].

$$\text{The desired resolution} = f_s / windowSize \quad (13)$$

If the given parameters are substituted into (13),

$$\text{The desired resolution} = 2048 / 512$$

$$\text{The desired resolution} = 4 \text{ Hz}$$

This means that each bin in the frequency spectrum represents a 4 Hz bandwidth.

In the CZT configuration, each data segment's processing time is clocked. This provides invaluable insights into computational requirements. Data segments, produced with 512 samples and 256-sample overlap, ensure a consistent data flow. Unlike traditional Fourier Transforms, CZT allows focused spectral analysis in the range of 1 Hz to 512 Hz (as defined by f_{start} and f_{end}).

If M is defined as the number of points between f_{start} and f_{end} based on a desired frequency resolution, then M is computed by using (14). As mentioned in (10), M is not equal to N .

$$M = \frac{f_{end} - f_{start}}{\text{desired resolution}} + 1 \quad (14)$$

If the given parameters are substituted into (10),

$$M = \frac{512 - 1}{4} + 1$$

$$M = 128.75$$

M is rounded to 128 using the floor command.

The parameters α and ω for the CZT calculation are derived from (10) to apply (15) and (16). These parameters are essential for tuning the CZT to focus on the specified frequency range.

$$\alpha = e^{-1j \times 2\pi \times f_{start} / f_s} \quad (15)$$

$$\omega = e^{-1j \times 2\pi \times (f_{end} - f_{start}) / (M \times f_s)} \quad (16)$$

Instead of producing a spectrum with 512 points (which would have been the case with a regular FFT of a 512-point signal), the CZT method produces a spectrum with only 128 points. This reduction is possible because CZT focuses only on the frequencies between f_{start} and f_{end} , with the defined resolution. In essence, for each segment of the data, this reduction enables to focus on the frequency components that are most relevant to the analysis, reduces the computational overhead by processing fewer data points and provides a more streamlined visualization that emphasizes dominant frequencies within the desired range while discarding information outside the desired frequency range.

In the real-time processing simulation, the main loop simulates real-time data acquisition and processing. For each iteration, the algorithm captures a data segment. CZT is applied to the windowed segment, producing a frequency spectrum for the desired range. The computed frequency domain data is stored for later visualization. In Acra KAM-500 modules,

signals are sampled many times faster than specified by the user [55]. The KAD/ADC/111 is a dedicated hard-wired state machine which performs oversampling on all available channels at a rate within the range of 16,000 samples per second (16 ksps) to 32,000 samples per second (32 ksps). Additionally, the state machine incorporates digital filtering mechanisms to remove any noise components that exceed the user-defined cutoff frequency. This system ensures precise and efficient signal processing in the device. By using the information from [56], the average sample per second is calculated as 24 ksps. A simulated acquisition delay of 0.021 seconds is added to replicate the real-world acquisition timings by using (17).

$$\text{Acquisition Delay} = \frac{\text{Segment Size}}{\text{Average ksps}} \quad (17)$$

If the given parameters are substituted into (17),

$$\text{Acquisition Delay} = \frac{512}{24}$$

$$\text{Acquisition Delay} = 0.021 \text{ seconds}$$

In the visualization stage, the algorithm generates two plots: a time domain plot and a frequency domain plot. In the time domain plot, the vibration data is plotted against time, providing insights into the acceleration values over time. In the frequency domain plot, the CZT-derived frequency spectrum highlights the top 5 magnitudes to emphasize dominant frequencies [29]. A simulation 'pause' introduces a realistic feel during playback.

In the performance assessment, the processing time for each segment is recorded, and the average segment processing time is computed by using (18).

$$\text{average time} = \frac{1}{\text{iterations}} \sum T \quad (18)$$

Where:

T: Elapsed time for each iteration.

Using the CZT algorithm for propulsion system vibration analysis, despite its effectiveness and providing great solutions, presents challenges. These challenges include harmonic vibrations generated by rotating machinery, potential interactions with other propellers leading to instant frequencies, the presence of broadband noise unrelated to specific harmonics, and variations in vibration profiles across different operational states of the rotorcraft. To manage these, it's crucial to ensure sufficient resolution in frequency analysis, especially for distinguishing close frequencies when propeller

interactions are a concern. Additionally, having data from other propellers, even for reference, can be advantageous. Higher resolution analysis in spectral analysis requires more distinct frequency bins over a given range, enabling better discrimination between closely spaced frequency components [47].

Result Analysis

The real-time simulation has been performed using MATLAB® R2023a with the license number 41077201. The algorithm incorporates the following optimization techniques to enhance performance: memory pre-allocation, vectorization, and usage of built-in functions [57]. PARFOR library has been used to increase the real-time performance of the calculations.

Vibration data is collected using the PCB 33931 model vibration sensor [58]. This sensor is designed to capture vibrations in its surroundings and convert them into electrical signals. To ensure accurate data acquisition, the raw vibration signals are first subjected to signal conditioning. This process is facilitated by Curtiss-Wright hardware, which is specifically configured for various operations such as amplification, filtering, and noise reduction data acquisition to enhance the quality and relevance of the vibration data. The effectiveness of the algorithm hinges on its capacity to optimize computations across multiple CPU cores, resulting in a substantial reduction in processing time for handling large datasets [59]. The real-time CZT simulation has been run on a PC which has 12th Gen Intel Core, i7-12700H and 2.30 GHz.

In a complete evaluation containing all relevant factors, such as the CPU, hardware, and processor, the average time per iteration, which includes acquisition time, is calculated at 0.0315 seconds. This holistic analysis offers a broad perspective on the computational process, accounting for the diverse variables that affect performance. However, a more detailed examination, specifically concentrating on the CZT analysis, shows a remarkable change in efficiency. When isolating this aspect from the overall computation, the time per iteration dramatically reduces to 0.0017 seconds.

Time domain vibration signals and frequency domain CZT magnitude plots have been presented in Fig. 2, Fig. 3, and Fig. 4, showing the results of a real-time simulation executed through the methods detailed in Chapter III. These graphics are captured by taking screenshots at three randomly chosen points during the simulation. This approach provides a

dynamic look into the evolving behavior of the system, offering valuable data that aids in the analysis and understanding of the simulated processes. The combination of time domain and CZT magnitude plots allows for a comprehensive examination of the system's response, making it an integral component of the case study in Chapter III.

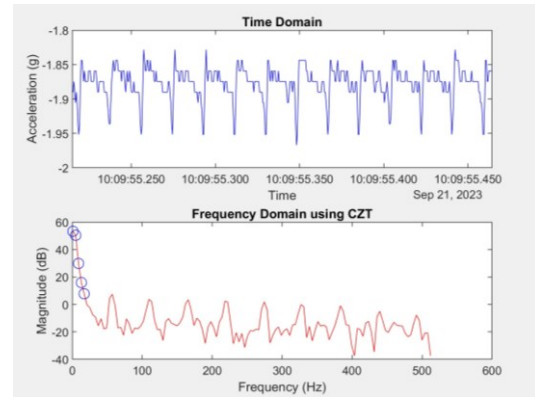


Fig.2. Time domain vibration signals and frequency domain Chirp Z Transform (CZT) magnitude plots.

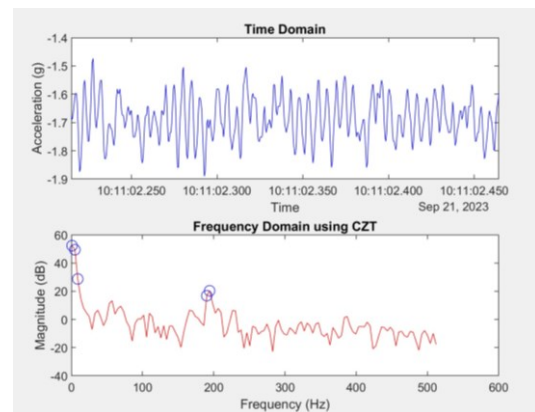


Fig.3. Time domain vibration signals and frequency domain Chirp Z Transform (CZT) magnitude plots.

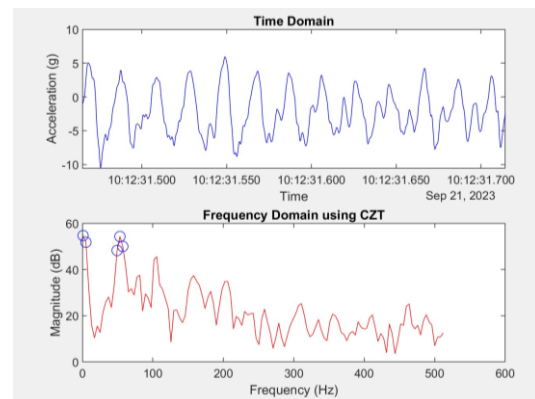


Fig.4. Time domain vibration signals and frequency domain Chirp Z Transform (CZT) magnitude plots.

Conclusion

Vibration data collected from sensors contains essential information about the mechanical behavior of structures and avionics, characterized by factors like frequency, amplitude, and phase. Time domain analysis reveals temporal behavior, while frequency domain analysis through CZT uncovers underlying frequency components. Real-time CZT analysis continuously processes incoming vibration data, finding applications in anomaly detection, pattern identification, and spectral analysis. This research seeks to enhance real-time data analysis, especially where high-frequency data is vital for decision-making. In the context of propulsion systems, vibration analysis is crucial for early issue detection, ensuring safety and efficiency [60].

This paper primarily focuses on optimizing high-frequency data payload using the CZT algorithm, regardless of sensor quality. The given methodology reduces the number of data points by a factor of 4 for each segment. To enhance the CZT algorithm, the Hann windowing technique is incorporated which minimizes spectral leakage, ensures a smooth frequency response, and is easy to implement [61]. In Chapter III, the CZT algorithm is applied to comprehensively analyze the prototype propulsion system. The process involves determining the desired spectral zoom range through harmonic calculation, leading to the definition of parameters like f_{start} and f_{end} . As outlined in Chapter II, f_s is calculated using the oversampling method. After determining the f_s , the desired resolution is also calculated. These parameters play a crucial role in assigning CZT-specific coefficients, including M , α , and ω , significantly improving the precision and clarity of the engine harmonics analysis.

When existing similar studies are examined, it has been observed that FFT Algorithms are generally used in many real-time applications such as [12] and [16], and CZT is preferred for post-processing applications [62]. When the review results in Chapter II are evaluated, it is concluded that the best method for the case study given in Chapter III was a real-time CZT Algorithm. Additionally, this algorithm stands out among other CZT-based approaches by strategically utilizing pre-calculated exponential factors and a careful buffering scheme, which collectively ensure a computationally efficient execution without compromising the transformative precision. These attributes are particularly advantageous when dealing with high-volume or streaming vibration data in dynamic systems.

In summary, the CZT offers a focused and efficient way to analyze and represent vibration data, which can lead to substantial reductions in the amount of data that needs to be transmitted, especially when specific frequency bands are of interest. This results in a reduced payload on communication channels in DAQ systems.

In a forthcoming study, while real-time CZT analysis offers numerous benefits, it also leads to some challenges, such as its computational complexity for large datasets and optimized algorithms to handle data in real-time. Additionally, sensor quality, data transmission speed, and noise interference can affect the accuracy of results. To manage these challenges effectively, a custom CZT function may be developed. This custom function will handle specific research requirements, potentially enhancing accuracy and computational efficiency in the analysis.

Appendix

Appendix A - Pseudocode of the algorithm

```

start
read the vibration data from the TDMS file
set vibrationData to data{1, 1}.vibrationData
set time to data{1, 1}.Time2048Hz
set fs (sampling frequency) to 2048 Hz
set windowSize to 512
set overlap to 256
set segmentSize to 512
set f_start (start frequency) to 1
set f_end (end frequency) to 512
create window = hann(windowSize)
calculate desired_resolution = fs / windowSize
calculate M = (f_end - f_start) /
desired_resolution + 1
calculate a = exp(-1j * 2 * pi * f_start / fs)
calculate w = exp(-1j * 2 * pi * (f_end - f_start) /
(M * fs))
compute iterations =
floor(length(fullVibrationData) / segmentSize) -
1
for iteration from 1 to iterations
start a timer (tic)
calculate startIndex = (iteration - 1) *
segmentSize + 1
calculate endIndex = iteration * segmentSize

```


calculatevibrationData=fullVibrationData(startIndex:endIndex)

calculate timeSegment = fullTime(startIndex:endIndex)

reshape the vibration data into overlapping segments using the 'buffer' function

compute the CZT of the reshaped data with the Hann window, M, w, and a

store the results, time segment, and original vibration data in a data structure

pause for 0.021 seconds (simulated processing time)

record and store the elapsed time for this iteration

end of loop

create a frequency vector 'frequencies' from f_start to f_end with M points

initialize an array 'top5Handles' to store handles for the top 5 plotted points

create a figure with two subplots for time and frequency domains

for iteration from 1 to iterations

update the time domain plot with current time and vibration data

calculate the magnitude of the CZT in decibels

if 'top5Handles' is not empty, clear the previous top 5 points

find the top 5 indices with the highest magnitude

extract the corresponding frequencies and magnitudes

plot the top 5 points on the frequency domain subplot

pause for 0.25 seconds for visualization

end of loop

calculate the average processing time per segment

display the average processing time

end

Acknowledgement

Here, sincere gratitude to the eRC Systems GmbH and Turkish Aerospace for their invaluable contributions to advancing research and scientific endeavors, providing researchers with a robust platform for innovation and discovery.

References

- [1] O. B. Ozseven, S. Tambova and H. Helvacı, "A Risk Analysis Study: Model Development for Risk Mitigation and Systematic Approach to FTI System Design Activities," *2022 IEEE International Symposium on Systems Engineering (ISSE)*, Vienna, Austria, 2022, pp. 1-6, doi: 10.1109/ISSE54508.2022.10005323.
- [2] S. A. Kilpatrick and T. A. Newton, "The Unique Challenges of Testing Specialized Network-Based Data Acquisition Systems," *2014 IEEE AUTOTEST*, St. Louis, MO, USA, 2014, pp. 233-238, doi: 10.1109/AUTEST.2014.6935151.
- [3] Ş. Tambova, and A. Aybar, "Colored Petri Nets Model for Network Based FTI Systems", *Journal of Communications*, vol. 16, no. 9, pp. 400-405, September 2021, doi: 10.12720/jcm.16.9.400-405.
- [4] NASA SP-6105, *Systems Engineering Handbook*, Revision 2, 2016.
- [5] T.D. Scharton, *Force Limited Vibration Testing Monograph*, NASA Reference Publication RP-1403, 1997.
- [6] M. Mosher, A.H. Pryor and D. G. Lewicki, "Detailed Vibration Analysis of Pinion Gear with Time-Frequency Methods," NASA, 2003.
- [7] P. K. Aggarwal, "Dynamic (Vibration) Testing: Design Certification of Aerospace System." *Encyclopedia of Aerospace Engineering*, 2010.
- [8] A. Halfpenny and T. C. Walton, "New Techniques for Vibration Qualification of Vibrating Equipment on Aircraft", *Aircraft Airworthiness & Sustainment 2010*, 2010.
- [9] Crouse, David R., "Flight Test Instrumentation", AGARD Flight Test instrumentation Series, AGAR Dograph No. 300 Vol 14, Introduction to Flight Test Engineering, 1995.
- [10] R. Benjamin, et al. "Fourier could be a data scientist: From graph Fourier transform to signal processing on graphs." *Comptes Rendus. Physique*, 2019, pp. 474-488.
- [11] G. Toh and J. Park, "Review of Vibration-Based Structural Health Monitoring Using Deep Learning," *Applied Sciences*, vol. 10, no. 5, p. 1680, Mar. 2020, doi: 10.3390/app10051680.
- [12] D. Łuczak "Mechanical vibrations analysis in direct drive using CWT with complex Morlet wavelet." *Power Electronics and Drives*, vol.8, no.1, 2023, pp.65-73.
- [13] N. K. Govindaraju, B. Lloyd, Y. Dotsenko, B. Smith and J. Manferdelli, "High performance discrete Fourier transforms on graphics processors," *SC '08: Proceedings of the 2008 ACM/IEEE Conference on Supercomputing*, Austin, TX, USA, 2008, pp. 1-12, doi: 10.1109/SC.2008.5213922.
- [14] L. Muślewski, M. Pająk, A. Grządziela, and J. Musiał, "Analysis of vibration time histories in the time domain for propulsion systems of minesweepers," *Journal of Vibroengineering*, Vol. 17, No. 3, pp. 1309–1316, May 2015.
- [15] T. Yang, *Telemetry Theory and Methods in Flight Test*. China: Springer, 2021, pp. 1-475, doi: 10.1007/978-981-33-4737-3.
- [16] P. Quinn, "Optimizing PCM Bandwidth Usage in Flight Test by Real-Time Data Analysis During Flight," *International Telemetering Conference Proceedings*, 2022, pp. 1-6, doi: 10.5162/ettc2022/7.3.
- [17] A. Devasa, M. Chorro and B. Vidal, "Comparison of computing efficiency among FFT, CZT and Zoom FFT in THz-TDS" *ArXiv*. 2021, pp. 1-10, doi: /abs/2108.03948.
- [18] O. ÇUlha and Y. Tanik, "Low Complexity Keystone Transform and Radon Fourier Transform Utilizing Chirp-Z Transform," in *IEEE Access*, vol. 8, pp. 105535-105541, 2020, doi: 10.1109/ACCESS.2020.3000998.
- [19] Y. Wang, L. Zheng, Y. Gao and S. Li, "Vibration Signal Extraction Based on FFT and Least Square Method," in

- IEEE Access*, vol. 8, pp. 224092-224107, 2020, doi: 10.1109/ACCESS.2020.3044149.
- [20] M. Nie, and W. Ling, "Review of condition monitoring and fault diagnosis technologies for wind turbine gearbox," *Procedia Cirp*, vol. 11, 2012, pp. 287-290, doi: 10.1016/j.procir.2013.07.018.
- [21] R. Wald, T. Khoshgoftaar and J. C. Sloan, "Fourier transforms for vibration analysis: A review and case study," *2011 IEEE International Conference on Information Reuse & Integration*, Las Vegas, NV, USA, 2011, pp. 366-371, doi: 10.1109/IRI.2011.6009575.
- [22] B. N. Mohapatra and R. K. Mohapatra, "FFT and sparse FFT techniques and applications," *2017 Fourteenth International Conference on Wireless and Optical Communications Networks (WOCN)*, Mumbai, India, 2017, pp. 1-5, doi: 10.1109/WOCN.2017.8065859.
- [23] A. D. Das and K. K. Mahapatra, "Real-Time Implementation of Fast Fourier Transform (FFT) and Finding the Power Spectrum Using LabVIEW and Compact RIO," *2013 International Conference on Communication Systems and Network Technologies*, Gwalior, India, 2013, pp. 169-173, doi: 10.1109/CSNT.2013.45.
- [24] L. Wenqiu and C. Peng, "GHz wideband real-time FFT algorithm based on FPGA," *2013 International Conference on Information and Network Security (ICINS 2013)*, Beijing, 2013, pp. 1-5, doi: 10.1049/cp.2013.2475.
- [25] P. Pariyal, D. Koyani, D. Gandhi, S. Yadav, D. Shah, and A. Adesara, "Comparison based Analysis of Different FFT Architectures," *International Journal of Image, Graphics and Signal Processing*, vol. 8, no. 6, 2016, pp. 41-47, 2016, doi: 10.5815/ijigsp.2016.06.05.
- [26] L. Zengqiang, et al. "Application of FFT interpolation correction algorithm based on window function in power harmonic analysis." *IOP Conference Series: Earth and Environmental Science*, vol. 252, no. 3, pp. 1-8, 2019, doi: 10.1088/1755-1315/252/3/032184.
- [27] D. Jwo, I. Wu and Y. Chang, "Windowing Design and Performance Assessment for Mitigation of Spectrum Leakage," *International Symposium on Global Navigation Satellite System 2018*, vol. 94, pp. 1-8, 2019, doi: 10.1051/e3sconf/20199403001.
- [28] "Windows and Spectral Leakage," [community.sw.siemens.com](https://community.sw.siemens.com/s/article/windows-and-spectral-leakage). <https://community.sw.siemens.com/s/article/windows-and-spectral-leakage> (accessed Sep. 5, 2023).
- [29] D. Jwo, W. Chang and I. Wu, "Windowing techniques, the welch method for improvement of power spectrum estimation," *Computers, Materials & Continua*, 2021, pp. 3983-4003.
- [30] P. Podder, et al. "Comparative performance analysis of hamming, hanning and blackman window." *International Journal of Computer Applications*, vol. 96, no. 18, pp. 1-7, 2014, doi: 10.5120/16891-6927.
- [31] Y. Xiong, et al. "Accurate and robust displacement measurement for FMCW radar vibration monitoring," *IEEE Sensors Journal*, vol. 18, no. 3, pp. 1131-1139, 1 Feb. 2018, doi: 10.1109/JSEN.2017.2778294.
- [32] J. Rabi, T. Balusamy, and R. Raj Jawahar. "Analysis of vibration signal responses on pre induced tunnel defects in friction stir welding using wavelet transform and empirical mode decomposition," *Defence Technology*, volume 15, No 6, pp. 885-896, 2019, doi: 10.1016/j.dt.2019.05.014.
- [33] A.D. Poularikas, *Transforms and Applications Handbook*. Arkansas: CRC Press, 2010.
- [34] J. Wang, Y. Peng and W. Qiao, "Current-Aided Order Tracking of Vibration Signals for Bearing Fault Diagnosis of Direct-Drive Wind Turbines," in *IEEE Transactions on Industrial Electronics*, vol. 63, no. 10, pp. 6336-6346, Oct. 2016, doi: 10.1109/TIE.2016.2571258.
- [35] B. Xu, T. Han, Z. Zhang, X. Liu and M. Ju, "Research on Sub-Nyquist Rate Sampling Method Based on Sparse Fourier Transform Theory," *2021 IEEE 4th International Conference on Electronics Technology (ICET)*, Chengdu, China, 2021, pp. 742-747, doi: 10.1109/ICET51757.2021.9450919.
- [36] D. Vazhenina and K. Markov, "End-to-End Noisy Speech Recognition Using Fourier and Hilbert Spectrum Features," *Electronics*, vol. 9, no. 7, pp. 1-18, Jul. 2020, doi: 10.3390/electronics9071157.
- [37] H. Jeon, Y. Jung, S. Lee, and Y. Jung, "Area-Efficient Short-Time Fourier Transform Processor for Time-Frequency Analysis of Non-Stationary Signals," *Applied Sciences*, 2020, vol. 10, no. 20, pp. 1-10, Oct. 2020, doi: 10.3390/app10207208.
- [38] O. Arslan and M. Karhan, "Effect of Hilbert-Huang transform on classification of PCG signals using machine learning," *Journal of King Saud University - Computer and Information Sciences*, Volume 34, No 10, pp. 9915-9925, 2022, doi: 10.1016/j.jksuci.2021.12.019.
- [39] M. Rhif, A. Ben Abbes, I. Farah, B. Martínez, and Y. Sang, "Wavelet Transform Application for/in Non-Stationary Time-Series Analysis: A Review," *Applied Sciences*, vol. 9, no. 7, pp. 1-22, Mar. 2019, doi: 10.3390/app9071345.
- [40] M. Mishra, "Power quality disturbance detection and classification using signal processing and soft computing techniques: A comprehensive review," *Int Trans Electr Energ Syst*, vol. 29, no. 8, pp. 1-41, 2019, doi: 10.1002/2050-7038.12008.
- [41] Y. Hu, Z. Wang, X. Wang, et al. "Efficient full-path optical calculation of scalar and vector diffraction using the Bluestein method". *Light: Science & Applications* 9, vol. 9, no. 1, pp. 1-11, 2020, doi: 10.1038/s41377-020-00362-z.
- [42] S. Scherr, et al. "An efficient frequency and phase estimation algorithm with CRB performance for FMCW radar applications." *IEEE Transactions on Instrumentation and Measurement*, vol. 64, no. 7, pp. 1868-1875, July 2015, doi: 10.1109/TIM.2014.2381354.
- [43] M. Shuohan, M. A. Qishuang, and L. Xinbo. "Applications of chirp z transform and multiple modulation zoom spectrum to pulse phase thermography inspection," *NDT & E International*, vol. 54, pp. 1-8, 2013, doi: 10.1016/j.ndteint.2012.11.006.
- [44] K. Wang, L. Wang, B. Yan and H. Wen, "Efficient Frequency Estimation Algorithm Based on Chirp-Z Transform," in *IEEE Transactions on Signal Processing*, vol. 70, pp. 5724-5737, 2022, doi: 10.1109/TSP.2022.3224648.
- [45] P. A. Milder, F. Franchetti, J. C. Hoe and M. Püschel, "Hardware implementation of the discrete fourier transform with non-power-of-two problem size," *2010 IEEE International Conference on Acoustics, Speech and Signal Processing*, Dallas, TX, USA, 2010, pp. 1546-1549, doi: 10.1109/ICASSP.2010.5495517.
- [46] G. Plonka, D. Potts, G. Steifdl and M. Tasche. *Numerical Fourier Analysis*. USA: Birkhauser, 2018, pp. 1-615.
- [47] I. Kubiak and A. Przybysz, "Fourier and Chirp-Z Transforms in the Estimation Values Process of Horizontal and Vertical Synchronization Frequencies of Graphic Displays," *Applied Sciences*, 2022, vol. 12, no. 10, pp. 1-18, May 2022, doi: 10.3390/app12105281.
- [48] T. T. Wang, "The segmented chirp Z-transform and its application in spectrum analysis," in *IEEE Transactions on Instrumentation and Measurement*, vol. 39, no. 2, pp. 318-323, April 1990, doi: 10.1109/19.52508.
- [49] S. Murugan and K. Jayakumar, "A DSP based real-time 3D FFT system for analysis of dynamic parameters," *2014 IEEE International Conference on Advanced Communications, Control and Computing Technologies*, Ramanathapuram, India, 2014, pp. 1489-1492, doi: 10.1109/ICACCCT.2014.7019351.
- [50] Z. D. Tsai, H. S. Wang, J. C. Chang, and J. R. Chen, "Development of an On-line System for Vibration

- Measurement and Tracing" *Particle Accelerator Conference (PAC)*, Canada, 2009, pp. 3660–3662.
- [51] G. Wang, X. Wang, and C. Zhao, "An Iterative Hybrid Harmonics Detection Method Based on Discrete Wavelet Transform and Bartlett–Hann Window," *Applied Sciences*, vol. 10, no. 11, pp. 1-16, Jun. 2020, doi: 10.3390/app10113922.
- [52] L. Sevgi, "Numerical Fourier Transforms: DFT and FFT," in *IEEE Antennas and Propagation Magazine*, vol. 49, no. 3, pp. 238-243, June 2007, doi: 10.1109/MAP.2007.4293982.
- [53] R. Puche-Panadero et al., "New Method for Spectral Leakage Reduction in the FFT of Stator Currents: Application to the Diagnosis of Bar Breakages in Cage Motors Working at Very Low Slip," in *IEEE Transactions on Instrumentation and Measurement*, vol. 70, pp. 1-11, 2021, Art no. 3511111, doi: 10.1109/TIM.2021.3056741.
- [54] J. Semmlow, *Circuits, Signals, and Systems for Bioengineers*. New Brunswick: ELSEVIER, 2005.
- [55] "TEC-NOT-019," [curtisswrightds.com. https://www.curtisswrightds.com/resources/tec-not-019-introduction-digital-filtering](https://www.curtisswrightds.com/resources/tec-not-019-introduction-digital-filtering) (accessed Oct. 15, 2023).
- [56] "KAD/ADC/111," [curtisswrightds.com. https://www.curtisswrightds.com/products/flight-test/data-acquisition/acrakam500/analog/kadadc111](https://www.curtisswrightds.com/products/flight-test/data-acquisition/acrakam500/analog/kadadc111) (accessed Oct. 22, 2023).
- [57] C. Moler, and L. Jack, "A history of MATLAB." *Proceedings of the ACM on Programming Languages*, vol. 7, no. OOPSLA2, pp. 1-67, 2020, doi: 10.1145/3622797.
- [58] "Model 339B31 Accelerometer," [pcb.com. https://www.pcb.com/products?m=339b31](https://www.pcb.com/products?m=339b31) (accessed Nov. 2, 2023).
- [59] S. Chen, and X. Li, "A hybrid GPU/CPU FFT library for large FFT problems," *2013 IEEE 32nd International Performance Computing and Communications Conference (IPCCC)*, San Diego, CA, USA, 2013, pp. 1-10, doi: 10.1109/PCCC.2013.6742796.
- [60] H.C. Lin, and Y. Ye, "Reviews of bearing vibration measurement using fast Fourier transform and enhanced fast Fourier transform algorithms," *Advances in Mechanical Engineering*, vol. 11, no. 1, pp. 1-12, 2019, doi: 10.1177/1687814018816751.
- [61] W. Tian, J. Yu, X. Ma, and J. Li, "Power System Harmonic Detection Based on Bartlett-Hann Windowed FFT Interpolation," *2012 Asia-Pacific Power and Energy Engineering Conference*, Shanghai, China, 2012, pp. 1-3, doi: 10.1109/APPEEC.2012.6307426.
- [62] D. Hou, H. Qi, H. Luo, C. Wang, and J. Yang, "Comparative study on the use of acoustic emission and vibration analyses for the bearing fault diagnosis of high-speed trains," *Structural Health Monitoring*, vol. 21, no.4, pp. 1-23, 2021, doi: 10.1177/1475921721103602.

Integration of FTI Configuration Management with Flight Test Database for an Enhanced Digital Twin Development

Ali Tahsin KAYMAK¹, Mehmet KEKEÇ², Raşit UZUN², Selma AYDIN²

¹ Turkish Aerospace, Kahramankazan, Ankara / TURKIYE,

² Turkish Aerospace, Kahramankazan, Ankara / TURKIYE

alıtahsin.kaymak@tai.com.tr mehmet.kekec@tai.com.tr rasit.uzun@tai.com.tr ses@tai.com.tr

Abstract

Flight test instrumentation configurations traced on aircrafts are carried out across various projects and multiple experimental platforms in each. Up to now, managed our configurations in Excel spreadsheets, ERP systems, Jira, Teamcenter, Doors, in-house tools etc... Apart of these multiple complex systems, flight test data management part requires additional systems such as Optimus (in-house), IADS, etc..., much more complex. Managing all these independent media, causes the work effort to divide between time management optimization and FTI configuration management.

Consolidated FTI Configuration management systems with flight test data management system in one FTI medium will ensure data integrity, accuracy and reliability. This more accessible and unified system will also be the foundation for us to develop a digital twin to presents the unpredictable correlation between flight test data and FTI architecture in the future so that condition monitoring based on Deep Learning and ML algorithms, and configuration management operations can be used in our pre-flight and post-flight activities.

Key words: FTI, Big Data, Configuration Management, Digital Twin, ML/DL

Introduction

Efficient Flight Test Instrumentation configuration management is a must in a multi-project environment. Current methods involve disparate systems, causing division in effort and accessibility. This paper advocates for integrating FTI configuration management and flight test data management systems into a unified medium to enhance efficiency and traceability. With this unified system, the main goal is to create an FTI digital twin.

FTI Management History

Having a dynamic FTI network that can and will change in almost every flight test also means monitoring and managing multiple media to monitor the sub-parts of the system. Although the management of these media is essential to trace the system, it also brings the following difficulties.

Each media is in a different medium. Followed system and their sub-medias can be categorized as follows according to FTI management purposes.

1. FTI Operations

Teamcenter by Siemens ^[1] is the media used for management of flight test instrumentation product tree.

A sheet-based list where we track the instrumentations on the aircraft based on their naming format and the data acquisition unit they are installed in.

Jira by Atlassian ^[2], where the health status and anomalies of instrumentations in flight tests are monitored & reported to FTI engineers and malfunction activities are initiated based on the findings.

1.1 A/C Configuration

Aircraft configuration management in Teamcenter is not in true focus to picture FTI systems in 3D model based to track. FTI parameters are not just names, they are supposed to carry multiple imprints within them to trace.

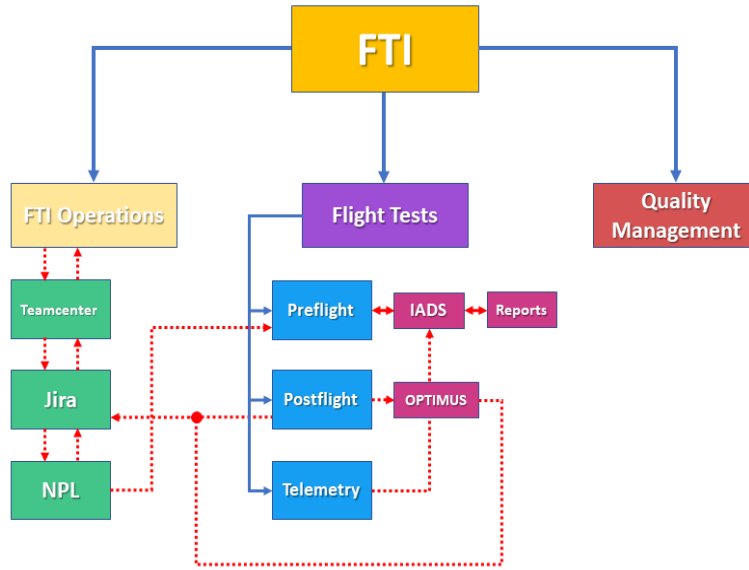


Figure 1 FTI Management Flowchart

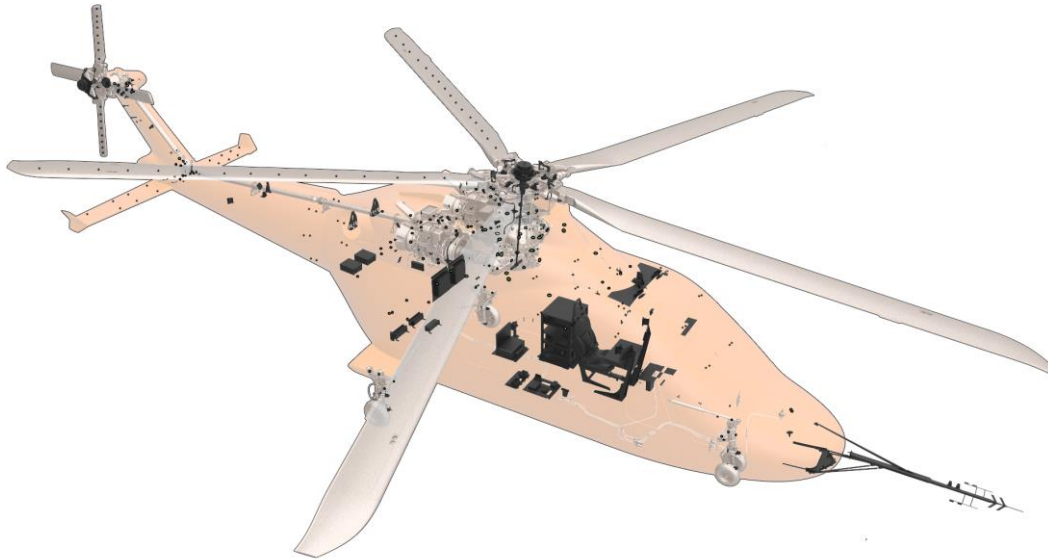


Fig. 2. Figure of FTI system in 3D, Teamcenter.

Even though the 3D model-based configuration given in Figure 2 provides information about the instrumentation to the user, it is insufficient in parameter tracking because it does not contain information such as sensor serial number, structural part serial number and calibration date. Hence reaching the desired resolution becomes a difficulty.

To manage daily changes made on FTI system in Teamcenter requires transitions between different medias. One of them is Numbered Parameter List.

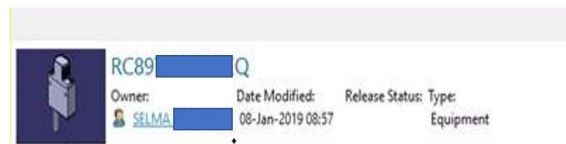


Fig. 3. Teamcenter sensor naming format, RC short for Rotor Craft, 89 as FTI ATA chapter.

Parameter No	Zone	Requester	Measurement Name
TAC701	7	ATA0330	TR Rotation Speed

Fig. 4. Numbered Parameter List sensor naming format, TAC short for Tacometer, 701 as the first tacometer of 7th zone on aircraft.

Flight tests campaigns performed on multiple prototypes and the same day changes that may come with it create conflicts between the product and FTI, and the traceability of this kind of dynamic configuration management creates engineering challenges and increased work effort. In addition, Teamcenter does not indicate the correlation between instrumentation and post flight data.

1.2 Numbered Parameter List

Numbered Parameter List, aka NPL, is a sheet-based file in which to keep track of parameters in the FTI system on the aircraft and can be called the backbone of FTI configuration management. Through this file, monitoring and managing the sensors and digital lines on the aircraft can be done. Even though it is a file full of tables, NPL actually makes a sheet meaningful thanks to its set of rules. Parameter naming rules is determined at the beginning of a project, can only give a first impression of both the type of a sensor and its location on the aircraft. If a parameter is named POT805, one understands that this is the 5th potentiometer located in the 8th zone through the imaginary divided zones of the helicopter. By checking the potentiometer sheet in NPL, one can access the identity of this sensor and how the data it depicts is interpreted.

Of course, the only purpose of this 6-digit name format is not to represent the type of sensor and the region where it is located. Parameter number represents a region, mechanism, the parameter itself, where data will be collected on the rotary wing. In every prototype of the project, on board or not, the name of that parameter where data is collected by FTI, is always the same.

Although this situation ensures traceability and sustainability in a way, it also becomes possible to form conflicts between FTI configuration of the aircrafts. NPL files are updated with a new version name with each change, to reflect the dynamic FTI system. The user records the changes in a history log file. Since it is a human-based system, there is room for greater errors on working for multi-projects and platforms.

Each experimental platform of a project has its own NPL file. To manage the parameter history and match them with the aircraft's own configuration and flight tests, the NPL version is updated with every minor change. This method was applied so that the monitoring of a parameter is more accessible. Although this situation also ensures traceability and sustainability in a way as well, it also becomes possible to form conflicts between FTI

configuration of the aircrafts since it is still a human-based system on a multi-project and platforms environment. Which shows that the parameter name may be insufficient for the NPL entries in the FTI configuration management in the Teamcenter product tree.

1.3 Jira by Atlassian

Flight Test Instrumentation deficiencies can be detected during flight tests and these deficiencies can be flight abort or can be solved as soon as condition permit. FTI Jira system deficiencies can be defined by flight test engineer, system designers, flight test instrumentation engineer. The system log status presents not only the instrumentation improvement history also keeping the knowledge about the problems.

Having Jira to track and record these problems or improvements is not completely sufficient for FTI management. In order to understand the problems and interpret what kind of action should be taken, it is essential to first make sense of the post flight data and view it from the FTI perspective. To achieve this, data has to be plotted and examined over time intervals. For this case, OPTIMUS, the in-house flight test database, is used and the connection between the FTI configuration of the flight test and the Jira findings gets to be accessible.

2. Flight Test Managements

There are formalized processes to control and maintain the FTI system before, during and after each flight tests or campaigns. In this process, the FTI engineer has to access different media in various locations, without a network between them. These can be summarized as follows.

- IADS, to monitor parameters before and during flight tests in telemetry rooms
- Numbered Parameter List, to obtain the FTI configuration
- Preflight reports, to access previous activities performed on the aircraft
- OPTIMUS, the in-house flight test database developed to share flight tests' post data with design teams

2.1 Pre-Flight Tests Activities

Preflight test activities performed before the flight test, to see that the FTI system is ready for this operation and to prove that the flight test critical parameters are healthy and consistent. To document and prepare the report of this, an FTI engineer should first obtain the real-time data gathering from the analog and digital

parameters on the aircraft to the data acquisition system with IADS, match it with a numbered parameter list, to see that the configurations match. Anomalies should be recorded and indicate the activities that have occurred on the aircraft since the previous preflight, if any, such as a sensor to be removed from the network.

Although this activity is only valid for 24 hours, dedicating the work effort spent to perform it to more than one project and the multiple platforms requires serious planning ahead of time. Documents reflecting these activities are recorded in FTI database and informed via e-mail and shared with the relevant teams, and knowing that these works have been completed remains specific to the person performing the activity.

Reviewing the parameters in preflight with the human eye inspection increases work effort, especially on a platform with different types of sensors & data protocols. It requires experienced personnel to carry out these actions and to interpret them well when necessary. Which, may not, fully provide traceability and reliability.

2.2 Post Flight Tests

After a flight test, an FTI engineer must obtain the data collected by the data acquisition unit on the aircraft and share it through the internal network so that it can be examined in detail by the analysis/design teams. For this, the raw data needs to be matched and interpreted with our configuration files created via NPL. In the past, FTI engineer would share this after matching the data with configuration files through IADS. This process would take a long time and effort, sometimes more than half a day. Nowadays, thanks to OPTIMUS, the flight test database developed by TUSAS Helicopter FTI & AI Teams, engineer responsible for the platform only needs to use a single system to share flight test post data and it takes a few minutes to perform the necessary set-ups.

2.3 OPTIMUS

After approximately 1 hour of flight test, the data collected from the FTI system on the T625 platform can consist of 100GB even in compressed UDP packets. In the past, in order to make sense of such large and raw data, IADS data manager was used and hours were waited for the data to be interpreted and exported corresponding to the desired test points.

OPTIMUS is a flight test database and framework developed by TUSAŞ. Created to manage such a large data, even in its

compressed form, and to make it more accessible and faster for export.

3. Quality Management Processes

FTI engineer makes a statement on behalf of the truth of the collected data. Evidence must be provided to document that the data collected during flight tests reflects the conditions during flight as it is and the calibrations of the sensors are valid. A calibration laboratory system is used to keep the calibration details of the sensors and process them into NPL. This system keeps calibration reports of sensors based on their serial numbers. Values such as the expiration date of the calibration and the sensitivity factor used during the interpretation of the data collected from the sensor are obtained by these reports. Keeping track of sensors that have a short time until their calibration date expires only through reports requires extra workload and continuous monitoring, as there is no countdown-based system that will warn the user in time.

Just accessing these reports requires a separate work effort. Similar types of sensors are used in multiple projects and platforms. Therefore, it must first be known whether the serial number on the sensor in the aircraft matches the serial number value in the NPL of the aircraft with respect to parameter name. Since there are situations where the sensors on the aircraft cannot be physically accessed, this process cannot always be accurate. All these processes are personnel-based and may cause serial number/sensor conflicts due to the human factor. This not only reduces traceability but also increases peer effort.

FTI Digital Transformation

Almost each of the systems used to manage the FTI configuration is on a separate media. This increased the work effort and limited the accessibility. Based on this, a project has been initiated on a system that is traceable and accessible, aims to collect media in a single environment, reduce work effort and the need for experienced personnel.

As a first step, NPL files were included in the environment of OPTIMUS, the flight database. Along with the flight data of each project and platform in OPTIMUS, the NPL reflecting the FTI configuration of the prototypes is now accessible here and sheet-based tracing is left behind.

By combining these two systems in the beginning, matters below is aimed.

- To follow aircraft data and parameters from the same system.

- Developing a system that will send timely e-mails to FTI staff for parameters that require date-based tracking (Re-Calibration dates, KAD Module Acceptance Tests [3]), while taking advantage of OPTIMUS's user-friendly web interface.
- Accessing reports and documents that track the history and identity of parameters or sensors, based on serial number, from a single place.
- Keeping a log of every change made to the NPL based on versions.

With these changes, all reports regarding the sensor can be accessed via OPTIMUS NPL instead of the distributed systems. Instead of going through the calibration reports for each sensor one by one and checking the re-calibration dates, 3 months before the re-calibration date, warning e-mails are being sent to the user automatically at regular intervals. Only with these changes, work effort has decreased significantly and NPL has become more trackable and accessible.

Future Work and Digital Twin

Main purpose of moving NPL and OPTIMUS to the same environment is just a preliminary preparation for the FTI Digital Twin [4]. Divided into three phases, FTI Digital Twin will display the FTI configuration on a 3D model in a game engine, perform FTI data management & condition monitoring and initiate predictive maintenance activities by making an estimation of sensor health before test campaigns is carried through imitating the environmental conditions beforehand.

The aim of the first phase is to reflect the FTI configuration, sensors and parameters on the helicopter shell within a 3D framework. With this application, which will eliminate the inadequacy of the information provided by parameter names about sensors and reduce multi-media transitions in product tree management, traceability will increase and by communicating with the OPTIMUS NPL system, the imprint information entered into NPL about the sensors will be accessible from a single media.

Phase 2 will combine real-time data with the FTI parameters collected on the 3D framework in Phase 1, and perform health monitoring by passing it through machine learning models that will establish data characteristics on the sensor data in static or dynamic conditions. This system is going to quickly depict the anomaly in the acquired sensor data in preflight activities, as a result, there will be a reduction in work effort. Necessity on the experienced FTI

engineer will lessen. Through the data characteristics that cannot be established by the human eye, performed preflight activities will be less prone to deficiencies.

In order to adapt the machine learning models in this process to a dynamic FTI system, the models will be re-trained with offline data, constantly. Therefore, bringing OPTIMUS and NPL together is essential to communicate them with the FTI digital twin system.

In the 3rd Phase, these models were trained with data collected in different environmental conditions, already in the FTI database; and the data characteristic established between the data, it will be able to predict the situations that the sensors will exhibit during flight test campaigns and warn FTI before anomalies occur by simulating flight tests on the game engine. The system will initiate malfunction activities on the sensor before the flight tests, making work effort more efficient.

Conclusion

To sum up, efficiency has been increased even by combining the 2 systems included in the FTI configuration, which is managed within multi-media systems that limit work effort and accessibility, the Digital twin will further optimize this management. It will gather the systems in a single framework and make the activities performed on the aircraft more controlled and accessible by combining Machine learning algorithms within FTI data management.

References

- [1] *PLM software | Siemens Teamcenter*. (n.d.). Siemens Digital Industries Software. Retrieved May 22, 2024, from <https://plm.sw.siemens.com/en-US/teamcenter/>
- [2] Atlassian. (2019). *Jira*. Atlassian. Retrieved May 22, 2024, from <https://www.atlassian.com/software/jira>
- [3] *Acra KAM-500 | Curtiss-Wright Defense Solutions*. (n.d.). www.curtisswrightds.com. Retrieved May 22, 2024, from <https://www.curtisswrightds.com/products/flight-test/data-acquisition/acrakam500>
- [4] AIAA. "DIGITAL TWIN: DEFINITION & VALUE." An AIAA and AIA Position Paper, Dec. 2020, www.aiaa-aerospace.org/wp-content/uploads/Digital-Twin-Institute-Position-Paper-December-2020-1.pdf. Accessed 22 May 2024.

IQRF® Communication Standard: Reliability for Lossy, Low-Rate Wireless Mesh Networks

Vladimír Šulc
IQRF Tech s.r.o.

vladimir.sulc@iqrf.org

Abstract

Wireless mesh networks are still a topic even over twenty years from the first indication of market success at Gartner Hype Cycles.

Too many trade-offs and limitations exist in latency, hop count limits, determinism, and reliability through all the globally supported wireless mesh networking technologies until today. The reason is simple: technical concepts focused primarily on routing optimization rather than reliability.

Contrary to that approach, the IQRF® has focused on reliable message delivery as the primary value. With 250+ routing hops and reliable message delivery, the IQRF® excels nowadays, especially in street lighting applications, where the long-range should be achieved, and high reliability must be guaranteed.

After two decades on the market, the IQRF® gets standardized, allowing everyone to use and implement all technical achievements and reliable protocols protected by dozens of patents under one royalty-free license.

Key words: iqrf, wireless, mesh, iot, reliability

IQRF® main features and benefits

IQRF® is a complete technology, standard and ecosystem including hardware (transceivers, gateways, repeaters, complete electronic devices, accessories, development tools), software, protocols, support, commissioning tools and services.

Since 2004, MICRORISC and IQRF Tech have developed IQRF®, a reliable, low-power, bidirectional, wireless mesh communication technology. With its IQMESH® protocol, IQRF® enables extremely robust and sophisticated mesh topology. Thousands of wireless systems worldwide are the proof of that.

More than 20 years of continuous research and development for and with customers crystalized in state-of-art communication technology featuring:

- **industrial reliability**

Thanks to the IQMESH® protocol, more network nodes mean higher reliability.

It is deterministic and reliable even in difficult environments.

It delivers robustness and industrial reliability to the wireless IoT.

In the IQRF® network using the IQMESH® routing protocol, the FRC® (Fast Response Commands) protocol can be used, which enables fast data aggregation and confirmation of broadcasts or multicasts.

With 200+ repeating nodes in one network cooperating in a mesh topology you can cover huge facilities, industrial halls, and streets and reliably deliver the message despite bad RF conditions in area.

- **simple integration**

Modular architecture, lightweight yet efficient DPA protocol, hardware and software development tools, plenty of guides, examples, and tutorials along with excellent technical support make development easy.

- **ultimate security**

The complex approach from device association to a network to automatically encrypted communication is based on security standards.

The security services layer is responsible for ensuring the following security objectives: frame integrity, networking frame authenticity, footer and payload confidentiality, replay protection.

- **interoperability and huge ecosystem**

The interoperability of devices from different manufacturers is based on IQRF interoperability standards.

Products certified on IQRF interoperability are listed in the IQRF Alliance marketplace at a website and can be easily used in complex IoT projects.

- **IQRF True Low Power® consumption**

IQRF® is designed to operate efficiently with minimal power consumption, making it suitable for battery-powered devices and applications where energy efficiency is crucial.

Low wireless consumption pushes battery limits to the new boundaries defined only by the battery's self-life.

A smart combination of different power consumption modes, from transmit mode to deep-sleep mode, makes it possible to achieve really low total power consumption.

For example, a sensor transmitting data every minute can run for more than 20 years on a single AA battery, twice the actual battery life.

IQRF® network with IQMESH® protocol

IQRF® networks are managed and organized^[1]. The controlling element for other network devices called Nodes is the Coordinator. Nodes with routing capabilities are called routers. Network communication is always encrypted and authenticated according to the latest security standards.

Association process

Nodes are associated with the network by the Coordinator. During the association, the Coordinator transmits the association data to the Nodes in a secure way through an encrypted message. The IQRF MAC is the unique identifier of the IQRF® device used for authentication. The coordinator securely shares information such as communication keys and network settings and assigns each Node a unique logical address used for addressing.

Topology discovery process

During this process, the Coordinator discovers the topology of routing Nodes (routers) and assigns them a virtual routing number (VRN), a unique number reflecting the distance from the Coordinator in hops and defining the time period for routing a given Node.

Each router knows its position in the network and has its dedicated time slot. TDMA-based directional flooding guarantees deterministic and collision-free routing. The IQMESH® routing protocol ensures that routing works well even in large networks. No vectors or routing tables are stored on routers or passed in communication messages.

Communication using the IQMESH® routing protocol is primarily synchronous. It is initiated by the Coordinator and the Nodes only respond to the request. Timing is strictly deterministic. Each Node of the router type forwards the message in a precisely given time slot corresponding to its VRN. The answer goes back the same way in exactly the opposite order. For a better idea of how sending a message on an IQRF® network using the IQMESH® routing protocol is done, see www.iqrf.org/technology/iqmesh/unicast (Figure 1).

Routing extends the range and enables to deliver data to difficult areas. IQRF® mesh routing protocol is called IQMESH®. It is based on an optimized directional flooding. Its main advantages are higher throughput and much higher robustness which primarily becomes apparent in industrial and other applications where a high reliability is a must.

IQMESH® is implemented above the IQRF OS by the DPA framework layer:

- Up to 240 devices in the network - 1 Coordinator + 239 Nodes
- Up to 240 hops
- Low latency (STD) as well as low power (STD+LP) network types supported
- Routing in real time:
 - Max. 60 ms per hop for STD network, based on the payload
 - Max. 100 ms per hop for LP network, based on the payload
- Payload up to 64 B
- All communication is automatically encrypted by AES-128
- Autonetwork functionality for automated network build-ups

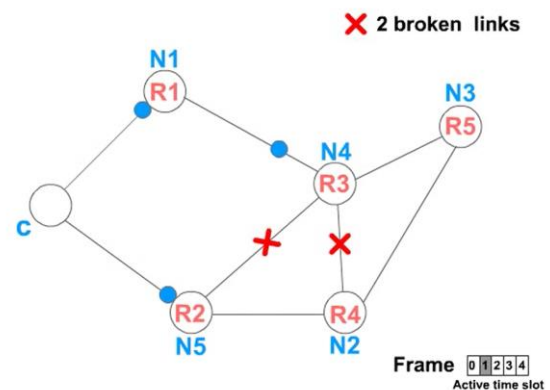


Figure 1 Routing in the IQRF network

FRC® (Fast Response Commands) protocol

The FRC® protocol allows to quickly send a command to multiple Nodes in the network and collect small data from them. It is a significantly faster method than polling individual Nodes one after the other using unicasts.

FRC® in its current implementation allows sending up to 30 B of user data to all or selected Nodes and collecting:

- 2 b from up to z 239 Nodes
- 1 B from up to 63 Nodes

- 2 B from up to 31 Nodes
- 4 B from up to 15 Nodes

The FRC[®] protocol has three phases:

1. A request is sent to the network. Once received, all devices are synchronized and ready to execute the desired command.
2. The addressed devices send the requested data to their neighbours.
3. The required data is aggregated step by step and sent back.

The command execution time is strictly deterministic and independent of the topology. Watch the animation of the whole process on <https://www.iqrf.org/technology/iqmesh/frc> (Figure 2).

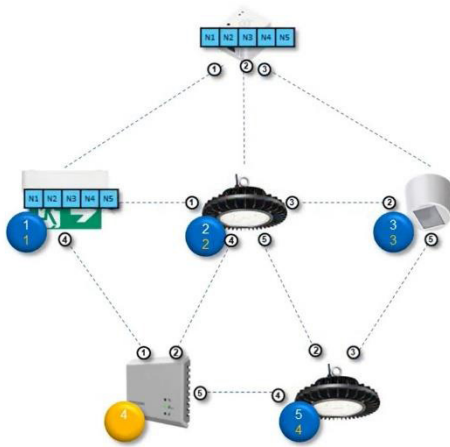


Figure 2 FRC[®] protocol

IQRF[®] interoperability certification

Companies that manufacture products for the IQRF ecosystem join together in the IQRF Alliance^[3]. IQRF Alliance tests products for interoperability at the application level.

You can find detailed description of IQRF Standard for sensors and other devices in the section IQRF Interoperability on IQRF Alliance website^[3]. When a product manufacturer follows the description of IQRF standard on the communication level, then from the point of view of integrators it does not matter if they communicate with sensors from one manufacturer or another, because they communicate uniformly and get predictable, uniformly structured responses.

The IQRF interoperability certification procedure includes getting HWPID for the certified product, inspecting required documents and the product, checking its compliance with the IQRF interoperability standard, fixing possible issues, and finally,

product listing in the IQRF repository and marketplace.

When manufacturers use certified IQRF[®] transceivers, they don't need to care about this lower basic part of the IQRF[®] interoperability.

Otherwise, they need to follow also guidelines for IQRF Communication Standard Specification, which defines IQRF Standards Association^[2].

IQRF Standards Association is a non-profit organization responsible for the IQRF Communication Standard Specification, royalty-free licensing of the open IQRF Communication Standard, and the IQRF MAC's management.

The IQRF Communication Standard specifies communication in the IQRF wireless mesh network and enables electronic devices to communicate reliably and securely. Manufacturers can implement the IQRF Communication Standard in their devices under a single royalty-free license. IQRF Standards Association certifies interoperability at the basic communication level. It means manufacturers can implement IQRF[®] technology directly into the electronics of their products or can manufacture their own IQRF[®] transceivers. It is a lower-level, basic part of the IQRF interoperability certification.

Conclusion

Today's market is deeply fragmented, there is no globally accepted standard due to many limitations. So, there is a plenty of different wireless technologies available on the market.

They are usually assorted according the range to personal, local, neighbourhood or wide area networks.

Thanks to the routing, IQRF[®] can reliably communicate from short distances up to few kilometres.

Thus, perfectly addresses many low power applications from monitoring, automation or control.

It perfectly fits to applications from security, through building automation, up to Smart City.

The benefit of IQRF[®] technology lies in its combination of low-power operation, the ability to operate in a mesh topology with high reliability and range, the interoperability of IQRF[®] ecosystem products, security features, and ease of integration, making it a versatile solution for a wide range of IoT applications using wireless transmission.

References

- [1] IQRf - Technology for wireless. Online. 2024. Available at: <https://www.iqrf.org/>
- [2] IQRf Standards Association. Online. 2024. Available at: <https://standard.iqrf.org/>
- [3] IQRf Alliance. Online. 2024. Available at: <https://www.iqrfalliance.org/>

Flight Test Instrumentation System: Tailoring MBSE Methodologies for Prototype Aerial Systems Development

Claudia Pérez Rus¹, Stéphane Le Gal²

¹ Airbus Defence and Space, Avenida del Aeropuerto, s/n, 41020 – Sevilla, Spain

² Airbus Defence and Space, Avenida del Aeropuerto, s/n, 41020 – Sevilla, Spain

claudia.perez.rus@airbus.com

stephane.le-gal@airbus.com

Abstract

This paper investigates the application of Model – Based Systems Engineering (**MBSE**) methodologies to prototype aerial systems, with a specialized focus on the complex modelling requirements of Flight Test Instrumentation (**FTI**) system. Unlike conventional embedded aircraft systems, FTI possesses unique characteristics and challenges. Traditional design and implementation approaches often struggle to accommodate the specialized nature of FTI, leading to misunderstandings and inefficiencies in system communication and integration. New Airbus programs are bringing the shift towards MBSE, evidencing the necessity of adapting these methodologies to address the particularities of FTI. This article emphasizes the need for tailored modelling techniques capable of capturing the nature of FTI systems. This study proposes a structured framework that enhances system-wide visibility, facilitates seamless integration with other aircraft systems, and enables more effective collaboration among multidisciplinary teams. This research goes through the challenges of customizing MBSE methodologies to suit the specific requirements of FTI, ultimately contributing to more efficient, sustainable (**zero-paper**) and reliable **prototype** aerial system development processes.

Key words: MBSE, FTI, zero-paper, prototype

1. Introduction

Model – Based System Engineering (MBSE) methodologies are on the rise as a basis for system engineering activities. The definition of aerial systems can greatly benefit from this approach, evolving towards digitalized processes.

MBSE approaches integrate a set of models as analytical, system architectural, verification, mechanical, electrical, software models, among others. This document addresses the possibility of including Flight Test Instrumentation (FTI) system in the system architectural model in particular. This type of model emphasizes how pieces fit together into a consistent whole and are used to capture functions, behavior, structure, components, objects, information flows, interfaces, interactions and scenarios [1].

During the definition of aerial systems, FTI system are developed in parallel, ensuring that the system can gather all required data during flight tests to successfully reach certification.

FTI systems can benefit of MBSE methodologies in various aspects which will be later described. Nevertheless, the different lifecycle, together with the particular nature of FTI interfaces towards other systems, leads to the necessity of a tailored approach to MBSE to cover prototype development requirements.

1.1. State of the Art

The research referenced in [1] introduces the MBSE development of civil aircraft and then establishes an integrated platform for civil aircraft development based on this process. Moreover, the article referenced in [2] deals with simulation models for MBSE applied to aircraft systems, mostly focusing on the technical discipline of fluid dynamics with embedded hardware and software. It mentions how as the use of MBSE increases, the usage of flight test data for model validation increases. It is also highlighted how the proper definition of flight test installations on aircraft are critical to this duty. Continuing the literature research, [3] approaches the creation of flight test scenarios

This information is of origin Airbus Defense and Space/Spain and does not contain any export controlled information

Airbus Amber releasable to ETTC

ETTC 2024– European Test & Telemetry Conference

based on model - based system engineering artifacts represented in System Modelling Language (SysML). In the current literature, there is a lack of concrete studies covering how FTI systems can be introduced into system architectural models from early design stages, benefiting from MBSE methodologies.

1.2. Objectives

The objectives of this paper are to:

- analyze the crucial interfaces between serial aerial system and FTI definition processes,
- evaluate the opportunities and difficulties of applying MBSE methodologies to FTI systems,
- and propose key aspects to be tailored when including FTI in the system architectural model.

1.3. Structure

To meet the previously enumerated objectives, this article is structured as it follows:

- **Model Based System Engineering:** This first introductory chapter summarizes the principles of MBSE. The differences with respect to traditional system engineering approaches are gathered.
- **Flight Test Instrumentation System:** This second introductory chapter describes the basics of a flight test instrumentation system.
- **FTI Specific Development Process:** This chapter defines the how FTI systems are usually defined and developed. Interactions during aerial system and FTI definition processes are analyzed.
- **Opportunities of applying MBSE to FTI:** Based on the previous one, this chapter identifies how MBSE can bring opportunities to enhance FTI definition and development process.
- **Difficulties of applying MBSE to FTI:** This chapter identifies difficulties to be taken into account when tailoring MBSE methodologies to FTI.
- **Prototype and serial system: Variants:** This chapter covers the fact that the architectural model of a prototype evolves in parallel to the serial system one.
- **System architecture model structure:** This chapter addresses FTI presence in the overall model structure.

- **System architecture model views:** The model of an architecture can be approached from different views, which is handled along this chapter.
- **Modelling of internal FTI:** This chapter focusses on a model of the internal FTI architecture.
- **Modelling of FTI interfacing with other systems:** This chapter covers the integration of FTI architecture into an architecture model of the overall aerial system of which FTI is part.
- **Conclusion:** This concluding chapter collects future steps, lessons learnt and overall conclusions of tailoring MBSE methodologies for prototype aerial systems development.

2. Model Based System Engineering

The traditional way of working in systems engineering is document centric: the primary focus is to create and manage various documents such as requirements documents, design specifications, interface control documents, etc. In this approach, the information is primarily conveyed through text, diagrams, tables, and other traditional document formats. The changes and updates of the system are managed by updating the relevant documents, which can sometimes lead to version control challenges and inconsistencies. See Fig. 1.



Fig. 1: Document centric approach schema

MBSE is a model centric approach: the documents are replaced by a model, that graphically represents the system, its components, interactions and requirements. Instead of relying on textual documents, MBSE employs standardized modelling languages like SysML (which stands for System Modelling Language). The model serves as master source of information, enhancing traceability and consistency. See Fig. 2.

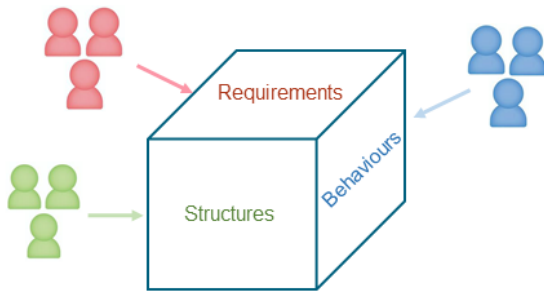


Fig. 2: Model centric approach schema

MBSE is an approach that:

- Improves communication and collaboration across disciplines,
- Improves ability to predict system behavior,
- Ensures design data consistency and completeness,
- Allows to perform cross domain impact analysis of changes,
- Supports interface management, enabling efficient system integration.

The International Council of Systems Engineering (INCOSE) formally defines MBSE as the formalized application of modelling to support system requirements, design, analysis, verification and validation, beginning in the conceptual design phase and continuing throughout development and later life cycle phases.

3. Flight Test Instrumentation System

Main purpose of a FTI system is to gather flight test data - in a safe and secure manner - which are later used to validate and certify the aerial system (e.g., aircraft, Remotely Piloted Aerial System (RPAS), Unmanned Aerial Vehicle (UAV), etc.).

When designing a new aerial system, the prototypes need to be fitted with a considerable amount and variety of instrumentation, whose installation may impact the system design from the very beginning.

As depicted in Fig. 3, FTI systems core functions are aiming to:

- Acquire flight avionics data and aircraft structural/environmental data,
- Record flight test data on-board and on-ground for offline data analysis,
- Encrypt flight test data (if needed),
- Transmit on-board data by telemetry means to FTGS (Flight Test Ground Station) for real-time monitoring during test flights,

- Contribute to execution of specific flight tests by the means of special instrumentation, as for example:
 - Envelope expansion by using flutter excitation system,
 - Real-time monitoring of weapons jettisoning by using video cameras,
 - ...

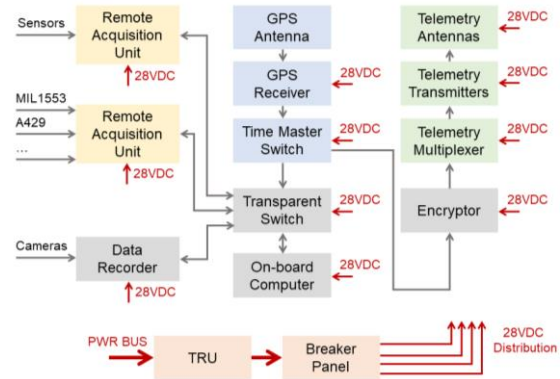


Fig. 3: FTI conceptual block diagram

Additionally to these core functions, FTI system relies on its own support functions which guaranty FTI proper operation:

- Power management and distribution,
- Time synchronization,
- Data management and distribution,
- Health status monitoring.

FTI is usually not considered as a L2 system (see Section 8 for the definition of a L2 system) itself because of its particularities and for being only implemented on prototypes. Therefore, it has a very specific lifecycle which is described in the following section.

4. FTI Specific Development Process

Following conceptual design phase, any aerial system development will follow standard system engineering approach as depicted in Fig. 4 (known as V model). This illustrates main system engineering principles which goal is to deliver the suitable system on-time, minimizing risk, controlling cost and quality along the whole project. It relies on:

- Properly capturing customer needs,
- Defining and validating system functional requirements early in the project,
- Proceeding with system and subsystems design,
- Building the right system and subsystems,

*This information is of origin Airbus Defense and Space/Spain and does not contain any export controlled information
Airbus Amber releasable to ETTC*

- Performing coherent and exhaustive verification and validation of the whole system.

Fig. 4 points out particularities of FTI system development process, which is characterized by a much more time-constrained lifecycle compared to aerial system development one:

- Even if system testability requirements shall be considered from the beginning, L1/L2 systems requirements toward FTI come late in the development phase as a certain design maturity is usually required to properly assess qualification and certification needs, and therefore the needed flight test instrumentation. Consequently, FTI requirements definition and validation arise once aerial system is already in design phase, requiring many interactions to follow design changes (❶).
- In design phase, FTI can anyhow be impacted by systems late design modifications, originated from implementation/realization issues, implying requirements update and therefore quick FTI system definition update (❷).
- As FTI is mainly based on COTS and well-known equipment, implementation/

realization of FTI system is much more agile than for a standard L2 systems.

- Anyhow, FTI verification phase may require involvement of other L2 systems (combined tests ❸). This imposes FTI system to be already available during L2 systems verification test, shortening its own verification phase.
- Same occurs for FTI system validation as FTI is involved in aerial system verification process (❹).
- Finally, as FTI is a key contributor to whole system validation and qualification, it has to be fully validated at this point of the project (❺).

In conclusion, FTI development process is much shorter than aerial system development one, requiring a lot of interactions with various stakeholders, agility and synchronization efforts to guaranty consistency of the end-to-end definition. In this regard, opportunities arise for FTI to benefit from MBSE features, which are gathered in the following Section 5.

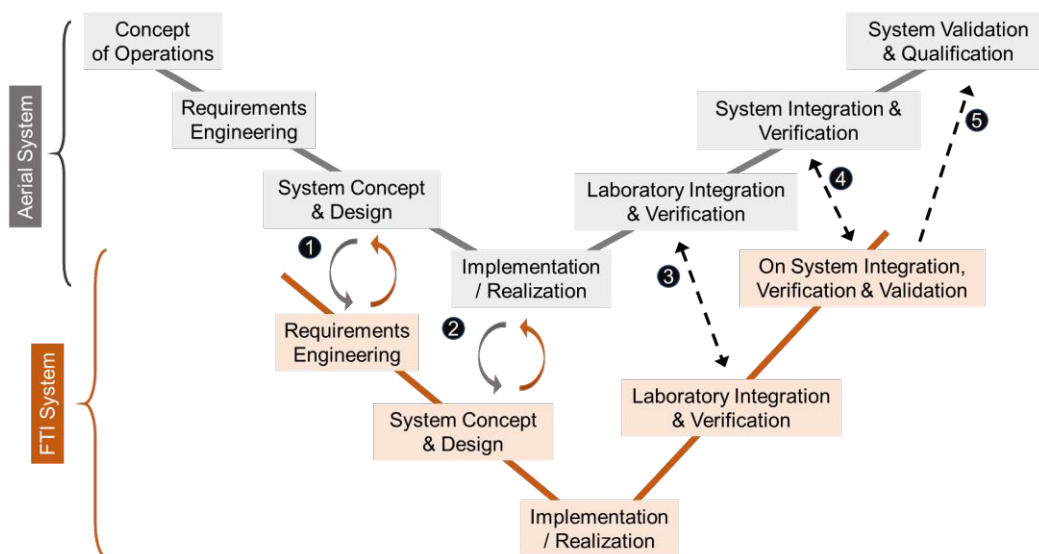


Fig. 4: FTI Development process

5. Opportunities of applying MBSE to FTI

Observing in detail the previously described FTI development process, it is noticeable that there is room for improvement, especially regarding:

- **FTI Visibility:** In a traditional FTI development process, FTI is visible to other

systems at late stages of the definition phase.

- **System Visibility:** The visibility of other systems is arduous for FTI as different aspects are defined in a multitude of individual and non-interrelated documents. This implies difficulties in cross – domain

*This information is of origin Airbus Defense and Space/Spain and does not contain any export controlled information
Airbus Amber releasable to ETTC*

ETTC 2024– European Test & Telemetry Conference

analysis regarding security and safety (among other things) of the architecture as a whole.

- **FTI Integration in the system:** In a traditional FTI development process, FTI is likely to be integrated once the system is defined, which can lead to inconsistencies.
- **FTI Design Review:** In a traditional approach, the verification of the FTI design is done by means of a manual review of the documentation that defines the system.

Tab 1 compiles a comparison between traditional and model – based system engineering regarding the previously enumerated points. Based on that, the opportunities of applying MBSE to FTI development process are extracted and summarized in the right – hand side column.

Tab 1: Opportunities of applying MBSE to FTI

	Traditional SE	Model - based SE	Opportunity
FTI Visibility	Late visibility	Enhanced visibility from early design stage	FTI design can be optimized being part of the system as a whole. The L2 systems can define their architectures considering interfaces with FTI.
System visibility	Multitude of individual and non-interrelated documents	Integrated picture of the whole system, including cross – domain system properties such as safety criticality, vulnerability, etc.	Support cross – domain analysis (safety, security, etc.).
FTI Integration in the system	FTI is integrated post system definition.	Anticipated FTI interfaces definition for further integration within the overall system	Enable earlier definition of interfaces towards FTI. Systems can consider the implication of FTI interconnections and mechanical installations in their design.
FTI Design Review	Manual review of the documentation.	Formal model validation rules	Support automatic consistency checks.

6. Difficulties of applying MBSE to FTI

A change towards MBSE inevitably implies the emergence of difficulties and challenges. The obstacles that may be encountered by the nature of both MBSE and FTI are identified and listed below:

- **Methodology change:** The changes in processes towards digitalization imply high anticipation and cost, time and resource efforts.
- **Robustness vs agility:** On the one hand, MBSE is a robust and formal approach to define a system. On the other hand, the nature of FTI requires agile processes. A trade – off between robustness and agility has to be found.
- **End-to-end visualization:** The end-to-end describes a process that takes a system from the very beginning to the end of its

definition. Following MBSE methodologies, the system is defined in an integrated tool chain.

Modelling particularities of intrusive FTI interfaces: FTI has very particular interfaces towards other systems as it needs to gather transparently data within sub-systems interconnection (e.g., avionic bus tapping), without compromising system function. This requires specific and unclassical modelling technics. Tab 2 compiles a comparison between traditional and model – based system engineering regarding the previously enumerated points. Based on that, the difficulties of applying MBSE to FTI development process are extracted and summarized in the right – hand side column.

*This information is of origin Airbus Defense and Space/Spain and does not contain any export controlled information
Airbus Amber releasable to ETTC
ETTC 2024– European Test & Telemetry Conference*

Tab 2: Difficulties of applying MBSE to FTI

	Traditional SE	Model - based SE	Difficulty
Methodology Change	Well known skills, tools and methodologies	Acquisition of new skills + adaptation of existing tools and methodology or development of new ones	High adaptation and anticipation required, which is translated into cost, time and resource efforts. Risk of not reaching sufficient maturity versus project milestones.
Robustness versus Agility	A robust system engineering methodology can be easily tailored for FTI for increased agility with a minimum of constraints.	Robustness is ensured through well-defined methodology and integrated tool chain. Agility is possible, but limited by a constrained framework.	Anticipation needed to tailor the methodology to be able to cope with agile implementation for FTI. Modelling rules have to be extended and customized beforehand.
End-to-End Process	The end-to-end process does not require the system to be defined in integrated tools.	The end-to-end process requires the system to be defined in an integrated tool chain.	The increased number of tools and the interdependencies between them make difficult the visualization of the end-to-end process and the understanding of the implications of a change along the whole tool chain.
Modelling particularities of intrusive FTI interfaces	Managed directly together with system owner and FTI.	Definition of specific modelling rules and responsibilities are required to be able to manage intrusive FTI interfaces.	Definition of serial and prototype system in the same model makes difficult to segregate both architectures in the case of intrusive FTI interfaces.

7. Prototypes and serial system: Variants

There are two important concepts in product line engineering and configuration management: variants and versions. On the one hand, versions are sequential revisions replacing each other; on the other hand, variants exist in parallel.

A prototype is developed in parallel to the serial system: it can be seen as a variant of the product. Fig. 5 provides a visual representation of this concept.

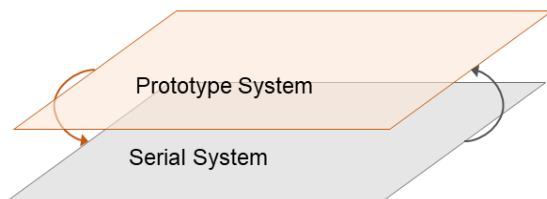


Fig. 5: Prototypes as variants of serial systems

The need for prototypes responds to high-level requirements: the system must have the functionality of being able to be tested. This justifies the existence of the particularities of the prototypes in the model as a concrete variant.

To use the same system architectural model to represent a set of system variants requires a high configuration control effort. As said before, a prototype responds to additional high-level functions than those of serial systems. A prototype evolves in different versions together with the aerial system. As prototypes development occurs in parallel of serial system development, both system architectures must be synchronized so that coherency is kept over whole system definition, including FTI.

8. System architecture model structure

A common approach in the development of complex systems involves conceptually decomposing the system into a multi-level hierarchy of interacting systems [4]. An aerial system could be decomposed in the following layers:

- **L0 System:** System of Systems (SoS). It represents the System of Interest (SoI) in its context. For example, a RPAS embedded in its operational environment. It answers to stakeholder requirements and operational concept analysis. The actors (e.g., Air Traffic Controller (ATC) and external systems (e.g., Ground Positioning System (GPS)) are also defined.

*This information is of origin Airbus Defense and Space/Spain and does not contain any export controlled information
Airbus Amber releasable to ETTC*

ETTC 2024– European Test & Telemetry Conference

- **L1 Systems:** Systems of Interest (Sol). These are major systems, as for example, the aircraft or the ground control station composing an RPAS.
- **L2 Systems:** Major Subsystems, as for example the electrical system of an aircraft. The definition of these systems answers to requirements that emerge during preliminary design phases.
- **L3 Systems:** Equipment, composing a L2 System. For instance, a battery of the electrical system of an aircraft.

In the system's hierarchical decomposition, FTI can be located at L2 level, but it is only part of a concrete variant of the system: the prototype.

Observing the prototype as a variant of the serial system as presented in Section 7, there are implications at all layers of the system (L0, L1, L2). Fig. 6 depicts graphically how the context of a prototype differs from the one of the serial systems. Note how there are also specific Flight Test (FT) actors and external systems that will be interacting with the FTI, as for example Flight Test Engineers (FTE) or the Flight Test Ground Station (FTGS).

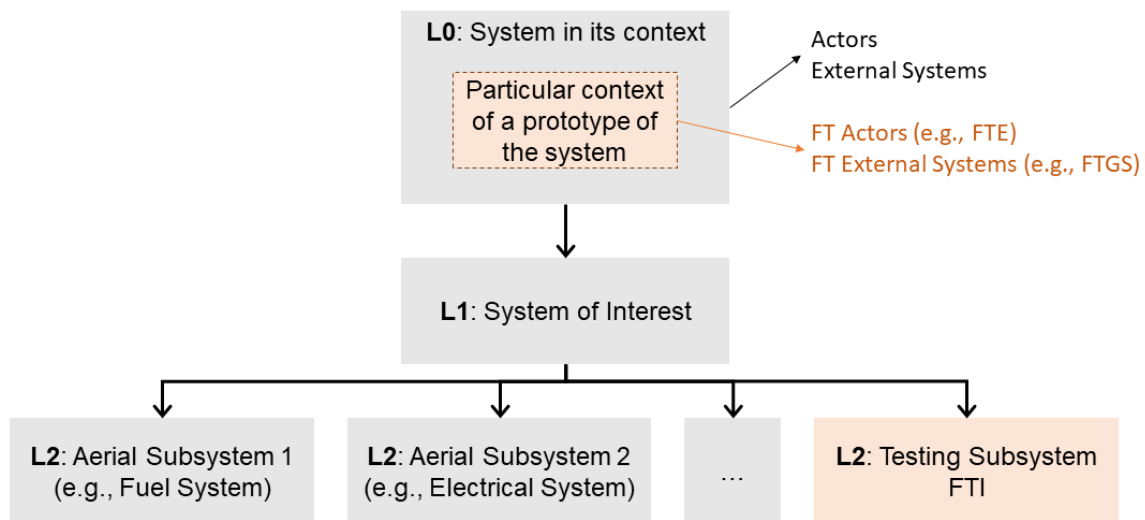


Fig. 6: FTI in the hierarchical structure of the system

9. System architecture model views

In usual MBSE methodologies to define a system architecture, the model can be observed from different views:

- **Requirements view:** A system can be observed as a set of requirements that, by *well-formed textual "shall" statements [...] communicate in a structured, natural language what an entity must do [...]* [5].
- **Functional view:** A system can be observed by a set of interrelated system functions, defining the capabilities, the services, or the functions provided by the system.
- **Logical view:** A system can be observed by a set of interrelated logical systems that compose the logical architecture, which consists in *decomposing and partitioning the system into logical elements. [...]* The

elements interact to satisfy system requirements and capture system functionality. Having a logical architecture mitigates the impact of requirements and technology changes on system design [6].

- **Physical view:** A system can be observed by allocated and interconnected hardware and software resources.

Fig. 7 shows how the previously defined views are traced and linked one to each other [7] [8]. System functions are defined **satisfying** functional requirements. These are **allocated** to logical systems. And these latter systems are an **abstraction** of the physical systems, that are defined and interrelated in the physical view. This tracing enhances impact analysis; for example, if a system is replaced by another, one can traced back, knowing which logical system, system function and requirement may be affected by the change.

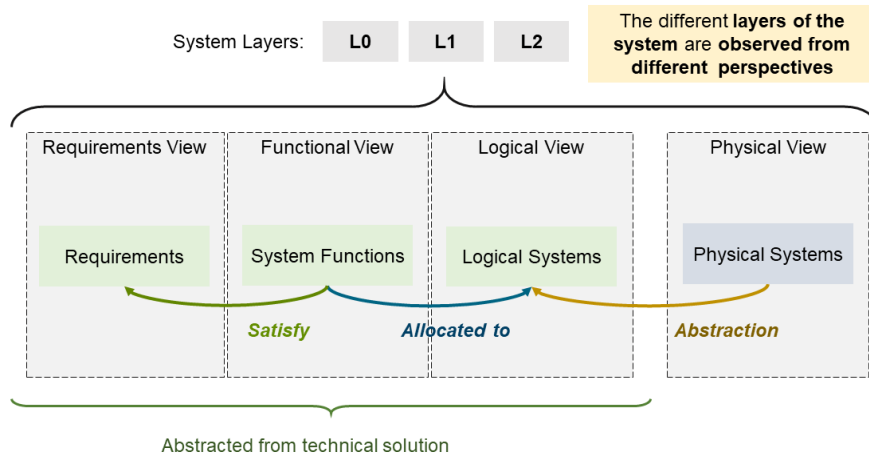


Fig. 7: Model views observed from model layers

10. Modelling of internal FTI

The layers of the system described in Section 8 can be defined through the different perspectives gathered in Section 9, and so can FTI also. Fig. 8 shows how FTI requirements can be traced down to FTI system functions using *satisfaction* links in the system architecture model.

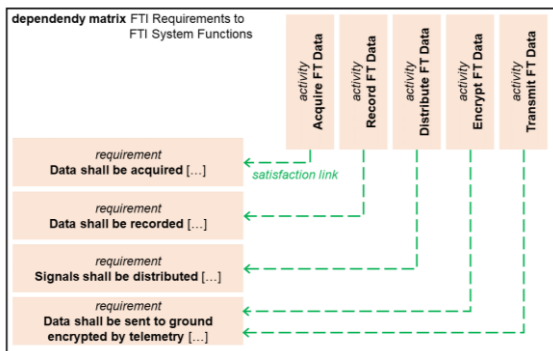


Fig. 8: System functions satisfy system requirements

Then, Fig. 9 depicts the modelling of the relationships between these system functions, defining the functional inputs and outputs of each function. The system functions are then allocated to logical system defining a logical architecture abstracted from the technical one. The black border shows the functional boundary of the system function "Provide FT Data to Ground", which is higher level than the ones represented inside. The lines that cross it represent functional flows coming/going from/to other higher level system functions outputs/inputs, or from external systems or actors.

To refine the logical architecture detailing the technological solution, concrete physical systems are defined realizing the logical ones,

as shown in Fig. 10. Note that this tracing is done at all levels: L2 logical systems as an abstraction of L2 physical systems, and analogously to L3 logical and physical systems.

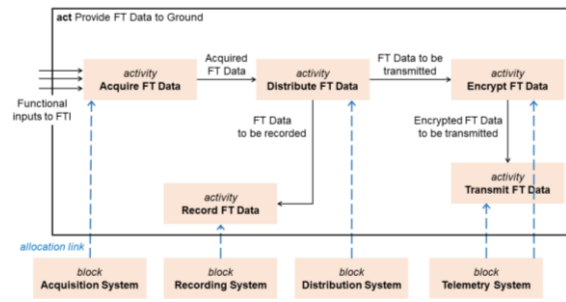


Fig. 9: Logical systems allocated to system functions

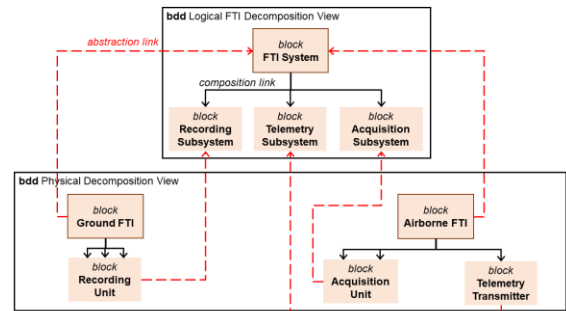


Fig. 10: Logical systems are an abstraction of physical systems

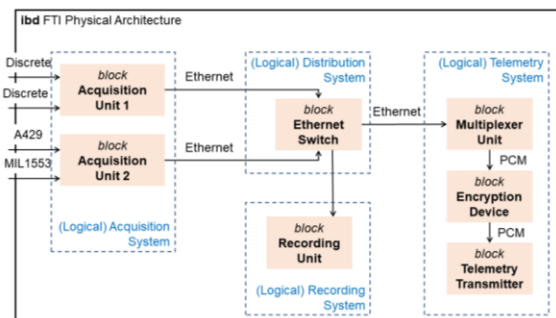


Fig. 11: FTI internal physical architecture

This information is of origin Airbus Defense and Space/Spain and does not contain any export controlled information
Airbus Amber releasable to ETTC

Once the physical systems are defined and traced up to the logical ones, the connectivity between them can be shown (see Fig. 11). It is depicted again how a group of physical systems constitute the realization of a logical one, which in turn has specific system functions allocated that satisfy concrete functional requirements. The black box represents the boundary of FTI physical architecture. The lines that cross it represent physical inputs/outputs coming/going from/to other systems, external systems or actors.

11. Modelling of FTI interfacing with other systems

As shown in the previous section, the FTI architecture can be designed following an MBSE methodology. Nonetheless, it is important to keep in mind that the real benefit is to integrate FTI architecture into an architecture model of the overall aerial system of which FTI is part.

Fig. 12 illustrates the fact that the FTI architecture implemented in the prototypes is defined on top of the serial system architecture. change.

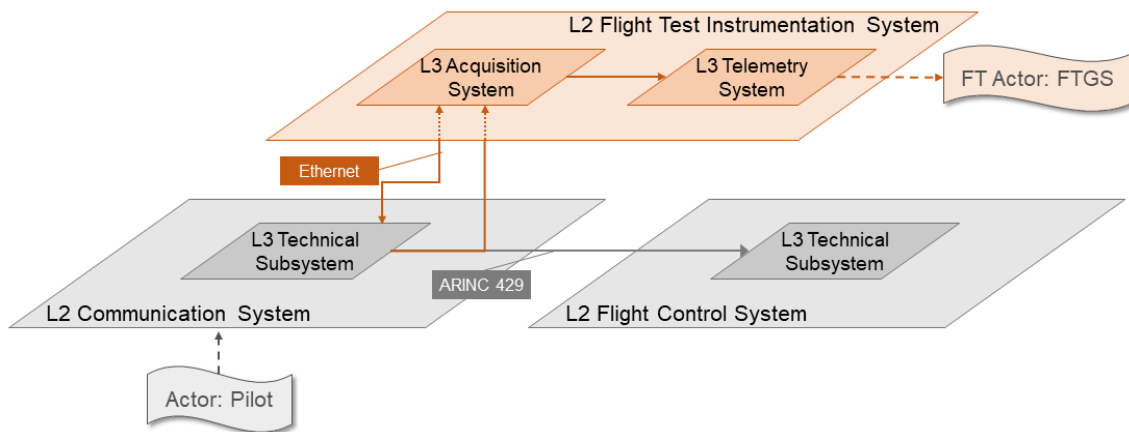


Fig. 12: FTI architecture on top of serial aircraft architecture

The same procedure as the one followed in Section 10 is adopted at the level of the complete aerial system. Fig. 13 shows a diagram analogue to the one in Fig. 10, but corresponding to the physical decomposition of the whole aerial system. In this example, also communication and flight control systems are shown in the composition tree.

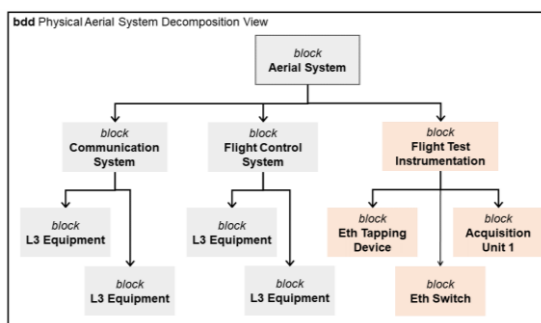


Fig. 13: Physical system decomposition view

The interconnections of FTI with other systems can be modelled: this is one of the key aspects from which FTI can benefit, since the communication and collaboration across disciplines is enhanced. Fig. 14 shows a diagram analogue to the one in Fig. 11, but one level of decomposition above. In this case, the

black border depicts the boundary of the whole aerial system (instead of the one of FTI), so the lines that cross it come/go from/to external systems or actors (e.g., the Air Traffic Controller (ATC) or the FTE). The blocks inside the diagram are systems at the same decomposition layer of FTI (e.g., Communication System, Flight Control System (FCS), etc.).

Note the different types of interconnections shown in Fig. 14:

- The connection ❶ between FTI and FCS is “direct”. FCS actively provides data to FTI through that connection. In the serial system, that connection would simply not exist.
- The connection ❷ between FTI and FCS represents the splice of a harness. FTI sniffs the information that flows between the two L3 FCS equipment. In the serial system, that connection would disappear, but the connection between FCS equipment remains.
- In the connection ❸ between FTI and Communication System an intermediate equipment is installed to sniff the data

flowing between the L3 Communication System equipment. Note that the red (FTI) and black (serial system) connections are mutually exclusive: as in the previous

connections types, the red one does not exist in the serial system. But the black also has to be removed in the prototype architecture.

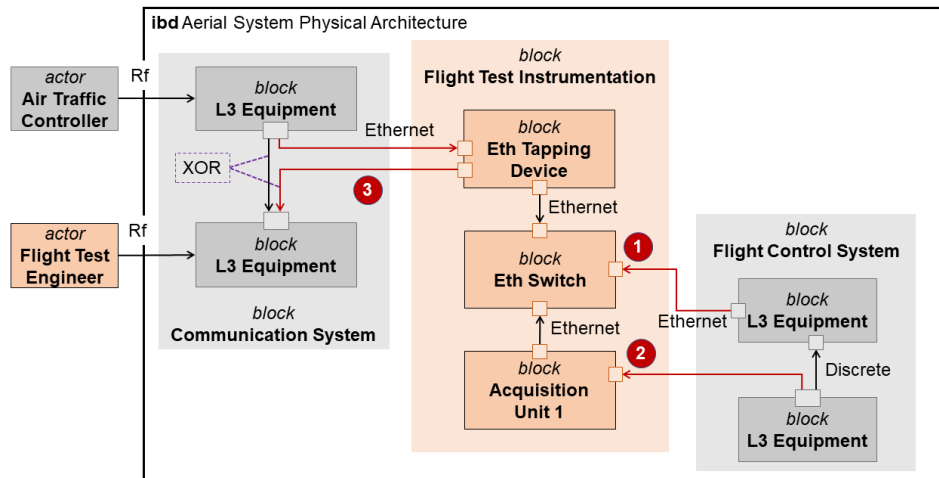


Fig. 14: Technical FTI interfaces towards other systems

Summing up, it is important to keep the serial and prototype architectures well decoupled.

12. Conclusions

Model - based systems engineering methodologies bring with them the **need to adapt to new ways of working**. It is necessary to familiarize oneself with the characteristics of the methodology, **understanding the opportunities (and challenges)** that it brings to the definition of complex systems.

As a FTI engineer, you need to make a deep study of the gaps that you will encounter when trying to bring your system definition into a model - based environment. It is a good idea to think deeply what parts of FTI definition can benefit from this process, which are, for example, the interconnections towards other systems and the repetitive part of the architecture (excluding sensors).

As a model - based system engineer, understand how different FTI lifecycle, as well as its operational concept. For this reason, FTI requires a tailored MBSE approach that enables agility in processes and tools. This has to be reflected at all levels of the system. Moreover, at a physical layer, there are very "FTI specific" types of interconnections with other systems. Awareness of specific processes, methods and tools towards prototypes particular needs and development lifecycle has to be achieved from the very beginning of the project

To conclude, this paper addresses just one piece of the complete MBSE environment: the system architectural model. Further assets are required for the complete definition of the FTI,

from detailed measurement chain definition, pin-to-pin design, electrical wiring establishment, etc. All these elements have to be taken into account for the realization of the system as a whole. This will be subject to further publications.

References

- [1] L. Hart, "Introduction to Model-Based Systems Engineering (MBSE) and SysML", in Delaware Valley INCOSE Chapter Meeting, Delaware Valley, USA, 30th July 2015
- [2] W. Bi, W. Wang, A. Zang and Y. Wang, "Extending Model-Based Systems Engineering into Integrated Platform Designed for Civil Aircraft Development", 8th August 2021; doi: 10.1590/jatm.v13.1218.2021
- [3] J. Alvarado and T. Bradley, "Developing Model-Based Flight Test Scenarios", *Journal of Test and Evaluation*, vol. 44, n° 4, December 2023
- [4] N. Chiriac, K. Hölttä-Ottom D. Lysy and E. Suk Suh, "Three Approaches to Complex System Decomposition", in 13th International Dependency and Structure Modelling Conference, Cambridge, Massachusetts, USA, September 2011.
- [5] INCOSE, "Guide to Writing Requirements", 2022.
- [6] INCOSE, "INCOSE Systems Engineering Handbook: A Guide for System Life Cycle Processes and Activities". Wiley, 2015.
- [7] Magic Draw, Accessed on May 18th 2024 [Online], Available: <https://docs.nomagic.com/plugins/viewsource/viwpagesrc.action?pagelid=36311025>
- [8] "What is MBSE? Introduction to Model-Based Systems Engineering". Capella | Open Source MBSE Tool. Accessed on May 18th 2024. [Online] Available: https://mbse-capella.org/what_is_mbse.html

*This information is of origin Airbus Defense and Space/Spain and does not contain any export controlled information
Airbus Amber releasable to ETTC*

ETTC 2024– European Test & Telemetry Conference

ENCRYPTION OF PACKET TELEMETRY: A RISK ANALYSIS

Cédric Tavernier
 Encryption Expert
 Hensoldt France,
 115 avenue de Dreux – 78370 Plaisir, FRANCE
cedric.tavernier@hensoldt.net

Jean-Guy Pierozak
 Test Range Business Line Manager,
 Hensoldt Nexeya France
 Route d'Elne, 66200 Montescot, FRANCE
jean-guy.pierozak@hensoldt.fr

ABSTRACT

Telemetry systems are evolving from Continuous Streaming (IRIG106-CH4) to Packet Streaming (IRIG106-CH10, iNET, TmNS...), resulting in the latest version of IRIG106-CH7 mixing both. In Telemetry, packet streaming relies on UDP protocol which is unidirectional and allows some loss of packets. Besides, the need to secure the confidentiality of TM data is growing, leading to cipher part or all of it. We propose in this paper to start build a solution from a rigorous risk analysis. A description of state of the art solution compliant with the risk analysis results will be performed.

INTRODUCTION

Our telemetry system addresses the classical problem of protection the information transmission field: the main objective is to transmit securely some telemetry data through a radio channel. We will deploy the Risk Analysis Scheme described in Figure 1, with the main following steps: Context Analysis, Fear Events Analysis, Scenarios of attacks, Risk Analysis and resulting Security Countermeasures.

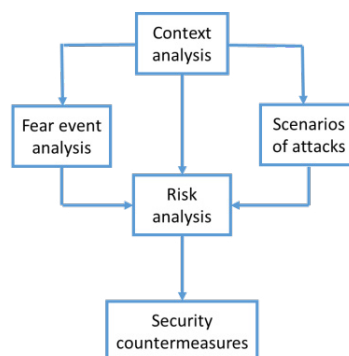


Figure 1: Risk Analysis Scheme

There exist a huge number of risk analysis model in practice. In order to be understood from the largest community, we recommend choosing a model compliant with the popular ISO 27005 [1].

1. CONTEXT ANALYSIS

As shown in Figure 1, the context of the operation is crucial. We consider an aircraft which is equipped of some sensors. During a mission the sensors data are gathered by a Data Acquisition System which transmits the telemetry data to some ground bases (Figure 2). The receiver is in charge of receiving the radio transmission, demodulating it, and encapsulate the data in UDP frames. Besides, the channel is unidirectional and noisy.

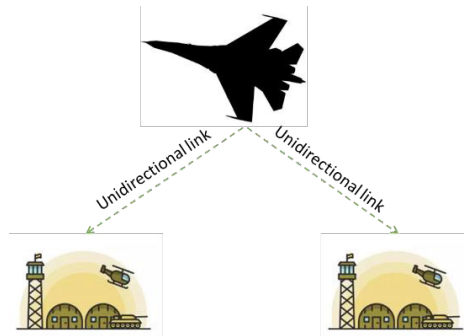


Figure 2: Operational Context

To collect the data, the decommutator is in charge of capturing a certain number of frames which could be stored in well denominated files.

At this stage, we can consider that the essential good is the telemetry data and the support goods are the transmitter, the receivers, the sensors/Data Acquisition System and the storage capacity of the different bases.

2. FEAR EVENT ANALYSIS

Confidentiality: The telemetry data are considered sensitive, thus breaking the confidentiality is a fear event.

Integrity: transmission of wrong, altered or transformed information compromises the interest of the mission, then, it is also a fear event.

Authenticity: the receiver must be sure to get the telemetry data from the right source, otherwise the mission is compromised: this a feared event.

Availability: A very noisy channel may cause a loss of information and may alter the interest of the mission, thus this is also a feared event.

3. SCENARIOS OF ATTACKS

Interception: an attacker may intercept the transmission and break the confidentiality.

Reordering packets: an attacker may intercept some packets and replay it. He can also reorder the packets before sending it to the receiver, and break consequently the integrity.

Attacks from the bases: if the data are not correctly protected, a cyber attack may compromise the telemetry data. If the storage is not protected, some passive or active attacks could compromise the data.

4. RISK ANALYSIS

It is clear that attacking the system inside the aircraft when flying is unlikely. The most likely attack can be over the air with jamming or simply interception. A cyber attack must be able to compromise the data in the bases itself, either in the aircraft, or in the data bases servers. On our opinion, the fear events are likely equally probable.

5. SECURITY COUNTERMEASURES

This brief risk analysis shows the need in term of security. We identify where the potential threats can act. Protecting the transport information is necessary but not enough because an attacker may intercept the telemetry data inside the data bases servers, or he could install a spy inside the aircraft when this one is parked at the airport of a base. We deduce that an applicative ciphering would be much more appropriate than a classical solution as VPN (virtual private network) encryption solution. However, we propose to analyse the potential solution by measuring the advantages and drawbacks.

- **VPN ANALYSIS**

Generally, VPN are bidirectional, especially IPsec VPN that works over TCP/IP. It is possible to implement the RFC 3948 and to encapsulate IPsec in UDP. Unfortunately, even in this case, the mandatory initial step consists in the handshake establishment that requires a bidirectional channel. This step allows a mutual authentication and the symmetric key secret sharing. To be compliant with our context, the handshake step (IKEV2) must be bypassed.

- **UDP FORWARDER**

The idea is to forward TCP/IP or UDP packets coming from a port toward another port and cipher the UDP frames in the middle. This method has the advantage not to require any bidirectional channel. Regarding the drawbacks, the UDP forwarder as the VPN only protect the transportation by building a ciphered tunnel, but outside the tunnel, data are not ciphered (clear text).

We deduce at this point that UDP forwarder is much more convenient because it aims to build a ciphered tunnel compliant the unidirectional link issue without requiring strong modification of any standard.

However, to protect the data from the source, to the destination and storage, these tunnel solutions must be associate with a ciphered storage:

- **FULL DISK ENCRYPTION**

For this technology, the disk is fully ciphered and the operating system manages to cipher the data coming from the interfaces and decipher data that come from disk and are directed toward the physical interfaces (hdmi, ethernet, serial,...). It is important to note that this technology do not warrant the integrity of the data. When the server is running, data are available in clear text.

- **FILE SYSTEM ENCRYPTION**

Only files containing the telemetry data are ciphered. It means that between the ciphered tunnel and the ciphered file, the data are in clear text. When the file is created, then only user with the correct key can read the file.

We deduce from these features, that the association between file system encryption and UDP forwarder is more appropriate. We must examine now the impact due to the noisy channel.

All frames must be ciphered using an IV (initial vector of 128 bits in general) which is transmitted in clear. If integrity is requested, then a tag (of 128 bits in general) must be also transmitted in clear. If any error appears on the IV, then the full frame could not be deciphered and shall be discarded. If an error appears on the tag, only the integrity guarantee shall be affected. We note that we cannot avoid this issue. Bypassing the IV means that a fixed word is ciphered in a unique manner: it makes the ciphered text not resilient against statistical attacks.

- **BLOCK CIPHER VS STREAM CIPHER**

We consider here a bloc cipher used with counter operation mode, then the only difference concerns the quantity of data lost. A bit error affects only one bit of a stream cipher whereas it affects a complete bloc (128 bits in general) for a bloc cipher. Regarding the IV and tag, there is no difference.

- **SYNCHRONOUS VS ASYNCHRONOUS**

Encryption can be synchronous or asynchronous. Synchronous cryptography is mostly used for data at rest, and also for digital signature. Asynchronous cryptography is usually used for data in transit and in cases where encryption and decryption keys need to be shared or exchanged.

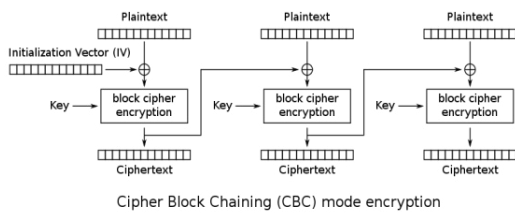
Synchronous ciphers have the advantage that key stream can be pre-computed before plaintext or ciphertext is provided, often with parallelism. They have the disadvantage of ciphertext malleability (a known change in ciphertext produces a known change in plaintext) and so will need to be combined with some form of message authentication. If a transmission is only received in part, it can be difficult to recover the fragment as the exact position in the key stream needs to be identified (synchronisation).

Asynchronous ciphers are largely serial in the encryption process (though not necessarily the decryption process) and the key stream can only be computed once the plaintext/ciphertext is provided. However, changing the ciphertext changes subsequent key stream and so there is considerably less malleability and a degree of message authentication. They also allow easy synchronisation at any point in transmission as the receiver can infer key stream after an initial run up of cipher bits (self-synchronisation).

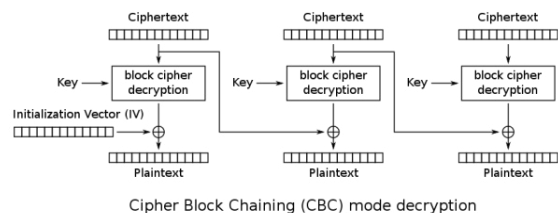
Hence, we deduce that according to the context, an asynchronous cipher is recommended since it brings more resilience regarding the resynchronization. A lost of packet is dramatic for counter operation mode for example whereas it implies only a lost of two blocs for a chaining mode like CBC. We present as example an asynchronous operation mode that is suitable with our scenario.

We remind that a block cipher mode of operation is an algorithm that uses a block cipher to provide information security such as confidentiality or authenticity. A block cipher by itself is only suitable for the secure cryptographic transformation (encryption or decryption) of one fixed-length group of bits called a block. A mode of operation describes how to repeatedly apply a cipher's single-block operation to securely transform amounts of data larger than a block.

In CBC mode, each block of plaintext is XORed with the previous ciphertext block before being encrypted. This way, each ciphertext block depends on all plaintext blocks processed up to that point. To make each message unique, an initialization vector **IV** must be used in the first block.



Cipher Block Chaining (CBC) mode encryption



Cipher Block Chaining (CBC) mode decryption

The encryption corresponds in term of computation to:

$$C_i = E_K(P_i \oplus C_{i-1}),$$

$$C_0 = IV,$$

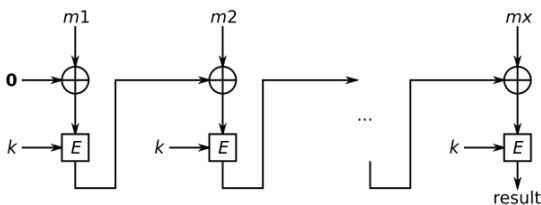
The decryption corresponds to the following formulas:

$$P_i = D_K(C_i) \oplus C_{i-1},$$

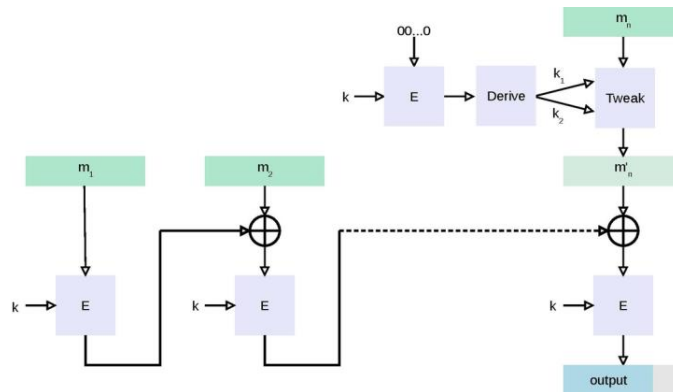
$$C_0 = IV.$$

We note that the decryption formulas imply that in case of erroneous bloc, only two consecutive blocs are affected. This mode does not require any counter: even if a bloc disappears, the resynchronization is done after losing one bloc maximum.

Regarding the integrity, the CBC-MAC provide this feature without involving much more calculation. To calculate the CBC-MAC of message m , one encrypts m in CBC mode with zero initialization vector and keeps the last block. The following figure sketches the computation of the CBC-MAC of a message comprising blocks $m_1 || m_2 || \dots || m_x$ using a secret key k and a block cipher E :



CBC-MAC on its own is not secure for variable-length messages, but it can be slightly modified by using the standard One-key MAC (OMAC) which is a message authentication code constructed from a block cipher much like the CBC-MAC algorithm:



CONCLUSIONS

After deploying a Risk Analysis Scheme on the topic of cyphering the Packet Telemetry, we deduce at that UDP forwarder is much more convenient because it aims to build a ciphered tunnel compliant the unidirectional link issue without requiring strong modification of any standard.

Besides, the association between UDP forwarder and file system encryption is more appropriate. About the impact due to the noisy channel: stream cyphering seems be more convenient, as a single bit error will affect a single bit of the ciphered stream but the use of IV may compromise the integrity of the complete frames and the synchronization may be an issue.

Finally, by studying the synchronous and asynchronous mode of cyphering we recommend using asynchronous chaining mode that brings a certain resilience in term of resynchronization, number of impacted packets in case of errors et integrity checking.

Our future work is to combine the need of segregating the Telemetry data depending on their security level, and the implementation of a cyphering solution compliant with this risk analysis.

REFERENCES

- [1] [ISO/IEC 27005:2018 - Information technology — Security techniques — Information security risk management.](https://www.iso.org/standard/75281.html)” <https://www.iso.org/standard/75281.html>, 2018

Quality Assurance through Leak Testing of Telemetry Components during Production

Dr. Joachim Lapsien¹

¹ CETA Testsysteme GmbH, Marie-Curie-Strasse 35-37, 40721 Hilden, Germany
Mail: joachim.lapsien@cetatest.com | Phone: +49 2103 2471-19

Abstract

Products used in telemetry applications (e.g. sensors, transmitters, receivers, power supply units) must function reliably under a wide range of conditions. If they are used outdoors or are exposed to liquids or moisture, there is a risk of malfunction due to the ingress of liquids. These products must be leak-tight.

During IP protection class testing, prototypes are tested in the laboratory. This is a type test.

To minimise risk a leak test is integrated into the production process as routine test – usually as an end-of-line test. Every part produced is tested. The test medium compressed air is widely used.

Operation and external influences lead to cyclic temperature-related pressure changes in the product. Mechanical stress on seals and seams can lead to leaks in encapsulated products.

In other products, pressure compensation elements (membranes) are used to reduce this mechanical stress. These membranes are watertight but permeable to air. During the leak test, the product must be filled via the membrane. Sometimes an opening is provided in the plug connector through which the product can then be filled directly.

Depending on the type of product (encapsulated, filling via a membrane, direct filling), there are specific aspects to be considered in the leak test.

Key words: IP protection class, type test, routine test, leak test

Telemetry – Applications and risks

The demand for telemetry solutions is continuously increasing. According to a market study by Verified Market Research (VMR), an annual growth rate of more than 8% is expected until 2030 [1].



Fig. 1. Security camera with with telemetry module [2]

Traditionally long used is telemetry in industry, aerospace and space industry, the motor sport

sector, transportation, logistics and remote imaging.

More and more branches profit from the advantages of telemetry solutions, like medical applications, internet of things, wearables, security, environmental protection, agriculture, animal tracking, oceanography, condition monitoring, regenerative energy sector, just to mention some branches (see Fig. 1 and 2).

In telemetry, numerous sensors are used to measure various parameters such as pressure, acceleration, temperature, angle, speed, rotational speed and displacements. And the use of remote image transmission is widespread.

Typical components of telemetry networks are the sensor systems with amplifier, the transmitting unit, the wireless connection, the receiving unit, supporting units for power supply and systems for data evaluation and storage.

The sensor systems, the transmitter and receiver units in particular are exposed to many

external influences, such as temperature, harsh environments and outdoor conditions.

If one of these components is not functioning properly due to a leak, this can lead to malfunctions in this telemetry channel, which can result in serious problems.



Fig. 2. Moisture sensor with telemetry module used in agriculture [3].

To reduce the risk of leaks and to ensure that only properly manufactured and leak-tight products are used, they are also tested for leaks during the production process in the integrated end-of-line leak test as part of quality control.

Type test and IP protection classes

In the definition of the IP protection classes the tightness resp. the impermeability against particles, contamination, liquid and moisture is described by the IP code (DIN EN 60529 / ISO 20653).

The IP code consists of two digits IP XY: The first digit X indicates the impermeability to particles, while the second digit Y indicates the water resistance.

Tab. 1 describes the IP protection classes for water tests and the corresponding test conditions.

Tab. 1: IP protection classes for water tests and test conditions [4], [5], [8]

IP code	Description	Test
IP X0	Not protected	None
IP X1	Water drips vertically	Vertical drips
IP X2	Water drips (inclination by 15°)	Enclosure is tilted at any angle up to 15° on either side of the vertical.
IP X3	Water spray	Water spray at an angle up to 60° on either side of the vertical
IP X4	Splash water	Water splashes against the enclosure from any direction

Tab. 1 – continued

IP code	Description	Test
IP X4K	Splash water with increased pressure	Water splashes against enclosure from any direction with Increased pressure
IP X5	High-velocity water	Water directed against the enclosure from any direction as a jet
IP X6	Strong high-velocity water	Water directed against the enclosure from any direction as a strong jet
IP X6K	Strong high-velocity water with increased pressure	Water directed against the enclosure from any direction as a strong jet with increased pressure
IP X7	Temporary immersion in water	Enclosure is immersed in water temporarily (1 m depth for 30 min)
IP X8	Continuous immersion in water	Enclosure continuously immersed in water Conditions agreed between supplier and manufacturer Tests are more severe than IP X7.
IP X9	High-pressure steam-jet cleaning	Water directed against the enclosure from any direction Control panels or electrical equipment
IP X9K	High-pressure steam-jet cleaning	Water directed against the enclosure from any direction Equipment installed in road vehicles

The prerequisite for compliance with the corresponding IP protection class is that no harmful or performance-impairing influences occur.

The IP protection class tests are type tests. Prototypes and samples are tested in the laboratory for tightness against the ingress of moisture strictly in accordance with the specifications of the desired IP protection class. The test result is summarised in a certificate. This certificate is only valid for the tested product.

Leak test as routine test during production

Carrying out a type test involves a great deal of experimental work. These tests are carried out by specially equipped laboratories and institutes. Special test equipment is used, and the test part is exposed to moisture or liquid with varying intensity and exposure time, depending on the IP protection class.

It is obvious that such tests cannot be integrated in the manufacturing process. It is not possible to work with moisture or liquids.

And the test duration (exposure time to moisture or liquid) does not correspond in any way to the production cycle times commonly used in industry.

The IP protection class test does not provide any direct parameters for the specification of the leak test during production.

A parameter regime for the leak test must be found here, considering the test conditions of the IP protection class test and the loads that occur on the product during operation. For this purpose, the test pressure and the leak rate must be defined.

Information on the test pressure and leak rate can be derived indirectly from some definitions of the IP protection classes. For example, the conditions of the diving test provide an indication of the test pressure. As a rule, the test pressure and the direction of pressurisation (i.e. test with positive or negative gauge pressure) are determined by the manufacturer, taking into account the product properties and the loads during operation.

The following information on tightness and leak rate as a function of hole size can often be found in the literature (see Tab. 2):

Tab. 2: Overview about tightness, leak rate and hole size [6], [7], [8].

Tightness	Leak rate less	⊙ Hole
Water tight	10^{-2} mbar*l/s	10 μ m
Vapor tight	10^{-3} mbar*l/s	3 μ m
Bacteria tight	10^{-4} mbar*l/s	1 μ m
Oil tight	10^{-5} mbar*l/s	300 nm
Virus tight	10^{-6} mbar*l/s	100 nm
Gas tight	10^{-7} mbar*l/s	30 nm
Virus tight (assured)	10^{-8} mbar*l/s	10 nm
"Absolute tight"	10^{-10} mbar*l/s	1 nm

Leak rate 1 mbar*l/s = 60 cm³/min

This information is based on a simplified model: there is an ideal hole in a housing that has been evacuated to a negative gauge pressure of -1 bar (relative). If this is suddenly opened, the column of air above the cross-section of the opening streams into the housing at the speed of sound. This results in a relationship between the hole size and the volume flow, the so-called leak rate.

In reality, however, the leakage results from a large number of micro-leaks (e.g. in glued or welded seams). The leak rates listed in table 2 therefore serve as orientation values. In practice and depending on the product, other

leak rates may prove to be more suitable. If orientation values are used as a basis, there is a risk that the test may be too stringent with an excessively high reject rate. To be on the safe side, the determination of the leakage rate should be verified by laboratory tests. Here, test parts with different production qualities are tested for leaks using compressed air. A laboratory test is then carried out under the conditions of the desired IP protection class. A correlation can then be used to decide which leak rate is still tolerable.

Leak test using compressed air

The use of compressed air as a test medium is widespread in industrial leak testing. Compressed air is available in all production facilities. Measuring the pressure change due to leaks is an objective and quantitative measurement method that can be easily integrated into automated production lines. In contrast to testing in a water bath, the product is not wetted during the test and can be further processed immediately after the test (e.g. packaging and delivery).

Compressed air can be used for leak rates down to 10^{-3} mbar*l/s, corresponding to 0.06 cm³/min. A leak rate of 0.6 cm³/min is often used for industrial leak testing of products that are to be tested for watertightness.

The differential pressure method is often used to detect small leak rates with compressed air.

Here, the leakage-related pressure change in a pressurised or evacuated product is measured against a sealed reference volume (usually an encapsulated volume inside the test device) that is at the same pressure level. A sensitive differential pressure sensor with an internal resolution of 0.01 Pa is used for this purpose.

Such small pressure changes occur due to thermal noise, micro-vibrations and minimal movements in the test part, in the adaptation and in the pneumatic lines.

For this reason, the measured values are averaged, and the displayed value is usually rounded to 0.1 Pa or 1 Pa (= 1/100,000th of the atmospheric pressure).

Pressure gradients from approx. 1 Pa/s can be detected with leak test methods using compressed air. Test devices from the CETATEST 825 leak tester series (manufacturer: CETA Testsysteme GmbH, Hilden), for example, are suitable for leak tests using the differential pressure method.

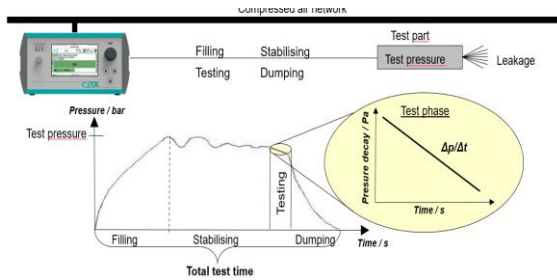


Fig 3: Principle of the pressure decay test [8]

A complete test process (see Fig. 3) for a directly fillable test part consists of successive phases: Filling, stabilising, measuring and dumping. Ideally, the filling and stabilisation times should be selected so that a stable state is achieved in the measuring phase. This is characterised by the fact that the pressure decay changes proportionally to the time. If the measured pressure decay value is within the permitted limit values, it is a good part. A sufficiently large spread of the measured value distribution between good and bad parts is necessary for a reliable testing process.

The leakage-related pressure gradient can be calculated using the so-called leak rate formula (1):

$$\frac{\Delta p [\text{Pa}]}{\Delta t [\text{s}]} = \frac{Q_L [\text{cm}^3/\text{min}]}{V_{\text{eff}} [\text{cm}^3]} \cdot \frac{100.000 \text{ Pa}}{60 \text{ s/min}} \quad (1)$$

Q_L Leak rate

V_{eff} Effective test volume
(test part, measuring line, adaptation,
test device measurement circuit)

$\Delta p/\Delta t$ Pressure gradient

The commonly used units for leak rates are "mbar*l/s" or "cm³/min", whereas (1 mbar*l/s = 60 cm³/min).

The leak rate formula can be used to estimate whether the compressed air test medium and the pressure decay method can be used.

Many industrial leak testing applications have pressure gradients of 10 to 50 Pa/s.

It should also be noted that the leak rate formula is based on ideal conditions, which rarely exist in the real production line.

So-called test leaks are used to simulate the allowable leak rate. These have a defined flow rate at a certain pressure. If they are connected in parallel to a master tight part, they can be used to simulate borderline test parts.

Application of the leak rate formula

A telemetry component is to be tested for leaks. The plug connector has an opening through which the product can be filled directly. The adaptation is carried out on the burr-free edge

of the connector housing. The fillable volume of the control unit is 80 cm³ including the plug connector area. The measuring line and the internal measuring circuit volume of the leak tester have a total volume of 14 cm³. This results in an effective test volume of 94 cm³. If a leak rate of 0.6 cm³/min is to be detected at a test pressure of 500 mbar (positive gauge pressure in relation to atmospheric pressure), this results in a calculated pressure gradient of 10.6 Pa/s in a stable regime. If the measuring time is 4 s, this corresponds to a leakage-related pressure decay of approx. 43 Pa as the rejection limit.

Types of products and their leak test

Directly fillable products

Some products have a plug connector that is not leak-tight. In the plugged-in unit consisting of plug and mating connector, the system is sealed to the outside.

In this case the plug connector can be used to fill the product directly.

Sometimes the plug connector is provided with a filling opening (see Fig. 4). A hole with a diameter of 1 mm to 2 mm is sufficient. The product can then be filled very reliably via this opening. For the sake of completeness, it should be noted that the "hole in the plug connector" feature is not accepted by all end customers.



Fig. 4: Example of a product with a hole in the connector area [8]

Sometimes a filling opening is only provided for the purpose of the leak test, which is then closed in a controlled manner after the successful leak test.

When adapting in the connector area or at an opening, it must be ensured that the test adapter does not move during the leak test.

This can be achieved with an end position lock of the test adapter or with a rigid stop. A "floating" adaptation should be avoided. Micro-movements can lead to movement-induced pressure fluctuations, which can have a disadvantageous effect on the test process (especially during the measurement phase).

Encapsulated products

Encapsulated products cannot be filled directly with compressed air. These are placed under a test hood that surrounds the outer contour as closely as possible and is pressurised. The

leakage-induced pressure decay into the product is measured. This type of test is known as a "closed component " or "hood test".

The following problem arises here: If the test part has a gross leak, it is filled directly with compressed air during the filling phase of the hood. In this case, only the tightness of the hood would be tested. Therefore, the first step is to check that the test part does not have a gross leak. This is followed by the fine leak test using the pressure decay measurement.

During the gross leak test, a reservoir volume integrated in the test device is filled to a starting pressure p_1 and disconnected from the pressure regulator. The shut-off valve of the internal reservoir volume is then opened, and the air streams into the hood connected to the test device. As the air from the reservoir volume is distributed over a larger volume, a lower pressure p_2 is created. The ratio p_2/p_1 can be used to pneumatically determine which volume is being filled and in this way is possible to detect of gross leaks.

If the test part does not have a gross leak, the fine leak test follows. The pressure decay from the pressurised hood into the interior of the test part is measured. The residual hood volume (i.e. the empty hood volume minus the displacement volume) represents the actual test volume. Taking into account the measuring line and the internal measuring circuit volume of the test device, the effective test volume is obtained.

The test hood is designed to be product specific. The test part tolerances and handling aspects must be taken into account when designing the hoods. Typical hoods have a gap distance between the maximum tolerated product and the hood of approx. 0.5 mm to 2 mm. The smaller the residual volume of the hood, the better the resolution for detecting gross leaks and the more sensitive the measurement of pressure losses.

A feasibility criterion is that the tolerance-related volume variation of the displacement volume is less than the internal volume of the product that is filled in the case of gross leakage.

It should also be noted that fully potted products cannot be tested for leaks using this method.

Products with pressure compensation element

Products in outdoor areas are exposed to a variety of environmental influences. Temperature-related pressure fluctuations can lead to overpressure or underpressure inside the system. As a result, the seals, welded and bonded seams are subjected to high stress and can become leaky. If there is then negative gauge pressure in the

product, there is a risk of moisture and liquid being drawn into the interior of the system. This can lead to serious faults in electronic components and severely impair their function.

For this reason, pressure compensation elements (membranes) are often used for ventilation. These enable pressure compensation while at the same time protecting against oil, water and particles. The pressure compensation element is often mounted behind a cross or perforated grid to protect it from dirt and mechanical damage.

Membranes made of expanded polytetrafluoroethylene (ePTFE) are widely used. The hydrophobic and oleophobic material is produced in thin layers and the flow is adjusted by stretching. These membranes are available in weldable and adhesive versions. A fundamental problem with this type is that often only the minimum flow rate is specified in the data sheet. The typical flow rate can be up to 2 to 3 times greater than the minimum flow rate.

In addition to this very common type of membrane, there are also membranes that are perforated by exposure to ion beams. This is followed by a chemical etching process. In this way, the pore density and pore size can be "adjusted" in a defined manner. These track-etched membranes are characterised by the fact that the average flow rate including the flow spread width can be specified and is indicated in the data sheet. This is very helpful for the planning of projects.

There are also membranes in which a granulate of porous PTFE is pressed under isostatic pressure and then sintered. This processed material is peeled to produce sintered membranes. These also have a relatively defined flow range.

Due to the handling of the pressure compensation element and its assembly, it must be checked whether it is undamaged and has been assembled correctly. During the membrane test, a reservoir volume inside the test device is brought to a defined pressure. When the air flows from this reservoir volume through the membrane into the test part, the pressure decrease is delayed due to the limited flow through the membrane. The change in pressure over time depends on the condition of the membrane (not fully welded or bonded, damaged, missing membrane). If the pressure is measured shortly after the start of the flooding process, the state of the membrane can be qualified in this way (see Fig. 5). The batch-dependent variation of the membrane flow rate must be considered critically here. This must be considered when planning the test process.

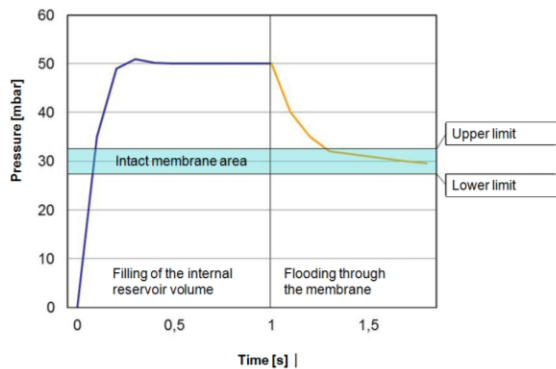


Fig. 5: Pressure-time diagram for the membrane test [8]

Once the membrane has been checked for correct installation, the leak test follows. The product must be filled via the pressure compensation element, which is installed on top of the ventilation opening. The required filling time depends on the permeability of the membrane, the flow-active area of the membrane, the applied pressure, and the volume to be filled. This time is significantly longer than for a test part with the same volume that can be filled directly.

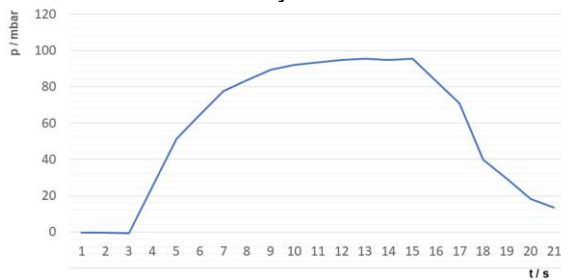


Fig. 6: Pressure-time diagram inside a test part when filled with a constant pressure of 90 mbar through the membrane (prepared test part with the possibility of measuring the pressure inside the part) [8].

Hereby only the pressure in front of the membrane can be measured. Preliminary tests must be carried out to ensure that the test pressure inside is actually reached (see Fig. 6). The filling process and therefore the overall test time can be shortened in some circumstances by pre-filling with a slightly higher pressure before the actual filling phase. The specifications regarding the sudden pressure load on the membrane must be considered. Overfilling must be avoided. Batch scattering must also be taken into account when planning the process.

If the product also has plug connectors that only need to be tight when plugged in, it is recommended that these are also pressurised with the test pressure during the leak test. This prevents the pressure in the test part from

gradually decreasing via the plug connector and pseudo leaks from being measured.

Additional comments

The leak test in the production line usually takes place at ambient temperature. The pressure loads on the product due to hydrostatic pressure and thermally induced pressure changes during operation can be simulated during the leak test by selecting the appropriate test pressures.

Micro-gaps that form under thermal stress due to the different material expansion coefficients (metal, plastic) cannot be simulated by different test pressures. Other test methods, tests or appropriate material selection must be used to ensure that this does not pose a problem during operation of the product.

The mating connector used for the electrical test can also be used as a leak test adapter with modifications. As the electrical test is associated with temperature input, it should not be carried out at the same time as the leak test. If consideration is given to carrying out the two tests in parallel and in one clamping, the heating phase must be completed before the measuring phase of the leak test begins. Then the test would always take place in the same thermal state. The feasibility should be verified by preliminary tests.

References

- [1] Verified Market Research (VMR) Global Telemetry Market Size and Forecast Report ID: 38312 | Published: Jan 2024 www.verifiedmarketresearch.com/product/telemetry-market/
- [2] © jakit17 - stock.adobe.com
- [3] © Sittichok - stock.adobe.com
- [4] Overview IP protection classes ITS GmbH Innovative Mess- und Testsysteme GmbH
- [5] Overview IP protection classes Asskühl GmbH & Co. KG
- [6] Leybold GmbH, Köln https://www.leyboldproducts.de/media/pdf/10/0f/8b/FVT_Grundlagen_der_Vakuumtechnik_DE591eea2256c34.pdf
- [7] Deutsche Gesellschaft für Zerstörungsfreie Prüfung e.V., Berlin | FAQ, V9 <https://www.dgzfp.de/foerdern-ernetzen/fachausschuesse/fa-dp/>
- [8] Measurements, photos, graphics, tables CETA Testsysteme GmbH, Hilden

Achievements and Challenges in Catalytic Combustion Hydrogen Sensors: Commercial Use in Fuel Cell Vehicles and Miniaturization using MEMS Technology

G. Yamamoto, S. Nakao, H. Miyazaki

*New Cosmos Electric, Co., Ltd. 748-7 Kamiarakawa, Yokawa-cho, Miki-shi, Hyogo, 673-1111, Japan
yamamoto.go@new-cosmos.co.jp, nakao.shoichiro@new-cosmos.co.jp,
miyazaki.hiroshi@new-cosmos.co.jp*

Abstract

Safe use of hydrogen in future low-carbon society requires hydrogen sensors that detect hydrogen leakage with high sensitivity and selectivity. For this purpose, we developed bead-shaped catalytic combustion sensors for hydrogen detection. The sensors consist of an alumina bead loaded with precious metal and a platinum heater coil. Developing the proprietary catalysts and downsizing the sensor elements led to very fast startup, extremely quick response to hydrogen, and long-term stability of the sensors. These features make the sensors very suitable for detecting hydrogen leakage in fuel cell vehicles (FCVs). Indeed, the sensor modules equipped with the sensor elements fulfilled strict demands such as high detection accuracy and durability against various harsh environments possible in FCVs. Consequently, the sensor modules have been installed in a commercial FCV (MIRAI, Toyota Motor Co., Ltd.) since 2020.

An important challenge in catalytic combustion sensors is miniaturizing the sensors using micro electro-mechanical systems (MEMS) technology. Miniaturized sensors exhibit reduced power consumption and thus can be operated with a battery. Indeed, we have already launched battery-operated city gas alarms equipped with MEMS chemo-resistive sensors in Japan and the USA. In this paper, we present various properties of MEMS catalytic combustion sensors together with bead-shaped ones.

Key words: hydrogen, hydrogen sensor, catalytic combustion, FCV, MEMS

1. Introduction

The safe use of hydrogen as a sustainable energy source is necessary to realize a low-carbon society in the future. To deal with the explosion danger of hydrogen in a wide concentration range (4~75 volume% in air), affordable, robust, and reliable hydrogen sensors capable of detecting leakage are essential. To address this assignment, New Cosmos Electric, which specializes in gas alarms and detectors, developed various hydrogen gas sensors fulfilling the requirements in emerging hydrogen use. For example, the installation of hydrogen alarm systems has become mandatory under the High-Pressure Gas Safety Act at Japanese hydrogen stations for automobiles. Presently, our gas detection and alarm systems are installed in approximately 80% of the hydrogen stations Japan, illustrating our contribution to realizing a low-carbon society.

Another example is the use of our hydrogen sensors in commercial fuel cell vehicles (FCVs).

Sensor modules equipped with hydrogen sensor elements have been installed in commercial FCVs as crucial components for hydrogen fuel sources. These sensor modules must ensure the detection of hydrogen leaks just in case of an accident, and high-performance hydrogen sensors capable of enduring various harsh environments possible in FCVs are required. We developed hydrogen sensors suitable for such uses by developing proprietary catalysts and downsizing the sensor elements. Furthermore, we have ensured a stable supply of gas sensors based on mass-production technology built on household gas alarms. As shown in Fig. 1, these sensors have been adopted in a commercial FCV (MIRAI, Toyota Motor Co., Ltd.) since 2020 [1].

This paper is organized as follows. We first briefly review the requirement for hydrogen sensors in FCVs and discuss the selection of hydrogen sensors suitable for the use. We then explain the working principle of the selected sensor for this purpose: catalytic combustion

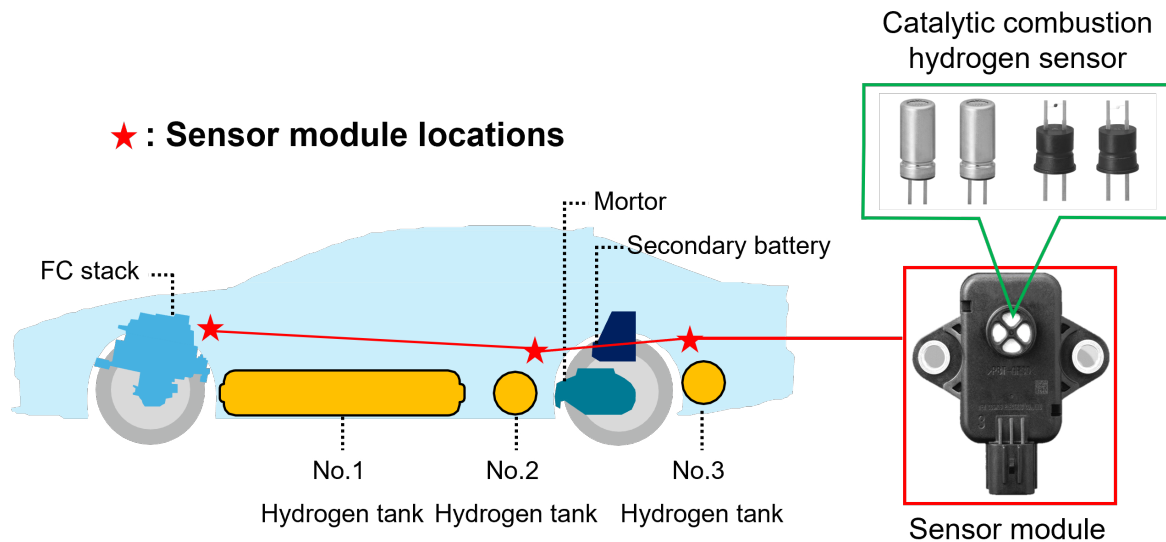


Fig. 1 Commercial FCV and the sensor module equipped with a catalytic combustion hydrogen sensor.

sensors [2]. We in detail present two important technical advances required for hydrogen sensors for FCVs: miniaturization of sensor elements and developing the proprietary catalysts. Before conclusion, we show a more advanced miniaturization using micro electro-mechanical systems (MEMS) technology for future emerging hydrogen use.

2. Requirement for hydrogen sensor in FCVs

Hydrogen sensors are important devices that detect and quantify hydrogen by its reaction with hydrogen present in the atmosphere and convert the change into an electrical signal or change in resistance. Given that gas sensors must be continuously exposed to their surrounding environment, the required specifications vary significantly based on factors such as environmental temperature, humidity changes, durability against toxic gases that degrade catalytic activity and gas selectivity. Furthermore, hydrogen exhibits numerous physical properties distinct from other gases, including its low mass density, combustibility, and high diffusion velocity. To date, hydrogen sensors with various detection principles have been extensively studied and developed. To name a few, these include thermoelectric, electrochemical, quartz crystal type, and hydrogen sensors that utilize the hydrogen absorption reaction in Pd alloys.

Presently, hydrogen sensors employed for leak detection in hydrogen stations and production facilities are mainly based on semiconductor and catalytic combustion detection principles. In addition, gas thermal conduction type is used in special applications such as hydrogen

concentration measurement in inert gas. Each sensor type has a different hydrogen detection range and is suitable for specific applications.

FCVs represent a sustainable alternative to traditional internal combustion engine vehicles, offering zero-emission transportation powered by hydrogen fuel cells. However, the safe handling and use of hydrogen in FCVs require robust sensing technologies to detect hydrogen leaks and ensure driving safety. Therefore, hydrogen sensors to be installed in FCVs satisfy the following important requirements:

- (1) a wide detection range (0-40,000 ppm)
- (2) detection accuracy ($\pm 10\%$ above 10,000 ppm)
- (3) fast startup (< 2 seconds) and 90% response speed (< 3 seconds)
- (4) durability against harsh environments
- (5) long life (> 10 years) and Driving time ($> 10,000$ hours)
- (6) operating temperature (-35 to 85°C)
- (7) low power consumption
- (8) low cost (mass producibility).

To fulfill these strict demands, we selected a catalytic combustion gas sensor, which has a track record the service for many years. However, objectively demonstrating the maintenance of hydrogen detection accuracy was a major challenge, especially over a service life of 10 years or more and under the harsh environmental conditions typical of vehicles. For this purpose, we developed an improved catalytic combustion hydrogen sensor.

3. Catalytic Combustion gas sensor

The catalytic combustion gas sensor has two key elements: a detector element reactive to combustible gases and a compensator element that remains inert. The detector element consists of an alumina bead loaded with precious metal such as Pd or Pt (Pd-Pt/Al₂O₃ catalyst), in which a Pt heater coil is embedded. On the other hand, the compensator element consists of an alumina bead without a precious metal and a Pt heater coil.

To detect a target gas, the Pt heater coil is heated to an appropriate temperature, e.g., 350°C by self-heating due to voltage application. In the presence of combustible gas, combustion occurs on the detector element, raising the temperature of the sensor and increasing its resistance. On the other hand, the compensator element, unaffected by combustion, maintains a constant temperature and resistance. By incorporating these elements in a bridge circuit (Fig. 2), the difference in sensor resistance causes an imbalance in the bridge circuit, and this change can be detected as a sensor output (ΔV), which is proportional to the concentration of combustible gas.

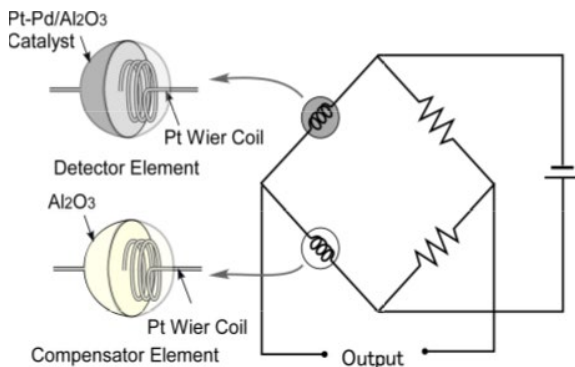


Fig. 2 Basic measuring circuit of the sensors.

4. Miniaturization of sensor elements

Hydrogen sensors for FCVs have strict requirements for fast startup and quick response to hydrogen within a few seconds. Thus, we attempted to downsize the sensor elements to improve thermal response and reduce response time to hydrogen. Figure 3 shows scanning electron microscope (SEM) images of the conventional and the improved sensors. The diameter of the bead-shaped element for the improved sensor was approximately 0.5 mm, which was half of that for the conventional sensor, 1.0 mm. That is because we used a smaller Pt coil heater for the improved sensor than that for the conventional sensor. The volume of the

improved sensor elements is thus approximately 1/8 of that of the conventional sensor. This miniaturization first of all reduced power consumption. The improved sensor required 125 mW for operation, which was one-third of that for the conventional sensor, 400 mW.

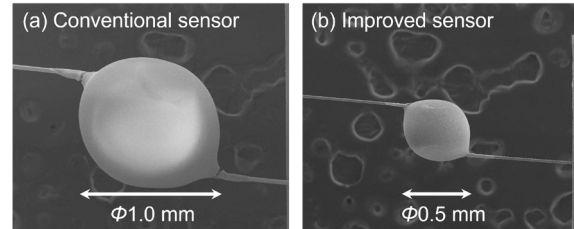


Fig. 3 SEM images of (a) the conventional and (b) the improved sensors.

Figure 4 shows a comparison of the thermal response characteristics of the conventional sensor and the improved sensor in air. The startup time, which can be evaluated by the return of a stable baseline after energization, of the conventional sensor was 10 seconds. In contrast, the improved sensor required only 1 second for startup. Such a quick startup of the hydrogen sensor can reduce explosion risk at system startup if a hydrogen leak occurs during system shutdown.

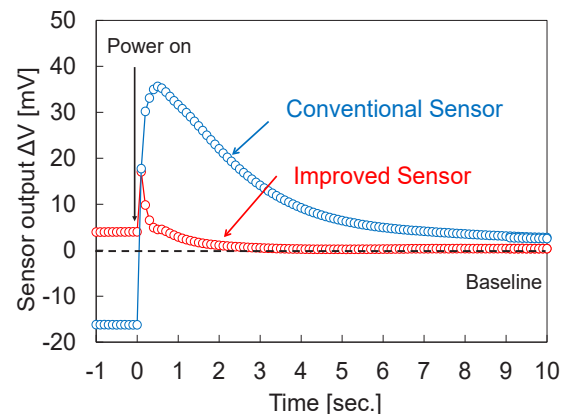


Fig. 4 Thermal response characteristics of the conventional and the improved sensors in air.

Figure 5 shows the hydrogen response characteristics of the improved sensor and conventional sensor to 10,000 ppm hydrogen in air. T_{90} response time, which is the arrival time to 90% of saturated output, of the conventional sensor was 5.8 seconds. On the other hand, T_{90} of the improved sensor was as short as 2.1 seconds. These results (Figs. 4 and 5)

demonstrate that miniaturization effectively improves startup and response time. Both values satisfied the requirement (3) in section 2.

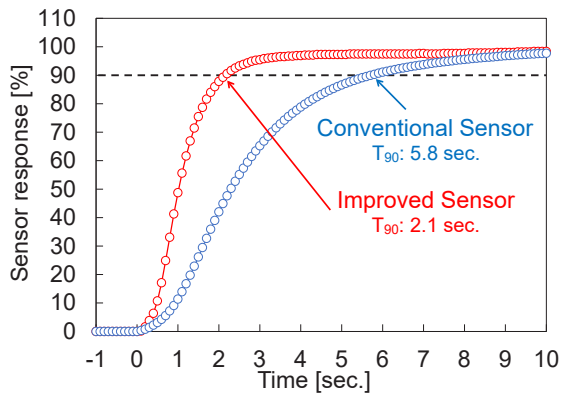


Fig. 5 Hydrogen response characteristics of the conventional and the improved sensors to 10,000 ppm hydrogen in air.

5. Developing proprietary catalysts

Catalytic combustion gas sensors commonly decreased sensitivity due to catalyst poisoning on the catalyst surface [3], particularly in the presence of siloxane vapor coexisting in the environment of FCVs. To enhance the durability of the active catalyst for the detector element [4], we fabricated highly dispersed Pd-Pt nanoparticles on alumina supports. Figure 6 shows transmission electron microscope (TEM) images of the Pd-Pt/Al₂O₃ catalyst. These images visualized highly populated and yet well-dispersed Pd-Pt nanoparticles on the surface of Al₂O₃ support. The improved sensors were fabricated with this proprietary catalyst.

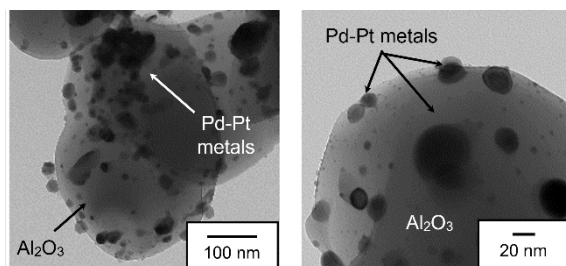


Fig. 6 TEM images of Pd-Pt/Al₂O₃ catalyst.

Figure 7 shows the hydrogen sensitivity of the sensor before and after exposure to 1 vol.% hexamethyldisiloxane for 20 hours. Surprisingly, the sensitivity of the sensor remained almost unchanged even after exposure to such a high concentration of siloxane vapor. Interestingly, SiO₂ precipitations were observed on the

surface of the detector element after exposure to siloxane. Such SiO₂ particles at the surface are supposed to adsorb siloxane vapor preferentially and keep the sensor inside free from siloxane. Thus, we consider SiO₂ particles as the origin of the excellent siloxane durability, at least after their formation.

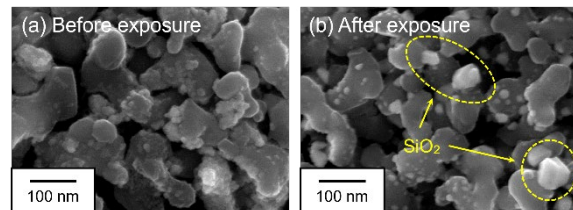
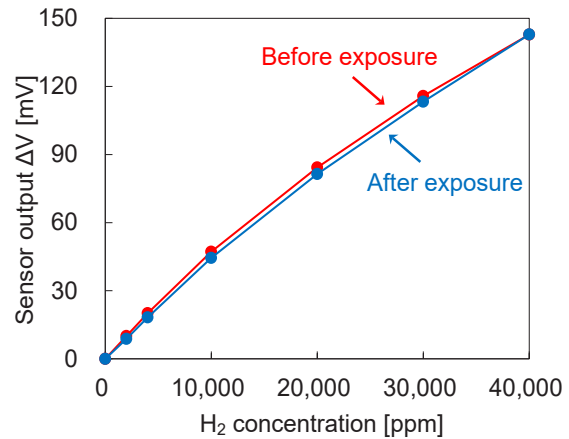


Fig. 7 Hydrogen sensitivity and SEM images of before and after exposure 1 vol.% hexamethyldisiloxane at 20 hours.

Another degradation mechanism affecting catalytic activity is the sintering of the catalyst particles due to long-term heating. We solved this problem by alloying Pd with Pt. Figure 8 shows the long-term stability of the improved sensor continuously energized in air. The change of hydrogen sensitivity for 16 years was less than 10% at hydrogen concentrations of interest ((2) in section 2), demonstrating excellent long-term stability of the sensor. In actual use, no sensors are continuously energized; sensors are heated only when in use and unheated when not in use. Because empirically catalytic combustion gas sensors show no sensitivity deterioration during no heating, a longer sensor life than that in Fig. 8 can be expected.

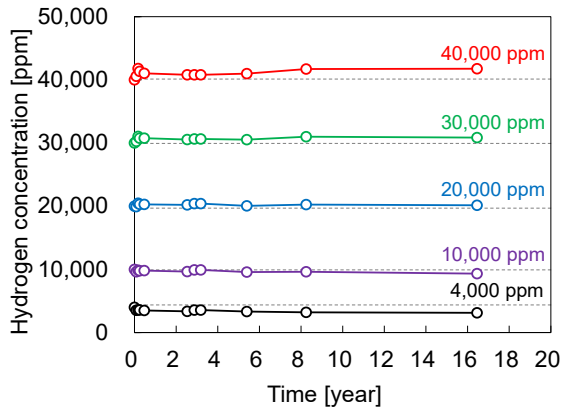


Fig. 8 Long term stability of the improved sensor in air.

6. MEMS catalytic combustion sensor

As shown in section 4, miniaturization of sensor elements is very effective for improving response time and power consumption. Thus, we are currently endeavoring to further miniaturize catalytic combustion gas sensors using MEMS technology [5], which fabricates microstructures on a Si substrate. This technology enables miniaturization of a Pt heater coil into a micro-heater as shown in Fig. 9, allowing for the fabrication of two micro-heaters on a single chip. Furthermore, MEMS technology enables the mass production of gas sensors at a reduced cost, facilitating its commercialization and widespread deployment. By depositing the sensor material on the micro-heater, we succeeded in miniaturizing the sensor elements to only 0.15 mm. The volume of the MEMS catalytic combustion gas sensor element is approximately 1/60 of that of the improved sensor for FCVs. Consequently, the miniaturized sensors exhibit dramatically reduced power consumption, enabling operation with a battery. Indeed, we have already launched battery-operated household city gas alarms equipped with MEMS chemoresistive sensors in Japan and the USA [6].

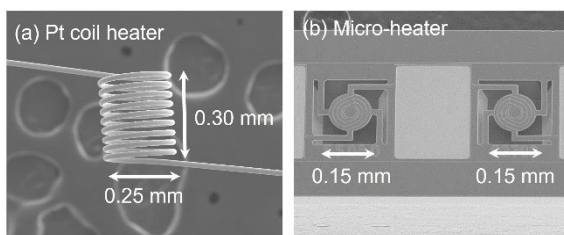


Fig. 9 SEM images of (a) a Pt heater coil of the improved sensor and (b) micro-heaters of the MEMS catalytic sensor.

The thermal response characteristics of the MEMS catalytic sensor are shown in Fig. 10. The heating time required to reach a prescribed temperature for hydrogen detection was only 100 milliseconds, for both the detector and the compensator elements. This represents an extremely fast startup time, as compared with the bead-shaped sensors (Fig. 5). Furthermore, the power consumption of the MEMS catalytic sensor is only 0.8 mW owing to its operation by pulsed voltage drive. The pulsed voltage operation is preferable for reducing power consumption, as compared with continuous operation in the bead-shaped sensors. This means that the MEMS catalytic sensor has ultra-low power consumption, which is sufficient for battery operation.

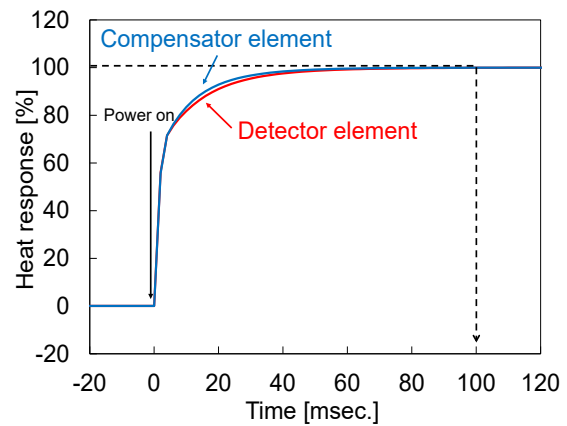


Fig. 10 Thermal response characteristics of the detector and the compensator elements of the MEMS catalytic sensor.

Figure 11 shows the gas sensitivity characteristics for hydrogen, methane, and isobutene operated with a pulsed voltage drive (100 milliseconds on and 7 seconds off). The MEMS catalytic sensor was designed to detect various combustible gases. The sensor output was proportional to the gas concentration and particularly linear to lower explosive limit (LEL) concentration for all combustible gases, indicating similar high accuracy performance to the conventional bead-shaped sensor.

Finally, the long-term stability of the MEMS catalytic sensor to hydrogen was tested, as shown in Fig. 12. The MEMS catalytic sensor was very stable with no significant sensitivity change for 540 days (approximately 1.5 years) in a laboratory environment (20°C and 60%RH), similar to that for the improved sensor. The test is still ongoing and we will carefully investigate the durability of the MEMS sensor.

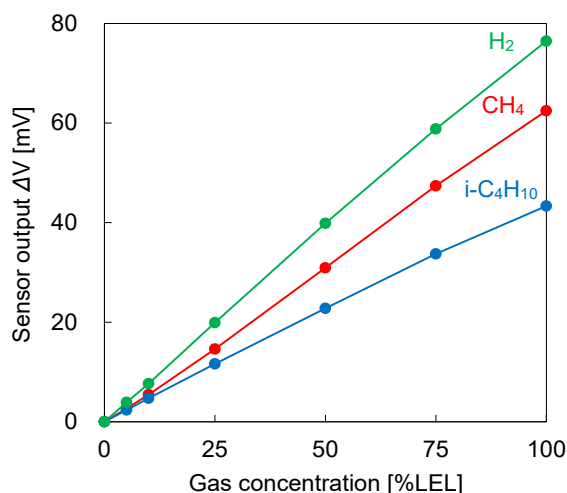


Fig. 11 Gas sensitivity characteristics of the MEMS catalytic sensor to hydrogen, methane, and isobutane.

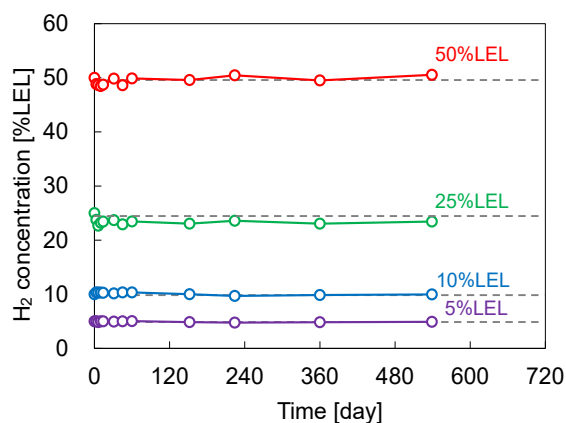


Fig. 12 Long term stability of the MEMS catalytic sensor in air.

7. Conclusion

We have successfully developed a catalytic combustion hydrogen sensor for FCVs. The improved sensor with the development of proprietary catalysts and miniaturization of sensor elements offers the following features compared to the conventional sensor.

- (1) Very fast startup (< 2 seconds)
- (2) Extremely quick response to hydrogen (< 3 seconds)
- (3) High durability against siloxane vapor
- (4) High accuracy with a hydrogen sensitivity change rate within $\pm 10\%$ even after 15 years

As a result of these achievements, our improved sensor has been adopted and installed in a commercial FCV (MIRAI, Toyota Motor Co., Ltd.).

Furthermore, we are currently challenging to develop MEMS catalytic sensors using MEMS technology, which enables further sensor miniaturization and extremely fast startup (only 100 milliseconds). In addition, this development enables low power consumption because the MEMS catalytic sensor operates by pulse voltage drive.

In the future, MEMS catalytic sensors will be applied to battery-powered hydrogen alarms and portable detectors. With our life-saving sensor technology, we aim to contribute to the prevention of gas accidents all over the world toward hydrogen energy society.

8. Acknowledgement

We gratefully acknowledge Kengo Suzuki for his contribution before his retirement.

References

- [1] Toyota Motor Co., Ltd., NEW MIRAI PRESS INFORMATION, available at https://global.toyota/pages/news/images/2020/12/09/1200/20201209_01_02_jp.pdf
- [2] H. Miyazaki and K. Suzuki, Chem. Sens. 45, 46 (2008). [in Japanese]
- [3] P. Albers, J. Pietsch and S. Parker, J. Mol. Catal. A: Chem. 173, 275 (2001).
- [4] K. Murata, J. Ohyama, Y. Yamamoto, S. Arai and A. Satsuma, ACS Catal. 10, 8149 (2020).
- [5] D. Briand and J. Courbat, Micromachined semiconductor gas sensors, in Semiconductor Gas Sensors (2nd Ed.), p413 (2020).
- [6] T. Taniguchi *et al.*, ECS Meet. Abstr. MA2020-01, 2327 (2020).

Measuring the aeroelastic properties of a tiltrotor aircraft in a wind tunnel model

Bjorn van der Meulen¹, Michiel Bardet¹, Theo ter Meer¹, Erik Brehl², Keith Soal³

¹ NLR Anthony Fokkerweg 2, Amsterdam, The Netherlands,

² DLR FT, Otto Lilienthalplatz 7, Braunschweig, Germany

³ DLR AE, Bunsenstrasse 10, Göttingen, Germany

bjorn.van.der.meulen@nlr.nl, michiel.bardet@nlr.nl, theo.ter.meer@nlr.nl, erik.brehl@dlr.de
keith.soal@dlr.de

Abstract

The EU-funded Advanced Testbed for Tiltrotor Aeroelastics-project (ATTILA) aims to investigate whirl flutter in *tiltrotor* aircraft. In order to do this, a *wind tunnel model* was developed, which represents a scaled version of a section of Leonardo's Next Generation Civil Tilt Rotor – Technical Demonstrator. The model was successfully tested in DNW's Large Low-speed Facility in the Netherlands in November 2023.

This paper focuses on the sensors, electronic instrumentation and channel synchronization. The system consists of *rotating* and *static* model parts, complemented by several computer systems which capture and store the data.

Both the stator and rotor parts of the model contain electronic sensors, such as strain gauge bridges, vibration sensors, and digital rotary encoders. Additionally, the rotor blades contain Fiber Bragg Gratings, sampled by an interrogator, supplied by PhotonFirst.

The dedicated Data Acquisition System for the rotor (RDAS) is a bespoke development by NLR. The physical implementation of the RDAS consists of three disc-shaped boards, with interconnects to the sensors, and two Ethernet interfaces to connect to both the data storage computer and the interrogator. The measurements enable the comparison between 'classical' strain gauge measurements and FBG measurements.

To acquire the sensor signals in the static domain, the Static Data Acquisition System was realised by DLR-FT, with the TEDAS-system at its core. Model vibrations were measured by a separate acquisition system of DLR-AE for an online modal analysis during the wind tunnel test.

All measured signals are collected by a storage computer, and simultaneously passed to the piloting station, both supplied by DLR-FT.

Key words: tiltrotor, wind tunnel model, rotating, telemetry

Introduction

Whirl flutter is a significant consideration in the design of tiltrotor aircraft. No less so in the Next Generation Civil Tilt Rotor Technology Demonstrator (NGCTR-TD) which is currently under development by Leonardo Helicopters. To aid in these development efforts, the Advanced Testbed for Tiltrotor Aeroelastics project (or ATTILA for short) was conceived.

Multiple parties were involved. NLR provided the model itself, along with the rotary data acquisition, the latter of which was augmented by a fibre-optic measurement solution by PhotonFirst. The DLR Institute of Flight Systems (DLR-FT) provided static domain data sampling

and model piloting. The DLR Institute of Aeroelasticity (DLR-AE) provided aeroelastic stability measurements and real-time monitoring.

This paper discusses the measurement system as it was implemented in the ATTILA model. First, a brief overview of the model is given, followed by a discussion of the requirements. This is followed by an overview of the sensor and data acquisition setup. Finally, the data storage and display are discussed, and a brief synopsis of the test campaign is given.



Figure 1: The ATTILA model in the LLF at DNW Marknesse, Netherlands

Model overview

The model is a scaled representation of a wing and nacelle, including a powered rotor. The wing is composed of a carbon fibre rectangular beam, which is enclosed by removeable wing sections. The nacelle is made up of several parts. The rotor pylon acts as a central mounting, to which all other key parts are attached, such as the balance, drive train and so-called TEDs, which allow for trim control and a mechanical excitation device to stimulate the flutter effect. A water-cooled electric motor and gearbox are used to drive the rotor.

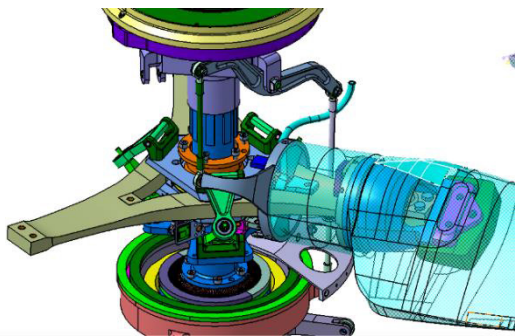


Figure 2: Detail of the rotor system

The rotor system consists of a central shaft, on which the other parts are mounted. The system incorporates a cyclic swashplate and collective control chain for blade pitch control. The rotor consists of a hub, gimbal joint and yoke, which

connects the blades to the hub, and the blades themselves.

The driveline includes an in-line torque meter. At the aft-end of the rotating collective tube, which is part of the collective control chain, the rotary data acquisition assembly is mounted.

Measurement and other requirements

In summary, the following is to be measured:

- Strains and torsion in the blades
- Strains in the yoke
- Forces (normal and side) on the shaft.
- Torque of the shaft
- Yaw and pitch in the hub
- Position data from the blades (pitch) and gimbal flaps;
- Temperatures in the blade pitch bearings and static balance
- Strains from the pylon balance
- Strains from the wing balance
- Vibrations in the rotor shaft
- Vibrations in the wind and pylon

Other related requirements included:

- Produce a synchronization signal (one-per-rev) (1P);
- Transmit data and 1P-signal to storage devices and pilot station
- For the rotating acquisition electronics: withstand the acceleration and vibrations caused by flutter excitation at maximum RPM and whirl flutter as well.
- For the rotary system, the following mechanical constraints had to be considered:
 - Limited space due to enclosure/nacelle covers;
 - Minimum imbalance;
 - Placement at end of shaft: mass constraint;
 - No forced cooling: conductive thermal dissipation.

Sensor overview

To measure flap bending, two pairs of strain gauge bridges are placed to measure the lag bending, at different radial locations in the blades. Furthermore, one bridge was placed as a torsion meter. This setup is similar for all three blades, with one exception. That being that one blade is instrumented with an additional lag bending and torsion sensor.

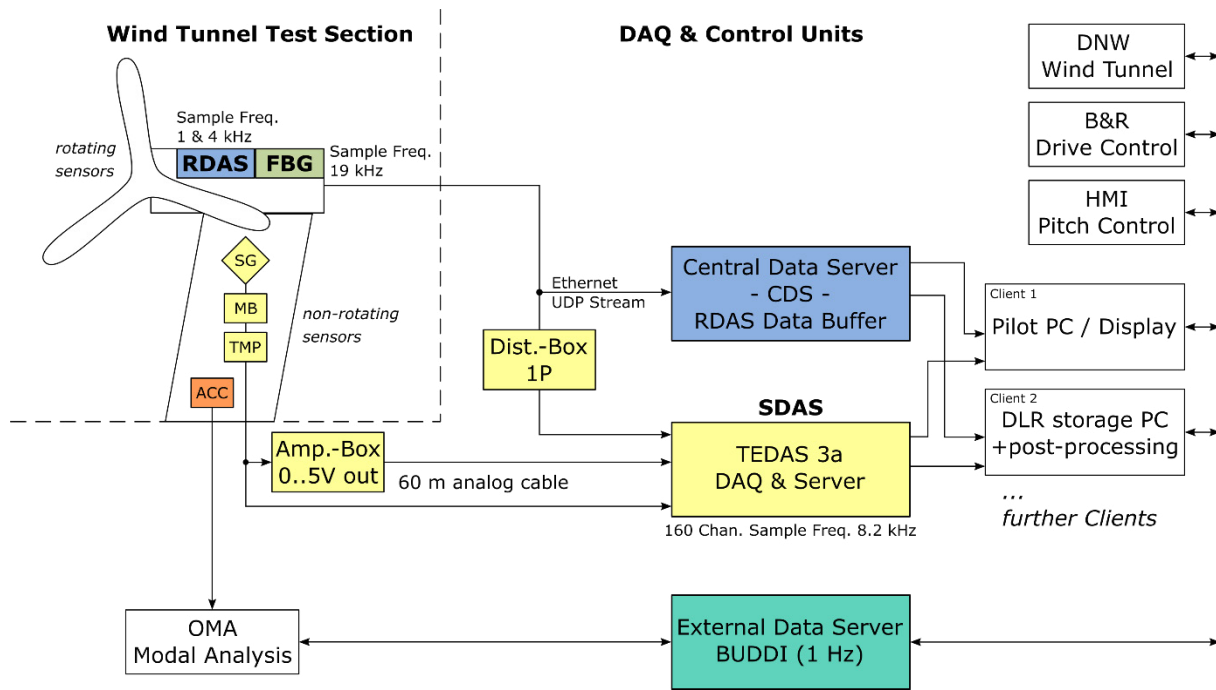


Figure 3. ATTILA System Setup.

In addition to the strain gauge bridges in the blades, optical fibers with Bragg gratings (FBG) are installed. Eight of these FBGs are contained in a single fiber. A number of FBGs are placed near the strain bridges, to allow for a direct comparison of the data produced by the different types of sensor. Two fibers were installed per blade, resulting in a total of six fibers containing 42 FBG strain and 6 FBG temperature measurements.

In the yoke, two flap and lag strain bridges are installed per arm. Another direct strain sensor is placed as a safety sensor.

For measuring the torque in the shaft, a torque sensor using a strain gauge bridge is used. In addition, bending moments in the mast are measured to enable derivation of rotor in-plane shear loads. For this, two pairs of bridges are placed under 90 degrees offset.

For all the measurements mentioned above, 750 Ohm-bridges are used.

To measure yaw and pitch, the hub is instrumented with two tri-axial accelerometers. These are placed 180 degrees apart. Dytran's 3333A3T MEMS-sensors were used to achieve this.

To measure rotary position data, incremental encoders are used. These are placed on the blade pitch bearings, and in the swashplate. The latter give rotational information, as well as the one-per-rev signal. The sensors used are the

Celera Motion Optira-sensors. These are A-quadrant encoders, with RS422-output.

Furthermore, there are a number of sensors in the fixed frame of the wind tunnel model which are acquired by the SDAS. Table 1 shows these sensors.

The wing bending moments are strain gauge full bridges which are located at the root section of the wing beam. The rotor balance is an NLR-designed mechanical structure which connects the wing beam with the nacelle. It also features full strain gauge bridges. All the strain gauges in the non-rotating part are connected to the DLR Amplification Box which is placed close to the model below the test section.

Table 1. Static sensor list

Description	Unit
Wing Beamwise bending	Nm
Wing Chordwise bending	Nm
Wing torsion	Nm
Balance Fx (thrust direction)	N
Balance side force	N
Bal. vertical force (spanwise)	N
Balance Mx	Nm
Balance yaw bending	Nm
Balance pitch bending	Nm

Description	Unit
Temperature balance 4 measuring points	°C
Temp. gearbox 3 measuring points	°C
Temperature cable	°C
Temperature collective tube bearing front	°C
Rotor speed from digital/analogue conversion	V
1P encoder signal	V

For the placement of accelerometers in the static domain, a sensor optimization was performed using QR factorization and the Finite Element (FE) model. The target was to accurately identify and track the first four elastic modes which were predicted to be critical to the dynamic stability. Based on these results, uniaxial and triaxial accelerometers were mounted in the leading and trailing edge of the wing, as well as on the tilting, and non-tilting part of the nacelle. The sensor positions and directions can be seen in Figure 4. In total twenty-nine signals are measured at 13 positions. This setup allows optimal identification of the 1st normal wing bending, 1st chordwise bending, first wing torsion and nacelle yaw modes.

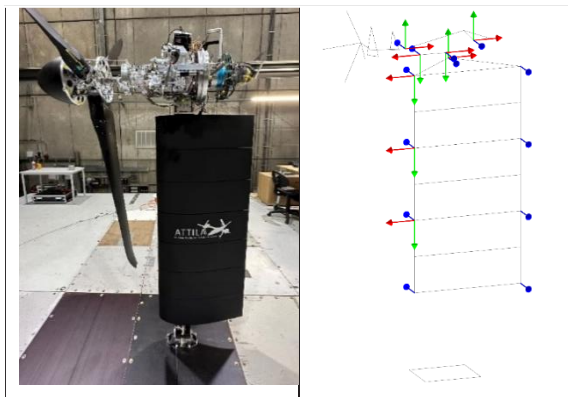


Figure 4. Accelerometer locations and directions for whirl flutter monitoring

Data acquisition

The signals coming from the sensors are sampled by three different systems: one for the rotating domain, and two in the static domain. The Rotating Data Acquisition System (RDAS) handles the rotating subsystem, while the Static Data Acquisition System (SDAS) tends to the static domain. In turn, the RDAS is split up into two subsystems. The Rotating Sensor

Conditioning System (RSCS) acquires all the data from the electronic sensors, while the Fibre Optic Sensor System (FOSS) acquires the data from the fibres in the blades.

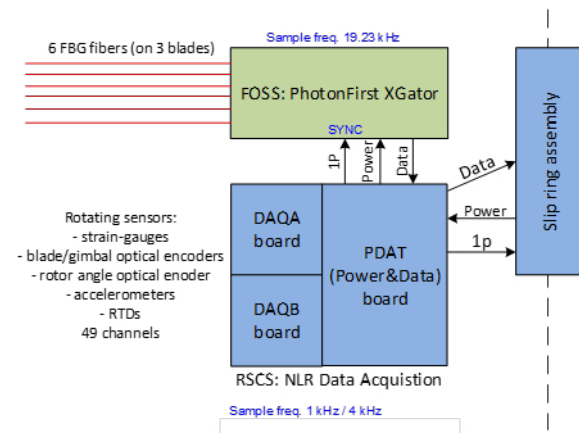


Figure 5. RDAS block schematic.

The core of the RSCS is formed by the Power Supply and Data Processing board (PDAT). It receives 28 VDC electrical power from the slip ring and converts this in switch-mode power supplies to a range of supply voltages that are needed internally for operation of the electronics. An extensive sequencing scheme is built in to ensure a proper and safe power-up procedure. Electrical power is forwarded to the other printed circuit boards in the RSCS.

The PDAT also contains a Field-Programmable Gate Array (FPGA). The FPGA implementation supports the collection of data, and transmission to a receiving computer. The design can be split up into three parts.

The first part handles control of the hardware elements in the acquisition chain, i.e. the setup of, and data readout from, the ADCs, and conditions the 1P signal for external application.

The second part collects the data, and packages it into Ethernet packets. Since the data comes in three different frequencies, care had to be taken to ensure consistent data output. This was achieved by having set packets lengths, containing:

- 28x 4 kHz-samples per package
- 7x 1 kHz-samples per package
- 1x 'slow' samples per package (temperatures, time-since-1P)

Finally, the data is sent out by the third part. This part controls the Ethernet link, which performs the required buffering, as well as arbitrating

between passing through the data from the FOSS or own data.

The different sampling speeds and signal processing result in different ADC group delays. This yields significant, but deterministic time offsets between the different data types. If these time offsets are known, they can be compensated for in the FPGA firmware.

The true group delays were determined through measurements, using a custom-made calibration source that applies synchronous signals to all types of channels. Measurements were initially taken without group delay compensation. The next step was to program the FPGA to correct for the observed relative group delays, so that a true synchronous-sampling DAQ system is established. A check measurement was performed to confirm proper implementation of the correction. The determination of the relative group delays from the measurement data is a tedious and time-consuming task; for this reason, NLR automated this step through a dedicated MATLAB program. Using MATLAB's App Designer, an application was developed to speed up this process. This 'Channel Synchronization Tool' reads the data in Excel format or CSV format of two channels with the same common frequency and determines the phase difference in degrees, seconds and 'time since 1P increment' counts.

The application uses FFT to compute the fundamental frequencies of both signals and uses these as initial values for the MATLAB *fit* and *fitype* functions to precisely determine the three coefficients of the expression $a \cdot \sin(b \cdot t + c)$ to reconstruct the original waveform without any DC-offset. The phase '*c*' is then used to compute the phase difference between both signals. This phase difference is specified to 0.01 'time-since-1P increment' count, 0.1 μ s and 10^{-7} degree. This is in line with the manual results, but can be done in tens of seconds.

Sensor conditioning and digital-to-analogue conversion are performed by the DAQA and DAQB-boards. These data acquisition boards have very similar functions. Both feature 16 strain gauge bridge measurement channels with 10 VDC excitation supply. Readings are taken with 16-bit resolution in a 500 Hz bandwidth. Local electronics temperature readings are taken to allow temperature-dependent calibration and posterior correction of the channels' transfer functions.

The DAQA board is complemented with seven IEPE measurement channels with 4 mA excitation. These are used for the aforementioned two triaxial hub-mounted

accelerometers. Readings are taken with 16-bit resolution in a 3 to 2000 Hz bandwidth.

The DAQB board is complemented with four RTD channels, for Pt100 temperature measurement on the pitch and centrifugal bearings. Sampling occurs with 15-bit resolution at a rate of 1 kS/s.

All of the sensor connections are on the outer perimeter of the RSCS printed circuit boards, with locking connectors to counteract centrifugal forces. The stack of boards is supported by a metallic structure with spokes, providing both structural integrity and a thermal frame for removal of generated heat, see Figure 6. The latter aspect is relevant because of possible future application of the electronics in a low-pressure heavy-gas wind tunnel environment in which convective cooling is less efficient.

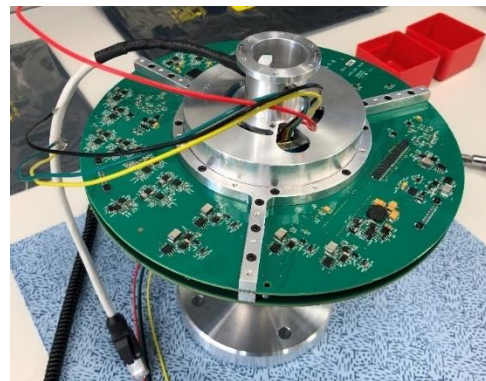


Figure 6. Partly assembled RSCS, showing thermal frame.

An XGator interrogator takes care of acquisition of the FBG sensors. This XGator interrogates the six different fibres sequentially, the sensors in each fiber are measured in parallel at 19.23 kHz. The fiber interrogated changes every 50 ms. The acquired data is sent to the storage computer (via the RSCS) through an UDP Ethernet-link.

The XGator allows up to 8 connections. Six connections were used for the different fibers, while the eighth was used as an input for the 1P-signal. The electronic 1P-signal coming from the RSCS is converted into a light input using a laser based optical sync signal. The XGTR interrogator is built on an integrated photonics platform which allowed the system to function in this harsh environment.

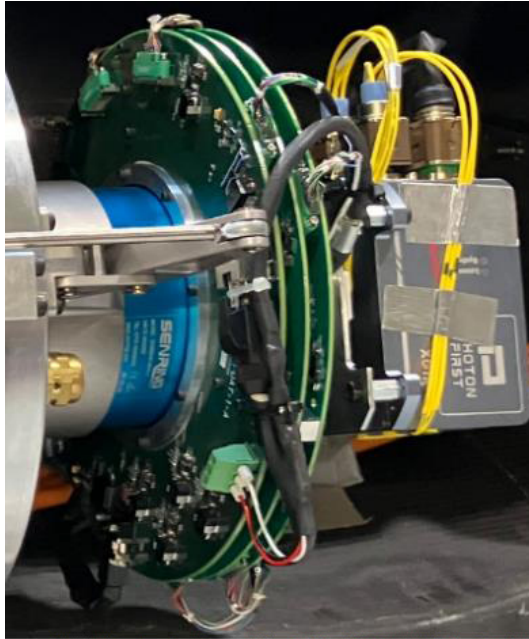


Figure 7. The complete RDAS, as mounted in the model.

In the stationary domain, the SDAS consists of two parts, namely the AmpBox and TEDAS.

The AmpBox is used for strain gauge sensor supply and signal conditioning of up to 48 input channels. The output is in the range of 0 to 5V and directly connected to the TEDAS signal input. Figure 8 shows this box which was specially designed for the usage within wind tunnel models.



Figure 8. Signal Conditioner – Amplification Box

The millivolt signal from a strain gauge is connected to programmable gain amplifiers (PGA) which allow offset adjustment to reach that suitable output range. The parameters from the PGAs can be remotely adjusted through a sophisticated network-communication interface over Ethernet (software “AmpManager”) such that no hardware changes or soldering is necessary. Apart from the PGAs, the AmpBox contains constant-current sources for Pt100 temperature sensor supply.

The AmpBox passes the conditioned signal to the TEDAS. DLR-FT developed the TEDAS (Throughput Enhanced Data Acquisition

System) for rotor-triggered measurement in combination with several software modules for online monitoring, pre-processing and data analysis. It is custom developed by DLR. Key specifications of the TEDAS 3 DAQ system are:

- 496 channels analogue DAQ
- Simultaneous sampling
- 16-bit ADCs
- ± 5 V buffered signal input
- Up to 3000 rpm = 50 Hz sampling
- 1024/2048 samples per revolution
- Rotor triggered measurement or fixed frequency
- Independent simulator/rotor switching

The complete system is currently mounted in a modular rack (see Figure 9) so that the measurement system can be used for different types of wind tunnel models or test rig configurations. The hardware front-end performs simultaneous sampling on all channels. The data volume for the internal ring buffer is about 100 MB/s.



Figure 9. TEDAS 3 rack system.

The overview in Figure 10 shows the structure of the rack-mounted hardware components.

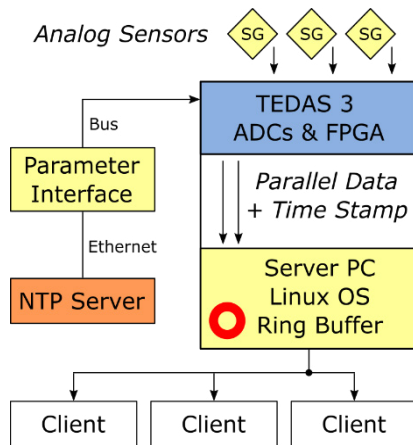


Figure 10. TEDAS 3 Block Diagram.

The sensors are electrically connected through buffers to the sampling hardware (ADCs) on the analogue frontend. The digital part of the system gets configuration parameters from a separate parameter interface (e.g. simulator/rotor switch point etc.). Apart from these parameters, a time stamp with 1 ms accuracy is included in the data block. This feature was provided for data merging in a separated DAQ system approach. The sampled data are continuously streamed out through a digital interface. A Linux-based Server PC reads the data stream and saves these data in a ring buffer with a special-developed server application. Multiple client requests can be handled simultaneously.

For the ATTILA test campaign, the system was configured in a fixed clock setup with a sampling frequency of 8.2 kS/s.

This setting was used to obtain a software compatibility for data analysis tools which are based on handling samples per revolution (rotor-triggered data packets).

The wing and nacelle acceleration signals are measured with an analogue to digital measurement system called CRONOSflex from IMC. All signals are acquired with 500 Hz sample frequency and the appropriate low pass anti-aliasing filters. The model RPM is also measured as an analogue input to the IMC system. Furthermore, a synchronization signal (sine sweep) is created by a signal generator and shared between the DLR-FT measurement system and the DLR-AE measurement system for post test data synchronization. A real-time interface was developed using ActiveX to acquire the data measured by IMC directly from the measurement computer RAM. This data is received by the DLR online monitoring OLM software in MATLAB. A listener function is used to execute appropriate events each time a new data block is received.

Data storage and processing

To store the data from both the RSCS and FOSS, a separate computer system, known as CDS (Central Data Server) was implemented.

The data was first received by the Rotary Data Processor. This processor performs sanity checks on the incoming packets and parses these. From here, the data was spread in three different streams.

First, the data is sent to the Data Storage Handler. This unit is responsible for the continuous data storage. It writes the parsed data into a binary file. This file can then be processed (offline) by a separate script to either a .csv or .m (MATLAB) file.

To be able to have a real-time overview of the data, quick-look functionality has been implemented, using Grafana for the presentation. The RDAS-message processor sends the parsed data by MQTT to a database. In turn, the Grafana dashboard periodically requests data from this database, and displays it.

Moreover, the processed data was stored in a ring buffer. A separate TCP message handler receives requests from the DLR pilot and measurement stations, and serves the data according to these requests.

The pilot station is the main monitoring and control station for the wind tunnel model during a test campaign. The responsible engineer at that station is in close contact via an intercom system to the wind tunnel operator and experimental systems operator. The pilot station constantly monitors the model's sensor data and actual load limits and can control further actuators (TEDs) mounted in the model with a dedicated HMI system (Figure 11).



Figure 11. ATTILA HMI system – pitch control.

For the ATTILA test the HMI system was able to control the collective pitch of the rotor blades, which is essential for the rpm control in power off condition (model acts as windmill). In addition, actuators for longitudinal and lateral cyclic pitch, similar to a conventional swash plate, control rotor tilt.

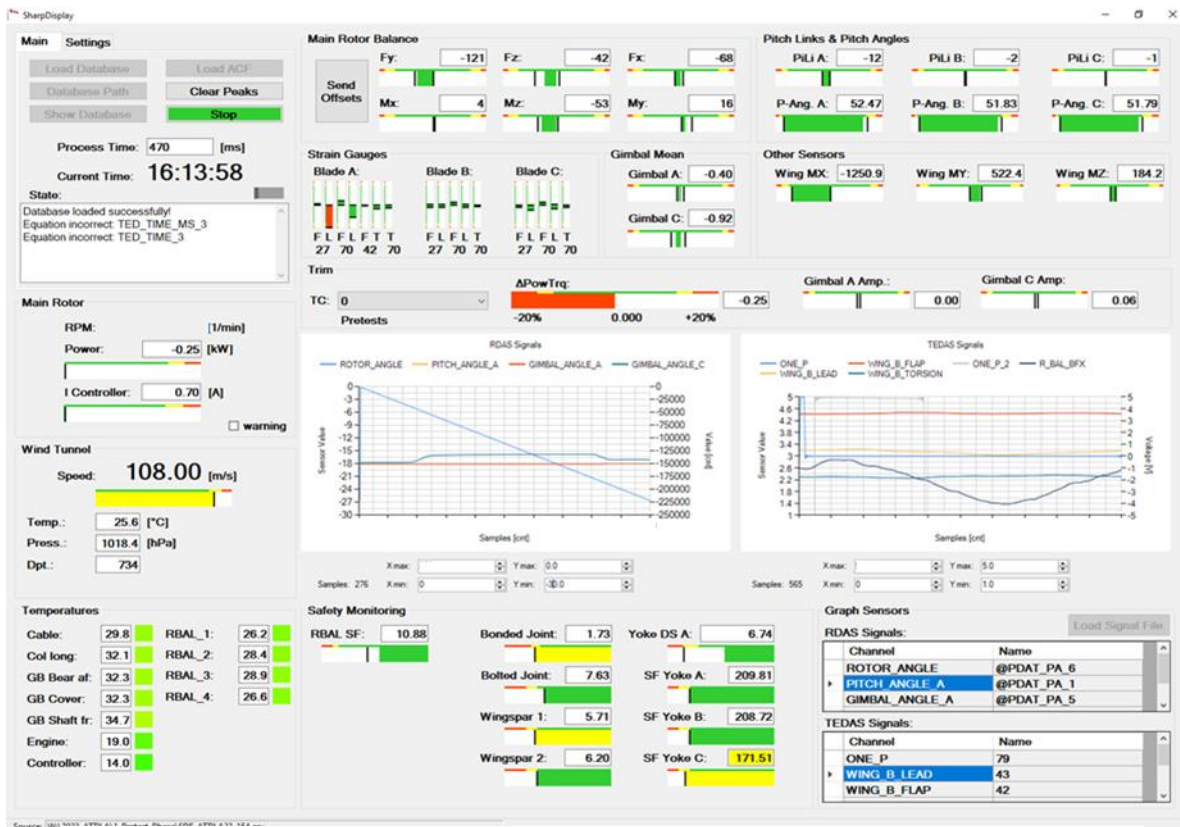


Figure 12. ATILA Pilot Display.

In power-on condition (electric motor drive) there is a dedicated RPM control system for the model's drive system. With that separate system a target rotational speed could be set and the actual speed was controlled automatically.

The main monitoring device is the pilot display PC with specially developed online monitoring software: The Pilot Display.

The Pilot Display collects the data from different acquisition systems:

- CDS – Central Data Server, stores and buffers all RDAS + FBG data
- SDAS – Stationary DAQ TEDAS, stores and buffers all non-rotating data
- EDS – External Data Server, operates the Basic Utility for Double Data Interchange, handles slow data (update rate ~ 1 Hz) between different network participants (see Figure 3 \rightarrow system setup)

All these raw data streams are merged by the display program which shows all necessary data in engineering values.

For the ATILA test the SDAS internal ring buffer memory was extended to realize the decay measurement after flutter excitation. A maximum

of 60 seconds decay time can be requested from the server.

Due to the model setup with different data acquisition systems for rotating and non-rotating sensors, the request order had to be defined to get a synchronized data-set after post-processing the data. Figure 13 shows the setting used for the ATILA test. The CDS collects the RDAS data stream and handles client requests comparable to the TEDAS server. First, the CDS is requested which delivers data "from now on" to the requested length. Next, the TEDAS server is requested to deliver historical data from the internal ring buffer. This procedure ensures an overlap of both data blocks from the two different DAQ systems.

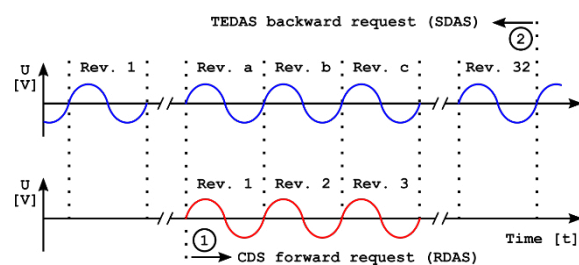


Figure 13. Overlapping data.

Apart from the request order that ensures data

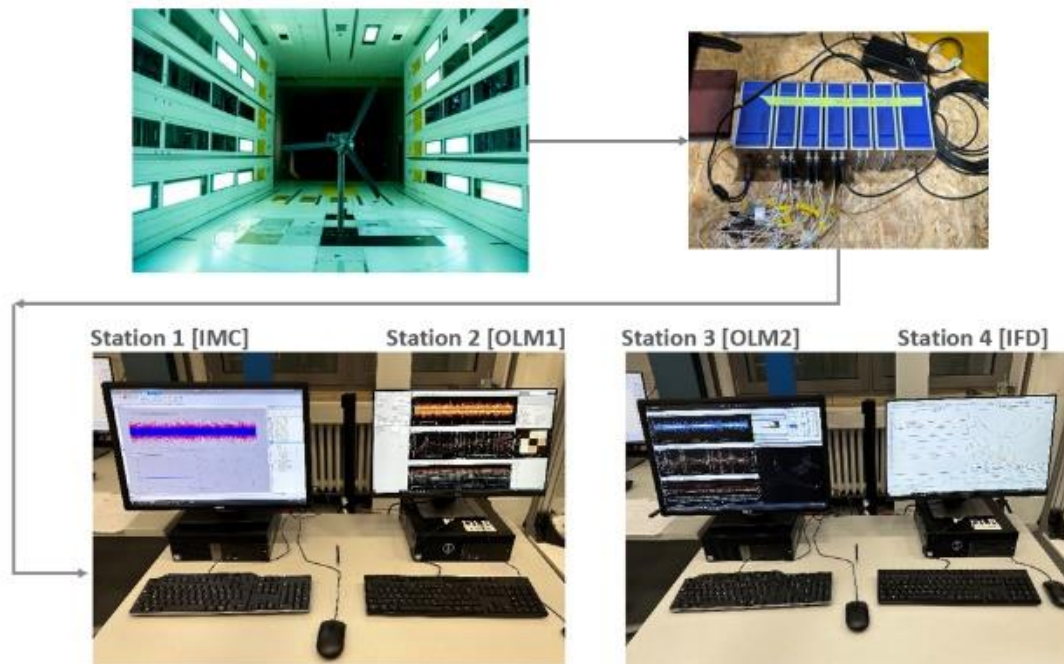


Figure 14. Whirl flutter stability monitoring system.

overlapping in time, the same 1P signal is measured on both systems. This rotor position sensor is mounted in the rotating model part. It is connected to one analogue RDAS input channel as well as fed through the slip ring to the distribution box which is connected to one analogue SDAS channel.

The DLR-AE OLM software performs signal processing, operational modal analysis (OMA) and mode tracking in near real time – updated every 2 seconds. When a new data block is received the data is processed using optimized code for the specific modal analysis method selected e.g. SSI or LSCF. If filtering, decimation and spectral calculations are required these are performed first. The data is then passed to the OMA algorithms which estimate the natural frequencies, damping ratios and mode shapes. The modal parameters are then tracked using various quality indicators and a machine learning method called DBScan. A configurable GUI is used by the engineer to monitor the results during the test. The data is saved at each stage of the above-mentioned process, and is fully traceable. Raw data is saved on the measurement PC in binary file format. The results of the OMA and tracking are saved locally on each PC and finally to an SQL data base on a network attached storage NAS. Finally, all data is batch copied each day to the NAS. An overview of the OLM system can be seen in Figure 14. Whirl flutter stability monitoring system.

Model commissioning and exploitation

After the completion of the sub-assemblies, the model was functionally integrated at the workshop facilities located at NLR Marknesse in May 2023. Following integration, a first low-RPM test was performed, to check the functioning of the drive train and to investigate any surface issues or defects. Following these tests, the model was then transported to the DLR Institute of Flight Systems, where the data acquisition and actuation systems in the model were integrated with the piloting and measurement stations. Further checks, such as balancing and calibration measurements were made.

After transport back to Marknesse, the model was prepared for the first wind tunnel campaign, aimed at testing the model in real conditions. Furthermore, testing and communication procedures were evaluated. This campaign was performed in August 2023.

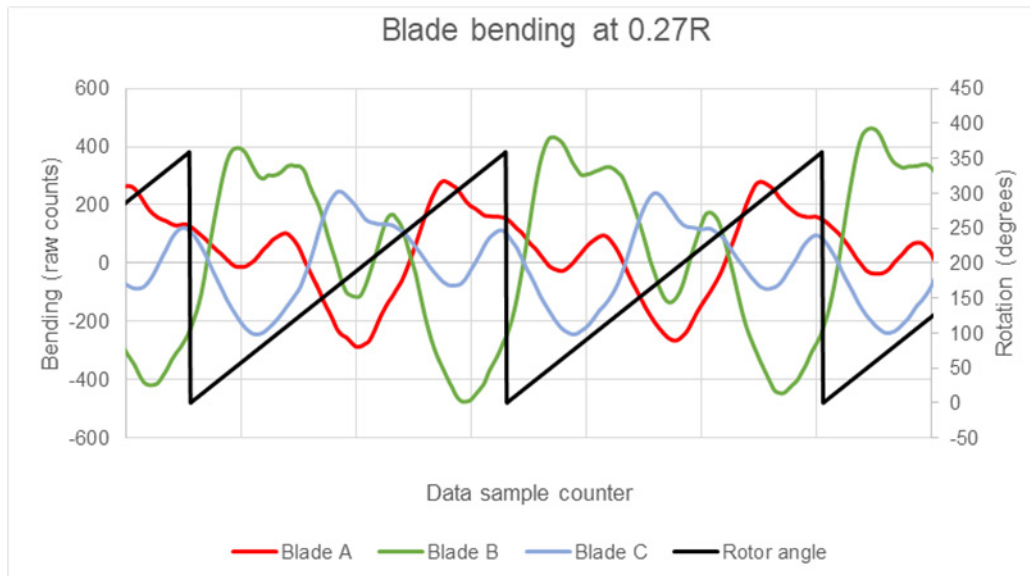


Figure 15. A data snippet representing blade bending signals, related to the rotor angle.

The shakedown campaign revealed a few issues. For the measurement system, these were a communication error between the piloting station and the CDS, as well as a signal integrity issue of the 1P-signal. The first was addressed with a software fix in the CDS, while the latter was eventually compensated for in the FPGA firmware. Furthermore, CAN communication issues between HMI and TED were solved successfully.

Having addressed these issues, and after performing final tasks such as synchronization and final calibration of RDAS, the system was ready for the final wind tunnel campaign which was performed during the late November and early December 2023.

To give a small insight into the collected data, Figure 15 provides a data snippet collected during this campaign. The sawtooth (in black) shows the rotor angle, as measured by the encoder mounted in the swashplate. The red, green and blue lines are the signals coming from the strain gauge bridges in the blades. As can be seen, the peaks (although differing in amplitude) are shifted 120 degrees with respect to each other.

In general, the measurement system was able to perform to expectation. A comprehensive analysis is still underway, but sanity checks of the data have found no data breaks or other anomalies. Accurate RPM control in unpowered state, i.e. controlling the RPM by changing the pitch of the blades has been possible thanks to the successful integration of encoder data coming from the RDAS and served through the CDS to the pilot station, as displayed in figure 12. In addition, the data coming from the strain

gauge bridges was also able to be used for monitoring the safety factors in the model.

Preliminary results have identified near-flutter behaviour, in unpowered state. [1]

Acknowledgement

This project has received funding from the Clean Sky 2 Joint Undertaking under the European Union's Horizon 2020 research and innovation programme, under grant agreement N. 863418.

References

- [1] S. van 't Hoff, F. Fonte, K. Soal, O. Schneider und K. Kaptein, „Whirl Flutter Testing of ATTILA Tiltrotor Testbed - Initial Results,“ in *Vertical Flight Forum*, Montreal, 2024.

High Innovative Telemetry Solutions for Demanding Applications in the Aerospace Industry

Dr.-Ing. Stephanie Manner¹, Dr.-Ing. Ernst Manner², Dr. Julia Manner³

^{1,2,3} MANNER Sensortelemetrie GmbH, Eschenwasen 20-24, 78549 Spaichingen, GERMANY
manner@sensortelemetrie.de

Abstract:

The aerospace industry is a field of its own. Always driven by innovations, safety and efficiency, this sector plays a vital role in shaping global transportation, communication and defense capabilities. Innovations and developments in this industry have far-reaching impacts on various sectors and contribute to the progress of technology as a whole.

Providing measurement solutions with contact free energy and real-time data transmission for aerospace applications is a supreme discipline and has ever been a core competency of our telemetry solutions.

Not only the high demands on environmental conditions such as temperature, humidity and shock/vibrations but also a highly precise and robust signal measurement and signal transmission in a system without foreseen space for measurement tasks is a challenge by itself.

In this paper we will discuss different solutions for measurement tasks in the aerospace industry with a focus on helicopter applications.

Key words: near field telemetry, sensor telemetry, helicopter applications, time synchronous data acquisition, PTP V2, IRIG B, IENA.

Space Constraints for Measurement Systems

Developing complex systems as aircrafts or helicopters means not only a lot of moving parts but also quite some loops during the engineering phase and test campaigns. Each loop will help getting closer to reaching the goal but often there arise problems the engineers did not think about. All the parts are carefully engineered and designed, the stress on the parts is simulated in FE models and if in doubt a measurement campaign for the part is done on test benches. Anyhow, once the subsystems are assembled to systems of the aircraft or rotorcraft, totally new behaviors might be identified during a ground test.

To understand the new behavior of the systems and to overcome the challenge a physical measurement is aimed for. Since the major part of engineering is already done there is no space foreseen for measurement systems or sensors. Additionally, the parts should not be manipulated in any way but measurement signals are needed. Adding e.g. weight to a shaft might change the behavior, stiffening or weakening shafts will also result in a different behavior. Here it is very important to choose very light weight measurement solutions. A high

grade of customization is necessary to push the borders of the feasible. Modular and adaptable components and a variety of package sizes are important to be able to solve such demanding tasks. This is called retrofit, meaning enabling measurement systems in locations where this seems impossible.

Environmental challenges

Since the constraints of available installation space are known and identified and can be addressed by the means in the passage before, the environmental conditions such a measurement system has to stand are to be defined.

The exact environmental conditions an aircraft system has to withstand can be studied in the standards like DO160 or CS-23, CS-27 or CS-29. The most challenging conditions are a significant range of temperature. Reaching from -50°C to up to 160°C or even 200°C the challenge for those systems is big. Components not only have to survive these temperatures, they also have to perform with nor or only minor degradation of the measurement accuracy and lifecycle of the system. The most challenging for electronic components as telemetry systems are temperature cycles. Going through the

freezing point and the dew point each time as well as cold starts are demanding.

Humidity and especially salt water tend to creep under the potting and sealing of the sensor installations.

Oil, especially gearbox oil is very aggressive. There are telemetry systems necessary to be installed in oil or oil mist. This is an additional challenge. Together with temperature cycles and vibrations as well as accelerations and high rpm this is nibbling on the potting and sealing and the oil tends to creep under the potting even more than salt water.

The circuit boards are the heart of the telemetry system. Electronic components are very vulnerable and cannot stand any force to them. These electronic circuit boards are highly complex with a lot of layers and the smallest electronic components on the market. Driven to the edge to perform in temperatures that are not even possible according to their electronic components data sheets but somehow realized with the fines engineering teams of the telemetry manufacturers. This means that the packing of the electronics needs to be done with a lot of knowledge. The resins need to be chosen wisely and several layers of different sealings and enforcement techniques need to be done to lead to success. There is a lot of sensitive and intellectual knowledge coming to this.

At the end the customer needs to choose the best fitting technology and industrial partner and telemetry manufacturer for a system to be operated in such demanding environments.

Electromagnetic Interferences (EMI) Awareness and Proofness

Part of such standards as DO160 or CS-23, CS-27 or CS-29 is EMI. EMI is not just the immunity against external fields and disturbances but also the EMI emissions of the telemetry system that could possibly disturb other systems of the aircraft or rotorcraft, especially the NAV/COM frequency band. Two decades ago the main focus has been to gather all the data during the flight campaigns or ground tests. A disturbed frequency was seen a minor issue.

This point of view changed drastically. A major trigger has been the NAV/COM systems that read signals as small as -90dBm using enormous amplification on the signals. On the contrary with the higher data rates and bigger bandwidths needed, EMI becomes even more prominent in telemetry systems. Therefore, the suppliers had to address this and eliminate the root causes. Highly innovate filtering techniques

perform fine tuning and optimize the EMI behavior of measurement systems.

At the end, the EMI behavior of a system is vastly influenced by the sensor application and especially the wiring and shielding of sensor wires. This is not always part of the installment done by the telemetry manufacturer. Anyhow, the manufacturers that provide installation on customer parts have gained a lot of knowledge and are willing to help their customers out with support to lead them to success.

State of the art systems and their components proofed their EMI behavior in certified labs.

Flexibility in a Custom Specific Telemetry System

This sounds like a contradiction but it is possible with the new generation of multi-channel telemetry systems.

The more flexibility a telemetry measurement system has, the shorter is the period of time necessary for customization. This is often a game changer in fast development cycles.

Some of the new generation of multi-channel telemetry systems on the market are software configurable. This means, that a majority of sensor interfaces are foreseen as hardware and can be activated as necessary. E.g. strain gauges (1/4- bridge, 1/2- bridge, full bridge, RTD, PT100, high voltage sensors, ICP and more). This is even possible after the system has been delivered and installed.

The number of channels can be upgraded by adding another module and this is possible up to 256 channels by multiples of 4 channel systems.

A huge advantage is the remotely configurable filter frequency using digital filtering onboard the amplifier electronics. Digital filtering on top allows very sharp edges of the filter function.

This often is a crucial advantage once the realization during a measurement campaign is made that e.g. the cutoff frequency needs to be changed. Of course, the necessary bandwidth has to be granted.

Monitoring of the System and Sensor Health Status

The new multi-channel telemetry systems are equipped with a monitoring function. The software allows the user to set alerts for critical system parameters and few the telemetry health data on a dedicated page of the software.

This can be measurement values, supply voltages, onboard temperature of the amplifier as well as forward and reflected power in

inductive systems. A logging function for an alert will allow the user to replay the system data recorded during the alert and help to understand certain issues.

On top, there is the possibility to recognize sensor losses such as disconnected wires or shorts.

Single channels can be shut down to avoid further harm or energy loss to the system and guarantee a successful measurement even when one sensor has failed.

E.g. turbine telemetry systems especially for aeronautical engines need this to be addressed. Those systems are highly integrated and a disassembly of the system to do certain problem solving is impossible.

To be able to check the overall telemetry system health can be a game changer and avoid issues during a test campaign.

Accurate Data without Loss

Data loss during a flight campaign are very aggravating. Even during ground test this is a scenario nobody wants to encounter. The majority of our telemetry systems are engineered as inductive systems. This is due to their robustness for signal transmission and the omission of maintenance of the system. The inductive transmission path is very robust and secure against disturbance or signal loss.

Besides inductive telemetry solution, we provide also radio telemetry systems that either can be used with batteries to supply the rotating part of the system or an inductive supply can be used with radio signal transmission for the data.

Each sample has a checksum, so corrupt signals get not passed through.

High Data Rates

Especially for flight test instrumentation (FTI) a lot of different measurement channels are needed. Looking at turbine telemetry system the number of channels and necessary bandwidth explodes. Our new technology can handle up to 256 channels with a total system data rate of up to 320Mbit/s.

Time Synchronous Sensor Data

The aim for a fully synchronized measurement is clear. On a complex system as a rotorcraft or aircraft it is very important to bring the different samples back to one master clock. Then being able to compare the sensor data especially in case of conspicuous data.

There are a lot of protocols available on the market. Thus, making this whole task even more demanding.

The most common protocol in the aeronautics is the PTP V2 IENA protocol but the older protocol like IRIG B is also demanded by some customers.

PTP v2 or IRIG-B

Both standards provide precise time synchronization. Even though PTP v2 is more common these days, our telemetry systems can handle both standards.

IRIG-B being a time code format that is able to provide time information up to an accuracy of milliseconds (when used in conjunction with PTP) and synchronized to a reference clock. The precise time information can also be integrated in the IENA format.

PTP v2 is designed to provide precise time information over local area networks using a master slave hierarchy. PTP v2 has a sub-microsecond accuracy.

The precision time protocol (PTP) allows to have one master clock e.g. GPS grand master and to synchronize every sample with this master clock.

By performing this every sample is defined in time with very high accuracy.

The time accuracy is about 10 ns and also depending on the sample rate.

IENA Format

The IENA format is used for encapsulating data in a standardized manner to allow data exchange over Ethernet networks. It is often used in the defense and aerospace industry where real time telemetry data is critical. It is a network-centric approach and allows efficient distribution of data across complex networks.

Combining PTPT v2 or IRIG-B with the IENA Format

Both approaches are promising even though the most common solution is using PTP v2 with the IENA format making the telemetry data easily accessible via Ethernet and having a precise timestamp.

Conclusion

Depending on the measurement task of a telemetry system the choice which technology is the best fit should be made after consulting your telemetry manufacturer of trust. There are many different realizations on the market each having its own advantages and disadvantages.

Major criteria are the available space and the number of channels needed together with the bandwidth and environmental conditions the system will be operated in.

Especially for telemetry systems used in flight there should be a focus on reliability, EMI proofness and time synchronous data acquisition together with time stamping.

For a measurement task that might get more complex after having obtained the first measurement data, highly flexible solutions are to be preferred. Using the new innovations on the market and being able to readjust the system down to the sensor interface and filter frequencies comes with a huge advantage not only for the flexibility of the measurement task but also for the lead time of customized telemetry systems.

Different systems can be operated on one bus by daisy chaining the evaluation units. One grandmaster for time stamping and resulting in time synchronous data. Analyzing all data and compare sensor data is possible not being limited to the telemetry sensor data but all sensors participating in the time stamping and using the same protocol. The majority of the systems nowadays use PTP v2 IENA but IRIG-B combined with IENA is available.

The sacrifices that have been made a few years ago are now able to overcome with the innovations and new technologies on the market. A reinvest in telemetry equipment might have enormous benefits.

HIL & HTB – challenges and solutions

Joerg Collrep, Bob Judd, Erik Goethert
¹ United Electronic Industries. Norwood, MA, US,
² joerg.collrep@ametec.com

Abstract:

Hardware in the Loop (HIL) and Hybrid Test Benches (HTB) plays a key role in avionic testing and more data streams are introduced and need to be managed or simulated. There is clear industry need for more simulation to reduce cost and safe time. Nevertheless, the impact of real hardware can't be neglected and therefore it is essential to consider them also in future bench plannings. Detailed planning and alignment with all stakeholders are essential to achieve major milestones in a new development or program update. It's about the "what, why, and how" and potential challenges you might face. We will explore them in context of HIL Testing in an avionics environment, highlight how hybrid test benches can provide potential solutions, elaborate on the why it is important to consider various types of sensors and signals before setting up the test and what solutions are available to deal with these challenges. We will talk about specifics on RVDT's, LVDT's, strain gauges, Thermocouples and synchros. The paper will describe a typical HIL set-up and will help you to understand the potential challenges, give an idea how to manage and provide solutions for implementation and connectivity of modern & smart HIL testing.

Key words: HIL, HTB, Testing, Simulation, DAQ,

Time to Market (TTM) plays a key role in the success of a product or it's upgrades, and the known V-model is part of this approach as it directly describes the contributors from Concept to the final system. Hardware in the Loop (HIL) testing is part of this model and already quite common in the industry to get early feedback of the potential system set-up and functionality while Hybrid Testbenches (HTB) are just beginning to enter the industry. Hybrids can use different set-ups depending on the needs of the users like a mix of simulated and actual hardware or even dislocated hardware in other facilities. The challenge is now beside high expectations on shorter TTM also the integration of multiple sensors & signals within an already complex test scenario. We will discuss potential contributors in an Avionics test bench and what needs to be considered in the selection process for a successful bench test.

Avionic Test bench

In a typical Avionic test bench, you will find the different data bus like e.g. MIL-Std.1553, AFDX, Arinc 429/708/453/825, General Purpose and Specific I/O's like e.g. Thermocouples, RTD's Strain Gauges, Synchro, Resolvers, LVDT, RVDT, Motion Sensing and of course, communication interfaces like e.g. RS-

232/422/485, SDLC/HDLC or Can bus. We want to focus Special I/O's in this paper to provide details on what needs to be considered in a good selection process and to set realistic expectations on your sensors/signals.

Thermocouples

You will find many options on Thermocouples (TC) with a typical accuracy of +/- 1°C which is quite common except you go for a special one. Keep an eye on the Cold Junction Compensation (CJC) as it directly impacts the system. A CJC error can create directly errors in your signals. Don't specify your system to run at 1kHz if your TC constant sits at 500ms, align your expectations & selection. Prepare for an open-circuit simulation to test for open-TC circuit. Furthermore, be careful on grounding if you select isolated TC's you need to make sure your system does the same.

RTD's

When using a Resistance Temp Detector (RTD) and board consider a RTD simulator before as this might be easier to get. The scale factor is getting greater as larger the resistance is. Most of the cryogenic users opt for 1000Ω and some of them are fragile. You need to have realistic expectations on your measurement speed. An

RTD with a rise-time (in air) of less than 1 sec is already a very fast one. Keep an eye on the wiring as this is typically the most critical one so your system should be able to detect and simulate short circuits as well.

Strain Gauges

Most of the time well under control but watch for the correct selection ¼, ½ or full bridge incl resolution and installation. Influencing factors are also the excitation voltage and you need to check the simulator’s full scale output voltage.

Synchros & Resolvers

In Aerospace application you will find mostly 400Hz ones but always double check, 28Vrms are the typical but you will find 90/115 Vrms as well. Some of them have only a 12-bit resolution so check whether that meets your expectations. Furthermore, check regarding isolation as some “real” signals coming off fully isolated coils.

RVDT and LVDT

Typical sensors provide accuracy levels of 0.1% and they require a power output is around 7 Vrms and 0.35 VA. The excitation frequency has a direct influence on the sensor linearity.

Control & Monitoring Computers

The most critical topic on this topic is the latency. Will the chosen I/O system match with the expectations of the real-time performance? The Windows operating system is most likely acceptable while the Linux one is typically lower and choose for the most critical RT tasks a VxWorks, QNX or RTLinux. Make sure that your system can be supported long enough to avoid obsolescence issues later.

Potential Solution

They key for a successful set-up of your HIL or HTB system is carefully selected sensors, signals, and I/O configurations. A full understanding of the impact of the various

elements is essential to meet your expected output. One of the supporting elements are the chosen communication protocols. On Hybrid Test benches (HTB) the ED 427 Virtual Interoperable Simulation for Tests of Avionic Systems (VISTAS) could be one potential candidate to achieve these goals (fig.1). It can provide e.g. detection of anomalies and debugging, software integration tests, functional verification, fault injection and system limit testing. The idea of VISTAS is to create a protocol for testing avionics system. Very often a particular avionics device can’t be tested alone – it requires other parts of avionics suite to be present and deliver information. To accomplish that, VISTAS allows easy substitution of missing parts to be emulated using hardware such as avionics interfaces. Additionally, it is possible to create a virtual bridge between test setup and an avionic device which could be in some remote area. To do that, one set of avionics interfaces talks to the device and another set talks to the test bench. Two sets are connected via a local or global TCP/IP network. Although the virtual link between the emulation and the emulation hardware could have latency or jitter, if set up correctly, the emulation hardware can use the hardware schedulers we discussed to solve these problems. Avionics are typically more sensitive to schedule than message content. Stale messages may be OK for one cycle. This is a perfect match for hardware-based message handling.

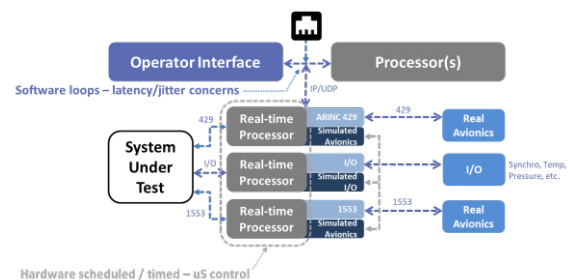


Fig. 1. Example of a ED247 (VISTAS) set-up.

A Hybrid Approach Using Near-Field Scanning in Combination with Field Simulations

Dominik Schröder¹, Christian Hedayat¹, Alexander Weiß², Harald Kuhn²

¹ Fraunhofer ENAS, Warburger Str. 100, 33098 Paderborn, Germany

² Fraunhofer ENAS, Technologie-Campus 3, 09126 Chemnitz, Germany
dominik.schroeder@enas-pb.fraunhofer.de

Abstract

This contribution shows the principle of near-field scanning (NFS) used in combination with electromagnetic field simulations across various domains of applications including automotive, IoT and industrial). With a near-field scanner, the field probes capture the electric and magnetic field strength within a few milli- or centimeter distance to the device under test (DUT). On the one hand, the near-field scanning results can be directly used in order to characterize and to investigate the DUT regarding functionality, security, electromagnetic compatibility (EMC), electromagnetic immunity (EMI) and field propagation characterization. On the other hand, using the so-called Huygens-principle, equivalent near-field sources of the DUT can be derived from near-field scans. These sources can then be imported into a field simulation tool to further post-process the NFS results. This hybrid approach can be used to extrapolate the near-field into the far-field at e.g. 3 meter or to evaluate the influence of the DUT on the environment and adjacent devices (cars, airplanes, humans, housing, others devices). It will be shown, that near-field scanning is a beneficial technique in every design phase of an electric component all along the way until its integration into the whole final system.

Key words: Near-Field Scanning, Field Simulations, EMC, EMI, Huygens-principle

Introduction

The trend towards electrification and digitalization is becoming increasingly important for all industries and daily life. Higher frequencies, increasing integration factors and the smartification of all devices lead to an increasingly crowded electromagnetic spectrum throughout the place. This fact leads to increasing electromagnetic interference (EMI) between different components and systems and their close environment. [1] Especially in the transportation sector, electrification of vehicles, vessels or airplanes is one of the dominant topics as politicians and industry try to reduce the carbon footprint and the consumption of fossil energy sources. However, electronic systems and components cover a wide range of possible operating points, ranging from very low power to kilowatts of power and from low frequencies to high frequencies. On the one hand, 77 GHz radar modules and 5G communication are used for autonomous driving, while on the other hand, motors and battery chargers operate at a few tens or hundreds of kilohertz and power from 11 kW to a few hundred kilowatts.

To avoid interference with other devices, each subsystem must be tested for electromagnetic

compatibility (EMC). In addition, the EMC compliance of the overall system must be tested under realistic operating conditions (e.g. in a fully equipped car). These component tests are often based on conducted measurements for cable-induced problems or far-field measurements for radiation-based problems. To get a quick, simple and comprehensive overview of the EMC characteristics of such devices, these test methods are good and sufficient. When such tests fail, manufacturers and developers start troubleshooting only based on these results, which usually do not provide any concrete information about the cause of the problem. Moreover, this very often ends in a trial-and-error approach, as EMC problems usually vary from one application to the next.

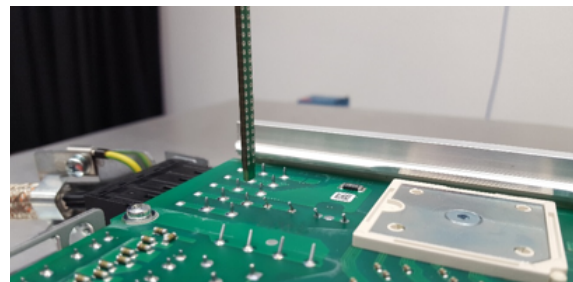


Figure 1. Example of a near-field measurement

This is where near-field scanning (NFS) based test methods can help. Traditionally rooted in antenna testing, NFS has evolved to address these critical issues. By using a near-field scanner to measure the electric and magnetic field strengths in close vicinity (typically within millimeters or centimeters), a detailed insight into the electromagnetic behavior of the device-under-test (DUT) is obtained. This gives developers immediate feedback on issues such as noise sources, malfunctions, coupling paths and safety aspects. [1,2]

In addition to evaluating the pure NFS results, equivalent near-field sources of the test specimen can be derived using a near-field scanner. These can be used in electromagnetic (EM) field simulation tools for advanced post-processing. Using the surface equivalence principle, the tangential near-fields must be recorded on a closed surface around the test object, which then forms the near-field source, also known as the Huygens surface [3]. This source has the same EM properties towards its outer space as the original measurement object. Various investigations can be carried out with such a field source. The simplest is far-field extrapolation, which provides a prediction of the far-field behavior and can therefore estimate the results of EMC-compliant measurements [4].

Furthermore, the integration of additional devices, systems, components, enclosures, vehicles or other units into the simulator significantly improves the utilization of the near-field source. This enables the evaluation of the electromagnetic effects of the DUT on its environment in terms of EM susceptibility, radiation optimization, positioning of the DUT in its intended environment and various other factors [5].

Near-Field Scanning and the Huygens-Principle

Near-Field Scanning

In general, a near-field scanner consists of a positioning robot, a measurement receiver (for near-field sources: dual-channel for phase-related measurements) and near-field probes. Additional components such as a 3D scanner and peripheral devices can be integrated to improve system accuracy and automation. A Cartesian-based scanner, for example, usually has at least four probes: tangential (x, y) and normal (z) probes for H- and E-fields. While a spectrum analyzer is sufficient for pure amplitude measurements, a two-channel concept is required to obtain phase information, each of which has its own advantages and disadvantages. Such a near-field scanner, such

as the NFS3000 from Fraunhofer ENAS, is used for the measurements examined in the following chapters.

Huygens-Principle

The transformation of the near-field into the far-field can be described using the surface equivalence theorem, also known as Huygens' principle. This principle states that every point on a propagating electromagnetic wave can be considered a source of a new electromagnetic wave. Based on this concept, a set of equivalent sources positioned on a closed surface around the DUT can determine the device's electromagnetic radiation in the far-field. The space surrounding the DUT, which is filled with homogeneous, linear, and isotropic material, is referred to as D_0 . This space is divided into two regions, D_+ and D_- , by the enclosing surface S , as illustrated in Figure 2.

The equivalent sources on this surface S are defined by the fictional magnetic current density \vec{M} and the fictional electric current density \vec{K} . Each of these densities can be expressed by their related tangential electric or magnetic near-field, which are defined as

$$\vec{K} = \vec{n} \times \vec{H}|_S,$$

$$\vec{M} = \vec{n} \times \vec{E}|_S.$$

This means, that the surface-equivalence-theorem is a good and easy way to use near-field scanning data as an equivalent field source, which can replace the DUT in the inner region of S . For NFS systems, usually working with a cartesian coordinate system, the surface S has the shape of the box. Therefore, it is often and from now on called Huygens-Box.

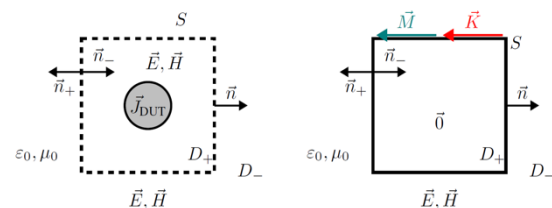


Figure 2. Basic principle of the surface equivalence theorem [5]

Having the current densities at hand the electric and magnetic field in the area D can be calculated using the STRATTON-CHU equations. With k_0 as free-space wave number and Z_0 as wave impedance in free-space the electric field can be represented by

$$\vec{E}(\vec{r}) = -jk_0 Z_0 \vec{A}_e(\vec{r}) - \nabla \Phi_e(\vec{r}) + \nabla \times \vec{A}_m(\vec{r}), \vec{r} \in D_-$$

and the magnetic field is defined as

$$\vec{H}(\vec{r}) = j \frac{k_0}{z_0} \vec{A}_m(\vec{r}) - \nabla \Phi_m(\vec{r}) + \nabla \times \vec{A}_e(\vec{r}), \vec{r} \in D_+$$

The electric and magnetic vector potentials

$$\vec{A}_e(\vec{r}) = \int_{\Sigma} G_0(\vec{r}, \vec{r}') \vec{K}(\vec{r}') dA(\vec{r}')$$

$$\vec{A}_m(\vec{r}) = - \int_{\Sigma} G_0(\vec{r}, \vec{r}') \vec{M}(\vec{r}') dA(\vec{r}')$$

$$\Phi_e(\vec{r}) = j \frac{k_0}{z_0} \int_{\Sigma} G_0(\vec{r}, \vec{r}') \nabla_{\Sigma} \cdot \vec{K}(\vec{r}') dA(\vec{r}')$$

and

$$\Phi_m(\vec{r}) = j \frac{1}{z_0 k_0} \int_{\Sigma} G_0(\vec{r}, \vec{r}') \nabla_{\Sigma} \cdot \vec{M}(\vec{r}') dA(\vec{r}')$$

complete the set of equations, whereas ∇_{Σ} is the tangential NABLA operator and G_0 is the GREENS function. Solving this equation system e.g. the boundary element method can be used, which was shown in [1] and [6]. In [6] also an approach to use only magnetic near-field components for the far-field calculation were examined. For the results within this publication, electric and magnetic fields are used.

Near-Field Scanning Application

Basically, near-field scanning results are evaluated with respect to the corresponding location at the DUT to find any issue related to EMC, functionality or security. The following two examples will show different purposes to use NFS results.

Solving EMC an issue

One of the main reasons for using electro-magnetic near-field scanning is to detect EMC problems. These can be unexpected electrical or magnetic hotspots caused, for example, by unwanted antennas, unsuitable component selection and design or poor routing and coupling on the PCB. Especially for DC-DC converters with high currents and voltages, the output filter must be designed very carefully, as even relatively small ripples can cause conducted or radiated EMC problems that lead to failing the compliance tests.

The following example shows such an output filter of a DC-DC converter for an on-board car charger. The converter operates at a frequency of several tens of kHz and the first version had problems with conducted interference. Figure 3 shows the near-field results of the normal electric field E_z . On the right side, the output filter (between $x = 500$ and 600 mm) ends at about $x = 500$ mm. To the left of $x = 500$ mm, however, there is still a considerable amount of alternating fields, which should ideally be filtered down to direct current. From the near-

field scan, it is possible to deduce where the filter is not working properly.

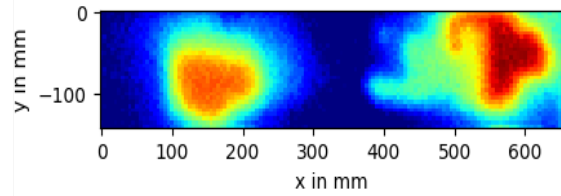


Figure 3. Measurement of the DC-DC converter with EMC issue

Utilizing these results, the filter can be redesigned and improved based on near-field measurements instead of using trial-and-error approaches to improve the EMC behavior. The result of the new version is shown in Figure 4. There, the electric field is much smaller at $x = 400$ to 500 mm. The EMC test carried out was also subsequently passed.

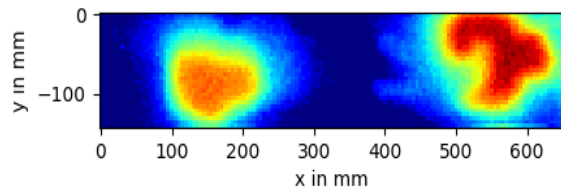


Figure 4. Measurement of the DC-DC converter after redesign

Functional Analysis

The second example shows a 2.4 GHz antenna test board, which is shown in Figure 5. This is one of the standard antennas for IoT applications with WiFi or Bluetooth connectivity. The PCB design is imported into the 3D field simulation tool CST Studio Suite. On the one hand, it is simulated and the H-field at 2.4 GHz and at a distance of 2 mm is examined. On the other hand, the H-field is measured the same points using the NFS3000 near-field scanner. For validation purposes and to check the functionality of the antenna, simulation and measurement are compared with each other.



Figure 5. 2.4 GHz antenna test board

The results are shown in Figure 6. It can be seen that both results are looking quite similar, and therefore measurement and simulation can be considered equal. In numbers it is a root mean square error of 4% over the measured space.

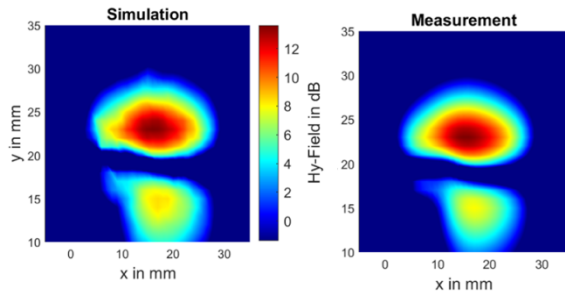


Figure 6. Measurement and simulation of antenna test board

Combination with Simulations

Using the Huygens-principle described before, near-field scanning results can be used within electromagnetic field simulation tools. For this purpose, CST Studio Suite will be used. This hybrid approach combines measurement results with field simulations to give an added-value to the near-field scanning technique. It can be used for different purposes, which will be shown in the following examples.

Device-under-Test

The Universal Spherical Dipole Source (USDS) from Applied Electromagnetic Technology is used as a test specimen to validate the broadband far-field transformation. The USDS, a spherical dipole antenna with a diameter of 10 cm, emits dipole-shaped fields from 10 MHz to 16 GHz. It has an internal comb generator with selectable frequencies (10, 64, 100 and 133 MHz) and is powered by a rechargeable battery to avoid cable interference. The USDS is primarily used for EMC-related characterization and shielding effectiveness testing.

The USDS is placed on Styrodur panels to minimize electromagnetic interference from the metal base plate of the NFS3000. The Styrodur cut-outs have a height of 15 cm to reduce the influence of the base plate of the near-field scanner. The comb frequency is set to 10 MHz. Measurements are taken on a Huygens-box around the USDS, with a minimum distance of 1 cm to the sphere. The cubic measurement box with an edge length of 12 cm has points at a grid distance of 1 cm, a total of 169 points per field component per side. Only the tangential field components are measured for the far-field transformation. To measure the bottom-side the sphere is mirrored to obtain a six-sided measurement. The spectrum is measured from 50 MHz to 1 GHz.

Near-Field to Far-Field Extrapolation

The simplest application of a near-field source is the simulation of the far-field. For antennas, this provides information about the radiation behavior such as directivity and total radiated

power. In EMC assessment, the far-field simulation helps to estimate EMC conformity for measurements in an anechoic chamber.

The measurement results of the Huygens-box are presented below. Figure 7 shows the magnetic field strength and Figure 8 shows the electric field strength, both at 300 MHz. The distance between the USDS and the base plate is 15 cm for these measurements. The results of the magnetic field are quite comparable with the simulation results shown in Figure 7. The results of the tangential electric field are in line with the expectations for a dipole antenna. In addition, the near-field data on the box are symmetrical to the axis of rotation of the USDS.

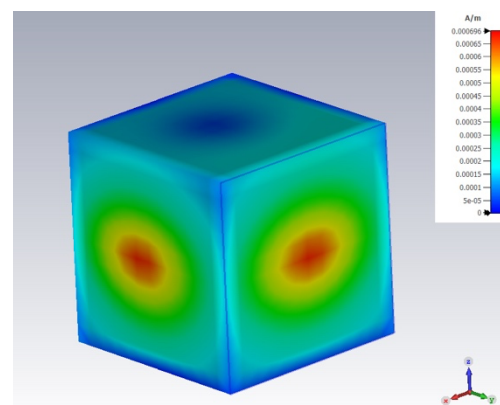


Figure 7. Measurement of the tangential magnetic field strength on the Huygens-Box at 300 MHz

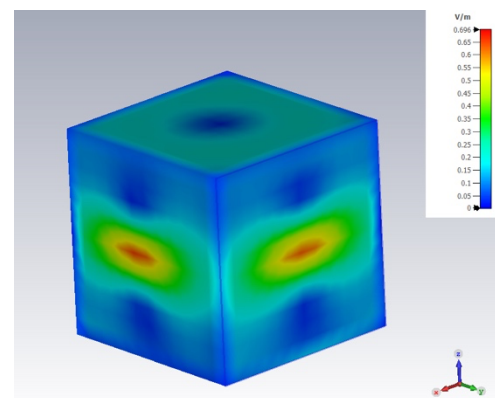


Figure 8. Measurement of the tangential electric field strength on the Huygens-Box at 300 MHz

The near-field data is now transformed into the far-field at a distance of 1 meter. The theoretical principles have already been discussed. A special solver developed in [6] deals with the equations for NFS Huygens-box measurements. For the following analysis, the CST integral solver (with the boundary element method) is used due to its advanced post-processing capabilities. The Huygens-box measurements are imported and simulated for

each frequency. A far-field monitor at 1 meter distance is defined to obtain the E-field in dB($\mu\text{V}/\text{m}$), which later facilitates the comparison with measurements in an anechoic chamber.

Figure 9 compares the transformation results with measurements in an anechoic chamber. The figure shows that both sets of results agree well in terms of data quality and quantity. The overall pattern of the transformation closely follows the measurement peaks, and the local minima at 230 MHz and 410 MHz are accurately reproduced. The maximum error occurs at 870 MHz, with a difference of 5 dB, while the mean error is around 2 dB. This evaluation shows that the far-field transformation from near-field scan data for highly radiating devices is very effective and comparable to far-field measurements.

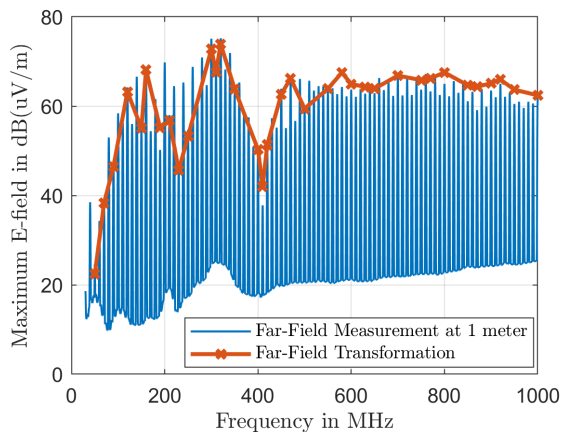


Figure 9. Comparison of far-field measurement in an anechoic chamber with the near-field to far-field transformation

Radiation Inside a Car

In addition to simply using the near-field source to predict far-field radiation, it can also be used in 3D field simulations. The source can be imported and placed anywhere in a given environment, e.g. in cars, enclosures, halls and so on. In the last two examples, the radiation of the USDS is shown inside and outside a simplified model of a car.

The car model is made of only three materials. The chassis is made of a perfect electrical conductor (PEC). The main internal parts are made of plastic and the wheels are made of rubber. It is sufficient at this point to demonstrate the basic concept of using near-field sources. For real problems, of course, a more detailed model of the vehicle would be required to achieve the most accurate results.

For the first demonstration, the near-field source is placed in the vehicle near the entertainment system (see Figure 10). This may

represent an electromagnetic interferer causing EMI problems inside the vehicle. The evaluation frequency for this and the next case is $f = 500$ MHz. A representative result of the simulation is shown in Figure 11. It shows the electric field on a cross-section of the vehicle. The source with the highest field strength is clearly visible. Most of the radiation goes beyond the windshield or remains in the passenger compartment, but a considerable proportion of the electric field is also present at the headlights and rear lights.

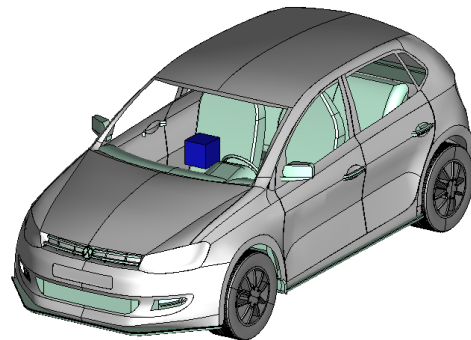


Figure 10. Simplified car model with near-field source inside

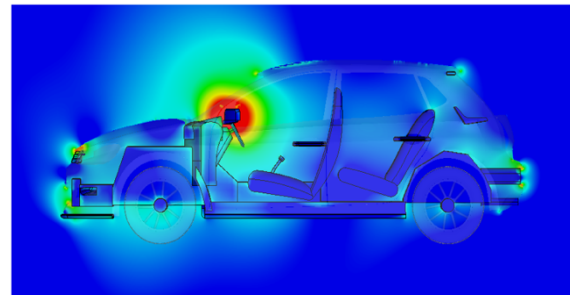


Figure 11. Simulation of radiation inside the car

The conclusion for this case is that if a component with EMC problems or even intended radiation is placed inside the vehicle, it can also interfere with parts further away. The simulation can help to replace the component, place or improve the shielding of the component itself or other sensitive parts, or even improve the positioning of these sensitive components.

Radiation Outside a Car

In addition to EMI cases, intended radiation is also of great importance in the automotive sector. Communication and radar sensors must function well and reliably to enable a safer driving experience and future autonomous driving. By placing the near-field source, e.g. at the front or on the roof of the vehicle, the radiation into the environment can be evaluated to optimize the positioning and function of the subsystems.

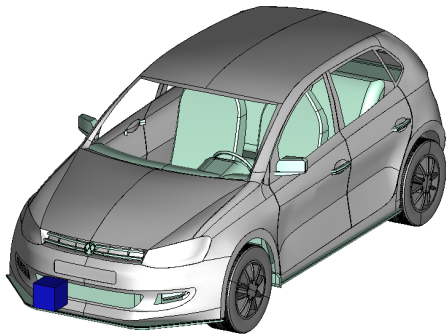


Figure 12. Simplified car model with near-field source outside

In Figure 12, the near-field source is positioned at the front of the vehicle and represents a type of sensor system that is intended to radiate. Here too, the evaluation frequency is $f = 500$ MHz. The results for this simulation are shown in Figure 13. Here, too, the cross-section of the vehicle and the corresponding electric field at 500 MHz are shown. The radiation of the device placed on the car can be assessed on the basis of the field distribution. Reaction effects could improve or worsen the desired directivity, which can be compared with the directivity without a car, for example.

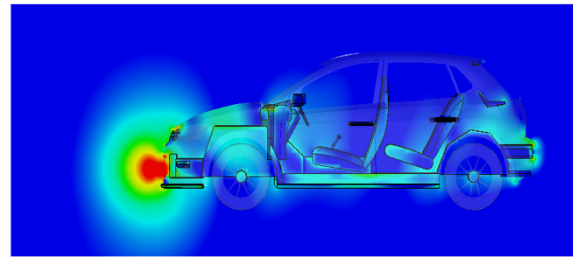


Figure 13 Simulation of radiation outside the car

Conclusion

To conclude, this paper emphasizes the benefits of near-field scanning in automotive applications by presenting the results of near-field scanning for different DUTs and demonstrating their benefits for different use cases. The effectiveness of addressing EMC issues and performing functional analysis is demonstrated. Using the Huygens principle, a near-field scanner captures near-field sources that can be seamlessly integrated into field simulation tools. This hybrid methodology significantly expands the field of application and the added value of this technique. Three different use cases integrating measurement and simulation were presented: a basic extrapolation from near-field to far-field and two scenarios illustrating radiation effects both inside and outside a vehicle.

References

- [1] M. Ramdani, E. Sicard, A. Boyer, S. Ben Dhia, J. J. Whalen, T. H. Hubing, et al., "The electromagnetic compatibility of integrated circuits - Past present and future", IEEE Trans. Electromagn. Compat., vol. 51, no. 1, pp. 78-100, Feb. 2009.
- [2] B. Deutschmann, H. Pitsch and G. Langer, "Near-field measurements to predict the electromagnetic emission of integrated circuits", 5th Int. Workshop Electromagn. Compat. Integr. Circuits, 2005, Nov
- [3] C. A. Balanis, Advanced Engineering Electromagnetics, New York: John Wiley & Sons, Inc., 1989, chapter 7
- [4] D. Schroeder, C. Hedayat, F. Goelden and H. Kuhn, "Broadband Far-Field Estimation of a Spherical Dipole Using Near-Field Scanning Data Up to 1 GHz," 2023 Smart Systems Integration Conference
- [5] M. Sørensen, I. Bonev, O. Franek, G. Petersen and H. Ebert, "How to handle a Huygens' box inside an enclosure", 2013 IEEE International Symposium on Electromagnetic Compatibility, 2013
- [6] C. Marschalt et al., "Far-field Calculation from magnetic Huygens-box Data using the Boundary Element Method," 2022 Smart Systems Integration (SSI), 2022
- [7] S. Lange et al., "Investigation of the Surface Equivalence Principle on a Metal Surface for a Near-Field to Far-Field Transformation by the NFS3000," 2020 EMC EUROPE, Italy, 2020

Research into equivalent Bidirectional Telemetry

Francisco M. Fernandez Casuso¹
¹ Airbus DS, Getafe, Spain,
 francisco.m.fernandez@airbus.com

Abstract:

The purpose of this paper is to illustrate the efforts made by the Flight Test Centre in Spain towards achieving robust, efficient, and high-quality bidirectional telemetry: from exploring potential uses to integrating it into ground stations and aircraft, including testing and searching for technologies.

The approach involves two main strategies. Firstly, internally redefining the telemetry paradigm to identify new applications benefiting from the technology's advantages. Secondly, exploring the market for suppliers to meet the specific needs of the Flight Test Center.

The goal is to develop bidirectional telemetry with equal capabilities in range, bandwidth, and latency, while also leveraging new features such as mesh networking or beyond line-of-sight (BLOS) capabilities. This requires implementing a new system, integrating high-gain antennas with dipoles, and utilizing various transmitter/receiver technologies like beamforming and MIMO.

Testing and integration of this system are already underway at the Flight Test Centre in Spain, with different configurations and providers being evaluated to gain confidence and measure capabilities.

The paper aims to showcase initial steps taken in this new technology, presenting theoretical and practical results achieved so far and their impact on telemetry practices. It also discusses challenges encountered and expected in the future, with the outcomes determining potential changes in test procedures.

Key words: Telemetry, Bidirectional, RF Design, Receivers, Antennas

1. Introduction

Aeronautical telemetry is one of the mainstays of flight testing, and has been for a long time. Since the 1950s, telemetry has been used to monitor from the ground what is happening in the aircraft. This saves a lot of costs. It is also a safety feature: it reduces the pilot's workload and helps to monitor a multitude of parameters that would otherwise be difficult to monitor (many eyes see more than two).

The future promises to be different. Technology has evolved a lot in recent years, but telemetry has hardly evolved at all, especially from the transmission point of view. In this technological project we address one of the many solutions we can find for the telemetry of the future. We will show the needs we see in the future and justify them. In addition, we will tell the evolution of the technology project we are leading at Airbus DS to address those needs, we will talk about the technologies and need and the tests we are doing.

This is a project with a long history in which we are just beginning to take the first steps. In this paper we will explain the basis of the project, how it came about and the first steps we are taking: needs and technologies that cover it, first tests and results, changes in mentality when it comes to understanding what the system will be like in the future. We will also talk about the next steps, what we want to do and how we want to do them and, of course, what we expect from them.

2. Context and Justification

Recently, the demand for telemetry resources has increased. More and more parameters are requested at higher rates, more and better-quality videos and even more prototypes simultaneously.

The evolution of telemetry transforms the way testing is performed and analysed. This evolution is a competitive advantage that can simplify operations, reduce costs and make testing safer and more efficient. But it also means big and profound changes. Changes in the way aircraft instrumentation is done and

changes in how to approach the aircraft/ground radio link.

The Flight Test group has been identifying different needs for improving telemetry for a long time. Although until now these needs may not have been sufficiently important to tackle a technological project like the current one, they have always been present. But the future is coming. And new programmes and new needs appear. It is no longer something desirable, it is a 'necessity'. The platforms of the future will need telemetry with capabilities that are not only far superior to those of today in terms of bandwidth or quality, but also very different. New technologies will have to be integrated with our ecosystem. This is a paradigm shift in the way we approach telemetry.

But let's take a step back. This coming future is starting to be built today. We have to be ready for it and we cannot start tomorrow. That's why we proposed this technology project to develop now the technology we will need tomorrow.

To support this technology, the Flight Test group consulted with a wide range of teams that use or will use telemetry. For them, we developed 'Voice of the Customer' sessions, in which we gathered all kinds of requirements. It was a very interesting exercise in which we unleashed the imagination of the users and found new ways to use telemetry.

Once we are clear about the potential needs, i.e., how this technology could be used, we need to see how to implement it. To do this, in parallel with the VoC exercise, we started to analyse the technical changes needed both in the aircraft and on the ground for this technology to be able to cover these needs. We studied the market and the different technical solutions and started with the different testing stages to validate the solution.

This paper aims to show the first steps we are taking in this technological project, as well as the conclusions obtained so far. We will also present the next steps we plan to take.

3. Voice of Customers

Voice of Customer is the example that technology cannot be ahead of users. Because it is not interesting to develop a new technology or way of working if it is not something that will later be used.

Once we had identified the future need and while we were looking at possible solutions, it was necessary to study with the end users the future uses that the different solutions could have. One must consider that what may be an excellent idea for one system or user may not

be necessary for another, and vice versa. The paradigm shift introduced by the use of bidirectional telemetry necessitates a change in the current mode of operation. Consequently, it is imperative that the principal users of telemetry—whether direct, potential, or future—engage in this process to ensure that the forthcoming technological solution is widely adopted.

We therefore consulted all the departments involved. Their responses, which varied widely, often included innovative ideas that enhanced the project and confirmed its necessity.

Some of the most notable suggestions included:

- Regarding instrumentation: being able to replay tests during execution, adjust data rates depending on the point to be tested or cease transmission of certain data to allocate BW for more critical data at that point and thus be more efficient.
- The possibility of stimulating aircraft systems from ground (flutter, dynamic change of control laws)
- Reducing the workload of the pilot or FTE/FTC by direct intervention of non-critical systems. This point is particularly important as it directly impacts flight safety.
- Implementing feedback systems to monitor changes in the aircraft made via other links (e.g. Link16, satcom)
- Integration of tests with simulators, rigs, etc.

In conclusion, the new solutions would enable new types of tests that have not been considered so far, which would be more time-efficient, cost-effective and safer.

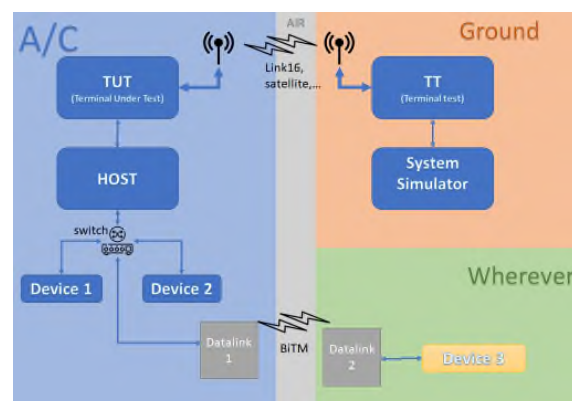


Figure 1. VoC example

4. Description of the project

For the last 50 years telemetry has been mainly an aircraft transmitting and a ground station listening; and its way of transmitting the

information has not varied too much, it has always been based on a coded digital signal passing through a pre-equalization filter to become an adapted signal that a modulator (FM, SOQPSK or similar) modulated to transmit, resulting, at the end, in an efficiency of 0.5 Bit/s/Hz [1]. Although there have also been uplink systems, these have always been asymmetric, with very narrow bandwidths and usually using a different channel for uplink (V/UHF radio, satellite, etc.).

With this project at Airbus DS we are looking for a new way to do telemetry, that has new capabilities (uplink/downlink), that is efficient in terms of spectrum and that allows to achieve a new way to do flight tests. This new telemetry will have to be:

- Bidirectional, the new technology must facilitate ground-to-aircraft and aircraft-to-ground connections and to prioritize between 'must carry' and 'sacrificable' traffic.
- To use MIMO technology that allows different data streams to be managed by different antenna arrays.
- Equalization, signal adapting to changes in the channel
- Diversity, capability to send and receive from different paths
- Beamforming, enabling the signal to better adapt to different aircraft situations and contexts.
- Mesh capability, enabling a telemetry network in its broadest sense, a telemetry network in the air connected to the ground.
- Connection, the technology must be IP-based and capable of managing TCP and UDP connections, with special attention to multicast traffic

But we also have to keep in mind that we do not want to lose capabilities, therefore our project must look for a telemetry that can maintain certain imposed conditions.

- Everything must operate in C-band (5091 - 5250MHz).
- We have to keep reaching long distances or as long as possible. In our case, the limit is at LoS. If this is not achievable, perhaps the solution is to rethink how to cover an area.
- The latency between data recording and data display should be similar to today, or at least should not increase significantly.

Within the broad scope of these limitations, and considering additional constraints (time, resources, budget), we have defined and limited our project to the following:

- The objective is to establish a radio link at a distance of >150 km with LoS and a 2x2 MIMO system.
- The aircraft antenna is limited to two dipoles and also due to aircraft issues the maximum power to be transmitted should be around 20W per antenna.
- The modulation scheme could be variable or fixed, in order to be able to test the behavior of the technology.
- With these premises, we calculated the link budget [2] and the ground antenna has to be a high gain parabolic antenna (>30dB) and 360° continuous rotation.
- The latency of the system should be as low as possible, but always less than 250ms. If this is not the case, needs to be re-evaluated.

In the market we have found different datalinks and antennas that could potentially meet the needs. It has not been easy because although many of them meet the requirements described above, with some of them we have encountered the problem that not all of them work exactly in terms of power and frequency we were looking for, as well as other configuration parameters that did not fit our needs.

In the end, we found a combination of equipment and antennas that met all the needs we required to be able to realize the project. It does not have to be the final technology to be implemented in the future, but it will be the technology we start testing with.

5. Stages of the project

From a testing point of view, we are approaching the project as different testing stages. Initially, as we have already explained, we have done basic research, technological research as well as applied research with proofs of concept. This would correspond to initial TLR1-TLR3 [3] stages of technological maturity. The following stages can be classified as follows:

- Laboratory testing: integration into the ground network and technology awareness. This would conform to a TLR4 level of maturity.
- Proximity testing: distances less than 1km with dipole antennas This would meet TLR4 level of maturity.

- Remote testing. This would conform to a TLR5 level of maturity.
- Testing on the move. This would conform to a TLR6 level of maturity.

At the end of each test we had a decision gate that gives us guidance on the maturity status of the project. Each of these stages and the conclusions are explained in more detail below.

The lab tests were mainly focused on the integration of the new technology into the ground station network. The way of working in a network implies a radical change in the current network configuration and several tests were necessary until the system was mature and perfectly integrated in the station. These tests served to familiarize with the environment and get to know the technology before moving on to the next step. There were traffic configuration problems that implied structural changes in the network configuration. At this stage it was concluded that the system was successfully integrated with the ground station network and that the system was fully integrable and fully operational.

The next step was to go outdoors and we started testing in a close environment (1km). Even without focusing in terms of power, we started to perform static tests in multipath environments, with very good results. In NLoS areas the system capabilities were powerful and beamforming substantially improved the results. Stress tests of the system were performed but still without parabolic antenna, using 1 or 2 streams and going deeper into the different options offered by the system interface. The conclusion of this stage of the project was satisfactory and promising and it was decided to continue with the next stage.

The next stage consisted of remote tests with two main objectives: to validate the link budget and to evaluate the performance of the system, all at a greater distance: between 3 and 65 km. Transmitting in a system that tried to simulate as well as possible an aerial environment, that is, with conditions of few reflections, clear environment at a considerable distance, using amplifiers and antennas, we intended to perform tests to verify the mathematical model of link budget that we were handling. The tests consisted of estimating how realistic the theoretical link budget is. To do this we have to play with the 'safety margin' estimates. This parameter is the safety margin needed to make a theoretical link budget and compare it with a real one. In our case, we estimate losses of maximum 10dB and minimum 5dB. Taking into account that we are transmitting from the ground, we estimate that the results obtained

here would be in any case, the worst case of when we would go out to fly. Presented below are several figures illustrating different scenarios:

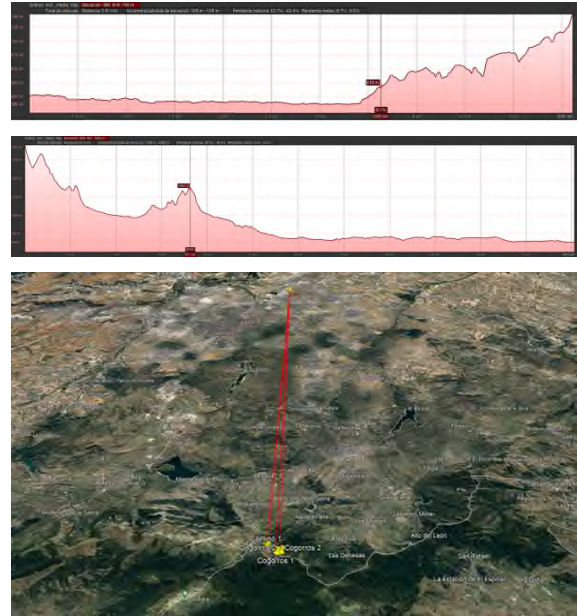


Figure 2. Long range scenarios

These measurements have always been done statically. In the configuration, different bandwidths, data rates and distances have been tested and as a test, UDP multicast and TCP connections have been made to fill the channel as theoretically fixed. Included in these connections there are audio, video, remote desktop connections and latency tests.

Although we have a large number of samples done, this figure serves as a representative result:

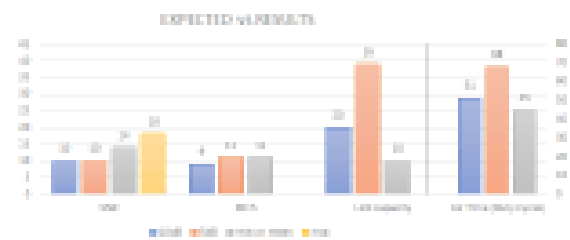


Figure 3. Expected vs result

It can be seen that the measured SNR is better than the estimated SNR in both cases, the modulation scheme is slightly better and the channel utilization time (Air Time) is slightly lower than expected.

Regarding latency, we were able to evaluate that, in general and as long as the channel is not saturated, which logically implies packet loss or excessive delay, the delay was low and acceptable, according to expectations.

*This information is of origin Airbus Defense and Space/Spain and does not contain any export controlled information
Airbus Amber releasable to ETTC
ETTC 2024– European Test & Telemetry Conference*

Therefore, the conclusion of this stage of the project was satisfactory and we considered the theoretical system to be valid, considering the real results to be slightly better than the theoretical ones.

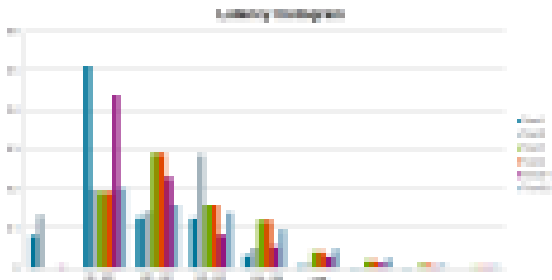


Figure 4. Latency

The next stage of testing is currently under development. In this stage, the system will be evaluated in a more realistic environment, a dynamic mobile environment and in flight. Concepts such as direct link stability or real link balance will be fine-tuned. We will study how it affects the shape of the aircraft, the shadows it can make and the ground-to-air pointing. We will also see in a realistic way how the traffic behaves. In a real flight we expect outages or micro-outages, unexpected link losses, misalignment and a multitude of untested scenarios. In this environment we expect to test what happens to TCP or UDP connections in these cases, how nodes behave and how connections are recovered. We also of course expect to measure latencies and see how the link budget model performs in a real air/ground environment. All this will be key to verify if the stability requirements we are looking for are met or not.

6. Future

In the immediate future we have to mature the current state of the project, we must ensure this state of maturity and finally test the current technology in a completely real environment. But the project goes further and as said at the beginning we seek to achieve an equivalent bidirectional telemetry. To this end, once the necessary maturity level has been reached in a real environment with two nodes, the project intends to continue advancing in different phases.

Next steps:

- Deepen the aircraft configuration
- Test the system with a remote centre
- Test the system with 2 aircraft (nodes) on local
- Test the system with 2 aircraft in a remote hub (or 2)

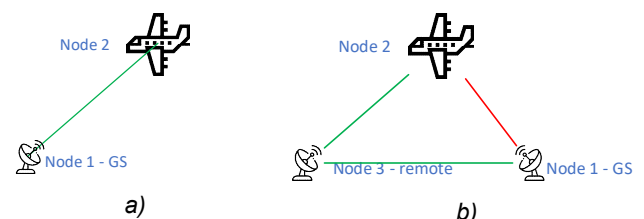
- Test new technology

From a 2-node point of view, we have to integrate the system on a large aircraft and see how the technology performs. Integrating the system on the aircraft will not be as trivial as it was not on the ground network. Recall that we left behind the concept of 2 separate networks where telemetry worked with a 'data extractor' from the aircraft and a 'data injector' on the ground. Of course, with the lessons learned from ground integration, on aircraft it should be less complicated, but the aircraft architecture is very rigid and other problems will arise.

From a testing point of view there is still a lot to do. So far, we have tested a 2-node network [Figure 5, image a)], which is a first step to get to know and learn how to handle the technology, but it is not representative of what we want to do. To 'replace' our telemetry with the concept of an aircraft flying over a large area where different antennas are following it on its path, we have to confirm that this overlapping area is done correctly and that the overlapping areas are equivalent and compatible in range with the current ones. If this is not the case, it may be necessary to consider a larger number of antennas to cover the same area.

On the other hand, a next step following on from the above, would be to do this same concept but with several nodes, flying first locally (2 ground nodes, one aircraft node [Figure 5, image b)]) and then remotely or remotely/locally (2 aircraft nodes, one ground node; and 2 aircraft nodes and 2 ground node [Figure 5, image c) and d))). This would increase the complexity of the network to at least 4 nodes and would allow testing the system at what for us would be a high level in complexity, understanding that adding more nodes would already be smaller hops.

Each step of these tests is a leap in complexity and will involve a multitude of tests and keeping an eye on different parameters. From seeing how the different types of connections behave, measuring latencies, bandwidths achieved, etc.



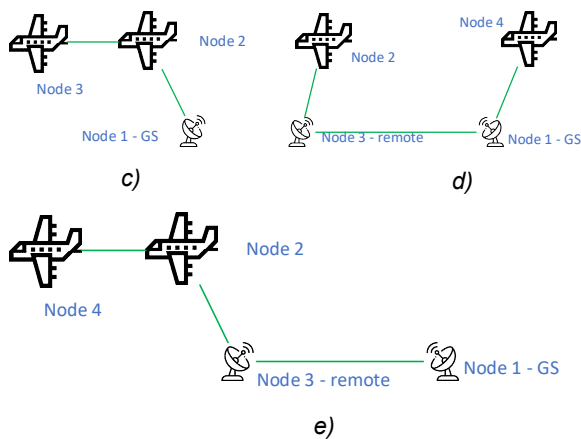


Figure 5. Different kind of scenarios: a) two nodes, currently in use; b) one aircraft with two ground nodes; c) two aircraft one node; d) and e) two aircraft with two ground nodes

But the project does not end here. The market has different datalink providers. We are currently betting on one of them and the results are promising, but technology is advancing very fast. Once the system has matured, changing supplier is neither so expensive nor so complex. Using the test system presented in this paper, testing a second radio system provided by another supplier would be as 'simple' as swapping one for another and repeating the tests. The most complex part is setting up this test bed for the first time. Once built, it could be used as a test bed for testing any similar technology with little change.

7. Conclusions

In this paper we have extensively presented the technological project that aims to study the capabilities of a future new telemetry with radically different capabilities to the current ones. We have identified the needs that are demanded by future programmes, we have presented the solution found and we have identified the uses that could be made of this technology from the different systems. Then we have explained the project and its different stages of maturity so far. Finally, we looked at the steps we still have to take.

Of course, this promising technology has its drawbacks. It implies such a radical change in the way telemetry is done that current systems

will not work. New installations would have to be made, or old ones would have to be modified and thus made incompatible with the old system. This will, of course, involve initial investments. This is a hot point when it comes to implementing the technology in the future.

In addition, until now, telemetry under the umbrella of the standard allowed for vendor-independence, with different telemetry datalink providers being compatible with each other. Currently, the providers of this type of datalink have proprietary solutions that are not compatible with other providers, which means that they are dependent only on this new provider. This would be a problem for the more distant future: the adoption of this technology requires a long-term projection of the supplier to keep the system compatible with new versions.

In summary, like any new technology, it has its advantages and disadvantages. So far, the different maturity tests have been passed one by one and we will work to keep it that way until it is fully implemented. It is a very promising technology and will be a paradigm shift in the way we do telemetry, in the way we work with it. It will bring new capabilities to testing, which can be done better and safer, saving a lot of costs both in testing and in direct costs, as this technology promises to be significantly cheaper than its predecessor.

Much remains to be done. We will be ready for them.

References

List and number all bibliographical references at the end of the paper. When referenced within the text, enclose the citation number in square brackets, i.e. [1]

- [1] <https://www.irig106.org/>
- [2] José María Hernando Rábanos, *Transmisión por radio*, ed *Universitaria Ramón Areces*
- [3] "Technology Readiness Level Definitions": https://www.nasa.gov/pdf/458490main_TRL_Definitions.pdf

Comparing architectures for bi-directional telemetry ground stations

S. BONNART¹, P. KLAEYLE²

¹ Safran Data Systems, Aerodrome Villemarie 33260 La-Teste-de-Buch, FRANCE,

² Safran Data Systems, 5, esplanade Anton Philips 14460 Colombelles, FRANCE
sebastien.bonnart@safrangroup.com

Abstract:

Over the past decades, data recorded onboard test aircrafts has expanded much faster than downlink capacity. Given the bandwidth and power limitations, a bi-directional link appears as the best way to ensure delivery of the largest amount of relevant data per test by leveraging in-flight reconfiguration capabilities. Moreover, an uplink improves communication reliability when offering on-demand data retransmission during the flight.

Transmission capability comes with a set of constraints for the ground station that depend on communication protocols and other characteristics of the test case. In this paper, we address these challenges and compare the trade-offs and performance of several ground stations architectures using state-of-the-art components and technologies in order to achieve bi-directional communication.

Key words: RF Design, Receivers, Antennas, Ground Stations, Bi-directional

Introduction

Bidirectional telemetry systems are a developing trend in flight test telemetry as they come as a solution for many new functionalities:

- Retransmit important data: makes tests more reliable
- Reconfigure in flight: makes testing more flexible depending on test results and environmental conditions. Also allows transmitting the most important data for each step of the test and to combine more tests in a single flight
- Send data from the ground to recalibrate the on-board inertial measurement unit in the case of a launcher stage recovery
- Command the transmission of on-board recorded data. One example is for a launch vehicle to record massive videos during the launch. Beyond a certain distance, it is not possible to recover the data in real time as the link budget does not provide enough bandwidth, however the video can be stored on-board, and transmitted during the first stage descent.
- Provide another voice channel, in addition to VHF link for redundancy

Bi-directional links between the test article and the ground is a vast topic that encompasses a whole stack of functions and protocols. In this paper, we focus on the physical layer of communication [1].

At the Radio Frequency (RF) level, the biggest challenge brought by bi-directional telemetry is the Receive (RX) – Transmit (TX) isolation: preventing the High Power Amplifier (HPA) output to damage the low Noise Amplifier (LNA), especially if using the same frequency band. Fortunately, the throughput need in telemetry is non-symmetrical: we want to downlink as much data as possible but only need to send seldom commands to the aircraft.

In order to propose and study bi-directional architectures, we first analyze the Inter-Range instrumentation Group (IRIG) 106 standard, before proposing ground station architectures that answer to various potential use cases.

IRIG 106 Telemetry Network Standard (TmNS)

IRIG 106 [2] is the comprehensive telemetry standard developed in the United States of America by the Range Commanders Council and sponsored by the International Foundation for Telemetry.

IRIG106 describes a bi-directional functionality as the Telemetry Network Standard in chapters 21,22, 25, 26, 27 and 28.

The prescribed modulation are Feher Quadrature Phase Shift Keying (FQPSK) or Shaped-Offset QPSK (SOQPSK) for high data rate and Pulse Code Modulation/Frequency Modulation for low data rates. Communication is in C-band, within 0-20MHz carriers at frequencies between 4900 and 4922MHz. Access sharing of the communication medium is Time Division Multiple Access (TDMA). Effective Isotropic Radiated Power (EIRP) of all transmitters is limited to 25W.

IRIG's standard provides a very powerful structure in order to build a reliable network between aircrafts and the ground, allowing air-to-air communications and many advanced functions [3]. Unfortunately, this ambitious architecture also comes with challenges:

- Identical 25W EIRP limitation for on-board and ground imply a symmetric RF communication that does not benefit of having the capacity to use large antennas on the ground while having small ones onboard. For a 1Mbps bidirectional link, the maximum distance for communication with 3dB link margin is about only 6km.

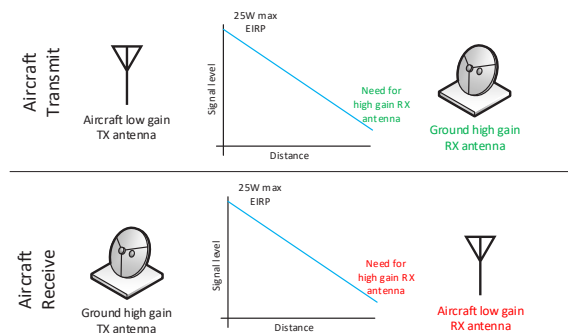


Fig. 1 challenge of EIRP limitation

- TDMA infrastructure represents a very costly investment for the network scheduler both to initially develop and then to equip every range
- TDMA signals are not compatible with current auto-track technologies
- Transmitting and receiving at identical frequencies is a significant challenge on the antenna side for RX-TX isolation
- Only the C band is considered

Fast RX-TX switching system

Including a fast RX-TX switch in the ground station is a classic TDMA way to ensure for good isolation between RX and TX signals.

With today's technology and IRIG's switching speed requirement, the switch should be pin-diode based.

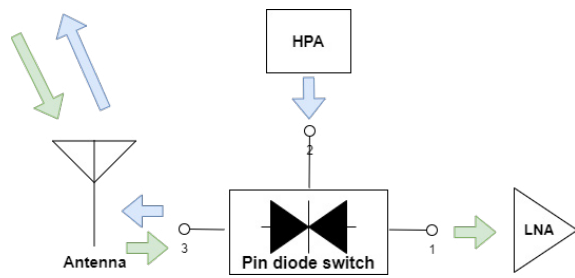


Fig. 2 Fast RX-TX switching

This architecture is compatible with IRIG, and could handle high TX power.

However the switch causes a high loss on the RX channel before LNA which has a strong negative impact (almost 2dB) on the figure of merit (G/T). Moreover, the switching times needs to be precisely controlled by the modem. Finally power dissipation is a significant integration challenge as they require huge heat sinks to sustain the transmit signal.

Circulator based architectures

Another idea to isolate TX power from LNA is to use circulators that route TX signal towards the antenna and RX signals coming from the antenna towards the LNA.

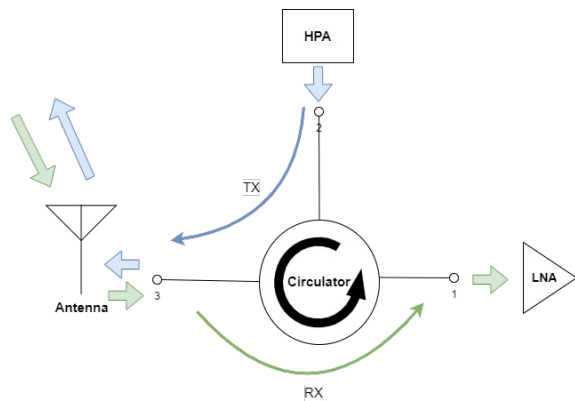


Fig. 3 Ideal circulator architecture

A single circulator architecture allows for a low power transmit only because the TX signal reflected by the feed's Voltage Standing Wave Ratio (VSWR) and the circulator's isolation leaks are quickly saturating the LNA.

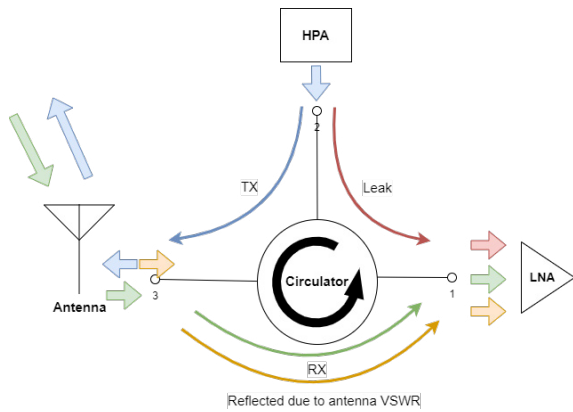


Fig. 4 Real circulator behavior

A partial mitigation is to optimize VSWR of the feed for the TX frequency and to use two circulators in series in an architecture that cancels most of the leak [4].

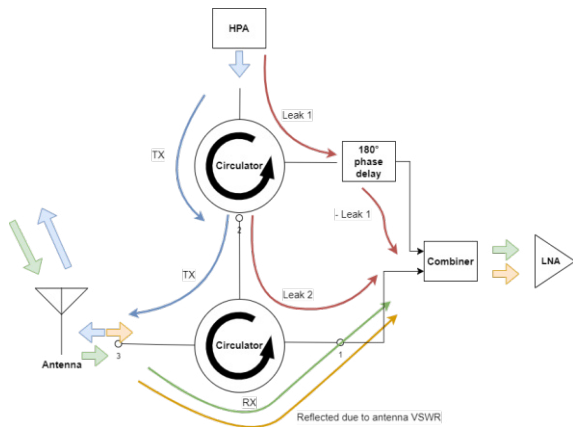


Fig. 5: Dual circulators architecture

This architecture is a compromise between maximum feed input transmit power, flexibility on the transmission frequency and has a G/T degradation of about 0.7dB in L/S-bands and 1.1dB in C-band. This solution is entirely passive which makes it more robust. Integration complexity is higher with more equipment to fit into the feed and requires per-system tuning.

Multiple antenna systems

RX-TX isolation can be achieved by using different antennas, to be installed on the same pedestal or on two distinct pedestals whose pointing direction is slaved. A tradeoff needs to be made between TX antenna gain and HPA power.

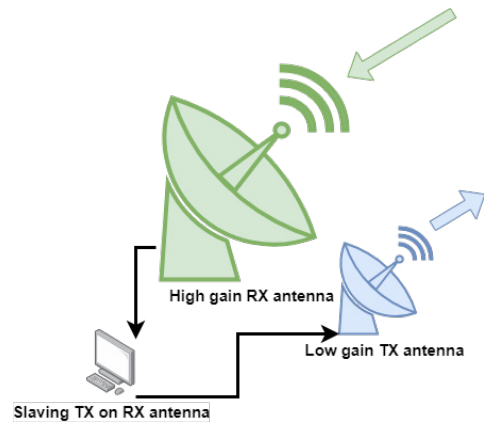


Fig. 6: slaved pedestals

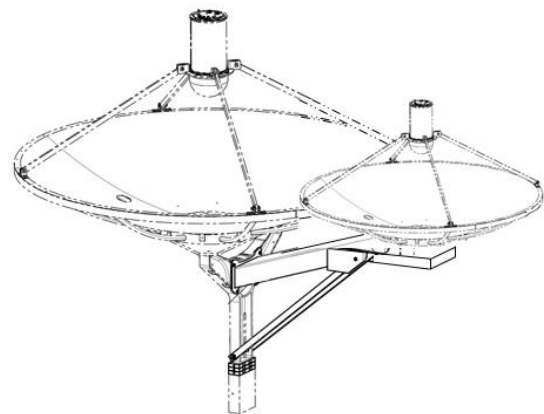


Fig. 7: dual reflectors

This architecture is compatible with IRIG, handles high TX power, is flexible but usually costly. Coupling between RX and TX feeds needs to be analyzed in order to determine spatial separation constraints.

In order to assess how relevant this solution is, we computed multiple uplink budgets in SOQPSK for various antenna sizes and computed the maximum communication distance assuming the target is visible at 5° over the horizon. We supposed that the transmitter power is 20W regardless of the gain of the transmit antenna and the gain of the board antenna is 1dBi.

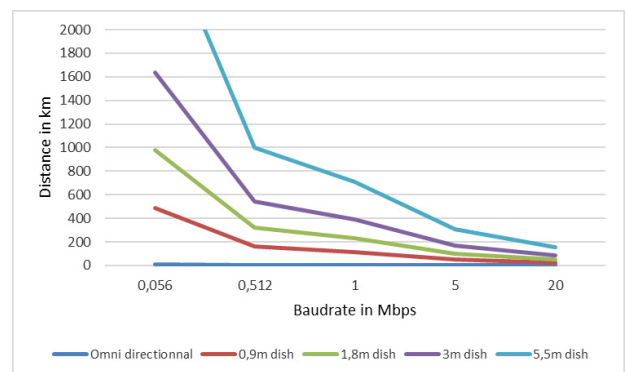


Fig. 8: Maximum communication distance depending on the baud rate

When considering the multiple antennas architecture, ground based omnidirectional antenna can only close the link over distances of a few kilometers or less. However, we notice that even the smaller dishes can provide uplink data rates sufficient for most use cases over long distance as long as the link can be non-symmetric.

Separated RX-TX frequency systems

The easiest way to prevent LNA saturation by TX signal is to use dedicated frequency bands. It is even possible to add switches to the design in order to remotely configure which of the L, S and C band is used to transmit and the two others are receiving.

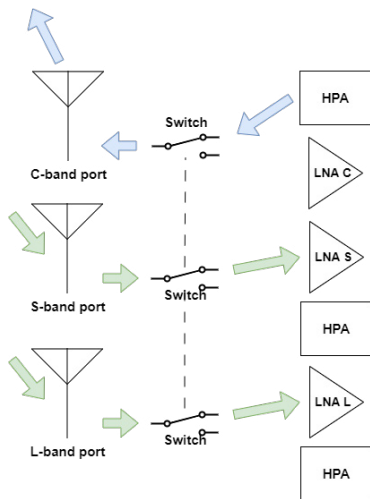


Fig. 9: Band-switching

This architecture has a low G/T degradation (0.4 to 0.5 dB), lowest cost and complexity impact but is not compatible with IRIG's TDMA used both for receive and transmit.

The other way to use frequency separation is to use a diplexer splitting RX and TX signals based on frequency within the same band.

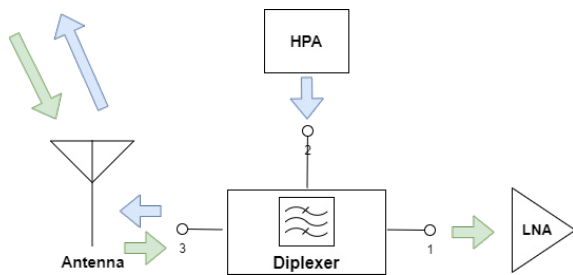


Fig. 10: Diplexer architecture

Separating RX & TX frequencies has G/T and integration difficulty impacts that mainly depend on the maximum power to transmit and the frequency separation between RX and TX signals. For Telemetry, this solution is always custom based on TX & RX frequencies whereas the Consultative Committee for Space

Data Systems has standardized frequencies for space communication [5]. Safran has years of experience implementing diplexers on bidirectional feeds, with a typical 1.1dB loss on S-band G/T when integrating a 200W diplexer allowing transmit between 2.025-2.120GHz and receive between 2.2-2.3GHz.

Comparison of architectures

There is no one size fits all solution to bidirectional telemetry. We proposed four families of architectures in an attempt to cover most of the needs. Here is a comparison of the strength and weaknesses of each solution.

Tab. 1: Architecture's features comparison

	Fast switch	Circulator based	Multiple antennas	Separated frequencies
Max TX power	✓✓✓	-	✓	✓
G/T impact	- -	-	=	-
Flexibility	=	-	✓	- -
Cost effectiveness	-	✓	- -	✓
Suitable for TDMA	=	=	=	only for links in the same direction
Suitable when TX baudrate is lower than RX	-	✓	✓	✓
Single Channel Monopulse compatibility	✗	✓	✓	✓

We assumed in this table that when the downlink baud rate requirement is lower than the uplink one, fast switching will be unaffected (and still poor) while circulator based architectures can be optimized for performance rather than isolation, side antennas can be made smaller and diplexer based architectures can prioritize low insertion loss over isolation.

Focus on a band-switching solution

Safran developed a band-switching feed that allows transmitting up to 20W CW in any of the L, S or C bands while receiving and Single Channel Monopulse (SCM) auto-tracking in the other two. Switching is remotely controlled, and transmission only occurs in one polarization at a time. Reception is simultaneous in both polarizations.

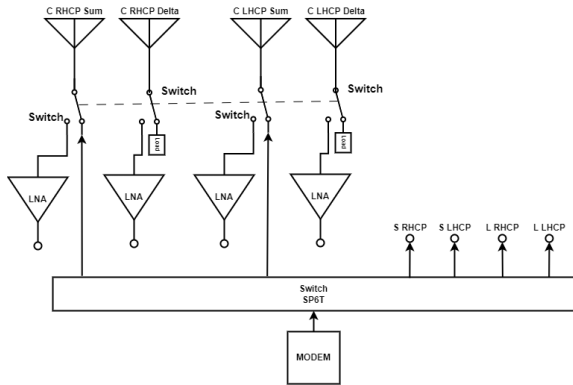


Fig. 11 Triband switching

The same architecture is employed for all 3 bands but for clarity, only the C-band has been fully represented on the diagram.

Tab. 2: Performance measured

	Lower L-band	S-band	C-band
TX losses (dB)	2	2.5	2.8
TX return loss (dB)	< -9.6	< -14.2	< -16
RX return loss (dB)	< -10.6	< -13	< -9.7

The table summarizes key performance of the feed.

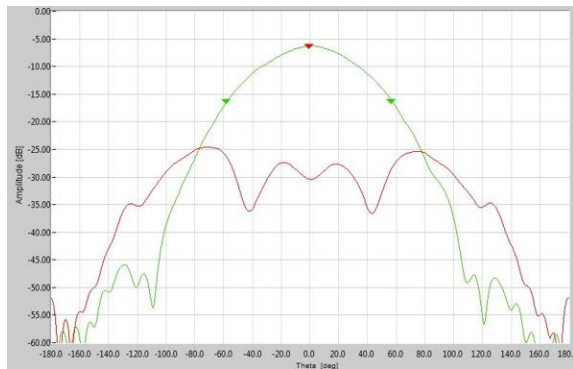


Fig. 12: TX pattern in S-band

In green is the co-polarization and in red the cross-polarization of an anechoic chamber measurement of a triband TX feed. One can see that the pattern is clean and that there is about 23dB between the transmission in the selected polarization and the other one.

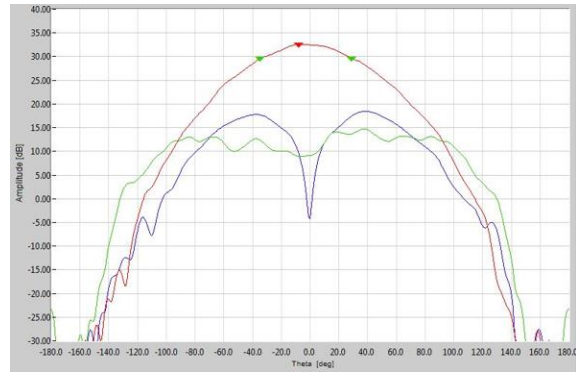


Fig. 13: RX patterns in C-band

In red is the co-polarization sum channel, in blue the delta one and in green the cross-polarization sum of an anechoic chamber measurement of a triband TX feed. This diagram features a clean sum pattern and a deep, well centered null on the delta diagram.

System level performance measured on a 1,8m pedestal delivered to an experimented customer are: G/T of 2dB/K in L-band, 3.3dB/K in S-band and 10.1dB/K in C-band with a 20W transmit capability. These are compliant with the customer's needs to enable bi-directional communication with test articles.

Modem and HPA integration considerations

Flight test pedestals are usually of type Elevation (EL) over Azimuth (AZ) as shown on the following diagram.

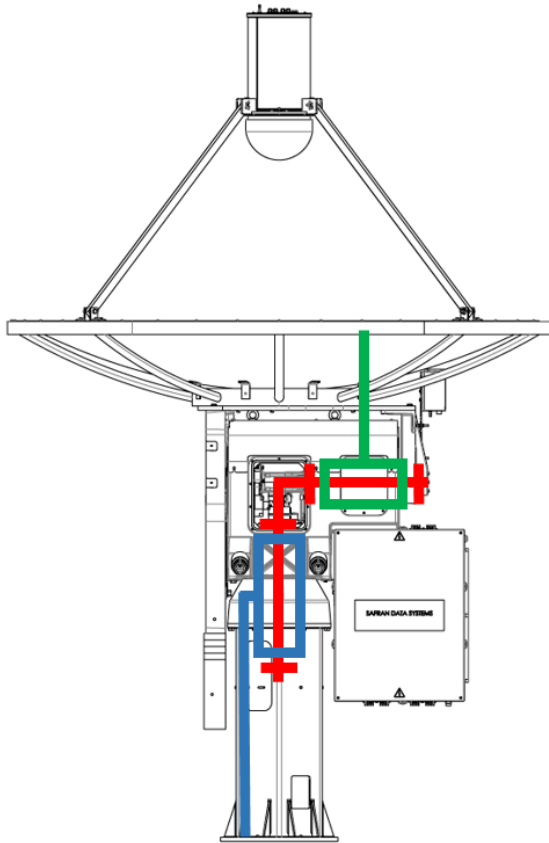


Fig. 14: EL over AZ pedestal joints

Test cases require unlimited AZ motion and therefore a RF rotary joint is installed on the AZ pivot. Rotary joints are much more expensive with increasing number of channels. As a consequence, integrating the HPA and the modem over the AZ axis (blue-red joint on the figure) is a good way to reduce cost. As long as power remains below 50W, signal is transmitted to the feed using cables whose flexibility is suitable to handle the elevation axis range (red-green joint on the figure) of the pedestal. This drives the need for outdoor HPAs as well as small modulators suitable for pedestal integration and adapted for use during antenna motion.

Conclusion

In this paper, we presented the challenges that bi-directional telemetry represent for ground stations and introduced multiple technical solutions. We compared the solutions and presented the performance of a field tested product that offers bi-directional telemetry capabilities.

References

- [1] International Telecommunication Union, Recommendation X.200 : Information technology - Open Systems Interconnection - Basic Reference Model: The basic model, (1994)

- [2] Telemetry Group, DOCUMENT 106-17 TELEMETRY STANDARDS, (2017)
- [3] T. Young, iNET: Impacts to Telemetry Community (2018); <https://www.itea.org/wp-content/uploads/2018/05/Young-Tom.pdf> accessed 16/04/2024
- [4] M.N.A. Tarek, M. Roman, E.A. Alwan, Power Efficient RF Self-Interference Cancellation System for Simultaneous Transmit and Receive, *2021 IEEE International Symposium on Antennas and Propagation and USNC-URSI Radio Science Meeting (APS/URSI)*, 113-114 (2021); doi: 10.1109/APS/URSI47566.2021.9704722.
- [5] CCSDS, RADIO FREQUENCY AND MODULATION SYSTEMS— PART 1 EARTH STATIONS AND SPACECRAFT, (2021); ref CCSDS 401.0-B-32

First experimental Results and Beamforming Features of Ground Antenna Implementing AESA Technology

C. Mellé¹, A. Robert¹, B. Lesur¹, G. Kipfer¹, C. Deville¹

¹ Safran Data Systems, La Teste de Buch, France
Christophe.melle@safrangroup.com

Abstract

This paper describes the last experimental results and studies of Safran telemetry ground antenna implementing Active Electronically Steerable Antenna (AESA) technology. Telemetry ground antennas play a key role in telemetry systems, by receiving data transmitted by the flying object and sending it to a ground system for data processing. The use of AESA technology allows for more precise targeting and tracking, making it ideal for high dynamic applications. The design presented in this paper is a 1-axis electronically steerable antenna, which is used for elevation axis while azimuth axis is mechanically driven. This S-band antenna is specifically intended for short to medium range telemetry and is able to handle high target dynamics. The paper presents the results achieved with a first prototype, at system level, with targets in real condition like rockets and LEO satellites. Moreover, beamforming shaping are likewise detailed in this paper in order to solve critical cases of propagation phenomena.

Key words: telemetry ground antenna, AESA, tracking, beamforming shaping.

1. Introduction : architecture and principles

To respond to short and medium range S-band telemetry applications, Safran began by developing a small ground station called Comtrack. The Comtrack antenna is a receive-only antenna with a gain of 21 dBi and a G/T of -2.5dB/K. This antenna has an automatic tracking function but only for azimuth axis and the half-power beamwidth in elevation is not considered large. Therefore, one other acquisition aid antenna has to complete the system to cover a certain number of missions. Taking into account the analysis of customer feedback and development advances in Active Electronically Scanned Antenna technologies, Safran decided to develop a new station enriched with new possibilities, while remaining transportable and economically relevant.

It is a new hybrid antenna, named Sparte e-100, with both mechanical rotation and electronic beam scanning, and which has a larger surface area as shown in Fig. 1. The antenna is equipped with a second degree of freedom on the radius diagram with an electronic elevation adjustment. The mechanical azimuth alignment is conserved in order to maintain 360° scanning. Note that the panel is tilted by 45°, which allows for an optimized coverage of 90° in elevation with an electronic offset of +/- 45°. Concerning the

antenna array, a new elementary radiating element has been developed.



Fig. 1. Picture of Sparte e-100 ground station.

In order to achieve automatic tracking on both axes, the entire surface of the network is divided into four identical sub-networks named A, B, C and D as shown in Fig. 2. Automatic tracking is done according to the Single Channel Monopulse principle from the sigma and delta channels generated by specific circuit networks. We can thus express:

- Sigma channel :

$$\Sigma = A + B + C + D \quad (1)$$

- Delta channel for azimuth:

$$\Delta z = (A + C) - (B + D) \quad (2)$$

- Delta channel for elevation:

$$\Delta e_l = (A + B) - (C + D) \quad (3)$$

Each sub-array A, B, C or D is a matrix of 8 lines of 4 radiating elements excited according to two polarizations H and V. Each line of four elements includes low noise amplification and a phase shifter. Right and left circular polarizations, sigma and delta channel generation are obtained using a passive BFN (Beam Forming Network) in multilayer PCB technology designed by Safran with 3dB 0-90° hybrid couplers.

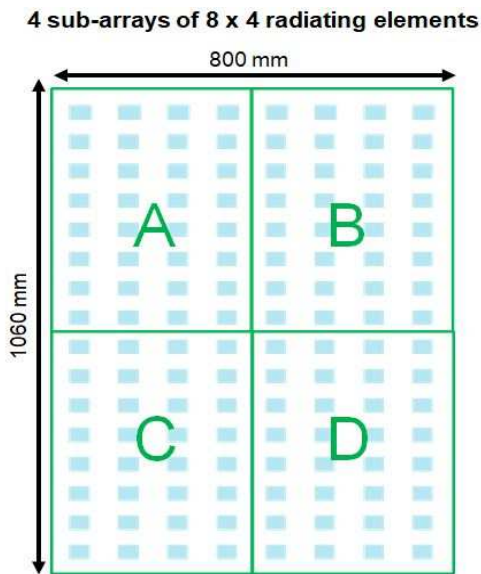


Fig. 2. Architecture of the complete array divided by four sub-arrays A, B, C and D.

Active RF modules designed by Safran for antenna feeds are used. These modules are equipped with a pre-filtered amplification stage, and generate the RHCP and LHCP circular polarizations for the sigma channels as well as the delta channels for the azimuth and elevation axes. The delta channels are phase shifted by a step of 90°, generally during one period of 2 ms, in order to obtain the four tracking error components Az+, El+, Az- and El-. Thus, there are two RF channels RHCP and LHCP after summation of delta and sigma including both telemetry data and tracking error information. The function of the RTR (Radio Telemetry Receiver) is used to demodulate the telemetry and tracking signals. Tracking errors are then processed by the ACU in order to adjust the beam orientation to the target in azimuth mechanically, and in elevation electronically: the synoptic of station is presented in Fig. 3 and performances in Tab.1.

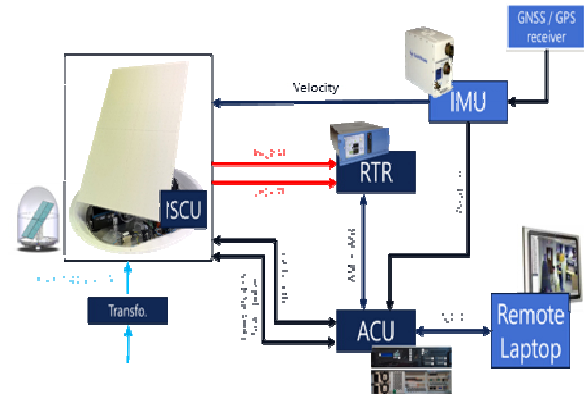


Fig. 3. Synoptic of Sparte e-100 ground station.

Bandwidth	2.2-2.4 GHz
Gain	27 dBi
G/T EI 45°	6 dB/K
Beamwidth 3dB	Az 8° / El 6°
Tracking Accuracy	+/- 0,5°
Azimuth Velocity	30°/s
Azimuth Acceleration	30°/s ²

Tab. 1: Main performances of Sparte e-100

2. Antenna experimental results in anechoic chamber

Several antenna prototypes have been manufactured. Before validating the 4x8 sub-array with the active elements, it was necessary to validate the radiating elements without the active components, such their Sii parameters adaptation and the radiation patterns in the H and V polarizations. Furthermore, this made it possible to know the efficiency of the radiating element and the losses of the power lines up to the input of the low noise amplifiers.

Firstly, a single sub-array was validated on the following points: routing of power supplies and phase shifter controls, radiation and function efficiency diagrams, and S parameters. One of the difficulties is to be able to evaluate the gain AESA because the presence of active elements with additional gain and losses. This gain measurement is done indirectly by measuring microwave lines with the same characteristics as those between the radiating elements. It is important to note that a correct consistency has to be established between gain measurements in the room and G/T measurements carried out outdoors.

Secondly, a complete set of the antenna with four subarrays was validated with the sigma/delta recombination and polarization

formation circuit RHCP and LHCP: Fig. 4 and Tab. 2 show radiation patterns and directivities of sigma RHCP and LHCP channels. The single channel monopulse tracking function could also be tested: some examples of radiation patterns of both sigma and delta channel are given in Fig. 5 and Fig 6; the tracking slopes in Fig. 7. The tests were carried out in one of the anechoic chambers of Safran Data Systems. These results show a good agreement between measurement and expected performances as demonstrated in [1] and [2].

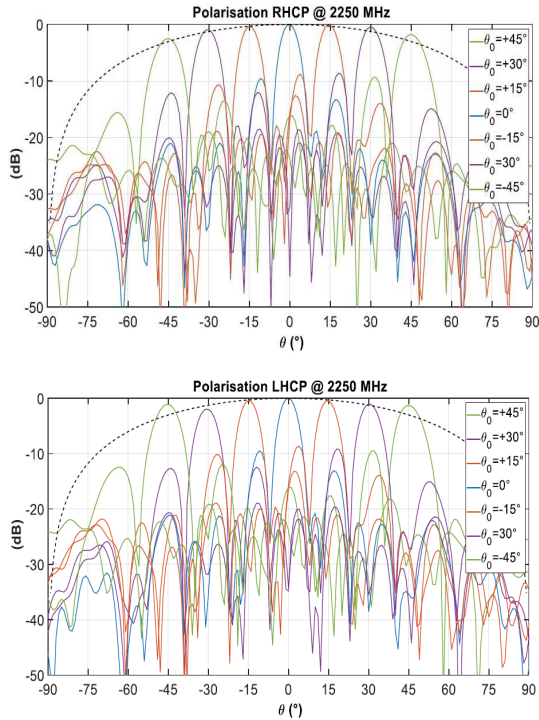


Fig. 4. Measures of sigma radiation patterns $\theta = -45, -30, -15, 0, +15, +30$ and $+45^\circ$ @2250MHz.

Theta(°)	Directivity (dBi) Simulation	Directivity (dBi) Measurement
-45	27	25.7
-30	27.8	26.5
-15	28.3	26.9
0	28.5	27.2
+15	28.3	26.9
+30	27.8	26.5
+45	27	25.7

Tab. 2: Directivities by simulation and measurement.

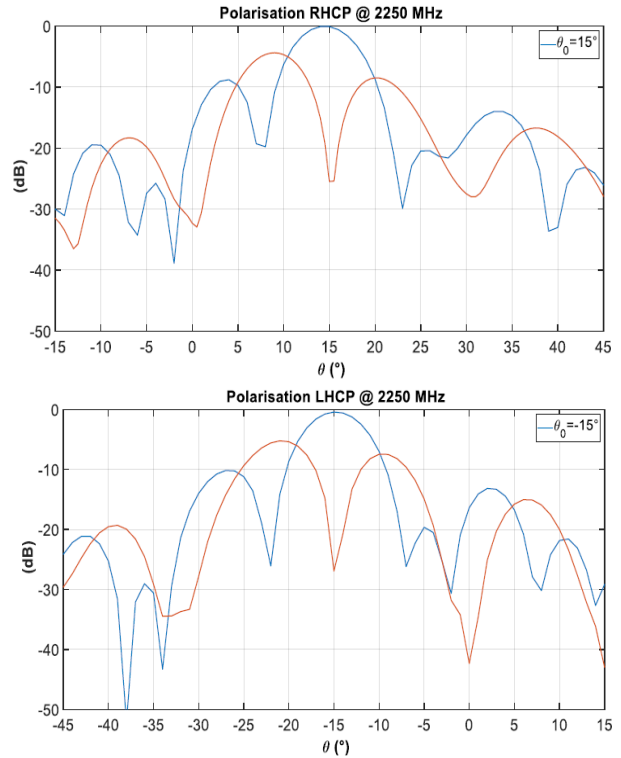


Fig. 5. Examples of sigma & delta radiation patterns RHCP $\theta = +15^\circ$ & LHCP $\theta = -15^\circ$ @2250MHz.

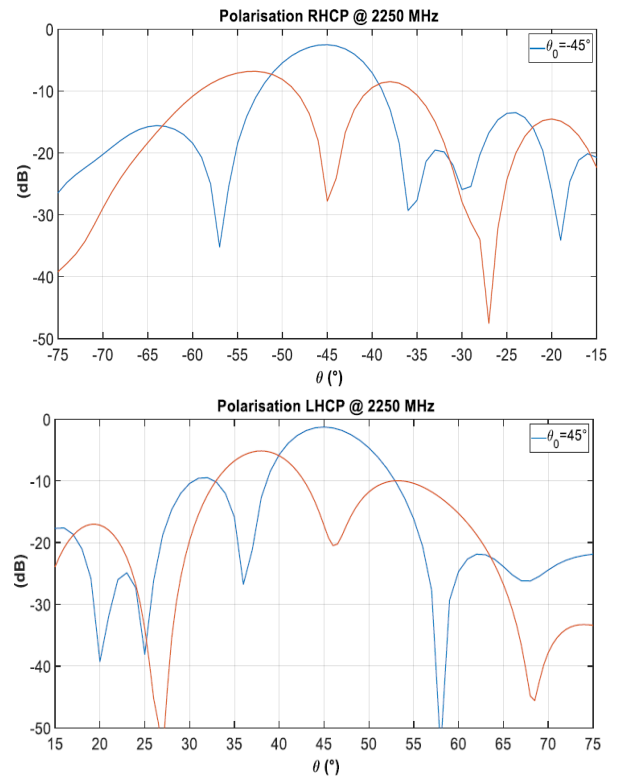


Fig. 6. Examples of sigma & delta radiation patterns RHCP $\theta = -45^\circ$ & LHCP $\theta = +45^\circ$ @2250MHz.

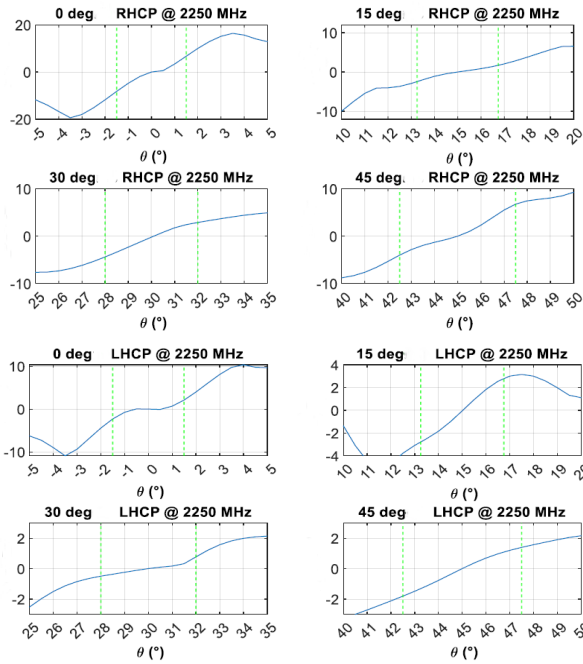


Fig. 7. Tracking slopes from delta / sigma measured @ 2250MHz.

3. Outdoor static and dynamic results

A second part of validation consists of validating the station system parameters. These tests proceed in two phases. The first phase consists of making adjustments to the servo control, software and RF on a static target. Safran teams has performed following:

- carry out the integration of the electronic beam steering functions in the ACU,
- ensure the tracking function on a fixed target in the far field: adjustments of gains and phases, calibration on the Az and El axes. See the homing tests (Fig. 8),
- validate the G/T measure on Sun to ensure the good value of figure of merit.

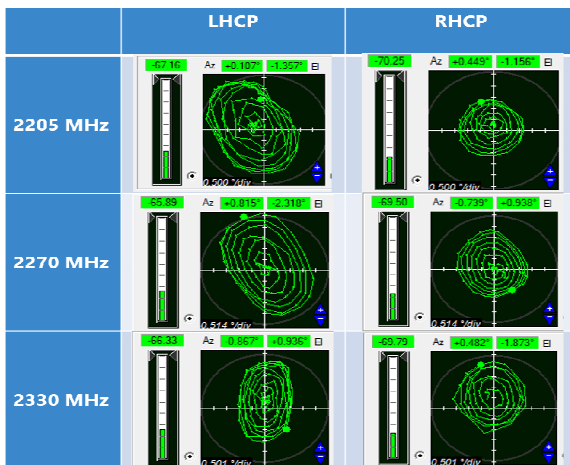


Fig. 8. Tracking homing tests for three frequencies.

The second phase consists of testing in dynamic mode on moving targets. The tests were carried out on satellites and on a rocket. Here are the main tests carried out in the factory or on site:

- Measurement of G/T on Sun (Fig. 9)
- C/N measurements and tracking tests on LEO satellites: Pleiades 1B, Pleiades 1A, Jason 3, Spot 6 and Calipso.
- Measurements of Eb/No on satellites (CNES).

G/T measurements are summarized in Fig. 9 for the both polarizations (LHCP and RHCP) and measured at 2350 MHz and 2250 MHz. Note that these performances are observed for an antenna of 1m² and the angle El = 0° corresponds to the beam towards the horizon. These measurements show the capacity of the 1m² antenna to reach a mean G/T of 5.9 dB/K.

TEST	Date	Time	Channel	Sun noise	Sky noise @ Sun EL	Sky noise @ 0 EL	Y factor, measured
Type	dd/mm/yyyy	UTC	Signal-polar	(dBm)	(dBm)	(dBm)	(dB)
Validation	13/06/20223	14:26:00	TM LHCP	-58.20	-65.30	-65.00	7.10
Validation	15/06/20223	15:48:00	TRK LHCP	-57.90	-65.00	-64.32	7.10

TEST	Date	Time	Channel	Sun noise	Sky noise @ Sun EL	Sky noise @ 0 EL	Y factor, measured
Type	dd/mm/yyyy	UTC	Signal-polar	(dBm)	(dBm)	(dBm)	(dB)
Validation	13/06/20223	14:23:00	TM RHCP	-58.20	-65.20	-64.90	7.00
Validation	15/06/20223	16:00:00	TRK RHCP	-57.60	-64.80	-64.12	7.20

LHCP									
Frequency	Sun EL	Sun Radio Flux	Antenna Beam width @ 3dB	A	K1	K2	K4	S = K1*K2*K4 *Freq	G/T @ 0 EL
(MHz)	(°)	Wm ² /Hz	(°)	(dB)	-	-	-	-	(dB/K)
2250,00	65,00	0,00	7,22	0,036	0,99	1,00	1,0	1,85E-20	6,09
2350,00	65,20	0,00	6,91	0,036	0,99	1,00	1,0	2,01E-20	5,73

RHCP									
Frequency	Sun EL	Sun Radio Flux	Antenna Beam width @ 3dB	A	K1	K2	K4	S = K1*K2*K4 *Freq	G/T @ 0 EL
(MHz)	(°)	Wm ² /Hz	(°)	(dB)	-	-	-	-	(dB/K)
2250,00	65,00	0,00	7,22	0,036	0,99	1,00	1,0	1,85E-20	5,97
2350,00	65,20	0,00	6,91	0,036	0,99	1,00	1,0	2,01E-20	5,86

Fig. 9. Measurements of G/T level.

In the following, measurements of Eb/No are realized for some satellites passes. Eb/No is a normalized signal-to-noise, or the ratio of energy per bit to noise density, and depends on C/N and G/T of the system. This measurement allows to evaluate the capacity of the station to receive a correct level of modulated signals. This can be linked to the BER (Bit Error Rate) which gives the number of bits altered by noise, interference, distortion or bit synchronization errors.

Many satellite passes and test configurations have been realized and, for this paper, only 2 satellite passes with their configuration are presented. The configurations used for these passes are presented in Tab. 3 and implemented in a RTR.

Satellite	JASON 3	Pleiades 1A
Frequency	2 215.92 MHz	2 269.2 MHz
Rate	3 355 444 bits/s	941 176 bits/s
Modulation	QPSK	QPSK
Polarization	LHCP	LHCP

Tab. 3. Configuration of JASON 3 and Pleiades 1A.

First, the measurements for JASON 3 satellite passes are presented using a RTR. Sparte e-100 is able to track Jason 3 satellite (Fig. 10) with an error of 0.05° rms in azimuth and 0.07° rms in elevation in auto-tracking mode. Then, Fig. 11 shows its capacity of receiving modulated signals with a maximum Eb/N0 of 7dB.

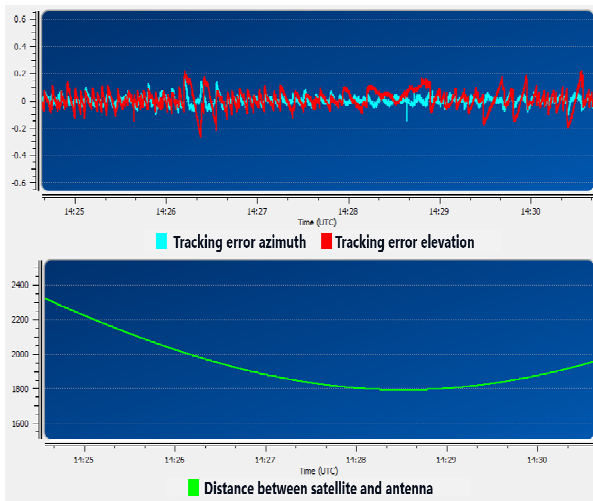


Fig. 10. Tracking tests with Jason 3 Satellite.

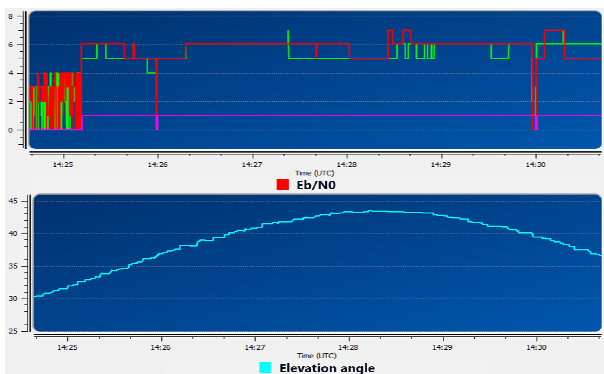


Fig. 11. Eb/No evaluation and elevation with Jason 3 Satellite.

The following figures show the results for Pleiades satellite, version 1A. Tracking errors

are plotted in Fig.12 and present an error between -0.5° and 0.5° in azimuth and in elevation during the tracking mode. These values are higher than the tracking errors seen with Jason 3, but the antenna still offers very good tracking capability. During Pleiades tracking, the antenna is able to reach a maximum Eb/N0 of 14 dB (Fig. 13).

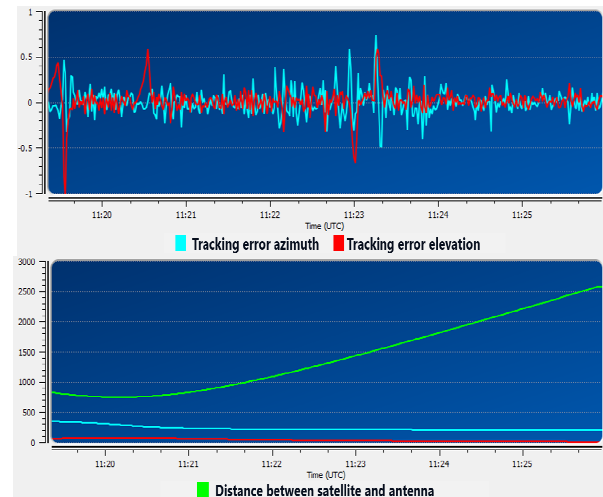


Fig. 12. Tracking tests with Pleiades Satellite.

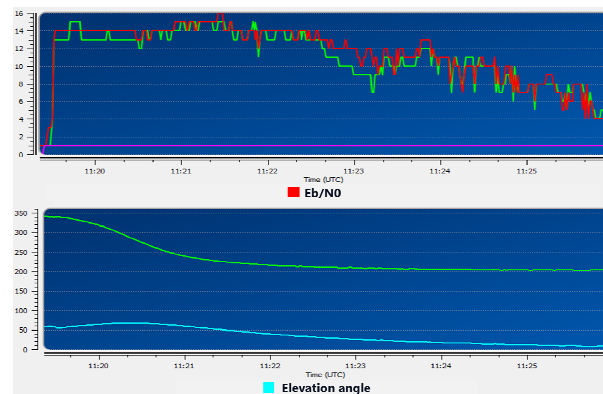


Fig. 13. Eb/N0 evaluation vs elevation with Pleiades Satellite.

All the link budget parts impact Eb/N0 levels as climatic conditions and ephemeris, this can explain the difference of Eb/N0. For both cases, these results validate the capacity of receiving modulated signals.

It is possible to get the value of G/T thanks to this formula, obtained in the literature [3]:

$$\left(\frac{G}{T}\right)_{dB/k} = \left(\frac{Eb}{N0}\right) + (R)_{dB} - (flux)_{dBW/m^2} + (k)_{dB/J/Hz} - 10\log_{10}\left(\frac{A^2}{4\pi}\right)$$

The corresponding computations for both passes are presented in Tab. 4.

Satellites crossing			Satellite -		
Date	Satellite	Cortex	Frequency (MHz)	lambda (m)	flux (dBW/m ²)
08/12/2023	Jason 3	RTR Safran	2215,92	0,14	-134
22/12/2023	Pleiades	RTR Safran	2269,2	0,13	-133

Ground Station link		G/T comparison		
lambda ² /4pi	R (bit/s)	Measured Eb/N0	Measured G/T (EI=0°) (dB/K)	Computed G/T (dB/K)
-28,36	3355444	7	5,91	6,02
-28,57	941176	14	5,91	6,70

Tab. 4. Computations of G/T with measured Eb/N0.

Many conclusions can be done thanks to these computations. First, they allow to estimate the minimum flux level received by the antenna. Then, this method (measurements of Eb/N0 and computations of G/T) is less time-consuming than experimental measurements of G/T on sun. In this context, it is important to have a good knowledge of flux levels to avoid computation errors of G/T.

For Jason 3 and Pleiades, the estimated flux levels are respectively -134 dBW/m² and -133 dBW/m² at the antenna input. These computations give the sensitivity of the antenna with a given G/T in tracking conditions and for different satellite links.

About the performances achieved with rocket, one demonstration done in November 2023 has given excellent results, but the details cannot be communicated for confidentiality purpose.

4. Conclusion and tracking with possible beamforming shaping features.

The results achieved in factory and during demonstrations with the CNES or other Customers show that the Sparte e-100 is close to a production prototype. The hybrid technology is a very good trade-off between technical performances and cost. The dimensioning of the antenna, the hybridization

References

- [1] C. Melle, G. Kipfer, A. Lohou, A. Karas, B. Lesur, R. Contreres, A Ground S Band Hybrid Active Electronically Scanned Array: Concept, Design and Performance, *ICORT 2021*; doi: 10.1109/ICORT52730.2021.9581364
- [2] A. Lohou, A. Robert, B. Lesur, G. Kipfer, P.-M. Bastie, Implementation of AESA Technology for High-Target Dynamic Telemetry Ground Antennas pt, Design and Performance, *ITC 2023*; doi: *unavailable*.
- [3] Orfanidis, S.J. (2002) Electromagnetic Waves and Antennas. Rutgers University, New Brunswick, NJ.

of the mechanical and electronic axes and its good sensitivity are well suited to launcher or micro-launchers missions, and more generally for applications which require only one beam. It should also be noted that in principle it is a by-design scalable antenna: it is indeed possible to assemble more than 4 sub-arrays or tiles for higher gains and G/T.

Note that in the context of multi-contact applications, Safran Data Systems is oriented more towards developments of analog-digital AESA, digitization of each analogical channel from sub-array or digitization of the analogical channel from each antenna. These developments are possible, if the frequencies allow it from an economic point of view towards full Digital Beam Forming network antennas.

To conclude for improvement of Sparte e-100, considering the propagation difficulties experienced during missions, such as multi-path effects and possible saturation of the amplification stages, it seems interesting to exploit the real-time agility and shaping capacity of the beam to reduce these undesirable effects. Thus, Safran Data Systems currently study advanced processing algorithms of beam shaping. This concern the opening of the beam in elevation and possibly the use of information given independently by the four sub-arrays (A, B, C, D) mentioned above.

5. Acknowledgments

The authors wish to thank the French Space Agency (CNES) for supporting this work through contracts R&T R-S20/TC-0006-048-92 and ORANUM202301764. This work is associated with the joint laboratory XSELANS (Xlim-Safran Electronics Lab for ANtennaS), in the context of the French National Research Agency program ANR-19-LCV2-0008.

Embedded Recording in Flight Test Telemetry Receiver

Florian Sandoz¹, Grégory Blanc², Maxime Cariou², Philippe Klaeyle²

¹ Safran Data Systems, 5 avenue des Andes – 91978 Courtaboeuf Cedex, France

² Safran Data Systems, 5 esplanade Anton Philips – 14460 Colombelles, France

florian.sandoz@safrangroup.com gregory.blanc@safrangroup.com
maxime.cariou@safrangroup.com philippe.klaeyle@safrangroup.com

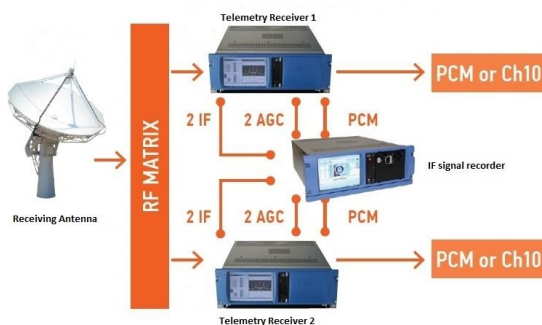
Abstract:

Telemetry hardware has continuously evolved over the decades pursuing the goal of evermore-integrated and easy-to-use systems. Digital signal processing techniques and FPGAs enabled manufacturers to develop Telemetry receivers with multiple channels in a single box. Yet, recording of ground station signals was left to separate units because of technical impossibilities. This paper presents an all-integrated Telemetry system embedding a best in class Telemetry Receiver and an IRIG-CH10 compliant Recorder. First, the system technical specifications are presented, with a focus on the type of signals to record and the required playback capabilities. Then, the technical approach that enables to run both the receiver and the recorder tasks on the same signal processing FPGA board is described. Finally, the performance of the system is assessed in terms of BER degradation of the playback signals.

Key words: Telemetry, Flight Test, Recorder & Reproducer, Multi-channel Recording, IRIG106.

Introduction

In this paper, we consider the following setup as the benchmark to evaluate the complexity of a ground station:



Two telemetry channels are transmitted at different RF frequencies. Each telemetry channel consists of two polarization signals (LHCP and RHCP) generated by the antenna, and demodulated by a dual-channel telemetry receiver. This reception configuration is named “polarization diversity”: both polarization signals are demodulated independently, and a third demodulation channel is being created after combination of the two polarization signals (pre-detection combination), leading to an improvement of the budget link up to 3dB.

An additional 3dB improvement on the budget link and a better robustness to multi-paths are possible if the same data is being transmitted on the two telemetry channels : the outputs of the pre-detection combiner of each dual-channel telemetry receiver can be recombined, creating a four channel pre-detection combined signal. This mode is named “polarization and frequency diversity”. It will not be studied in this article, and shall be considered as a possible improvement of the presented ground station setup.

There are four RF signals coming from the antenna via a RF matrix : two per dual-channel telemetry receiver. Each receiver is able to translate them to IF (70Mhz) for further recording by a four-channel IF recorder.

Each dual-channel telemetry receiver is able to output three PCM data : one for each received signal, plus one for the internally created combined channel. A PCM data consists of a pair of data and clock signals, which are sent to a decommutator and data processing unit.

Simultaneous processing by the decommutator and recording by the IF recorder is possible, at the cost of TTL splitters.

The presented ground station is then made of the following elements:

Tab. 1: Equipments

Item	Description	Nb
Receiver	Dual-channel telemetry receiver with embedded screen and keyboard for control and connectors in the backpanel 4U height	2
Recorder	Four-channel IF recorder with embedded screen and key board for control and connectors in the backpanel 4U height	1

Tab. 2: Interconnection

Item	Type	Nb
Antenna to RF splitters/matrix	N-type coax	2
	RF splitters (1 to 2)	2
RF splitters/matrix to receivers 1&2	N-type coax	4
Receivers 1&2 to IF recorder (IF signals recording)	BNC coax	4
Receivers 1&2 to IF recorder (AGC signals recording)	Custom cable RS422 D-sub44 to D-sub9	2
Receivers 1&2 to TTL splitters (PCM outputs of each receiver)	BNC coax	12
	TTL splitters (1 to 2)	12
TTL splitters to IF recorder (PCM inputs of the IF recorder)	BNC coax	12
TTL splitters to decommutator (PCM inputs of the decommutator)	BNC coax	12
Network to receivers 1&2 and IF recorder (Monitoring&control)	RJ45 cable	3
Receivers 1&2 to decommutator (Telemetry data)	RJ45 cable	2
Power supply to to receivers 1&2 and IF recorder	Power supply cable	3

The total of each element sorted by category is depicted below:

Tab. 3: Cables by category

Item type	Nb
N-type coax	6
BNC coax	40
RJ45 cable	5
Power supply cable	3
AGC custom cable	2
TOTAL	56

Tab. 4: Splitters by category

Item type	Nb
RF splitters (1 to 2)	6
TTL splitters (1 to 2)	12
TOTAL	18

More than 70 interconnection items of various types are needed, making harsh assembly, maintenance and flexibility of the ground station.

An all-integrated ground station

This article introduces an all-integrated ground stations, whose functionality and performances are strictly equivalent to those of the setup presented previously in this article. The new setup is then simplified as follows:



A single equipment performs the features of two dual-channel telemetry receivers and one IF signal recorder, reducing drastically the number of interconnection items needed. In addition, the new equipment embeds only two RF inputs (instead of four in the original setup): several telemetry channels (i.e. different carrier frequencies) can be processed on a single RF input, so that the equipment receives the two polarity signal (LHCP/RHCP) directly from the antenna. Splitters (or RF matrix) upfront the receiver are no longer required.

In the following, the all-integrated telemetry equipment is named receiver-recorder. As the IF and PCM recording is performed in the same box as the receiver, the cables required to perform IF, AGC and PCM recording are no longer required. Furthermore, three 4U equipments are now replaced by a single 4U equipment.

Below is the list of the required interconnection in a ground station using the new receiver-recorder:

Tab. 5: Interconnection (receiver-recorder)

Item	Type	Nb
Antenna to receiver-recorder	N-type coax	2
Receiver-recorder to decommutator (PCM inputs of the decommutator)	BNC coax	12
Network to receiver-recorder (Monitoring&control)	RJ45 cable	1
Receiver-recorder to decommutator (Telemetry data)	RJ45 cable	1
Power supply to to receiver-recorder	Power supply cable	1

The total of each element sorted by category is depicted below:

Tab. 6: Cables by category (receiver-recorder)

Item type	Nb new setup	Nb initial setup
N-type coax	2	6
BNC coax	12	40
RJ45 cable	2	5
Power supply cable	1	3
AGC custom cable	0	2
TOTAL	17	56

Tab. 7: Splitters by category (receiver-recorder)

Item type	Nb new setup	Nb initial setup
RF splitters (1 to 2)	0	6
TTL splitters (1 to 2)	0	12
TOTAL	0	18

The number of required cables is reduced drastically, and the need for splitters disappears.

Embedded recording specifications

By focusing on the use case presented earlier, we can easily write the specifications of the embedded recording. First, we can list the type of channels needed in the recording.

The quad channel receiver generates four down-concerted channels (IF1-4) centered at 70 MHz, with reduced level dynamics thanks to the AGC loops. Those AGC loops generate four signals (AGC1-4), each one holding the information of the gain that is applied to a particular channel. Recording of both those IF and AGC signals is of critical importance for two reasons. First, for post mission analysis. On a first order approximation, the profile of the AGC signal over time reflects the evolution of the link budget during the test scenario. Secondly, for playback. During playback, the receiver will require the AGC signals as inputs of its pre-detection algorithm, along with the IF signals. Without the AGC signals, the receiver will not be able to weight the IF contributors as expected in a MRC. The pre-detection combined signals that the receiver generates out of IF1-4 are considered as intermediate, redundant, signals that do not need to be recorded to save storage space, and system bandwidth.

The recording of IF and AGC signals might seem to be enough to keep track of the test

scenario. Upon playback, a quad channel receiver with adequate AGC inputs would indeed be able to perform the MRC again, and provide the PCM outputs. This raises an important limitation of recording only IF and AGC channels: one depends on the receiver to be able to recover the PCM data again. However, PCM streams cost only a fraction (typ. 2%) of the bandwidth and storage space that are required for IF signals recording. It is evident that having the ability to access directly to PCM data without the need of the receiver is a must-have in a modern recorder. Most of the time, only the PCM data would be required for playback, possibly on remote CH10 compatible PCM recorders. A quad channel receiver as depicted earlier generates 6 PCM streams (4 individual channels, 2 combiners). It consequently seems a good option to record all six PCM channels (PCM1-6) along with IF (IF1-4), and AGC (AGC1-4) signals.

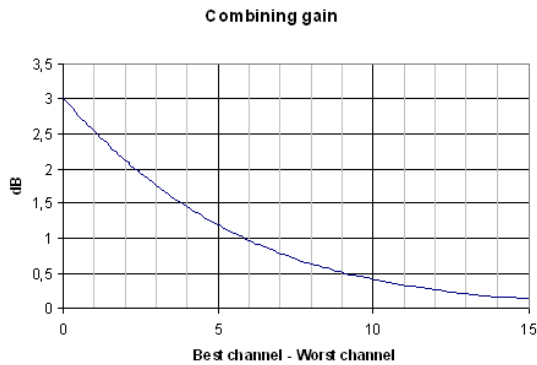
Now that the number and type of channels are clearly identified, we can elaborate on the required playback abilities. As explained in previous paragraph, the system shall be able to playback the PCM data on the usual connection with the decommutator. This means the data playback should be made available either through PCM electrical connection (TTL, RS-422) or through UDP streaming (RCC218-20, or CH10 UDP).

For IF replay, two principles can be investigated. First, it shall be possible to output the IF signals through the usual IF output of the receiver for external analysis or shortloop testing. In the same manner, the AGC signals shall be reproduced on the AGC outputs of the receiver. From an MRC point of view, in case of shortloop testing of the playback IF, it is important that either

- The receiver can process external AGC signals, along with IF signals whose level are set
- The IF level differences between the four IFs are reproduced.

For better interoperability of the system, we chose to implement the second solution. As the IF outputs of the receiver have a static and limited dynamic range (usually a digital scale, with Full-Scale at 10 dBm), it is not possible to cover the whole dynamic range of a low bitrate configuration (up to 100 dB) while keeping quantization error low. Yet, if we take a look at the combining gain, as a function of the level difference for a two channel MRC, for a same noise level under AGWN, it appears that the combining gain becomes hardly noticeable (0,1 dB) when the level difference reaches 15 dB.

This last value is compatible with a digital scale reproduction of the original dynamic range. Consequently, the playback shall reproduce the level *differences* among the sources, on a scale of at least 20 dB.



The second principle for playback of IF signal is to feed the IF signals directly in digital domain at the input of the receiver, to eliminate the need for external IF loopback. This, however, raises technical challenges that are not addressed in the present article.

Finally, other specification elements, such as time alignment, quantization scale, storage, can be extracted from the specification of a typical external flight test recorder, such as the Cortex RSR. The next table summarizes the technical specifications for the embedded recording.

Tab. 8: Embedded recording specification

Item	No.	Details
0	File format	IRIG106 CH10
1	IF channels	4 70 MHz, 8 bits/16 bits selectable
2	AGC channels	4 16 bits, > 300 kHz.
3	PCM channels	6 Bitrate bits per second. PCM throughput.
4	IRIG channels	2 Decoded time reference + 16b analog recording
5	Storage	Single cartridge, NVMe, 15 TB (> 4h at full speed)
6	Aggregate bandwidth	8000 Mbps
7	IF outputs	4 70 MHz, receiver outputs Ability to reproduce the level difference between IFs. 4 ns time alignment precision.
8	AGC outputs	4 Use of receiver outputs
9	PCM outputs	6 Either PCM or UDP

			streaming.
10	IRIG output	1	Use of one high-BW video output of the receiver.
11	Recording and replay		Shall be operable independently from the receiver tasks. No impact of the recorder on the receiver operation of performance.

Embedded recording implementation

This paragraph depicts the challenges and the advantages of integrating the receiver and the recorder into a single box. The reduction of the number of cables required has been previously mentioned.

Software and Cybersecurity

The application software of the three equipment have been modified in order to be able to run on a single kernel and on the same operating system. The required effort to secure the ground station is then reduced accordingly.

Apart from this modification, the legacy of the software of each equipment is maintained, and the software interface remains the same as the one of the stand-alone equipment.

Implementation wise, the recorded and playback flow all pass through the PCIe interface between the high-level software and the low-level firmware. Even though both products are now inside a single platform, a particular attention has been given to the separation during the implementation in an effort to minimize any potential perturbation between the receiver and recorder operation. As an example of this effort, a second microcontroller is deployed onto the FPGA platform to process specific recorder functionalities and compartmentalize low-level application.

Filtering

One of the main advantage of this new compactness is that the recording can directly benefit from the several analog and digital filtering and decimation stages of the receiver. The IF signal recorded correspond exactly to what is seen by the demodulator inside the receptor. The recording configuration (acquisition bandwidth, input frequency, input selection) is automatically adjusted to correspond to the IF filter bandwidth.

Gain (AGC)

The recorder captures the sum of every variable gain inside the receiver downlink: analog AGC and digital gain. The gain of the IF signal is automatically recorded alongside the IF signal in the form of an additional CH10 flow. It creates analog packet with 16 bits samples that represent fixed-point (Q8.8) value of the gain in dB extracted at the defined rate of 390 kHz.

The TMATS contains for the CH10 packets of the IF signal information of the ADC full scale in Vpp and the input impedance. Combining those information with the recorded AGC gain allows the reconstitution of the signal input level in dBm.

It also enables a new functionality during the replay: the Dynamic Gain Replay. This allows to playback the variation of level between IF signals and therefore correctly use the pre-detection combiner. When the dynamic gain replay is disabled, the output IF signals during playback are at a constant level of -13 dBm. When the dynamic gain replay is enabled, the stronger of the two IF signals, based on AGC value, will playback at -13 dBm and the weakest signal will playback at -13 dBm less the difference of level between the two IF signals. Thus, only the difference of level is provided during the playback and not the absolute level.

PCM

The PCM streams are directly captured inside the digital domain the nearest possible of the demodulation output, before the physical output and the usual bitrate reconstruction algorithm. In the case where a FEC is present, the PCM streams are sampled after the decoding. This proximity has the advantage of always having a valid clock available for the recorder. Therefore, problematic case such as a discontinued clock does not have to be handled.

The PCM bitrate inside the recorder is automatically adapted to the receiver channel configuration.

Replay

A specific new filter for the up sampling process has been developed to adapt the sampling between what is inside the CH10 packet and what is needed for the DAC frequency. This filter is future proof in a way to adjust for the potential replay at RF Frequency (telemetry

bands) and with others recorded sampling (i.e. from others vendors).

The same timing performance as expected of a recorder is kept. The RTC is at the center of the alignment process between the different types (IF and PCM) of signals. The RTC is also used to generate a coarse approximation of the frequency for the playback clock. The receiver outputs handle the fine final tuning.

Results

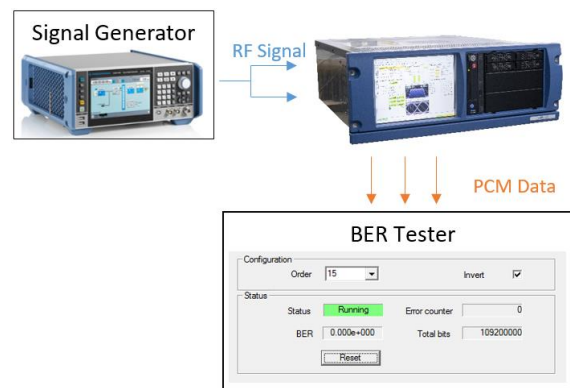
Setup presentation and expectations

The result part here will be focused on the capacity of this new equipment to both receive two IF signals with polarization diversity and record them. In the same time, the setup will show the capacity of the pre-detection combiner to create a third demodulation channel with a noticeable BER improvement.

After that, the setup is rearranged to focus on the playback mode (IF replay and PCM replay), showing the capacity of the embedded receiver to conserve the quality of the original IF signals and the PCM frames originally transmitted.

Note that the pre-detection combiner will be used again on the replayed IF signals to demonstrate that the performance gain during playback is the same as the original one.

Results will be demonstrated with the following setup:



This include a Signal Generator that simulates a signal we could receive through an antenna.

The RF signal is splitted on the two RF inputs, then converted to IF signals. Using the RF inputs gives the opportunity to use thermal noise by slowly decreasing the RF level on the generator. Due to the differences of the noise factor between the two RF channels, a slightly

different BER on demodulation channel 1 and demodulation channel 2 maybe observed.

The pre-detection combiner is expected to demonstrate a significant performance improvement on demodulation channel 3.

The setup is limited to one dual-channel telemetry receiver-recorder that includes:

- a pre-detection combiner for the third PCM channel.
- The new recording part to capture both the two IF channels input and the three PCM channels. (2 from the direct inputs and one resulting of the pre-detection combiner).

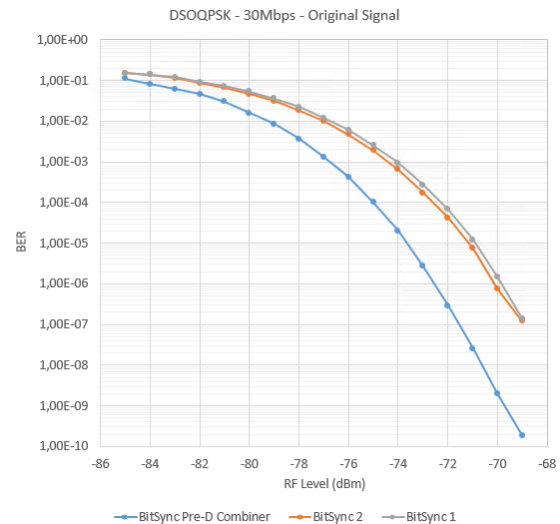
To ensure that the PCM outputs are correct, the BER is measured externally with an independent BER measurement system with three PCM inputs (data and clock signals).

Original signal measurement

The steps are the following:

1. Configure two IF signals on the two IF inputs of the receiver. (Generator IF output stays OFF)
2. Connect the three PCM outputs to the BER Tester Inputs.
3. Start Recording.
4. Switch ON the IF output on the generator.
5. Measure the BER and the number of frame received on the BER Tester.
6. Switch OFF the IF output on the generator.
7. Stop recording.

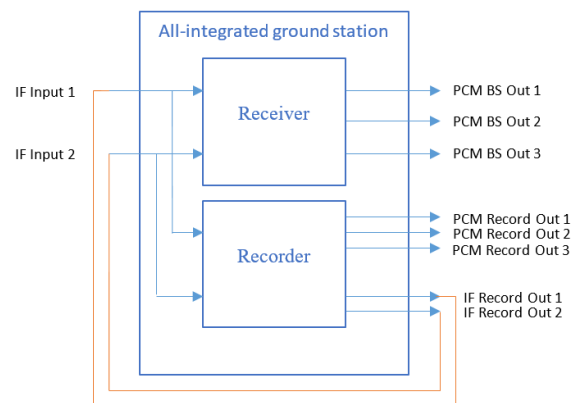
Those first steps allow us to get a first chart of three BER measurements for each demodulation output.



The performance improvement on the pre-detection combined channel is observed as expected.

IF Replay

Now that IF signals have been recorded, we can play them back on the embedded receiver with the following setup:



As mentioned earlier, the receiver and the recorder are two independent part.

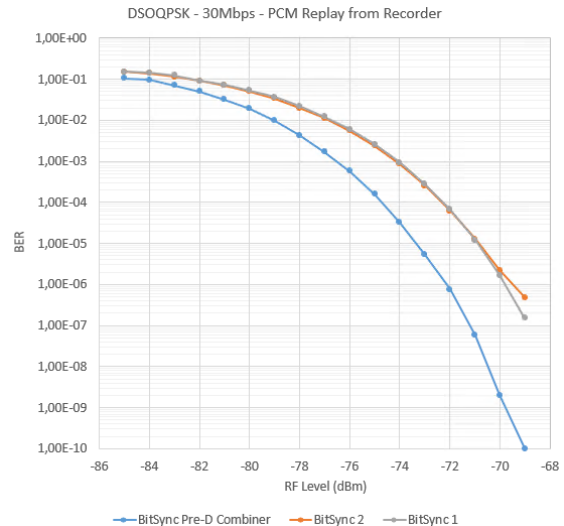
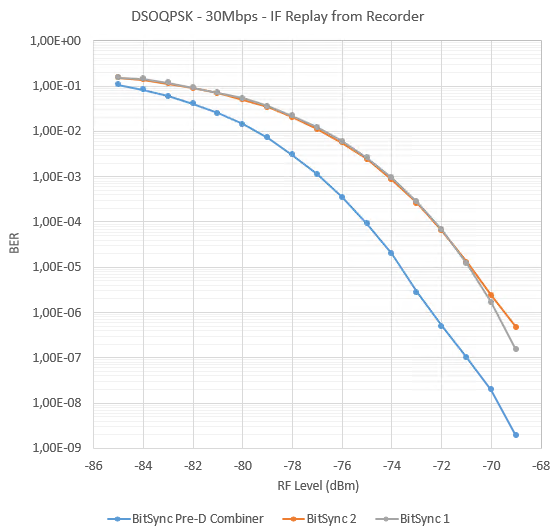
The recording starts with the signal OFF, then switched ON for a certain duration and finally switched back OFF before stopping the recording. This procedure ensure that the presence of the useful signal is fully recorded.

The steps are:

1. Connect the three PCM outputs to the BER Tester Inputs.
2. Start playing the record.
3. Measure the BER and the number of frames received on the BER Tester during the presence of the useful signal.

4. Wait for the end of the record.

By recording several files with a different RF level each time, we are now able to get the following charts:



This replay shows the capacity of the recorder to ensure that the original IF signals are recorded without losing any data.

Moreover, the pre-detection combiner is able to improve the BER on the 2 IF replay signals, showing that the IF signals are recorded without any timing difference.

PCM Replay

Now that the IF replay confirmed the good recording of both IF signals, we need to check that the PCM recorded after the demodulation units are consistent and give the same results.

To prove these, we don't need the receiver part anymore, we just have to replay the file and monitor the PCM Recorded Outputs (instead of the PCM Demodulated Outputs) with the external BER Tester.

Conclusion

This article presented the advantages of merging the telemetry receiver and IF signal recorder into a single box. The architecture choices were explained, and the record and playback capability without any performance loss was demonstrated.

The increasing integration presented in this article will continue to bring opportunities for new features in the near future, the first challenge being the implementation of a four channel pre-detection and post-detection combination.

Glossary

- RHCP: right-hand circular polarization
- LHCP: left-hand circular polarization
- BSS: best source selector
- RF: radio-frequency
- IF: intermediate frequency
- TMoIP: telemetry over IP
- SNR: signal-to-noise ratio

- PCM: pulse coded modulation
- MRC: maximum ratio combining
- ADC: analog to digital converter
- DAC: digital to analog converter

A modified OQPSK detection for MIL-STD SOQPSK in the satellite communication

Ding Xingwen, Song Jianyong, Chen Ming, Lu Manhong
Beijing Research Institute of Telemetry, Beijing, China

Abstract:

Military-standard (MIL-STD) shaped-offset quadrature phase-shift keying (SOQPSK) is a highly bandwidth-efficient constant-envelope modulation so that it has been applied in the satellite communication widely. We develop a simple detection of MIL-STD SOQPSK which is based on a modified OQPSK detection. The simple detection has the advantages of low complexity and good performance. And it's also suitable for other varieties of SOQPSK and FQPSK.

Key words: MIL-STD SOQPSK, Precoder, Modified OQPSK Detection, Detection Efficiency.

Introduction

In the recent years, many commercial companies have come up with ambitious commercial satellite launch plans[1][2]. The detection efficiency of satellite communication modulation has become increasingly important.

Dapper and Hill [3] described a form of continuous phase modulation (CPM) known as shaped BPSK (SBPSK) in the early 1980s. This modulation evolved into the constrained, ternary, full-response CPM using a rectangular frequency pulse that forms the basis for the MIL-STD 188-181 UHF Satcom standard. This modulation is also known as "Shaped Offset QPSK" (MIL-STD SOQPSK or SOQPSK-MIL) since it looks like an offset QPSK with smoothed phase transitions. An even more bandwidth efficient version of SOQPSK, called SOQPSK-TG, was adopted as an interoperable alternative to FQPSK in the IRIG 106 standard for aeronautical telemetry [4]. The family of SOQPSK waveforms, as described by Hill [3], are constant envelope signals with excellent spectral containment and detection efficiency. Furthermore, they can be detected using a standard OQPSK receiver. Performance results from Hill [5] indicate that a penalty of about 1 dB is incurred with MIL-STD SOQPSK, if a suboptimum OQPSK detector is used.

The objective of this paper is to investigate a modified OQPSK detection for MIL-STD SOQPSK to improve detection efficiency. The remainder of the paper includes a brief review of SOQPSK modulation characteristics, an introduction of precoder for SOQPSK, a comparison between the standard OQPSK detector and the modified OQPSK detector with simulation results, and the conclusion.

Characteristics of SOQPSK Modulation

The SOQPSK signal can be defined as a CPM signal[6]

$$s(t; \mathbf{a}) = \exp \{ j\phi(t; \mathbf{a}) \} \quad (1)$$

where the phase is a pulse train of the form

$$\phi(t; \mathbf{a}) = 2\pi h \sum_i \alpha_i q(t - iT) \quad (2)$$

and α_i is an M -ary symbol, T is the duration of each α_i , and h is the digital *modulation index*. The *phase pulse* $q(t)$ is usually thought of as the time-integral of a *frequency pulse* $g(t)$ with area $1/2$ and duration LT .

$$q(t) = \int_0^t g(\tau) d\tau \quad (3)$$

$$\int_0^{LT} g(\tau) d\tau = q(LT) = 1/2 \quad (4)$$

For SOQPSK, α_i is drawn from a *ternary alphabet*, i.e. $\alpha_i \in \{-1, 0, 1\}$, where $M = 3$. The *modulation index* is $h = 1/2$. The SOQPSK variants differ by their respective frequency pulses. Fig. 1 gives two typical examples: MIL-STD SOQPSK and SOQPSK-TG.

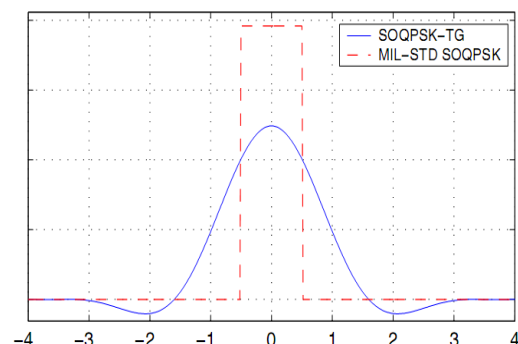


Fig. 1. The frequency pulses for SOQPSK-TG and MIL-STD SOQPSK.

As shown in Fig. 1, MIL-STD SOQPSK is full-response ($L = 1$) with a rectangular-shaped frequency pulse $g_{MIL}(t)$:

$$g_{ML}(t) = \begin{cases} \frac{1}{2T}, & 0 \leq t < T \\ 0, & \text{others} \end{cases} \quad (5)$$

SOQPSK-TG is partial-response ($L = 8$) with a frequency impulse shaping filter function $g_{TG}(t)$:

$$g_{TG}(t) = n(t)w(t) \quad (6)$$

Where[4]

$$n(t) = \begin{bmatrix} \frac{A \cos \pi \theta_1(t)}{1 - 4\theta_1^2(t)} \\ \frac{\sin \theta_2(t)}{\theta_2(t)} \end{bmatrix} \quad (7)$$

$$\theta_1(t) = \frac{\rho B t}{2T} \quad (8)$$

$$\theta_2(t) = \frac{\pi B t}{2T} \quad (9)$$

$$w(t) = \begin{cases} 1, & \left| \frac{t}{2T} \right| \leq T_1 \\ \frac{1}{2} \left[1 + \cos \left(\frac{\pi \left(\left| \frac{t}{2T} \right| - T_1 \right)}{T_2} \right) \right], & T_1 < \left| \frac{t}{2T} \right| \leq T_1 + T_2 \\ 0, & \left| \frac{t}{2T} \right| > T_1 + T_2 \end{cases} \quad (10)$$

The function $n(t)$ is a modified spectral raised cosine filter of amplitude A , rolloff factor ρ , and an additional time scaling factor B . The function $w(t)$ is a time domain windowing function that limits the duration of $g_{TG}(t)$. The amplitude scaling factor A is used to normalize the pulse shape such that the phase shift induced by a single frequency pulse is $\pi/2$ radians, as

$$\int_{-2(T_1+T_2)T}^{2(T_1+T_2)T} g(t) dt = \frac{\pi}{2} \quad (11)$$

For SOQPSK-TG, other parameters are $\rho = 0.7, B = 1.25, T_1 = 1.5, T_2 = 0.5$.

Using Hill's article [5] for reference to a visual revelation, the top trace in Fig. 2 shows that, for unshaped OQPSK, the frequency pulse is simply a delta function, $g(t) = (1/2)\delta(t)$. In each bit period, the frequency pulse is either present or absent. If present, the phase will shift by $\pi/2$ radians, but it can only go in the "allowed" direction for that bit period. Because of the offset between the I and Q channels, the allowed direction will depend on the current state, such that the signal will change in I value, or Q value, but never both at the same time.

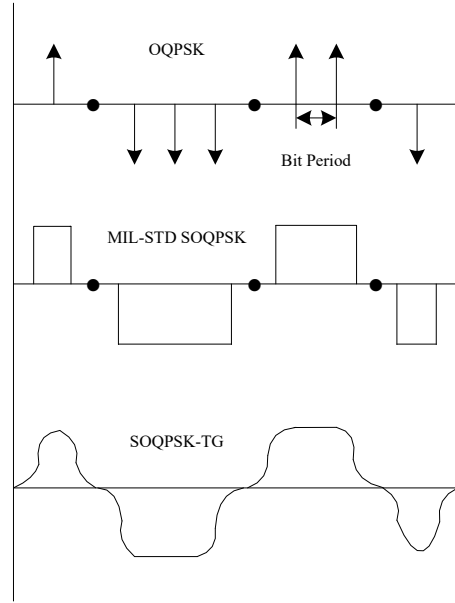


Fig. 2. Frequency pulses for Offset QPSK variants.

MIL-STD SOQPSK is depicted by the middle trace in Fig. 2. Again, the area of the frequency pulse is exactly $\pi/2$ radians, but the shape is rectangular, with a duration of one bit period. This has the effect of shifting the phase of the carrier by exactly one-quarter rotation over a span of one bit. At any instant in time, the phase is either stationary, or is moving at a constant rate of one-quarter of the bit rate.

The bottom trace in Fig. 2 represents the frequency pulse of SOQPSK-TG, which will also shift the phase of the signal by $\pi/2$ radians in one bit period. It is important to note that all of these waveforms are perfectly constant envelope; only the phase trajectory differs from one variant to the next. It is also significant that all of them can be demodulated with a conventional OQPSK detection.

Fig. 3 shows the power spectral density of MIL-STD SOQPSK and SOQPSK-TG. The primary difference between them is that SOQPSK-TG improves its sidelobes more effectively, which is achieved by partial-response characteristic at the expense of higher complexity. To emphasize the highly bandwidth efficiency of SOQPSK, unfiltered BPSK and OQPSK are also shown for reference.

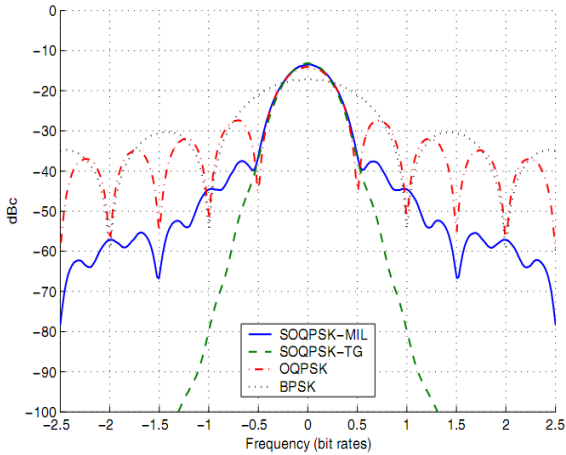


Fig. 3. Power spectral density of MIL-STD SOQPSK and SOQPSK-TG.

In this paper we concentrate on MIL-STD SOQPSK.

Precoder for SOQPSK

The characteristic that sets SOQPSK apart from ordinary CPM is that the ternary data is the output of a precoder, as shown in Fig. 4.

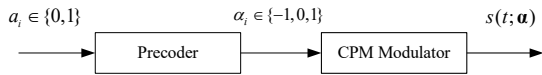


Fig. 4. Signal model for SOQPSK.

The precoder converts the binary data $a_i \in \{0,1\}$ into ternary data $\alpha_i \in \{-1,0,1\}$ according to the mapping [7]

$$\alpha_i = (-1)^{i+1} d_{i-1} \left(\frac{d_i - d_{i-2}}{2} \right) = (-1)^{i+1} (2a_{i-1} - 1)(a_i - a_{i-2}) \tag{12}$$

Where $d_i = 2a_i - 1 \in \{+1, -1\}$ and $a_i \in \{0,1\}$.

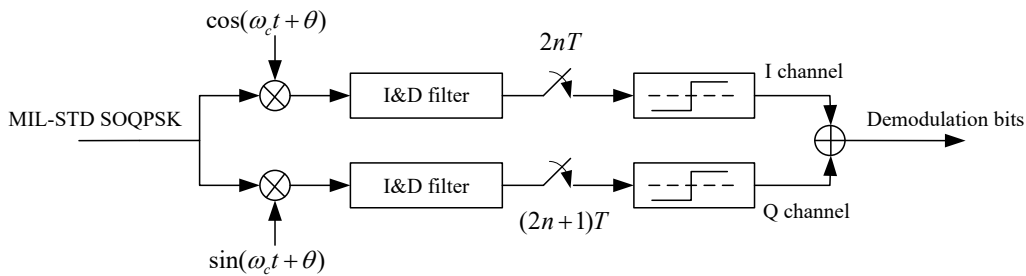


Fig. 5. Block diagram of a standard OQPSK detector.

To improve the detection efficiency, a modified OQPSK detector for MIL-STD SOQPSK is investigated, as shown in Fig. 6. The only difference between two detectors is the detection filter before data judgement. For standard OQPSK detector, the detection filter is just an

Therefore, SOQPSK is viewed as a *constrained* ternary CPM. The mapping in Equation (12) imposes three important constraints on the ternary data [8]

- 1) While α_i is viewed as being *ternary*, in any given symbol interval α_i is actually drawn from one of two *binary* alphabets: $\{0, 1\}$ or $\{0, -1\}$.
- 2) When $\alpha_i = 0$, the binary alphabet for α_{i+1} switches from the one used for α_i , when $\alpha_i \neq 0$, the binary alphabet for α_{i+1} does not change.
- 3) A value of $\alpha_i = 1$ can not be followed by $\alpha_{i+1} = -1$, and vice versa.

The original motivation for SOQPSK is that Equation (12) leads to a simple symbol-by-symbol detection architecture [5]. Conceptually speaking, we can separate the input bits for even symbol times and odd symbol times into *inphase* and *quadrature* bit streams, as in

$$a_{I,n} = a_{2n}, \quad a_{Q,n} = a_{2n+1} \tag{13}$$

The role of the precoder is to ensure that the phase state of the CPM modulator is oriented correctly so that the *inphase* and *quadrature* bits can be recovered using a standard OQPSK detector.

A Modified OQPSK Detector for MIL-STD SOQPSK

As mentioned above, MIL-STD SOQPSK can be demodulated using a standard OQPSK detector [3][5], as shown in Fig. 5. The detector is simple and easy for hardware implementation, whereas with a detection penalty of about 1 dB.

integrate and dump (I&D) filter. For modified OQPSK detector, the detection filter is a modified filter, which can match MIL-STD SOQPSK better, so as to improve the bit error rate performance with only little increased

complexity. The wave shape of the modified filter is shown in Fig. 7.

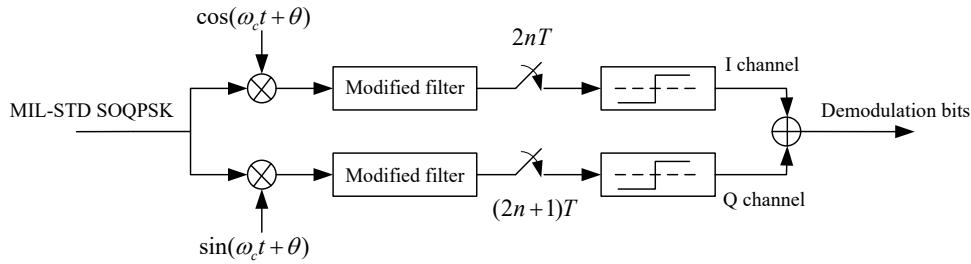


Fig. 6. Block diagram of a modified OQPSK detector.

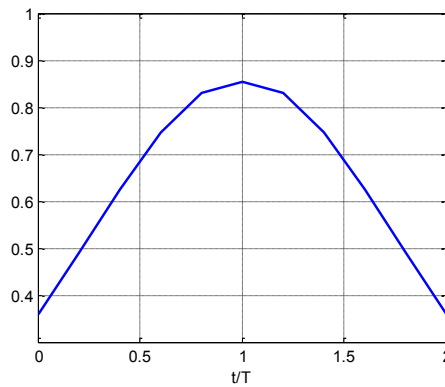


Fig. 7. Wave shape of the modified filter.

Simulation Results

The performances of MIL-STD SOQPSK with both detectors are simulated by MATLAB Software. The results are shown in Fig. 8, along with the theoretical curves of OQPSK and MIL-STD SOQPSK. A simple comparison between two detectors is also given in Tab. 1.

Tab. 1: Comparison of two detectors

Modulation Type	Eb/No (dB) required for BER = 10 ⁻⁵		
	Standard OQPSK Detector	Modified OQPSK Detector	Theoretical Optimum Detector
MIL-STD SOQPSK	11.01	10.54	9.90

Compared to the standard OQPSK detector with I&D filter, the modified detector with a better matched filter has an improvement of 0.47 dB at BER = 10⁻⁵ for MIL-STD SOQPSK, although is still worse than the theoretical optimum detector about 0.64 dB. From Fig. 8, we also see that at BER = 10⁻⁵, MIL-STD SOQPSK is about 0.3 dB worse than OQPSK, both in theory. But MIL-STD SOQPSK has the higher bandwidth efficiency than OQPSK, as shown in Fig. 3.

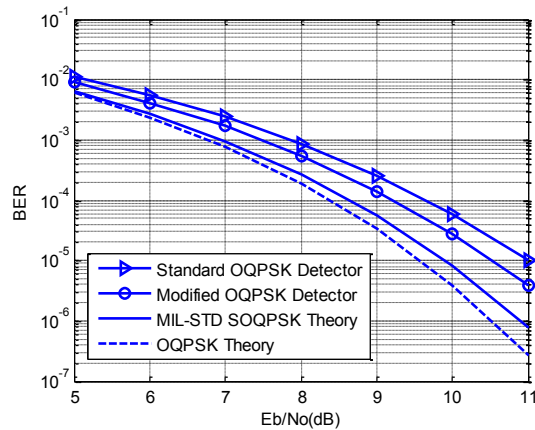


Fig. 8. Performances of MIL-STD SOQPSK with both detectors.

Conclusion

We have investigated a modified OQPSK detector for MIL-STD SOQPSK to improve detection efficiency. Compared to the standard OQPSK detector with I&D filter, the new modified OQPSK detector with a better matched filter has an improvement of 0.47 dB at BER = 10⁻⁵ for MIL-STD SOQPSK, with only little increased complexity. And this modified OQPSK detector is also suitable for other varieties of SOQPSK and FQPSK[9].

M. J. Dapper and T. J. Hill, SBPSK: A robust bandwidth-efficient modulation for hard-limited channels, Proceedings of IEEE MILCOM, October 1984; doi:10.1109/MILCOM.1984.4794893

References

- [1] Zhang Xianhui and Shen Guosong, Application of SQPSK Modulation in TDRSS, *Journal of Telemetry, Tracking and Command*, 2007, 28(z1):26-29; doi:10.3969/j.issn.2095-1000.2007.z1.005.
- [2] Yan Jianhua, Li Xiaomei and Zhang Tao, Research on ETSI TCR standards and TT&C system of commercial satellite, *Journal of Telemetry, Tracking and Command*, 2020, 6(41).
- [3] M. J. Dapper and T. J. Hill, SBPSK: A robust bandwidth-efficient modulation for hard-limited channels, Proceedings of IEEE MILCOM, October 1984; doi:10.1109/MILCOM.1984.4794893.
- [4] Range Commanders Council Telemetry Group, Range Commanders Council, White Sands Missile Range, New Mexico. IRIG Standard 106-23: Telemetry Standards, 2023. [Online]. Available: <http://jcs.mil/RCC/manuals/106-23>.
- [5] T. Hill, An Enhanced, Constant Envelope, Interoperable Shaped Offset QPSK (SOQPSK) Waveform for Improved Spectral Efficiency, *Proceedings of the International Telemetry Conference*, San Diego, CA, October 2000.
- [6] J. B. Anderson, T. Aulin, C-E. Sundberg. Digital Phase Modulation, *Plenum Press*, New York, 1986.
- [7] M. K. Simon, Bandwidth-Efficient Digital Modulation with Application to Deep-Space Communication, *New York: John Wiley & Sons, Inc.*, January 2003. Also published as part of the JPL Deep Space Communications and Navigation (DESCANSO) Monograph Series, JPL Publication 00-17, Jet Propulsion Laboratory, Pasadena, California, June 2001.
- [8] M. Simon and L. Li. A cross-correlated trellis-coded quadrature modulation representation of MIL-STD shaped offset quadrature phase-shift keying. *IPN (Interplan. Network) Progress Report 42-154*, August 2003.
- [9] Ding Xingwen, Song Jianyong, Chen Ming and Lu Manhong, A modified OQPSK detection for SOQPSK-TG in aeronautical telemetry. *Proceedings of the International Telemetry Conference*, San Diego, CA, October 2014.

AESA.....	B7.5	helicopter blade dynamics	A5.2	Security of data	A8.1
AI: Artificial Intelligence	A6.1, A9.1	helicopter rotor blade	A5.2	Sensor	A6.2
Airborne Mobile Telemetry	A4.1	High-voltage safety	B1.1	sensor telemetry	B5.2
anomaly detection	A2.2	HIL	B6.1	Shielding Concept.....	B1.4
Antennas	B7.3, B7.4	HTB	B6.1	Signal Processing	B2.2
Applications.....	A8.1	Huygens-principle	B6.3	Simulation	B6.1
autonomous vehicles	A3.2	hydrogen.....	B4.2	SNMP	A10.2
Bandwidth	A9.1	hydrogen sensor.....	B4.2	Store Separation Flight Test	A9.2
battery testing.....	B1.1	Icing Probes.....	A1.4	strain gauge measurement	B1.1
BDA.....	A8.3	IMU	B5.2	SWaP Optimized.....	A8.2
beamforming shaping.....	B7.5	increased efficiency.....	A3.2	Telemetry.....	B5.1, B7.3, B7.6, A9.1
Bidirectional.....	B7.3, B7.4	INS	A3.1	telemetry ground antenna	B7.5
Big Data	B2.3	Instrumentation.....	A1.4, A10.1	Telemetry spectrum	A4.1
catalytic combustion	B4.2	IP protection class	B4.1	temperature measurement.....	B1.1
Chirp-Z Transform.....	B2.2	IRIG B.....	B5.2	TENA	A8.3
common operational picture	A6.2	IRIG106	B7.6	Testing.....	A10.1, B6.1
Configuration Management	B2.3	JMETC.....	A8.3	Thermal Modelling	B1.2
connected environment	A6.2	Kubernetes	A8.4	tiltrotor.....	B5.1
Container Cloud	A8.4	leak test	B4.1	time series analysis.....	A2.2
CWT: Continuous Wavelet Transform	A6.1	LEO constellations.....	A2.3	time synchronous data acquisition	B5.2
Data Acquisition	B6.1, A8.1, A8.2	lidar.....	A1.1	Tornado.....	B1.4
data fusion.....	A6.2	LIDAR.....	A10.1	torsion	A1.1
Data Management.....	A8.1	links and networks	A8.1	tracking	B7.5
Data Management Applications	B2.1	LoRa	A2.1	TSPI.....	A3.1
Data Management Standards ...	A8.1	Machine learning	A2.2, A6.2	TT&C Software	A8.4
Decentralized Systems.....	A2.1	MBSE	B3.2	type test	B4.1
decision tree.....	A6.1	MEMS.....	B4.2	Vibration Testing.....	B2.2
Deep Q-network	A2.3	MIL-STD SOQPSK	B7.7	Video.....	A1.4
Detection Efficiency.....	B7.7	ML/DL.....	B2.3	Virtualization	A8.4
Digital Telemetry	B1.4	Modified OQPSK Detection	B7.7	wavelets.....	A6.1
Digital Twin.....	B2.3	Multi-channel Recording.....	B7.6	Weather	A1.4
Distributed Networks	A8.2	multi-domain	A8.3	Wind.....	A10.1
Elasticsearch.....	A6.1	multi-site	A8.3	wind tunnel model	B5.1
electrical strain gauges.....	A5.2	near field telemetry	B5.2	wing deformations.....	A1.1
EMC	B1.4, B6.3	Near-Field Scanning.....	B6.3	Wireless Sensor Networks	A2.1
EMI.....	B6.3	Networked telemetry system	A2.3	zero-paper.....	B3.2
Energy Efficiency	A2.1	Networks & Architecture	A8.1		
Ethernet.....	B1.4	Object Tracking	A9.2		
Fast Fourier Transform.....	B2.2	on board processing	A2.2, A9.1		
FCV	B4.2	optical fibre sensors.....	A5.1, A5.2		
Fiber Bragg Grating.....	A5.1, A5.2	pattern recognition	A6.1		
Field Simulations.....	B6.3	Photogrammetry.....	A9.2		
flexion.....	A1.1	Power Over Ethernet (PoE).....	A8.2		
Flight Test	B7.6	Precoder.....	B7.7		
Flight Test Campaign	A1.4	prototype.....	B3.2		
Flight Test Instrumentation.....	B2.2	PTP V2	B5.2		
Flight Test Network Management	A10.2	R2: correlation coefficient	A6.1		
Frequency spectrum encroachment	A4.1	Real-Time Data Acquisition	B2.2		
FTI.....	B2.3, B3.2	Receivers.....	B7.3, B7.4		
FTI monitoring	A10.2	Recorder & Reproducer.....	B7.6		
FTI Refurbishment	B1.4	Reduced Wiring.....	A8.2		
GNSS.....	A3.1	Reinforcement Learning	A2.1		
GPS.....	A3.1	Resource Reorganization	A8.4		
GPS/GNSS interference monitoring	A3.2	Resources	A2.3		
Ground Stations	B7.4	RF Design.....	B7.3, B7.4		
Hardware Architecture.....	A9.2	rotating.....	B5.1		
helicopter applications.....	B5.2	Rotorcraft.....	A10.1		
		Rough Order Model (ROM)	B1.2		
		routine test.....	B4.1		
		Satellite telemetry data	A2.3		